CIICT 2009

Proceedings of the China-Ireland Information and Communications Technologies Conference

National University of Ireland Maynooth
19th-21st August 2009

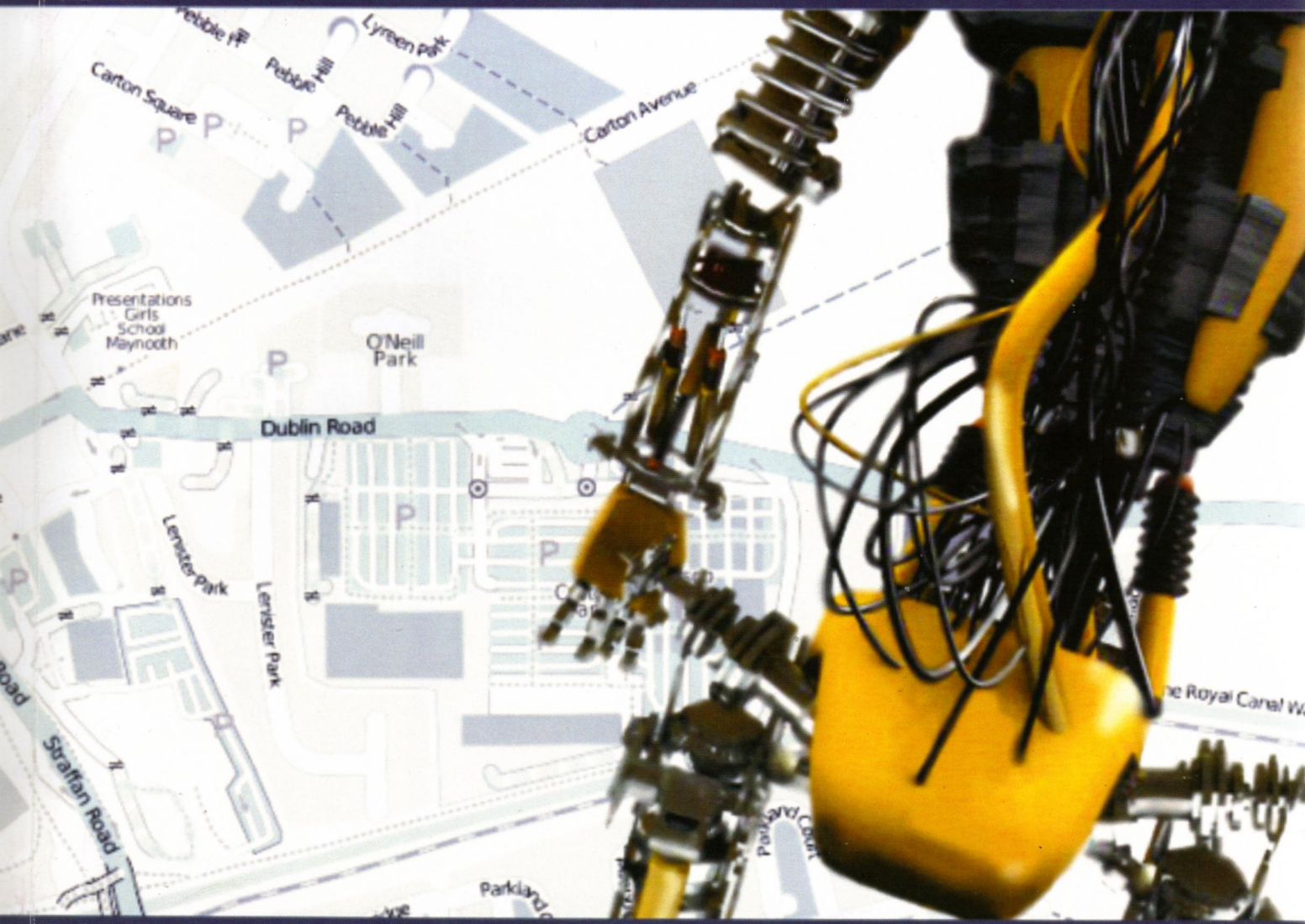

Edited by Adam C. Winstanley

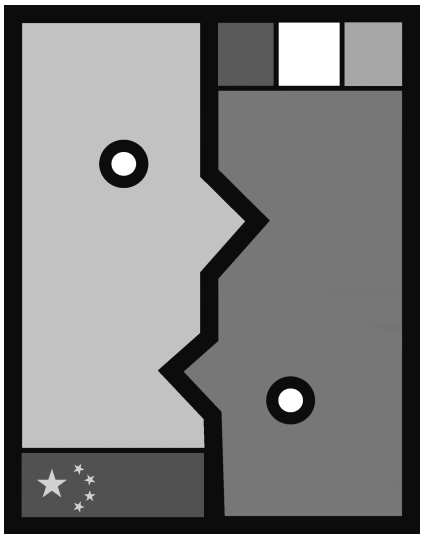

CIICT 2009

Proceedings of the China-Ireland Information and Communications Technologies Conference

National University of Ireland Maynooth
19th – 21st August 2009

Edited by Adam C. Winstanley

Adam C. Winstanley (ed.)

CIICT 2009

China-Ireland Information and Communications Technologies Conference

19th – 21st August 2009

Department of Computer Science
National University of Ireland Maynooth
County Kildare, Ireland

ISBN 978 0 901519 67 2

Published August 2009, NUI Maynooth, Ireland

Additional copies may be ordered from: CIICT 2009, Department of Computer science, NUI Maynooth, county Kildare, Ireland.
ciict@cs.nuim.ie

Cover design by Justyna Ciepluch.

Printed by Cahill Printers Limited, Clonshaugh, Dublin 17.

Foreword

On behalf of the organising committee I would like to extend my warmest welcome to all speakers and attendees at the 2009 *China-Ireland Information and Communications Technologies* conference (CIICT) being hosted by the Department of Computer Science, NUI Maynooth in association with several other departments and research institutes on campus including the Department of Electronic Engineering, the National Centre for Geocomputation (NCG) and the Institute of Microelectronics and Wireless Systems (IMWS). The NCG and IMWS were founded as the result of grants from Science Foundation Ireland recognising the importance of these areas in modern science and engineering. Many thanks are also due to Science Foundation Ireland for awarding a generous grant to support a keynote speaker and enabling us to offer 20 bursaries to assist student participation at CIICT 2009.

In 2009, the China-Ireland Information and Communications Technologies conference again brings together theoreticians, practitioners and academics from the numerous related disciplines that are painted within the broad brush of ICT. This is the fourth conference in the series following events held in Hangzhou Dianzi University (2006), Dublin City University (2007) and Beijing University of Posts and Telecommunications (2008).

The initial call for papers for CIICT 2009 was issued in March 2009. Contributions were sought from researchers in China and Ireland (and also worldwide) on all aspects of Information and Communications Technology. The conference organisers received 65 papers from both China and Ireland with several having authors from both countries. Each paper was subject to a review by at least three members of the program committee. 31 papers were accepted for oral presentation and publication as full papers in the proceedings. In April 2009, a further call was made for short papers describing work in progress and preliminary results. These were each reviewed by two programme committee members and this resulted in a further 22 papers for short presentation at the conference.

I wish to thank the members of the programme committee without whose comments and prompt reviews a conference of this type could not be successful. I am also grateful to the members of the local organising committee, the Maynooth Conference and Accommodation Centre and the support staff of NUI Maynooth and St. Patrick's College, Maynooth.

CIICT has prospered due to the generosity of sponsors who every year support the conference and the many associated prizes, competitions, workshops and social events. This year is no exception and we wish to thank our current sponsors for their generosity: Science Foundation Ireland, Failte Ireland, Microsoft Ireland and the Maynooth Campus and Conference Centre.

So welcome CIICT delegates to Maynooth. We hope the conference is beneficial and you leave after having a useful and enjoyable experience.

Adam Winstanley
Chair CIICT 2009

Committees

Conference Chair
Adam Winstanley, CS NUIM

Conference Co-Chairs
Ronan Farrell, EE NUIM
Lei Yan, Peking University

Proceedings sub-editor
Jianghua Zheng

Local Organising Committee
Yanpeng Cao
Blaceq Ciepluch
Padraig Corcoran
Ricky Jacob
Laura Keyes
Paul Lewis
Eoin McAiodh
Peter Mooney
Zheng Pan
Bashir Shalaik
Jianghua Zheng

CIICT Steering Committee
Charles McCorkell (Chair), Dublin City University
Thomas J. Brazil, University College Dublin
Gabriel M. Crean, University College Cork
Stephen Holland, Synopsys
Chris Horn, Iona Technologies PLC
Fiona O'Brien, Lenovo International BV
Donal O'Mahony, Trinity College Dublin
Lingling Sun, Hangzhou Dianzi University
Roger W. Whatmore, Tyndall National Institute
Yinghai Zhang, Beijing University of Posts and Telecommunications

CIICT 2009 Programme Committee
Rob Brennan, Trinity College Dublin
Donggang Cao, Peking University
Gang Chen, Wuhan University
Jiming Chen, Zhejiang University
Padraig Corcoran, NUI Maynooth
Ronan Farrell, NUI Maynooth
Amy Fitzgerald, NUI Maynooth
Ivan Ganchev, University of Limerick
David Gray, Dublin City University
Boran Guan, Hangzhou Dianzi University
Ron Healy, NUI Maynooth
Matthieu Hodgkinson, NUI Maynooth
Peter Hung, NUI Maynooth
Hai Jin, Huazhong University of Science & Technology
Yan Ma, Beijing University of Posts and Telecommunications
Jonathan Maycock, NUI Maynooth & Bielefeld University
Conor McArdle, Dublin City University
John McDonald, NUI Maynooth
Seamus McLoone, National University of Ireland, Maynooth
Derek Molloy, Dublin City University
Rosemary Monahan, NUI Maynooth
Aidan Mooney, NUI Maynooth
Peter Mooney, NUI Maynooth
Diarmuid O'Donoghue, NUI Maynooth
Aidan O'Dwyer, Dublin Institute of Technology
Derek C W Pao, City University of Hong Kong
Philip Perry, QoSTech Ltd, Dublin
James Power, NUI Maynooth
Robert Sadleir, Dublin City University
Ronan Scaife, Dublin City University
Bashir Shalaik, NUI Maynooth
Xiaojun Wang, Dublin City University
Chuangbai Xiao, Beijing University of Technology
Hongwen Yang, Beijing University of Posts and Telecommunications
Yonglin Yu, Wuan National Laboratory for Optoelectronics
Jianghua Zheng, NUI Maynooth
Sheng Zheng, China Three Gorges University
Anding Zhu, University College Dublin

For further information about this and future CIICT conferences see:

`www.ciict.org`
`ciict.cs.nuim.ie`

TABLE OF CONTENTS

Section 1A

ANTENNAS AND CIRCUITS 1

DEMONSTRATOR PLATFORM FOR ANTENNA ARRAY CALIBRATION

Gerry Corley, Justine Mc Cormack, Ronan Farrell
Centre for Telecommunications Value-Chain Research (CTVR),
Institute of Microelectronics and Wireless Systems,
National University of Ireland Maynooth,
Ireland.

Abstract-**This paper presents a hardware platform for antenna array calibration research in tower top electronics. The platform has eight phase and amplitude controlled transmit channels and a novel antenna coupler array structure which provides non-radiative calibration capability. The phase and amplitude of each channel can be varied between 0 and 360° and over 25dB respectively under full software control. The platform has been used to test and develop array calibration routines which achieve amplitude variances of less than 1dB and phase variances of less than 5° measured between eight channels at the antenna connections.**

I. INTRODUCTION

In order to achieve accurate beamforming it is essential that the elements of an array are amplitude and phase matched or that the differences are known, in addition these relationships must be maintained in demanding environmental conditions such as a tower top over long periods of time. Traditionally this has been achieved through the use of tight tolerance components, phase matched cables and the use of factory measured calibration tables, however this is an expensive approach and offers little adaptation to the ambient environmental conditions.

Amplitude and phase errors between array elements distort the antenna radiation pattern in terms of beam pointing direction, sidelobe level, half power beamwidth and null depth [1] . The extent of the distortion has been well covered in antenna array literature [2], [3], [4].

There are several approaches to array calibration including tight tolerance design with factory determined calibration tables, calibration using internal and external radiating sources and non-radiative dynamic calibration [5]. The third approach was chosen as it does not require external radiators, high tolerance cables and components or extensive array modelling. In addition dynamic calibration allows continuous monitoring of the array status for network management purposes; this is a critical requirement for all cellular and wireless network operators.

Desirable features of any research platform are: that it be simple to use, that the controlling software be easy to modify and that the hardware be easily expandable, for example, through the addition of more array elements. In hardware, this was achieved through the use of off-the-shelf phase and amplitude adjustment components configured in a modular easily expandable fashion. As regards software it was decided to use Labview to control the system, implement the calibration algorithms and collect measurements. Labview is a graphical programming language aimed and test and control applications, it is easy to implement graphical user interfaces and can call both C and Matlab functions [6].

II. PLATFORM ARCHITECTURE

Effective non-radiative array calibration relies on the ability to measure the transmit or receive signals as close to their antennas as possible and to compare the measured signals with reference signals to ascertain the phase and amplitude relationship between the elements. The reference signal(s) can be the actual transmit signal in the case of live calibration or a pilot signal in the case of off-line calibration. A block diagram of a distributed transceiver array with integrated calibration/reference blocks is shown in Figure 1. This system consists of interconnected transceivers and calibration blocks where the calibration blocks provide at least one and in most cases multiple calibration paths to each transceiver, in addition every transceiver calibration path is linked to every other path through the tessellated transceiver and calibration block structure. This multiplicity and interdependence of calibration paths for each transceiver facilitates the development of powerful calibration algorithms [7].

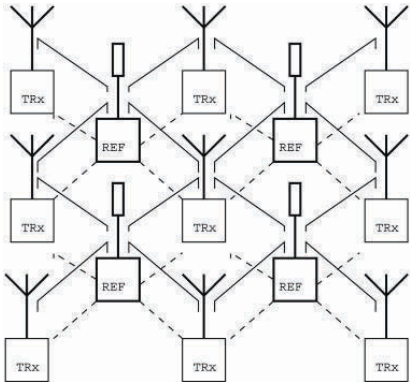

Figure 1: Distributed Transceiver System, with built in Calibration Infrastructure

A block diagram of the platform is depicted in Figure 2. The heart of the demonstrator is a 2x4 antenna coupler array; this novel design consists of an array of couplers where each coupler output provides coupling from the four surrounding transceiver through paths; a more detailed description of this coupler array and its operation is provided in [8] and [10]. In the case of transmission, the coupler outputs provide attenuated versions of the forward TX signals present at the through path inputs. The loss and phase shift between the through path input

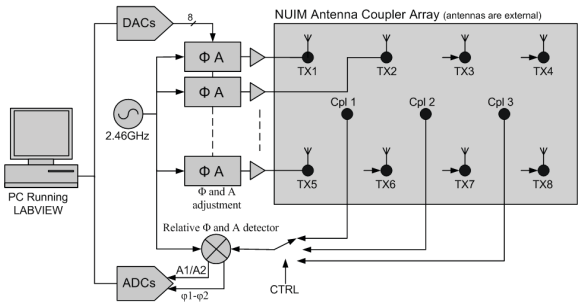

Figure 2: Block diagram of calibration and beamforming platform

and output is small, less than 1dB and the phase variation across all through paths is less than 2°. The coupler array variations can be included as a calibration offset table in the calibration algorithms.

The coupler outputs are connected through an RF switch to the vector voltmeter module which compares the coupled signal with a reference signal and produces DC outputs corresponding to the phase and amplitude difference between its inputs. The detector module is comprised of two Analog Devices AD8302 RF Gain and Phase Detector IC's configured to give I and Q outputs (cos φ & sin φ), from which it possible to generate a linear monotonic output for all angles between 0 and 360°.

$$I = A.\cos\varphi$$
$$Q = A.\sin\varphi$$

$$\varphi = \tan^{-1}(Q/I) \qquad (1)$$
$$\varphi` = \varphi \quad \text{for } I > 0,\ Q > 0 \qquad (1.1)$$
$$\varphi` = \varphi + 180° \quad \text{for } I < 0,\ Q > 0 \qquad (1.2)$$
$$\varphi` = \varphi + 180° \quad \text{for } I < 0,\ Q < 0 \qquad (1.3)$$
$$\varphi` = \varphi + 360° \quad \text{for } I > 0,\ Q < 0 \qquad (1.4)$$

The phase shift is described by equation (1) however this produces discontinuities at 90° and 270° so the response is modified according to equations (1.1 - 1.4). As regards relative amplitude, the AD8302 produces a linear output voltage for amplitude difference from -60dBm to 0dBm.

The phase and amplitude adjustment modules, one for each array element, allow the phase and amplitude of the RF signal to be varied from 0 to 398° and -7 to -32dB with respect to (wrt) the input by applying DC voltages to the phase and amplitude control inputs. The modules comprise continuously variable voltage controlled phase shifters (Mini-circuits JSPHS-2484) and a variable attenuator (Mini-circuits RVA-3000). These components are mounted on a printed circuit board with some control voltage level adjustment circuitry and the ensemble placed in a shielding can to minimise electromagnetic interference between array channels. Figure 3 shows a photograph of the phase and amplitude adjustment modules. An external amplifier was added in series with the phase and amplitude adjustment modules to compensate for their insertion loss and to ensure that the signal fed back to the phase and amplitude detector module would be at the input mid-range point.

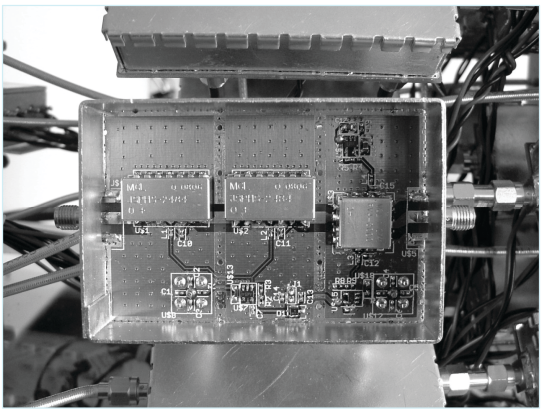

Figure 3: Phase and amplitude adjustment module

The control voltages for the phase and amplitude adjustment modules are generated by a National Instruments multi-channel 13 bit digital to analogue (DAC) card (NI PCI 6723); similarly the outputs of the vector voltmeter are digitised using a NI 16 bit analogue to digital (ADC) card (NI PCI 6251). The control of the ADC's and DAC's as well as the implementation of the control loop and the calibration algorithms were all done through Labview.

III. Platform Measurements

In the previous section the operation of the phase and amplitude adjustment and vector voltmeter modules was explained. In this section, measurements from these modules which are the core components of the platform are presented and discussed.

The phase and amplitude adjustment module was tested using a vector network analyser. By sweeping the module control voltages, the phase and amplitude of the RF signal at the output were plotted against the RF signal at the input, this is shown in figures 4 and 5. All RF

measurements were taken at 2.46GHz. The amplitude response is very non-linear but nonetheless monotonic. The phase response covers 398° and has some non-linearity at low voltages but again is monotonic. Non-linearity in the module's responses is not critical as phase and amplitude are set within a control loop which uses the vector voltmeter response to set reference points.

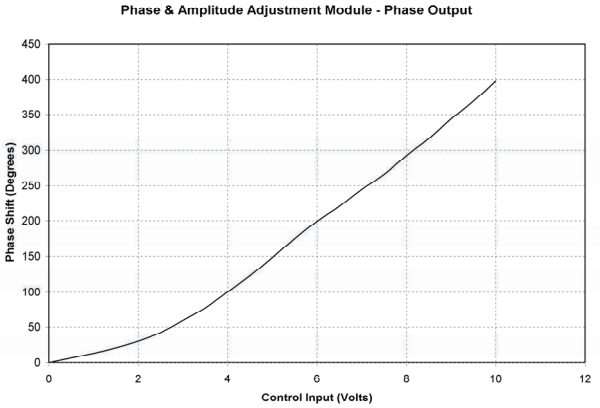

Figure 4: Phase and Amplitude Adjustment Module - Phase Output

The phase and amplitude adjustment module was reused to generate phase and amplitude differences between the RF inputs of the vector voltmeter module. The module DC output levels were recorded over the full platform phase and amplitude range between its RF inputs.

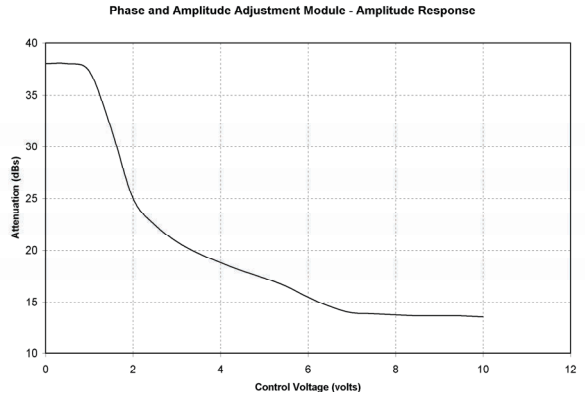

Figure 5: Phase and Amplitude Adjustment Module – Amplitude Output

Figures 6 shows the vector voltmeter phase output against phase input; the phase output is calculated from the I and Q outputs as described in the previous section. The response covers 360° before wrapping back to 0°, there is some non linearity but this could easily be adjusted for with a look up table. The relative amplitude plot in figure 7 shows a range of 25dBs for the platform; this is much greater than the expected amplitude mismatches in a beamformer.

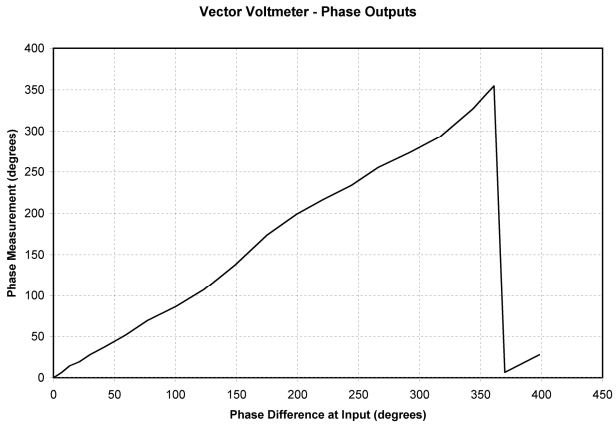

Figure 6: Vector Voltmeter - Phase Output

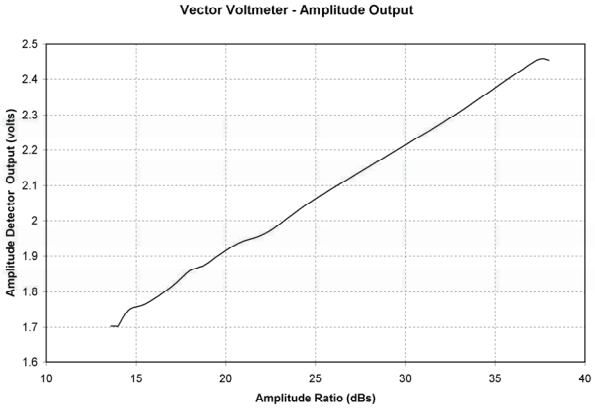

Figure 7: Vector Voltmeter - Amplitude Output

IV. Calibration Algorithm Demonstration

The initial application for the platform was to test calibration algorithms developed at the Institute. The calibration algorithms work by defining a single antenna element as a reference and calibrating all other antennas relative to that reference by following a particular route through the elements of the array. The choice of reference element and the path chosen determines the efficacy of the algorithm in terms of accuracy and speed. The results of testing on different algorithms have been presented in [9]. In this paper the measurements from testing one of these algorithms will be presented as an illustration of the capabilities of the platform.

The dual path algorithm is a comparison based calibration algorithm. It selects a reference element in the left hand corner of the array and then performs comparisons with the elements coupled to the reference antenna element; it takes two paths of identical length to each element of the array from the reference antenna.

These two paths are averaged to reduce the effect of coupler errors.

Figure 8 shows a photograph of the calibration algorithm test set-up. The antenna connections on the 2x4 coupler array were connected to the inputs of a high speed digital oscilloscope (Agilent Infinium 5483A DSO 2.5GHz); unused antenna connections were terminated with 50Ω loads. The oscilloscope offers resolutions of better than 1° in phase and better than 0.1dB in amplitude which is sufficient to verify the operation of the platform and algorithm.

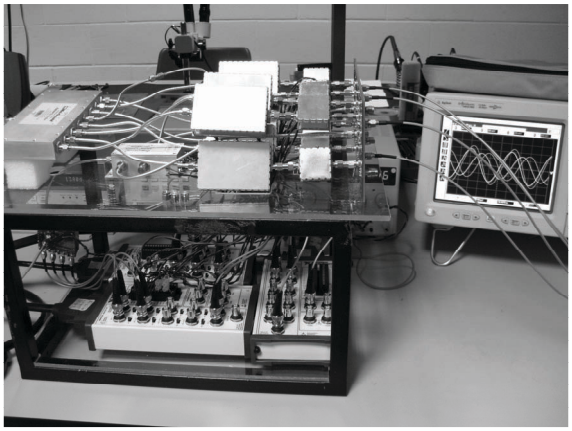

Figure 8: Calibration and beamforming platform with antennas replaced by a high speed digital oscilloscope

To represent an uncalibrated system, each channel was set to a random phase shift and amplitude attenuation by applying control voltages to the phase and amplitude adjustment modules. An oscillogram of the random phase and amplitude relationships on four of the antenna connections is shown in Figure 9. The dual path algorithm was then run in Labview on the platform PC and the phase and amplitude relationships were measured on the oscilloscope; Figure 10 shows an oscillogram of the signals at the antenna connectors after calibration.

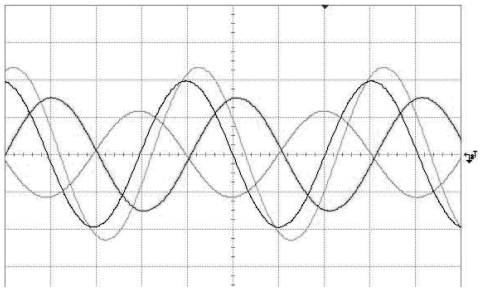

Figure 9: Oscillogram of uncalibrated output signals

From the oscillograms it is clear that after calibration there is no visible phase difference and a small visible amplitude difference between the channels. More precise measurements for each TX output of the array are presented in Table 1

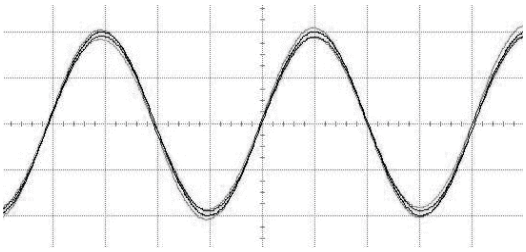

Figure 10: Oscillogram of antenna connections after calibration

Table 1: Transmit phase and amplitude measurements wrt TX1

	TX1	TX2	TX3	TX4	TX5	TX6	TX7	TX8
Phase wrt TX1 (°)	0	1.8	-2.2	-2.2	-1.6	0.18	0.4	-0.4
Amplitude wrt TX1 dB	0	0.11	-0.27	-0.03	-0.49	-0.56	-0.22	-0.3

The results table shows that the maximum phase difference from the reference element (TX1) was 2.2° and between elements was 4°. The maximum amplitude difference between the reference and the other elements was 0.56dB and between all elements was 0.67dB.

V. Conclusions

This paper presented a test platform for the exploration and development of tower top antenna array calibration algorithms and technology. The platform operates at 2.46GHz and uses off-the-shelf components in a modular easily expandable architecture. The software, Labview, allows easy configuration of the hardware and implementation of calibration algorithms. Platform measurements were presented which showed a phase and amplitude control range of 0 to 360° and 25dB respectively for each array output. Additionally a calibration routine was run on an array with antenna outputs preset to random amplitudes and phases, the routine succeeded in reducing the phase and amplitude difference between outputs to less than 1dB amplitude and 5° phase.

Acknowledgment

The authors would like to thank Science foundation Ireland for their generous funding of this project through the Centre for Telecommunications Value Chain Driven Research (CTVR).

REFERENCES

[1] J. K. Hsiao, "Design of error tolerance of a phased array," Electronics Letters, vol. 21, pp. 834-836, 1985

[2] N. Jablon, "Effect of element errors on half-power beamwidth of the Capon adaptive beamformer," Circuits and Systems, IEEE Transactions on, vol. 34, pp. 743-752, 1987

[3] R. Elliott, "Mechanical and electrical tolerances for two-dimensional scanning antenna arrays," Antennas and Propagation, IRE Transactions on, vol. 6, pp. 114-120, 1958

[4] K. Carver, W. Cooper, and W. Stutzman, "Beam-pointing errors of planar-phased arrays," Antennas and Propagation, IEEE Transactions on, vol. 21, pp. 199-202, 1973.

[5] J. McCormack, T. Cooper, and R. Farrell, "Tower-Top Antenna Array Calibration Scheme for Next Generation Networks," EURASIP Journal on Wireless Communications and Networking, vol. 2007, pp. 12, 2007

[6] Y. Huang, "Design of a Dynamic Beamforming Antenna for Wimax Radio Systems", Aerospace Conference 2008 IEEE, pp.1 – 6, 2008

[7] J. McCormack, T. Cooper, and R. Farrell, "A Multi-Path Algorithmic Approach to Phased Array Calibration," presented at Antennas and Propagation, 2007. EuCAP 2007. The Second European Conference on, 2007

[8] T. S. Cooper, G. Baldwin, and R. Farrell, "Six-port precision directional coupler," Electronics Letters, vol. 42, pp. 1232-1233, 2006.

[9] J. McCormack, G. Corley, and R. Farrell, "Experimental Results of Non-Radiative Calibration of a Tower Top Adaptive Array", 3rd European Conference on Antennas and Propagation, EuCAP 2009. *Awaiting publication.*

[10] T. S. Cooper, J. Mc Cormack, R. Farrell and G. Baldwin. "Towards Scalable, Automated Tower–Top Phased Array Calibration", Vehicular Technology Conference, Dublin, Ireland April 23 – 25, 2007

A Numerical Model to Estimate PIFA (Planar Invert F Antenna) Performance with Rotation Effect in Proximity to the Human Body

Z. Duan, D. Linton, S. Jeyakumar
The Institute of Electronics, Communications, and Information Technology (ECIT)
Queen's University Belfast, Queen's Road, Queen's Island, Belfast, UK, BT3 9DT
Fax: +44(0) 28 9097 1702; Tel: +44(0) 28 9097 1778
E-mail: zduan01@ecit.qub.ac.uk

Abstract

This paper investigates a typical PIFA performance in wearable applications. The antenna input impedance has close correlation with its positions which should include not only its distance to the body surface but also its rotation angles. The radiation efficiency also plays an important role in the overall antenna performance due to electromagnetic absorption by the human body in its near field range. A numerical model is first reported according to the simulation result as far as we know, so that it simplifies evaluation of PIFA performance when it is used in mobile phones or wireless sensor nodes.

1. Introduction

PIFA is the most popular antenna in personal wireless networks due to its low profile, low cost and good bandwidth. Any antenna design requires careful consideration regarding proximity coupling, particularly for a compact design with a limited volume. High antenna efficiency, enough bandwidth and good tolerance of human movement are several key factors to antenna engineers for optimum performance in conjunction with not only the RF circuit but also for the specific application environment [1][2].

Strong coupling occurs through the near field between the antenna and the human body in a wearable communication system [3]-[5].Any distortion, such as the body-antenna separation or antenna rotation, has considerable effect in the near field. In general, the distance between the antenna and the human body surface refers to the degree of coupling intensity, which may be applied for a fixed incident antenna position and orientation [6]-[12]. Considering the wave incidence at different angles, with various antenna orientations, the radiation performance will alter in terms of the maximum radiation direction, the antenna bandwidth and efficiency.

2. PIFA port impedance variations with distance and rotation angle

In this paper we investigate a 2.4 GHz PIFA antenna rotating along its center point as shown in Figure 1. A numerical electromagnetic phantom used in the simulation has a permittivity (ε_r) of 45, a loss tangent of 0.3, with dimensions of 150 × 150 × 20 mm. The size of this body model was found after comparing the simulation results in terms of antenna performance when a larger model was used. No significant differences were found. The angle is formed by the ground plane of the PIFA antenna and the top surface of the phantom as shown in Figure 2. In the initial simulation, the PIFA antenna is located parallel to the phantom but having a 1 mm separation. The PIFA antenna is then rotated along y axis while keeping the separation from the axis edge to the phantom surface given separation. The rotations angles (θ) are chosen depending on the given separation where the lowest edge can not touch the phantom surface as listed in Table 1. Simulations are employed to check port impedance, radiation pattern and antenna efficiency. However some larger separation and rotation angles could be verified, but this condition is not often met in a wearable scenario. Only a limited range is selected in this paper.

Table 1: The rotation angles at different separation

Separation	Rotation Angle		Separation	Rotation Angle
1 mm	-2^0, -1^0, 0^0, 1^0, 2^0		2 mm	-4^0, -2^0, 0^0, 2^0, 4^0

3 mm	-8^0, -6^0, -4^0, -2^0, 0^0, 2^0, 4^0, 6^0, 8^0		4 mm	-10^0, -8^0, -6^0, -4^0, -2^0, 0^0, 2^0, 4^0, 6^0, 8^0, 10^0
5 mm	-12^0, -10^0, -8^0, -6^0, -4^0, -2^0, 0, 2^0, 4^0, 6^0, 8^0, 10^0, 12^0		10 mm	-20^0, -16^0, -12^0, -8^0, -4^0, 0^0, 4^0, 8^0, 12^0, 16^0, 20^0
20 mm	-30^0, -25^0, -20^0, -15^0, -10^0, -5^0, 0^0, 5^0, 10^0, 15^0, 20^0, 25^0, 30^0			

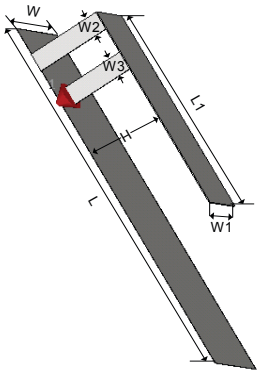

L—39.78 mm
W—9.17 mm
H—7.75 mm
L1—22.65 mm
W1—5.6 mm
W2—2mm
W3—2mm

Figure 1: The PIFA antenna in free space

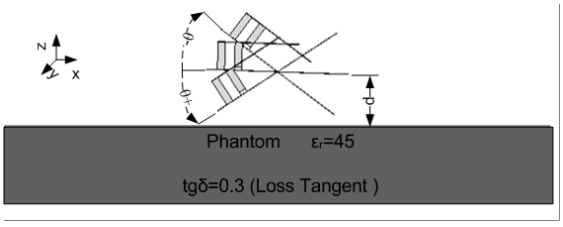

Figure 2: The PIFA rotating along the y axis (Clockwise rotation represents a negative angle and counterclockwise rotation represents a positive angle)

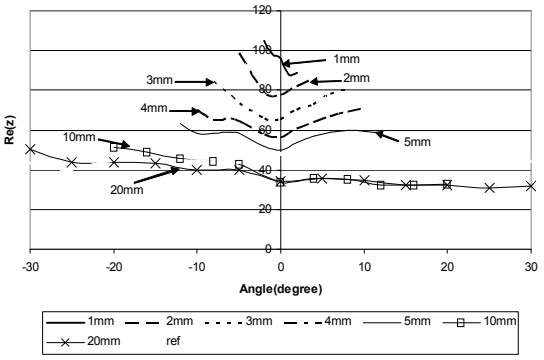

(a)

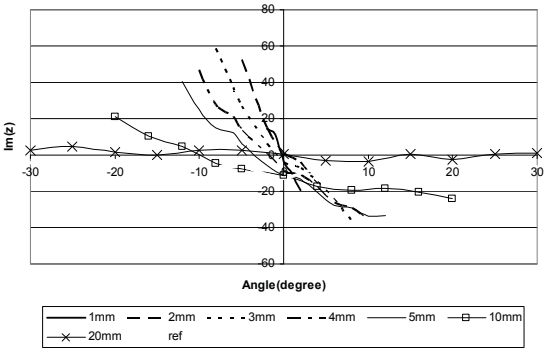

(b)

Figure 3: (a) The real part and (b) imaginary part of port impedance variations with separation and rotation angles at 2.44 GHz. The curves of *ref* represent the PIFA port impedance in free space, where the ripple is caused by simulation numerical errors

Port impedance is a parameter to demonstrate antenna detuning effects in a complex user environment, which impacts the resonant frequency and available power to antenna. To list the detail effects to antenna, the impedance is divided into real and imaginary parts instead of the usual S_{11}. As exhibited in Figure 3 (a), the real part of the port impedance decreases with rising separation and the deviation decreases as well. Figure 3 (b) shows the imaginary part of the port impedance, the slopes of the curves are gradually reduced with the growing separation which could be explained by weaker coupling between the PIFA and the human phantom. Approximate equations are introduced to described these variations.

Equation 1: The real part of the port impedance

$$\mathrm{Re}(z) = f(d) + n(\theta, d) \qquad [1]$$

$$f(d) = \begin{cases} 96.354 - 28.546 * \ln(d) & d < 10mm \\ 35 & 10mm \le d \le 20mm \end{cases}$$

$$when \quad 1\text{mm} \le d < 10mm$$

$$n(\theta, d) = (4.77 - 1.94 * \ln(d)) * |\theta|$$

$$when \quad -30 < \theta < 0 \; and \; 10mm \le d \le 20mm$$

$$n(\theta, d) = (0.0161 * d - 0.8488) * \theta$$

$$when \quad 0 \le \theta \le 30 \; and \; 10mm \le d \le 20mm$$

$$n(\theta, d) = -0.1357 * \theta$$

Equation 2: The imaginary part of the port impedance

$$when \quad 2mm \le d < 20mm$$

$$\text{Im}(z) = g(d) * \theta + m(\theta) \qquad [2]$$

$$g(d) = 3.1713 * \ln(d) - 8.7871$$

$$m(\theta) = -10.723 * \ln(\theta) + 14.409$$

$$when \quad d \ge 20mm$$

$$\text{Im}(z) \approx 0 \qquad [3]$$

3. PIFA radiation efficiency variations with distance and rotation angle

The radiation efficiency is defined as being the total radiated power divided by the maximum available power when the antenna is impedance matched. Especially in wearable antenna, the human phantom will absorb part of the radiator energy due to the microwave heating effect. The efficiency indicates the total obtainable gain of the PIFA, which also has an impact on battery lifetime.

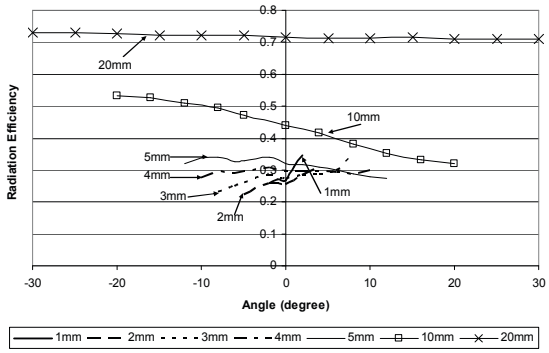

Figure 4: The radiation efficiency changing with separation and rotation angle

$$\eta_r = \begin{cases} s(d) * \theta + 0.29 & 1mm \le d \le 5mm \\ q(d) * \theta + w(d) & 5mm < d \le 20mm \end{cases} \qquad [4]$$

$$s(d) = -0.0149 * \ln(d) + 0.0212$$

$$q(d) = 0.0079 * \ln(d) - 0.0242$$

$$w(d) = 0.0285 * d + 0.1527$$

4. PIFA radiation pattern variations with distance and rotation angle

The radiation pattern always changes with different antenna orientation whatever a PIFA antenna is utilized in off-body or on-body channels. Off body channel need more energy propagating away from body surface, however on-body channel need energy propagating along body surface.

Here we display several radiation patterns at different distance and angles that will provide us a clear picture about the body effect on PIFA radiation performance.

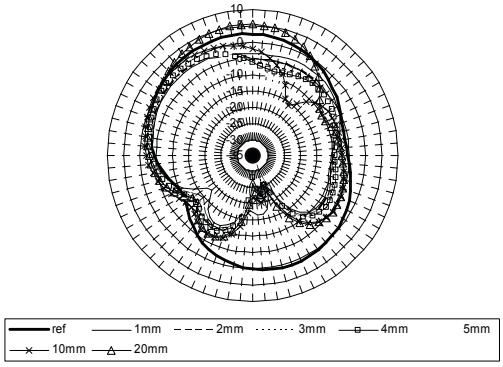

(a)

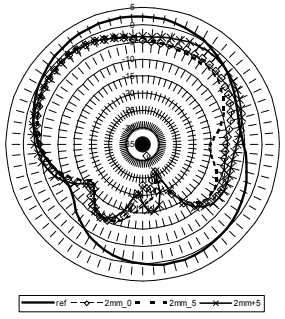

(b)

Figure 5: The E plane (ZX plane) Gain pattern (a) at 0 degree rotation with different separation (b) at 2mm separation with different rotation angle

The results show that the separation (D) has a more influence on gain pattern. The available gains in the main lobe increase with the rising separations which agree with the antenna efficiency variations in Figure 4. There have clear attenuation in the lower half plane compared to that of free space due to the phantom absorptions regardless of the separation.

Small rotation has limited impact on antenna radiation pattern as shown in Figure 5 although it sufficient affects the port impedance and efficiency explained in previous sections.

5 Conclusions

A PIFA antenna used in WPN (Wireless Personal Network) is reported in this paper considered its different separation and rotation angles. Simulations prove that the port impedance and the radiation efficiency have strong correlation with its positions and orientation. Several equations are first reported to describe the port impedance and efficiency as functions of D (the separation) and θ (rotation angle). The radiation pattern is not sensitive to small rotations. In the future, detailed measurement will be carried out confirm those equations.

6. Acknowledgement

This work has been supported financially by the Engineering and Physical Sciences Research Council (EPSRC), United Kingdom under Grant EP/D053749/1. The authors wish to thank our consortium partners: Zarlink, Taconic, European Antennas and the Home Office Scientific Development Branch for their encouragement and support.

7. Preferences

[1] P. S. Hall and Y. Hao, *Antennas and propagation for body-centric wireless communications*, Boston, Mass. London, Artech House, ISBN 978-1-580-53493-2, 2006.

[2] T. A. Milligan, *Modern antenna design —2nd ed*, Hoboken, New Jersey, John Wiley & Sons, ISBN-13 978-0-471-45776-3, 2005.

[3] A. Christ, A. Klingenbock, T. Samaras, C. Goiceanu and N. Kuster, "The dependence of electromagnetic far-field absorption on body tissue composition in the frequency range from 300 MHz to 6 GHz," *IEEE Trans. Microwave Theory Tech*., vol. 54, no.5, pp. 2188-2195, 2006.

[4] H. R Chuang,. "Numerical computation of fat layer effects on microwave near-field radiation to the abdomen of a full-scale human body model," *IEEE Trans. Microwave Theory Tech*, vol. 45 iss:1, pp.118-125, 1997.

[5] Http://niremf.ifac.cnr.it/tissprop/, 2009.

[6] K. L. Wong and C. I. Lin, "Characteristics of 2.4-GHz compact shorted patch antenna in close to a lossy medium," *Microwave Opt. Technol. Lett*., vol. 45, pp. 480-483, 2005.

[7] H. R. Chuang, W. T. Chen, "Computer simulation of the human-body effects on a circular-loop-wire antenna for radio-pager communications at 152, 280, and 400 MHz," *IEEE Trans. Vehicular Technology*, vol. 46, pp.544-559, 1997.

[8] W. G Scanlon, N. E Evans and M. Rollins, "Antenna-body interaction effects in a 418 MHz radio telemeter for infant use," *Annual International Conference of the IEEE Engineering in Medicine and Biology - Proceedings*, pp. 278-279, 1996.

[9] H. E. King and J. L. Wong, "Effect of a Human Body on a Dipole Antenna at 450 and 900 MHz," *IEEE Trans. Antennas Propag*, Ap-25, no. 3, pp. 376-379, 1977.

[10] H. R. Chuang, "Human operator coupling effects on radiation characteristics of a portable communication dipole antenna," *IEEE Trans Antennas Propag*, vol. 42, no. 4, pp. 556-560, 1994.

[11] M. F. Iskander, Z. Yun and R. Q. Illera, "Polarization and human body effects on the microwave absorption in a human head exposed to radiation from handheld devices," *IEEE Trans. Microwave Theory Tech*, vol. 48, no. 11, pp.1979-1987, 2000.

[12] D. Nashaat, H. Alsadek and H. Ghali, "Investigation of the mutual effect between human head and new shapes of PIFAs used in mobile communication systems," *Microwave Opt. Technol. Lett,* vol. 46, pp.243 -248, 2005.

Design of Compact Annular-Ring Patch Antennas for Circular Polarization

X. L. Bao and M. J. Ammann

Centre for Telecommunications Value-chain Research,
School of Electronic & Communications Engineering,
Dublin Institute of Technology, Kevin Street, Dublin 8, Ireland

Abstract

Several novel compact annular-ring patch antennas for circular polarization are presented. Two techniques are employed to reduce the antenna size and provide a suitable input impedance match, one is to insert strips into the annular ring and the other is to place a cross-slot into the ground plane. The proposed annular-ring patch with a cross-slotted ground plane can obtain a much smaller size for a given frequency. The resonant frequencies of these novel antennas can effectively be reduced due to increased path length of surface current. Dual annular-ring patch antennas with an embedded circular patch can provide dual frequency circular polarization characteristics. The performances of the proposed antennas are discussed.

Keywords: Annular-ring antennas, circular polarization, cross-slot, dual-frequency

Introduction

With the increased development of wireless communications systems, miniaturization of circularly polarized antennas have become more attractive to the engineering researcher. Annular-ring patch antennas have a smaller dimension compared to other square and circular patch antennas [1-5]. If annular ring is embedded with a pair of notches and a strip in inner circle, the antenna will exhibit circular polarization characteristics. Aperture-coupled microstrip fed annular-ring patch antennas have also been shown to produce circular polarization [6].

In this paper, two techniques are applied to the circularly polarized annular-ring patch antenna: embedding strips in the annular ring and cutting a crossed-slot into the ground plane. For a patch antenna with a narrow annular-ring, it is very difficult to achieve a good match to the 50 Ohm impedance of the coaxial probe. To obtain compact patch size and circular polarization at a given frequency, these branch strips are employed to match the coaxial probe. The proposed structures can effectively miniaturize the patch antenna size. A significant further size reduction can be achieved by augmenting the annular-ring patch antenna with a crossed-slot in the ground plane [7-8]. Various novel annular-ring circularly polarized antennas are designed and studied experimentally, and the circular-polarization performances are evaluated.

Annular Ring Patch with Embedded Strips

It is well know that annular-ring patch antenna is smaller than the rectangular patch or circular patch antenna. At the same time, the investigations on the annular-ring indicate when the inner radius of annular-ring is increased, the resonant frequency is decreased. But as the inner radius becomes large, a high impedance is created and it is difficult to provide a suitable match to 50 Ohms. So, some matching strips are placed inside the annular-ring to obtain good matching at the low frequency. In this paper, three new structures embedded into cross-strip patch are presented in Figure 1 a, b and c. If the position of feed point is properly selected, the two orthogonal modes of the annular-ring patch antennas can be excited with equal amplitude and 90 degree phase difference at a given frequency. Thus, the characteristics of circular polarization for annular-ring are realized. Three patch antennas presented in this paper are printed on FR4 substrate, of relative permittivity 4.2, of thickness 1.52mm, loss tangent 0.02. Using optimized results, the antenna dimensions for Antenna A, B, C are list in the table 1. For the

same size of annular-ring outer radius, the measured return loss and axial ratio properties of three different circular polarized annular-ring antennas are plotted in the Fig 2 and Fig 3, respectively. It is found that three antennas have good impedance bandwidth and axial-ratio performances. The normalized spinning radiation patterns in the XoZ plane for the three types are shown in Fig.4 (a), (b), and (c) at their individual centre frequencies (1.562GHz, 1.556GHz, 1.452Ghz), respectively.

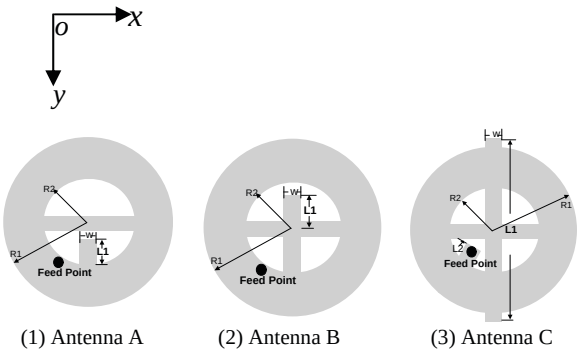

(1) Antenna A (2) Antenna B (3) Antenna C

Figure 1. Annular-Ring Patch with embedded strips

Table 1 The parameters of three annular-ring patch antennas embedded cross-strips

Parameters(mm) No.	R1	R2	W	Feedpoint	L1	L2
Antenna A	24.8	8.2	1	(-7,7)	4	-
Antenna B	24.8	7.8	2	(-6.6,6.6)	3.8	-
Antenna C	24.8	12.8	2	(-3,3)	59	9.8

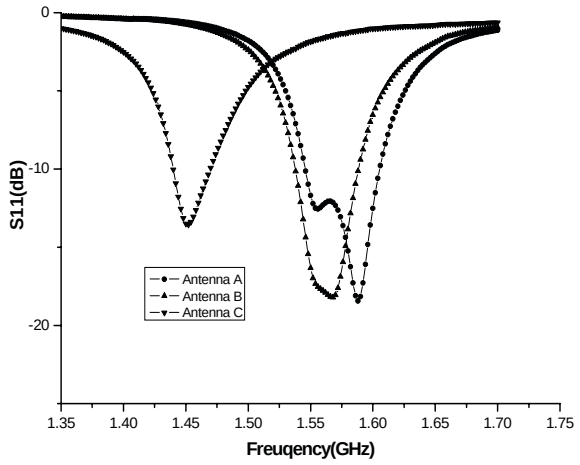

Figure 2. S11 for three annular-ring patch antennas

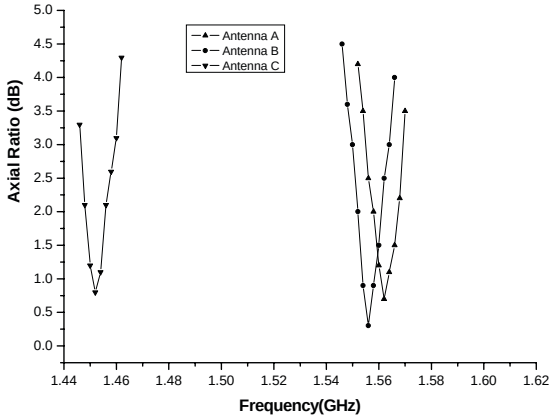

Figure 3 Axial ratio for the three antennas

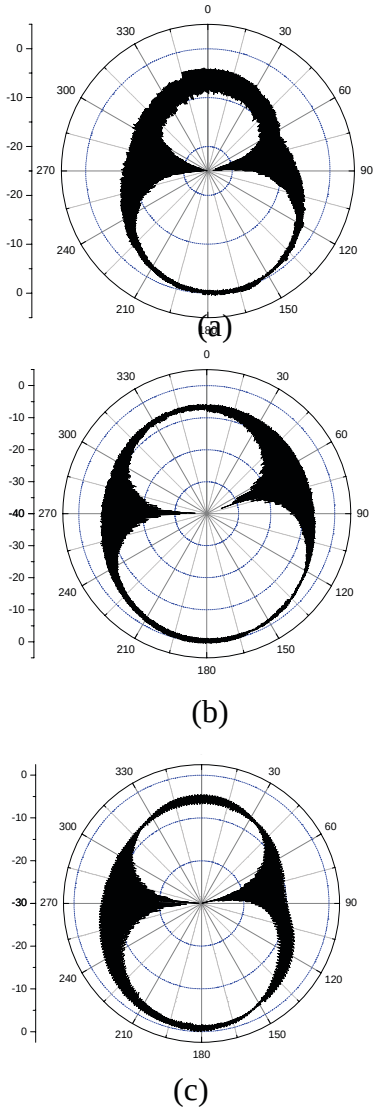

Figure 4. Spinning dipole radiation patterns for the antennas at different frequencies

Annular-ring Patch Antenna with Embedded Circular Patch and a Cross-slotted Ground Plane

In order to miniaturize the annular-ring antenna, a cross-slot in the ground plane is employed to compact annular-ring due to increased surface current path. To match the annular-ring patch, a circular patch placed in the centre of annular-ring patch is used, as shown in Figure 5 (a). Figure 5 (b) shows the geometry of the proposed dual-frequency circular polarized characteristics. These patches are printed on FR4 substrate, of permittivity $\varepsilon_r = 4.0$ and thickness 1.52 mm. The crossed slot in the groundplane has unequal lateral lengths, L1 and L2, with a slot width *w*. This structure can excite two degenerate orthogonal modes with equal amplitude and 90 degree phase difference by tuning various parameters (R2, R3, L1, and L2) and right-hand circular polarization (RHCP) radiation is obtained. The optimized dimensions selected are listed in table 2. In order for better matching of input impedance, a circular slot of radius R4 = 4mm is located at the centre of the cross slot. This antenna is excited by a 50 ohm coaxial probe, and position of feedpoint along the diagonal line is also listed in table 2.

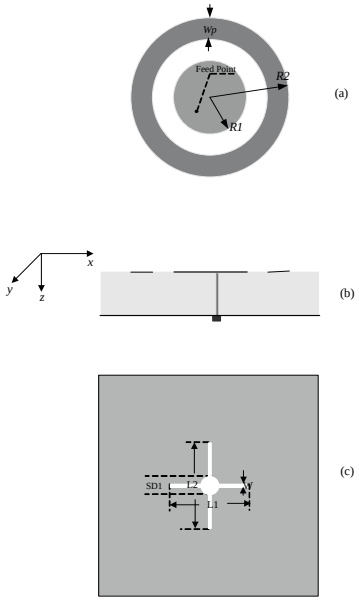

(a) The proposed single-frequency CP antenna

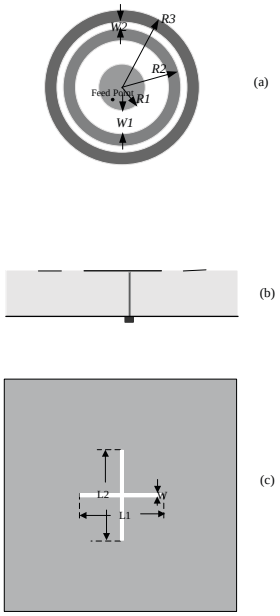

(b) The proposed dual-frequency CP antenna

Figure 5. The geometries of the annular-ring patch antennas loaded by circular patch with cross-slotted ground plane

For the single frequency CP antenna, in comparison to the conventional circular patch antenna, the centre frequency of the proposed annular-ring patch antenna is smaller by 55 % for the same substrate and outer circular radius. The measured 10 dB return loss impedance bandwidth for the proposed antenna is approximately 65 MHz (6.1%) from 1.039 GHz to 1.094 GHz, as shown in Figure 6.

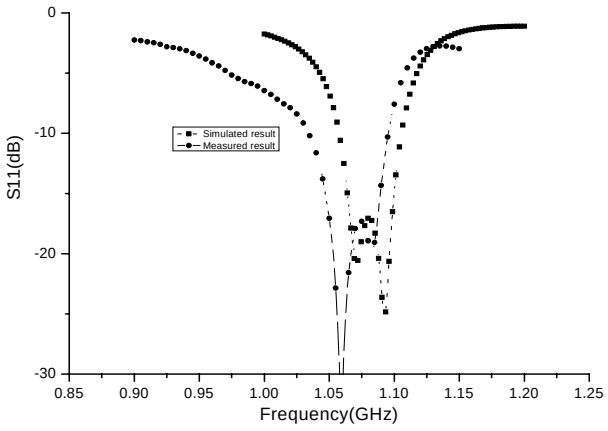

Figure 6. Measured and simulated S11 for the single frequency CP antenna.

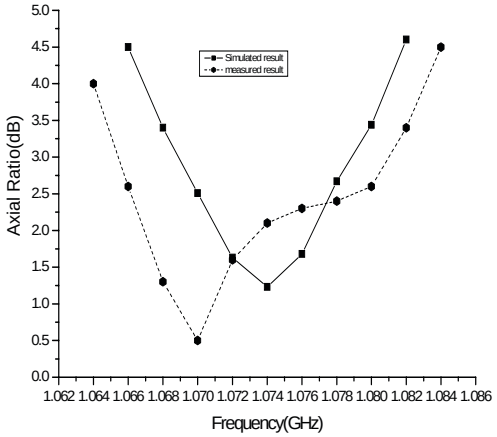

Figure7 Axial ratio for the single frequency CP antenna.

The simulated and measured axial-ratio (AR) is shown in Figure 7. The measured axial-ratio bandwidth, determined for AR <3 dB, is about 16 MHz (1.6%) from 1.065 GHz to 1.081 GHz.

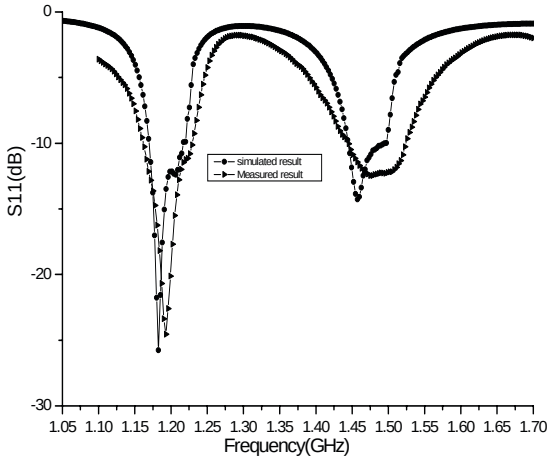

Figure8 Return loss for the dual-frequency CP antenna

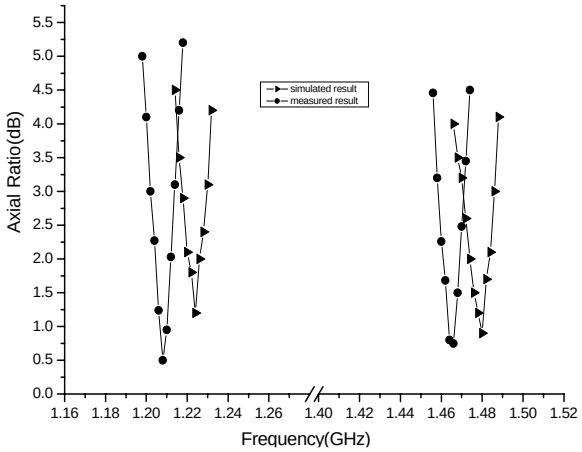

Figure 9 Axial ratio for the dual-frequency CP antenna

For dual CP antenna, the simulated and measured results for return loss and axial ratio are shown in Figure 8 and Figure 9, respectively. The measured results are in agreement with the simulated results. The measured results show bandwidths of input impedance for a S11 less than 10 dB are about 5.88% (72 MHz) at 1.224 GHz and about 6.08% (90 MHz) at 1.480 GHz. The proposed antenna is reduced by about 53 % compared to the conventional circular patch antenna. The measured axial ratio bandwidth for the first band is 12 MHz (0.98% with respect to 1.224 GHz) from 1.218 GHz to 1.230 GHz, and for the second band, the axial ratio bandwidth is 16 MHz (1.08% with respect to 1.480 GHz) from 1.470 GHz to 1.486 GHz.

Conclusions

Two techniques are presented which reduce the size of annular-ring patch antennas, while maintaining the circular polarization characteristics. Several new compact annular-ring patch antenna geometries are examined numerically and experimentally. These novel annular-ring patch antennas can significantly reduce the patch size and also produce good circular-polarization characteristics. An annular-ring placed around a circular patch antenna and loaded with a cross-slot in the ground plane is shown to reduce the antenna size by 55 percent compared to the strip-loaded annular-ring patch. Good bandwidths of impedance and axial ratio are also obtained.

References

[1] J.S.Dahelle and K.F.Lee, Characteristics of Annular Ring Microstrip Antenna, *Electronics Letters*, Vol.18, No.25, 1982, pp.1051-1052

[2] A.K.Bhattacharyya, L.shafai, A Wider Band Microstrip Antenna for Circular Polarization, *IEEE Transactions on Antennas and Propagation*, Vol.36, No.2, 1988,pp.157-163.

[3] G.J.K.Moernaut and G.A.E.Vandenbosch, Size Reduced Meander Line Annular Ring Microstrip Antenna, *Electronics Letters*, Vol.40, No.23, 2004, pp.1-2.

[4] C.Y.Sim, K.W.Lin, J.S.Row, Design of An Annular-Ring Microstrip Antenna for Circular Polarization, *IEEE Antennas and Propagation Society International Symposium*, Vol.1, 2004, pp.471-474.
[5] H.M.Chen and K.L.Wong, On the circular polarization of annular-ring microstrip antennas, *IEEE Transactions on Antennas and Propagation*, Vol.47, No.8, 1999, pp.1289-1292.
[6] J.S.Row, Design of Aperture-Coupled Annular-Ring Micrsotrip Antennas for Circular Polarization, *IEEE Transactions on Antennas and Propagation*, vol.53, No.5, 2005, pp.1779-1784.
[7] X.L.Bao and M.J.Ammann, Compact Annular-ring Embedded Circular Patch Antenna with a Cross-slot Ground Plane for Circular Polarization, *IEE Electronics Letters*, 2006, 42, (4), 192-193.
[8] X.L.Bao, and M.J.Ammann, A single-layer Dual-frequency Circularly-polarized Patch Antenna with Compact Size and Small Frequency Ratio, *IEEE Transaction on Antennas and Propagation*, Vol.55, No.7, 2007, pp.2104-2107.

Table 2. Dimensional parameters for the antennas

Parameters(mm)	R1	R2	R3	W1	W2	L1	L2	SD1	Wp	FeedPoint
Single CP Antenna	24.8	9.0	-	-	-	48.0	50.0	4.0	2.8	(-5,-5)
Dual CP Antenna	24.0	18.9	6.5	0.8	7.5	40	42.4	--	--	(-3,-3)

Section 1B

LOCATION-BASED SYSTEMS

Interpretation of Spatial Movement and Perception in Location Based Services

Eoin Mac Aoidh
National Centre For Geocomputation
National University of Ireland Maynooth
Ireland
Email: eoin.macaoidh@nuim.ie

Adam Winstanley
Department of Computer Science
National University of Ireland Maynooth
Ireland
Email: adam.winstanley@nuim.ie

***Abstract*—Location Based Services should deliver pertinent information to the user at the right place and at the right time. Such is the range of available content, that it must be filtered and prioritised according to the user's context to reduce wait time and eliminate the delivery of unwanted information. While some contextual information can be inferred from the device sensors, such as location and time, a deeper understanding of the user's context can be inferred by combing these sources with an implicit interpretation of the user's actions. This paper proposes an experiment to compare the user's actions in a real world environment to his actions in an identical virtual world, enabling accurate contextual inferences to be made. The real world study allows an analysis of real movements, which can be correlated with movements in the virtual world, with a greater potential for additional psychological analysis as part of the virtual world.**

I. Introduction

As the proliferation of location aware mobile devices increases due to continuous technology improvements, the demand for Location Based Services (LBS) is increasing. The goal of a LBS is to deliver appropriate content relevant to a specific location (usually the user's current location) at the time when it is required. For example, a LBS might deliver information on nearby restaurants to the user, however, a well designed LBS must take account of more than just location. Several other contexts, such as time of day, menu preference, and whether the user is hungry or not, in this example, are crucial to the development of an intelligent service. The LBS must employ any contextual information which can be gleaned implicitly to its advantage. In this case, if it can be inferred, based on device location, that the user has been sitting in a restaurant for the last 45 minutes, it is likely that the user has eaten, and that restaurants are no longer a priority for the user. Therefore the order of priority content must be recalculated according to the user's changing context.

LBS are designed for use on a mobile device, over a wireless network. Transmission of information is often affected by poor network coverage and slow processing on the device. Furthermore, the quantity of spatially referenced information available is continuously growing. As a result, it is crucial for the most important content to be prioritised for delivery to the user's device to reduce latency for the user. Moreover, irrelevant information must be elided to avoid swamping the user with information. In order to provide such a contextual, personalised LBS, the user's context, intentions, interests and preferences must be accurately interpreted from all available sources. We propose the development of a testing environment for the interpretation of a user's spatial movements and perceptions, both in a real world and in an identical 3D virtual environment. By understanding the user's actions and correlating them to what the user can see in the world around him, in relation to what is visible on the device screen, issues such as the user's concept of proximity, i.e. what services are 'nearby', and relevance, i.e. features that are used for orientation purposes, those which correspond to features/services of interest, and those which are irrelevant, can be explored. An improved understanding of these user context issues paves the way for the delivery of an improved LBS, adding value to the service, and enhancing the user's experience.

II. Related Work

Implicit Interest Indicators (III) [1] are employed by many applications with a user modelling component. They are a means of interpreting the user's interest in a particular item. For example, the printing of a Webpage as an III signifies an interest in the contents of the page [1]. In the context of a spatial browser, zooming in on a specific area signifies an interest in its contents [2] [3]. By studying sequences of operations, it is apparent that certain combinations of operations have different meanings, depending on their order of execution [4]. Furthermore, the strength of inferences made based on user interaction varies depending on the context in which they were executed [2]. For example, it has been shown that at times when the mouse is not actively engaged in interface manipulation, user's eye movements, and consequently the mental processing of the information on screen is connected to the location of the mouse cursor [5]. At other times, however, when the mouse is being actively engaged to pan and zoom through the map for example, its location in relation to the contents of the map is not as indicative of the user's objects/areas of interest [2].

The cognitive processes involved in the human brain while processing traditional 2D maps on paper, and in digital form are explored in [6] [7]. The authors explore the possibilities of exploiting Cognitive Load Theory (CLT) for more

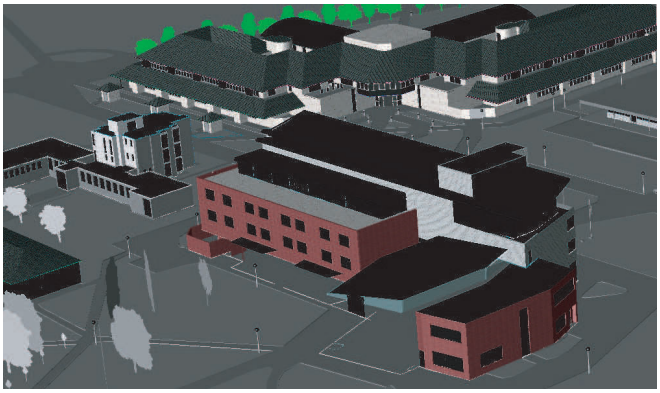

Fig. 1. A screenshot showing a section of the 3d campus model.

comprehensive and robust methodologies for 2D map construction and analysis. Human cognition in relation to virtual 3D environments is explored in [8]. The human perception of directionality between virtual landmarks is exploited for the improvement of spatial learning. The test environment proposed in this paper is concerned with the inferences about the user's notions of spatial perception in both two and three dimensions which can be made from the *physical movements* of the user through both real, and virtual 3D space. The inferences which can be made from user's physical interactions with a map interface, including mouse movements and map manipulation interactions, were explored in [2]. It is intended to bring this concept of physical movement analysis for the interpretation of the user's spatial perception to both the real, and virtual 3D space for experimentation.

III. Proposed Experiment

The test bed for the proposed experiment is a university campus. An accurate 3D model of the campus has been generated from LiDAR point clouds. The model covers an area of 500m by 700m, containing 14 buildings represented in exceptional detail. The internal representations of some of the main buildings have also been built. This gives us an identical, accurate 3D virtual representation of the real world campus, a section of which is shown in Figure 1. Such is the scale and detail of the model, that experiments could be carried out at scales varying from an area covering 5m to 500m, or even internally within the buildings, over multiple floors.

In the proposed set of experiments, users will carry a mobile device offering an interactive 2D map of the campus with information on all of the points of interest. A number of predefined tasks will be carried out, requiring them to navigate through the campus. Similar tasks will subsequently be carried out in the virtual environment. The same 2D application on the mobile device will be available to the user. Their navigation through the real world environment will be assessed, and compared to their navigation through the virtual environment at a range of scales. Of primary interest are physical movement patterns which could act as implicit interest indicators about the user's context, and the contents of the map on the mobile device in relation to the objects which the user can see in the real/virtual world. Such an experiment comparing and contrasting navigation in identical real and virtual worlds is of importance, as further analysis can be conducted in the virtual world which is not possible in a real world scenario. Analysis including eye tracking and EEG monitoring in the virtual world would follow, which are not feasible in the real world as the equipment is intrusive and cumbersome. Inferences about the user's eye movements and brain activity in the real world, e.g. for navigation, can be made if the correlation between real and virtual world performance is well tested and documented.

IV. Conclusion

Location Based Services must deliver contextually relevant content in order to provide a useful service to the user, minimising download time and reducing information overload. Certain fundamental inferences about location and time etc. can be made based on the device sensors. Our goal is to enrich this contextual information by implicitly inferring additional information about the user based on the relationship between his/her physical movements and corresponding interactions with an associated 2D map on a mobile device. We propose an experiment to examine the relationship between physical movements through space and 2D map browsing in identical real and 3D virtual worlds. By assessing the correlation between the real and virtual worlds, it could be possible to conduct an additional psychological analysis on interactions in the virtual world using equipment which would be inappropriate in a real world scenario.

Acknowledgment

Research presented in this paper was funded by a Strategic Research Cluster grant (07/SRC/I1168) by Science Foundation Ireland under the National Development Plan. We gratefully acknowledge this support.

References

[1] M. Claypool, P. Le, M. Waseda, and D. Brown, *Implicit Interest Indicators* In Proceedings of IUI'01, pp. 33-40, 2001, Santa Fe, New Mexico, USA. ACM. 2001.

[2] E. Mac Aoidh, M. Bertolotto and D.C. Wilson, *Understanding Geospatial Interests by Visualising Map Interaction Behaviour* In Information Visualisation, Vol. 7, No. 3-4, pp. 257-286, Palgrave, 2009.

[3] T. Tezuka and K. Tanaka, *Presentation of Dynamic Maps by Estimating User Intentions from Operation History* In Proceedings of MMM2007, pp 156-165, January 2007, Singapore. Springer Verlag.

[4] M. Hirose, R. Hiramoto, and K. Sumiya, *GeminiMap - Geographical Enhanced Map Interface for Navigation on the Internet* In Proceedings of W2GIS'07, pp. 279-292, November 2007, Cardiff, UK. Springer Verlag.

[5] M.C. Chen, J.R. Anderson and M.H. Sohn, *What Can a Mouse Cursor Tell Us More? Correlation of Eye/Mouse Movements on Web Browsing* In Proceedings of CHI'01, pp. 281-282, Seattle, Washington, USA. ACM. 2001.

[6] A.K. Lobben, *Tasks, Strategies, and Cognitive Processes Associated With Navigational Map Reading: A Review Perspective*,The Professional Geographer,56:2, pp. 270281, 2004.

[7] R.L. Bunch and R.E. Lloyd, *The Cognitive Load of Geographic Information*,The Professional Geographer,58:2, pp. 209220, 2006.

[8] W.S. Albert, R.A. Rensink and J.M. Beusmans, *Learning relative directions between landmarks in a desktop virtual environment*, Spatial Cognition and Computation 1: pp. 131144, Kluwer. 1999.

Location Based Services of University Town Based on OpenStreetMap: NUI Maynooth as an example

Jianghua.Zheng , B. Ciepłuch, Peter. Mooney, and Adam Winstanley

Dept. of Computer Science
National University of Ireland Maynooth
Maynooth, Co. Kildare, Ireland
Jianghua.zheng@nuim.ie

***Abstract*— The university campus of NUI Maynooth forms a substantial part of Maynooth town. Location based services (LBS) could be important for visitors to the campus and town in assisting them to make the most of their stay, particularly if they are not familiar with the town. In this paper we discuss an LBS application for Maynooth university campus and Maynooth town based on OpenStreetMap. The solution uses open source software and public participation rules to build its database. The work provides a prototype LBS system for NUI Maynooth which is currently under active development. The paper mainly describes some completed components of the work: data acquisition and pedestrian navigation algorithm design. Future work on path optimization and 3D applications is also discussed.**

Keywords: location based services, pedestrian navigation, walking area, path planning, OpenStreetMap, university town

I. INTRODUCTION

University towns usually are situated in a quiet environment and beautiful scenery. These characteristics attract visitors to tour university towns. As strangers, these tourists could use a powerful and convenient Location Based Service (LBS) to help them get familiar with the unfamiliar environment and lead them to the interesting sites. Such applications need accurate spatial data and detailed geographical attribute information. Such products are not usually provided by mapping and cartography companies as this attribute information is often expensive to collect. Without these data and information products the problem of pedestrian navigation cannot be solved satisfactorily. We describe a system that adopts and integrates Web 2.0 technologies and open source tools as a promising way to serve LBS applications for pedestrian navigation. We take the university town of Maynooth in Co. Kildare Ireland as a case study example.

The work is part of the eCampus project, which is constructing a major test bed for StratAG, the Strategic Research Cluster in Advanced Geotechnologies (www.stratag.ie) at National University of Ireland Maynooth. It focuses on constructing a university campus related information system including diverse location-based services.

II. FUNCTION DESIGN AND SYSTEM ARCHITECTURE

Visitors can use the LBS applications from two types of terminals. The first type is through a standard desktop computer interface using an Internet browser. The other is mobile terminals which can acquire LBS information through wireless communication networks. In terms of the delivery of content, the location based services for a university town are similar to other LBS applications. The major types of service include highlighting and querying Point of Interests (POI) and pedestrian navigation. Figure 1 displays the system architecture in outline. The main functionality can be described as:

POI services

- Where am I?
- Where is an organization or a place located?
- Where is nearest ATM or other type of POI?
- etc

A. *Pedestrian navigation*

- 2D & 3D navigation;
- Outdoor & Indoor navigation
- Navigation inside & outside walking areas
- User preferred route planning
- Natural language description
- etc

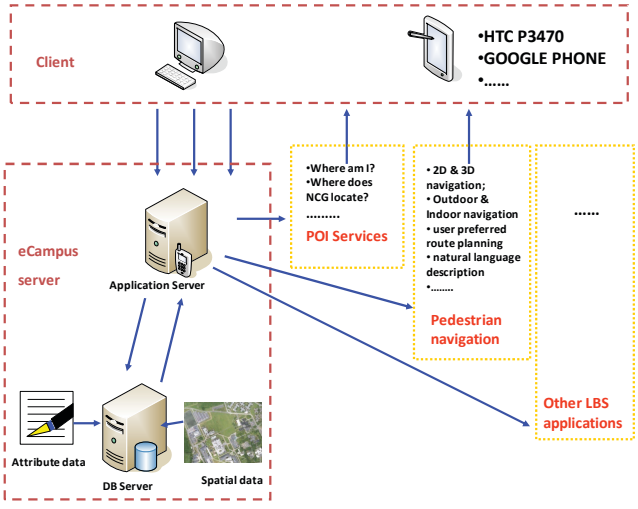

Figure 1 system architecture

III. DATA COLLECTION

Accurate spatial data and detailed geographical attribute information are the basis of LBS applications for any environment including university towns. In Ireland there are generally no suitable free data that can be directly used for such applications. In Maynooth, for example, Google Earth does not provide good resolution remote sensing images for navigation. Also Google Maps does not provide attribute data for POI queries and pedestrian navigation. Furthermore, obtaining high resolution remotely sensed imagery from commercial companies would incur a large financial cost that the project cannot support.

Beginning in 2008 a cost effective method for creating a map of the campus was sought for NUI Maynooth and the surroundings area. This map creation task was necessary because this map data was required for use in the prototyping pedestrian navigation application. The fastest way to solve this problem would have been to use an "out of the box" mapping system like Google Maps or Virtual Earth. The other more costly option was to purchase the data about streets and paths in this area from a company which prepares maps for GPS devices.

For pedestrian navigation a very detailed map of the campus area is required. This map must, by default, include all streets on which it is possible to drive but the map must also include pedestrian ways (paths, lanes, walkways, trails). A quick, efficient, and accurate solution to this problem was to create the map ourselves. OpenStreetMap is a free and open map of the world.

OpenStreetMap allows users to upload GPS data, aerial photography, and other spatial sources for inclusion on the OpenStreetMap (OSM) map of the world. There are many documents on the OSM Wiki pages to get started with map creation. A GPS logger device was obtained for GPS coordinate collection. A GlobalSat® DG-100 GPS Data Logger was used. This device is not a complicated GPS device. It contains a button for on/off and three diodes which show current status and a simple trigger to allow the operator to choose how frequently the measurement of position is captured and recorded into the device's internal memory. This device is very widely use by the OpenStreetMap community. It is very easy to use this device with Linux servers as drivers are available using an application called GPSbabel [1]. Based on the same code, a special plug-in for an OSM editor called JOSM was manufactured by the OpenStreetMap community which downloads routes of journeys directly to a spatial data editor.

At the initial stages of map creation for Maynooth, it was decided that we would collect as much geographical data and information as possible about the vicinity. The final versions of the maps could be used then by members of the local Maynooth community and for us in university projects such as this project on pedestrian navigation. We are hopeful that the "open access to data" philosophy of OSM [2] will mean that it will not be necessary for other projects requiring mapping to re-invent the wheel and collect their own data. The OSM map can be continually updated and edited as geographical features change in the area or as more detailed or new geographical data is collected and uploaded to OSM. Due to this work, at present the OSM map of Maynooth better represents the geographical reality of the area than Google maps or Virtual Earth. It also offers the University the opportunity to quickly add or remove geographical features to the OSM map to accurately reflect changes in the physical campus structure – for example new footpaths or the relocation of facilities such as postboxes.

OSM data can be accessed in XML format. The XML format is verbose and shows all of the attributes for a line (roads, streets, paths) or point (Point of Interest, shop, amenity) feature on the map. An example is shown below for one point of interest (POI) which is Brady's Public House on Main Street of Maynooth. The subset of the XML is shown as follows.

```
<osm version="0.5" generator="OpenStreetMap server">
<node id="344721377" lat="53.3815013" lon="-6.5902968"
user="Blazejos" visible="true" timestamp="2009-02-
13T11:06:12+00:00">
<tag k="created_by" v="Merkaartor 0.12"/>
<tag k="amenity" v="pub"/>
<tag k="name" v="Brady's"/>
</node>
</osm>
```

In graphical format Brady's pub is displayed on a graphical map tile by the Mapnik software package (figure 2).

Figure 2 data collection sample

The first step in building the OSM map starts with traveling along streets, lanes and paths, in the town and capturing GPS coordinates for these features. This is a time consuming process. Before map data collection began the Maynooth town area was divided into small manageable

segments. The process of data collection, editing, and final production upload to the OSM servers took between two and three days for each segment. In Ireland it is difficult to access high resolution aerial imagery without incurring a very large cost. This meant that the only method to capture high resolution data was to physically visit every geographical feature in Maynooth which we would like to have on the map.

The typical procedure was to travel the streets and lanes by bicycle to capture their shape in GPS coordinates. Data capture by bicycle was useful for several reasons. Firstly there were some examples of footpaths hidden between trees and bushes and could only have been captured using ground survey. The bicycle also allowed travel along pedestrian-only streets and lanes. At the same time the relative location of the geographical details was captured of all other important information particularly POIs such as speed bumps, street lights, bus stops and shops. Photographs were taken with a digital camera to enhance the accuracy of the placement of these POIs on the map and in their physical description.

Upon returning to the laboratory the data from the GPS logger were uploaded. Street and line feature data was uploaded first followed by adding information on POIs. The Java OpenStreetMap (JOSM) [3] editor was used for this task. The JOSM has a special plug-in which allows the editor to match digital photographs taken during the survey with points on the line representing the line feature. This is done by comparing points on the GPS coordinate line with the time stamps of the JPEG photographs taken by the digital camera.

Figure 3 data collection sample

This approach to map creation is not perfect as it is difficult to capture the shapes (plan view) of buildings. It is possible to create reasonable approximations to the shape of large buildings by simply walking around then and recording coordinates with the GPS device. However this is not suitable for all buildings as it is often the case that not every corner or side is accessible by pedestrians. Therefore, the National Centre for Geocomputation (NCG) at NUI Maynooth provided us with an aerial photograph of the Maynooth campus.

The dimensions of this image are 7113x8810 pixels and it was resolution-rectified using the on-line tool "Map wrapper" [4]. The aerial photograph does not cover all of Maynooth. However the photograph has allowed us to create a complete map of Campus buildings and campus path ways. 'Map wrapper' provides a Web Map Service (WMS) which, in combination with the JOSM plug-in, allows a direct connection. It was then a simple task to place this aerial photograph as a background in JOSM and simply transfer the necessary features onto the map. The final result of this map production work is a high quality map of our university campus as figure 3).

The map offers greater resolution and more geographical attribute detail than maps offered by Google Maps or Microsoft Virtual Earth for the same location. The map of Maynooth (town and campus) is presented by the OSM public server but can be used freely by any third party. In particular, university research projects can use this map without constraints of map license structure or map purchase/usage costs. OSM is far from being "the finished article" for Ireland. Many locations in Ireland are very poorly mapped and contain little or no geographic detail. It is our intention to disseminate our knowledge of OSM and map production widely to other researchers and the general public in Ireland. It is hoped that this will help inspire other citizens to become part of the OSM community and assist in improving the representation of the island of Ireland in OSM. This data collection solution makes the geographical data updating of the OSM maps a very minimal cost exercise. It provides an opportunity for users to add new POI or other information into the database. For pedestrian navigation it is very important to have the information updated frequently.

IV. PEDESTRIAN NAVIGATION

When visitors use LBS applications in a university town most of their travel mode is walking. Pedestrians are not constrained to the road network (for example the lanes, turn restrictions, one-way streets) unlike vehicle drivers [5], [6]. In addition there are some special features that are unique to pedestrian navigation. These include "walking areas" where pedestrians can walk freely such as squares, grassland, parks and open ground. This is one of the key differences compared with the road networks used for vehicle

navigation. We define a walking area in 2D Euclidean space as an area where pedestrians can walk at random without using fixed paths. A walking area is generally represented by a polygonal feature. Zheng [6] discussed data modeling of pedestrian networks including walking areas. In former work [8] we classified walking areas into three types with orthogonal attributes including the character of their boundaries and entrances, concave-convex characteristics of their shape and the presence of impenetrable islands. Walking areas can be divided further into three subtypes derived from the access character of the boundaries and entrances: fixed entrances, open boundary (free entrance), and open boundary with restrictions. Considering the subtypes of the other orthogonal factors in characterizing polygon shapes there should be 12 general situations. For developing robust pedestrian navigation services the entire set of situations must be taken into account.

Pan [7] put forward an algorithm generating optimal paths within a polygon (a walking area) with interior obstacles. This algorithm was based on Dijkstra's algorithm. This work also provided some solutions for the special behaviors of pedestrians, such as preference for easy walking routes and preference for indoor routes.

Zheng [8] describes a Two-Level Path Planning Algorithm for pedestrian navigation. In a related paper currently under peer review the author describes the solution for pedestrian navigation with open boundary areas. The solution solves the problem to represent the link passing through open boundaries in any directions by building up the connecting relationships between the open boundary area and other related spatial nodes (including simplified adjacent open boundary areas). At the first level this takes an open boundary area as one node of a link-node network for path planning outside walking areas. The second level is used for optimal path planning inside the walking areas. The detailed algorithm will be published in the near future.

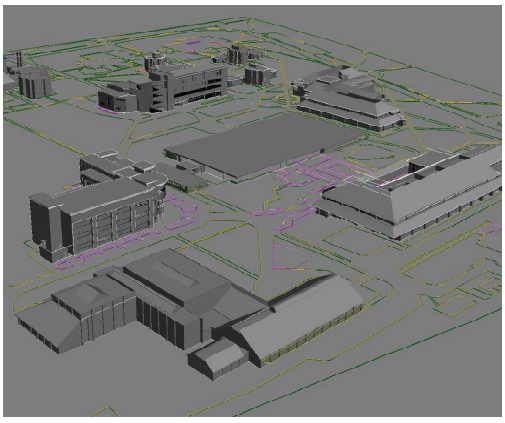

Figure 4 3D data sample

V. CONCLUSION AND FUTURE WORK

Our goal is to obtain a cost effective way for data collection and software deployment for LBS applications for the case study of pedestrian navigation in a university town. A 2D data collection solution has been adopted based on OpenStreetMap. This paper has described our preliminary work so far. Future work will focus on better optimal path representation for various topographic situations. Furthermore, we will develop test applications for mobile terminals to allow user testing to be performed. Figure 4 shows a 3D data sample of NUIM campus obtained as part of the StratAG project. The extension of pedestrian navigation to 3D scenarios (for example, inside buildings) will also be investigated.

ACKNOWLEDGMENT

Research presented in this paper was funded by a Strategic Research Cluster grant (07/SRC/I1168) by Science Foundation Ireland under the National Development Plan. The authors gratefully acknowledge this support.

REFERENCES

[1] Christoph Eckert, GPS Babel application, http://www.gpsbabel.org

[2] Mordechai (Muki) Haklay and Patrick Weber, OpenStreetMap: User-Generated Street Maps, IEEE Pervasive Computing, 7, (4), 12-18, Oct.-Dec. 2008.

[3] Immanuel Scholz, JOSM application, http://josm.openstreetmap.de/

[4] Tim Waters, Map Wraper application, http://warper.geothings.net/

[5] Christian Gaisbauer and Andrew U. Frank. Wayfinding Model for Pedestrian Navigation, 11th AGILE International Conference on Geographic Information Science 2008.

[6] Jianghua Zheng, Jianwei Tao, Jianli Ding, Abudukim Abuliz, and Hanyu Xiang. Pedestrian Navigation Data Modelling for Hybrid Travel Patterns, Geoinformatics 2008. Proc. SPIE, 7144, 71442Y (2008)

[7] Zheng Pan, Yuefeng Liu, Adam C. Winstanley, Lei Yan, Jianghua Zheng. A 2-D ESPO Algorithm and Its Application In Pedestrian Path Planning Considering Human Behavior, Proceedings of MUE'09 (to be published in June 2009), IEEE CS.

[8] Jianghua Zheng, Adam Winstanley, Zheng Pan, Seamus Coveney. Spatial Characteristics of Walking Areas for Pedestrian Navigation, Proceedings of MUE'09 (to be published in June 2009), IEEE CS.

Wiimote as a Navigation tool for Pedestrians

Ricky Jacob, Adam Winstanley, Declan Meenagh
Computer Science Department
National University of Ireland Maynooth
Maynooth, Kildare, Ireland
rjacob@cs.nuim.ie, adam.winstanley@nuim.ie

Eoin Mac Aoidh
National Centre for Geocomputation
National University of Ireland Maynooth
Maynooth, Kildare, Ireland
eoin.macaoidh@nuim.ie

Abstract — **Pedestrian Navigation requires effective communication between the mobile device and the user. The Mobile device should be able to give feedback to the user ensuring there is minimum input and attention of the user required. Mobile interaction for navigation has mostly been through the use of visual interfaces with maps and annotations. This paper describes a Multi-modal, haptic interface with the visual interface of an OpenStreetMap on a mobile platform. The Wiimote is used as the haptic tool which will vibrate based on the navigation path to be taken by the user with signals from the mobile application via a wireless connection using bluetooth.**

Keywords- Multi-Modal, Haptic, OpenStreetMap, Wiimote, Pedestrian navigation

I. INTRODUCTION

According to a new study from ABI Research [5] the number of subscribers to handset-hosted location based services (LBS) increased in 2008 to more than 18 million. Thus we can see an enormous growth during the coming years in the use of mobile services. For good Location Based Services (LBS), there is always the need of an effective medium of interaction between the human and the mobile device. The various ways in which we can achieve that can roughly be classified under the following: graphical user interfaces (GUI), speech user interfaces, haptic user interfaces, gaze interfaces, and computer vision.

When selecting an interaction technique, we must know what is the task that we are looking to make easier and more natural for the user and how do we plan to do that decides upon which modalities we are going to use for input and output.
Part of this is

- graphic feedback, haptic feedback, auditory feedback, speech synthesis
- manual (haptic) input, speech input, voice input, eye tracking, computer vision.

If multimodal interaction is going to be used, then how do we overcome the complexities that come with it? The need for psychological aspects is required inorder to assess which of the methods are easy and hard for understanding and which people prefer using. We must select the programming platform and additional software packages based on the modalities we choose for our work. Lots of work to make the browser a location-aware one is going on and with the Geolocation API, the browser will now be able to recognize you current location and give you search results based on that. This will cut down on the human interaction part. Mozilla [6] has recently included a new experimental add-on called Geode to their famous web browser - Firefox. Geode provides a rudimentary implementation of geolocation for the current version of Firefox by using a single hard-coded location provider to enable Wifi-based positioning conforming to the W3C Geolocation specification [7] so that developers can begin experimenting with enabling location-aware applications today.

Since mobile devices have issues such as small memory, small display, latency, and user input constraints, we need to ensure the application does not overlook those factors. Also the need to choose between broswer based and widget based application is of importance. The use of graphical display like maps or texual description, requires the user to look into the screen while he is on the move thus interupting the user's other major work. Use of audio feedback also requires the users attention at all times just limiting the user from performing other tasks at the same time.

Car navigation systems have evolved well over the years to provide better communication between the user and the system. These navigation systems work better with the GPS satelliites as the cars travel on roads and it is quite easy to get good signals from the satellites. Also in case of the car, the user's context does not vary also his field of view, thus it is comparitively easier to provide effective navigation to the user. The pedestrian navigation system is much more complex, as user context various quite rapidly and the system should dynamically change accordingly. Also it requires the user's attention if the system is a visual interface or audio feedback. Haptics on the other hand will not need much of the user's attention when on the move. In this paper. we propose the need for haptic feedback for pedestrian navigation along with the visual interface on the mobile device.

II. NAVIGATION USING HAPTIC FEEDBACK

The word haptics refers to the capability to sense a natural or synthetic mechanical environment through touch. Haptics also includes kinesthesia (or proprioception), the ability to perceive

one's body position, movement and weight (Hayward et al. [1]).

An exploration of haptic output for indoors pedestrian guidance (e.g., a room in a hospital) which is what GentleGuide [2] does is limited to indoor navigation and has fixed paths. Most of the other work done with respect to haptics is focuses on people with a visual disability, like the wearable navigation system by Ertan et al. [3]. Our work is to maximize use the sense of touch efficiently to help users navigate in an outdoor environment, similar to Keyson [4].

So here we are designing for various contexts and for a broad range of users. We also keep in mind various other aspects while we model the system which includes the user's level of experience, cultural background, physical abilities, cognitive abilities, work domain, including others. We also plan to model the location or travel history and then try to provide context aware results based on digital dairy/calendar inputs for reminders and also current weather and other environmental information too.

III. SYSTEM IMPLEMENTATION

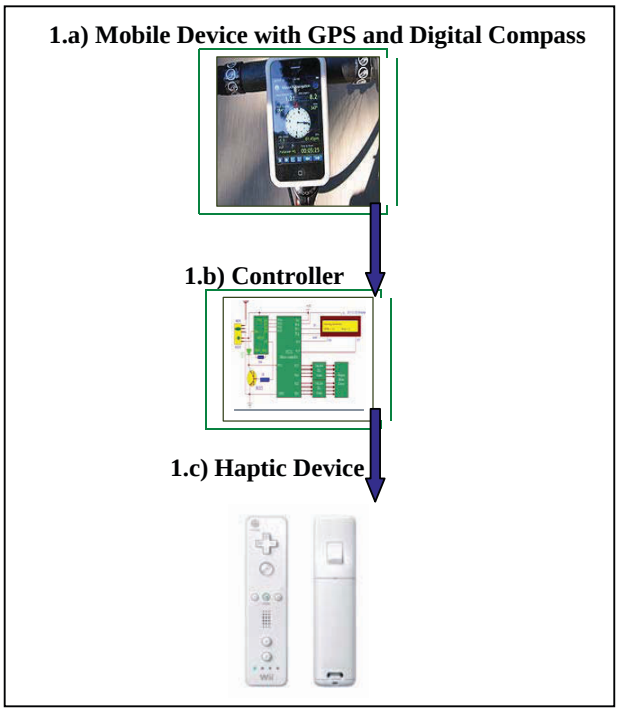

Figure 1. Flow of information in the haptic feedback system.

The digital compass along with the GPS embedded in the mobile will let the user navigate in open space. We also attempt to provide the best modality combination based on the current environment. So if it the user wants to view the path on a map in the middle of his/her navigation, he can switch to the map mode.

Our haptic feedback system (Fig 1) allows the user to keep his mobile device (Fig 1.a) inside his pocket or bag and with the help of a Bluetooth connection to a Wiimote (Fig 1.c) or with the use of the mobile phone itself, we can guide the user to his location with the help of haptic feedback in the form of vibrations. We need a controller (Fig 1.b) to decode the encoded signals that is received by the Wiimote to interpret the signals. The user will be guided toward the right path to his location by altering the intensity and/or time of duration of the vibrations. If the user changes his position to a entirely different location from the specified path (e.g., if it suddenly rains, the user might have ran towards a building for shelter), then we also plan to dynamically re-route his/her path and provide the best route to the user based on his/her current position.

IV. CONCLUSION

Getting the mobile device to interact wirelessly with the Wiimote was the first challenge and now we need to understand as to how usable the Wiimote is going to be. For this we are doing some user trials where paths have been predefined and we ask the user to reach the destination based on the haptic feedback and also by using the visual navigation and take feedback to see how effective the haptic feedback is.

We intend to use OpenStreetMap as the visual interface as it is freely available for download and we can customize it as per our requirements. During the initial stages we will use the data for Ireland which we have downloaded as our test bed. Haptic feedback will be useful as it enables the user to be involved in other work and would not need his/her attention as in the case of audio or visual feedback.

ACKNOWLEDGMENT

Research presented in this paper was funded by a Strategic Research Cluster grant (07/SRC/I1168) by Science Foundation Ireland under the National Development Plan. The authors gratefully acknowledge this support.

REFERENCES

[1] V. Hayward OR. Astley, M. Cruz-Hernandez, D. Grant, G. Robles-De-La-Torre, "Haptic interfaces and devices", Sensor Review 24(1), pp 16-29, 2004.
[2] S. Bosman, et al., "GentleGuide: An exploration of haptic output for indoors pedestrian guidance", 2003.
[3] S. Ertan, C. Lee, A. Willets, H. Tan, A. Pentland, "A Wearable Haptic Navigation Guidance System", 1998
[4] D.V. Keyson, "Touch in User Interface Navigation", 1997.
[5] ABI Research http://www.abiresearch.com/, 2009
[6] Mozilla http://www.mozilla.com/, 2009
[7] W3C Geolocation http://www.w3.org/TR/geolocation-API, 2009

Feedback Control Models and Their Application in Pedestrian Navigation Systems

Lei Yan[1] Zheng Pan[1,3] Adam C. Winstanley[2] A. Stewart Fotheringham[3] Jianghua Zheng[2]

1. Beijing Key Lab of Spatial Information Integration & Its Applications, Institute of RS&GIS, Peking University, Beijing, China

2. Department of Computer Science, National University of Ireland, Maynooth, Co. Kildare, Ireland

3. National Centre for Geocomputation, National University of Ireland, Maynooth, Co. Kildare, Ireland

Abstract—Feedback control theory has been widely used in many fields; this paper introduces this theory into a model for a pedestrian navigation system. Based on the model, several feedback channels are designed and analysed using control theory. The pedestrian is not only a data receiver but also a data collector. All collected information is stored in a temporal database and can be used for spatial-temporal analysis. At the same time, feedback control theory can integrate all modules of the system as whole, which can help to improve the overall effectiveness. Based on information fed back and feedback control theory, the pedestrian navigation system will help users to "see more, understand better, and decide more quickly."

Keywords—Feedback control model, pedestrian navigation system, LBS (Location based services)

I. INTRODUCTION

With the advancement in communication, GPS and GIS technologies, vehicle navigation systems are now widely used. In recent years, pedestrian navigation systems have been increasingly an active research field. It is not always easy for pedestrians to find the right way to reach their destination in an unfamiliar environment. Pedestrian navigation systems can help them to find an optimal route. Navigation for pedestrians is different from that for vehicles. Different pedestrians may choose totally different routes. They can walk along a road, or across a square. They can also follow a twisting narrow pass, or even cross a muddy grass field. The pedestrian needs a highly efficient and individualized navigation service. Furthermore, the pedestrian may also want to know the current traffic situation before they decide which means of transportation to use.

There are many pedestrian navigation systems available, but most of their implementation focuses on how to accurately determine the user's location or how to add more functional modules to the system. However, improving the overall effectiveness between several collaborating modules is still a problem that needs further study.

Some pedestrian navigation systems can collect and process information from different sources. This information can help users to choose a more suitable route. However, this data is usually considered transient and discarded after a short time. Archiving data for profiling user preferences or route information has not been used very much.

In this paper, we focus on the task of how to improve the efficiency of pedestrian navigation systems. In section 2, we briefly introduce related work in the field of pedestrian navigation and feedback control theory. In section 3, we describe why feedback control theory can be usefully applied in pedestrian navigation systems and how it may be modelled. The paper closes with some concluding remarks and suggestions of enhancements for a practical pedestrian navigation system.

II. RELATED WORK

A. Pedestrian Navigation Systems

Pedestrian navigation systems have been discussed for a long time. However, despite the fact that many navigation solutions include a pedestrian mode setting, none of these were worthy of that name [1]. Maybe this is an extreme verdict on the available applications for pedestrian navigation. However, it reflects that there still is a lot to do in this key area of location based services. Recent advances in mobile phones, positioning technologies, and wireless networking infrastructures are making it possible to implement and operate large-scale pedestrian navigation in the real

world and will result in them being more widely available in the future. Among them, NAVITIME is probably the most successful commercial navigation service for the public in Japan. Pedestrian navigation is one of its main services. It became available early this century and now has over one million users in Japan [2].

As a whole, pedestrian navigation is still on the edge of new positioning and communication technologies and several of its requirements have not been fully achieved. These include modelling the full complexity of walking routes, indoor navigation, personalized services suitable for various pedestrian behaviours and not implementing full 3D applications [3][4][5].

With the advent of more powerful hardware and software technologies in several key areas, including communication, computing, positioning and spatial representation, and more friendly and powerful pedestrian navigation services will become a reality.

B. Feedback Control Theory

Control theory is an interdisciplinary branch of engineering and mathematics, which deals with the behaviour of dynamical systems. The desired output of a system is called the reference. When one or more output variables of a system need to follow a certain reference over time, a controller manipulates the inputs to a system to obtain the desired effect on the output of the system [6] [7].

To avoid the problems of the open-loop controller, control theory introduces feedback. A closed-loop controller uses feedback to control states or outputs of a dynamical system. Its name comes from the information path in the system: process inputs (e.g. voltage applied to an electric motor) have an effect on the process outputs (e.g. velocity or torque of the motor), which is measured with sensors and processed by the controller; the result (the control signal) is used as input to the process, closing the loop.

Feedback is a mechanism, process or signal that is looped back to control a system within itself. Such a loop is called a feedback loop. Intuitively many systems have an obvious input and output; feeding back part of the output so as to increase the input is positive feedback; feeding back part of the output in such a way as to partially oppose the input is negative feedback.

Negative feedback helps to maintain stability in a system in spite of external changes. Positive feedback amplifies possibilities of divergences (evolution, change of goals); it is the condition to change, evolution, growth; it gives the system the ability to access new points of equilibrium [8][9].

Feedback control theory is widely used in many fields, such as biology, climate science, economics, electronic engineering and mechanical engineering. But it is seldom used in navigation field, especially in pedestrian navigation system.

III. MODELING OF PEDESTRIAN NAVIGATION SYSTEM

The most important factor in a pedestrian navigation system is data. The system needs to get data from different sources and send processed data to users. Existing systems always take the pedestrian as an information receiver, which are typical open-loop systems. In this paper, the pedestrian is not only a data receiver, but also a data collector. The pedestrian can feed some information back to the system, which forms a closed-loop of information.

Fig. 1 is the feedback control model of pedestrian navigation system. As shown in the figure, there are three feedback channels in the system: user feedback, spatial-temporal analysis feedback and validity feedback. These three feedback channels all are negative feedback, which can help to maintain system stability.

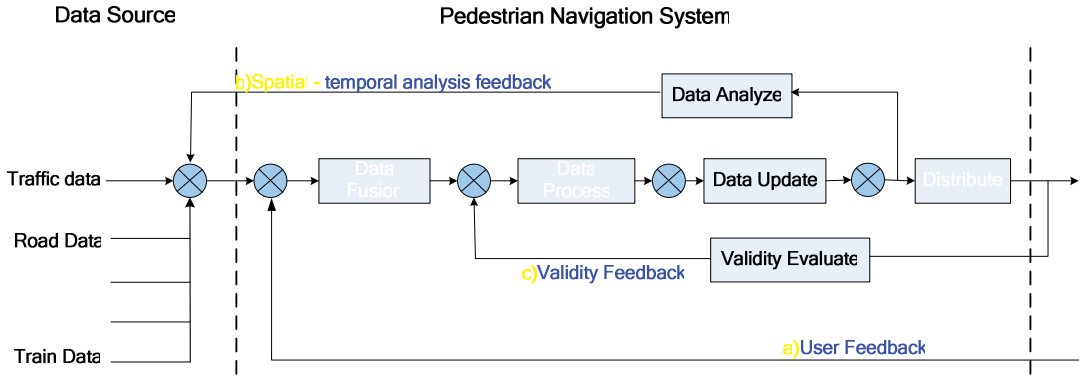

Fig. 1 Feedback control model

A. User Feedback

Because pedestrians are not limited in vehicle road network, they can walk across a square, or across a grass field. Therefore, compared with vehicle navigation systems, pedestrian navigation needs more information, including road network information, traffic information, POI (point of interest) information and some other information. One solution is to add more information source to pedestrian navigation system. In this system, the pedestrian is taken as an extra data source.

There are some data collecting interfaces in the system, so pedestrian can feedback data to the system in time. For example, if a pedestrian gets caught in a traffic jam, he can upload the congestion information to the pedestrian navigation system, which can help other people to avoid heavy traffic. For another example, if a pedestrian finds a new shop when he is walking along a street, he can send the name of the shop to the system. The exact location of the shop will be sent to the system at the same time. In this way, a pedestrian navigation system can get more general and timely information.

B. Spatial-temporal Analysis Feedback

Pedestrian navigation systems can get information from different data sources. Most systems use these data only once. In fact, we can find much useful information by analyzing historic data, which is another kind of feedback channel of the system.

A pedestrian navigation system needs to store several kinds of information. This information often evolves with time and location. So a temporal database will be constructed to store massive historic data. A temporal database supports the storage and retrieval of temporal data objects. Each entry in the database has one or more associated timestamps. All changes that occur are recorded and past states of the database may be retrieved. Two different timestamps may be used, the transaction time, corresponding to the moment when the information is introduced in the database, and the validity time, the time when that information is valid in the real world.

By analysing the spatial-temporal data stored in database, pedestrian navigation system can not only reconstruct the missing data, but also predict future data.

For example, real-time traffic information can help pedestrian to choose a suitable route. If the traffic information of some road segments is missing for some reason, we can reconstruct the missing data by analyzing historic temporal data. Results of spatial-temporal analysis can be feed back to the system as a kind of data source.

C. Validity Feedback

Different user may choose different routes. Some pedestrians want to choose a shortest route or a fastest path. While other pedestrians may want to choose an easy-walk route. The system will calculate a route according to the user's different requests.

But can the calculated results truly meet the needs of users? A sidewalk may be no longer a fastest path because of road-works. And a user may not think a path is easy to walk because of the mud after a rain storm. So it is very important to get the feedback from users about system validity.

In the process of navigation, the pedestrian can evaluate the precision of the data they receive and the validity of the calculated path. For example, each road segment will be assigned a number to represent the ease-of-travel over the road segment in advance. The smaller the number is, the easier the road segment is to walk. If a pedestrian thinks some road segment is not easy to walk, the system will increase the number after it gets the feedback from user. In this way, the system can obtain user's evaluation in time, which is also a kind of useful feedback to improve the data processing efficiency.

IV. CONCLUSION

This paper attempts to apply feedback control theory to pedestrian navigation. Three kinds of feedback channels are discussed. User feedback can be used to collect more information. Spatial-temporal analysis feedback can be used to reconstruct missing data and predict future data changes. And validity feedback is useful to improve system efficiency. Furthermore, these feedback channels connect different parts of the system into a unit. Based on these feedback channels, pedestrian navigation system will become more practical, more efficient and timely.

REFERENCES

[1] Dominique Bonte. The Mobile World Congress 2008: Pedestrian Navigation at Last, 11 Feb. 2008.

[2] Masatoshi Arikawa, Shin'ichi Konomi and Keisuke Ohnishi. NAVITIME: Supporting Pedestrian Navigation in the Real World. PERVASIVE computing, Published by the IEEE Computer Society, July–September 2007, pp21-29

[3] Masakatsu Kourogi,Nobuchika Sakata,Takashi Okuma,and Takeshi Kurata. Indoor/Outdoor Pedestrian Navigation with an Embedded

GPS/RFID/Self-contained Sensor System, ICAT 2006,LNCS 4282,pp.1310–1321,2006.

[4] Tracy Ross, Andrew May, and Simon Thompson. The Use of Landmarks in Pedestrian Navigation Instructions and the Effects of Context, MobileHCI 2004,LNCS 3160,pp.300–304,2004

[5] Christian Gaisbauer and Andrew U.Frank. Wayfinding Model for Pedestrian Navigation. Proc. Of 11th AGILE International Conference on Geographic Information Science 2008.

[6] Hao wang, Changcheng Huang, James Yan. A Feedback Control Model for Multiple-Link Adaptive Bandwidth Provisioning Systems. 2006 IEEE International Conference on Communications, Volume 3, June 2006, pp.987-993.

[7] Yu Chen, Qionghai Dai. A feedback control model for resource management on streaming media servers. Video Image Processing and Multimedia Communications, 2003, 4th EURASIP Conference, Volume 2, 2-5 July 2003 pp.835-840.

[8] Jeongho Hong, James C. Akers, Ravinder Venugopal, Miin-Nan Lee, etc. Modeling, Identification, and Feedback Control of Noise in an Acoustic Duct. Control Systems Technology, IEEE Transactions on Control Systems Technology, Volume 4, No. 3, May 1996, pp.283-291.

[9] B.G. Kim. Theoretic Framework for Feedback Control Models in High-Speed Networks. Database and Expert Systems Applications, 2003. Proceedings. 1-5 Sept. 2003. pp.134-138.

Tram and Bus Tracker: A Dynamic Web Application for Public Transit Reliability

Bashir Shalaik and Adam C. Winstanley
Department of Computer Science, National University of Ireland, Maynooth, Co. Kildare, Ireland

bsalaik@cs.nuim.ie

Abstract—*Currently transit quality information such as timetable adherence, bus arrival times and route performance has usually been disseminated through static environments on web-pages, paper documents or other different media. This paper describes a dynamic Geographic Information System-based Web application which displays the same information through a dynamic web application. Using data collected from an Automatic Vehicle Location System (AVL), a map-based interface has been created to allow travellers and operators to see routes, stops and buses in motion. The collected information is archived for off-line analysis. The system allows users to query and display day-to-day management of operations as well as to generate static performance reports to provide a complete view of the transit system reliability.*

I. I INTRODUCTION

Environmental occurrences such as traffic congestion or urban construction present new obstacles for transportation. Designing and implementation of a distributed transit vehicle information system will help reduce stress as well as improve confidence in and perception of transit systems [1]. Tram and Bus Tracker delivers real-time transit vehicle location and progress information highlighting any deviations from the published time-table or any bad services symptoms such as bunching of vehicles due to traffic conditions or incidents. Recent advanced techniques in communications, computing technology have made real-time transit information system an interesting area of research. In this project a web based application system has been developed to explore techniques of showing transit vehicle performance. This system was built using the PHP scripting language, a MySQL database, client-side JavaScript, XML and Microsoft Virtual Earth API.

This system has the ability to display transit vehicles locations in near-real-time on a map and offers user and operator interactive querying on a specific bus or route. In addition, it allows the operator to monitor and measure the vehicle fleet so as to improve the transit services provided.

II TRANSIT SYSTEM'S RELIABILITY INDICATORS

Improving the reliability of services is one of the main objectives of transit agencies. Many performance indicators have been developed to assess transit performance, the choice of which indicator depending on the frequency of the service. For high-frequency routes (a vehicle at least every ten minutes) these include Excess Waiting Time (*EWT*) [2], Headway Regularity Index (*R*)[3], Headway Reliability (*RH*)[4] and Travel Time Reliability (*RT*)[4]. On high frequency routes passengers are more concerned with regularity, whereas for low frequency their concern is more with punctuality.

EWT [2] is defined as "the measure of the additional wait experienced by passengers due to irregular spacing of buses or those that failed to run". EWT can be calculated by subtracting scheduled waiting time (SWT) from average waiting time (AWT) i.e.

$$EWT = AWT - SWT \qquad (1)$$

The term headway is used for the time interval between successive vehicles on the same route and in the same direction as they pass a particular point on that route [5].

The headway regularity index is a reliability performance indicator for buses at a stop, route, or system level [3]. Service regularity is measured by comparing the actual with the scheduled headway. A high headway index (R) indicates a regular service whereas low numbers indicate headway irregularities.

$$R = 1 - 2\sum_{r=1}^{n} \frac{r(h_r - H)}{n * H} \qquad (2)$$

where:
r rank of headway (1..n)
n total number of headway measures
hr series of headways
H mean headway

When the headway measures are equal for n observations the headway regularity index will be 1. In this paper the headway regularity index was calculated for one bus route in both directions.

Many factors such as traffic conditions, route characteristics, passenger characteristics, and operational conditions contribute to bus unreliability. The term reliability can be defined as "the ability of the service to provide consistent service over a period of time" [5]. In this paper two types of bus reliability are measured, travel time reliability and headway reliability.

Travel time reliability measures the variability in bus journey time for a specific bus route within a specific time interval at a specific level of service [4]. The travel time reliability is defined as the mean over standard deviation of travel time.

$$RT = \frac{\mu_t}{\sigma_t} \qquad (3)$$

The higher value of *RT* indicates a good reliability.

Maintaining the scheduled headways by keeping regular spacing between buses will minimise the average passenger wait time and eliminates buses bunching. Bunching of buses happens in the absence of service during the scheduled time causing high passenger demand for the next bus. Headway Reliability is another proposed reliability indicator; it is defined as the standard deviation over mean headway:

$$RH = \frac{\sigma_t}{\mu_t} \qquad (4)$$

Smaller values of *RH* indicate better headway reliability.

III Tram and Bus Tracker

Tram and Bus Tracker (www.bustracking.co.uk) is a joint project between NUIM and Blackpool Transport that uses various reliability measures to visualize the behaviour of vehicles in ways to allow the operator to better assess and improve the quality of service. The system uses off-the-shelf GPS/GPRS integrated units programmed to transmit location at regular intervals (45 seconds approximately) while the vehicle is in motion. The data is stored on a server and can be displayed through a standard web browser to show views representing current locations of vehicles in close-to-real-time. The system displays real time locations of buses pictorially, textually and, using the facilities provided by the Microsoft Virtual Earth API, with 2D and 3D maps(figure 1).

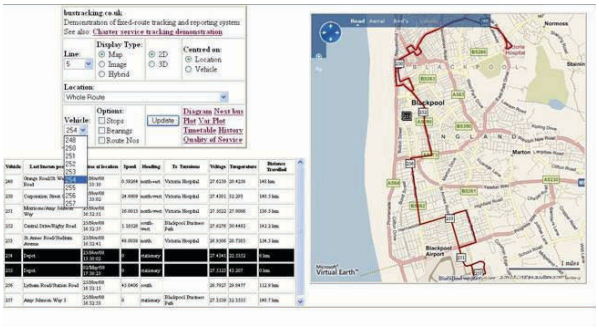

Fig (1) The public interface showing updating textual display plus moving locations on Microsoft Virtual Earth.

In order to improve services, as well as providing real-time information, this system builds up an archive of data that can be analysed and mined for information that can show behaviour of the transport system over time, indicating problems such as vehicle bunching and delays due to congestion. In addition, to qualify for public subsidies, operators must report Quality of Service metrics to government. These are usually calculated manually but the existence of a full archive of data gives the potential for automation.

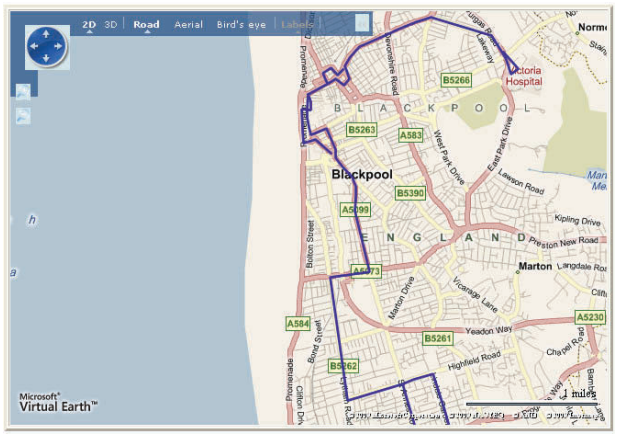

Fig (2) Route 5 in Blackpool city

IV. Blackpool Route 5

The City of Blackpool, UK lies along the coast of the Irish Sea. It has a population of 142,900, making it the fourth-largest settlement in North West England. The bus services in the city are operated by Blackpool Transport Services. For the purpose of demonstrating the analysis and evaluation of bus services in Blackpool, Line 5, a high frequency route, was selected to be a test case. This bus route contains 73 bus stops in both directions, 14 of which are timing-points where

departure times are quoted in the public timetable. Figure 2 shows Line 5 in Blackpool.

V. IMPLEMENTATION

Excess Waiting Time (EWT) is a standard metric used to measure the quality of service on high-frequency public transport. This indicator is a key performance indicator since it denotes how much time passengers had actually to wait in excess of what they would have expected if the service were perfect. EWT is calculated by subtracting Scheduled Waiting Time (SWT) from Average Waiting Time (AWT) and it is this which is used as the measure of reliability. The greater the EWT, the less reliable is the service [2]. EWT can be calculated on a daily, weekly or monthly basis. Figure 3 shows EWT values in a certain day for all bus stops along route 5 in Blackpool.

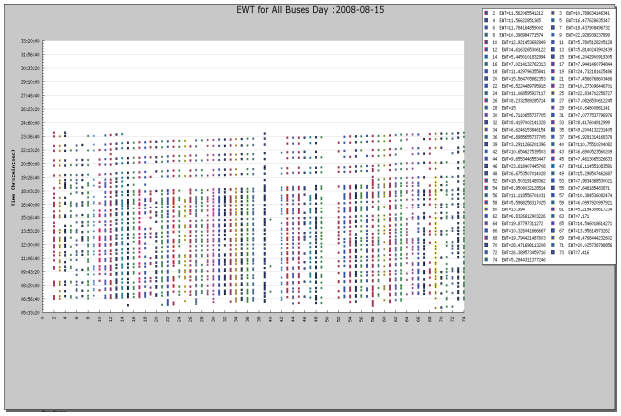

Fig (3) EWT values for different bus stops in route 5

Buses bunching and headway overlapping can easily be noticed. The headway regularity index indicator was calculated to measure the quality of service; the result is shown in figure 4. High index numbers indicate a regular service whereas low numbers indicate headway irregularities.

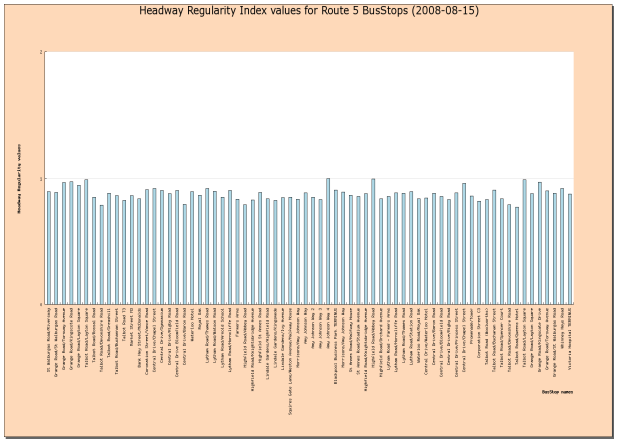

Fig (4) Headway regularity index values

It shows that there is a trend towards higher headway regularity for all bus stops on the day the headway index was calculated. Starting from the bus terminus, travel time reliability was measured for each bus stop in the same direction; figure 5 shows different bus stops with travel time reliability measure.

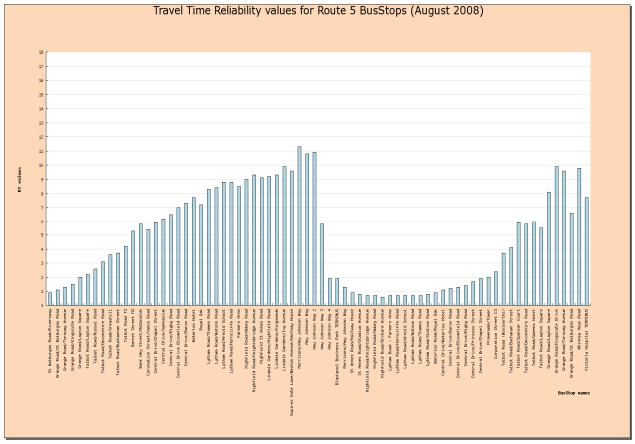

Fig (5) Bus stops with travel time reliability measure.

Bus stops located on the south direction have higher travel time reliability than stops on the north, which means that they have a more reliable travel time.

For headway reliability, a smaller values indicates better reliability. Headway reliability values seem to be high on the second segment of the route and tend to be lower before the end of the route (figure 6).

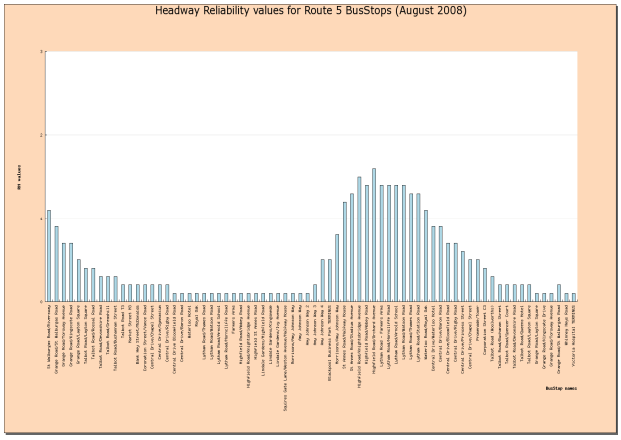

Fig (6) Bus stops with headway reliability measures

VI CONCLUSION AND FUTURE WORK

Tram and Bus Tracker is adynamic web application system with an intuitive interface and the ability to measure transit services' reliability. The system can be useful to users (travellers) and the operators in that, as well as providing transit information in close to real-time, it also provides tools to analyse performance and see where improvements are needed. The system architecture can be developed to be applicable to different transit services or regions.

VII ACKNOWLEDGEMENTS

Thanks are due to Blackpool Transport Ltd for facilitating this project and particularly to Oliver Howarth for his comments and feedback. One author is supported by a PhD studentship from the Libyan Ministry of Education.

REFERENCES

[1] D. S. Maclean, and D.J. Dailey, "*Busview: A Graphical Transit Information System*", **Proceedings of the IEEE Conference on Intelligent Transportation Systems, Oakland (CA) USA, August 25-29, 2001**

[2] *"Performance Information London Bus Services Ltd."* **London Bus Quality of Service Indicators, London, Fourth Quarter (2006/2007)**

[3] M. Hofman, and M O'Mahony, "*The Impact of Advers Weather Conditions on Urban Bus Performance Measures*", **Proceedings of the 8th International IEEE Conference on Intelligent Transportation Systems, Vienna Austria, September 13-16, 2005**

[4] *R.Liu, and S. Sinha, "Modelling Urban Bus Service and Passenger Reliability*", **Institute for Transport Studies, University of Leeds**

[5] S.*Zolfaghari, M. Y.Jaber and N. Azizi, "A Multi-Attribute Performance Measurement Model for Advanced Public Transit Systems* "**,Journal of Intelligent Transportation Systems,7:3, 295-314, July 01 2002**

Section 1C

SIGNAL PROCESSING

Digital Audio Watermarking by Magnitude Modification of Frequency Components Using the CSPE Algorithm

Jian Wang[#1], Ron Healy [#2], Joseph Timoney [#3]

[#]*Computer Science Department,*
National University of Ireland, Maynooth, Co. Kildare, Ireland
[1]jwang@cs.nuim.ie
[2]ronhealyx@gmail.com
[3]jtimoney@cs.nuim.ie

ABSTRACT:

In this paper we describe a process whereby the magnitude of either one or two frequency components of a signal is modified in order that it may be used to encode a hidden message within a signal in such a way as the casual observer would have no way of noticing the presence of a hidden message. Previous work has used filtering and signal addition to achieve the same goals. The current work improves on this by using a recent super-resolution component-identification technique to isolate the components to modify, limiting the impact on the quality of the signal.

Keywords: *Signal processing, digital audio watermarking, data hiding, Steganography*

1.0 INTRODUCTION

The concept of *Steganography,* defined as "*the art or practice of concealing a message, image, or file within another message, image, or file*" [1] is not new. Steganography may be combined with *Cryptography* in order to make message data more secure even if the presence of the message is discovered. Digital watermarking of audio and video is a form of Steganography, in that the audio/video can be used to 'hide' the presence of other information.

In recent years there has been a marked increase in research in the area of digital watermarking. This has been driven, in part, by the needs of the Entertainment Industry to find means for protecting, tracking or identifying intellectual property such as photographs, music and movies. The SDMI (The *Secure Digital Music Initiative*, a group consisting of more than 200 companies in the fields of I.T., Music and Entertainment, Consumer Electronics, Security and Internet Service Providers) challenge at the turn of the century, with regard to digital music, contributed to much investigation into the area of digital watermarking over the intervening years. Eventually, the SDMI folded, claiming that it was awaiting developments in technology before implementing digital rights management technologies. One of the reasons identified for the SDMI's failure was that the technologies then available were insufficient to achieve the aim of completely hiding an added watermark from those expert or talented listeners described as 'golden ears'. This meant that there was no way of preventing detection and ultimate removal of the watermark. The watermarking technology that the SDMI purported to recommend to the Industry was broken almost immediately [2].

There have been a number of alternative propositions for hiding data in cover signals and most are successful to a certain extent or in a given context. A good overview of the theories in this area can be found in [3]. The basic premise of watermarking schemes is that the information to be watermarked w is added or embedded in the cover or host signal s to produce a watermarked signal s'

$$s + w = s' \tag{1}$$

This paper proposes a technique for hiding data in cover audio signals, specifically music or spoken word, by the identification and modification of the magnitude of frequency components in the cover signal itself.

In part, the work is inspired by [4], a technique designed for covert communications across a radio channel for military applications, and follows on from an earlier work which used the addition of multiple frequency components to achieve a similar aim [5]. In [5] it was proposed that the message to be embedded was to be separately generated. This was then added to the host or cover audio. In this paper, however, we instead propose that the host or cover is

itself modified in a controlled manner, rather than having potentially destructive and/or detectable content added to it. In both this paper and [5], the primary concern is for inaudibility of the watermark and blind or semi-blind detection, meaning that the decoder does not have any knowledge of either the content of the cover audio or of the embedded watermark prior to decoding. This restriction is guided by the intended use of the technology.

In this paper, we present the results of experiments performed to recover a bit sequence which was embedded in a synthesised cover audio signal consisting of randomly generated components. The decoding was performed without any reference to the original unwatermarked signal or the watermark itself.

2.0 METHOD

A component value is first chosen which is used as the basis for calculating which components to modify to hide the message. The initial component choice may be dependent on various factors, such as the type of audio used as host/cover. For example, human speech generally consists of lower frequency components – and less of them – than a modern Rock or Pop song so hiding data in a recording of speech would naturally limit the component of choice. However, even in such a limited range, there are still thousands of values to choose from.

The value of the chosen component becomes, in effect, a private key and this value is needed in order to decode the watermark – assuming that the *presence* of the watermark has previously been detected. This adds to the security of the technique when used in an environment where *security of the content* of the hidden message is an issue.

The signal intended as the cover or host audio is segmented into frames of uniform length and the frame is then analysed using 'Complex Spectral Phase Estimation' (CSPE) techniques [6] to identify the presence and magnitude of its inherent components. Previously, FFT techniques have been used to approximate the relative strengths of inherent components. This would be inadequate for this project, as exact measurement of components using the FFT is only possible if the component is aligned with an analysis bin. This is an unlikely occurrence in a real-world signal such as recorded music or speech. Therefore, the FFT is an inadequate solution to the problem of identifying exactly the components present.

2.1 CSPE INTRODUCTION AND DESCRIPTION

The CSPE algorithm was introduced as a method to accurately estimate the frequency of components that exist within a short time frame. It was also designed to be computationally efficient. It is actually related in some aspects to the cross-spectrogram technique of [7]. The principal of CSPE algorithm can be described as follows:

An FFT analysis is performed twice: firstly on the signal of interest and the second time upon the same signal but shifted in time by one sample. Then, by multiplying the sample-shifted FFT spectrum with the complex conjugate of the initial FFT spectrum, a frequency dependent function is formed from which the exact values of the frequency components it contains can be detected. The procedure of the CSPE algorithm is depicted in block diagram form in Figure 1.

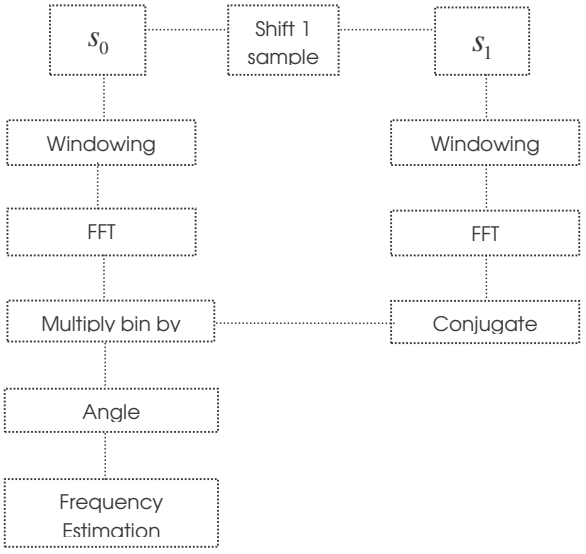

Fig. 1: The flow diagram of CSPE

Mathematically, the algorithm can be described as follows. Assume a real signal s_0, and a one-sample shifted version of this signal s_1. Say that its frequency is $\beta = q + \delta$ where q is an integer and δ is a fractional number. If b is an initial phase, w_n is the window function used in the FFT, F_{ws_0} is the windowed Fourier transform of s_0, and F_{ws1} is the windowed Fourier transform of s_1, then, from [6], we find

$$D = e^{\frac{j2\pi\beta}{N}} \tag{2}$$

The frequency dependent CSPE function can be written as

$$CSPE_w = F_{ws_0} F^*_{ws_1} = (\frac{a}{2})^2 \begin{bmatrix} D^* \left\| F_w(D^n) \right\|^2 \\ +2\mathrm{Re}\left\{ e^{j2b} D F_w(D^n) \otimes F_w^*(D^{-n}) \right\} \\ +D \left\| F_w(D^{-n}) \right\|^2 \end{bmatrix} \tag{3}$$

The windowed transform requires multiplication of the time domain data by the analysis widow, and thus the resulting transform is the convolution of the transform of the window function, w_f, with the transform of a complex sinusoid. Since the transform of a complex sinusoid is a pair of delta functions in the positive and negative frequency positions, the result of the convolution is merely a frequency-translated copy of w_f centred at $+\beta$ and $-\beta$. Consequently, with a standard windowing function, the $\|F_w(D^n)\|$ term is only considerable when $k \approx \beta$ and it decays rapidly when k is far from β. Therefore, the analysis window must be chosen carefully so that it decays rapidly to minimize any spectral leakage into adjacent bins. If this is so it will render the interference terms, i.e. the second and third terms, to be negligible in Eq.(3). Thus, the CSPE for the positive frequencies gives:

$$CSPE_w \approx \frac{a^2}{4} \left\| F_w(D^n) \right\|^2 D^{-1} \tag{4}$$

From Eq. (4). we find the CSPE frequency estimate

$$\begin{aligned} f_{CSPE_w} &= \frac{-N\angle(CSPE_w)}{2\pi} \\ &= \frac{-N\angle\left(\frac{a^2}{4} \left\| F_w(D^n) \right\|^2 D^{-1} \right)}{2\pi} \\ &= \frac{-N\angle(\frac{a^2}{4} \left\| F_w(D^n) \right\|^2 e^{-j\frac{2\pi}{N}\beta})}{2\pi} = \frac{-N(-\frac{2\pi}{N}\beta)}{2\pi} = \beta \end{aligned} \tag{5}$$

The frequency dependent function as illustrated in Equation (4) produces a graph with a staircase-like appearance where the flat parts of the graph indicate the exact frequencies of the components. The width of the flat parts is dependent on the main-lobe width of window function used to select the signal before FFT processing. An example of the output of the CSPE algorithm is shown in Figure 2. Consider the signal S_1 which contains components with frequency values (in Hz) of 17, 293.5, 313.9, 204.6, 153.7, 378 and 423. The sampling frequency is 1024 HZ. A frame of 1024 samples in length is windowed using a Blackman window and is padded using 1024 zeros. The frequency dependent CSPE function is computed as per Equation (5). As shown in Figure 2, each component can be calculated and these are identified with an arrow in the graph. The largest error among all the estimates of the components frequencies is approximately 0.15 Hz.

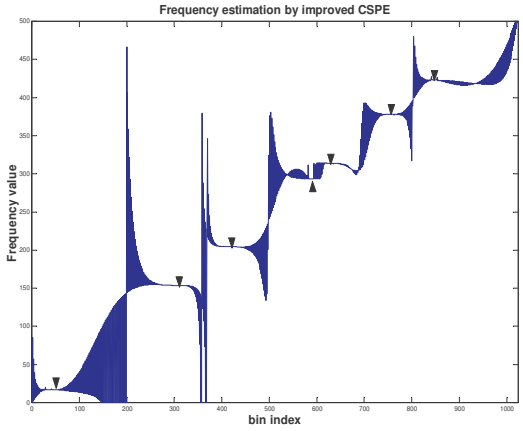

Fig. 2 Frequency estimation of S_1 by CSPE

Notice too in Figure 2 that at the flat sections in the graph of the CSPE result, the width of flat sections where the arrows point are related to the width of the window's main-lobe in the frequency domain.

In addition, with CSPE, we can get the amplitude and phase of the kth frequency component using the following equations, where $W(\omega\text{-}fcspe(k))$ is the Fourier Transform of window function which has been shifted to $fcspe(k)$ in frequency domain.

$$Amp_k = \left\| \frac{2 * F_{ws_0}}{W(\omega - fcspe(k))} \right\| \tag{6}$$

$$Phase_k = \angle\left(\frac{2 * F_{ws_0}}{W(\omega - fcspe(k))} \right) \tag{7}$$

2.2 EXPERIMENTAL EVALUATION OF CSPE

Experiments were designed to evaluate the performance of the CSPE algorithm in correctly identifying frequency components within a multiple-component signal. In each set of experiments, a total of 500 signals with Sampling Frequency 44100 Hz and containing components across the

human hearing range of 100 Hz to 20,000 Hz were generated. Each signal contained many equally spaced frequency components. The number of components in each generated signal was not consistent. For each individual signal, we have a unique, randomly-generated step constant which defines the space between two neighbouring frequency components of the signal. 500 step constants were created range from 169 Hz to 668 Hz for 500 signals. Equation (8) and (9) were designed to assess CSPE accuracy in frequency estimation.

Denoting $Freq_{estk}$ as the value of estimated Frequency components of signal k ; $Freq_{orgk}$ as the value of original Frequency components of signal k; M_k as the number of frequency components contained in Signal k; *FreqError* as the frequency estimation error between $Freq_{est}$ and $Freq_{org}$ of signal k; $MeanError_{cspe}$ as the mean error of the CSPE frequency estimation over N signals, for this experiment, N = 500, M changes with signal step constant.

$$FreqError_k = \frac{\sum_{i=1}^{M_k} \left| Freq_{estk}(i) - Freq_{orgk}(i) \right|}{M_k} \tag{8}$$

The frequency estimation error of each signal as computed using Equation (8) is shown as Figure 3:

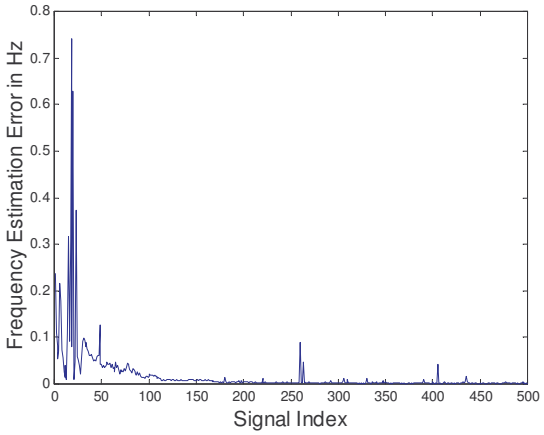

Fig. 3 CSPE Estimation Error for Each Signal

The distribution of frequency estimation error (*FreqError)* is shown in Figure 4.

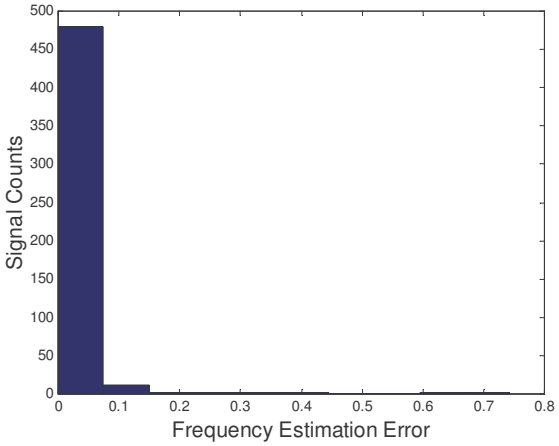

Fig. 4 The distribution of Frequency Estimation Error

The mean error is calculated according to Equation （9）

$$MeanError_{cspe} = \frac{\sum_{k=1}^{N} FreqError_k}{N} \tag{9}$$

By data analysis, we note that 97.8% of signals analysed using the CSPE algorithm resulted in a $FreqError$ value of less than 0.1 Hz, and the $MeanError_{cspe}$ is 0.0174 Hz, meaning that the algorithm identified the component to within 0.1 Hz in almost all cases. We conclude from these results that the CSPE is extremely accurate in frequency estimation for signals containing constant frequency signal components. With accurate estimation of the frequency, the amplitude and phase can be estimated using Eqs. (6) and (7).

3.0 MODIFYING COMPONENTS

Once the user-defined component has been identified in the signal by the CSPE algorithm, its magnitude is then calculated. It is then a matter of modifying the magnitude of this component, weighting it against a second value from within the signal, in order to represent a single bit ‘1’ or ‘0’.

We may choose to weight the user-defined components against the average power of the frame in which the bit is to be embedded. This was the procedure followed in both [4] and [5]. We may also choose to modify the user-defined component against a second component. This method has its advantages and disadvantages but it is not our intention to detail the process in this paper. However, using a second component from within the signal as a comparison against which the first user-defined component was weighted, led to some problems in that, while the CSPE algorithm is very

accurate in identifying the components in a synthesised signal with little variation, this may not be the same type of component make-up as would be encountered in real world signals, such as audio and speech.

3.1 DYNAMICALLY SELECTING COMPONENTS

We decided to make the process of choosing the component(s) to modify as flexible as possible by making this a dynamically chosen pair of values, dependent on the user-defined value but also dependent on the signal under consideration and reliant on the ability of the CSPE algorithm to detect and identify the components that the watermarking process would use. We defined the components which would be chosen for modification as being the nearest components above and below the user-defined value by more than a calculated threshold as illustrated in Equation (10) where *compA* is the highest CSPE-detected frequency component that is lower than the user-defined component *u*, by more than the threshold *k* while *compB* is a CSPE-detected frequency component above the user-defined component by the same threshold amount

$$(compA < (u - k)) < u < (compB > (u + k)) \quad (10)$$

What is interesting to note, using the formula in Equation (10) for defining which component we need to modify, and in which frames of the cover signal, is that only approximately half of the frames will require any modification. This is because the relationship between the values of the two chosen components in any given frame may already fit the criteria used for representing a '1' or a '0'. In this case they would not have to be modified in any way. This consideration makes this method far more favourable than [5],

When modifying the amplitude of a frequency component, care must be taken to ensure that we do not introduce any noticeable artefact which would result in an impact on sound quality. Similarly, we must ensure that the alteration we make to the magnitude of the chosen component is not so great as to have a negative impact on the timbre of the original signal.

We define a set of rules that would lead to the modification of only one of the components (*compA* or *compB*) in approximately half the frames. This is achieved by setting the rule (Amp refers to Amplitude)

If *bit*=1 let Amp(*compA)* > Amp (*compB*) + *margin*

If *bit*=0 let Amp (*compB*) > Amp(*compA)* + *margin*

The system would then compare the magnitude of both components (*compA* and *compB*) in any given frame before deciding if any modification would be required in order to satisfy these criteria, depending on the bit to be embedded and the magnitudes of the two components in that particular frame. If they are already in the correct relationship, no modification is required. If, however, they are not in the correct relationship, we must modify at least one of them. The decision to modify a component leads another question. Let us assume that the magnitude of *compA* is lower than that of *compB,* in a frame in which it needs to be of a higher magnitude to represent a '1' bit.

3.2 MODIFYING THE MAGNITUDE

As mentioned in Section 2.0.2, the CSPE algorithm can be used to accurately identify a component within a signal, and then to calculate its phase and amplitude. In order to increase the magnitude of a particular frequency component in the cover signal $S(t)$, we add a component at a defined magnitude and matched to the phase of the component it is being combined with, as illustrated in Equation (11):

$$S(t)= S(t)+(rAmp-lAmp+threshold)cos(2\pi(compA)t+lp) \quad (11)$$

where *rAmp, lAmp, compA* and lp define amplitude of *compB*, amplitude of *compA*, Frequency of *compA*, phase of *compA*.

Similarly, if we decide to reduce the magnitude of a component $S(t)$ so that it satisfies the requirements for embedding a '1' bit, we do this by reducing the magnitude of the component to the right of the user-defined component value, by adding in a component that is 180^{o} out of phase with the original component in the signal as follows:

$$S(t)= S(t)+(rAmp-lAmp+threshold)cos(2\pi(compB)t+ \pi-rp) \quad (12)$$

where *compB* and *rp* define amplitude and phase of *compB.*

4.0 DECODING

In order to process candidate audio for detection and decoding of a potential embedded watermarked message, the system must first be provided with the user-defined

value used as a basis for calculating the embedding values, along with the rules that define a '1' bit and a '0' bit. The candidate audio signal is then segmented into frames using the same frame size as was used for embedding. The system calculates the magnitude of the embedded component, and performs a simple comparison. From this comparison the watermarked bit sequence can be recreated. It would be a comparatively simple matter of applying the CSPE algorithm to identify the two components above and below the user-defined value by more than a pre-defined threshold. These two components would then have their magnitude compared and a '1' or a '0' bit would be determined according to the rules used in their embedding.

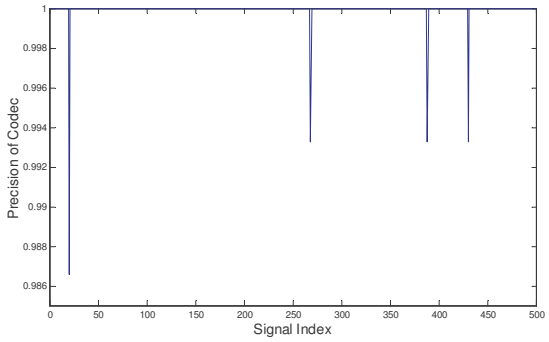

Fig. 5 Precision of Codec for each Signal

5.0 EVALUATION OF WATERMARKING SCHEME

A series of experiments was carried out to evaluate the performance of this codec, based on the same 500 signals as introduced in Section 2.2. For each signal, a randomly generated binary bit-sequence of length 150 was embedded by means of modification of the magnitude of components as described in Section 3. The system then decoded the modified signal in order to detect the watermarked code.

The difference between these two code sequences can be calculated in terms of equation below, where *DCode* denotes code sequence obtained in decode side, *ECode* denotes code sequence embedded in the signal. *CodecPrecision* denotes the precision of the decode process with code length L for signal k, *MeanPrecision* denotes average error of the decode process over N signals. In this experiment, L and N are set to 150 and 500 respectively. The results of this experiment are depicted in Figure 5.

$$CodecPrecision_k = \frac{L - \sum_{i=1}^{L} |DCode(i) - ECode(i)|}{L} \quad (12)$$

$$MeanPrecision = \frac{\sum_{k=1}^{N} (CodecPrecision_k)}{N} \quad (13)$$

The distribution of *CodecPrecision* is shown in Figure 6.

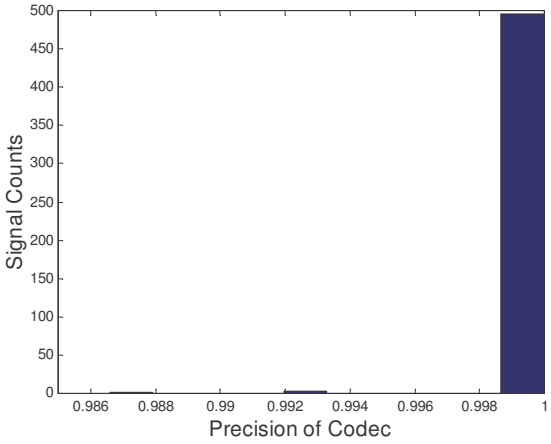

Fig. 6 The distribution of Precision of Codec

From the experiment results, it can be seen that 99.2% of signals produce a *CodecPrecision* value of 1 (100%). This means that, from 500 randomly generated signals with multiple components of different frequency spacing, watermarked with a binary bit-sequence of 150 bits, 99.2% of these signals were decoded to the *exact* 150 bit sequence. Only 0.8% (a total of 4) of the 500 signals was not decoded perfectly. Of those not *perfectly* decoded, the bit sequence recovery rate was above 98.66%. The *MeanPrecision* computed using Equation (13) is 0.9999 (99.99%). Therefore, the performance of this codec is almost perfect for this experiment with the synthesised signals.

Furthermore, the decode experiment in this case represented a single iteration of a bit sequence over the length of a signal. Given that any real world use of such a scheme would enable a bit sequence to be embedded repeatedly in a cover signal, it would be possible to increase the effectiveness of the decode process by, for example, repeated decoding and using the *mode* of the results.

6.0 CONCLUSION

We have proposed an application that utilises the super-resolution capabilities of the CSPE algorithm to accurately identify individual components of an audio signal, calculate their magnitudes and then alter magnitude as appropriate to represent a particular bit value.

Experimental tests using 500 synthesised signals incorporating multiple randomly generated components embedded with a bit sequence of length 150 showed an accuracy of completely perfect decoding of 99.2% with an average overall accuracy of 99.999%.

Future work will determine how to calculate and set the magnitude so signal watermarking is perceptually invisible, by evaluating whether to modify the component to the left or right of the user-defined frequency value, or both.

Also, the impact of accidental and deliberate attacks on the watermarked signal will be evaluated.

7.0 REFERENCE

[1] *Merriam-Webster Online Dictionary*.

http://www.merriam-webster.com/dictionary/steganography

[2] S. A. Craver, M. Wu, and B. Liu, "Reading between the lines: Lessons from the SDMI challenge," in *10th USENIX Security Symposium.* Washington, DC, 2001.

[3] Moulin, P., & Koetter, R., "Data-Hiding Codes", *Proc. Of the IEEE, Vol. 93, No. 12, Dec. 2005.*

[4] Gopalan, K., et al, 'Covert Speech Communication Via Cover Speech By Tone Insertion', *Proc. of the 2003 IEEE Aerospace Conference*, Big Sky, MT, March 2003.

[5] Healy, R. & Timoney, J. 'Digital Audio Watermarking with Semi-Blind Detection For In-Car Music Identification' *Audio Engineering Society 36th International Conference, Michigan, USA. June 2-4, 2009* (in press)

[6] K. M. Short and R. A. Garcia, "Signal Analysis using the Complex Spectral Phase Evolution (CSPE) Method", *Audio Engineering Society 120th Convention, May 2006, Paris, France*

[7] Douglas Nelson, "Cross Spectral Methods for Processing Speech", *Journal of the Acoustic Society of America, vol. 110, No.5, pt.1, Nov.2001, pp.2575-2592*

[8] The online *Webster* Dictionary. http://www.webster-dictionary.net/definition/interpolation

USING CONVOLUTIVE NON-NEGATIVE MATRIX FACTORIZATION ALGORITHM TO PERFORM ACOUSTIC ECHO CANCELLATION

XIN ZHOU, YE LIANG, NIALL CAHILL, ROBERT LAWLOR

Department of Electronic Engineering, National University of Ireland Maynooth, Maynooth, Co. Kildare, Ireland.
Email: zhou.xin@nuim.ie, liang.ye@nuim.ie, ncahill@eeng.nuim.ie, rlawlor@eeng.nuim.ie

In this paper Convolutive Non-negative Matrix Factorization (NMF) is used to perform acoustic echo cancellation. This modified version of NMF employs the idea of convolutive basis decomposition. CNMF makes use of a single basis function which spans the pattern length. This version of NMF allows us to reveal the underlying patterns which cross multiple columns as single bases. We use this idea, realize it in the simulation environment and implement it to perform AEC. This approach is evaluated through experiments on simulated data, from the results we find acoustic echo can be reduced using this approach.

1. INTRODUCTION

In recent years the use of hands free communication has increased significantly. A problem with such hands free communication is the occurrence of acoustic echo. Acoustic echo is an important issue for hands free communication. Acoustic echo exists in any communications scenario where there is a speaker and a microphone, e.g. hands-free car phone, hands-free conference phone, etc. Acoustic echo arises when sound from a loudspeaker is picked up by the microphone in the same room. When the far-end user speaks to the microphone, the microphone of the near-end user can catch the output speech from the near-end speaker and retransmit back to the far-end user side. Usually the loudspeaker-enclosure-microphone coupling (LEM) is presented as a time invariant linear FIR filter *h(t)*, however as a small changes in the enclosure environment can greatly affect the LEM filter, such as open or close a door, it is necessary to use an adaptive LEM filter to model the echo path over time. Call the far-end participant voice signal *x(t)*, the near-end speech signal *v(t)*, and the noise *n(t)*, then the echo signal *y(t)* can be stated as:

$$y(t) = n(t) + v(t) + \sum_{i=0}^{N-1} h(i)x(t-i) \qquad (1)$$

Here *N* is the length of the impulse response and *t* is the time index.

Most existing AEC techniques use Least Mean Square (LMS) or Normalized LMS (NLMS) [1] to estimate and update the LEM filter coefficients. It works by calculating an estimate of the acoustic echo based on the reference speech and the incoming captured speech signal. This acoustic echo estimate is then subtracted from the near-end speech before being sent to the far-end user.

There exist some problems to this approach: first of all, long estimation filters are needed for a LEM filter. The resulting long impulse responses can lead to convergence issues and large computation load. Secondly, the adaptive algorithm may diverge if the reference signal contains noise. Thirdly, changes in the LEM filter may lead to a period of misadjustment. Finally, the adaptive algorithm may diverge away from suitable FIR coefficients when both near-end and far-end users speak simultaneously [2].

In order to overcome these problems, a number of techniques have been developed [1]. However, the acoustic echo problem has not yet to be solved completely. In this paper an alternative approach to AEC is presented. A monaural sound source separation (SSS) technique based on Convolutive non-negative matrix factorisation (CNMF) is employed to perform AEC. It is shown that this approach can lead to significant echo reduction particularly during doubletalk.

The structure of the paper is as follows. In section 2 Monaural Sound Source Separation is described, sections 3 and 4 introduce the theory of NMF and CNMF. In section 5 we describe the experiments making use of CNMF to perform AEC followed by results and discussion in sections 6.

2. MONAURAL SOUND SEPARATION

Monaural sound source separation is a technique that attempts to separate any number of sound sources with only one mixture of the sources. As only one mixture

exists no spatial information of the sources is available. This means that blind source separation techniques such as Independent Component Analysis (ICA) or spatial filtering based on sensor arrays cannot be used as they require multiple sensors. Similarly, undetermined blind source separation techniques based on sparsity and spatial cues which require at least two mixtures such as DUET and ADRess are also not applicable [15].

In many situations, such as telecommunications and audio retrieval, only a monaural (one microphone) solution is available. The use of prior information about the source signals makes the monaural sound source separation possible. The idea of this technique is to train bases or models using training data for each speaker beforehand and then match these models with a mixture containing these speakers. Within this framework, many different approaches have been developed, including non-negative matrix factorization (NMF) [3] or sparse NMF (SNMF) [4], markov models [5], local NMF [6] bases, and in [7] time domain bases were trained using ICA and then matched to the mixture using a maximum likelihood technique.

In this paper we present the application of such an approach to the AEC problem. We made use of Convolutive NMF to perform both training and matching in the audio spectrogram.

3. THE ORIGINAL NONNEGATIVE MATRIX FACTORIZATION

Non-Negative Matrix Factorization (NMF) is a mathematical technique for linear non-negative data [8]. The non-negative constraint leads to a part-based decomposed representation because it allows only additive, not subtractive, combinations of the original data. The decomposition gives a more intuitive representation of the underlying data [8]. The basic idea of it is approximating a data set $V \in \mathbb{R}_{\geq 0}^{M \times N}$ as a multiplication of two matrices $W \in \mathbb{R}_{\geq 0}^{M \times R}$ and $H \in \mathbb{R}_{\geq 0}^{R \times N}$:

$$V \approx W \cdot H. \quad (2)$$

The non-negative constraint forces the factors W and H to be non-negative, i.e., all elements must be equal to or greater than zero.

By changing R the degree of the approximation can be varied. Big R leads to decreasing the reconstruction error and small R increasing it.

The next step is to estimate W and H which is an optimization problem. Lee and Seung [9] defined two approaches for estimating W and H, based on different cost functions. A generalized version of the Kullback-Leibler divergence is the cost function used in [2]:

$$D(V \| W,H) = \| V \odot \log(\frac{V}{W \cdot H}) - V + W \cdot H \|_{Fro} \quad (3)$$

Where $\odot$ is the Hadamard product. The purpose of this optimization is to minimize this cost function with respect to W and H with the constraint of non-negativity. The following update rules for calculating W and H are derived from equation (3) [9]:

$$H = H \odot \frac{W^T \cdot \left\lfloor \frac{V}{WH} \right\rfloor}{W^T \cdot 1}, W = W \odot \frac{\left\lfloor \frac{V}{WH} \right\rfloor \cdot H^T}{1 \cdot H^T} \quad (4)$$

The iterative procedure is halted when the cost function D reaches a per-defined threshold.

The matrices H and W express different aspects of the factorization: the columns of W contain the basis for the data and the rows of H contain the contribution of each basis to the data over time. When W and H are multiplied together, the data is reconstructed with an error. The magnitude of this error depends on R and the data.

4. CONVOLUTIVE NMF

The following theory of CNMF utilizes work from [10].

The original NMF represents regularly repeating patterns which span multiple columns of V matrix using a number of different bases to describe the entire sequence. CNMF uses a single basis function that spans the pattern length. This kind of situation can be very frequently found when analyzing audio signals. This version of NMF allows us to reveal the underlying patterns which cross multiple columns as single bases. By doing a series of experiments, we can find that this approach leads to a significant reduction in the level of acoustic echo.

As described in section 3 NMF using a matrix product $V \approx W \cdot H$ to reconstruct the estimated data matrix V, in the convolutive Non-Negative Matrix Factorization they extend this expression to:

$$V \approx \sum_{t=0}^{T-1} W(t) \cdot \overset{t\rightarrow}{H} \quad (5)$$

where $V \in R_{\geq 0}^{M \times N}$ is the input data matrix, $W(t) \in R_{\geq 0}^{M \times R}$ is the training bases, and $H \in R_{\geq 0}^{R \times N}$ is the weights. The $\overset{i\rightarrow}{(\cdot)}$ operator is a shift operator that moves the columns of its argument by i elements to the right, and conversely $\overset{\leftarrow i}{(\cdot)}$ shifts to the left. The columns that are shifted in from outside the matrix are set to zero.

Equation 5 is a summation of convolution operations between corresponding elements from a set of two-dimensional bases *W* and a set of weights *H*.

The set of i^{th} columns of *W(t)* defines a two-dimensional structure. This matrix will be shifted and scaled by convolution across the axis of *t* with the i^{th} row of *H*. The resulting reconstruction will be a summation of all the basis convolution results for each of the *R* bases [9].

The estimation of the appropriate set of matrices *W(t)* and *H* to approximate *V* is based on the framework of NMF that Lee and Seung used in [9]. In accordance to the NMF cost function, they defined the Convolutive NMF cost function as:

$$D = \| V \odot In\left(\frac{V}{\hat{V}}\right) | -V + \hat{V} \|_F \qquad (6)$$

Where $\hat{V}$ is the approximation of *V* defined as:

$$\hat{V} = \sum_{t=0}^{T-1} W(t) \cdot \overset{t\rightarrow}{H} \qquad (7)$$

They decomposed the above cost function to a series of simultaneous NMF approximations according to the linearity property, one for each value of *t*. Then they optimize the above cost function by optimizing this set of *T* NMF approximations. For each NMF approximation they updated the equivalent *W(t)* and the appropriately shifted *H*. This gives the convolutive NMF updates equations which are:

$$H = H \odot \frac{W(t)^T \cdot \left[\frac{V}{\hat{V}}\right]}{W(t)^T \cdot 1}, W(t) = W(t) \odot \frac{\left[\frac{V}{\hat{V}}\right] \cdot \overset{t\rightarrow T}{H}}{1 \cdot \overset{t\rightarrow T}{H}} \qquad (8)$$

They updated *H* and *W(t)* in every updating iteration and each *t*. Actually for each *t*, *W(t)* is updated by the corresponding NMF, but *H* is shared and shifted across all *t*'s in an iteration. Update *W(t)* and *H* for each *t* may result in a mistaken estimate of *H* with the update for *t = T −1* dominating over others. Therefore it is best to update all *W(t)* first and then assign to *H* the average of all the NMF subproblems:

$$H = \left\langle H \odot \frac{W(t)^T \cdot \left[\frac{V}{\hat{V}}\right]}{W(t)^T \cdot 1} \right\rangle, \forall t \qquad (9)$$

In terms of computational complexity this technique depends mostly on *T*. If *T = 1* then it reduces to standard NMF, otherwise it is burdened with extra matrix updates equivalent to one NMF per unit of *T*.

In this paper we utilize this idea, realize it in the Matlab simulation environment and implement it to perform the specific application which is Acoustic Echo Cancellation.

To perform monaural sound source separation with CNMF, two stages are required. First, acquire a sequence of spoken speech from each speaker, calculating a spectrogram for each sequence and performing NMF decomposition on each spectrogram separately. Then separate low rank *W* basis matrices are trained for each individual speaker. The resultant *W* matrices (one for each speaker) are then concatenated into a large *W* matrix called W_{train}. The second stage is the separation stage or a matching stage where a mixture of speech, containing known speakers, is separated into individual sources. This is achieved by performing CNMF decomposition on the speech mixture using W_{train} from the training stage. In this stage, this factorization W_{train} is updated by convolution with the *H* matrix in each iteration. This process gives the result that each individual speaker's basis matrix characterizes the mixture spectral energy depending on the contribution the speaker made to the mixture. After a prescribed number of iterations have been reached, W_{train} is separated back to the individual *W* matrices of the speakers. The resultant *V* matrix is combined by multiplying W_{train} with the corresponding portion of the *H* matrix from the separation stage.

5. EXPERIMENTS

The experiments in the paper demonstrate that the CNMF based approach to AEC can match and remove the echo with or without the presence of far-end speech in the near-end microphone signal. We use the condition of conventional AEC that the far-end speaker speech is used to excite the LEM system at the near-end user, so for this experiment we neglect the effect of noise on the overall system, neither measurement nor background noise, then divide and perform the processing in different groups.

We did the experiments using Matlab. We used pure speech from different speakers which were chosen randomly from the TIMIT database [13]. We used some speech as near-end and some as far-end, then added room response to the far-end speech to create the noise. After that we mixed these speech signals to create the mixture. Each mixture contains both near-end speaker contribution and far-end speaker contribution (here treated as noise).

We trained a *W* basis matrix for the near-end speaker using training data for each experiment. We also trained a separate specific *W* basis for use on the incoming far-end speech. The number of basis vectors *R* within *W* was set to 32 for both near-end and far-end speech bases. These bases were used to separate out the mixture spectrogram and remove the echo from the returning signal. The time base for convolution was set to 8, which means the algorithm will read in 8 frames of data, perform shift of *H* and update of *W*(*t*) 8 times in each

iteration, one NMF for each frame. This is because each frame of sound signal has only one column. As a result, to process sound signal the CNMF doesn't require extra computational load. From the experiment we found that estimating the contribution from the original mixture resulted in better results. The results of this test are listed as Output 1 in Table 1. We also performed an additional experiment to evaluate this approach when no knowledge of the local speaker is available. Speeches from other speakers were used to train generic and independent *W* basis and these bases were used to perform matching. The results of this experiment are listed as Output 2 in table 1. The third experiment was performed to compare and illustrate the benefit of having the reference signal in AEC, displayed as Output 3 of Table 1. For this experiment speaker specific bases were trained for near-end and far-end speakers without the specific reference speech provided.

We used both objective and subjective measurements to analyze the results of the experiments. In the subjective listening tests, a panel of subjects listened to the input and output speech to assess the effect of the algorithm. The objective analysis used three objective ratios based on the input and output speech to analyze the performance of the CNMF algorithm during doubletalk. Two of the three ratios were taken from a standardized set of energy ratios defined in [14]. The first is the signal to interference ratio (SIR), which measures the amount of echo still left in the returning near-end speech,

$$SIR = 10\log_{10}\left(\frac{\| s_{target} \|^2}{\| e_{interf} \|^2}\right) \qquad (10)$$

The second is signal to distortion ratio (SDR) which measures the amount of the distortion in the original signal due to the algorithm

$$SDR = 10\log_{10}\left(\frac{\| s_{target} \|^2}{\| e_{interf} + e_{artef} \|^2}\right) \qquad (11)$$

Where e_{interf} is the amount of interference energy left in the output, e_{artef} is the energy of processing artefacts left after processing and s_{target} the near-end speech. The third energy ratio is a measure of the level of echo suppression, the echo reduction loss enhancement (ERLE) defined as follows

$$ERLE = 10\log_{10}\left(\frac{E\{y^2(t)\}}{E\{e^2(t)\}}\right) \qquad (12)$$

Where *y(t)* is the echo signal and *e(t)* is the echo after processing. The first two measures were used to measure the performance on mixtures that contained both far-end and near-end speech together, and the third measure was only used to compare the level of echo reduction during the pauses in speech. The results of the SID and SDR ratios are shown in Table 1, and the results of the ERLE ratios are listed in Table 2.

a)

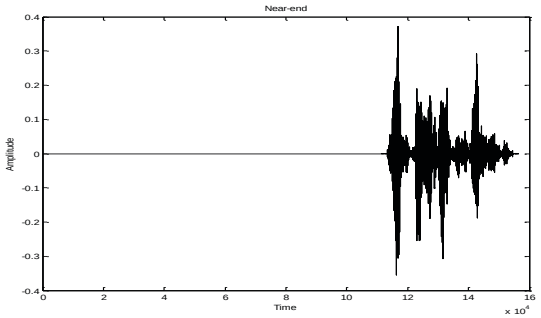

b)

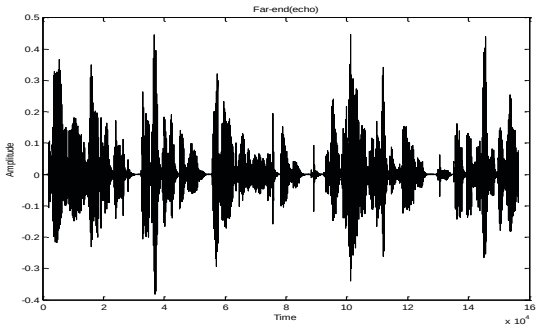

c)

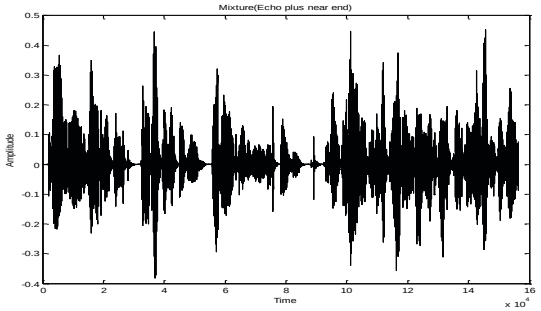

d)

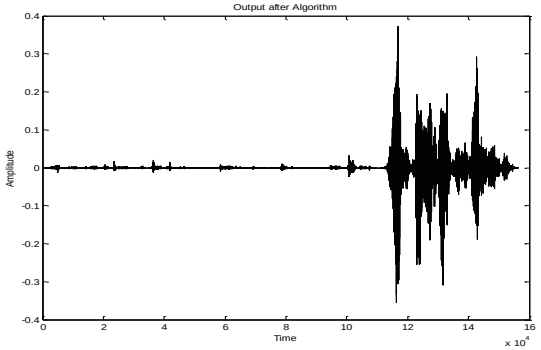

Figure 1 a) Near-end speaker with pause, b) Far-end signal (Noise), c) Mixture at near-end microphone, d) output from algorithm.

6. RESULTS AND DISCUSSION

The results of the experiments show that this approach leads to a significant reduction in the level of echo. SIR results in Table 1 show that the algorithm can achieve a significant reduction in the echo signal during doubletalk with speaker specific trained bases. The results from using the independently trained basis matrices (Output 2 Table 1) are similar as those of the experiments using speaker specific trained basis. This suggests that this approach is not speaker dependent. The Output 3 listed in Table 1 shows the results when the actual reference speech is not known. This result is not as good as previous experiments. This suggests that having the actual far-end reference signal is necessary (far-end speech) for improved overall performance.

The results listed in Table 2 show the performance of the AEC approach during pauses in the near-end speech. The results overall are quite good. However not all echo was removed because some of the local speaker basis matched some of the echo energy thus retaining it in the output.

In the subjective listening tests, three volunteers listened to the input speech and the output speech after ran of the algorithm. All of the listeners agreed that the echo was reduced significantly in the output speech. This is important for the practical application of the algorithm.

Further work on this topic includes combine features of different versions of NMF or other mathematical tools, find the optimal or best suitable algorithm for different applications such as AEC, musical separation, etc. Moreover the number of basic functions *R* for echo and near-end speech bases can be optimized. Alternatively some of the non-linear post-processing techniques used to improve LMS methods such as component zeroing could be employed to improve performance [1].

Near-end	Far-end (echo)	Input SDR dB	Input SIR dB	Output 1 SDR dB	Output 1 SIR dB	Output 2 SDR dB	Output 2 SIR dB	Output 3 SDR dB	Output 3 SIR dB
Speech 1	Speech 2	3.0204	3.0204	9.3880	24.4273	8.8893	22.7629	3.3207	9.8459
Speech 2	Speech 3	3.2072	3.2072	6.8427	23.5563	6.1803	21.3245	4.7592	8.7264
Speech 3	Speech 4	2.5625	2.5625	8.6977	22.5722	7.4898	18.3213	3.0983	8.1832
Speech 4	Speech 1	2.3412	2.3412	5.6212	17.5956	5.2179	17.2864	4.2391	6.7645
Average		2.7828	2.7828	7.6374	22.2879	6.9443	19.9237	3.8543	8.3801

Table1: Energy ratio results from experiments. Input SDR and SIR are input ratios. Output 1 SDR, SIR results from speaker dependent bases and output 2 independent bases. Output 3 is the results from not having the reference signal.

Near-end	Far-end (echo)	ERLE(dB)
Speech 1	Speech 2	10.2991 (see Figure 1d)
Speech 2	Speech 3	11.2945
Speech 3	Speech 4	10.1103
Speech 4	Speech 1	9.2382
Average		10.2355

Table 2: Calculated ERLE for pauses in near-end speech Experiments

7. CONCLUSIONS

In this paper we employed a new method called Convolutive Nonnegative Matrix Factorization and showed how this method can be used to perform acoustic echo cancellation. From the experimental results we can see that Acoustic Echo Cancellation can be reduced using CNMF in a monaural sound source separation framework. The CNMF can achieve good cancellation results, however combine its feature with some other techniques may lead to even better performance. Further work includes developing algorithms for faster convergence and improved performance in terms of minimizing the objective function.

REFERENCES

[1] S. Haykin and B. Widrow, Least-mean-square adaptive filters, Wiley-Interscience, Hoboken, N.J., 2003.

[2] Niall Cahill and Robert Lawlor. "A novel Approach to Acoustic Echo Cancellation", Department of Electronic Engineering, National University of Ireland Maynooth, Eurasip08

[3] P. Smaragdis, “Discovering auditory objects through nonnegativity constraints,” in SAPA, 2004.

[4] M. N. Schmidt and R. K. Olsson, “Single-channel speech separation using sparse non-negative matrix factorization,” in (INTERSPEECH), 2006.

[5] S. T. Roweis, “One microphone source separation,” in NIPS, 2001, pp. 793–799.

[6] Local Non-Negative Matrix Factorization as a Visual Representation, Tao Feng, Stan Z. Li, Heung-Yeung Shum, HongJiang Zhang Microsoft Research Asia, Beijing Sigma Center, Beijing 100080, China

[7] G. J. Jang and T. W. Lee, “A maximum likelihood approach to single channel source separation,” JMLR, vol. 4, pp. 1365–1392, 2003.

[8] D.D. Lee and H.S. Seung. “Learning the Parts of Objects by Nonnegative Matrix Factorization”, in Nature 1999 (401):788.

[9] D.D. Lee and H.S. Seung, “Algorithms for non-negative matrix factorization”, in Advances in Neural Information Processing Systems 13, 2000.

[10] P. Smaragdis, “Convolutive Speech Bases and their Application to Supervised Speech Separation”, IEEE Trans. on Audio, Speech and Language Processing, Vol. 15, Issue 1, pp. 1-12, January, 2007

[11] Roweis, S.T. “One Microphone Source Separation”, in Neural Information Processing Systems 13, 2000.

[12] J. B. Allen and D. A. Berkley, “Image method for efficiently simulating small-room acoustics,” J. Acoust. Soc. Amer., vol. 65, no. 4, pp. 943–950, Apr.1979.

[13] W.M Fisher, G.R. Doddington, and K. Goudie-Marshall, “The DARPA Speech Recognition Research Database: Specifications and Status,” Proceedings of DARPA Workshop on Speech Recognition, pp. 93-99, Feb. 1986

[14] E. Vincent; R. Gribonval; C. Fevotte; “Performance Measurement in Blind Audio Source Separation”, IEEE trans on Speech and Audio processing. Volume PP, Issue 99, 2005 Page(s): 1 – 8.

[15] T. Virtanen, “Monaural Sound Source Separation by Nonnegative Matrix Factorization with Temporal Continuity and Sparseness Criteria”, IEEE Transactions on audio, speech and language processing, VOL. 15, NO. 3, March 2007

Using Apodization to improve the performance of the Complex Spectral Phase Estimation (CSPE) Algorithm

Jian Wang[#1], Joseph Timoney[#2], Matthieu Hodgkinson[#3]

[#]*Computer Science Department,*
National University of Ireland, Maynooth, Co. Kildare, Ireland
[1]jwang@cs.nuim.ie
[2]jtimoney@cs.nuim.ie
[3]matthew.hodgkinson@nuim.ie

***Abstract*— The recently introduced Complex Spectral Phase Evolution (CSPE) algorithm is a super-resolution technique for the estimation of the exact frequency values of sinusoidal components in a signal. However, if a component of the signal does not exist within the entire data set, it cannot be identified out by CSPE algorithm, even though it still may be visible in the FFT magnitude spectrum. In this paper, we identify the source of this problem and propose a novel approach to resolve this issue. Specifically, we will show how to use a window apodization function to improve the CSPE algorithm. Experimental results are presented to illustrate the performance enhancement.**

***Keywords*— CSPE, Apodization, Kaiser Window**

I. INTRODUCTION

Most often the estimation of the frequencies of a signal composed of sinusoidal components is done in the frequency domain using peak-picking from the magnitude spectrum of the signal. However, this accuracy of this approach is severely limited to cases where a component frequency is not a multiple of the windowed signal length divided by the sampling frequency. In essence, this means only when a component frequency is aligned exactly with the analysis frequencies of the DFT, can it be measured accurately. When the component frequency does not satisfy this constraint, a common solution that is used in Sinusoidal Modelling algorithms is to apply quadratic interpolation to the component spectral magnitudes immediately either side of the true frequency to find the correct frequency and magnitude values. However, the performance of this method is highly dependent on the window function used [1] and the length of the data for analysis. The CSPE algorithm was introduced by [2] as a method to accurately estimate the frequency of components that exist within a short time frame. It was also designed to be computationally efficient. It is actually related in some aspects to the cross-spectrogram technique of [3].

However, the CSPE algorithm has been found to be unable to detect frequency components that do not appear throughout the entire signal source under analysis. This is puzzling because an associated peak can still appear for the component in the FFT magnitude spectrum. To resolve this issue it is necessary to investigate the CSPE algorithm in more detail and determine how it can be improved.

This paper is organized as follows: Firstly, we give a general introduction to the CSPE algorithm followed by an experimental evaluation that compares the CSPE algorithm with the widely-used frequency estimation method introduced in [4]. Then, we will explain in more detail the problem of identifying components that do not exist for the complete data frame and introduce the idea of apodization to solve it. Lastly, we will show the improvement to the CSPE result by using the apodization function by providing some experimental results.

II. CSPE AND ITS COMPARISON WITH ANOTHER FREQUENCY ESTIMATION APPROACH

The principal of CSPE algorithm can be described as below:

An FFT analysis is performed twice; firstly on the signal of interest, and the second time upon the same signal but shifted in time by one sample. Then, by multiplying the sample-shifted FFT spectrum with the complex conjugate of the initial FFT spectrum, a frequency dependent function is formed from which the exact values of the frequency components it contains can be detected. This frequency dependent function has a staircase-like appearance where the flat parts of the graph indicate where the exact frequencies of the components. The width of the flat parts is dependent on the main-lobe width of window function used to select the signal before FFT processing. Mathematically, the algorithm can be described as follows:

Assuming a real signal s_0, and a one-sample shifted version of this signal s_1. Say that its frequency is $\beta = q + \delta$ where q is an integer and δ is a fractional number. If b is an initial phase, w_n is the window function used in the FFT, F_{ws_0} is windowed Fourier transform of s_0, and F_{ws_1} is the windowed Fourier transform of s_1, then first writing

$$D = e^{\frac{j\,2\pi\beta}{N}} \tag{1}$$

The frequency dependent CSPE function can be written as

$$CSPE_w = F_{ws_0} F^*_{ws_1} = (\frac{a}{2})^2 \begin{bmatrix} D^* \left\| F_w(D^n) \right\|^2 \\ +2\,\mathrm{Re}\left\{ e^{j2b} D F_w(D^n) \otimes F_w^*(D^{-n}) \right\} \\ +D \left\| F_w(D^{-n}) \right\|^2 \end{bmatrix} \tag{2}$$

The windowed transform requires multiplication of the time domain data by the analysis widow, and thus the resulting transform is the convolution of the transform of the window function, w_f, with the transform of a complex sinusoid. Since the transform of a complex sinusoid is nothing but a pair of delta functions in the positive and negative frequency positions, the result of the convolution is merely a frequency-translated copy of w_f centred at $+\beta$ and $-\beta$. Consequently, with a standard windowing function, the $\left\| F_w(D^n) \right\|$ term is only considerable when $k \approx \beta$, and it decays rapidly when k is far from β. Therefore, the analysis window must be chosen carefully so that it decays rapidly to minimize any spectral leakage into adjacent bins. If this is so it will render the interference terms, i.e. the second and third terms, to be negligible in (2). Thus, the CSPE for the positive frequencies gives:

$$CSPE_w \approx \frac{a^2}{4} \left\| F_w(D^n) \right\|^2 D^{-1} \tag{3}$$

Finding the angle of (2) leads to the CSPE frequency estimate

$$f_{CSPE_w} = \frac{-N\angle(CSPE_w)}{2\pi} = \frac{-N\angle\left(\frac{a^2}{4} \left\| F_w(D^n) \right\|^2 D^{-1} \right)}{2\pi} = \frac{-N\angle(\frac{a^2}{4} \left\| F_w(D^n) \right\|^2 e^{-j\frac{2\pi}{N}\beta})}{2\pi} = \frac{-N(-\frac{2\pi}{N}\beta)}{2\pi} = \beta \tag{4}$$

The procedure of the CSPE algorithm is depicted in block diagram form in Figure 1.

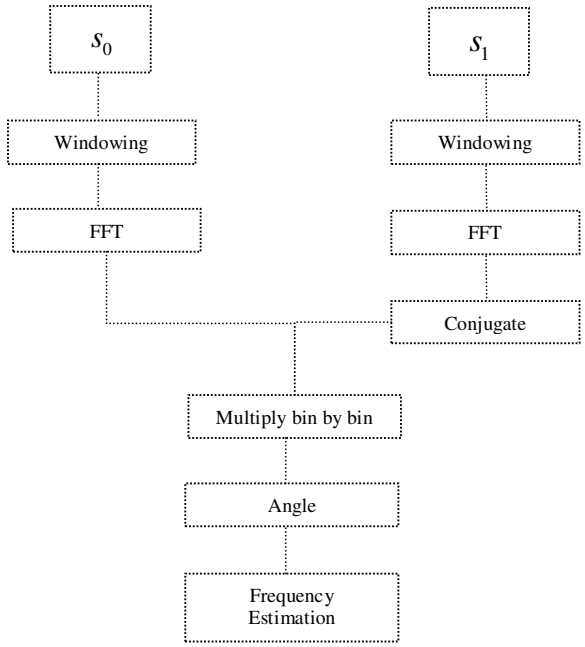

Fig. 1 The flow diagram of CSPE

An example of the output of the CSPE algorithm is shown in Figure 2. Consider the signal S_1 which contains components with frequency values (in Hz) of 17, 293.5, 313.9, 204.6, 153.7, 378 and 423. The sampling frequency is 1024 HZ. A frame of 1024 samples in length is windowed using a Blackman window and is padded using 1024 zeros. The frequency dependent CSPE function is computed as per eq. (2). As shown in Figure 2, each component can be identified exactly and are labelled with an arrow in the graph. The largest error among all the estimates of the components frequencies is approximately 0.15 Hz.

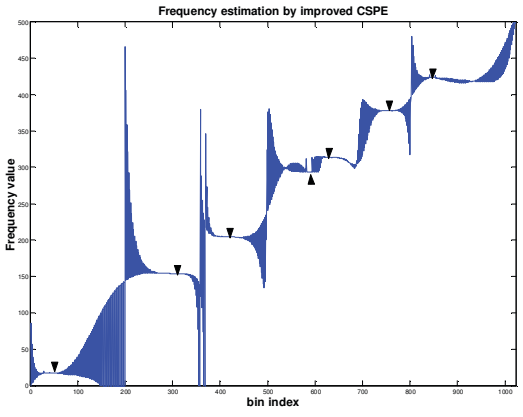

Fig. 2 Frequency estimation of S_1 by CSPE

Notice too in Figure 2 that at the flat sections in the graph of the CSPE result, the width of flat sections where the arrows point are related to the width of the window's main-lobe in the frequency domain.

2.1 Accuracy of the CSPE algorithm

An experiment was carried out to compare the accuracy of the Quadratic Interpolation Estimation Algorithm [4] with the CSPE algorithm. The procedure of this experiment can be described as below: defining twenty centre frequencies f_{c_i} ($0< f_{c_i} < \frac{F_s}{2}$) , for each f_{c_i} , M random frequencies were generated (each of which has a small random fluctuation of f_{c_i}) and thereafter M signals were created based on these M frequencies. The RMS error of the frequency estimation by CSPE and Quadratic Interpolation Estimation Algorithm for these M signals were calculated respectively for each f_{c_i} which shown in the figure below:

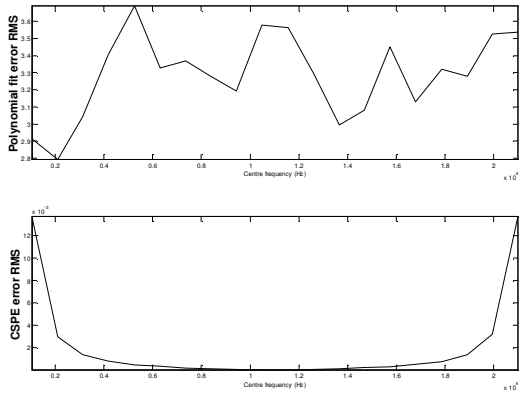

Fig. 3 Accuracy comparison of quadratic fit and CSPE frequency refinements

As shown in figure 3, the CSPE estimate was found to be more accurate than the quadratic interpolation approach, over a factor of 10^3 in many cases.

From the above experiment, it is clear that the CSPE algorithm works very well when the components contained in signal are constant and stable for over the entire data length. However, there can be cases where some components will only appear in half or even a quarter of the data frame length. We can run another experiment on the signal S_2 that has the same frequency components as S_1 , but restricting each component to appear in half or a quarter of the frame. The resulting output of the CSPE algorithm is shown in Figure 4:

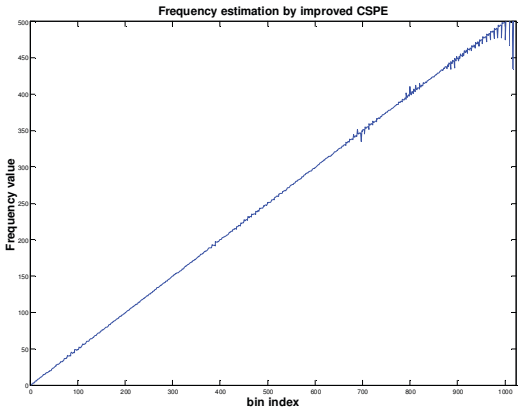

Fig. 4 Frequency estimation of S_2 by CSPE

Frome figure 4, it can be seen that there is no flat region in any part of the graph, that is, none of frequency components can be identified by CSPE algorithm . However, if the FFT magnitude Spectrum of S_2 is plotted, as shown in figure 5, each frequency component is still visible which indicates that there should be some information related to the component present in any FFT-based frequency domain analysis. So, the next section will try to understand this problem and propose a novel approach to deal with it.

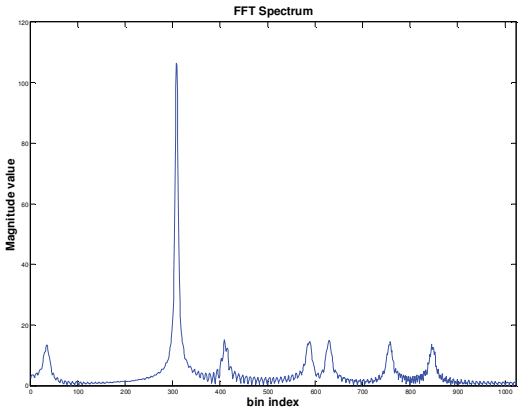

Fig. 5 FFT spectrum of the signal

III. Analysis of The problem and An improvement on the CSPE algorithm

Let's suppose there are three signals: $x_1[n]$, $x_2[n]$, $x_3[n]$ with the same length 1024 samples, with the same Sampling Frequency 1024 HZ, and all bearing the same frequency component at 123.5 HZ. The difference among the three signals being that the component appears over the entire

length of $x_1[n]$, while it only appears in a half and quarter length of signals $x_2[n]$, $x_3[n]$ respectively, the remaining values sample being zero. If we do a normal FFT analysis this component will not be centred on a frequency bin and instead will produce a representation with significant peaks at the 124th and 125th bins with smaller components dying away either side of them. Thus, this signal is an ideal candidate for a CSPE algorithm analysis.

It is possible to rewrite $x_2[n]$ and $x_3[n]$ in terms of the product of $x_1[n]$ and a step function. If $u_1[n]$ and $u_2[n]$ are two different unit step functions then,

$$x_2[n] = x_1[n]u_1[n]; \quad (5)$$

$$x_3[n] = x_1[n]u_2[n]; \quad (6)$$

Denoting $F(x_1)$ and $F(w)$ as the FFT transform of $x_1[n]$ and a suitable window function $w_{ks}[n]$, such as a Blackman window, the spectral representation of the signal $x_1[n]$ can be written as

$$F(x_{1_w}) = F(x_1) * F(w) \quad (7)$$

where * denotes the convolution operator.
Then, the spectral descriptions of the other signals can be written as

$$\begin{aligned} F(x_{2_w}) &= F(x_2) * F(w) \\ &= F(x_1) * F(u_1) * F(w) \end{aligned} \quad (8)$$

And likewise,

$$\begin{aligned} F(x_{3_w}) &= F(x_3) * F(w) \\ &= F(x_1) * F(u_2) * F(w) \end{aligned} \quad (9)$$

Examining equations (8) and (9) it is possible to interpret the terms $F(u_1) * F(w)$ and $F(u_2) * F(w)$ as the actual windowing operation that are applied to the signal $x_1[n]$ in the frequency domain. Now if we compare the original and alternative window functions frequency response that are all effectively applied to $x_1[n]$ we can see that there is an important difference between the original window and the others in terms of the main lobe size and the height of the side lobes. These are shown in Figure 6.

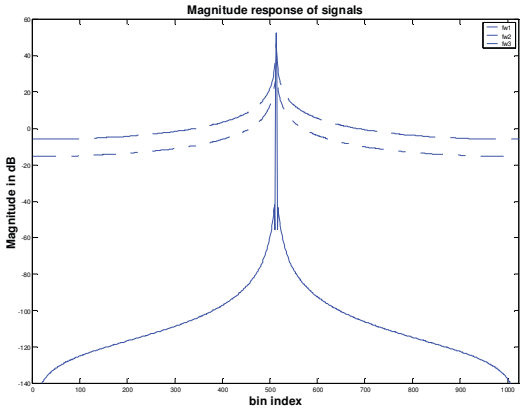

Fig. 6 Magnitude Response of three different actual window functions

From figure 6, when the signal doesn't appear over the entire frame, its actual window function spectrum is significantly different from the original window function. Specifically, the side-lobe hasn't been suppressed in a large extent and the width of main-lobe has been increased. This impacts the CSPE algorithm then in that the interference terms outline in eq. (2) are not sufficiently suppressed. Thus, because these terms are larger, the CSPE output is useless for finding the exact signal frequency of $x_2[n]$ and $x_3[n]$. Motivated by the idea of introducing window function in the first place Fourier analysis, we can introduce a second window function to suppress the greater side-lobes caused by the convolution effect of the spectrum with the unit step functions. This practice is known as apodization [6]. It is more commonly known in image processing than in 1-D signal processing. Normally, an Apodization Function is used to suppress the effects of side-lobes at the expense of lowering the spectral resolution. Some researchers, particularly in image processing [7], [8] have shown that the Kaiser window Function is a better for apodization than other window functions such as the Poisson, Gaussian or Tukey. The Apodization factor using the Kaiser Function can be written as

$$w_{ks}[n] = 1 - kaiser(N, \beta) \quad (10)$$

The side lobe suppression of the Kaiser window is dependent on the parameter β. The apodization of the signal analysis window is then given by

$$w_A[n] = w[n]\left(w_{ks}[n]^{\alpha}\right) \quad (11)$$

Experimentally the relationship between different values of β and effect of raising $w_{ks}[n]$ to an integer power α, to enhance the suppression effects, was evaluated. An example of the effects of suppression of the side-lobes is depicted in Figure 7. From the figure 7, we can find when $w_{ks}[n]$ is

raised to a cubic power, α =3, with β = 0.01, it has a side-lobe attenuation level greater than 300 dB.

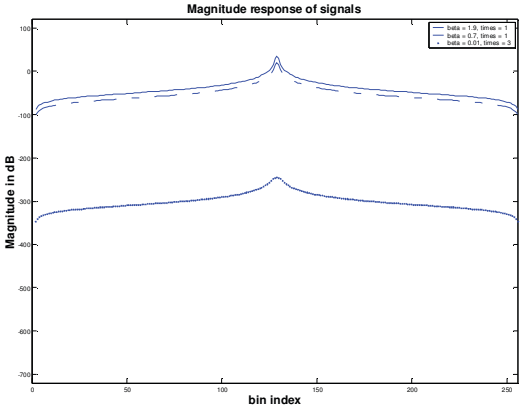

Fig. 7 Magnitude Response of Kaiser window function

Next, the signal S_2 can be analysed with the function $w_A[n]$ (beta = 0.01, α = 3) and the CSPE frequency detection result is shown in Figure 8 where the arrows label the detected frequency components. It can be seen that now the frequency components are identified in the CSPE function.

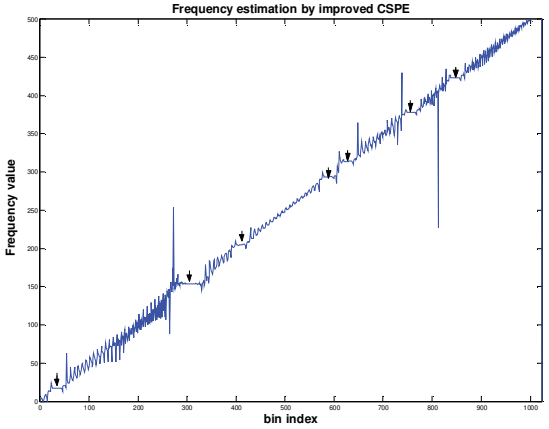

Fig. 8 Frequency estimation by improved CSPE

It was determined experimentally then that when components exist at a different proportion over a frame, the value of β and the power of $w_{ks}[n]$ have to be adapted to get a satisfactory result. Table 1 summarizes this configuration as a reference for users, where Y means a component can be detected, while N means that it cannot; and α means the power of the Kaiser window.

TABLE I
CONFIGURATION OF β AND T FOR THE DETECTION OF DIFFERENT PROPORTION OF A FRAME

	The Proportion of one Frame			
	$\frac{1}{2}$	$\frac{1}{4}$	$\frac{1}{8}$	$\frac{1}{16}$
β =0.01, α = 1	Y	N	N	N
β =0.01, α = 3	Y	Y	N	N
β =0.01, α = 10	Y	Y	Y	N
β =0.01, α = 18	Y	Y	Y	Y

IV. CONCLUSIONS AND FUTURE WORK

This paper has addressed a problem discovered with the CSPE algorithm, that is, when frequency component does not exist throughout the entire length of the data frame, that although it appears in the FFT magnitude spectrum, the CSPE algorithm is not capable of detecting this component. By focusing on changing the analysis window's frequency response, the idea of Apodization Function was introduced that was shown to over this difficulty. An experimental result has demonstrated that the performance of the CSPE algorithm has been improved by applying this solution. In future, the intention is to try to extend this CPSE algorithm to correctly identify the dynamic frequency evolution of a frequency modulated signal.

REFERENCES

[1] Florian Keiler, Sylvain Marchand, "Survey on extraction of sinusoids in stationary sounds", Proc. Of the 5 th Int. Conference on Digital Audio Effects(DAFX-02), Hamburg, Germany, September,2002

[2] Short ET AL, "Method and apparatus for compressed chaotic music synthesis", United States Patent 6,137,045; October 2000

[3] Douglas Nelson, Cross Spectral Methods for Processing Speech, Journal of the Acoustic Society of America, vol. 110, No.5, pt.1, Nov.2001, pp.2575-2592

[4] J. Rauhala, H.-M. Lehtonen and V. Välimäki, "Fast automatic inharmonicity estimation algorithm", Journal of the Acoustical Society of America, vol. 121, no. 5, pp. EL184-EL189, 2007.

[5] B. Frei, 'Digital_Sound_Generation – Part 1 Oscillators', Online Book, Institute for Computer Music and Sound Technology, Zurich University of the Arts, Switzerland.. 2007.

[6] H. C. Stankwitz, R. J. Dallaire, and J. R. Fienup, "Non-linear Apodization for Sidelobe Control in SAR Imagery", IEEE Trans. On Aerospace and Elect. Syst., Vol. 31, No. 1, pp. 267-279, Jan. 1995

[7] Thomas, G., Flores, B.C., Jae Sok-Son, "SAR sidelobe apodization using the Kaiser Window", Image Processing, 2000. Proceedings.

Computing Modified Bessel functions with large Modulation Index for Sound Synthesis Applications

Joseph Timoney, *Thomas Lysaght*
Dept. of Computer Science
NUI Maynooth, Co. Kildare, Ireland.
jtimoney@cs.nuim.ie

Victor Lazzarini,
Dept. of Music,
NUI Maynooth, Co. Kildare, Ireland.
victor.lazzarini@nuim.ie

Ruiyao Gao,
Dept. of Electronic. Eng.,
ITT Tallaght, Dublin, Ireland.
rgao@ittdublin.ie

***Abstract*-Ordinary Bessel functions are a common function used when examining the spectral properties of frequency modulated signals, particularly in sound synthesis applications. Recently, it was shown that modified Bessel functions can also be used for sound synthesis. However, to limit the impact of aliasing distortion when using these functions, it is essential to set an upper limit on the frequency-dependent modulation index used when computing these functions. However, it can be impossible to do this beyond a certain threshold when using standard mathematical software tools such as Matlab, or the scientific toolbox of the Python language, because of numerical overflow issues. This short paper presents an approach to overcome this limitation using the MaxStar algorithm. Results are also presented to demonstrate the usefulness of this solution.**

Keywords: Modified Bessel functions, numerical overflow, Maxstar algorithm.

I. INTRODUCTION

Frequency Modulated (FM) signals are important in both the fields of telecommunications and sound synthesis. Ordinary Bessel functions are a key mathematical tool for the understanding of the spectral properties of these FM signals [1]. The success of FM synthesis as a sound generating technique led to the exploration of other techniques similar in concept, specifically using Modified Bessel functions [2]. However, for a long period this work was forgotten until recently when it was shown that a synthesis technique based on Modified Bessel functions was very useful for the generation of high quality, low-aliasing digital reproductions of the periodic waveforms used in analog subtractive synthesizers [3], for example, sawtooth waves. Specifically, the synthesis equation is

$$s(t) = e^{m\cos(\omega_m t)}\cos(\omega_c t) \qquad (1)$$

where *m* is the Modulation index.
This can be expressed using Modified Bessel functions as

$$I_0(m) + \sum_{n=1}^{\infty} I_n(m)\left(\cos(\omega_c t - n\omega_m t) + \cos(\omega_c t + n\omega_m t)\right) \qquad (2)$$

where

$I_n(.)$ is a modified Bessel function of order *n* and ω_c and ω_m are the carrier and modulation frequencies respectively [3].

From (2), it can be seen that equation (1) generates a harmonic signal with a spacing of frequency ω_m and magnitude scaling given by the set of Modified Bessel functions $I_n(m)$ where $n = 0,\ldots,\infty$.

In practical applications (1) should be scaled by a factor [3]

$$g(m) = e^{-m} \qquad (3)$$

which leads to

$$s(t) = e^{(m\cos(\omega_m t)-m)}\cos(\omega_c t) \qquad (4)$$

If the ratio between the carrier and modulation frequencies is one, then Equation (5) describes a unipolar pulse train. The width, and thus the smoothness of the pulse, is determined by the value of the modulation index *m*.

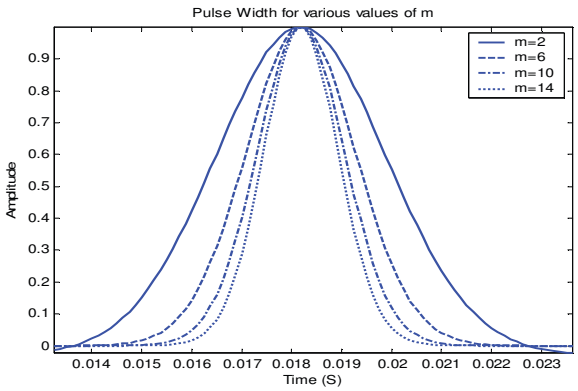

Figure 1. Plot of the pulseshape defined by (5) for various values of modulation index.

Lower values of *m* give a broader pulse shape. Figure 1 shows an example of this for values of *m* ranging from 2 to 14. For this plot the sampling rate was set to be 8 kHz and $\omega_c = \omega_m = 55$ Hz.

The spectrum of this pulse train is given by [3]

$$X(\omega) = \frac{1}{e^m} \sum_{n=1}^{\infty} (I_{n-1}(m) + I_{n+1}(m)) \cos(n\omega) \quad (5)$$

The harmonic amplitudes of the expression for the spectrum in (5) are determined by the modified Bessel functions $I_n(.)$ that are scaled by the factor $g(m)$. This factor gives a smooth low pass characteristic to the spectrum with the steepness of the roll-off being determined by the value of m. Figure 2 provides a spectral example of (5) for a carrier frequency of 100Hz.

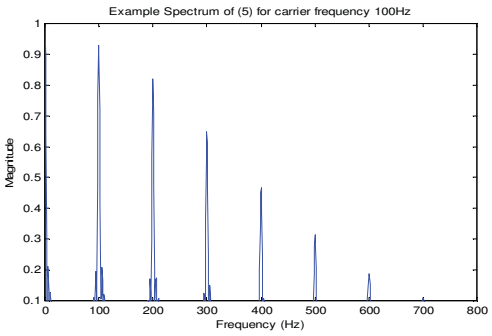

Figure 2. Plot of tan example of (5) showing the lowpass characteristic of the harmonic amplitudes.

The implications of this for the digital generation of the classic waveforms of subtractive synthesis is that by integrating this pulse train it is possible to create a signal spectrum that is an approximation to that of a sawtooth wave, whose harmonic magnitudes decrease with respect to the harmonic number. The equation for the integrated spectrum is

$$X'(\omega) = \frac{e^{-m}}{n\omega} \sum_{n=1}^{\infty} (I_{n-1}(m) + I_{n+1}(m)) \sin(n\omega) \quad (6)$$

If the integrated signal is then passed through a suitable DC blocker filter as described in [4], then the output waveshape should be close to that of a sawtooth, as illustrated in Figure 3. The example in Figure 3 was generated for carrier and modulator frequencies of 440 Hz and a sampling frequency of 44100 Hz. The modulation index was chosen to be 943 and was determined empirically. It is clear from Figure 3 that the waveshape is that of a sawtooth, validating the usefulness of this technique for the application.

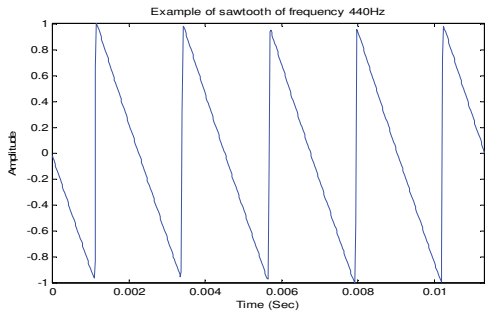

Figure 3. Sawtooth wave generated by integrating (4), followed by DC blocking, and whose spectrum is given by (6).

II. Optimising Bandlimited Signal Synthesis

What is of primary concern when creating this approximation is that the signal should be effectively bandlimited, that is, any aliased components should be of sufficiently low magnitude so as to be imperceptible. To ensure this, it is then a question of choosing a suitable value for m such that any harmonics that exist in theory beyond half the sampling frequency are sufficiently small such that their aliased version will not be heard. This can be posed as an optimsation problem, as given by ~~in~~ (7). Here, a figure of -90dB is chosen as the upper threshold on the spectral magnitude of the aliased components [3].

$$\max_m \left\{ 20\log_{10} \frac{I'_{N+1}(m)(N+1)^{-1}}{I'_1(m)} \right\} \leq -90 \quad (7)$$

where N is the number of harmonics in the sawtooth wave from DC to half the sampling frequency and

$$I'_n(m) = I_{n-1}(m) + I_{n+1}(m) \quad (8)$$

To perform this optimization it is possible to use a standard routine such as '`fmin`', for example, that is available as a routine in the Matlab software package. This routine uses a Nelder-Mead Simplex search method [5]. However, in the implementation of the optimization of (7) a problem was discovered. Specifically, when attempting to compute the magnitude of the Modified Bessel function for values of modulation index greater than 700 the algorithm used generates a numerical overflow and will return a value of infinity. A similar behaviour was observed when using the `Sci.py` module of python for the computation in [6].

A. Computing Modified Bessel Functions using Logs

To compute a Modified Bessel function of order n and modulation index m it is possible to use the formula [7]

$$I(n,m) = \sum_{k=0}^{\infty} \frac{(m/2)^{n+2k}}{k!(n+k)!} \quad (9)$$

From (9) both the numerator and denominator of the summation will grow to be infinitely large, but empirical observation found that the value of their ratio will first reach a maximum and then decrease to zero as *m* increases. In an implementation it can be surmised that the maximum number of terms in the summation can be restricted as long as it exceeds the point where the ratio reaches zero. This is a valid approach but fails when the maximum of the ratio is beyond the numerical precision of the machine. As stated already, this occurs for large values of modulation index and thus an alternative is required in such cases. An obvious choice for compressing the numerical values generated by each term of (9) is to use the logarithmic function

$$\log\left(\frac{(m/2)^{n+2k}}{k!(n+k)!}\right)=(n+2k)\log(m/2)-\log(k!(n+k)!) \tag{10}$$

and using the logarithmic property

$$\log x^{z} = z\log x \tag{11}$$

Equation (11) can then be rewritten using the multiplicative property given in (12)

$$\log(xz)=\log x+\log z \tag{12}$$

to give

$$\log\left(\frac{(m/2)^{n+2k}}{k!(n+k)!}\right)=(n+2k)\log(m/2)-\log(k!) -\log((n+k)!) \tag{13}$$

A number of possibilities exist for expressing the logarithm of a factorial. Firstly, the exact expression is [8].

$$\log(x!)=\sum_{z=1}^{x}\log z \tag{14}$$

Alternatively, a very good approximation for the logarithm of a factorial due to Ramaujan [8], for $x \neq 0$, can be written which would reduce the computational effort in evaluating the multiplications in $\log(x!)$ for each term.

$$\log(x!)\approx x\log x - x+\frac{\log(x(1+4x(1+2x)))}{6}+\frac{\log(\pi)}{2} \tag{15}$$

Furthermore, it also is more robust numerically. Particularly, in the case of Matlab [5], if the number of terms *k* selected exceeds 170, then $\log(k!)=\infty$.

Using (15), equation (13) can be rewritten to produce

$$\begin{aligned}&=(n+2k)\log(m/2)-k\log k+k-\frac{\log(k(1+4k(1+2k)))}{6}\\&-(n+k)\log(n+k)+(n+k)\\&-\frac{\log((n+k)(1+4(n+k)(1+2(n+k))))}{6}+\log\left(\frac{\pi}{2}\right)\end{aligned} \tag{16}$$

B. Applying the MaxStar algorithm

From (16) it can be seen that each term in (10) can be computed using logarithms which will significantly reduce the size of its numerical value, thus avoiding overflow problems. However, the next issue is how to add them without computing the exponential of each term. They should also be added in the log domain and then the exponential found of the overall result. To this end a very useful algorithm from the field of telecommunications is the MaxStar algorithm [9]

$$\ln\left(e^{x}+e^{z}\right)=\left\{\max(x,z)+\ln\left(1+e^{-|x-z|}\right)\right\} \tag{17}$$

where

$$\begin{aligned}\max(x,z)&=x \quad if\ x\geq z\\&=z \quad otherwise\end{aligned}$$

This expression is applied iteratively to the summation until the final term is reached [10]. An alternative approximation was recently given in [10], which was

$$\ln\left(e^{x}+e^{z}\right)=\frac{x+z}{2}+\ln\left(2\cosh\left(\frac{x-z}{2}\right)\right) \tag{18}$$

Once the sum of terms is found using (17) or (18) all that remains to compute (9) is to find the exponential of this sum. This procedure will work in Matlab [5] as long as the total value of the log of the sum of the terms in (9) is 709 or less as otherwise an infinite output will result because in this package

$$e^{710}=\infty \tag{19}$$

This could be problematic in the general case, but if all we want to do is solve the optimization problem of (7) then the logarithmic can also be rewritten as

$$\log_{10}\left(I'_{N+1}(m)(N+1)^{-1}\right)-\log_{10}(I'_{1}(m))$$

$$= \log_{10}(N+1)^{-1} + \log_{10}(I'_{N+1}(m)) - \log_{10}(I'_1(m)) \tag{20}$$

Ignoring the first term which is a constant and substituting (8) into (20) gives

$$= \log_{10}(I_N(m) + I_{N+2}(m)) - \log_{10}(I_0(m) + I_2(m)) \tag{21}$$

Both terms in (21) are structurally similar, so, for example, considering the first term only and defining the output of the MaxStar algorithm as $MS(.)$ leads to the definition

$$MS(I_n(m)) = \log\left(\sum_{k=0}^{\infty} \frac{(m/2)^{n+2k}}{k!(n+k)!}\right) \tag{22}$$

Then

$$\log_{10}(I_N(m) + I_{N+2}(m)) = \log_{10}(\exp(MS(I_N(m))) + \exp(MS(I_{N+2}(m)))) \tag{23}$$

where for clarity the function exp(x) is used to represent e^x. Applying the MaxStar algorithm to (23) produces the nested expression in (24)

$$= \log_{10}(\exp(MS(MS(I_N(m)) + MS(I_{N+2}(m))))) \tag{24}$$

It is possible then to apply the property

$$\log_y(x^z) = z \log_y x \tag{25}$$

which results in

$$= MS(MS(I_N(m)) + MS(I_{N+2}(m)))\log_{10} e \tag{26}$$

Thus, the exponential power has been removed and now is present in (26) in the form of a multiplication by a constant. In this form any issues with numerical overflow should be overcome. The optimization in (7) can finally be rewritten using the formulation in (26) as

$$\max_m \left\{ \begin{array}{l} \log_{10}(N+1)^{-1} + \\ MS(MS(I_N(m)) + MS(I_{N+2}(m)))\log_{10} e \\ -MS(MS(I_0(m)) + MS(I_2(m)))\log_{10} e \end{array} \right\} \le -\frac{90}{20} \tag{27}$$

For example, if we have a pitch frequency for the sawtooth wave of 146.8324 Hz (note D) and a sampling rate of 44100 Hz, the number of harmonics that will exist to half the sampling frequency is N=150. Setting the maximum number of terms in the summation to be 2000, the optimization routine returns a value of modulation index m=2131.7. Figure 4 is a plot of the lower portion of the spectrum of this sawtooth, after hanning windowing, showing its harmonics with no visible alias components present.

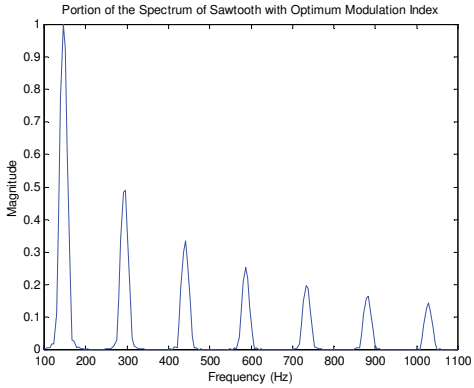

Figure 4. Lower part of spectrum of optimized sawtooth.

III. Conclusion

This short paper has presented an approach for the computation of Modified Bessel functions with high modulation indices that uses the MaxStar algorithm to overcome numerical difficulties currently experienced with mathematical software packages. Furthermore, it also has shown how an optimisation formulation can be rewritten using the MaxStar algorithm that obviates the need to explicitly compute large numbers that are raised to an exponential power.Future work will seek out other similar applications where the MaxStar algorithm would prove to be useful.

IV. Acknowledgment

Victor Lazzarini would like to acknowledge the funding support given by An Foras Feasa for this work.

References

[1] J. Chowning, and D. Bristow, *FM Theory & Applications - By musicians for musicians*, Yamaha, Tokyo, 1986.

[2] J.A. Moorer, ,"The Synthesis of Complex Audio Spectra by Means of Discrete Summation Formulas". *Journal of the Audio Engineering Society*, 24 (9), 1976.

[3] V. Lazzarini, J. Timoney and T. Lysaght, "A Modified FM synthesis approach to bandlimited signal generation", *Proc. 11th conf. Digital Audio Effects (DAFx)*, Espoo, Finland, Sept. 1-4, 2008.

[4] R. Yates and R. Lyons, 'DSP Tips & Tricks [DC Blocker Algorithms]', *IEEE Signal Processing Magazine*, vol. 25, no. 2, pp. 132 – 134, March 2008.

[5] *Matlab 5.3*, The Mathworks: 1999.

[6] *Sci.py*, Python Module: 2009. http://www.scipy.org/

[7] G. N. Watson, *A Treatise on the Theory of Bessel Functions*, 2nd Ed., Cambridge Univ. Press, Cambridge, UK, 1944.

[8] *Factorial*, Wikipedia entry, 2009: http://en.wikipedia.org/wiki/Factorial.

[9] J. A. Erfanian, and S. Pasupathy, "Low-Complexity Parallel-Structure Symbol-by-Symbol Detection for IS1 Channels," *IEEE Pacific Rim Conference on Communications, Computers and Signal Processing*, June 1st - 2nd, 1989.

[10] Motorola Inc, Apparatus and method for calculating the logarithm of a sum of exponentials, *European Patent Office*, EP20020293271, June 2004.

Section 2A

RADIO SYSTEMS 1

Wireless Billboard Channels over T-DMB

Zhanlin Ji, Ivan Ganchev, Máirtín O'Droma
Telecommunications Research Centre, University of Limerick, Ireland
{Zhanlin.Ji; Ivan.Ganchev; Mairtin.ODroma}@ul.ie

Abstract—**This paper describes wireless billboard channels (WBCs) established over terrestrial digital multimedia broadcasting (T-DMB), which are used by the service providers to broadcast advertisements of their services to mobile users so they may discover and associate with the 'best' service following the user-driven 'always best connected and best served' principle (ABC&S) in the emerging ubiquitous consumer wireless world (UCWW). A novel and more efficient IP datacasting (IPDC) operational mode for 'WBC over T-DMB' is proposed and evaluated.**

Keywords-Ubiquitous Consumer Wireless World (UCWW); Wireless Billboard Channels (WBCs); Advertisement, Discovery and Association (ADA); Terrestrial Digital Multimedia Broadcasting (T-DMB); IP Datacasting (IPDC).

I. INTRODUCTION

The WBCs are defined as simplex, unidirectional, narrowband and broadcast channels [1], which are solely used to 'push' (wireless) service advertisements to a large number of mobile users (MUs). WBCs are fundamental part of the ubiquitous consumer wireless world (UCWW) – the University of Limerick's next generation network (NGN) proposal [2~4]. The UCWW will bring many benefits to MUs, teleservice providers (TSPs), and access network providers (ANPs) including: greatly enhanced user freedom of choice in accessing the services, elimination of roaming charges, 'level playing field' for new ANPs and much greater commercial openness and fairness in the ANP market, realization of truly user-driven always best connected and best served (ABC&S) [5], user-driven integrated heterogeneous networking, etc.

The following technologies are suitable carrier candidates for WBCs: the digital audio broadcasting (DAB), terrestrial digital multimedia broadcasting (T-DMB), digital radio mondiale (DRM), digital video broadcast - handheld (DVB-H), and multimedia broadcast / multicast service (MBMS). Among these, T-DMB is a new multimedia broadcasting technique developed by Korea in 2005 based on the European DAB standard. Comparing with DAB, T-DMB adds a Reed-Solomon (RS) forward error correction (FEC) to improve communication in wireless channels and uses a highly efficient MPEG4 part 3 bit sliced arithmetic coding (BSAC) or advanced audio codec (HE AAC) to replace the DAB's MPEG Audio Layer 2 (MP2) audio codec scheme [6-8]. To improve spectrum efficiency, T-DMB uses orthogonal frequency division multiplexing (OFDM) modulation scheme, and supports a single frequency network (SFN). T-DMB suits well as a carrier for WBCs.

The 'WBC over T-DMB' system is developed along three layers: a service layer, a link layer, and a physical layer.

The error protection of service advertisements is an important issue in WBCs, since even a single bit error may cause discarding a full WBC segment [9]. In the 'WBC over T-DMB' system, the physical layer reliability is ensured by a Reed-Solomon (RS) code, convolutional interleaver, punctured convolutional code, and inner interleaver. The service layer reliability is ensured by an advertisement delivery protocol (ADP) [10]. For extra error protection, a DVB-H compatible link layer is proposed in this paper to smooth IP datacasting (IPDC).

There are four T-DMB transmission modes defined by ETSI 300-401 [7], respectively with 1536, 384, 192, and 768 subcarriers in one OFDM symbol. This paper focuses on WBCs established over T-DMB operating in all four transmission mode.

The rest of the paper is organized as follows. Section II presents the new 'WBC over T-DMB' IPDC mode. Section III describes the 'WBC over T-DMB' software testbed and the obtained performance evaluation results. Section IV summarizes the conclusions.

II. 'WBC OVER T-DMB' IPDC MODE

The T-DMB standard [7, 8] supports two operational modes: a stream mode – for broadcasting audio stream datasets, and a packet mode – for IP packets broadcasting. However, the stream mode is not suitable for WBCs, whereas the packet mode does not provide sufficient error protection for WBC data broadcasting in wireless fading channels. Thus, a digital video broadcasting - handheld (DVB-H) compatible module [11] was added on the top of the T-DMB as the link layer operating in a new 'WBC over T-DMB' IP datacasting (IPDC) mode (Figure 1). With the strong outer layer of a FEC scheme, i.e., multi-protocol encapsulation - forward error correction (MPE-FEC) solution, the reliability of 'WBC over T-DMB' can be improved without changing the T-DMB standard.

The MPE-FEC frame is the core element in the link layer. MPE-FEC is introduced in DVB-H for compensating the performance degradations due to the use of wireless fading channels. It is a frame which consists of 255 columns and a number of rows (256, 512, 768 and 1024 rows are supported [11]). Every cell in the MPE-FEC frame is one byte. A MPE-FEC frame carries a number of WBC segments. The 255 columns are divided into two parts: from 1st to 191st column is the application data table (ADT), and from 192nd to 255th column is the RS data table (RSDT). Flexibility is allowed by

This publication has been supported by the Irish Research Council for Science, Engineering and Technology (IRCSET), Science Foundation Ireland and the Telecommunications Research Centre, University of Limerick, Ireland (http://www.ece.ul.ie/trc).

puncturing some parity RSDT columns to achieve different code rates, i.e., 1/2, 2/3, 3/4, 5/6, 7/8.

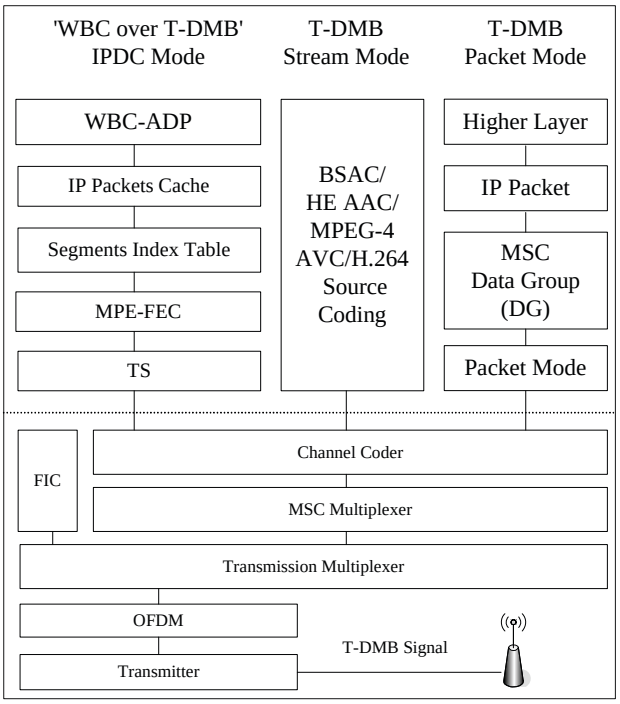

Figure 1. The new 'WBC over T-DMB' IPDC mode vs. standard T-DMB stream mode and packet mode.

III. 'WBC OVER T-DMB' SOFTWARE TESTBED

A. Layers Implemention

The WBC service layer has a three-tier software architecture [12]. Thanks to this architecture, the Internet-based enterprise application on the WBC-SP node and the portable-device-based application on the mobile terminal are able to run in an intelligent, flexible, and extensible way.

The 'WBC over T-DMB' link layer software testbed was designed and implemented in C++. The encoder's functional model is depicted in Figure 2. The decoder running on the mobile terminal uses a reversed functional model.

The 'WBC over T-DMB' physical layer testbed was designed based on the ETSI-EN-300-401 [7] and ETSI-EN-102-427 [8] standards. The transmitter side first generates a 3008B[1] dataset, which is further processed as shown in Figure 3. In the outer coding section, a Galois field (GF) array is created with the dataset. Then the array is encoded by a RS(204,188) module for extra error protection at the physical layer. In the outer interleaving section, the output matrix is first reshaped to one-row dataset; then a convolutional interleaving algorithm is used for permuting the one-row dataset with the help of an internal shift register algorithm; finally, the output is translated into a bit array by a byte-to-bit convertor. In the inner coder section, the bit array is first encoded by the convolutional encoder and then punctured by the predefined

[1] 3008 = 16 × 188 (transport stream packet length).

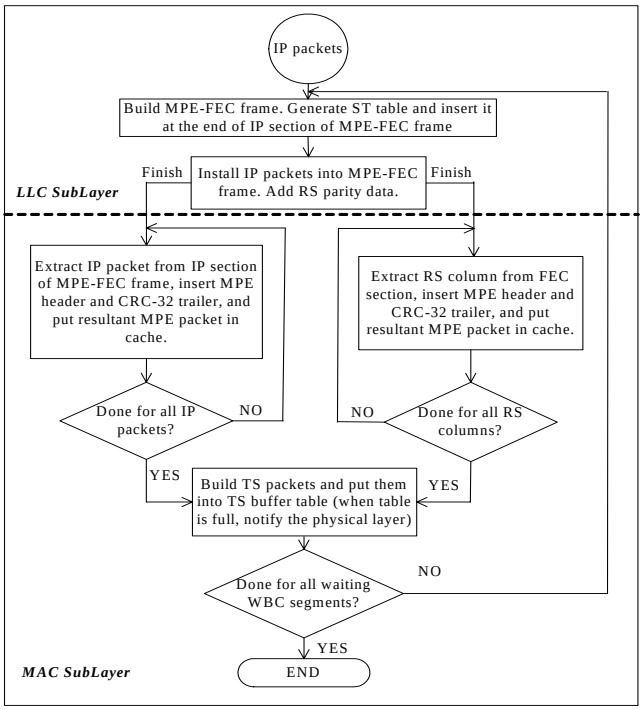

Figure 2. The 'WBC over T-DMB' link layer encoder's functional model.

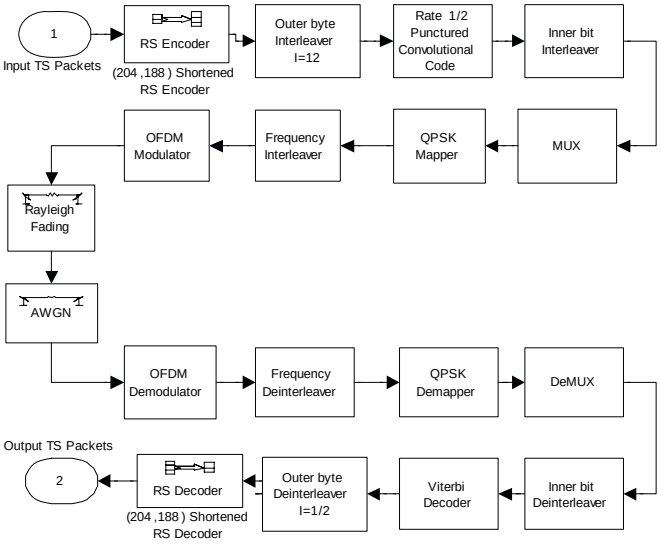

Figure 3. The 'WBC over T-DMB' physical layer testbed.

convolutional code rate. In the inner interleaving section, an inner bit-wise interleaving algorithm is used to provide extra reliability. The output of the inner interleaving dataset acts as a main service channel (MSC), which together with a random dataset fast information channel (FIC) and a Sync channel produces a T-DMB transmission bit frame in the MUX module.

In the mapping section, the T-DMB transmission bit frame is QPSK modulated. Then the output is processed by a frequency interleaving algorithm to improve reliability. The output is modulated by an inverse fast Fourier transform (IFFT) algorithm in the OFDM modulation section. Then a T-DMB OFDM symbol transmission frame is built, which is passed

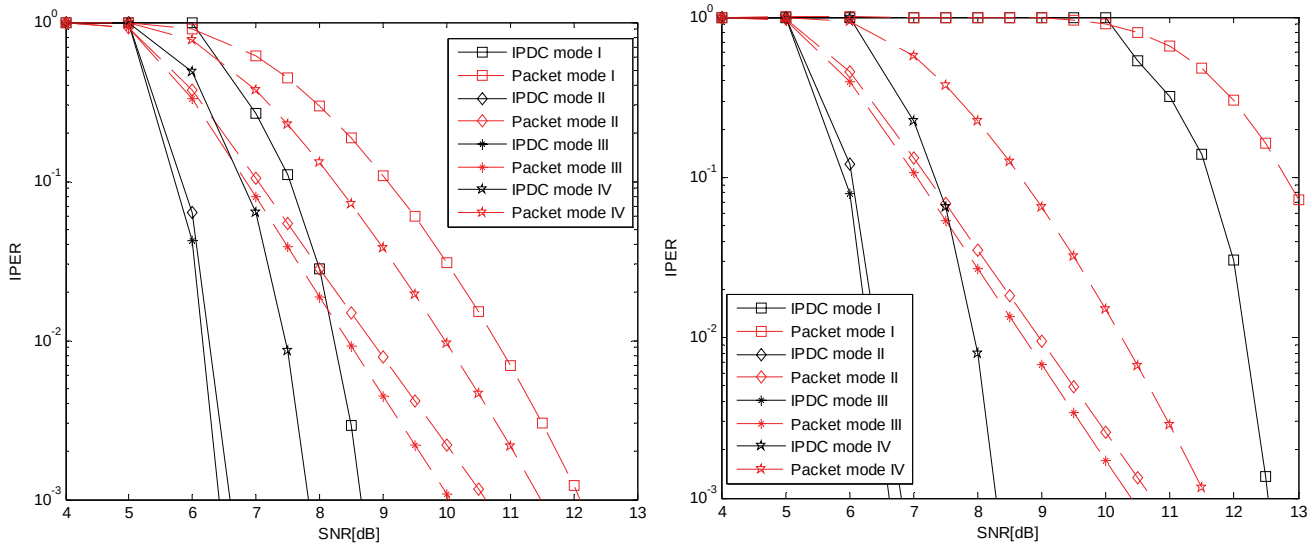

Figure 4. The IPER in packet mode and IPDC mode: (a) Doppler frequency= 10Hz; (b) Doppler frequency = 80Hz.

first through a Rayleigh fading channel and then through an additive white Gaussian noise (AWGN) channel. In the receiver, the data processing is performed in reversed order.

The physical fading channel design follows the COST 207 model in typical urban reception conditions [13], which has been commonly used for wireless broadcasting simulations.

B. Simulation Results

The IP packet error rate (IPER) is an important criterion to measure the performance of 'WBC over T-DMB'. For the purposes of simulation, at the service layer 5000 distinct WBC segments were produced by means of the ADP protocol and sent down to the link layer for broadcasting using the following parameters: WBC segment size - 4016B, IP packet length – 1024B, ADP (n=6, k=4). To test the IPER in offline mode, the link layer first stores all IP packets into a database, and processes them one by one. The MPE-FEC frame has 1024 rows and 255 columns. At the physical layer, the following parameters were used: WBC source rate – 384 Kbps, data length in 24ms – 9216 bits, convolutional code rate – 1/2, interleaving depth – 16, cyclic prefix ratio – 0.25.

Figures 4(a) and 4(b) show the IPER simulation results for the packet mode and IPDC mode when the Doppler frequency is equal to 10Hz and 80Hz, respectively. The results confirm that the IPDC mode outperforms the packet mode with approximately 2.5dB SNR gain at IPER value of 10^{-2}. The results also show that the transmission modes III and II have better anti-Doppler effect resistance than modes IV and I. The reason for that is that they use higher subcarrier frequency (8kHz and 4kHz, respectively) than transmission modes IV and I (2kHz and 1kHz, respectively), which gives better results in fading environments. So with same Doppler value, the normalized Doppler frequency's order is: mode III< mode II < mode IV < mode I.

From the results it is clear that in order to sustain the effects of fading and noise in WBCs, and thus to achieve better QoS, the 'WBC over T-DMB' IPDC mode – a novel solution for broadcasting service advertisements to mobile terminals – must be employed.

IV. CONCLUSION

The establishment of wireless billboard channels (WBCs) over terrestrial digital multimedia broadcasting (T-DMB), for facilitating the service advertisement, discovery and association (ADA) in the ubiquitous consumer wireless world (UCWW) has been presented in this paper. A software testbed has been designed in Java, C++ and Matlab to evaluate the T-DMB operational modes. The performed simulation has confirmed that with the proposed novel IP Datacasting (IPDC) solution, the 'WBC over T-DMB' system is able to operate more reliably and efficiently.

REFERENCES

[1] Flynn, P., I. Ganchev, M. O'Droma. "Wireless Billboard Channels: Vehicle and Infrastructural Support for Advertisement, Discovery, and Association of UCWW Services," Annual Review of Communications, Volume 59 (Chicago, Ill.: International Engineering Consortium), ISBN: 978-1-931695-53-4, Pp. 493–504. 2006.

[2] O'Droma M. and I. Ganchev. "Towards a Ubiquitous Consumer Wireless World," IEEE Wireless Comm., Vol. 14, Issue 1, Pp. 52-63. ISSN: 1536-1284. DOI: 10.1109/MWC.2007.314551. February 2007.

[3] O'Droma M. and I. Ganchev. "Techno-Business Models for 4G, " Proc. Int'l. Forum on 4th Generation Mobile Commun., King's College London, U.K. May 2004.

[4] O'Droma M. and I. Ganchev. "Strategic Innovations through NGN Standardisation for a Ubiquitous Consumer Wireless World". ITU-T Kaleidoscope Conference (K-INGN 2008). 12-13 May 2008, Geneva, Switzerland. Proceedings book [ITU 2008; IEEE CN CFP083E-PRT],Pp. 135-142,

[5] O'Droma M. S. and I. Ganchev. “Enabling an Always Best-Connected Defined 4G Wireless World,” Annual Review of Communications, Volume 57 (Chicago, Ill.: International Engineering Consortium, 2004), ISBN: 1-931695-28-8, Pp. 1157-1170. 2004.

[6] Byungjun Bae, Joungil Yun, Sammo Cho, Young Kwon Hahm, Soo In Lee, and Kyu-Ik Sohng, “Design and Implementation of the Ensemble Remultiplexer for DMB Service Based on Eureka-147,” ETRI J., vol. 26, no. 4, pp. 367-370, Aug. 2004.

[7] ETSI, Radio Broadcasting Systems; Digital Audio Broadcasting (DAB) to mobile, portable and fixed receivers, ETSI EN 300 401 V1.3.3, May 2001.

[8] ETSI, "Digital Audio Broadcasting (DAB); Data Broadcasting - MPEG-2 TS streaming," ETSI TS 102 427, V1.1.1, July 2005.

[9] Ji Zh., I. Ganchev, M. O'Droma. “Efficient Collecting, Clustering, Scheduling, and Indexing Schemes for Advertisement of Services over Wireless Billboard Channels,” Proc. of the 15th International Conference on Telecommunications (ICT 2008), Pp. x.1-x.6, St. Petersburg, Russia, 16-19 June 2008. ISBN 978-1-4244-2036-0. DOI 10.1109/ICTEL.2008.4652649.

[10] Ji Zh., I. Ganchev, M. O'Droma. “Reliable and Efficient Advertisements Delivery Protocol for Use on Wireless Billboard Channels,” Proc. of the 12th IEEE International Symposium on Consumer Electronics (IEEE ISCE 2008), Algarve, Portugal, 14-16 April, 2008. DOI 10.1109/ISCE.2008.4559488.

[11] ETSI, "Digital Video Broadcasting (DVB); DVB-H Implementation Guidelines, " ETSI TR 102 377, V1.2.1, 2005.

[12] Ji Zh., I. Ganchev, M. O'Droma. 2008. “Intelligent Software Architecture for the Service Layer of Wireless Billboard Channels,” Proc. of the 6th Annual IEEE Consumer Communications & Networking Conference (CCNC09), Pp. 1-2, Las Vegas, USA, 10-13 January 2009. ISBN 978-1-4244-2309-5/09. DOI 10.1109/CCNC.2009.4784824.

[13] COST 207 Report, "Digital land mobile radio communications, Commission of European Communities, Directorate General," Telecommunications, Information Industries and Innovation, Luxemburg, 1989.

RF SDR for Wideband PMR

Ling Gao, Ronan Farrell
(Centre for Telecommunications Value Chain Research,
National University of Ireland, Maynooth, Co. Kildare, Ireland;
lgao@eeng.nuim.ie, ronan.farrell@nuim.ie)

ABSTRACT

TErrestrial Trunked Radio (TETRA) offers capabilities equivalent to the second generation of mobile phones with voice and limited data capabilities. TETRA needs to evolve to satisfy increasing user demand for new services and facilities as well as gleaning the benefits of new technology. An initial enhancement (TETRA Enhanced Data Service, TEDS) has been agreed. The enhanced TETRA services allows for more flexibility in the communication modes used, so as to provide adaptability in applications. We propose that it is possible to deploy Software Defined Radio (SDR) technologies into the basestation to economically provide this level of flexibility and to further extend the capability of TETRA services by deploying a WiMAX channel into the proposed TETRA tuning range. Thus delivering true broadband data service while simultaneously supporting the original and enhanced TETRA services.

1. INTRODUCTION

TETRA is a Private Mobile Radio (PMR) standard that has been developed by the European Telecommunications Standards Institute (ETSI) for the needs of the transport, civil and emergency services [1]. TETRAPOL is another PMR standard, developed by Matra Nortel Communications. TETRA and TETRAPOL are competitors in the PMR market in Europe. In this paper we focus on TETRA services as it is a more recent standard than TETRAPOL. For perspective, we will compare the radio characteristics between TETRA and TETRAPOL later (Table 1).

There is increased interest in the delivery of broadband data services over the TETRA network, for example video imagery of accident scenes. An enhanced form of TETRA (TEDS) has been agreed which can offer data rates of up to 600 kbps [2]. However successful deployment of TEDS requires additional spectrum to be allocated and this has proved to be problematic. An investigation was carried out by ETSI which concluded that a single standardised frequency band cannot be agreed; however the concept of a tuning range for enhanced TETRA services is gaining acceptance. In addition to the difficulty in agreeing a standardised spectrum allocation, enhanced TETRA supports a range of communication modes depending on individual user bandwidth and signal quality. This implies a greater complexity on the radio systems. Though the new TETRA services will offer improved capabilities, it is necessary to provide backward compatibility with existing TETRA users and as there are over 1000 networks currently deployed around the world [3]. The greatest challenges will be experienced by the TETRA basestations which must support new and legacy systems. SDR, specifically in the concept of flexible hardware transceiver systems, offers an economical solution to both the challenges of implementing TEDS and supporting legacy systems and provides a development route for new TETRA services.

This work is on integration of deploy a WiMAX sub-channel into the TETRA framework for true broadband services on demand. Similar initiatives, WiMAX overlay over TETRA demonstration for emergency call-handling system by Alcatel Lucent and TelMAX project by Teltronic have also explored the issue of integration WiMAX channels over TETRA bands. This work is focussed on the integration of TETRA and WiMAX standards within a single physical layer SDR transceiver rather than the use of separate radio front-ends.

This paper will present the requirements for a SDR platform with an investigation of various radio architectures to support the proposed and legacy schemes. Then we will show the implementation of our proposed RF receiver architecture plus the design challenges for this experimental platform.

2. COMBINING WIMAX AND TETRA

TETRA services were initially deployed in Europe in a 20 MHz band between 380 and 400 MHz as two 5 MHz bands with a 10 MHz duplex separation [1]. To deploy the new enhanced TETRA data services additional spectrum is required to complement the existing band. The Electronic Communications Committee (ECC) within European Conference of Postal and Telecommunications

Administrations (CEPT) has proposed a "tuning range" within which enhanced TETRA services can be deployed [4]. It recommends three bands within that tuning range, including the original TETRA band, as shown below (Figure 1). The tuning range requirements are further complicated as non-European deployments have used other frequencies ranges. One particularly interesting aspect is the Federal Communications Commission (FCC) proposed national public service network at 758-793 MHz [5] which would be attractive to any future TETRA-type network.

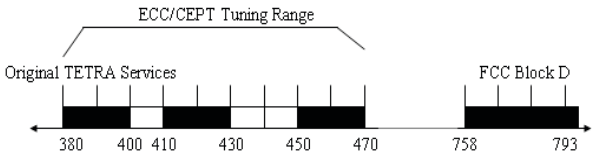

Figure 1 system tuning range

Enhanced TETRA allows for channel widths up to 150 kHz, offering users a range of data rates, up to 600 kbps. This is a significant improvement on existing TETRA services, however it does not offer data rates that would support full multimedia transmissions or rapid delivery of large files. Though TEDS has identified a maximum channel width of 150 kHz, there is nothing inherent in the TETRA framework that prevents wider channels to be used. We propose that WiMAX (IEEE 802.16e) offers features that are highly suited to TETRA-type applications such as quality-of-service guarantees and scalable OFDM access. The WiMAX standards allows for 1.25 MHz channel [6] which would allow up to three 1.25 MHz WiMAX channel to be deployed with the remaining spectrum then used to support voice and data services whether using TETRA or TEDS, thus maintaining legacy support (Figure 2).

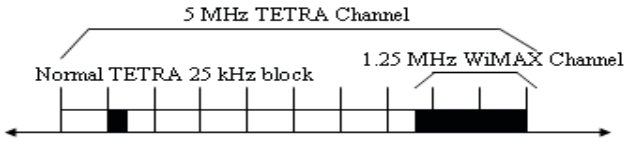

Figure 2 5 MHz TETRA channel

The key advantage to using the WiMAX standard is scalable OFDM access schemes (OFDMA) where users are dynamically allocated bandwidth as needed for their application, according to their quality of service metric and allow users to obtain bursts of data throughput of up to 6 Mbps when needed. WiMAX presents low cost of delivery of higher data rates over large geographical areas and also perform very well in mobile conditions. With WiMAX's enhanced channel efficiency of up to 5 bits/hertz, greater number of users plus applications can be supplied.

The use of high data rate OFDMA modulations brings in challenging requirements for the transmitter in terms of spectral quality and Error Vector Magnitude (EVM). Also the receiver faces some difficulties. The high EVM required is difficult to attain because it demands a high Signal-to-Noise Ratio (SNR) from the Low Noise Amplifier (LNA), about 35 dB. Other challenges are that the receiver must exhibit low power consumption, high bandwidth and high dynamic range. [7]

If basestations are to be designed using full channel capture and channelisation in the digital domain, implementing this WiMAX sub-channel requires only a small modification of the software implementation of the physical layer and then subsequently a separate WiMAX stack.

3. SOFTWARE DEFINED RADIO PLATFORM REQUIREMENTS

To develop a new system suits our proposal, the main radio characteristics of the TETRA, TEDS, TETRAPOL and WiMAX standards are studied as follow:

Table 1 Compare radio characteristics of TETRA, TEDS, TETRAPOL and WiMAX

	TETRA	**TEDS**	**TETRA POL**	**Mobile WiMAX**
Frequency (MHz)	380-410	350-470	80/380/450	410-470, 758-793
Spectrum Allocation	Two 5 MHz bands	additional 5 MHz bands	similar to TETRA	similar to TETRA
Duplex Spacing (MHz)	10	10	similar to TETRA	similar to TETRA
Channel BW (kHz)	25	25-150	<8	1250
Channel Spacing (kHz)	25	matches channel spacing	10/12.5	50-100
Access Scheme	TDMA FDMA	TDMA FDMA	FDMA	SOFDMA
Modulation	$\pi/4$ DQPSK	$\pi/4$, $\pi/8$ DQPSK up to 64 QAM	GMSK	QPSK, up to 64 QAM
Tx Power (dBm)	28 to 46	similar to TETRA	42	similar to TETRA

Rx Sensitivity (dBm)	-103 to -106	similar to TETRA	-113 to -111	-90.8
Efficiency (bits/Hz)	1.4	<3.5	similar to TETRA	3-4

TETRA and WiMAX are two different standards, the terminologies of the system specifications are described quite differently (TETRA is an ETSI standard, WiMAX is an IEEE standard). To explore the viability of this approach, a low-cost demonstrator is going to be developed according to an initial suggestion for an integrated wideband transceiver as shown below (Table 2) that can offer the necessary tuning range and channel capture. It is challenging to produce common specs as different standards and modulation schemes are involved in each channel. Linearity and dynamic range are key transceiver criteria.

Table 2 Combined system specs for transceiver

	Combined TETRA, TEDS, TETRAPOL and WiMAX
Receiver	
Signal Sensitivity (dBm)	-106
Signal Sensitivity (dBm / Hz)	-152
Maximum Acceptable Signal (dBm)	-30
SNR/CNR @ BER = 1e-4 (dB)	24
NF (dB)	7 (MS), 4(BS)
Linearity IIP2 (dBm)	37
Linearity IIP3 (dBm)	-13
ACPR (dBc)	-70 @ 75 kHz offset
Transmitter	
Tx Power (dBm)	42
Tx Dynamic Range (dB)	80
EVM (%)	<3

4. PROPOSED TEST PLATFORM

For our investigation of the combined radio system, we propose to adapt an existing mobile communication system SDR platform MARS developed by the Institute of Microelectronics and Wireless Systems (IMWS) at NUI Maynooth, operating in the frequency range 1.8 to 2.4 GHz [9]. This platform functions, sub-optimally, in the range 380-480 MHz and requires further work to meet linearity and noise requirements. The main issues that need to be addressed are attenuation induce due to matching networks; oscillator performance, and linearity. This platform works with the software framework developed within the Centre of Telecommunications Value Chain Research (CTVR) and is being integrated with the OSSIE framework developed by Virginia Tech.

Our two candidate architectures are a homodyne (direct-to-RF) transmitter and receiver, or a homodyne transmitter with a superheterodyne receiver. With the development of modern transmitters, the direct-to-RF transmit path is an increasingly mature technology and with new developments in wideband mixers and PAs, achieving the needed reconfigurability will be relatively straightforward. For the receiver, the challenges are more difficult. In any implementation, there will be a strenuous sensitivity and linearity requirements. This will be complicated by the large tuning range. While MARS SDR receiver is currently configured to support a direct-from-RF architecture, this approach faces challenges in terms of linearity, noise and DC offset cancellation. An alternative approach, which we have chosen, is to use a more traditional two-stage approach with a low frequency IF stage. The following table lists some of the advantages and disadvantages for the two approaches for the receiver stage [7]:

Table 3 Summary of Tx/Rx architectures suitable for our system

	Direct	**Superheterodyne**
Adv	• Fewer components • simple frequency plan for multi-standard, • high integratability, no image problem	• more reliable performance • flexible frequency plan • no DC offset • no 1/f noise issues • high blocker and interferer rejection • improved tunability
Dis	• LO leakage and DC offset issue • 1/f noise • Vulnerability to blocker and ACPR issues • More challenging RF filters	• More components • Potentially more power • IF bandwidth typically fixed

Compared with the two candidate radio architectures (Table 3), we use a more traditional superheterodyne approach for the receiver. This offers advantages in that we have a fixed 5 MHz slot. The RF stage can deal with tuning, linearity and noise, while the IF stage can use highly selective filters to achieve the required adjacent channel & blocker rejection. The proposed test platform is shown below:

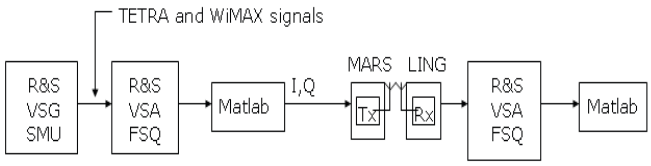

Figure 3 Proposed Test Platform

The equipments needed are Rohde Schwarz Vector Signal Generator SMU, Rohde Schwarz Vector Signal Analyzer FSQ, PC, low cost experimental SDR system MARS from IMWS NUIM. We plan to get TETRA+WiMAX I&Q analog signals from R&S vector signal generator SMU200, connect it to R&S vector signal analyzer FSQ. Use R&S matlab transfer toolbox to get the IQ files from FSQ. The reason for doing this is due to the internal IQ files within the firmware of the SMU200 is not available to users. Then we transmit the IQ data to the MARS transmitter and our new designed superheterodyne receiver (Figure 3). This platform requires further work to meet linearity and noise requirements. The main issues that need to be addressed are gain, matching networks, oscillator performance and singal/power level. Then we will connect Tx & Rx to the FSQ to see how the TETRA + WiMAX signals perform.

5. RECEIVER IMPLEMENTATION

The SDR receiver is implemented using as many off the shelf parts as possible. The receiver implementation diagram is shown in figure 4.

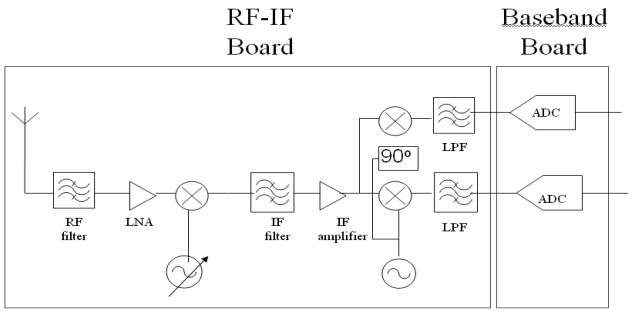

Figure 4 Receiver Implementation

We will have one RF-IF board on top of a baseband board.

The RF bandpass filter is designed of 3rd order Chebyshev filter operating a frequency range from 380 MHz to 480 MHz. The LNA is Agilent ATF55143, with a gain of 17.7 dB at a noise figure of 0.6 dB and an IP3 of 24.2 dBm capable of operating across a frequency range from 450 MHz to 6 GHz. Although 380 MHz to 480 MHz is out of this LNA frequency range, we re-designed the matching network then simulated it in Agilent Advanced Design System tool. An Analog Devices part AD8348 was chosen as a downconverter. It has a conversion gain of up to 44 dB by the use of AGC, with a noise figure of 11dB, and IIP3 of 28 dBm. The AD8348 can be interfaced with a detector such as the AD8362 rms-to-dc converter to provide an automatic signal-levelling function for the baseband outputs. The ADF4360-7 is an integrated integer-N synthesizer and voltage controlled oscillator (VCO). The ADF4360-7 centre frequency is available and is set by external inductors. This allows a frequency of between 350 MHz to 1800 MHz.

The IF filter that we have chosen is an EPCOS SAW filter. Its centre frequency is 140 MHz with a bandwidth of 8.8 MHz. The ADL5530 is a broadband, fixed-gain, linear amplifier that operates at frequencies up to 1000 MHz. This provides a gain of 16.5 dB and achieves an OIP3 of 37 dBm with an output compression point of 21.8 dB and a noise figure of 3 dB. The IF downconverter is the same component as the RF stage, an Analog Devices part AD8348. Separate I and Q outputs of the mixers. The oscillator signal comes from ADF4360-9, an integrated integer-N synthesizer and voltage controlled oscillator (VCO). This configuration is capable of producing a frequency in a range from 65 MHz to 400 MHz, which the fixed centre frequency is 140 MHz. Two low pass filters are followed which the bandwidths are 3.5 MHz for both I and Q.

Next the signal is digitised using two 16-bit Analog Devices ADC's capable of operating up to 80 Msps in the baseband board developed by IMWS at NUIM. This digitised information is then transferred to the host computer for final processing and data extraction over a USB2 interface.

The receiver PCB board layout is then developed in Easily Applicable Graphical Layout Editor (EAGLE) (Figure 5).

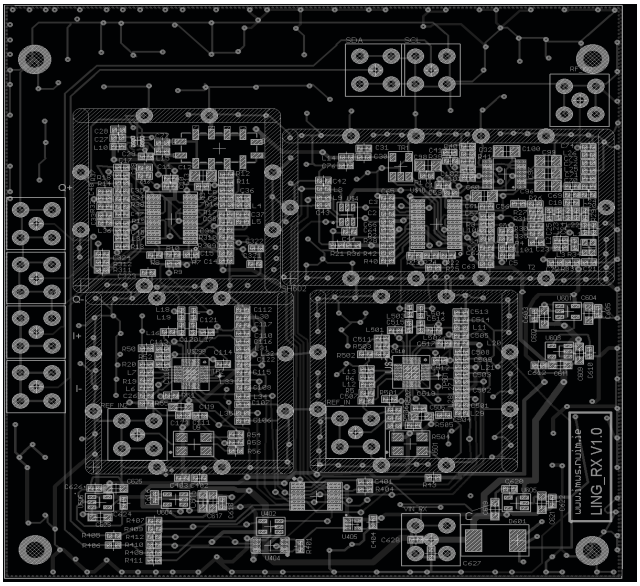

Figure 5 Receiver PCB Board

6. DESIGN CHALLENGES

From a basestation perspective, this proposed test platform offers a number of challenges, specifically maintaining noise and linearity performance over such a range of frequencies and handling the different modes of operation. One of the challenges of designing a combined communication systems is that it must remain compatible with legacy TETRA services. This is particularly challenging as the TETRA specifications were designed for very narrowband 25 kHz channels, specifically the figures on linearity and sensitivity. High sensitivity is needed as TETRA basestations are not typically as densely populated as comparable mobile telephony systems. Complicating the matter is the needs for TETRA clients to be capable of sustaining high receive power levels when close to such basestations [8]. The basis of our analysis was the need to be compatible with legacy systems, while accepting that some compromises would be needed on adjacent channel specifications as the legacy values are not appropriate to our wideband solution. As we are focussed on basestation radios, we are also assuming that receiver power levels can be assumed to be low.

The challenges for a SDR platform are focused on the RF-IF stages rather than the software framework. Specifically there are demanding receiver requirements on signal sensitivity, adjacent channel rejection, and linearity. These issues were manageable when dealing with narrowband signals at a specific frequency but become much more challenging when dealing with a wide tuning range. One particular issue is the problem of the transceiver filter which must be wideband or reconfigurable in some way. This will limit our ability to minimize adjacent channel interference. To address the issue of varying sub-channel widths, it will be necessary to undertake full channel capture and subsequently digitally undertake channelisation, filtering and de-modulation. If this approach is taken minimizing wideband noise contributions from the electronics and adjacent channels becomes particularly important. To investigate the interference issue, we had a look into blocker specifications for TETRA 25 kHz QAM receiver is shown (Figure 6).

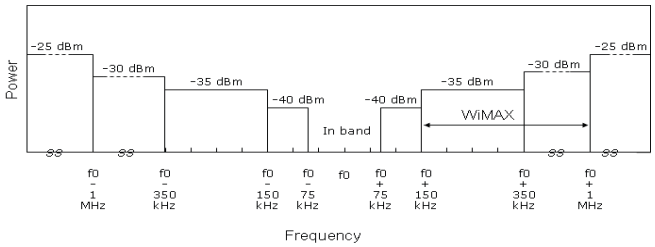

Figure 6 Blocker Specifications for TETRA 25 kHz QAM receiver

At +/-75kHz offset, the level of interfering signal is -40dBm. At +/-150kHz offset, the level of interfering signal is -35dBm. At +/-350kHz offset, the level of interfering signal is -30dBm. At +/-1MHz offset, the level of interfering signal is -25dBm. WiMAX signal has to be lower than -35dBm/-30dBm. The max tolerated input power is 0 dBm. The filter specs and how far we put WiMAX channel next to TETRA channel are critical.

7. CONCLUSION

In this paper, we have reviewed the TETRA, TEDS, TETRAPOL and WiMAX standards. A new combined system specification for the transceiver has been presented to show how a WiMAX sub-channel can be integrated into a TETRA channel and retain legacy compatibility. We focused on RF frontend receiver architectures with a discussion of the relative benefits of homodyne and heterodyne architectures. The challenge of adding a broadband channel into the existing TETRA framework is complex and places significant constraints on future TETRA receivers, but we propose that following a software-defined radio philosophy allows for implementation with minimal additional hardware complexity. Our next step is to adapt the LING superheterodyne receiver with an existing MARS transmitter and demonstrate this proposed reconfigurable radio platform. If successful, this approach may allow future TETRA users to avail of broadband data rates minimal additional cost for either the user or the basestation provider.

ACKNOWLEDGEMENTS

The authors wish to thank Philippe Mege, Gilles Latouche and Laurent Martinod of EADS Secure Networks for their assistance and support. Also the authors extend thanks to the sponsors EADS and IRCSET for the PhD programme.

REFERENCES

[1] Whitehead, P., "The other communications revolution [TETRA standard]", *IEE Review,* volume 42, pp. 167-170, 1996

[2] Nouri, M., Lottici, V., Reggiannini, R., Ball, D., Rayne, M., "TEDS: A high speed digital mobile communication air interface for professional users", *IEEE Vehicular Technology Magazine*, volume 1, issue 4, pp. 32 - 42. 2006

[3] Juan Ferro, "A TETRA market overview", TETRA Experience China, TETRA association, 2006

[4] Draft ECC Report on Public Protection and Disaster Relief Spectrum Requirements, ECC/CEPT/102, Electronic Communications Committee, September 2006

[5] Don Bishop, "Coming to America: TETRA-One way or another", *Mobile Radio Technology (MRT) Magazine*, January, 2001

[6] IEEE 802 Working Group, http://standards.ieee.org/getieee802/802.16.html

[7] Luis Abraham Sanchez-Gaspariano, Alejandro Diaz-Sanchez, "IEEE802.16e design issues and transceiver architecture selection for mobile WiMAX systems", *IEEE Computer Society*, February, 2008

[8] Private conversation with Philippe Mege, Gilles Latouche and Laurent Martinod of EADS Secure Networks.

[9] G. Baldwin, L. Ruíz, R. Farrell, "Low-Cost Experimental Software Defined Radio System", *SDR Technical Forum 2007,* November 2007

Q-Learning for Cognitive Radios

Neil Hosey
Dept. of Computer Science
NUI Maynooth
Maynooth, Co. Kildare
Email: nhosey@cs.nuim.ie

Susan Bergin
Dept. of Computer Science,
NUI Maynooth,
Maynooth, Co. Kildare

Diarmuid O'Donohue
Dept. of Computer Science,
NUI Maynooth,
Maynooth, Co. Kildare

***Abstract*—Machine Learning approaches such as Reinforcement Learning (RL) can be used to solve problems such as spectrum sensing and channel allocation in the cognitive radio domain. These approaches have been applied to other similiar domains such as in mobile telephone networks and have shown much greater performance than the static channel allocation schemes used.**

The objective of this research is to use an RL technique known as Q-Learning to provide a possible solution for allocating channels in a wireless network containing independent cognitive nodes. Q-Learning is an attractive algorithm for such a problem because of the low computational demands per iteration. Many of the current proposed techniques suggest using a negotiation policy between two nodes to decide on which channel each may use, however a considerable problem with this is the overhead involved in the negotiation involved between the nodes. This paper suggests an approach where each node acts as an individual independant node, with minimal interaction with the other nodes.

Results have shown that using such a technique gives fast convergence on an optimal solution when correct rates are chosen. It has also shown that the algorithm is very scalable, in that as the network grows, the state-action space does not grow sufficiently to cause major memory or computational demands.

I. Introduction

Research in the area of cognitive radio (CR) has broadened significantly in the past number of years since it was first presented by Mitola in 1999 [1]. It is now recognised as being an essencial replacement for the current regulation of the electromagnetic spectrum where vast bands of usable spectra is being underutilised. One such example of this was in the USA where the Spectrum Policy Task Force [2] had found that for a particular period on a police broadcasting channel, the typical channel occupancy was less than 15% , while the peak usage was nearly 85%. This has led to much research into the area of opportunistically accessing underutilised spectrum where no primary user is currently active.

The goal of this research is not to focus on primary and secondary users in a frequency domain, but rather to allow each cognitive node to learn by its own mistakes. In this case, the agent considers the environment to include all other cognitive nodes, and any other transmitters working on the same channels as being part of the environment. This will ensure an even distribution of channels not only for the cognitive nodes, but also for any other type of wireless communication device. It is hoped that future work will look at primary and secondary users working in the same environment using a Q-Learning approach. Much of the research in this area has focused on cooperative sensing where nodes within a cognitive radio network share information about the environment. There has been very little work focusing on reinforcement learning techniques such as Q-Learning, currently there is only one other paper which looks at Q-Learning for channel allocation in cognitive radios[3]. There are several levels on which this can happen [4], which at the very least have a need for a control channel to pass information between nodes. This alone can lead to massive overheads on a network as the number of nodes and the amount of data shared increases. The proposed solution is individual sensing where each node is a single cognitive entity having the ability to acquire information about the environment or network without the help of other nodes in its vicinity.

This is achieved using a reinforcement learning algorithm known as Q-Learning whereby the agent goes through a phase of *learning* before it can converge on an optimal solution for channel allocation. In this learning phase, the node makes decisions on what channels to select pseudo-randomly, the outcome of taking these actions will weigh strongly on what decisions are made later on. Once a node has finished learning, it can then make decisions on what it has learned. The ability for a node to be able to preempt whether a channel is going to be in use before accessing it allows it to optimise bandwidth usage for itself and any other nodes that may be accessing the same channel.

The remainder of this paper is organised as follows. First, an overview of reinforcement learning is presented, along with an in-depth look at Q-Learning and how it is applicable to this domain. Details on how Q-Learning has been applied in channel selection in cognitive networks are provided. Results and outcomes of simulations performed are then given, followed by current and future work. Finally, conclusions from this work and possible future work in this area are provided.

II. Reinforcement Learning

A. Application of Reinforcement Learning

Reinforcement Learning is a machine learning technique whereby an agent interacts with an environment in the hope of achieving a goal. This interaction occurs on a continual basis with the hope of the agent being able to learn to function

in an optimal fashion within that environment. The way in which the agent interacts with the environment is through a series of actions that can be performed. These actions can have positive or negative outcomes which can, over time, be used to determine how best to work in the current environment. At each point in time, an agent can be in a particular state, with the ability to choose an action based on what it has learned in previous iterations.

The overall goal is to find an optimal policy that maps each state to an action an agent should take in those states [6]. Figure 1 shows how the agent interacts with the environment and uses this to determine its next state.

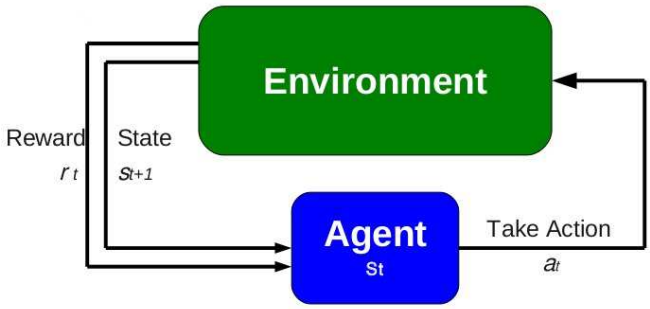

Fig. 1. Agent-Environment Relationship

To represent this formally, we assume the agent receives the next state from the environment as shown in figure 1 at each iteration of the algorithm, $s_t \in S$, where S is the set of possible states and $t = 0, 1, 2, ...$ for each individual discrete timestep or iteration. On receiving this state, an action is chosen, $a_t \in A(s_t)$ where $A(s_t)$ is the set of possible actions that can be taken in state s_t. On taking this action, the agent observes the result, and receives a reward r_{t+1} where $r_{t+1} \in \Re$. After taking this action, the agent has now moved into a new state, s_{t+1}. At each iteration of the algorithm, a policy is created that maps the action taken, a_t to the state s_t and this policy is denoted by $\pi_t(s_t, a_t)$. The way in which this mapping occurs is dependent on each RL algorithm and is usually based on one of a number of action selection strategies which will be described in the next section.

B. Q Learning Algorithm

Q-Learning is an RL off-policy temporal-difference learning algorithm introduced by Watkins in 1989. The algorithm works by learning an action-value function that gives an expected utility of taking an action in a particular state and following that policy thereafter [7]. The environment in which the agents exist can be modelled as a Markov Decision Process. The agent-environment shown in Figure 1 consists of a number of steps:

- Agent examines state $s_t \in S$
- Action $a_t \in A$ is taken based on s_t
- A transition occurs as a result of action a_t being taken, and a new state s_{t+1} is taken into account. A reward is generated based on this transition, r_t.
- The reward, r_t, that is returned is then stored or learned for that state action pair, and the above process is repeated.

The goal of repeating this process is for the agent to find an optimal policy $\pi^* \in \pi$ for each state $s_t \in S$ in a recursive manner. The fact that the Q-Learning algorithm can converge on π^* without having any prior knowledge of the environment makes it very suitable for cognitive radio channel selection because of the unpredicability of other nodes and the electromagnetic spectrum.

The algorithm can be described as a simple value iteration update as shown below:

$$Q(s_t, a_t) \leftarrow Q(s_t, a_t) + \alpha(s_t, a_t) \times [r_t + \gamma \times max_a Q(s_{t+1}, a) - Q(s_t, a_t)] \quad (1)$$

where $\alpha(s_t, a_t)$ is the learning rate where $0 < \alpha \leq 1$ and which represents to what extent newly acquired information will be taken into account. A learning rate of 1 will mean that only the most recent rewards will be taken into account whereas a learning rate of 0 will mean the agent will learn nothing, and any current reward will be discarded. The discount factor, γ, $0 < \gamma \leq 1$, decides how important future rewards are for the agent. Another thing that makes the Q-Learning algorithm suitable for this type of problem is because it has been shown [8] that Q-Learning will converge with a probability of 1 as long as each state action pair is visited infinately as the learning rate approaches zero. The way in which the Q function in Equation 1 is implemented can be shown in the pseudocode:

```
For each episode, while s is not terminal
   Sense environment and state s
   For each iteration:
      Choose a from s using certain policy
      Take action a, observe output, r, s_{t+1}
      Update Q value for state-action pair (eqn. 1)
      s ← s_{t+1}
   Loop
Loop
```

The electromagnetic spectrum environment that the agent is working in is very unpredictable, making it suitable to use an off-policy RL algorithm such as Q-Learning so as to allow a period of random exploration before following the target policy of the agent. The policy used in selecting which action to take is dependent on the type of policy used. The simplest example is to select the action with the greatest reward for that state, although this may not always lead to an optimal solution as it would lead to a totally greedy policy that would not explore parts of the state space that would not appear to be advantageous but could lead to an optimal solution in the future.

ε-Greedy is an example of a strategy that overcomes this problem. It does so by only selecting the best action $1-\varepsilon$ of

the time and another action is chosen randomly selected for the remainder of the time, ε. The value of ε is in the range $0 < \varepsilon \leq 1$. The higher the value, the more random exploration will occur. A similiar strategy known as ε-decreasing strategy is what is used in this experiment. The main difference between this and ε-Greedy is that ε decreases over a period of time so that the agent goes through a period of random exploration or learning before becoming totally exploitative.

III. Algorithm Implementation

To explain how Q-Learning was used for this problem, an examination of how each state, action, and reward is structured is provided. First, the available spectrum was broken up into a number of channels which could be used for communication. The number of channels available, C, that was used in this experiment was 4, but can change depending on available spectrum. This amount of channels was chosen to provide a simple case, although any number of channels could be chosen as this implementation does not suffer from scalability problems.

The state was defined as a 2-dimensional structure

$$s_t(tr_t, if_t) \tag{2}$$

where the 1st dimension, tr_t, represents the number of channels that a node is currently transmitting on at that time, $0 < tr_t \leq C$ and, the 2nd dimension, if_t, represents the number of channels that an agent attempted to transmit on but were in use at that time, $0 \leq if_t \leq tr_t$. The number of interfering channels is based on the number of channels in use, either by other nodes or through interference that are within range of the node. Through sensing the environment, a binary 2 dimensional vector, $if_t(c)$ is populated as per equation 2.

$$if_t(c_t) = \begin{cases} 1 & \text{if channel } c \text{ at time } t \text{ is in use.} \\ 0 & \text{otherwise} \end{cases} \tag{3}$$

where $c_t = 1, 2, ..., C$. This vector is scanned at each iteration upon taking an action to move to the next state. As the network may be spread over a large area, and would not be a fully-connected network as a result of wireless restrictions on distance, a connectivity vector, V is used to store what cognitive nodes are within range. This is only needed for simulations as a real world implementation would only be able to sense nodes within the wireless transceivers maximum distance. There are 3 possible actions that can be taken by an agent at a particular timestep:

- *I* - do nothing.
- *II*- acquire a channel.
- *III* - drop a channel.

Action I will not acquire or drop any channels, action II will acquire a channel for transmission, and action III will drop a channel that it already has in use. The channel that is selected for drop or acquire is completely random in this implementation, but future work may allow an agent to learn which channels are good and which are bad.

There is an immediate reward or punishment received for taking action a_t while in state s_t. Although there are many posible ways in which to calculate a reward in such an instance, it is important to ensure that the agent doesn't act in a greedy manner, by acquiring as many channels as possible leaving other nodes in the network, or surrounding networks starved of bandwidth. The proposed function shown in equation 4 ensures that the number of active channels is proportionately greater than the number of intefering channels. The weighted interfering channels forces a punishment to any agent that acquires a hnigh proportion of channels in an environment where channel usage is high.

$$r(s_t, a_t) = tr_t - (tr_t \times if_t) - 1 \tag{4}$$

This function ensures the channels are evenly distributed between all the nodes of the network, and also for other devices operating in the same environment. A simple example would be where an agent is transmitting on 2 channels and had also attempted to transmit and failed on another channel after action 1 or *acquire channel* was chosen, the state the agent would be in is $s_t(2, 1)$. So the reward calculated based on equation 4 is

$$r(s(2, 1), 1) = 2 - (2 \times 1) - 1 = -1 \tag{5}$$

In this case, it is a small punishment that the agent receives for this state-action pair. It shows that because the agent is transmitting on 2 channels, but interfering on one of them channels, the reward is negative.

As mentioned in the previous section, the policy by which the actions are chosen for Q-Learning is based on a particular strategy, and in this case a hybrid on ε-Greedy known as the ε-Decreasing strategy. The idea of this is, as explained in the previous section is to allow the agent to go through a period of random learning or exploration before exploiting what it has learned.

Many of the simulations that we have carried out have used a value for ε of 0.8. An example of how action selection occurs is as follows. In the first iteration of the algorithm, there is a 80% probability that a random action will be chosen (exploration) and a 20% probability that the best (or max Q value) action will be chosen (exploitation). As the algorithm progresses, this value decreases to allow the agent to slowly transform into an agent that selects the best action based on what it has learned rather than randomly hopping through the state space, thus exploiting the information it has gathered. As ε approaches zero, the agent should eventually converge on a stable, non-greedy state that uses an appropriate amount of channels without causing interference to other nodes in the environment. It then converges on a fixed state where the agent is transfering over a fixed number of channels until the environment changes enough to warrant a re-learning. These changes could be due to other nodes leaving or joining the network or other outside interference.

As this value reduces overtime and effectively controls

whether the agent is in a *learning mode* or not, it should be possible to adjust this value during the running of the algorithm. There are numerous reasons why we would want to do this but the most important is that the electromagnetic spectrum is an ever changing environment, and as long as it is slow changing, the agent can re-enter the learning phase when the environment has changed enough as to make what it has learned redundent. This forces the agent to re-learn so that it can effectively operate in the altered environment again. This can be an ongoing process where the agent goes in and out of a learning phase whenever some metric that measures environmental change reaches some threshold. The function used in decreasing ε is the same as the one used in decreasing α, which is explained below.

The convergence of a discrete algorithm to an optimal policy is vital for this algorithm, and Watkins and Dayan have proved that Q-Learning does converge [8] as long as a number of conditions hold. The learning rate, α_t, where $0 \leq \alpha \leq 1$ decreases at each iteration. We looked at 2 ways of decreasing α_t, the first being to simply decrease it by a fixed value each time as shown in Equation 6.

$$\alpha_t = \alpha_t - (\alpha_t \div EstNumI) \tag{6}$$

where $EstNumI$ is the estimated number of iterations needed for the algorithm to converge. Another method for decreasing α suggested by Watkins was to decrease it based on the number of times a particular state-action pair, $\alpha(s, a)$ is visited.

$$\alpha(s, a) = \frac{1}{n(s, a)} \tag{7}$$

where $n(s, a)$ is the number of times that state action pair has been visited. This $alpha$ value will give 1, $\frac{1}{2}, \frac{1}{3}, ..$ at each visit to a particular state-action pair.

Eventually the algorithm needs to converge on a particular state which tells the agent the optimal amount of channels it can transmit on without causing interference. This is achieved by allowing the policy to continue choosing actions until action 0, *'do nothing'* is chosen for a fixed number of iterations, meaning that the algorithm has reached a stage where it will stay in the same state forever.

Finally, the greatest advantage of using this particular implementation is the small amount of memory and computational requirements needed. The state-action space would be considered substantially smaller than many other problems that use Q-Learning. In a 4 channel network there is a maximum of 16 possible states, with 3 possible actions making a total state-action memory space of 48. Assuming the use of floating point numbers, the memory space used storing these Q values is only 192 bytes.

IV. Results and Findings

A. Simulation

This work was based on a simple 4-node network as shown in figure 2 for simulation purposes.

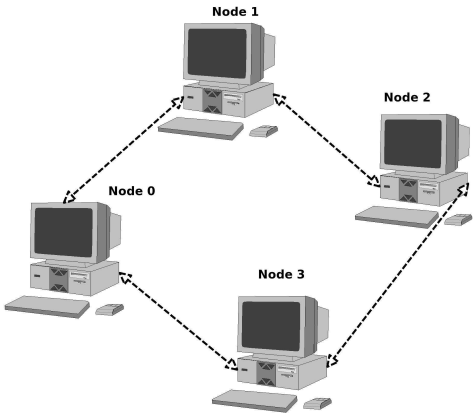

Fig. 2. 4-Node Network

We simulated an environment where there was 4 channels available for transmission, although the number of channels could be altered for each individual node to simulate a real world environment where there may be other radio operating in the same environment. As we wanted to model this as accurately as we could, we used nodes that could only transmit on 1 channel and in some cases 2 to ensure that the algorithm, for each agent or node would converge on an optimal solution each time in different scenarios. The way in which interference was represented in the simulated environment was using a 2 dimensional vector. An example of one is shown in the table below.

	N0	N1	N3	N2
N0	0	1	1	0
N1	1	0	0	1
N3	1	0	0	1
N2	0	1	1	0

Table 1. Sample interference vector over all nodes where 0 represents if two nodes are not in interferable range and 1 if they are in range.

Each node, as mentioned above has an interference vector which holds details on which nodes are within range that could cause interference upon acquiring a channel. The connecting lines in Figure 2 represent 2 nodes being within interfering range. For example, node 0 is within interfering range of nodes 1 and 3. For the purpose of these simulations, this table was used for determining interferable nodes within the network. In a real world case, each node would need to determine which nodes are within range themselves. We implemented this in Java, as this was the first authors main language. Although this sufficed, future work will include implementing this on a number of SDR's, which would require a C implementation.

B. Results

The simulations carried out were mainly focused on different rates and different decreasing factors for ϵ, γ and λ. We also looked at how the overall interference throughout the

network reduced as the agents neared convergence. Finally, we looked at using different forms of action selection strategies.

1) Experiments and final states: As discussed above, for each independent node, it will eventually settle on a state which would hopefully maximise spectrum usage without causing any interference with other nodes. Simple 4-node experiments have shown that this is the case. A sample of some of the experiments is shown in Table 2 and have shown good results. In each case, the output shows that the algorithm has converged on an optimal solution that uses the maximum amount of channels possible for each node without causing interference.

	Node0	Node1	Node2	Node3	Output
1	4	4	4	4	2,2,2,2
2	4	1	4	4	2,1,2,2
3	4	1	1	4	3,1,1,3
4	4	4	1	1	2,2,1,1
5	4	2	3	4	2,2,2,2
6	4	1	4	1	2,1,2,1

Table 2. Output of results of channel usage

The values shown in Table 2 for each experiment represent the number of channels available for transmission for each node. The output is the number of channels the algorithm converged to for each node respectively. In each of these cases, the number of channels is the maximum amount possible without causing interference with other nodes. The channels have also been divided equally without any communication or passing of information.

2) ϵ-reduction: The speed at which the algorithm converges on a solution depends alot on how ϵ is reduced. The faster this value is reduced, the quicker the algorithm moves into the exploitation phase. Results have shown that the faster ϵ is reduced the less chance it has to explore the state-action space in full and thus usually results in the algorithm converging on a bad solution. Figure 3 shows sampled results of how the interference of a single node transitions during the course of the learning of the environment every 1000 iterations.

It can be seen that for a large amount of the iterations at the beginning of the algorithm, the node is interfering on all four channels available, but as it begins to transition into the exploitation phase, this number slowly digresses and eventually does not interfere on any channel. It has been explained that one of the rates at which ϵ decreases is based on the function:

$$\epsilon_t = \epsilon_t - (\epsilon_t \div EstNumI) \tag{8}$$

In the case above, a value of 100,000 has been set for $EstNumI$, meaning that at each iteration, it will be decreased by $\epsilon_t \div EstNumI$. If $EstNumI$ is decreased substantially, thus causing a faster decrease in ϵ, the algorithm will act in a much more erratic manner and will fail to converge on a fair solution. Figure 4 illustrates an example where $EstNumI$ is set to 15000. It shows how in comparison to Figure 3,

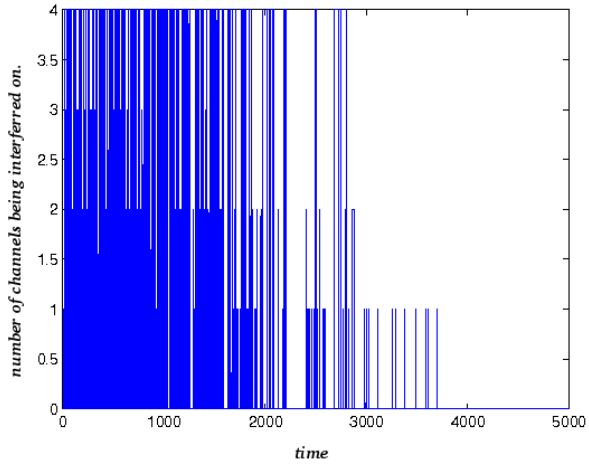

Fig. 3. Single Cognitive Node Interference Pattern over the course of learning environment in a 4 node 4 channel network.

the algorithm fails to reduce the number of channels it is interfering on, and although it converges much quicker than a higher $EstNumI$, each node will not acquire a fair amount of channels, with the one below acquiring all 4 channels, causing interference on the network with some nodes, whilst causing other nodes to not acquire any.

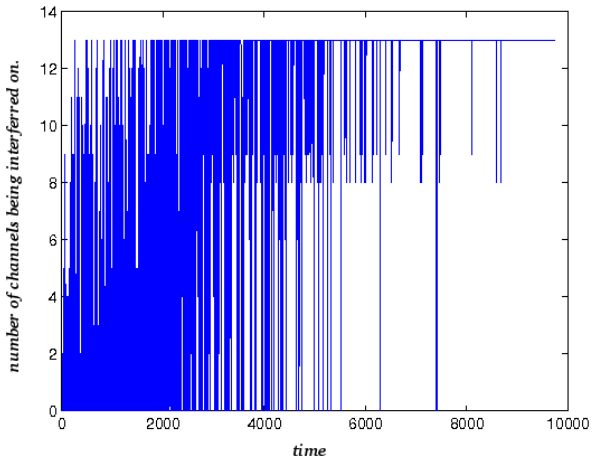

Fig. 4. Single Cognitive Node Interference Pattern where the algorithm does not converge on a good solution.

Therefore the selection of $EstNumI$, must be large enough to allow an agent to traverse the state-action space enough before reaching an exploitative phase.

3) ϵ-Decreasing vs. ϵ-Greedy: The action selection strategy which appeared to work best was ϵ-Decreasing. Many of the experiments carried out using ϵ-Greedy resulted in the algorithm taking much more iterations to converge. While in comparison to ϵ-Decreasing, which converged very quickly as long as robust values were chosen for the different rates. ϵ-Decreasing allowed for greater exploration at the beginning, and greater exploitation towards convergence. This suited the

needs of the experiments as the goal was to find an optimal solution for channel allocation.

4) γ-Selection: How much of the future rewards the algorithm takes into account during the exploration phase very much depends on the initial selection of the discount factor, γ. It has already been shown that Q-learning will converge with a probability of 1, but what it converges to may not be *good* for what the algorithm hopes to achieve. It has been noted that the smaller γ is, the less the probability that the algorithm could converge on a good solution, and usually resulted in a number of the nodes acting in a greedy fashion while other nodes not being able to acquire any channels. A lower bound on the learning rate was discovered, and if it was set below this bound, these problems would occur. As long as γ is greater than the lower bound specified in Equation 8, the algorithm will strive to find a long term goal as opposed to only focusing on current goals.

$$\gamma \geq 0.5 \tag{9}$$

It was also noted that any value over this threshold made very little difference in the both the number of the iterations needed to converge and the solution that the algorithm converged to. What is different between λ and the other variables is that it is fixed. It does not decrease or increase throughout the course of the algorithm. This threshold is based on the fact that γ is a discount factor for future awards. As this approaches zero, the less the algorithm considers future rewards of importance. This makes each individual agent work in a greedy fashion and only consider current rewards.

5) α-Selection (initial): The learning rate, α as discussed earlier determines how much the algorithm takes into account what it learns at each iteration over what it has previously learned. In comparrison to other uses of Q-Learning, the importance of $alpha$ is quite low. It has been noted, through multiple experiments, that as long as there is robust selection for ϵ and γ, it does not matter what initial value is selected for α as long as it follows the basic criteria of being decreased appropriately through time (iterations) and in the range $0 \leq \alpha \leq 1$.

V. Future Work

This research is still in the early stages, and current work is focusing on implementing such an algorithm on a number of Software Defined Radios (SDR) to develop a working example of how Q-Learning could be used in solving this problem. The Maynooth Adaptable Radio System (MARS) has been under development at NUI Maynooth's electronic engineering department since 2004 [9].

Current software demonstrations allow for transmission of images using the IRiS software architecture developed at the CTVR, Trinity College, Dublin and a large number of waveforms using a MARS demonstration application from a transmitter to a receiver. Implementing the Q-Learning algorithm on the MARS boards will give us a working example of a machine learning algorithm to this problem in a real world

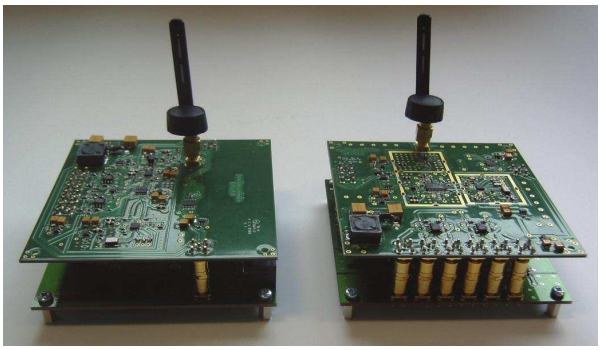

Fig. 5. MARS Receiver and Transmitter Boards

environment, although there are a number of challenges to overcome first. Currently the transmitter and receiver boards run off separate machines, and since cognitive radios need to be fully duplex for both scanning and receiving, there is a need to have both boards running on the same machine. Current work will focus on determining if the kernel will be able to recognise both boards running concurrently.

There are also a number of improvements to be made to the current algorithm. For example individual channels can be included so that agents will be able to differentiate between good channels and bad channels as opposed to whether a number of channels to use is good or not. This would vastly improve the performance of the algorithm in terms of avoiding interference.

Although this is a completely independent learning algorithm with no co-operation with other nodes, it may be worth exploring what advantages some limited communication may have between nodes. One such example could be passing information about *bad channels* between nodes based on some threshold of the Q-Values. It has been mentioned that there is no communication between nodes, but in the real-time implementation, there may need to be a small low bandwidth control channel for communicating which channel a node is going to transmit on to another node.

It may also be worth exploring how well a centralised approach would work using the Q-Learning algorithm by using a master-slave setup in a network. This would involve one fat node doing much of the computation and using a control channel to transmit channel usage information back and forth.

VI. Conclusion

In this paper, we have presented a simple RL technique for channel assignment in a network of independent cognitive nodes. This is achieved using a self-learning scheme based on a TD learning algorithm known as Q-Learning using a 2 dimensional state in an unknown environment. Q-Learnings suitability to this is has been shown as it can take in unknown situations and act upon them using its own experiences.

Simulations carried out on a 4 node network with 4 channels have shown good results in fair non-greedy channel

assignment, so much so as to pursue implementing this on a number of Software Defined Radios in a real time environment with the future goal being to use this as a benchmark to measure other machine learning algorithms abilities to perform this task.
The most significant advantage of this implementation is how small the memory, bandwidth and computational requirements are in comparison to many other cognitive radio channel assignment schemes.

VII. Acknowledgements

This work has been carried out with the support of Science Foundation Ireland (SFI) through the Centre for Telecommunication Value Chain Research (CTVR), the Institute of Microelectronics and Wireless Systems at the National University of Ireland, Maynooth and Irene Macaluso of the CTVR, Trinity College, Dublin.

References

[1] J. Mitola and G. Q. Maguire, *Cognitive Radio:Making Software Radios More Personal*, IEEE Personal Communcations 1999
[2] FCC *Spectrum Policy Task Force Report*, ET Docket No. 02 - 135, 2002.
[3] Husheng Li *Multi-Agent Q-Learning of Channel Selection in Multi-User Cognitive Radio Systems: A Two by Two Case*
[4] S. M. Mishra, A. Sahai and R. W. Brodersen, *Cooperative Sensing among Cognitive Radios*, In Proc. of the IEEE International Conference on Communication(ICC), pp. 1658 - 1663, 2006.
[5] N. Lilith and K. Dogancy, *Dynamic Channel Allocation for Mobile Cellular Traffic using Reduced-State Reinforcement Learning*, WCNC 2004 pp. 2195-2200.
[6] L. Kaelbling, M. L. Littman and A. W. Moore, *Reinforcement Learning: A Survey*, Journal of Artificial Intelligence Research 4-237-285, 1996.
[7] C. J. Watkins, *Learning from Delayed Rewards*, Ph.D Thesis, Cambridge, 1989.
[8] C. J. Watkins, *Q Learning*, Machine Learning , Volume 8 pp279-292, 1992.
[9] R. Farrell *Software-Defined Radio Demonstrators: An Example and Future Trend*, Centre for Telecommunications Value Chain Research, Institute of Microelectronics and Wireless Systems, National University of Ireland Maynooth, Maynooth, Co. Kildare, Ireland

Section 2B
GEOCOMPUTATION

Extracting Localised Mobile Activity Patterns from Cumulative Mobile Spectrum RSSI

John Doyle*, Ronan Farrell, Seán McLoone, Tim McCarthy, Peter Hung
Institute of Microelectronics and Wireless Systems,
National University of Ireland Maynooth,
Maynooth, Co. Kildare,
Ireland
Email: *jcdoyle@eeng.nuim.ie

***Abstract*—Techniques for observing the flow of people are creating new means for observing the dynamics between people and the environments they pass through. This ubiquitous connectivity can be observed and interpreted in real-time, through mobile device activity patterns. Recent research into urban analysis through the use of mobile device usage statistics has presented a need for the collection of this data independently from mobile network operators. In this paper we demonstrate that by extracting cumulative received signal strength indication (RSSI) for overall mobile device transmissions, such information can be obtained independently from network operators. We present preliminary results and suggest future applications for which this collection method may be used.**

***Index Terms*—RSSI, Erlang, human monitoring, geo-temporal weighting.**

I. Introduction

Mapping applications which present the flow of human activities are now becoming increasingly common, one of the main contributions to this is the vast amounts of information made available from mobile devices. In 2007 the number of mobile phones in Ireland numbered 5.3 million [1] while the human population numbered 4.3 million [2]. It is quickly becoming the norm in the developed world that mobile phone devices are outnumbering people. The developing world too has seen a rapid surge in mobile device numbers as mobile networks are often easier and cheaper to install compared to that of landline networks.

As a result of this ever expanding technology, activities that once required a fixed location and connection can now be achieved with higher flexibility, which enables users to act and communicate more freely. The usage patterns obtained from mobile device activity can enable us to model the dynamics of human flow in modern environments [3].

The ability to detect such activity has become increasingly important due to growing interest in the provision of location based services (LBS). LBS researchers have developed techniques for the detection of people in the proximity of an area other than through examining mobile usage statistics. One common approach is to use vision based techniques which utilises camera surveillance systems to identify crowd numbers and behaviour [4], [5], [6]. However, theses types of systems invoke certain social issues with regards to privacy [7], [8].

As stated in Doyle *et al.* [9], the mobile phone usage statistic commonly employed in mobile usage mapping applications is a measure of network bandwidth used. Typically, this is collected at a base station within a mobile operator's network, or by use of special software installed on mobile phones. The metric by which this activity is measured is known as an Erlang. An Erlang is one person-hour of phone use, which could represent one person talking for an hour, two people talking for half an hour each, 30 people each speaking for two minutes, and so on [10]. A more modern interpretation of this metric would be to consider the quantity of digital data transferred, regardless of the form of communication, such as voice, SMS, and data. This method was valuable in the past due to the restricted nature of mobile telecommunications which were fundamentally voice-only networks. Modern networks have an progressively diverse range of usages which do not linearly correspond to intensity of communication. For instance text messaging uses very little bandwidth though is an important form of communication.

As an alternative to collecting data throughput measurements, we have adopted a technique for monitoring the cumulative electromagnetic energy in the frequency band of client-side mobile phone transmissions (i.e. mobile device to base station transmission band). By analysing these RSSI values over time and space through a collaborative network of sensors, we propose that results can be obtained that are of comparable quality to the more invasive network bandwidth metrics (Erlang). Such measurements can be easily achieved using well known circuitry for Received Signal Strength Indication (RSSI) [11], [12]. The information gathered is inherently anonymous due to the absence of information decoding. As a result, it is impossible to deduce individual identities or phone information content from the raw data collected and stored in the proposed system, thus avoiding the potential ethical issues faced by both vision based and network operator polled systems.

In the rest of this paper, we highlight the use of an energy detecting device to monitor mobile spectrum activity for the purpose of mapping mobile device activity. Section II gives an overview of some related work in this field. Section III

describes the proposal put forward by this paper. Section IV details the experimental setup adopted to measure the temporal RSSI data, from which useful information is extracted. Section V presents the results of experiments carried out focusing on the collection of RSSI mobile device data under different scenarios. Section VI summarises the conclusions of the work to date and outlines future directions for research.

II. Background

This section presents on overview of some work related to the collection and analysis of human movement data. This can be grouped into real time urban flow mapping, location tracking and spectrum strength collection.

A. Real Time Urban Flow Mapping

The emergence of new mapping applications which present the flux of people in an attempt to demonstrate the dynamics of metropolitan cities highlights the recent growth and interest relating to tracking human flow on urban scales. Over the last few years this research area has seen steady growth with large projects starting in European and Asian cities. The monitoring of mobile phone usage patterns has been the major data source used to extract the human behavioural patterns needed for these applications. Other sources such as passive tolling of Bluetooth devices, as well as techniques including GPS tracking and short range tracking have been utilised in the past but theses do not scale easily in urban environments.

Amsterdam Real Time [13] and Cityware Research Group [14] are examples of such projects. The Amsterdam Real Time project aimed to construct a dynamic map of Amsterdam, Netherlands, based on trace lines produced from the collection of GPS data relating to peoples movements. Each person volunteered in the experiment and was equipped with a GPS receiver. This receiver fed the GPS coordinates of the volunteer to a central system in real time. Maps produced were solely based on this GPS data. In the UK, the Cityware research group supplemented the pedestrian flow data typically gathered as part of a space syntax analysis with data on Bluetooth devices passing through pedestrian survey gates.

To date there are two main methods for the gathering mobile usage information: data collection at the operator level; and through modified mobile phone software. The first area requires the cooperation of mobile operators to provide data on a macro level of urban areas. Graz in Real Time [15], the Mobile Landscapes project [3], Real Time Rome [16] and Bangkok Metropolitan Project [17] are examples of projects which utilised this network operator data.

The Graz in Real Time project is a real time mobile phone monitoring system based on cell phone traffic intensity, traffic migration (hand overs) and traces of registered users as they moved through the city of Graz.

The Mobile Landscapes project collected network usage data in the Milan, Italy. When combined with the geographical mapping of cell areas, a graphical representation of the intensity of urban activities and their evolution through space and time was produced. From this they were able to detect events such as national holidays and major sporting events.

The Real Time Rome was MIT's SENSEable City Laboratory contribution to the 10th International Architecture Exhibition in Venice, Italy. The project was the first example of an urban-wide real time monitoring system that collects and processes data provided by telecommunications networks and transportation systems. It used location data from mobile phone subscribers provided by Telecom Italia, public buses ran by a local transport company Atac and taxis run by the cooperative Samarcanda.

Horanont and Shibasaki [17] presented an implementation of mobile sensing for large-scale urban monitoring in Bangkok Metropolitan, Thailand. They used Erlang data from Advanced Info Service PLC (AIS), a leading mobile operator in Thailand. They showed that large scale monitoring of clusters of Erlang data from mobile base stations were able to provide indirect interpretations of spatial patterns of urban life and its temporal dynamics.

However, there are difficulties with this approach, most notably the legal and privacy issues that prevent operators delivering such information to outside researchers. In addition, even with best efforts, there is no guarantee that data from theses sources is always available, complete or accurate. Network operators continually optimise their network throughout the day, using temporary towers. This adds to the level of uncertainty into these fixed point measurements as network topologies become more dynamic. A more fundamental issue arises regarding spacial accuracy as the spatial resolution of the usage statistics is dependent on both the operators network topology and base station hardware.

As a result approaches have emerged which aimed to address these issues by placing embedded software applications on the mobile devices to log data. Estonia group project [18] and MITs Reality Mining project [19] are examples of projects which utilise this approach.

Ahas and Mark [18] tracked the mobile phones of 300 users for a social positioning application. They combined spatio-temporal data from phones with demographic and attitudinal data from surveys, creating a map of social spaces in Estonia.

MITs Reality Mining project illustrated that it was possible to extract common behavioural patterns from the activities of 94 subjects. The subjects were issued with mobile phones pre-installed with several pieces of software that record and sent research data on call logs, Bluetooth devices in proximity, cell tower IDs, application usage, and phone status. This yields valuable, person specific results but the solution may not be easy to scale considering the large numbers needed to represent urban and suburban populations.

B. Mobile Phone Location Tracking

Most indoor environment based localisation research to date has focused on the accurate localisation of objects and people using short-range signals, such as WiFi [20], [21], [22], Bluetooth [23], ultra sound [24], and infra-red [25]. Outdoor

localisation is almost exclusively performed using the Global Positioning System (GPS).

Otsason *et al.* [26] showed that an indoor localisation system based on wide-area GSM fingerprints can achieve high accuracy, and is in fact comparable to an 802.11-based implementation. To date there are two major ways for mobile phone locations to be tracked in mobile networks, namely network-centric and device-centric localisation. In network-centric systems, base stations make the measurements of distance to a mobile phone and send the results to a centralised location at which the location of the mobile device is calculated. In device-centric systems, the handset performs the calculation itself on the basis of environmental information gathered from the network. Hybrid solutions are also possible, which try to combine the advantages of both.

The American National Standards Institute (ANSI) and the European Telecommunications Standards Institute (ETSI) stated that mobile positioning systems can be classified under the following technologies: cell identification, angle of arrival, time of arrival, enhanced observed time difference, and assisted GPS [3].

- *Cell identification;* The available coordinates of the serving base station are associated with the mobile device. The accuracy of the locational information depends upon the physical topology of the network.
- *Angle of arrival (AoA);* The AoA method uses data from base stations that have been augmented using arrays of smart antennas. This allows the base station to determine the angle of incoming radio signals, making it possible to then determine the location of a handset by triangulating known signal angles from at least two base stations.
- *Time of arrival (ToA);* Position here is determined by triangulating the time needed for a packet to be send from a phone to three finely synchronised base stations and back.
- *Enhanced observed time difference (E-OTD);* This requires handsets to be equipped with software that locally computes location. Three or more synchronised base stations transmit signal times to the mobile device, the embedded software of which calculates time differences and therefore distance from each base station making triangulation possible.
- *Assisted global positioning system (A-GPS);* Here devices use both GPS and a terrestrial cellular network to obtain geographic positioning.

C. Spectrum Signal Strength Collection

To collect the cumulative electromagnetic energy in the frequency range of client-side mobile phone transmissions, one must be able to measure and quantify the energy in the specific energy band occupied by client-side mobile phone transmissions. This is effectively measuring the signal strength in a specific frequency band of energy [11], a common technique in wireless communications. To do this reliably an energy detecting device is used which returns a received signal strength indication (RSSI) parameter. Energy detecting devices can easily be purchased or built. Due to such readiness in availability, RSSI has been considered in the past as a sensing parameter. A number of applications have provided insight into its usefulness, both Wu *et al.* [27] and Stoyanova *et al.* [28], in particular, describe the key issues which affect RSSI accuracy. They are summarised as:

- The orientation of the antenna;
- Transceiver variation;
- Multipath fading and changes in environment.

Multipath fading and environment changes contribute the main variance in RSSI data. This relates to part of the electromagnetic energy radiated by the antenna of a transmitter reaching a receiver by propagating through different paths. Along these paths, interactions known as propagation mechanisms may occur between the electromagnetic field and various objects. To model theses mechanisms, propagation prediction models have been devised to provide an accurate estimate of the mean received power or path loss (PL) for a specified frequency band based on geographical information about the environment. Empirical, semi-deterministic, and deterministic models are the main classes which describe mobile channel characteristics [29]. As these propagation models describe how a signal may act in a given environment, they must be used when trying to gain insight into positions of signal sources.

In recent years cognitive radio systems [30], [31], [32] have become increasingly viable and signal strength measurement is a key element in the detection of primary user spectral occupancy. To improve performance, they have explored a number of techniques that can be used to address these issues, such as collaborative sensing between multiple RSSI detectors [33], [34]. By cross-correlation and signal processing, non-random signals can be detected and analysed. Similar approaches can be applied with existing transmissions to detect usage and extract statistical patterns.

III. Proposal

Our proposal is based on the measurement of localised cumulative strength of mobile device emissions through the use of an RSSI sensor. We propose that this data can provide a suitable alternative to operator obtained data. Results will demonstrate the proposed method can capture mobile phone activity and display the spacio-temporal patterns contained within.

As an alternative sensing parameter, cumulative received signal strength (RSSI) offers several advantages over network usage data;

- RSSI data can be collected without the cooperation of mobile operators or mobile device user.
- RSSI as a metric is independent of modulation type, so RSSI can be used for GSM protocols and 3G protocols.
- Geo-spatial RSSI data can provide fine resolution making it possible to localise events very accurately and quickly.
- RSSI collection hardware can easily be modified to observe different metrics, making a network deployment very flexible.

However, individual sensor measurements of wideband signal strength measurements have limitations in terms of localised accuracy. This is due to limiting channel characteristics and the inability to distinguish between a single near device transmitting with high power and several users far away transmitting with low power. The question then is how to reliably collect this information taking into account such factors.

By adopting techniques commonly utilised in cognitive radio systems, we propose that these accuracy issues may be mitigated. First, by spatially and temporally weighting each RSSI data point form a sensor with corresponding points from other radios in the geographical area nearby, the RSSI accuracy can be improved [33] [34]. Second, modelling the environment with accurate models will help quantify the data and give insight into its behaviour. Third, calibration with respect to base station coverage will reduce effects caused by mobile device transmission power variation. Finally, the spatial sampling topology of the sensor network will be a dominant factor in determining performance, particularly when variable sensor heights are also considered. Thus methods for insuring topology uniformity must be taken into account.

To distinguish between the RSSI signal generated by one user near the sensor and several users further away we will deploy a dense network topology. This will insure that spectral energy readings from each sensor can be localised to some degree. To localise such activity there are several possible solutions. One is to localise activity based on a sensor identification technique, similar to the cell identification used to identify a mobile device position in a cellular network. Here the sensor node with the associated highest RSSI value is deemed to be the coordinate of the activity. This will however offer reduced spatial resolution. Thus a more advanced technique, which combines multi-sensor information, would be a more suitable approach.

IV. Experimental Work

A. Experimental Setup

Our experiments were based on the measurement of localised cumulative strength of mobile device emissions through the use of a custom-made RSSI sensor. The main component used to measure the RSSI intensity was a true power detector from Analog Devices (chip part number AD8362) paired with a single omni-directional GSM 900 antenna. The AD8362 device returns a voltage which linearly corresponds to the RF spectrum power passed through it. It operates with a 65dB dynamic range, ranging from -55dB to 10dB. To obtain a measure of the performance, experiments were carried out within a building on NUI Maynooths North Campus. The measured performance of two such sensors were compared to that of a spectrum analyser, the results of which can be found in Section V.

Doyle *et al.* [9] described the capabilities of such a sensor with respect to picking up different types of phone activity. This paper highlighted the capability of such sensors for picking up even shorter bursts of mobile transmission energy with both text message and phone call activity clearly identified. A technique for the extraction of areas of high temporal dense activity was also demonstrated. From this information, areas around each hour mark of high temporal density were highlighted, these times coincided with the starting and finishing times of lectures, thus demonstrating that RSSI can provide the information needed to monitor human behaviour.

To further validate the capabilities of the sensing devices and feature extraction methodology, we designed two experiments which tested different scenarios of mobile phone activity. The focus was to test our method for geo-spatial temporal weighted signal processing. Both experiments took place in the foyer of the Engineering building at NUI Maynooth under controlled conditions (no other phone activity). The result can be seen in Section V.

- **Experiment 1:** Obtain RSSI measurements from a phone call while a person is walking in a uniform direction. The path taken is depicted in Fig. 1a.
- **Experiment 2:** Measure readings from a phone call while a person is walking in a non-uniform direction. The path taken is depicted in Fig. 1b.

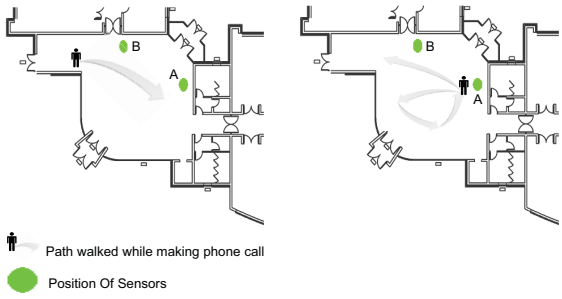

(a) Path taken in Experiment 1 (b) Path taken in Experiment 2

Fig. 1: Layout of sensors and path walked by a phone user for a controlled test carried out in Engineering foyer on NUI Maynooth's North Campus. A and B indicate the positions of sensors A and B respectively.

B. Processing Method

Various signal processing algorithms can be applied to assist with extracting interesting patterns from measured mobile phone signal strengths. Our approach has focused on a geo-spactial temporal based scheme that identifies time periods with interesting behaviour. One early implementation is explained in this Section. Its layout is depicted in Fig. 2.

The spectral energy, which was sampled at a rate of 2kHz, and is denoted as $s(k)$. The signal processing method applied to these samples consists of four stages.

- **Stage 1:** Detect the presence of a mobile transmission as governed by a cut-off threshold τ

$$s_\tau(k) = \begin{cases} 0 & \text{if } s(k) < \tau \\ s(k) & \text{if } s(k) \geq \tau \end{cases} \quad (1)$$

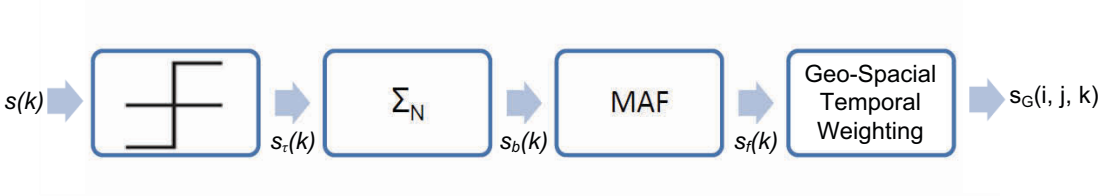

Fig. 2: Signal processing performed on raw RSSI data. Feeding output back into the geo-spactial temporal weighting stage gives an n^{th} order weighting.

where τ in this instance is chosen to be -55dBm, the minimum detectable level of the energy detecting chipset.

- **Stage 2:** Downsample the data by a factor of T, this is done by replacing every block of T samples by its average

$$s_b(i) = \frac{1}{T} \sum_{k=(i-1)T+1}^{iT} s_\tau(k) \tag{2}$$

where $s_b(i)$ is the downsampled data set and T is the downsampling factor. Decimation should be application specific. While it can trim down the noise within the data, excessive decimation may reduce the signal of short temporal events, such as text messages.

- **Stage 3:** Smooth the data using a moving average filter (MAF) of width $(2W + 1)$ samples

$$s_f(i) = \frac{1}{2W+1} \sum_{p=(i-W)}^{i+W} s_b(p) \tag{3}$$

where $s_f(i)$ is the resulting filtered data set.

- **Stage 4:** Given a vector of readings from a set of n sensors

$$\mathbf{s}(k) = [s_1(k), s_2(k), s_3(k), \ldots, s_n(k)] \tag{4}$$

apply a geo-spatial temporal weighting using a truncated Gaussian Kernel. Here, $s_i(k)$ the sensor reading from the i'th sensor, has an associated coordinate in space (x_i, y_i) relating to the position of the sensor. To achieve this weighting, points are calculated in space-time by a collaborative weighting of readings taken from each sensor node. A point in space-time $s_G(x, y, k)$ can be calculated using,

$$s_G(x, y, k) = \sum_{p=k-j}^{k+j} \sum_{i=1}^{n} g_{ip}(x, y, k) s_i(p) \tag{5}$$

where $g_{ip}(x, y, k)$ is the geo-spatial temporal weight corresponding to reading $s_i(p)$ and $2j + 1$ is the width of the truncating window in time. The weight $g_{ip}(x, y, k)$ is given by

$$g_{ip}(x, y, k) = g_\beta(x, x_i) g_\beta(y, y_i) g_\beta(k, p) \tag{6}$$

where

$$g_\beta(u, v) = e^{-\left(\frac{u-v}{\sigma_u \beta}\right)^2}. \tag{7}$$

Here, u and v are placeholders for the corresponding variables in Eq. 6. σ_u denotes the initial spreading factor assigned to each dimension and β is a scaling factor controlling the spread given to those points whose weight is over the lower limiting threshold γ such that,

$$\beta = \begin{cases} 1 & \text{if } s_i(k) < \gamma \\ c & \text{if } s_i(k) \geq \gamma \end{cases} \tag{8}$$

where $c > 1$. The effect of this stage is to weight each RSSI data point from a sensor with corresponding spatial and temporal points from other sources such that readings that are both spatially and temporally close are amplified.

V. Results

The results shown here reflect measurements of wide band mobile phone RSSI taken on NUI Maynooth North Campus. Fig. 4 illustrates the sensitivity comparison between a spectrum analyser and RSSI sensors, whose architecture is described in Section IV-A. It can be seen that the readings from RSSI sensors, though less precise, resemble that from a spectrum analyser.

Fig. 3 presents the measurements collected in an experiment prior to geo-spatial temporal weighting. The experiments are carried out to verify the ability of signal processing algorithm to highlight the movement of mobile devices in an indoor environment. Fig. 5 and Fig. 6 show how the geo-spatially temporally weighted points in space may be visualised in the form of contour maps that highlight device activity picked up.

The temporal shift of energy can clearly be observed as the positions of the phone calls, in voice communication mode, vary in space. Currently, a preliminary method is employed to interpolate the data over space. This consisted of adopting the sensor nodes positions as the centre of energy annealing the signal as we moved further out. Note weights represented in each contour plot are relative measures compared to that of surrounding areas. As a result the measure of dominance should be considered relative and not as an absolute value.

Future work will involve more advanced methods which may take into account pre-defined information gathered from geographical information systems (GIS) and channel models relating to the mobile spectrum band of interest. Nevertheless,

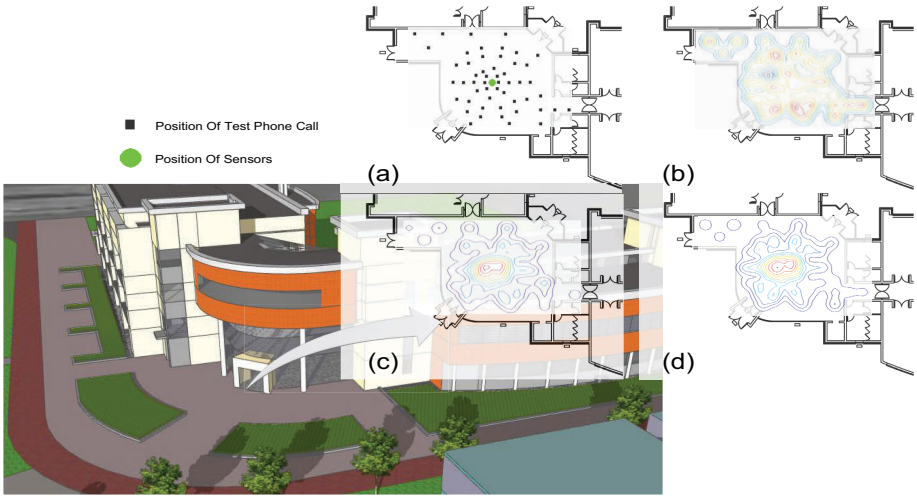

Fig. 4: RSSI measurements obtained in the foyer of NUI Maynooth's Electronic Engineering building showing the relationship between the sensor nodes used and a spectrum analyser: (a) locations of calls made in the foyer, the positions of the sensing nodes and spectrum analyser; (b) readings taken from a spectrum analyser; (c) readings taken from sensor A; (d) readings taken from sensor B

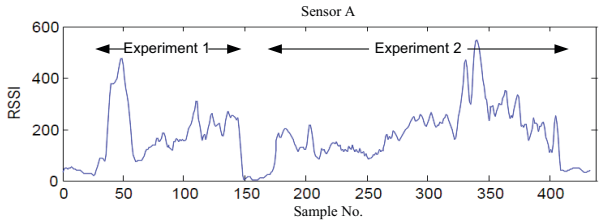

(a) RSSI measurements obtained from sensor A

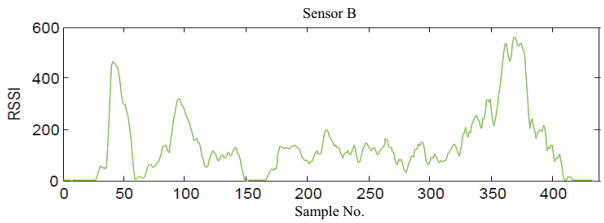

(b) RSSI measurements obtained from sensor B

Fig. 3: RSSI measurements obtained in the Engineering foyer of NUI Maynooth for both experiments 1 and 2.

these early results suggest that localised cumulative RSSI data could be a valuable source of information when trying to extract flow information from mobile devices.

VI. Conclusions

This paper summarised the work being carried out in the area of mapping mobile phone activity on urban and localised scales. At the same time, an overview is presented on popular localised tracking techniques and issues which relate to the reliable measurement of mobile spectrum RSSI. Experiments demonstrate that the detection of mobile spectrum RSSI can provide useful information when monitoring mobile device activity in a localised context. This information is gathered without the cooperation of mobile network operators or users and retains usage anonymity due to the lack of information decoding. We presented a preliminary technique for the detection and visualisation of mobile activity flow within indoor environments.

This proposed approach could also be used to complement traditional techniques for mapping mobile device activity. For instance, one could use the network operator data, if available, to model the dynamics of a city or town while localised RSSI data, within such an urban environment, is used to observe the dynamics of specific buildings or localised areas. Nonetheless, our research is still in its preliminary stages, so additional validation is needed.

For this purpose, a mobile sensor network aimed at the collection of RSSI data is under construction. It will first be distributed throughout the North Campus of NUI Maynooth with a view to expanding it into the nearby South Campus and town of Maynooth in longer term. This project will offer an opportunity to understand some of the dynamics relating to university student life. Moreover, focusing on temporal and spatial patterns of mobile phone activity may shed light on how we interact with our local environment.

We hope to address such questions as how buildings really used on campus, how to determine where people can be found as opposed to where they pass through and how to identify interesting localised events as they occur in time and space. The answers to these questions would pave the way for a number of interesting applications. A real time map of human

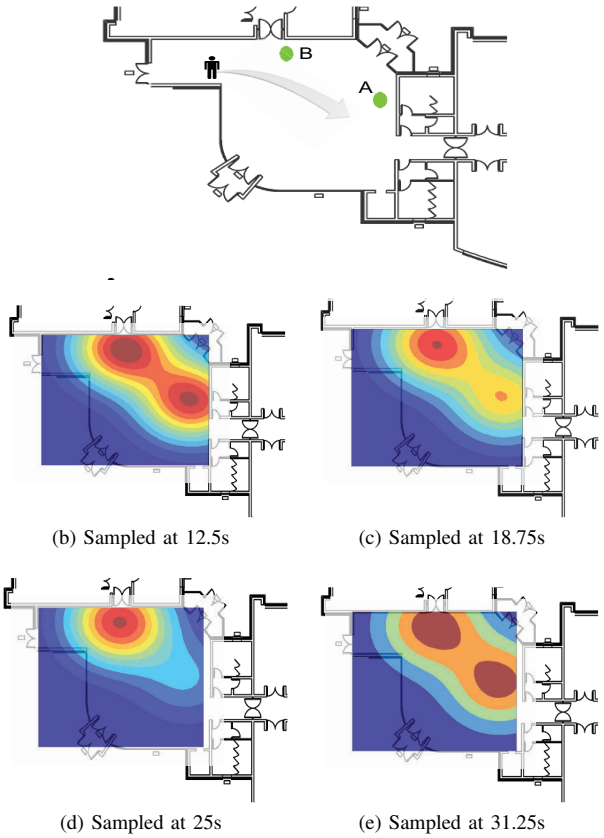

(b) Sampled at 12.5s (c) Sampled at 18.75s

(d) Sampled at 25s (e) Sampled at 31.25s

Fig. 5: Mapping of RSSI information obtained after the geo-spatial temporal weighting process for time slot of experiment 1 in Fig. 3 at different sampling times.

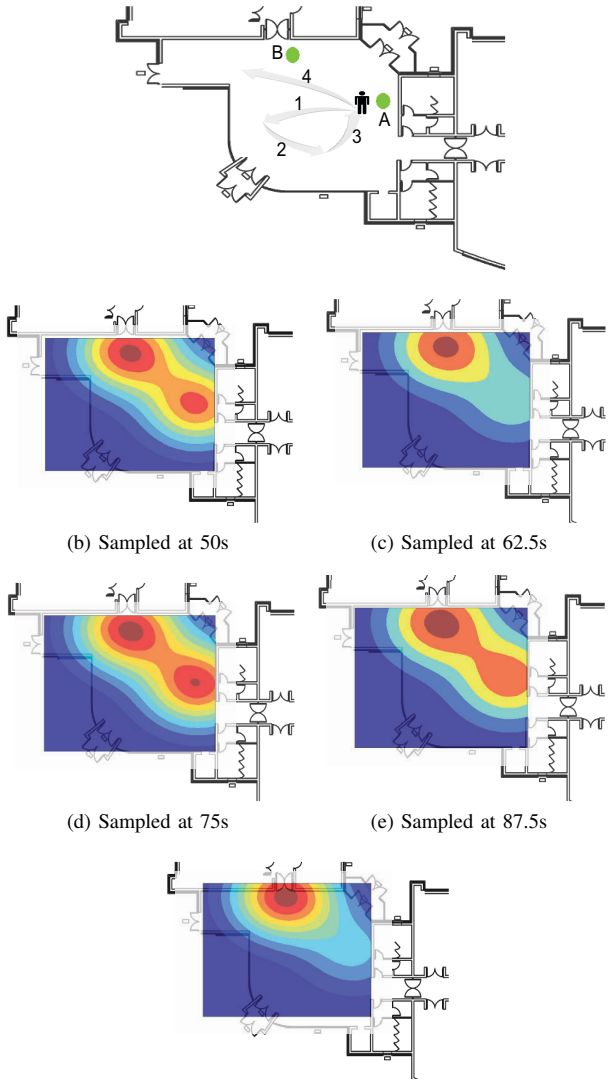

(b) Sampled at 50s (c) Sampled at 62.5s

(d) Sampled at 75s (e) Sampled at 87.5s

(f) Sampled at 100s

Fig. 6: Mapping of RSSI information obtained after the geo-spatial temporal weighting process for time slot of experiment 2 in Fig. 3 at different sampling times. The path numbers indicate the walking sequence of the phone user.

flow could be produced showing the real time movements of student population, both indoor and outdoor. The map could provide insights to university planning authorities to decide on the location of student services or emergency services in the event where rapid response is required.

Acknowledgements

Research presented in this paper was funded by a Strategic Research Cluster grant (07/SRC/I1168) by Science Foundation Ireland under the National Development Plan and by the Irish research Council for Science, Engineering and Technology under their Embark Initiative in partnership with ESRI Ireland. The authors gratefully acknowledge this support.

References

[1] I. C. R. (COMREG), "Quarterly report," Tech. Rep., March 2009.
[2] I. C. S. O. (CSO), "Population and migration estimates," Tech. Rep., April 2008.
[3] C. Ratti, S. Williams, D. Frenchman, and R. Pulselli, "Mobile landscapes: using location data from cell phones for urban analysis," *Environment and Planning B: Planning and Design*, vol. 33, no. 5, pp. 727–748, 2006.
[4] Y. Ivanov, C. Stauffer, A. Bobick, and W. Grimson, "Video surveillance of interactions," *IEEE Workshop on Visual Surveillance*, vol. 19, no. 12, pp. 82–89, 1999.
[5] D. Ayers and M. Shah., "Monitoring human behaviour from video taken in an office environment," *Image and Vision Computing*, vol. 19, no. 12, pp. 833–846, 2001.
[6] A. Davies, J. Yin, and S. Velastin, "Crowd monitoring using image processing," *Electronics And Communication Engineering Journal*, vol. 7, no. 1, pp. 37–47, 1995.
[7] K. Bowyer, "Face recognition technology: security versus privacy," *IEEE Technology and Society Magazine*, vol. 23, no. 1, pp. 9–19, 2004.
[8] L. Barkuus and A. Dey, "Location-based services for mobile telephony: a study of user's privacy concerns," *Proceedings of the INTERACT 2003, 9TH IFIP TC13 International Conference on Human-Computer Interaction*, pp. 9–19, July 2003.
[9] J. Doyle, R. Farrell, S. McLoone, T. McCarthy, P. Hung, and M. Tahir, "Utilising Mobile Phone RSSI Metric for Human Activity Detection," *Proceedings of the ISSC 2009, 20th Irish Signals and Systems Conference*, June 2009.
[10] J. Reades, F. Calabrese, A. Sevtsuk, and C. Ratti, "Cellular census: Explorations in urban data collection," *IEEE Pervasive Computing*,

vol. 6, no. 3, pp. 30–38, 2007.

[11] H. Urkowitz, "Energy detection of unknown," *Proceedings of the IEEE*, vol. 55, no. 4, pp. 30–38, April 1967.

[12] K. Srinivasan and P. Levis, "Rssi is under appreciated," in *Proceedings of the Third Workshop on Embedded Networked Sensors (EmNets 2006)*, 2006.

[13] E. Polak, "Amsterdam real time," *Waag Society, http://www.waag.org/realtime/*, 2002.

[14] E. ONeill, V. Kostakos, T. Kindberg, A. Penn, and S. F. T. Jones, "Instrumenting the city: Developing methods for observing and understanding the digital cityscape," *Lecture Notes in Computer Science*, vol. 4206, pp. 315–332, Sept 2006.

[15] C. Ratti, A. Sevtsuk, S. Huang, and R. Pailer, "Mobile landscapes: Graz in real time," in *Proceedings of the 3rd Symposium on LBS And TeleCartography*. Springer, 2005, pp. 28–30.

[16] F. Calaberse and C. Ratti, "Real time rome," *Networks and Communication Studies*, vol. 20, no. 3-4, pp. 247–257, 2006.

[17] T. Horanont and R. Shibasaki, "An implementation of mobile sensing for large-scale urban monitoring," *Proceedings of UrbanSense08, International Workshop on Urban, Community, and Social Applications of Networked Sensing Systems*, Nov 2008.

[18] R. Ahas, A. Aasa, lar Mark, T. Pae, and A. Kull, "Seasonal tourism spaces in estonia: Case study with mobile positioning data," *Tourism Management*, vol. 28, no. 3, pp. 898–910, 2007.

[19] N. Eagle, A. Pentland, and D. Lazer, "Inferring social network structure using mobile phone data," *Proc. of National Academy of Sciences*, 2006.

[20] P. Bahl and V. Padmanabhan, "Radar: An in-building rf-based user location and tracking system," in *IEEE INFOCOM*, vol. 2. Institute of Electrical Engineers Inc (IEEE), 2000, pp. 775–784.

[21] E. Elnahrawy, X. Li, and R. Martin, "The limits of localization using signal strength: A comparative study," in *In Proceedings of the 1st IEEE International Conference on Sensor and Ad Hoc Communications and Networks*. Institute of Electrical Engineers Inc (IEEE), Oct 2004, pp. 406–414.

[22] A. Ladd, K. Bekris, A. Rudys, L. Kavraki, and D. Wallach, "Robotics-based location sensing using wireless ethernet," *Wireless Networks*, vol. 11, no. 1, pp. 189–204, 2005.

[23] L. Aalto, N. Göthlin, J. Korhonen, and T. Ojala, "Bluetooth and wap push based location-aware mobile advertising system," in *Proceedings of the 2nd international conference on Mobile systems, applications, and services*. ACM New York, NY, USA, 2004, pp. 49–58.

[24] N. Priyantha, A. Chakraborty, and H. Balakrishnan, "The cricket location-support system," in *Proceedings of the 6th annual international conference on Mobile computing and networking*. ACM New York, NY, USA, 2000, pp. 32–43.

[25] A. Ward, A. Jones, and A. Hopper, "A new location technique for the active office," *IEEE Personal Communications*, vol. 4, no. 5, pp. 42–47, Oct 1997.

[26] V. Otsason, A. Varshavsky, A. LaMarca, and E. D. Lara, "Accurate gsm indoor localization," *Lecture Notes in Computer Science*, vol. 3660, pp. 141–158, Aug 2005.

[27] R. Wu, Y. Lee, H. Tseng, Y. Jan, and M. Chuang, "Study of characteristics of rssi signal," in *IEEE International Conference on Industrial Technology, 2008. ICIT 2008*. Institute of Electrical Engineers Inc (IEEE), 2008, pp. 1–3.

[28] T. Stoyanova, F. Kerasiotis, A. Prayati, and G. Papadopoulos, "Evaluation of impact factors on rss accuracy for localization and tracking applications," in *Proceedings of the 5th ACM international workshop on Mobility management and wireless access*. ACM New York, NY, USA, 2007, pp. 9–16.

[29] B. Fleury and P. Leuthold, "Radiowave propagation in mobile communications: an overview of european research," *Communications Magazine, IEEE*, vol. 34, no. 2, pp. 70–81, Feb 1996.

[30] S. Haykin, "Cognitive radio: brain-empowered wireless communications," *IEEE Journal on Selected Areas in Communications*, vol. 23, no. 2, pp. 201–220, 2005.

[31] J. Mitola III and G. Maguire Jr, "Cognitive radio: making software radios more personal," *IEEE Personal Communications*, vol. 6, no. 4, pp. 13–18, 1999.

[32] W. L. I.F. Akyildiz, M. Vuran, and S. Mohanty, "Next generation/dynamic spectrum access/cognitive radio wireless networks: A survey," *Computer Networks*, vol. 50, no. 13, pp. 2127–2159, 2006.

[33] X. Huang, N. Han, G. Zheng, S. Sohn, and J. Kim, "Weighted-collaborative spectrum sensing in cognitive radio," in *Communications and Networking in China, 2007*, 2007, pp. 110–114.

[34] A. Ghasemi and E. Sousa, "Collaborative spectrum sensing for opportunistic access in fading environments," in *New Frontiers in Dynamic Spectrum Access Networks, 2005. DySPAN 2005.*, 2005, pp. 131–136.

Evaluating Twitter for Use in Environmental Awareness Campaigns

Peter Mooney*†, Adam C. Winstanley* and Padraig Corcoran*
*Geotechnology Research Group,
Department of Computer Science,
National University of Ireland Maynooth (NUIM),
Maynooth, Co. Kildare. Ireland
Email: {peter.mooney, adam.winstanley, padraig.corcoran}@nuim.ie
†Environmental Research Centre,
Environmental Protection Agency Ireland,
Richview, Clonskeagh,

***Abstract*—Many studies have shown that the effective harnessing of ICTs is critical in local, national, and global efforts to adapt and mitigate the effects of climate change. Citizens must be provided with accurate information about environmental issues and should receive this through the most effective communication channels available. In this paper we describe work in progress in evaluating Twitter as a means of distributing environmental information to citizens. This work will attempt to measure how effective the Twitter medium can be in environmental awareness campaigns for issues such as climate change by carrying out an analysis of a regularly updated database of Twitter messages. This work will also look to establish if users are environmental issues through their Twitter networks.**

I. Introduction

The online social network Twitter.com (http://twitter.com/) and environmental issues such as climate change and pollution are both inextricably linked with today's popular culture and mass media. In this introductory section we provide a brief overview of both Twitter and the natural environment in order to emphasise their individual positions in modern society, popular culture, and the mass media. We also provide a brief literature review of research carried out on the applications of Twitter and its social impact.

A. Influence of Twitter

Twitter is used by millions of people around the world to stay connected to their friends, family members and coworkers through their computers and mobile phones. The interface allows users to post short messages (up to 140 characters) that can be read by any other Twitter user. Users declare the people they are interested in following, in which case they get notified when that person has posted a new message. A user who is being followed by another user does not necessarily have to reciprocate by following them back, which makes the links of the Twitter social network directed. Zeichick summarises Twitter as the ability to "post and follow text messaging using a browser, special desktop applications, or mobile applications on smartphones" [1]. He comments that with key news media, such as the New York Times and the Telegraph, writing frequently about Twitter we have an indication that "it (Twitter) has passed the stage where it is only for *early adopters*". Some newspapers have begun to publish *getting started guides* for Twitter such as "How to make the most of Twitter" from The Guardian [2]. The ubiquitous nature of Twitter is reflected in media reports in the UK from early 2009 where proposed primary school curriculum changes were discussed. These changes would allow schools greater flexibility in what they teach including plans to teach school children the fundamentals of using Web 2.0 technologies such as Twitter and Wikipedia [3].

B. Environmental Problems

Since the end of 2006 climate change has gradually become *the* hot topic [4] amongst all other environment problems. A large number of events, reports, movies, etc. for example the Stern Review, Fourth Assessment Report of the Intergovernmental Panel on Climate Change [5], Conference of Parties 13 in Bali, the Live Earth Global Concert have generated increasing media coverage on climate change issues [4]. Conventional environmental awareness campaigns strongly rely on information to change attitudes. To make climate change communication effective, more sophisticated alternatives are suggested, such as harnessing tools and concepts used by brand advertisers, so as to make being climate-friendly desirable rather than a duty or matter of obedience [6]. Climate change affects every citizen at every level - local, regional, national, and global [7]. Some authors [8] have looked at the reporting of climate change in the mass media. Results of this analysis[8] show that scientists tend to be associated with an emphasis on environmental problems and causes while politicians and special interests tend to be associated solutions and remedies. A major European Commission survey revealed that "pollution in towns and cities and climate change" are the most frequently discussed environmental topics amongst EU Citizens and this reflects the intense public discussion on these topics[9]. Almost 57% of EU Citizens surveyed placed climate change as the number one issue that "worried them about the

environment'. The report states that "this further reinforces the observation that climate change has become one of the top concerns in the environmental debate".

C. Users and Usage Patterns on Twitter

As we will discuss in Section II below Twitter.com provides an API to access the Twitter service. This has assisted researchers in carrying out research on various aspects of Twitter. Many novel applications have been developed. Twitter has allowed professionals in the area of health-care simulations [10] and education to begin "open sharing of relevant and useful knowledge allowing the community to adapt and evolve faster to the rapidly changing health care environment". The social possibilities of mobile technology in transitional spaces such as public transport has been investigated where researchers designed a location-based friend finder for Twitter that displays only people in the same train as the user in the Stockholm subway [11]. Java et. *al* present a taxonomy characterising the underlying intentions users have in making Twitter posts by aggregating the apparent intentions of users extracted from Twitter posting data [12]. This analysis shows that Twitter users with similar intentions connect with each other successfully and find each other amongst the many other millions of users. Other work [13] has gathered Twitter posts from nearly $100,000$ users using deep searches of the Twitter network sampled collections from the publicly available timeline. The authors identified *three* distinct classes of Twitter users. Firstly there are users who have a much larger number of followers than they are following themselves. These include media outlets, Hollywood stars, etc. The second group called *acquaintances* are users exhibiting a certain symmetry in their Twitter relationships - that is they follow people who follow them. The final group is a small group who have the common characteristics that they are following a much larger number of people than they have followers. These are usually people who contact *everyone* in the hope that they will get a high following. Other research has investigated if Twitter operates a form of online "word of mouth branding" [14]. The authors analysed almost $150,000$ Tweets containing branding comments, sentiments, and opinions. Of the 20% of these tweets found to contain branding comments almost 50% contained positive sentiments about certain brands. Twitter was seen to have had an influential role in the successful presidential campaign of Barack Obama. "On election day, the Obama campaign used Twitter to post toll-free numbers and texting strings for finding polling locations, connecting to volunteer opportunities, and making contributions" [15].

II. Using the Twitter API

Twitter.com provides a REST API (REpresentational State Transfer Application Programming Interface) which allows developers to perform most tasks that users might otherwise perform with their Twitter account using the forms on the Twitter website. With the API developers can retrieve the last 20 tweets of the accounts the authenticated user is subscribed to, of all unprotected users, or of a specific user. The API provides a means for the programmatic sending and deleting of tweets, direct messaging, friendships, notifications, account blocking, favorite messages, etc. The REST API is relatively easy to use from any programming language that can perform and handle HTTP GET actions for sending URLs to a server. For most popular programming languages developers can find a Twitter API library allowing the sending and receiving of tweets and performing of other Twitter-related search and query information using the syntax and data structures of the specific programming language. There are libraries for the Twitter API in Java, PHP, C++, Ruby, .NET, and PERL. To retrieve information (tweets, searches, user lookups, etc) from Twitter one can easily use command line tools such as `wget` or `curl` to send a specially formatted URL to the Twitter server and receive information back in plain text format (JSON or XML). To make use of this information it must be parsed. This is where the Twitter API Libraries for the programming languages mentioned above becomes very useful. By querying the Twitter system using the Twitter API within programming code the returned information can be parsed, analysed, searched, stored in a database, etc. It also provides developers with an opportunity to build in Twitter functionality to existing web-based applications.

A. Web-based Applications using the Twitter API

Given the simplicity of the the Twitter API several web-based applications have gained quick popularity on providing value-added services for Twitter users. **Twuffer** http://www.twuffer.com allows users to schedule tweets for a later date. A tweet is typed into twuffer with a specified date and time for broadcast. At the specified date and time twuffer posts the tweet on Twitter. **Twidentify** http://www.twidentify.com is a search engine for Twitter. There are 3 ways to search using a keyword. Trend search allows tracking the popularity of a keyword over time. The second is a basic Twitter search of who is using the keyword in their current tweets. The final search option is *Search on influence*. The results of this search are sorted in order of users who are retweeted (directly quoted in other tweets or conversations). This usually gives the opportunity to see what *influential people* on twitter are tweeting about your keyword search term. **TwitterCounter** http://twittercounter.com/ is a user statistics application allowing users to track their progress on twitter. The information is presented in time series graphs and allows customisation of the timeframe. Other functions includes the ability to compare your statistics to other users.

B. Offline analysis of Twitter messages

To supply data for this research it is necessary to build up a large corpus of Tweets. We downloaded and stored all tweets which contained revelvant keywords: climate, environment, *climate change*, etc. This corpus of Tweets is stored offline due to restrictions placed on the Twitter API in terms of number of server accesses per day. Figure 1 shows a flowchart of the process of accessing Twitter messages. A PHP script sends the appropriate HTTP GET (keyword search, user search,

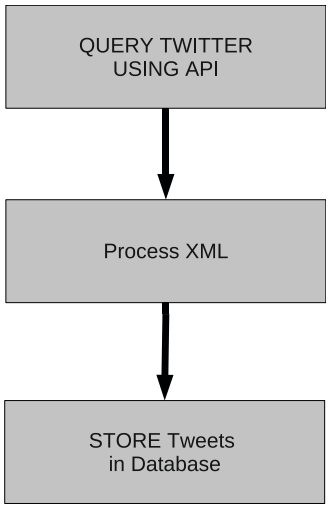

Fig. 1. Download of messages from Twitter.com using the Twitter API

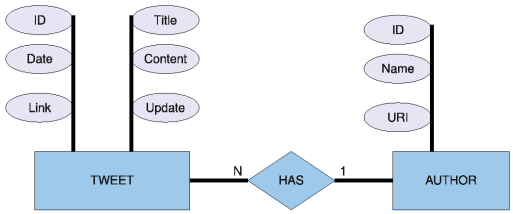

Fig. 2. Entity Relationship Diagram for Message Database

trend request, public timeline) request to the Twitter server. The Twitter server replies with XML formatted output. Each tweet object contains the message text, information about the author, and the timestamp of the tweet. This XML is processed by the PHP script. The PHP script parses each tweet message which includes reformatting of special characters and extraction of usernames within messages and inserts the tweet into a database. The Entity Relationship diagram for the message database is shown in Figure 2. The Twitter API restricts calling applications to 70 requests per hour unless otherwise arranged with Twitter.com. For this reason we cache the results of public timeline requests and keyword searches. Each tweet has a unique alpha-numeric identifier. This helps to avoid duplication of tweets within our offline database. Textual analysis of this dynamically updated database of Twitter posts is then performed. We are currently investigating a number of issues which are summarised as follows:

- Investigation of temporal correlations between the use of climate change related vocabulary during periods of major media coverage of climate change issues and events
- Specific analysis of Twitter messages from Ireland containing climate change related vocabulary. The Twitter API provides geocoding based on a user's location from their Twitter profile. A circle of N kilometers is searched centered on a $(lat, long)$ pair.
- Analysis of the number of *retweets* for climate change related issues. A retweet is when one individual copies a tweet from someone in their network and shares it with their network. It is acknowledged as the highest degree of content approval on Twitter.

III. Conclusions and Future Direction

In this short paper we have described research we are currently undertaking to establish how effective Twitter could be as a tool in environmental awareness campaigns. We looked at the specific issue of climate change to establish if people using Twitter were communicating about environmental issues in their Twitter networks.

A. Future Direction of Twitter

Honey et. *al* [16] predicts that tools such as Twitter "will soon come to be used in formal collaborative contexts, as well for example in work involving distributed teams just as instant messaging was used before". Other researchers [17] comment that as the new generation of scientists "grow up" with instant messaging, blogging, Twitter, they are beginning to explore ways to use these technologies for information exchange and collaboration. The future direction of Twitter is somewhat unknown with Lucky [17] stating that "we are in the middle of something happening around us and nobody really understands the consequences". Twitter has come "from nowhere to become the third most visited social networking site in the US in just three years by allowing its users to broadcast their thoughts, actions and news instantly" [18]. This rise has caused Google to "admit to losing out to Twitter in the race to meet web user demand for real-time information". Interestingly young adults and teenagers have not taken Twitter seriously yet according to Internet surveys such as Nielsen Net Survey [19]. Some research indicates that as long as teenagers can update their online status via MySpace and Facebook for their friends as well as Instant Messaging and SMS Texts, Twitter doesn't really add to the existing technology. Many young adults are only seeing the media and business aspects of Twitter.

B. Using Twitter Securely

We believe that as Twitter becomes more widely adopted by citizens the issues of information and personal security using Twitter will need to be addressed. This was also the case when email became ubiquitous [20][21]. Some literature has begun to appear regarding the security of Twitter. Some research shows that many users, often willingly, "share personal identifying information about themselves but do not have a clear idea of who accesses their private information or what portion of it really needs to be accessed" [22]. For those organisations who have "a business need to use Twitter then there must be training provided on how to use Twitter in a secure manner" [23]. The authors emphasise the need to "provide ongoing

awareness communications about Twitter information security and privacy issues". Vulnerabilities in Twitter's Javascript programming code leaves the "microblogging service with major holes in its security"[24]. This is expanded upon by Bradbury who gives examples of how worms and other malicious code could be transported around the Internet by the exchange of links within Twitter messages[25]. For Twitter to gain acceptance as a communication device for serious issues such as Climate Change the authors feels that it is necessary that the problems of the email world: spam, junk mailing, phishing, etc are tackled aggressively and effectively. Otherwise users will follow the same usage patterns as they use when managing their email - only trusting a small set of users, or friends, and deleting any material which looks dubious.

C. Public Awareness of Climate Change

Public awareness is key to making a real difference in fighting environmental problems such as climate change [4]. However, due to ineffective communication strategies, much effort to educate the public on climate change issues has not translated into a great degree of concrete progress. As outlined in [26] the authors show that the experiences of the UK, Canada and Sweden demonstrate that climate change communication campaigns appear to influence large numbers of people in relatively short periods of time. These campaigns were based on pro-social behavioral campaigns but had little success in changing peoples habits and behaviours. Harnessing the pro-social aspects of Twitter could prove a useful tool in informing the public better about environmental problems. "This is low-hanging fruit in the fight against climate change that our society really cant afford not to harvest" [26]. We believe that Twitter can assist in communicating information about Climate Change. Tools such as Twitter can address "the dichotomy of high awareness and low priority strongly related to ineffectiveness of some environmental communications"[4].

ACKNOWLEDGMENT

Dr. Peter Mooney leds a 5 year project (2008 - 2013) called "Geoinformatics Services for Improved Access to Environmental Data and Information" funded by the Environmental Protection Agency STRIVE research programme. Dr. Adam Winstanley is funded under StratAG (Strategic Research in Advanced Geotechnologies and is the Principal Investigator for the Location Based Services (LBS) Strand . Dr. Padraig Corcoran is a Lecturer at the Department of Computer Science.

REFERENCES

[1] A. Zeichick, "A-twitter over twitter," *netWorker*, vol. 13, no. 1, pp. 5–7, 2009.

[2] C. Arthur, "How to make the most of twitter," The Guardian: Thursday 8 May 2008. Technology news and features section (page 1), 2009.

[3] P. Curtis, "Pupils to study twitter and blogs in primary shake-up," The Guardian: Wednesday 25 March 2009. Top Stories (page 1), 2009.

[4] C. K. Tan, A. Ogawa, and T. Matsumur, "Innovative climate change communication: Team minus 6%," Global Environment Information Centre (GEIC), United Nations University (UNU),53-70, Jingumae 5-chome,Shibuya-ku, Tokyo 150-8925,Japan, GEIC Working Paper Series 2008-001, 2008.

[5] IPPC, "Climate change 2007: Synthesis report. the fourth assess- ment report of the intergovernmental panel on climate change," Intergovernmental Panel on Climate Change, IPCC, Geneva, Switzerland, IPPC Synthesis Report ISBN 978 0521 88009-1, 2006.

[6] G. Ereaut and N. Segnit, "Warm words: How are we telling the climate story and can we tell it better?" Institute for Public Policy Research, IPPR,30 - 32 Southampton Street,Covent Garden, London, WC2E 7RA, England., IPPR Technical Report 435, 2006.

[7] J. Laukkonen, P. K. Blanco, J. Lenhart, M. Keiner, B. Cavric, and C. Kinuthia-Njenga, "Combining climate change adaptation and mitigation measures at the local level." *Habitat International*, vol. 33, no. 3, pp. 287 – 292, 2009.

[8] C. Trumbo, "Constructing climate change: claims and frames in US news coverage of an environmental issue," *Public Understanding of Science*, vol. 5, no. 3, pp. 269–283, 1996.

[9] European Commision, "Attitudes of european citizens towards the environment," Directorate General Environment and coordinated by Directorate General Communication., Download at http://ec.europa.eu/public_opinion/archives/eb_special_en.htm, Special Eurobarometer Survey Report Ref: 295 Wave EB68.2, 2008.

[10] D. Weberg, "Twitter and simulation: Tweet your way to better sim," *Clinical Simulation in Nursing*, vol. 5, no. 2, pp. e63 – e65, 2009.

[11] N. Belloni, L. E. Holmquist, and J. Tholander, "See you on the subway: exploring mobile social software," in *CHI EA '09: Proceedings of the 27th international conference on Human factors in computing systems*. New York, NY, USA: ACM, 2009, pp. 4543–4548.

[12] A. Java, X. Song, T. Finin, and B. Tseng, "Why we twitter: An analysis of a microblogging community." in *Advances in Web Mining and Web Usage Analysis*, ser. Lecture Notes in Computer Science, H. Zhang and M. Spiliopoulou, Eds., vol. 5439. Springer, 2007, pp. 118–138.

[13] B. Krishnamurthy, P. Gill, and M. Arlitt, "A few chirps about twitter," in *WOSP '08: Proceedings of the first workshop on Online social networks*. New York, NY, USA: ACM, 2008, pp. 19–24.

[14] B. J. Jansen, M. Zhang, K. Sobel, and A. Chowdury, "Micro-blogging as online word of mouth branding," in *CHI EA '09: Proceedings of the 27th international conference on Human factors in computing systems*. New York, NY, USA: ACM, 2009, pp. 3859–3864.

[15] S. Greengard, "The first internet president," *Commun. ACM*, vol. 52, no. 2, pp. 16–18, 2009.

[16] C. Honey and S. Herring, "Beyond microblogging: Conversation and collaboration via twitter," in *System Sciences, 2009. HICSS '09. 42nd Hawaii International Conference on*, Jan. 2009, pp. 1–10.

[17] C. R. Aragon, S. Poon, and C. T. Silva, "The changing face of digital science: new practices in scientific collaborations," in *CHI EA '09: Proceedings of the 27th international conference on Human factors in computing systems*. New York, NY, USA: ACM, 2009, pp. 4819–4822.

[18] R. Wray, "Google falling behind twitter," The Guardian Online: Tuesday 19 May 2009. http://www.guardian.co.uk/business/2009/may/19/google-twitter-partnership, 2009.

[19] M. McGiboney, "Twitters tweet smell of success," Nielsen NetView Survey. 2009 (Feburary) Available at http://blog.nielsen.com/nielsenwire/online_mobile/twitters-tweet-smell-of-success/, 2009.

[20] A. Levi and c. K. Koç, "Inside risks: Risks in email security," *Commun. ACM*, vol. 44, no. 8, p. 112, 2001.

[21] P. Kumaraguru, Y. Rhee, A. Acquisti, L. F. Cranor, J. Hong, and E. Nunge, "Protecting people from phishing: the design and evaluation of an embedded training email system," in *CHI '07: Proceedings of the SIGCHI conference on Human factors in computing systems*. New York, NY, USA: ACM, 2007, pp. 905–914.

[22] B. Krishnamurthy and C. E. Wills, "Characterizing privacy in online social networks," in *WOSP '08: Proceedings of the first workshop on Online social networks*. New York, NY, USA: ACM, 2008, pp. 37–42.

[23] R. Power and D. Forte, "War and peace in cyberspace: Don't twitter away your organisation's secrets," *Computer Fraud and Security*, vol. 2008, no. 8, pp. 18 – 20, 2008.

[24] J. Sullivan, "Why tweeters should beware of worms," *The New Scientist*, vol. 201, no. 2706, pp. 18 – 18, 2009.

[25] D. Bradbury, "Twitter hit by worm attacks," *Computer Fraud and Security*, vol. 2009, no. 4, pp. 1 – 1, 2009.

[26] K. Akerlof and E. W. Maibach, "Sermons as a climate change policy tool: Do they work? evidence from the international community," *Global Studies Review*, vol. 4, no. 3, pp. 4–7, 2008.

Research on Unmanned Airship Low-altitude Photogrammetric Flight Planning and Pseudo-ortho Problems

DUAN Yi-ni
1.Geomatics College Shandong University of Science and Technology Qingdao, China
2.Peking University Beijing, China
email:yiniduan@126.com

ZHENG Wen-hua
Geomatics College Shandong University of Science and Technology Qingdao, China
email:zhenwenhua_sd@163.com

YAN Lei
Institute of Remote Sensing & Geographic Information System Peking University Beijing, China
email: lyan@pku.edu.cn

Abstract

Unmanned airship is a new method of aerial photogrammetry. This paper mainly focuses on airship low-altitude photogrammetric flight planning and parameters design. It gives a series of formulas to calculate flight altitude, flight route and other photogrammetric parameters. Moreover, this paper discusses the solution to pseudo-ortho problems for high buildings. According to the relationship among flight altitude, building height, offset from flight route center and deformation, the function models are used to correct the deformation.

Keywords

unmanned airship; low-altitude photogrammetry; flight altitude optimal design; flight route design; pseudo-ortho

1. Introduction

Compared with other photogrammetric platforms, unmanned airship is less stable and is easy to be influenced by airflow. As a result, some images' inclination angles are too large, with various grey degrees and irregular overlap. In order to overcome the disadvantages of unmanned airship low-altitude photogrammetry system, it is necessary to design optimal photogrammetric flight parameters based on the character of airship itself. Due to large orthophoto projection error of high buildings in the condition of center projection, the bottleneck of orthophoto production in the paper is researched on the solution to pseudo-ortho.

2. Photogrammetric flight planning and parameters' design

2.1 Optimal Flight altitude design

In ideal state (the ground is flat, the photo is level), the relationship between flight altitude and scale is shown in (1):

$$\frac{1}{m} = \frac{f}{H} \tag{1}$$

Where, m is the denominator of photogrammetric scale, f is the focal length of camera, H is flight altitude.

A. The first method of flight altitude optimal design

Map scale leads to photogrammetric one to calculate flight altitude by (1). The relationship between map scale and photogrammetric one[1] is shown in Tab.1. We also calculate the corresponding flight altitudes for the three map scales.

Tab.1 The relationship of some references

Map scale	Simulative photogrammetric scale	Digital photogrammetric scale	Flight altitude(m)
1：500	1：2000~1：3000	1：4000	96
1：1000	1：4000~1：6000	1：6000~1：8000	144~192
1：2000	1：8000~1：12000	1：12000	288

B. The second method of flight altitude optimal design

Flight altitude relies on the ground resolution (GR) of digital camera. The relationship between GR and H [2]is shown in (2)

$$GR = \frac{H \cdot N \cdot d}{f \cdot rows} \text{ or } GR = \frac{H \cdot N \cdot d}{f \cdot cols} \tag{2}$$

Where, f is the focal length of camera, H is flight altitude, N is pixel values in rows and columns, d is single pixel size.

With (2), the optimal flight altitude in different scales can be designed for precision requirements.

2.2 Flight route planning

Flight route planning is based on the formula of photogrammetric baseline. With the overlap degree Q, the image width l (the unit is pixel) and the ground resolution GR, the baseline b [3] is：

$$b= (1-Q) \times l \times GR \quad (3)$$

A. Flight route interval optimal design

Tab.2 shows that, for Canon 5D digital camera, l_y (the lateral width of image) =2912. If the ground resolution is 0.15m and the lateral overlap degree is 30%~50%, the lateral baseline length can be calculated with (3):

Tab.2 Parameters of Canon 5D digital camera

Camera Type	Image array (pixel)	CMOS (mm)	Lens focus length (mm)
Canon 5D	4368×2912	35.8×23.9	24

$b_{0.3}$=(l－0.30)×ly×GR=305.76 m

Or

$b_{0.5}$ =(l－0.50)×ly×GR=218.4 m

From the result, it's known that the suitable flight route interval is about 200 meters, which can make sure that the lateral overlap degree is 30%~50%.

B. Location of photographic station optimal design

As the flight direction is X, the location of photographic station n is [4]:

$$X_n=X_1+ (n-1)\times b_x \quad (4)$$

Where, b_x is calculated with (3), X_1 is the location of the first photographic station.

C. Image number in a flight route optimal design

$$n=int(\frac{L}{b})+2 \quad (5)$$

Where, L is the length of a whole flight route, b is the length of baseline in the flight direction.

3. Research on pseudo-ortho problems of high buildings

As the type of airborne photogrammetry belongs to center projection, the higher are the buildings, or the further is the airship offset from flight route center, the greater the projection error is. Fig. 1 shows the relationship among flight altitude H, building height h, radius vector r and projection error dh.

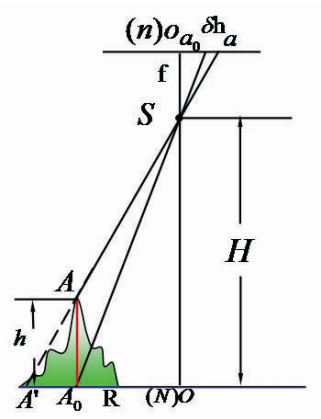

Fig.1 Projection error dh

With (6) we can calculate dh:

$$dh=\frac{h}{H}r \quad (6)$$

Where, r is the radius vector from image a to plate nadir point n, dh is projection error aa_0.

From (6), we can get two solutions to pseudo-ortho problems of building height:

A. $dh=\frac{h}{H}r$ If flight altitude H, building height h and radius vector r are given, projection error dh can be calculated. Input dh, the projection error i.e. pseudo-ortho deformation can be rectified in ERDAS software.

B. $r=\frac{dh\cdot H}{h}$ If the tolerance value of projection error Max dh, flight altitude H and height building h are given, the radius vector r can be calculated. Drawing a circle with the radius r, the deformation inside the circle is less than tolerable value. The orthophoto quality from the special part will be higher.

4. Photogrammetric flight test

On April 2008, the authors applied the unmanned airship low-altitude photogrammetry for the task of 1:2000 photogrammetric topographic maps and corresponding orthophotos of Shengjian Coal Mine in Sanhekou City, Shandong Province, China. Total flight area: 16.8 km^2; Ground resolution: 10.2cm; Forward overlap: 75%, lateral overlap: 55%.

With the Canon 5D digital camera parameters in Tab.2 and flight planning formulas, the flight parameters are designed as follows.

A. Flight altitude optimal design

W_r=0.102×4368=445.5m

Then the flight altitude is:

$$H = \frac{\mathrm{f} \cdot W}{N \cdot d} = \frac{f \cdot 445.5}{35.8} = 299m$$

B. Flight route interval optimal design

Length of lateral baseline:

$B_{0.55}$=(l－0.55)×ly×GR

=0.45×2912×0.102=133.66 m

From the result, we design that the flight altitude is 300m, the flight route interval is 133 meters, and the ground coverage area of every photo is 400m×300m. Fig.2 shows the aerial photos of "South 2" flight region of the coal mine. The precision of certain orientation points is shown in Tab.3 after aerial triangulation.

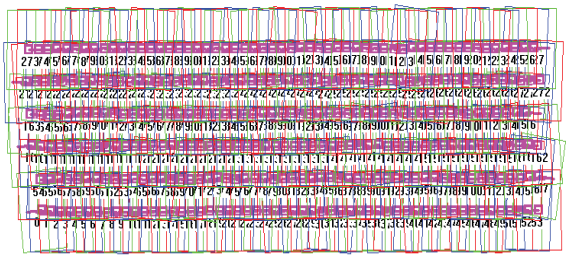

Figure 2 Flight routes and aerial photos of "South 2" flight region

The planar point mean square error: ±0.155m, elevation mean square error: ±0.103m.

Tab.3 The coordinate differences in stereo pair and RTK (Realtime Kinematic)

Test points	RTK coordinates			Coordinates measured in stereo pair			Coordinate differences		
	X	Y	Z	X	Y	Z	X	Y	Z
20001	508485.452	3856682.175	35.879	508485.369	3856682.134	35.882	0.083	0.041	-0.003
20002	508328.752	3854900.606	34.262	508328.536	3854900.571	34.366	0.216	0.035	-0.104
20005	508338.393	3855954.610	34.423	508338.346	3855954.430	34.560	0.047	0.180	-0.137
20006	508387.974	3856335.317	36.687	508388.124	3856335.204	36.886	-0.150	0.113	-0.199
20012	508097.988	3856711.690	35.254	508098.095	3856711.730	35.378	-0.107	-0.040	-0.124
standard deviation of overall sample							0.133	0.075	0.064

The results shows that the aerial triangulation precision satisfies the requirement of "1:500, 1:1000, 1:2000 topographic maps survey norms"

5. Conclusion

1) Before the photogrammetric flight, design the flight parameters with the formulas in this paper, to provide strict theory for flight planning. But in actual operation process, ground surface irregularity, flight off-course, image tilt and other factors must be taken into consideration. So flight parameters should be adjusted in different flight conditions.

2) To make sure that the designed flight parameters are valid, flight test can be done in a small part of the whole survey region. By analysis of the coordinate differences between the measured coordinates in stereo pair and the corresponded RTK coordinates, the precision of aerial triangulation can be obtained, which reflects the quality of airborne photogrammetry.

3) This paper introduces a method with function model to solve the pseudo-ortho problems. But it must be realized by perfecting the ERDAS software and adding the new pseudo-ortho rectification function, which will greatly improve the efficiency and quality of orthophoto production.

References

[1] CUI Hong-xia, LIN Zong-jian, LI Guo-zhong, and SUN Ying. UAVs for Generation of Digital Large-Scale Orthophotos, Journal, Chinese Journal of Electron Devices, 2008, Vol.31, No.1 (in Chinese)

[2] LIN Zongjian. The International Archives of the Photogrammetry, Journal, Remote Sensing and Spatial Information Sciences. Vol. XXXVII. Part B1. Beijing 2008

[3] YAN Lei, DING Jie, ZHAO Shi-hu, LIAN Zhou-hui, GAO Peng-qi, and LIU Yue-feng. Key Technologies and Implementation of a Ground-based Simulation System for Digital Aerial Remote Sensing, Journal, Image Technology, 2006, 1(in Chinese)

[4] Henri Eisenbeiss. A Mini Unmanned Aerial Vehicle (UAV): System Overview And Image Acquisition, Journal, International Workshop on "Processing And Visualization Using High-resolution Imagery", 2004

Spatial - temporal Simulation and Prediction of Sandy Desertification Evolution in Typical Area of Xinjiang

Dunli Liu[1], Jianghua Zheng[1]
1. College of Resources and Environment Science, Xinjiang University, Oasis Ecology Key Lab of National Education Bureau, Urumqi 830046, Xinjiang, China
e-mail: ldl_rain@126.com, itslbs@gmail.com

Zhihui Liu[1, 2, *], Fei Wang[1]
2. International Center for Desert Affairs-Study on Sustainable Development in Arid and Semi-arid Lands, Urumqi, 830046, China
e-mail: lzh@xju.edu.cn, moncak2008518@yahoo.com.cn

Abstract— **A quarter of territory in Xinjiang is covered with desertification landscape, and the monitoring results indicate that it's still expanding with the speed of 84.5km2 every year. The severity of desertification has become a threat to the sustainable development of oasis ecology and the living space of human. A topical research area was located in the northern part of Hotan Oasis. Following methods were used: Firstly, remote sensing data in three different time phases were used to classify and analyze sandy desertification of the area. Secondly, main factors of sandy desertification were selected and quantified to establish the Sandy Desertification Index (SDI, for short) model. Thirdly, sample points were chosen and data were collected based on sandy desertification types, taking the year of 2000 as the benchmark. The points were used to calculate SDI and match sandy desertification types, which were simulated by the changing of SDI in 1990. So the sandy desertification distribution map could be reconstructed by Interpolation Algorithm and matched with remote sensing image. Finally, Linear Regression model was used to predict main factors of sample points, and the forecast of potentially space evolution would be realized by the SDI, which set 2010 as a target. Four results were reached by the research. 1) Sandy desertification expanded quite obviously in the area nearly in past three decades, accounting for 5.98% of the total. The serious sandy desertification increased from 19.39 km2 to 41.86 km2, showing the most prominent evolution. The high and light ones expressed mild increase and the modest one declined in the meanwhile. 2) SDI model was built by seven main factors. The real sandy desertification types of forty sample points were matched with their SDI based on observational data in 2000, and the result showed 82.5% of the correct rate. 3) Sandy desertification map of 1990 that built through SDI had a quite high degree of simulation to remote sensing image, with only -2.72 percent of the relative error. 4) The situation of sandy desertification in study area would be aggravating in 2010 through the prediction. There would be 11.2 km2 farmland annexed by desert, the area of serious and light sandy desertification would increase 19.84 km2 and 8.88 km2 respectively. The conclusion is that the SDI of sandy desertification model can reasonably reflect sandy desertification types. We can realize the spatial-temporal simulation and prediction of sandy desertification evolution by the model. And it provides more effective and intuitive expression and decision support for sandy desertification research and prevention.**

Keywords-***Sandy desertification; spatial-temporal evolution; SDI; simulation and prediction; Xinjiang***

I. INTRODUCTION

As one of the important environmental problems, sandy desertification impacts and haunts the survival of all humankind and the sustainable development of society. Not only it threatens the entire human environment, but has become the barrier of global economic development and social stability. For current researches, such aspects as the types, distribution, monitoring, evaluation, prevention, trend forecast, movement mechanism, have been related worldwide [1-8]. At present, however, as one of developing words, there is no uniform definition of sandy desertification concept. The research integrates current views and defines sandy desertification as following: under the condition of sandy surface on arid, semi-arid and partly semi-humid areas, the fragile balance of natural ecosystem is undermined due to the impacts of natural factors or human activities, and then the land degradation gradually forms, which indicates by wind and landscapes of wind erosion, making the similar desert landscape comes into being in regions where never appeared before [9-12].

Xinjiang is located in the hinterland of Eurasia, which is a province where there are the widest desert distribution and severest harm in China. And it is one of the most serious regions which suffer sandy desertification in the world. The unique terrain of two basins clipped with three mountains causes the dry and windy natural climate, which provides a congenital condition for the formation and expansion of sandy desertification. The area of sandy desertification in Xinjiang has reached $4.3\times10^5 km^2$, which is 25.8% of the total, and recently increases by an annual rate of 84.5 km^2, according to the census data in 2000 by Forestry Survey and Design Institute of Xinjiang. Researches have been done since 1970's. The study area mainly focus on Tarim River valley and southern margin of the Tarim which relate to desertification types, trends, causes or drivers, as well as

* Corresponding Author. Tel: +86+991+8582378, Fax: +86+991+8585504, E-mail: lzh@xju.edu.cn

control measures and so on [13, 14]. However, it is very difficult to achieve expected results by purely theoretical expression and numerical analysis particularly for the large-scale desertification and the slow changing process. Management and policy-makers need a better visual and simulated process for the direct support of preventing and controlling desertification. In this research, SDI (Sandy Desertification Index) model was built based on the main effective factors of desertification while the classification and analysis of desertification was done by using of remote sensing data. And index and types of desertification were matched on the basis of selecting reasonable sample points and the spatial-temporal evolution of the latter was expressed by the model. At the same time, the spatial distribution of particular year was constructed by Interpolation Algorithm, achieving the expected effect and function of simulating and predicting spatial-temporal evolution of desertification. For this aspect, most scholars only used the impact factors of desertification to evaluate development or genetic type, while it is seldom to see using the research method, which utilizes impact factors of desertification to build SDI model. And it achieves the simulation and prediction of spatial-temporal evolution through changing SDI of desertification is quite few.

An area located in the northern regions of Hotan Oasis where has classic sandy desertification evolution is selected and researched. Three remote sensing images that of MSS (Jul., 1973), TM (Oct., 1990) and ETM+ (Oct., 2000) data are calibrated and used for sandy desertification classification. The desertification evolution is analyzed over the past three decades. The SDI model is constructed by the main effective factors based on sample points' data of 2000, and the desertification types of those points are analyzed according to the correlation between desertification types and their SDI. The types' statuses are simulated in 1990. Furthermore, spatial-temporal distribution of sandy desertification in study area is simulated by Interpolation Algorithm based on GIS software. The result shows a better effect with -2.72 percent relative errors after compared with remote sensing data. And for this reason, the data of sample points in 2010 are predicted based on relevant models, and so spatial-temporal distribution of desertification is realized. The results indicate that the situation is more and more serious in study area. There will be large area of farmland turns to desert, and the light and serious desertification expands substantially, so the control works are imminent.

II. ANALYSIS OF SANDY DESERTIFICATION CHANGE IN STDUY AREA

A. Overview of the study area

The oasis located in the southern margin of the Tarim Basin is one of the most affected areas with sandy desertification in Xinjiang. And Hotan Oasis has the severest threats because of the Taklimakan Desert's expansion, which becomes the poorest region in Xinjiang as far as to the whole country [15]. In view of these reasons, an area that in the northern of Hotan is chosen for research, where is 37°05'～37°11'N, 79°59'～80°06'E. The area is located in the junction of desert and oasis with all types of desertification, which gives a good representation. It has 400 (Row) ×400 (Line) elements and its real area is 144km^2, with 1353m altitude, 14.8 temperature, 23.8mm rainfall and 2.1m/s wind speed (data of 2007).

B. Remote sensing image process and analysis

MSS (Jul., 1973), TM (Oct., 1990) and ETM+ (Oct., 2000) data are used to geometric and radiometric correction by ENVI, combined with topographic map and other data. The coordinates of study area are treated as the basis for clipping image to ensure the consistency of images. The area is classified into different types on the basis of their image characters and interpretation keys, as well as the indicators system of land classification. And the standard of image interpretation is shown in table Ⅰ. The sandy desertification lands are divided into the light, modest, high and serious ones, based on the classification standard provided by the Federal Agriculture Organization (FAO, for short) and the United Nations Environment Program (UNEP, for short) [16-18].

There are complex lands in study area with both desertification and non-desertification ones, such as farmland, woodland, settlements and so on. In order to highlight the focus of this research, the desertification lands are classified minutely and the non-desertification ones combined into farmland. Classification results are shown in figure 1.

C. Change analysis of sandy desertification in study area

The spatial - temporal evolution of the research area in past 30 years are identified and analyzed based on discriminated standard of sandy desertification types, so the statistics of sandy desertification area for different types and periods can be obtained easily by built-in statistical functions of ENVI (Table Ⅱ).

The Shift Degree (SD, for short) is introduced to show the changing of different sandy desertification types' area more intuitively, which refers to the changes of sandy desertification in a time unit. One year is put as the time unit in this study because sandy desertification is a slow process. That is, SD is annual growth rate and is expressed by the formulary as follows:

$$\mathrm{SD} = \frac{\mathrm{A}_j - A_i}{A_i} \times \frac{1}{T} \times 100\% \qquad (1)$$

In formula (1), A_i means initial areas of desertification lands and A_j expresses final areas, T shows time interval [19-21]. The total SD of study area is 2.64% from 1973 to 1990, which can spot from table Ⅲ. The serious desertification has largest SD, arriving 6.13%. The second one is high desertification with 2.68% declines, but light and modest ones' are quite little. So it can be seen that the light, modest and high desertification have different degrees of reduction, and the reduced area have turned to be serious one. Between 1990 and 2000, the overall SD is 2.69%, which has slighter increase than 20 years ago. The SD of light desertification become larger with 2.59%, and the follows are modest, high

and serious ones in turn. Overall, the desert land increased from 91.59 km^2 to 100.10 km^2 in past nearly three decades, accounting for 5.91% of total area. The serious desertification shows the most obvious increase and the modest one reduces quite apparently. Modest desertification translates into serious one with large areas as a result of people's negligence to desertification, as well as overgrazing and reclaiming continuously.

III. SDI MODEL CONSTRUCTION

A. *Effective factors selection of sandy desertification*

Sandy desertification in Xinjiang has various reasons, which can be divided into two groups, natural group and cultural one. The desertification process is exacerbated by their interaction effects. Land surface with loose sand, arid climate and sparse vegetation leads to the weak ecosystem, which provides congenitally material basis and driving force for the occurrence and development of sandy desertification. Therefore, factors of wind speed, temperature and precipitation and vegetation of surface are the essential elements in process of sandy desertification. The annual wind speed, annual temperature, annual precipitation and vegetation coverage are used to express the factors above, taking one year as the time unit.

At the same time, the formation of sandy desertification in Xinjiang also has substantial connection with intensity and scale of socioeconomic human activities based on many studies. Yudong Song [15] said "Sandy desertification caused by unreasonable reclamation and utilization of water resources takes up 85% of all". Variety of excessively economic activities that result from population and livestock pressure are the main triggered factors of sandy desertification, and the population density and grazing capacity are used for represent them in this research. On the other hand, the degree of sandy desertification is also related to social economy, which represents the exponential increase with the level of economic development. It is expressed by the index of Net Revenue of Per Capita (NRPC, for short).

B. *Quantification and classification of effective factors*

Selected factors are annual wind speed, annual temperature, annual precipitation, vegetation coverage, population density, grazing capacity and NRPC. Their classification standard is proposed according to what was provided by FAO and UNEP in 1984, combining of internal research results and observed data over the years of study area. All the factors are divided into light, modest, high and serious types according to their values with reference to the classification of sandy desertification (Table Ⅳ) [22-24].

C. *SDI model construction*

SDI is the quantization of sandy desertification types in some study area or point. The model is constructed through intensity index values of desertification effective factors and their weight coefficients. In formula (2), η means adjustment coefficient, W_i expresses weight coefficient of factor i and F_i shows its intensity index, N is used to indicate number of factors, which is five in this study.

$$\mathrm{SDI} = \eta \bullet \sum_{i=1}^{N} W_i \bullet \mathrm{F}_i \qquad (2)$$

Reasons of using adjustment coefficient: There are other types of land except sandy desertification, such as farmland and woodland, which have high vegetation coverage as non-desertification land. For the performance of a more comprehensive type of land without detailed analysis for non-desertification, vegetation coverage is treated as the basis of discrimination. So the value of η is 0 when the vegetation coverage is more than 90%, otherwise 1.

The value field of intensity index F_i is [0, 1] for the calculation advantage. So different factors can identify their relevant intensity index by the classification standard shown in table Ⅳ, and their specific value can be obtained through interpolation method.

Commonly used methods for weight coefficient are Analytic Hierarchy Process, Delphi, and so on. They are intervened with subjective factors more or less, which make the results less scientific. Principal component analysis is introduced in this study based on statistical principle. The weight coefficient is shown by the proportion that each factor's eigenvalue of the total in the correlation matrix. Standardized method (z- score) is used to correlation matrix and eigenvalue calculation based on data of the factors during 1973 to 2000. The result is as follows through SPSS (Table Ⅴ) [25].

IV. SPATIAL-TEMPORAL SIMULATION OF SANDY DESERTIFICATION EVOLUTION

A. *Sample points selection and data acquisition*

Sample points should be selected from different land types as full as possible, which are light, modest, high, and serious and non-desertification area, combined with residents and livestock activities, vegetation types and distribution, and so on, according to distribution of desertification types and observation data in 2000. There are forty points in study area, eight ones in each land types. At the same time, sample points' areas choose 30×30 m totally, which can convenient for the resolution of remote sensing image. One method of averaging different data which observed by many times according to the characteristics of seasonal variation is used to ensure the effective factors' data more rationally and objectively, under the condition of not doing continuous observation.

B. *SDI calculation and type discrimination*

The value field of SDI model is [0, 1], which can be calculated by that of its parameters. Doing different calculation to the SDI value field, and then, relationships between them and sandy desertification types will come true based on the standard provided by FAO and UNEP, and real situation of study area (Table Ⅵ).

According to the relationship between SDI model and desertification types, sample points are treated with SDI calculation and sandy desertification type discrimination, and compared with the real situation. Result is shown in table Ⅶ.

There are forty points be selected and disposed, seven of which are wrong. The accuracy rate is 82.5% and it can meet research requirement. There are both lenient and overweight results among the error points. They are just between adjacent levels but not with skip-level ones. For a further step, data of SDI for those error points are almost in the brink of two types, which mainly caused by a little bigger or smaller data of some factor. It is indicated that the relationship between SDI and desertification types should need for further amendment. But it has reached the standard of this study due to the high discrimination rate.

C. Spatial-temporal simulation of sandy desertification evolution

Linear regression model and moving average model which are used to project their value in 1990 based on annual data sets from 1973 to 2000 and points' data in 2000 due to the limitation of effective factors' data for sample points. The SDI is calculated and sandy desertification is inverted of each point, and then interpolation method is used to simulate desertification distribution in design year, under the support of computing and image analysis functions of GIS (Figure 2a).

Statistical results of comparing the simulation with remote sensing image (Figure 1b) can be seen from table Ⅷ that light desertification shows biggest error with 13.90%, which mainly due to the selected points can not reflect slight smaller regions of light desertification in farmland. The relative errors of modest and high desertification are -10.04% and -6.64% respectively, performing smaller simulation area. However, the serious one shows bigger area than that of remote sensing image. It can be seen from both images that partly modest and high desertification are distinguished as the serious ones in northeast region of study area, mainly because of the limitations of points selection and interpolation method. In a word, the relative error is -2.72%, which means that the correct simulation of the total desertification area is 97.28%, showing a better simulation result.

V. SPATIAL-TEMPORAL PREDICTION OF SANDY DESERTIFICATION EVOLUTION

According to data characters of sample points in 2000, three methods that linear regression model, multiple regression model and time series model are used to predict the effective factors data of points in 2010, combined with observation of 35 years from 1973 to 2007 (Figure 3). So spatial-temporal of sandy desertification evolution can be obtained in the target year, which is expressed in figure 2(b).

The area of sandy desertification increase significantly in 2010, compared to 2000 based on the analysis of simulated status. There are large areas of light desertification in farmland, partly of which even turns to be modest or high ones, and the boundary of farmland moves inside apparently. The areas of various desertification types calculated in 2010 are as follows: light one 20.47km^2, modest one 9.12 km^2, high one 20.03 km^2 and serious one 61.70 km^2, a total of 111.33 km^2, which is 77.32 percent of study area. It can be seen that there are 11.2 km^2 farmland ate up by desert and serious desertification land increased by 13.8%, mostly come from modest and high ones. Overall, the growth rate of desertification after 2000 is more serious than before, which shows imminent management for sandy desertification in study area.

VI. CONCLUSION AND DISCUSSION

Research of desertification started in 1977, when the United Nations Conference on Desertification (UNCOD) was held in Nairobi, Kenya. And after that, the concept of "sandy desertification" was put forward for the first time in China. Based on existing research results, that is, the main effective factors of desertification, SDI model is established and combined with classification standard of desertification types. The function of expressing the latter changes through that of the former will come true, so as to the reconstruction and prediction of spatial-temporal of sandy desertification evolution. The results are as follows: Firstly, SDI model established by main effective factors can correspond to the types of desertification well， and the simulation and prediction of spatial-temporal of desertification evolution are carried out through changes of SDI. Secondly, there will be a phenomenon of significant desertification expansion in research area in next few years, and even more serious than before, if current land development patterns and policies are maintained all the same. So it is necessary to take remedial measures as soon as possible.

There is a certain lack in this research. The first one is the fewer selected sample points. There are no full points in the area and the representation of data is not enough because of the limited personnel and equipment constraints. Secondly, the data of effective factors failed to be observed and obtained continuously, resulting in incompletely correct rate in discriminating the type of desertification, and even not providing a better support for the possible prediction of the development. The man-machine data acquisition and wireless remote transmission used in further research can make up for these deficiencies quite well.

ACKNOWLEDGEMENT

This paper is supported by the Projects of Cultivate Foundation of Science and Technology Innovation Program of China (No.708090), National Scientific Foundation of China (No.70361001, No.40871023), Project of Meteorological Desert Research Foundation of China (Sqj2007004) and Open Project of the Key Laboratory of Oasis Ecology (Xinjiang University) Ministry of Education (XJDX0201-2008-10).

REFERENCES

[1] Mario G. Manzano, Jose Navar, Processes of Desertification by Goats Overgrazing in the Tamaulipan Thornscrub (Matorral) in North-eastern Mexico[J], Journal of Arid Environments, Vol.44, 2000, PP.1-17.

[2] J.C. Bathurst, J. Sheffield, X. Leng, G. Quaranta, Decision Support System for Desertification Mitigation in the Agri Basin, Southern Italy[J], Physics and Chemistry of the Earth, Vol.28, 2003, PP.579-587.

[3] Cheng Weiming, Zhou Chenghu, and Liu Haijiang, etc., Research of Oasis Expansion and Eco-envionmental Evolution during 50a in Manas River Basin[J], Science in China, Ser D Earth Science, Vol.35, No.11, 2005, PP.1074-1086.
[4] Kjeld Rasmussena, Bjarne Foga, and Jens E. Madsenb, Desertification in Reverse? Observations from Northern Burkina Faso [J], Global Environmental Change, Vol.11, 2001, PP.271-282.
[5] Zhao Wenzhi, Chang Xueli, and He Zhibin, etc., Ejina Oasis Vegetation Ecological Water Requirement Study[J], Science in China, Ser D Earth Science, Vol.36, No.6, 2006, PP.559-566.
[6] Wang Ninglian, Yao Shandong, and Yang xiangdong, etc., Trends of Sandstorms' Frequency in the 20th Century Reflected by Ice Core and Lake Sediment records in Northern China[J], Science in China, Ser D Earth Science, Vol.37, No.3, 2007, PP.378-385.
[7] Lei Jiangqiang, Mu Guijin, and Wang Lixin, A Brief Introduction on the Progress of Systematic Studies on Main Biological Events in the Eukaryotes [J], Science Foundation in China, 2005, PP.268-276.
[8] Li Xiangyu, Li Shuai, and He Qing, An Overview of Study on Sandy Desertification[J], Arid Mereorology, Vol.23, No.4, 2005, PP.73-82.
[9] M. Nael, H. Khademi, and M.A. Hajabbasi, Response of Soil Quality Indicators and Their Spatial Variability to Land Degradation in Central Iran[J], Applied Soil Ecology, Vol.27, 2004, PP.221-232.
[10] S.M. Herrmann, C.F. Hutchinson, The Changing Contexts of the Desertification Debate [J], Journal of Arid Environments, Vol.63, 2005, PP.538-555.
[11] Wang Xunming, Li Jiejun, and Dong Guangrong, etc., Response of Climate evolvement and sandy desertification in Sandy Area near 50a, Northern China[J], Science Bulletin, Vol.52, No.24, Dec., 2007, PP.2882-2888.
[12] Zhu Zhimei, Yang Chi, and Cao Mingming, etc., Analysis on the Soil Factor and Physiological Response of the Plants in the Process of Sandy Desertification on Grassland[J], Acta Ecologica Since, Vol.27, No.1, Jan., 2007, PP.48-57.
[13] Wang Ranghui, Fan Zili, Study on Land Desertification with RS and GIS Techniques in Alagan, the Lower Reaches of Tarim River[J], Journal of Remote Sensing, Vol.2, No.2, May, 1998, PP.137-142.
[14] Han Guihong, Tuerxun. Hasimu, and Shi Li, Discussion on Land Desertification and Causes in Lower Reaches of Tarim River[J], Journal of Desert Research, Vol.28, No.2, Mar., 2008, PP.217-222.
[15] Yi Deting, Study on the Desertification in Xinjiang and Its Causes of Population and Economy [D], Xinjiang: Xinjiang University, 2003.
[16] Wang Tao, Wu Wei and Xue Xian, etc., Time-space Evolution of Desertification Land in Northern China[J], Journal of Desert Research, Vol.23, No.3, May, 2003, PP.230-235.
[17] Wang Tao, Wu Wei, and Xue Xian, etc., Spatial-temporal Changes of Sandy Desertified Land during Last 5 Decades in Northern China[J], Acta Geographica Sinica, Vol.59, No.2, Mar., 2004, PP.203-212.
[18] Zhu Zhenda, Chen Guangting. Sandy desertification land in China[M], Beijing: Science Press, 1994, PP.132-133
[19] Chen Yalin, Chang Xueli and Cui Buli, etc., Dynamics Analysis on Development of Desertification in Hobq Desert[J], Journal of Desert Research, Vol.28, No.1, Jan., 2008, PP.27-34.
[20] Li Sen, Yang Ping and Wang Yue, etc., Preliminary Analysis on Development and Driving Factors of Sandy Desertification on Ali Plateau[J], Journal of Desert Research, Vol.25, No.6, Nov., 2005, PP.838-844.
[21] Dong Yuxiang, Liu Yihua, Study on Assessment Criteria System for Hazard Degree of Desertification Disaster[J], Journal of Catastrophology, Vol.9, No.1, mar., 1994, pp.8-12.
[22] Dong Yuxiang, Study on the Assessment Model for Hazard degree of Sandy Desertification[J], Scientia Geographica Sinica, Vol.15, No.1, Feb., 1995, PP.24-29.
[23] FA0 and UNEP. Provisional Methodology for Assessment and Mapping of Desertification [M], 1984.
[24] Zhu Zhenda, Judgment of Concept and development for sandy desertification [J], Journal of Desert Research, Vol.3, No.4, 1984, PP.2-8.
[25] Yang Shiqi, Gao Wangsheng, and Sui Peng, etc., Quantitative Research on Factors of Soil Desertification in Gonghe Basin[J], Acta Ecologica Sinca, Vol.25, No.12, Dec., 2005, PP.3181-3187.

TABLE I. REMOTE SENSING IMAGE CHARACTERS OF SANDY DESERTIFICATION LANDS

Sandy Desertification Types	Image Characters	Other Characters
Light	Massive and do not has rules, light red	There are red dots among light red region
Modest	Lumpy and do not has rules, pink	Uneven ground with sand distribution
High	Irregular patches, brown-yellow	Clear sand dunes and have brushwood dots
Serious	Broad distribution, brown-yellow	Apparent landform of sand dunes and ridges

TABLE II. STATISTICS OF DIFFERENT TYPES OF SANDY DESERTIFICATION [A]

Year	Light		Modest		High		Serious		Total	
	Area	*Percent*	*Area*	*Percent*	*Area*	*Percent*	*Area*	*Percent*	*Area*	*Percent*
1973	10.01	6.95	31.50	21.88	30.69	21.31	19.39	13.46	91.59	63.60
1990	9.21	6.39	17.14	11.91	28.93	20.09	39.58	27.49	94.86	65.87
2000	11.59	8.05	14.29	9.92	32.36	22.47	41.86	29.07	100.10	69.52

A. Units: area km^2, percent %.

TABLE III. SPREADING RATES OF SANDY DESERTIFICATION LANDS DURING DIFFERENT PERIODS IN RESEARCH AREA

Period	Shift Degree/%				
	Light	*Modest*	*High*	*Serious*	*Total*
1973-1990	-0.47	-2.68	-0.34	6.13	2.64
1990-2000	2.59	-1.66	1.19	0.58	2.69

TABLE IV. CLASSIFICATION STANDARDS OF MAIN EFFECTIVE FACTORS OF SANDY DESERTIFICATION

Effective factors	Light	Modest	High	Serious
Annual wind speed (m/s)	< 2.6	2.6～4.6	4.6～5.9	> 5.9
Annual temperature (℃)	< 10.0	10.0～12.5	12.5～15.0	> 15.0
Annual precipitation (mm)	> 80.0	80.0～55.0	55.0～15.0	< 15.0
Vegetation coverage (%)	> 50.0	50.0～30.0	30.0～10.0	< 10.0
Population density (person/km^2)	< 20.0	20.0～40.0	40.0～60.0	> 60.0
Grazing capacity (sheep unit/ km^2)	< 58.5	58.5～91.6	91.6～137.4	> 137.4
NRPC (Yuan)	< 450	450～700	700～1100	> 1100
Intensity index	0.25	0.25～0.625	0.625～1.00	1.00

TABLE V. CORRELATION MATRIX OF COMPONENT

Component	Annual Wind Speed	Annual Temp.	Annual Precipitation	Vegetation Coverage	Population Density	Grazing Capacity	NRPC
Annual wind speed	1.000	0.116	-0.402	0.571	-0.428	-0.560	-0.359
Annual temperature	0.116	1.000	-0.205	-0.425	0.500	0.412	0.494
Annual precipitation	-0.402	-0.205	1.000	-0.205	0.133	0.179	0.095
Vegetation coverage	0.571	-0.425	-0.205	1.000	-0.982	-.964	-0.950
Population density	-0.428	0.500	0.133	-0.982	1.000	0.934	0.972
Grazing capacity	-0.560	0.412	0.179	-0.964	0.934	1.000	0.944
NRPC	-0.359	0.494	0.095	-0.950	0.972	0.944	1.000
Eigenvalue	0.059	0.019	0.003	4.412	1.496	0.618	0.394
Weight coefficient	0.0084	0.0027	0.0004	0.6302	0.2137	0.0883	0.0563

TABLE VI. CORRESPONDING STANDARDS OF SANDY DESERTIFICATION INDEX TO ITS TYPE

Sandy Desertification Type	Light	Modest	High	Serious
Sandy desertification index	0.0～0.25	0.25～0.50	0.50～0.75	0.75～1.00

TABLE VII. DISCRIMINATION RESULT OF SANDY DESERTIFICATION TYPE

Points	SDI	Distinguishable Type	Real Type	Points	SDI	Distinguishable Type	Real Type
1	0.83	serious	serious	21	0.22	light	light
2	0.79	serious	serious	22	0.42	modest	modest
3	0.76	serious	serious	23	0.80	serious	serious
4	0.64	high	high	24	0.00	farmland	farmland
5	0.24	light	modest	25	0.31	modest	modest
6	0.53	modest	modest	26	0.24	light	modest
7	0.13	light	light	27	0.18	light	light
8	0.21	light	light	28	0.08	light	farmland
9	0.10	light	light	29	0.78	serious	serious
10	0.00	farmland	farmland	30	0.78	serious	high
11	0.00	farmland	farmland	31	0.28	modest	modest
12	0.63	high	high	32	0.27	modest	modest
13	0.77	serious	serious	33	0.00	farmland	farmland
14	0.54	high	modest	34	0.00	farmland	farmland
15	0.63	high	high	35	0.10	light	light
16	0.76	serious	high	36	0.55	high	high
17	0.63	high	high	37	0.26	modest	light
18	0.00	farmland	farmland	38	0.23	light	light
19	0.30	modest	modest	39	0.56	high	high
20	0.00	farmland	farmland	40	0.79	serious	serious

TABLE VIII. ERROR ANALYSIS OF SANDY DESERTIFICATION SIMULATION

Sandy Desertification Types	Light	Modest	High	Serious	Total
simulication/km^2	7.93	15.42	27.01	41.92	92.28
Remote sensing/km^2	9.21	17.14	28.93	39.58	94.86
error rate/%	-13.90	-10.04	-6.64	5.1	-2.72

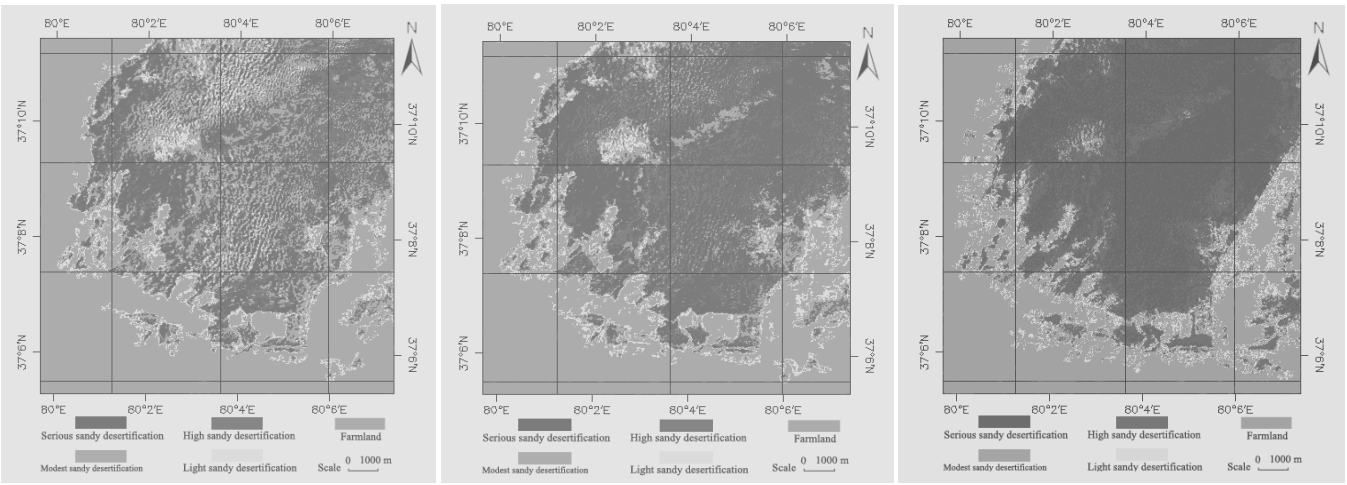

(a) 1973 (b) 1990 (c) 2000

Figure 1. Spatial - temporal change of sandy desertification lands during past nearly 30 years in research area

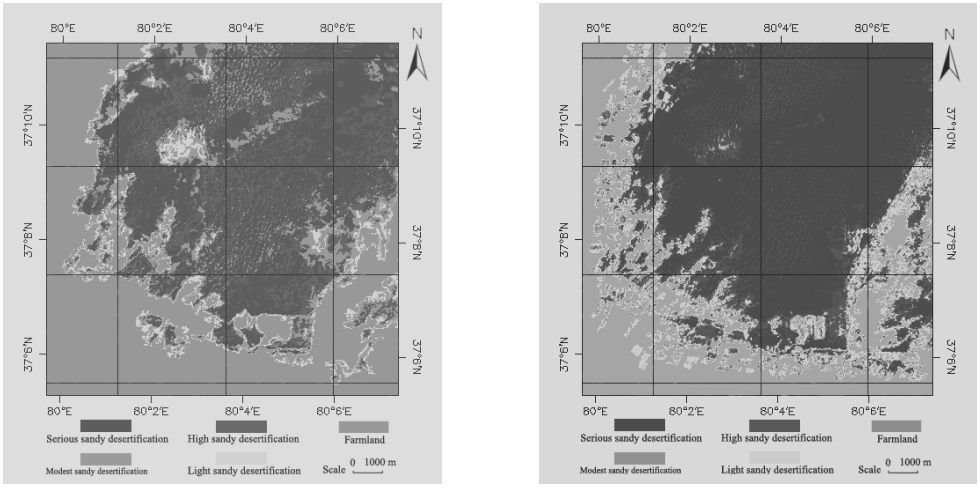

(a) Simulation of sandy desertification in 1990 (b) Forecast of sandy desertification in 2010

Figure 2. Simulation and forecast of the sandy desertification

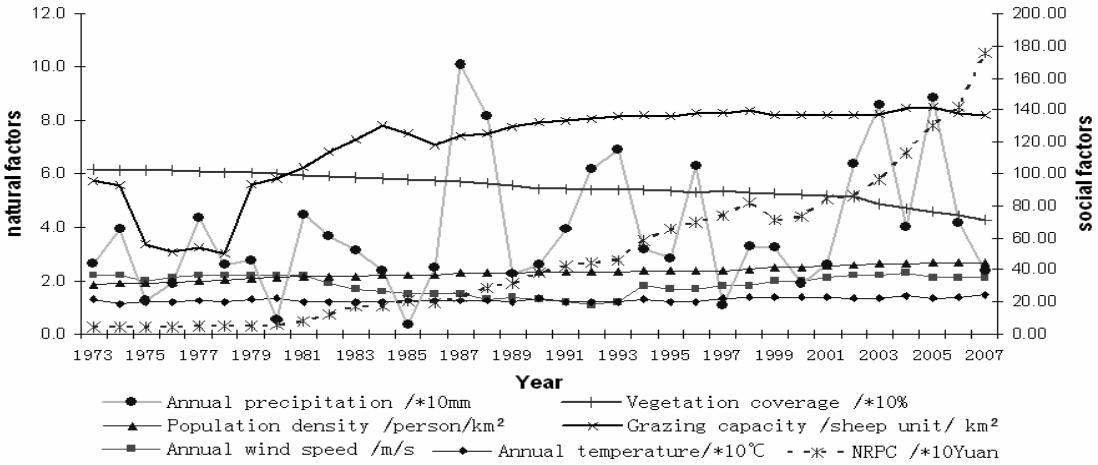

Figure 3. Effective factors data of research area from 1973 to 2007

Section 2C

COMPUTER NETWORKS 1

Effect of Hard RTOS on DPDC SCADA System Performance

A. M. Azad, C. M. Hussain and M. Alam
Electronics and Communication Engineering
BRAC University
Dhaka 1212
BANGLADESH
a.azad@bracuniversity.ac.bd

***Abstract*-Supervisory Control And Data Acquisition (SCADA) system is extensively used in power systems specifically for monitoring different power parameters, operating and controlling power electronics as well as other high voltage elements, for example breakers tripping or constant data procurement form current, voltage or power transformers. SCADA system failure can be an effect of inevitable consequences which include equipment damage, customer load losses even life losses. Dhaka Power Distribution Company Ltd. (DPDC) former DESA has been using SCADA over a decade which was developed by ABB. After its introduction in DPDC, the SCADA system hardly had any performance upgrade. At present the entire SCADA system is observing many problems that are rendering the whole structure obsolete. At the early stage ABB came across some limitations which later on were solved in such a way that may not convene the time precision that present technological development demands. ABB used soft real time operating system UNIX. This OS usually responses with high latency which sometimes caused some remote power elements (breakers) to fail in certain time frame. The communication structure is based on microwave links which certainly has some shortcomings in terms of SCADA security. Evaluating these consequences, this paper presents some draw backs of current DPDC, SCADA system and proposed Hard RT Linux as an operating.**

***Key words*:** Hard real-time, Soft real-time, PID tuning, SCADA, RT-Linux, RTU.

1 INTRODUCTION

SCADA refers to a system that accumulates data from different sensors at feeders, relays or in other remote locations and then propels this data to a central computer which then controls those elements according to constricted instruction based on the procured data. System analysis in this paper will be concentrated on former DESA SCADA system which has currently been reformed as Dhaka Power Distribution Company Ltd (DPDC) SCADA system. The control capability that SCADA systems provide is essential for the safe and efficient operation of our electric power grids.

The system-wide monitoring and control functions provided by such systems may contain slight shortcoming which makes the entire system less effective where strict time accuracy is in concern. SCADA systems are used in power systems to monitor, operate and control generation, transformer, and switching and load stations [1,2,3,5,18]. Such control can he automatic or manually initiated by operator commands. A typical SCADA system consists of three main components, namely, remote terminal unit (RTU), master control and telecommunication network. The failure of any of these components may disable the entire system. The master control however, takes part in controlling the entire network which expectedly should be much more compact with advanced equipments and as a same time highly sensitive with respect to time to be more efficient in sending instructions to its target.

The operating system using by SCADA is UNIX, DEC OSF/1, which is a soft RT operating system and can be replaced by hard RTOS for example RT Linux to ensure time criticalness in every possible measure. This paper will demonstrate how maximum delay time can be recuperated and confined the desired loop iteration time by integrating RTOS as DPDC SCADA operating system. In section 2 the formation of DPDC SCADA control system communication is described followed by section 3 where the method of SCADA protection is explained in brief. After that in section 4, the structure of SCADA hardware is given and in section 5 the SCADA software will be described with an experimental presentation of breaker operation in a subsection 5.1. In section 6 the hard real-time operating system is explained with one subsection 6.1 about real-time Linux and under section 7, related works on RT Linux at BRAC University is explained elaborate including result from the laboratory test with few subsections. The proposal for Hard RTOS for DPDC SCADA is provided in section 8.

2 SCADA, DHAKA POWER DISTRIBUTION COMPANY LTD

Electric network management is a unique and proven system, which after being introduced by former Dhaka Electric Supply Authority (DESA) back in 1995, has saved some Tk 2/3 crore every month [8]. Bangladesh can save crore of taka in the power sector by adopting a new system which will also improve quality and security of power distribution. SCADA system gives a overview of the network and update view of voltage levels and equipment states making them instantly aware from anything happening over a wide area, like spider in centre of a web. Such a control centre enables to operate to have a window into electrical network through computer station. In the greater Dhaka power communication network of SCADA, the Remote Terminal Unit (RTU) is located with quite a distance from master control unit and communication is established by microwave wireless communication.

One major wireless communication ring was developed by five cells connecting with one SCADA 'Master Control' (Dhanmondi CC). The five cells New MirpurCL-2(2/2), Tongi2CL-5(2/2), NarsingdiCL-3(2/3), BultaCL-3(3/3), and FatullaCL-7 (2/2) are involved with the signal relaying to the different sub cells or RTUs. The sub cells receive signals to execute the power elements. These sub cells are not in the communication ring and only can send the acknowledgment to the master control through the relay or transponders. The RTU adjacent to the base stations are connected with Ultra High Frequency (UHF) communication and some cases with the pilot cable.

3 SCADA PROTECTIVE SCHEME

Power systems are operating close to their design limits. These operating conditions leave little room for error in the protection and control systems. The pre-eminent approach to preserve the transient stability of the power grid High-speed is the fault clearing protection and control systems. These high-speed tripping schemes are called pilot protection because they utilize end-to-end communications to provide high-speed, simultaneous fault clearing or termination. Remote terminal(s) systems must receive a signal from master control to issue a local tripping signal. In case of DPDC (former DESA) SCADA, the microwave communication is in primary concern although applicable communications channels include audio tone, microwave, fibre optic, and spread spectrum radio. These schemes exchange a minimum of one information bit. Unlike blocking schemes, precise signal or message timing is usually not critical. The more time it takes for a relay at one end to receive notification that the remote terminal relay also senses a forward fault, the longer the tripping time. A slightly delayed trip during an internal fault does not comprise a disoperation. It is accepted that a failure to receive a valid tripping signal can result in a failure to operate at high-speed for an internal fault [9]. But at the same time this should be taken into the account that sharp time response can improve the efficiency of the system.

4 SCADA HARDWARE STRUCTURE

The ABB SCADA system consists of a series of servers, consoles, and networking components to build a hardware platform on which to install the ABB Energy Management Software suite. There is a central processing server which provides the central core for the SCADA system and includes database management, centralized communications, and other critical SCADA functions. The Central Processing server consists of a Compaq Alpha server running Tru64 release 5.1b. Disk storage is provided with six disk drives. A backup for these drives is provided in a split SCSI bus cage with 12 disk drives. Each set of six disk drives can be used as the primary drive system during boot. This allows a fully configured and functional backup copy of the central processing server to be available should testing crash the primary system.

The Real-time Database and Communications server consists of a Compaq Alpha server running Tru64 release 5.1b. Disk storage is provided by two disk drives acting as a primary and secondary drive. The primary drive is mirrored via a manually run script to the secondary drive. The consoles provide the Human Machine Interface (HMI) for the ABB SCADA/EMS system. In a typical system, there are many consoles, each providing control, analysis, and/or monitoring functions for the ABB system. All PCs on this system are HP Workstations with Xeon processors running Windows XP Professional. Disk storage is provided by a single disk drive. The NVIDIA Quadro NVS graphics system is capable of driving up to four computer displays.

5 SCADA SOFTWARE STRUCTURE

Digital Equipment Corporation (DEC) developed a new UNIX implementation based on the OSF/1 specification. Digital UNIX was formerly called DEC OSF/1It was initially marketed as DEC OSF/1[14]; DEC renamed the new operating system Digital UNIX, and then Tru64 UNIX when Compaq acquired the company. It is a 64-bit operating system for workstations and servers equipped with the Alpha processor [4]. Though it is fully System V-compliant, for both the user and administrator, it behaves more like a BSD system. On server type Digital AlphaStation 400 4/233 of server 6 and server 7 is dedicated as Application Servers of DPDC SCADA which is compatible with OSF/1 Rev 3.2 comprising different sort of application software for example DEC, (OSF-BASE, OSF-USR etc) and For Database architecture Data Engineering Tool is installed in Dhaka1 server comprising of Oracls7.1.3.2.1for DEC OSF/1 3.0, RDBMS 7.1.3.2.1 etc. In terms of Human Machine Interface (HMI) servers (WS400 Workstation) allocated for dhaka2, dhaka3, dhaka4 and dhaka5 (remote workstation, LDC) where different HMI software are installed [20].

SCADA may needs to operate more than one RTU of different substations in same time. To preserve their temporal behavior command applications require that the underlying systems provide soft real time Quality of Service QoS Guarantees. In the current DPDC SCADA operating system (UNIX DEC OSF/1) multi user, multi process and time sharing (TS) environment these applications do not perform well when they are scheduled concomitantly with the traditional non RT applications such as text editors compilers or computation intensive tasks. The real time RT applications also do not perform well when other RT applications are scheduled concomitantly. Untimely scheduling of processes is partially responsible for this kind of adverse phenomenon rather than insufficient CPU capacity. One potential solution for this problem is to serve RT application in UNIX environment is to dedicate the entire system to serve only one RT application. This involves blocking services to all other RT or non RT applications and users. This solution avoids the potential scheduling problem and it also defeats the UNIX environment goals of supporting multi user multi process and time sharing properties [17].

Therefore, this solution is not feasible in the UNIX environment.

5.1 Breaker Operation of DPDC SCADA

DPDC SCADA system in kataban, we conducted an experiment on breaker operation located quite a distance from master control. Remote Terminal Units (RTU) are designed to respond with the command given from the master control, provided the breakers are in automatic mood. If the breakers are set to manual condition, the master control of SCADA system does not have any hold on any of these RTUs or breakers in any circumstance. Since SCADA is a very sophisticated decentralized electrical control system we were not allowed to operate the breakers in extensive measure. We collected few breaker operational data which have been done on schedule. Master control operates few two breakers in Jigatala and other breakers from Kollyanpur substation. In each case breakers were tripped in different time period. It is to be noticed that the communication delay should be considered identical as we operated breakers located in two different substations not more than 30 Km apart from Dhanmondi CC. In case of any communication time deviation from the time taken by the communication system, we can neglect the delay in this regard because of microwave communication.

SCADA use to operate several breakers each day which are centrally controlled by Dhanmondi master control keeping all the records of tripping data on an event list. We procured few of those data which have been given in Table5.1 where all mentioned tripping timing was from two substations, Kollyanpur substation and Jhigatala substation. On the Table 5.1 the procured tripping data from DPDC SCADA is presented.

TABLE 5.1: BREAKER OPERATIONAL DELAY ANALYSIS

Substations	Date (day/month/year)	Command Time (hr : min : sec)	Tripping Time (hr : min : sec)	Delay Time (ms)
Kollyanpur	12/04/2009	21 : 15 : 26	21 : 15 : 27	1000
	13/04/2009	13 : 17 : 00	13 : 17 : 01	1000
	13/04/2009	14 : 17 : 54	14 : 17 : 56	2000
	13/04/2009	20 : 32 : 32	20 : 32 : 34	2000
	19/04/2009	19 : 16 : 18	19 : 16 : 20	2000
Jhigatala	20/04/2009	14 : 08 : 06	14 : 08 : 08	2000
	05/04/2009	11 : 49 : 59	11 : 50 : 15	16000
	08/04/2009	16 : 30 : 16	16 : 30 : 17	1000
	09/04/2009	12 : 25 : 03	12 : 25 : 05	2000
	09/04/2009	15 : 00 : 43	15 : 00 : 50	7000

At Kollyanpur substation for example, a breaker was commanded to trip at 21: 15: 26 which responded after 1000ms giving the tripping time at the event list 21: 15: 27. However, the desired loop time is to be mentioned as 2000 ms which we found on following day's event list. Master control sent a command to same substation to trip a breaker at 14: 17: 54 which was executed 2000ms later at 14: 17: 56. The same case we found as a majority except two deviations. We located two large time delay interims of breaker operational timing when the master control operated a breaker in Jhigatala in time of 11 hr 49 min and 59 sec (11:49:59) and the breaker was tripped at 11 hr 50 min and 15 sec (11:50:15) which indicates the operational time delay is 16 millisecond. In second case a dummy breaker of Jhigatala substation was operated at 15:00:43 and tripped at 15:00:50 giving operational time delay 7ms. The graphical presentation of the breaker operational time delay fluctuation is given in graph 5.1.

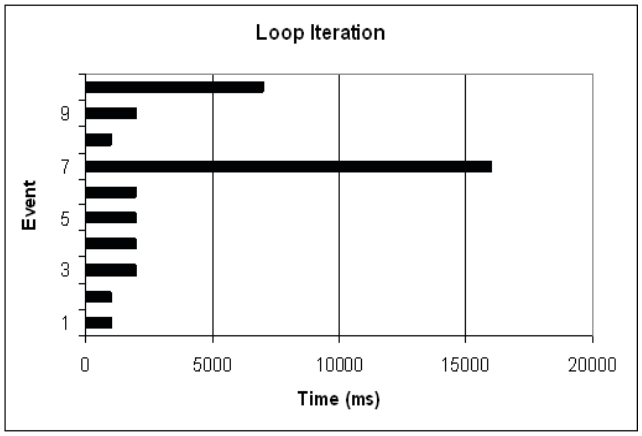

Graph 5.1: Breaker Operational Loop Iteration of DPDC SCADA

The in figure 5.1 shows the block diagram of SCADA system where the SCADA server end consists of Compaq Alpha server and UNIX operating system. The Remote Terminal Unit (RTU) end is having data acquisition and interfacing units like marshalling and data conversion blocks. The next block is the communication where all the modulation and demodulation take place before transmitting and receiving signals respectively. After transmitting any command signal it reflects back from the receiving substations with acknowledgment. In this experiment the time taken by the receiving ends are not prime concern. This research rather concentrate with the time taken by the SCADA master control and the process of restrict the breaker tripping loop iteration within desired time. The block diagram indicates the delay time taken by the six different blocks, SCADA server delay s_{server} transmitter and receiving data acquisition card time delay τ_{DAC} and the both transmitter and receiving end communication delay refers to τ_{Com} and in the receiving end the circuit breaker delay $\tau_{CB.}$ Since the communication system is using microwave, the delay regarding this can be negligible. The data acquisition card at RTU takes reasonable amount of time and it could be improved by increasing the pulse frequency of digital to analog converter or analog to digital converter.

Analyzing the nature of the time delay, the entire tripping loop iteration or in the other way the minimum desired loop time includes 2 * (τ_{Server} + τ_{DAC} + τ_{Com}) . These six parameters cumulatively give the time delay of

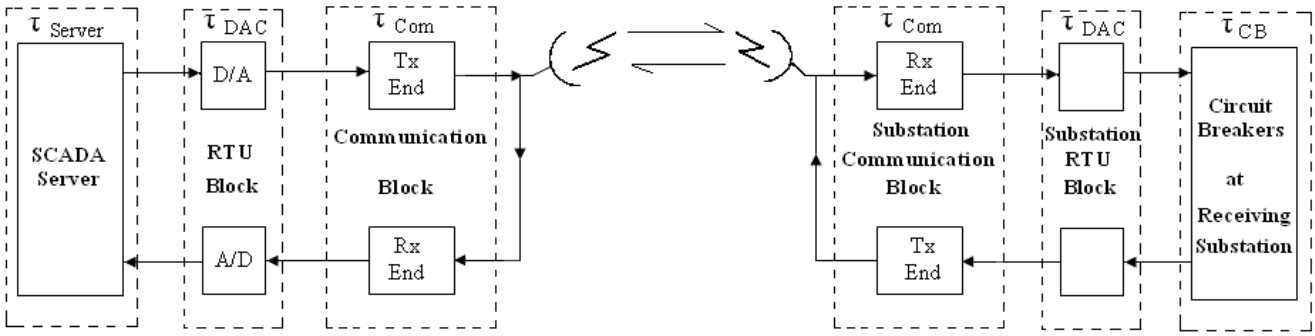

Fig. 5.1: Block Diagram of DPDC SCADA Communication between Server & Client

approximately 2000 ms and most of the time delay takes place from our findings in SCADA server end which is about 1500 ms. Breaker operational Time fluctuations occur due to multitasking operation and running other software for different applications. On the figure 5.1, minimum loop iteration was measured as 1000 ms few times. However, the desired loop iteration is counted as 2000 ms which in few cases can be exceeded drastically. In Jhigatala substation on 5th April and 9th April 2009 can demonstrate the scenario of maximum delay occurred in a breaker operation. On 5th April in a certain incident the breaker tripping loop iteration of 16000 ms provides in this case a Jitter of 14000 ms. Operational time delay variation depends on many parameters on which one of the most frequent reason is due to operating system. As soft RT operating system does not work well when other non RT tasks run simultaneously. Apparently the operating system of SCADA which is in this case DEC OSF/1 for DPDC causes the influential effect for the instability as soft RTOS is vulnerable to interruption while multitasking. SCADA operates their entire DPDC control network by five console computers on UNIX platform. Each of them may involve at different tasks at the same time for example printing data, breaker commands and status updates of RTUs. These multitasking may cause the operational periods to be fluctuated significantly in each command. The Jitter of 14000ms could have been halted by a time critical operating system like Real-Time Linux. RT Linux can reduce the maximum time delay and restrict the desired loop iteration within 2000ms.

6 Hard Real-time Os

A hard real time system is an information system, whose correction depends on moment in time when logic output occurs rather than the logic output of the algorithm. The hard real time application fails if their operating system timing requirements are not satisfied [7, 12]. The output is required to reach within a precise time interval. A real time system is not necessarily fast, but must be accurate in time rather then resulting correct output. The design of the real time system goes under multiple stages. Identification of the task, which suppose to be performed, and the satisfactory temporal restriction come at the first stage. The next stage goes under the code is developing and the measuring run time of each task and then precision of time constrain test is executed to ensure that the tasks will not miss their deadline while the system is running. However, the soft real time applications tolerate large latencies in what they have requested from the operating system. The real time system is implemented with a combination of Linux, RT-Linux, data acquisition cards, source code and standard PC.

7 Related Experiments On Real-time Environment

Evidently in case of multitasking soft real time operating system works less efficiently as traditional non RT tasks can be interrupted. Besides response of a system can be minimized and countered by running the tasks under hard RT operating system, for example RT Linux. An experiment has been performed under Control Application Research Group (CARG) of BRAC University by implementing a PID controller algorithm in RT-Linux environment to compare the PID controller step response in different environment (soft and hear real-time) and improving the performance over the Windows environment illustrated in [7]. The experiment regarding SCADA system was replicated with the PID controller because of two inevitable reasons, SCADA control equipments were far beyond our reach and to compare the performance between two operating system windows XP and RT Linux, Knopix3.0 since there was a unavailability of UNIX as DEC OSF/1. The Real-Time system is the accurate system which gives lowest latency on processing different parameters of proportional, integral and differential controller and through this real-time environment the servomotor control unit is controlled. This experiment shows that the delay performance of PID algorithm can be significantly countered under real-time implementation. Reducing the delay and enhance the stronghold controller act in RT-OS leads the system with minimized measurement noise. In order to obtain best response sampling rate of 10*msec* is chosen for soft real-time case and 1*msec* is chosen for hard real-time case. The time responses are examined both in hard real-time and soft real-time environment. The results which will be demonstrated on the subsequent part of this paper in hard real-time performed faster than in soft real-time due to the lower latency of RT-Linux. Multitasking is a very important factor in our cyber world. But it will be more efficient when it will be uninterruptible. On the other hand accuracy is another unavoidable factor [19]. In a different experiment another experiment has been done on implement a closed loop system for stepper motor using RT LINUX in case of multitasking. As a result the total system can drive parallel task simultaneously and error free driving of stepper motor. A large number of work and application has been

already done on error free system of stepper motor. Some are based on microcontroller, some are using LINUX based program and other are using modified driver circuit. But in this particular work the specialty is to drive the stepper motor with maximum accuracy in case of uninterrupted multitasking where the task is processing in a RT kernel. In this work the main factors are the DAQ card which is used for multitasking, an optical encoder to get the feed back from the stepper motor and finally a program which is run the entire system and if any type of error occur, it will take the necessary immediate action. So the accuracy in case of multitasking environment will be maximized. The results in subsection 7.2.1 showed that RT Linux can perform more consistently on multitasking condition with relatively less response time.

7.1 Hard Real-Time PID Controller

In this work the PID controller implementation under soft real-time is presented in the VCL program on MS15 –DC motor control module (Servo controller). The system included a 120 MHz Pentium laboratory PC with Windows XP installed, connected a servo system through a parallel port. The servo system module enables the user to perform closed-loop, positional or a speed control of a DC motor. Speed of rotation and positional feedback information are available in both analog and digital forms, but particularly in this experiment the module was controlled by analog system [16].The PID controller under RT-Linux environment comprised a 120 MHz Pentium laboratory PC had been in use for soft RTOS with the feedback modules and ax5411 data acquisition card. RT-Linux 3.0 has been loaded to execute the real-time thread of PID controller [7]. A real-time thread program is developed based on the PID algorithm in terms of the necessary requirements of the software [7, 13]. A priority scheduling real-time kernel was implemented for the data acquisition card with dissimilar sampling and hold rate. During the initialization step, the tasks are assigned to each module. The flow of data to and from the data acquisition card is implemented with real-time tasks through real-time FIFO. Interrupt-based techniques had been applied to handle three real-time tasks mentioned as A/D conversion, real-time thread program execution and D/A conversion. The inter-task communication among the three real-time tasks is done with shared memory. The RT-kernel receives a fixed set of tasks at the time of initialization and each of the tasks has a priority level assigned in the pre-emptive scheme. The real-time task communicates with non real-time Linux and the data acquisition card and the RT-FIFOs avoid message losses. High level interfaces between the user and the experiment had been provided by non real-time GUI program using GTK (GIMP Tool Kit) in the Linux environment. The non real-time critical set of tasks can be mentioned as data logging, display and GUI. The real-time tasks deliver results to Linux at a low rate and final data through shared memory and circular buffer under the data acquisition scheme.

7.1.2 PID Controller Experiment Result

Initially of the experiment, soft real-time PID controller has been considered [7]. The servo system was operated using Ziegler-Nichols parameters and the system response had been observed in terms of delay time, rise time, peak time, settling time and overshoot. The same experiment was performed using RT-Linux real-time thread program. The comparative results in soft real-time and hard real-time environment are as follows:

TABLE 7.3: T_D, T_I, T_P, T_S PARAMETERS [7]

Parameters	Soft real-time PID	Hard real-time PID	Faster rate
Delay Time, T_D	0.10s	0.064s	1.56 times faster
Rise time, T_R	0.19s	0.103s	1.84 times faster
Peak Time, T_P	0.31s	0.146s	2.12 times faster
Settling time, T_S	0.70s	0.35s	2 times faster
% Overshoot, M_p	25%	25%	Same

The delay time is the time required for the response to reach half the final value. From the table above it is found that the delay time $T_D = 0.10$ second for soft real-time PID controller and the hard real-time it is reduced to 0.064 second which is 1.56 times faster than the soft real-time. Responses of servo system with PID controller in soft and hard real- time environment with necessary parameters are illustrated in [7]. T_R is the time required for the response to rise from 0% to 100% of its final value. For the soft real-time, the rise time is 0.19sec and for hard real-time it is 0.103sec. Thus, the response time is 1.84 times faster in hard real-time PID controller. The peak time, T_P (time required for the response to reach the first peak of the overshoot) is 0.31sec for soft real-time where on the other hand for the hard real-time, it is 0.146 sec which gives 2.12 times improvement. Settling time T_s is also 2 times faster in hard real-time. The settling time zone is considered $\pm$ 2%. Percentage peak overshoot is 25% for both (hard real-time and soft real-time PID controller) case. Overall, it clearly illustrates that there is improvement in system response for hard real-time PID controller over soft real-time PID controller.

7.2 RT-LINUX Stepper Controller on Multitasking

To get the maximum performance of stepper motor, different types of improvement and work has been done. In this work a control system of stepper motor by using Real Time Linux has been implemented [19]. RT Linux program algorithm was used where the motor is controlled in Real time kernel so no other task can interrupt this task in case of multitasking. Data Acquisition Card (PCL-812PG) was connected to sent signal and receive signal from hardware interface. A GUI interface controller was also developed in this work to make it easier to use. The Linux based simulation program interacts with hardware interface to drive the stepper motor in real-time environment in case of multitasking mode. So the driver circuit drives the motor by using the command from the RT program by using the DAQ card. Stepper motor is largely used for the purpose of accurate and efficient movement. However, miss stepping leads to main problem, therefore many types of work have been done to find the remedy including developing many types of algorithm and programs. But in case of multitasking that work are not much efficient and the non RT task can be interrupt by other tasks in soft or non RTOS. The system can

be more If RT Linux takes the action in multitasking environment. In this work a RT Linux PC controlled the entire system in real-time method. A PC-812PG DAQ card is used to send and receive data from the hardware interface and multiple tasks can be controlled by this device. PC-812PG is a high performance, high speed and multi-function data acquisition card for IBM PC and compatible computers. It is ideal for wide range of applications in industrial & laboratory environments. These applications include data acquisition, process control, automatic testing & factory automation. The main purpose of this card is to receive and send signal to the external hardware interface. It is mainly used for multitasking in real-time environment. Driver circuit ULN2003 had been in use to receive data from the DAQ card and drives the unipolar stepper motor according to the data. The unipolar stepper motor is having 5 wired stepper motor with step size is 1.8 degree. It gives in clock wise or anti clock wise rotation. It mainly converts the electrical pulse into mechanical signal.

7.2.1 Stepper Motor Experiment Results

An experiment in BRAC University laboratory has been performed to compare the control of stepper motor in different environment (RT Linux, non RT Linux and Windows). DSO was used to measure the reading for each of the stator signal from the stepper motor in case of multitasking. At that time four programs were running simultaneously for each of the cases which make the CPU occupied near about 90% for RT LINUX and 70% for Non RT Linux and Windows. Then the compression of the procured result varying the time resolution for 10 ms, 1s and 2 second had been done. The table 7.2.1 illustrates that in case of 1 sec time resolution for 90 degree full rotation Windows takes 7.92s where non real-time Linux takes 6.16s and hard RT Linux takes 6.00s in multitasking mode. It is proved from this experiment that RT is better than Non RT Linux and performs much better than windows OS. Increment of the timing resolution up to 10ms allows non RT and windows to give irregular movement of the stepper motor, however RT Linux worked properly. After increasing the time duration up to 2s, some miss steps occurs both in soft RT Linux and windows but on the other hand RT Linux was working accurately.

TABLE 7.2.1: STEPPER MOTOR FOR 90 DEGREE ROTATION

Parameters	Windows	Soft RT Linux	Hard RT Linux
Time Difference (10ms period)	Random movement with severe interruption	Irregular Waveform	59.2 ms
Time Difference (1Sec period)	7.92 s	6.16 s	6.00 s
Time Difference (2Sec period)	0.31s	0.146s	2.12 times faster

This control system works in between 1ms < T < 3s. Because in case of 1ms there is irregular movement of motor is occurred and in case of using any time duration which is greater than 3s gives some irregular movement too. For closed loop control system of stepper in case of multitasking, RT Linux based algorithm is used to control the stepper motor and error correction as well. In this experiment had shown the response of the system in case of multitasking in both real-time and non real-time environment. In terms of controlling a stepper motor the RT Linux based control algorithm performed with real-time response and error correction feature comparing to any other soft or non real-time operating system.

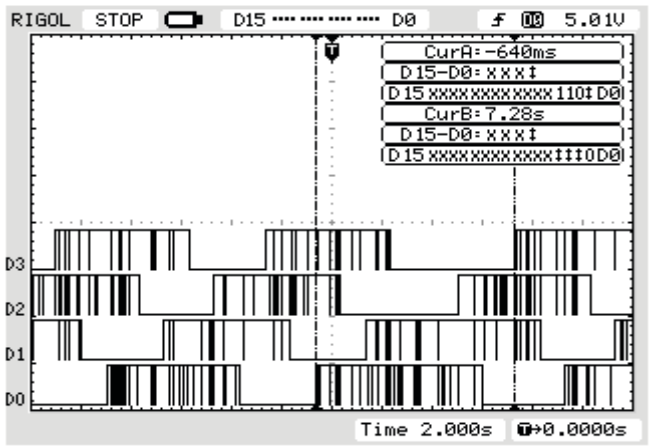

Fig. 7.2.1: Wave form of Windows under Multitasking (1sec delay/pulse)

The wave forms for soft RT Linux, windows and Hard RT Linux are given in the three consecutively on the figure above. There are other sets of responses can be found from 10ms, 2sec and the nature of wave form can be measured from those figures.

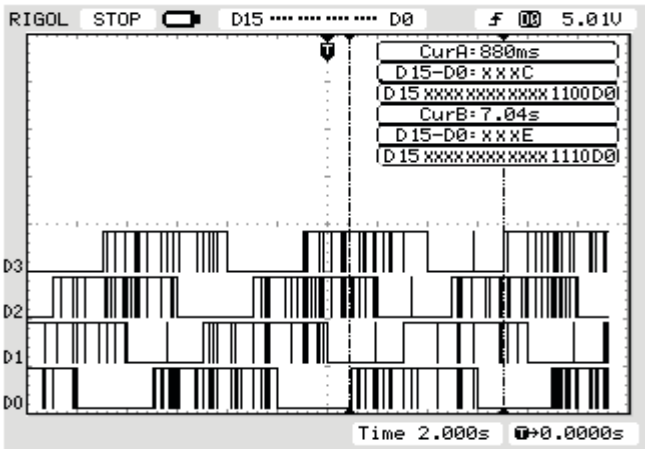

Fig. 7.2.2: Wave form of soft RT under Multitasking (1sec delay/pulse)

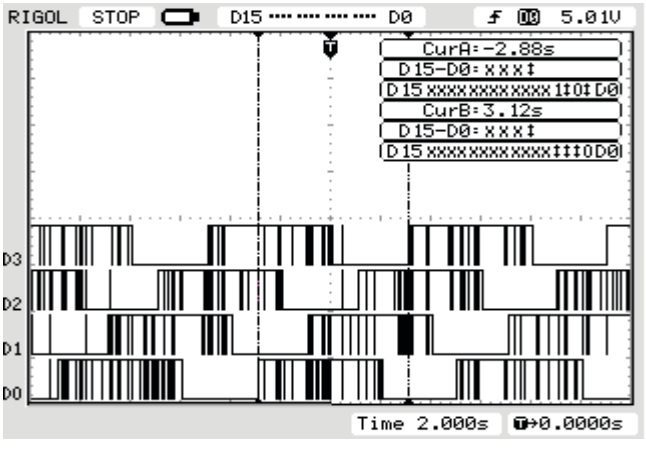

Fig. 7.2.3: Wave form of Hard RT under Multitasking (1sec delay/pulse)

8 Proposed Real-time Operating System For DPDC SCADA System

As it was mentioned before, the real-time applications also do not perform well when other RTs are scheduled concurrently. To keep this OS on progress one feasible solution is the current RT extension to UNIX. The UNIX POSIX.4 real time extension provides fixed priorities to real time applications. The priority scheduling rule dictates that higher priority processes are scheduled before the lower ones in a pre-emptive fashion. RT processes are assigned higher fixed priorities whereas non RT processes are assigned lower dynamic priorities. As a result the RT processes are served before non RT processes and higher priority RT processes are served before lower priority RT processes. This fixed priority mechanism provides a convenient way to implement the rate monotonic RM algorithm because the ordering of priorities between the RT processes depends on the ordering of the process rates the length of their periods. Under this RM schedule the RT processes with smaller periods are executed first followed by RT processes with larger periods and then non RT processes [17]. Prior to the start of any RT process the schedulability test is performed by checking its total CPU demand so that including this new process the CPU resource allocation will not exceed the CPU capacity. But this schedule has many problems described the following paragraph.

Priority should represent the importance of a process rather than whether this process is RT or non-RT. For example, a user giving command for printing RT application more important than other user giving command for trip a breaker non RT application RT and non RT applications must share the CPU time fairly. It is also unreasonable to assign priority for RT applications based on the length of their periods. This is called the fairness problem. There is no mechanism to meet the deadline and prevent overrunning and observe monopoly of CPU by a faulty RT process at high priority because it does not provide any protection between applications. Frequent over runs from a high priority process can cause massive interruption to other processes at lower priority. A RT process at very high priority can even block most of the system processes and lock up the entire system. This is called the enforcement problem. Root privilege is required to run the application under fixed priority. However when the UNIX security is in concern, it is impossible to give every user root privilege to run RT applications. This is called the security problem.

UNIX is an operating system created in the early days of computers. More recently, Linux was created as an open-source, freeware operating system. Hard RT-Linux can make a system to guarantee that predefined response times to certain hardware events to execute by activating kernel pre-emption. RT-Linux can use UNIX constructs and also departs from traditional UNIX. RT-Linux is faster than many of the other commercially available operating systems. It appears to also be far more robust than UNIX, DEC OSF/1. Linux is being used in many time critical applications because of its speed [10]. SCADA can be more efficient with RT-Linux without any major modification in their setup because it is used in many applications that need to maintain uptime as Linux, like UNIX, can run for months at a time without rebooting.

The reason why SCADA experts over a decade earlier had set the response time up to 30ms was because they found this time is a minimum to operate any power elements consistently. A soft real time OS like UNIX can not guarantee the system to execute in time because in case of soft Real-time the timing constrains are only failed in very rare cases which reflects the similar problem with the DPDC (former DESA) SCADA while operating the substation's RTUs. While operating substations from the master control some delay can be occurred as it was demonstrated earlier part of this paper due to multitasking environment which particularly in this experiment we found 14000ms. This 14000ms however, can be minimized by hard RT Linux operating system and confined the minimum desired loop time fewer than 2000ms by stopping all other non RT task during prioritize command under execution.

As microwave travels with the speed of light than it can be anticipated, the approximate distance of 70km from Dhanmodi CC to Narsingdi CL3 2/3 for example: it takes maximum of 0.233 ms which is less than one percent of entire time taken by the power component tripping process, and the relaying the signal, the transponders also do not contribute much time comparing to 30ms time frame if we take the maximum measurement of time taken by the master control to trip the breaks of Jigatala substation mentioned earlier in this paper. The signal transmission time is relatively negligible to the defined time span by the operating system and during the establishment of DPDC (former DESA) SCADA experts did not locate any other deviation with the system. There is a prospect to reduce that response time or desired loop time introducing hard RT operating system, preferably RT Linux in DPDC SCADA system.

Hard real time OS is positively faster and can meet the requirements for SCADA state of the art technology if the SCADA OS is replaced by RT-Linux. This particular OS can introduce task priority as an extra feature to the SCADA system. This operation will first identify the priority and according to that the execution will be done. The above experiments show the rise time of RT Linux is 1.56 times faster then any other soft real time OS. The faster rise offers the faster response to the system, in this case the response time of the SCADA system, if the maximum time taken for breaker tripping is taken into the account can be improved by 1.56 times which allows the system to response in approximately 18 ms and can improve the response time. Since RT Linux performs efficiently under multitasking environment by restricting any other non RT tasks. RT Linux executes the prioritize task as nonpreemptable and stop any other task on the processor so that no jitter can occur. Due to this specific feature of RT Linux the maximum delay time over the desired loop time can be recovered that can resist the delay operation of breakers on a certain instant. This is the radical improvement of DPDC SCADA system which our paper is suggesting.

9 CONCLUSION

SCADA system is a communication and control system used for monitoring, operation and maintenance of energy infrastructure grids and at the same time system has a harsh deadline for critical tasks comparing with traditional application. This paper has identified the motive of the failure of consistent execution of SCADA power components in different Remote Terminal Unit under specific time limit and proposed RT Linux as a primary Operating System for DPDC SCADA and with the help of advance communication system which will be concentrated on our further research to have better response time in terms of tripping or initiating any relays or breakers of different feeders or substations. These approaches will promote the existing SCADA technology towards future development and offers the time precision of supervisory control so that no command is failed to execute. RT Linux makes the SCADA system 1.56 times faster than ever before from operating system's point of view which compensates approximately 13ms from the previous maximum time taken by the master control to operate breakers. The fiber optics allows more security on communication by reducing the attenuation of the signal and data interception. The fastness of the response time and priority task handling property of the hard Real-Time operating system (RT-Linux) will improve the performance of the existing SCADA system which can save more resources and money; moreover it will improve quality and security of power distribution for new DPDC SCADA.

10 ACKNOWLEDGMENT

This work has been conducted and supported by Control Application Research Group (CARG) of BRAC University under the criterion of individual student research project. SCADA (Katabon) of Dhaka Power Distribution Company Ltd has been tremendously supportive while conducting this research. SCADA superintendent engineer, communication engineer had extended their helpful and effective information and expert opinions in this regard. The experiment of comparison between hard and soft Real-Time Operating System has been performed under Control Application Research Group (CARG) and a part or that experiment was provided by the members of CARG which unquestionably assisted to conduct the research on SCADA system of Dhaka Power Distribution Company Ltd.

11 REFERENCES

[1] CIGRE Study Committee B5/WG07. "The Automation of New and Existing Substations: Why and How," Report No: Draft Final Report, November 2002.

[2] Power Engineering Society Substations Committee *I Subcommittee* C3/Task Force 1, "Recommended Practice for Network Communication in Electric Power Substations," IEEE Project P1615.

[3] Hydro One Inc. "Transmission Control Room and SCADA Standard," Hydro One Internal Report, February 3, 1999.

[4] *J. R. Davidson ,M. R. Permann ,B. L. Rolston ,S. J. Schaeffer* ABB SCADA/EMS System INEEL Baseline Summary Test Report. November 2004

[5] Gomaa Hamoud Rong-Liang Chen Ian Bradley, "Risk Assessment of Power Systems SCADA" *Power Engineering Society General Meeting, 2003, IEEE Volume 2, Issue,13- 17 July 2003 Page(s): - 764 Vol.2,Digital Object Identifier*

[6] I. Kaya, N. Tan & D. P. Atherton, "A simple Procedure for improving performance of PID Controllers", Proceedings of IEEE Conference on *Control Applications,2003,* CCA 2003, Volume: 2, page(s): 882- 885.

[7] C. M. Hussain, M. Alam and A. M. Azad, "Performance of PID Controller both in Hard and Soft RTOS", *Proceedings of China-Ireland International Conference on Information and Communication Technologies 2008, Beijing, China.*

[8] ABB Utility Vice President of export sales "Bangladesh can save more money in power sector using SCADA system", Daily star, April11 2003,

[9] Allen Risley, Jeff Robertsand Teter Ladow,"Electronic Security of Real- Time protection And SCADA Communications Presented before the 5th Annual Western power Delivery Automation Conference Spokane, Washington, April 1-3 2003.

[10] http://wiki.answers.com/Q/What_is_the between_Linux_and_Unix

[11] M. Alam, C. M. I. Hussain, M. Moniruzzaman, S. Chowdhury. "PID Controller Of Servo System In Real-Time Linux Environment" A Thesis Submitted to the Department of Computer Science and Engineering of BRAC University.

[12] A. M. Azad, M. Alam and C. M. Hussain, "Delay Analysis of Sampled-Data Systems In Hard RTOS", Proceedings *of the 5th InternationalConference on Control, Automation and Systems* 2008, accepted to appear, Prague, Czech Republic.

[13] A. M. Azad, T. Hesketh & R. Eaton, "Real-time Implementation Multi-rate Sampling Systems in RT-Linux Environment", *Proceedings of The fourth International Conference on Control and Automation,* Montreal, Canada, 2003, pp.605-609.

[14] http:// www.desa.com.bd

[15] http://www.linuxfocus.org/English/May1998/article4.html

[16] K. OGATA, "Modern Control Engineering", *Pearson education, Inc,* 2002.

[17] Hao hua Chu, Klara Nahrstedt , "A Soft Real Time Scheduling Server in UNIX Operating System", Volume 1309/1997, Interactive Distributed Multimedia Systems and Telecommunication Services, *4th International Workshop, IDMS '97 Darmstadt, Germany, September 10–12, 1997 Proceedings*

[18] C. M. I. Hussain, M. Alam and A. M. Azad,"Performance Improvement of DPDC SCADA System Using Hard Real-Time OS", *The 2nd International Conference on Control, Instrumentation and Mechatronic Engineering CIM2009.*

[19] Ahmed Al Amin, Asaduzzaman All Faruk, Md. Asiful Alam, A. M. Azad, "Closed Loop Control Of Stepper Motor Using Real-Time Linux In Case Of Multitasking".

[20] Technical Reference Peter Nordvall, BTA, Date 11-08-98, ABB Network Control, S.P.I.D.E.R. System Program Versions No: 1KSE 6031-931 Reference L4654.1006, Page: 3(7).

HYBRID DECODING SCHEMES FOR TURBO-CODES

Shujun Huang[*], *Yinwei Zhan*[†]

Faculty of Computer
Guangdong University of Technology
Guangzhou 510006, China.

Charith Abhayaratne

Dept. of Electronic & Electrical Engineering
The University of Sheffield
Sheffield S1 3JD, United Kingdom.

ABSTRACT

Frequently used decoding algorithms for turbo decoding are the maximum a posteriori (MAP) algorithm and the soft output Viterbi algorithm (SOVA). The Log-MAP algorithm is a transformation of the MAP algorithm in logarithmic domain. It shows the better decoding performance, while the SOVA has the lower computational complexity. In this paper, we propose hybrid turbo decoding schemes using the SOVA and the Log-MAP algorithms. Both theoretical analysis and experimental results show that the proposed hybrid turbo decoding has less computational complexity than that of the Log-Map turbo decoder, and better decoding performance than that of the SOVA turbo decoder. The decoding performance can be close to that of the Log-Map turbo decoder with a small number of iterations.

Index Terms— Turbo-codes, SOVA, Log-MAP, hybrid decoding schemes

1. INTRODUCTION

In wireless mobile communication systems, powerful channel coding is essential in order to obtain sufficient reception quality. In 1993, Berrou *et al.* [1] proposed turbo-codes which take good advantage of random codes and the decoding condition of Shannon's noisy channel coding theorem to acquire good performance close to the Shannon's limit. This turbo-code integrates an interleaver and convolutional codes, so that, it can realize random coding and improve the low code weight. It adopts iterative decoding, presented in [2] *et al.*, to approach the maximum likelihood decoding. In [3], X. Qi *et al.* proposed a new iterative decoding scheme. Daneshgaran *et al.* [4] have presented a systematic method for design of interleavers. Perez *et al.* [5] proved that the performance of turbo-code can be improved by increasing the length of the interleaver. According to different design philosophies, interleavers can roughly be divided into two types: regular and random. A regular interleaver usually realizes interleaving on the basis of a certain rule. Thus, it can be easily realized. But for a random interleaver, it is difficult to realize deinterleaver.

The maximum a posteriori (MAP) algorithm and the Soft output Viterbi algorithm (SOVA) have become major decoding algorithms for turbo decoding. For example, Bahl algorithm is a MAP decoding method which minimizes the probability of the symbol error (or bit) for convolutional codes [6]. On the other hand, the SOVA is proposed on the basis of a Viterbi algorithm minimizing the probability of word error. It also suits for convolutional codes [7]. The Log-MAP algorithm is a variation of the MAP algorithm in logarithmic domain and yields lower computational complexity than that of the MAP algorithm and results in nearly the same decoding performance as that of the MAP algorithm. Compared to the Log-MAP algorithm, the SOVA is lower in computational complexity, but much worse in decoding performance. The complexity comparisons between the two algorithms have been presented in [8].

In this paper, we propose hybrid decoding schemes for turbo-codes by using the Log-MAP algorithm and the SOVA. This paper is organized as follows. In §2, we briefly review the structure of the turbo encoder, the decoder, the soft input and soft output (SISO) decoders based on the Log-MAP algorithm and the SOVA. Then in §3, we present our hybrid decoding scheme and its analysis. Experimental results are shown in §4 for comparing the hybrid decoding schemes with the original individual schemes, followed by conclusions in §5.

2. PRELIMNARIES

A turbo encoder uses a structure of parallel concatenated convolutional codes. Typically, it is at least composed of an interleaver and two recursion system convolutional (RSC) encoders as shown in Fig. 1. For an input bit $\{d_k\}$, the turbo encoder output is $\{X_k^s\} = \{d_k\}$, $\{X_k^{1p}\}$ and $\{X_k^{2p}\}$, where the last two components are the outputs of RSC encoders.

A turbo decoder, as shown in Fig. 2, mainly consists of two SISO decoders, interleavers and deinterleavers. For an AWGN channel and a binary modulation, the turbo decoder input comprises three random variables y_k^s , y_k^{1p} and y_k^{2p} with

[*]The authors would like to express their sincere gratitude to Mr. Jun Yang and Mr. Jiajun Wen for their comments.

[†]Correspondence author: ywzhan@ieee.org. The work of Yinwei Zhan is supported by Natural Science Foundation of China (grant no. 60572078).

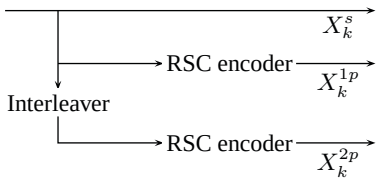

Fig. 1. The structure of the turbo encoder.

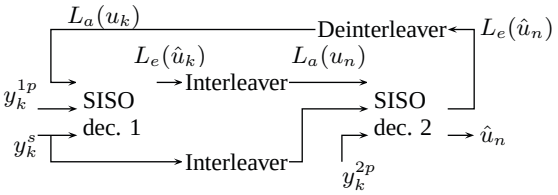

Fig. 2. The structure of the turbo decoder.

time k corresponding to the three output bits from the encoder. Let $u_k = 2X_k^s - 1$, $\hat{u}_k$ be the bit decision of the SISO decoder, $L_e(\hat{u}_k)$ is the extrinsic information (EI) generated by one SISO decoder which does not depend on the decoder input y_k^s, and $L_a(u_k)$ be the priori information (PI) associated with the EI generated by the other SISO decoder in the turbo decoder.

2.1. The Log-MAP decoder

An optimum soft output decoder should adopt a posteriori probability. The MAP algorithm based on codes trellis can minimize the bit error probability. The output of a MAP decoder for a transmitted "± 1" in the information sequence is defined as a posteriori log-likelihood ratio (LLR),

$$L(\hat{u}_k) = \ln \frac{p(u_k = +1|r)}{p(u_k = -1|r)} = \ln \frac{\sum_{(s',s),u_k=+1} p(s', s, r)}{\sum_{(s',s),u_k=-1} p(s', s, r)},$$

where r is the reception of the MAP decoder and the bit u_k is associated with the transition from time $k-1$ to k. The indexes s' and s correspond to the trellis states at times $k-1$ and k, respectively The transition from s' to s arises from the information bit u_k.
The Bayesian principle implies that

$$\begin{aligned} p(s', s, r) &= p(s', s, r_{t<k}, r_k, r_{t>k}) \\ &= p(r_{t>k}|s)p(s, r_k|s')p(s', r_{t<k}), \end{aligned}$$

where $r_{t<k}$ is the information received prior to the time k and $r_{t>k}$ is the information received after the time k.
Now we define $\alpha_k(s') = p(s', r_{t<k})$, $\beta_{k+1}(s) = p(r_{t>k}|s)$, and $\gamma_k(s', s) = p(s, r_k|s')$. Then we can write

$$\begin{aligned} \alpha_{k+1}(s) &= \sum_{s' \in \sigma_k} \gamma_k(s', s)\alpha_k(s'), \\ \beta_k(s') &= \sum_{s \in \sigma_{k+1}} \gamma_k(s', s)\beta_{k+1}(s), \\ \gamma_k(s', s) &= p(r_k|u_k)P(u_k), \end{aligned} \tag{1}$$

where σ_k is the state set at the time k and the $P(u_k)$ is the a priori probability of bit u_k.

The Log-MAP decoder can avoid calculating actual probabilities by using the logarithm of probabilities and the approximation $\max^*(x, y) \approx \ln(e^x + e^y)$. If the transition between s' and s exists, (1) can be updated as

$$\begin{aligned} \alpha_{k+1}^*(s) &= \max_{s' \in \sigma_k}^* \left[\gamma_k^*(s', s) + \alpha_k^*(s')\right], \\ \beta_k^*(s') &= \max_{s \in \sigma_{k+1}}^* \left[\gamma_k^*(s', s) + \beta_{k+1}^*(s)\right], \\ \gamma_k^*(s', s) &= \frac{u_k L_a(u_k)}{2} + \frac{L_c}{2} r_k \cdot v_k, \end{aligned}$$

where $v_k = (u_k, p_k)$, $p_k = 2X_k^p - 1$, $X_k^p = X_k^{1p}$ or X_k^{2p}, r_k is the reception in response to v_k, and $L_c = 4E_s/N_0$ is the reliable factor of the channel. Based on the above analysis, the output of a Log-MAP decoder can be written as

$$\begin{aligned} L(\hat{u}_k) = &\max_{(s',s)}^* \left[\alpha_k^*(s') + \gamma_k^*(s', s)|_{u_k=+1} + \beta_{k+1}^*(s)\right] \\ &- \max_{(s',s)}^* \left[\alpha_k^*(s') + \gamma_k^*(s', s)|_{u_k=-1} + \beta_{k+1}^*(s)\right]. \end{aligned}$$

2.2. The SOVA decoder

The SOVA uses soft decisions to calculate its metrics. In the AWGN channel, at time k, the metrics of the partial path of SOVA can be solved via

$$M([r|v]_k) = M([r|v]_{k-1}) + \sum_{j=0}^{n-1} L_c v_k^j r_k^j + u_k L_a(u_k),$$

where $v_k = (u_k, p_k)$, $p_k = 2X_k^p - 1$, $X_k^p = X_k^{1p}$ or X_k^{2p}, r_k is the reception in response to v_k, $M\left([r|v]_{k-1}\right)$ is the metrics of the former partial path, and $L_c = 4E_s/N_0$ is the reliable factor of the channel.

At time k and states $S_i, i = 0, 1, \cdots, 2^v - 1$, the difference of the maximum likelihood path $[v]_k$ and the error path $[v']_k$ can be written as $\Delta_k(S_i) = M([r|v]_k) - M([r|v']_k)$. At time k, the probability P_c of the maximum likelihood path correctly selected is equal to

$$P_c = \frac{p([v|r]_k)}{p([v|r]_k) + p([v'|r]_k)} = \frac{e^{\Delta_k(S_i)}}{1 + e^{\Delta_k(S_i)}}.$$

The log-likelihood ratio of the path decision can be formulated as $\Delta_k(S_i) = \ln \frac{P_c}{1-P_c}$ The larger the value of $\Delta_k(S_i)$ is, the more reliable the decision is. In other words, the decision is more reliable only if the probability of whether the survivor path is the maximum likelihood path or not is larger. At time k, the reliable value of the survivor path is $\Delta_{k-m}(S_i), m = 0, \cdots, \delta$, where δ is the decoding depth.

At time $k-m$, if the corresponding information bit of the survivor path is different from that of the competition path, the bit decision may be wrong. By using the method in [7]

Fig. 3. The succeeding structure of a hybrid turbo decoder.

Table 1. The computation complexity comparison of the decoding schemes

Operation	LM-LM	SV-SV	SV-LM / LM-SV
max ops	$10A-4$	$2A+6v+6$	$6A+3v+3$
additions	$30A+18$	$4A+16$	$17A+17$
multi by ± 1	16	16	16
look-ups	$10A-4$	0	$5A-2$
bit comps	0	$12v+12$	$6v+6$

updating the reliable value of the survivor path with backward tracking and according to the inference in [2], the soft output (or LLR) of the bit decision of the SOVA decoder can be written as

$$L(\hat{u}_{k-m}) \approx \hat{u}_{k-m} \min_{j=0,\cdots,m} \Delta_{k-j}(S_i),$$

where $\hat{u}_{k-m}$ is the bit decision at time $k-m$.

3. HYBRID TURBO DECODING SCHEMES

Based on the above analysis of the Log-MAP decoder and the SOVA decoder, both of them can output the LLR, $L(\hat{u}_k)$, of the bit decision, so the two SISO components of a turbo decoder can be different.

The succeeding structure of a hybrid turbo decoder, considering two SISO decoders can be shown as in Fig. 3. In the conventional schemes, The SISO decoders are either the Log-MAP only (LM-LM) or the SOVA only (SV-SV). In the hybrid case, we propose to use the Log-Map decoder in one SISO decoder and the SOVA in the other or vice versa (LM-SV or SV-LM). Table 1 shows the computation complexity comparison of the decoding schemes for a single iteration. In Table 1, eachquantity need to be multiplied by n which is the length of the information sequence and $A = 2^v$, where v is the count of registers of one component encoder. According to this analysis, when the $v = 2$, the number of operations of the Log-MAP turbo decoder is the highest out of all these decoding schemes. The number of its operations is about twice that of the SOVA turbo decoder. The number of operations of the hybrid turbo decoder is the compromise of that of the Log-MAP turbo decoder and that of the SOVA turbo decoder. Thus, it has less computational complexity than that of the Log-Map turbo decoder.

As regards to the hybrid turbo decoders, the soft output of each component decoder can be represented as

$$L(\hat{u}_k) = L_c \cdot y_k + L_a(u_k) + L_e(\hat{u}_k).$$

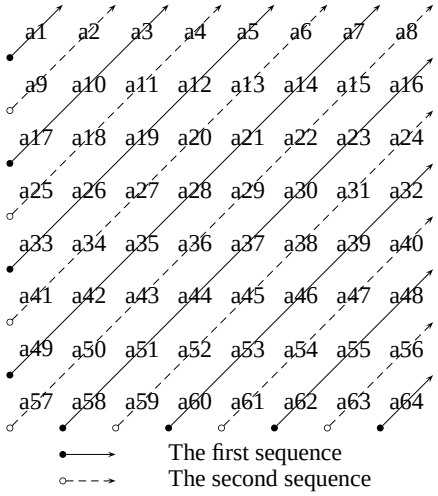

Fig. 4. The structure of a 8×8 sample for the interleaver.

In the process of iterative decoding, the EI can be solved by $L_e(\hat{u}_k) = L(\hat{u}_k) - L_c \cdot y_k - L_a(u_k)$. Then $L_e(\hat{u}_k)$ is exchanged between the two component decoders so that they can take advantage of the EI of each component decoder. Provided that $L_e(\hat{u}_k)$ is generated by the SOVA decoder, $L_e(\hat{u}_k)$ with interleaved can turn into the PI $L_a(u_n)$ of the Log-MAP decoder. $L_e(\hat{u}_n)$ of the Log-MAP decoder becomes the feedback for the SOVA decoder after deinterleaving and applied to the next iteration. This iterative mechanism improves the decoding performance.

4. EXPERIMENTAL RESULTS

We evaluate the performance of turbo decoders described above considering AWGN channels. For this, we choose the interleaver of a regular spiral structure, which can be easily realized. In the interleaving process, the bits data are written into an $m \times n$ matrix row wise and then read from the upper left corner to the lower right corner. Conversely, the process of the deinterleaving is that the bit data are written into an $m \times n$ matrix from the upper left corner to the lower right corner and then read row wise. Fig. 4 shows the organisation structure of 8×8 samples for the interleaver. In this way, the input neighboring information bits can be far away from each other after interleaving, so that it can certainly improve the performance of the turbo code. In general, while the interleaver is large enough, an input sequence interleaved can be considered as a random code.

The experiments are conducted in a system with the 2.66G CPU of Pentium 4, 512M memory of DDR and the C++ programming language. We also choose the (7, 5) RSC code as the component code of the turbo encoder. The decoding depth of the SOVA decoder is 18. The number of iterations is 10. For the interesting range of SNRs ($E_b/N_0 = 0.0\text{dB}, \cdots, 1.5\text{dB}$), Fig. 5 and Fig. 6 show the comparison

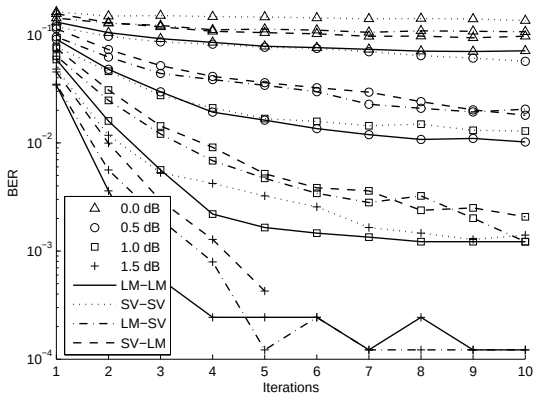

Fig. 5. The comparison of the decoding performance for the decoding schemes mentioned with the coding rate $R = 1/3$.

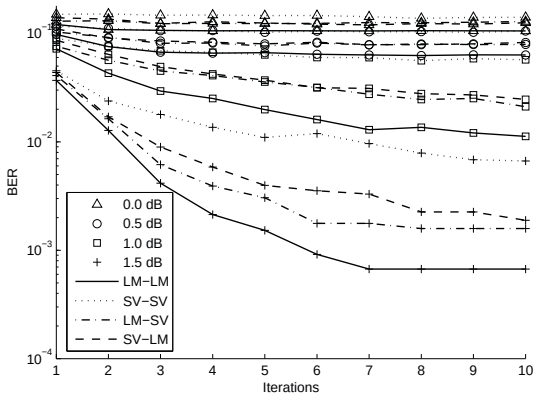

Fig. 6. The comparison of the decoding performance for the decoding schemes mentioned with the coding rate $R = 1/2$.

of the decoding performance for the decoding schemes mentioned with 16384 information bits with the coding rate $R = 1/3$ and $1/2$ respectively.

At $R = 1/3$, for the decoding performance, the SOVA turbo decoder is the worst while the Log-MAP turbo decoder is the best. The two hybrid turbo decoders perform nearly the same in decoding. At previous times, their BERs are about the mean of those of the Log-MAP turbo decoder and the SOVA turbo decoder. However, their BERs can be even close to that of the Log-MAP turbo decoder with a small number of iterations. At 0.5dB, they need about eight times iterations to approach the BER of the Log-MAP turbo decoder. At 1.5dB, they need about five times iterations to approach the BER of the Log-MAP turbo decoder. The higher the SNR (E_b/N_0) is, the fewer iterations they need to approach the BER of the Log-MAP turbo decoder. Similar performance are seen for $R = 1/2$. Table 2 shows the comparison of the cost for the decoding schemes with 16384 information bits.

Table 2. The comparison of the cost for the decoding schemes with 16384 information bits, $R = 1/3$

SNR	LM-LM	SV-SV	SV-LM	LM-SV
0.0 dB	5.094s	0.813s	2.938s	3.031s
0.5 dB	5.109s	0.813s	2.969s	2.938s
1.0 dB	5.079s	0.797s	2.953s	2.921s
1.5 dB	5.094s	0.813s	2.969s	2.968s

5. CONCLUSION

In this paper, we have proposed the hybrid turbo decoding schemes using the Log-MAP algorithm and the SOVA. Theoretical analysis on the number of their operations proves that the hybrid turbo decoders consist of fewer number of operations than those of the Log-MAP turbo decoder. Based on the experiments, we can draw the conclusion that their decoding performances are superior to those of the SOVA turbo decoder, and even close to the Log-MAP turbo decoder using a small number of iterations. Furthermore, their costs are lower than the Log-MAP turbo decoder. The proposed schemes would contribute to an effective strategy to wireless communication.

6. REFERENCES

[1] C. Berrou, A. Glavieux, and P. Thitimajshima, "Near shannon limit error-correcting coding and decoding: Turbo-codes. 1," *IEEE ICC 93*, pp. 1064–1070, vol. 2, 1993.

[2] J. Hagenauer, E. Offer, and L. Papke, "Iterative decoding of binary block and convolutional codes," *IEEE Transactions on Information Theory*, vol. 42, no. 2, pp. 429–445, Mar 1996.

[3] X. Qi, M. Zhao, S. Zhou, and J. Wang, "An iterative decoding scheme with turbo code and iteratively demapped multidimensional QPSK serially concatenated," *IEEE GLOBECOM '05*, vol. 3, Nov 2005, [CD-ROM].

[4] F. Daneshgaran and M. Laddomada, "An improved interleaver design technique for parallel concatenated convolutional codes," *IEEE ICC 03*, pp. 3100–3104 vol. 5, 2003.

[5] L.C. Perez, J. Seghers, and Jr. Costello, D.J., "A distance spectrum interpretation of turbo codes," *IEEE Transactions on Information Theory*, vol. 42, no. 6, pp. 1698–1709, Nov 1996.

[6] L. Bahl, J. Cocke, F. Jelinek, and J. Raviv, "Optimal decoding of linear codes for minimizing symbol error rate (corresp.)," *IEEE Transactions on Information Theory*, vol. 20, no. 2, pp. 284–287, Mar 1974.

[7] J. Hagenauer and P. Hoeher, "A viterbi algorithm with soft-decision outputs and its applications," *IEEE GLOBECOM '89*, pp. 1680–1686 vol.3, Nov 1989.

[8] P. Robertson, E. Villebrun, and P. Hoeher, "A comparison of optimal and sub-optimal MAP decoding algorithms operating in the log domain," *IEEE ICC 95*, pp. 1009–1013, vol. 2, 1995.

JavaScript code Fragment Analyzing for Cache Proxy

Yachao Zhou[1], Xiaofei Wang[1], Yi Tang[2], Jieyan Yang[3] and Xiaojun Wang[1]
[1] School of Electronic Engineering, Dublin City University, Ireland
[2] Department of Computer Science and Technology, Tsinghua University, Beijing, PRC
[3]China Unicom System Integration Limited Corporation, PRC
Email: yachao@eeng.dcu.ie

***Abstract*—The JavaScript language is used to enhance the client side display of web pages. Programs in JavaScript are deployed in HTML documents and they are interpreted by web browsers on the client machine, helping to make web pages richer, more dynamic. JavaScript is widely used in most popular websites, such as CNN, a famous news website in the world. We calculate the percentages of two popular JavaScript fragments and propose a proxy based scheme to reuse the same JavaScript fragments efficiently. The proxy could extract the same JavaScript code fragments as the JavaScript library and detect whether there are malicious codes in it.**

***Key Words*—JavaScript, cache proxy, web security.**

I. INTRODUCTION

Web browser`s role is becoming more and more important day by day. Web application can be broadly categorized into static web application and dynamic web application. Static web applications are those that display the information to the user and dynamic web applications accept input from the user and perform actions based on the input. It is not anymore just a tool for accessing static HTML-pages but today`s platform for Rich Internet Applications (RIA). Web2.0 makes browsing experience more and more like using a traditional desktop application. Since business needs are growing, the hypertext mark-up language continues to grow to meet the needs of business with the new, powerful, and exciting tags.

Most web applications employ a more distributed model, in which the client side is used not simply to submit user data and actions but also to perform actual processing data. This is done for two primary reasons:

(1) It can improve the application`s performance, because certain tasks can be carried out entirely on the client component, instead of making a round trip of request and response to the server.

(2) It can enhance usability, because parts of the user interface can be dynamically updated in response to user actions, without the need to load an entirely new HTML page delivered by the server.

Larbin is a web crawler, which is also called (web) robot, spider, or scooter etc. It is intended to fetch a large number of web pages to fill the database of a search engine. With a network fast enough, Larbin should be able to fetch more than 100 millions of pages on a standard PC.

In this paper, we use the web crawler Larbin to fetch some popular web sites and analyze the detailed information of some JavaScript fragments which we care about. Our contributions are listed as follows:

- Analyze some kinds of JavaScript codes fragment distribution in some popular website.
- Propose a proxy to extract the JavaScript codes fragment and rewrite the HTML pages.
- Enhance the efficiency of JavaScript code libraries via cache proxy engine.

This paper is organized as follows. The related works is presented in section II, the methodology is provided in section III. Section IV is the conclusion.

II. RELATED WORKS

Emre [2] presents AjaxScope, a dynamic instrumentation platform that enables cross-user monitoring and just-in-time control of web application behavior on end-user desktops. AjaxScope enables a large number of exciting instrumentation policies, such as: performance, runtime analysis and debugging, usability evaluation. It needs not to change anything of the web browsers. The AjaxScope proxy only dynamically rewrites the uninstrumented JavaScript code according to the instrumentation policies.

NeatHtml [3] and Caja [4] take an alternate approach by performing parsing of untrusted HTML using a client-side trusted JavaScript library. After parsing, untrusted content is filtered in a series of steps to ensure that it is free of script content. They both embed untrusted HTML in the web page using trusted client side JavaScript code via the innerHTML DOM property (for Caja this is a deliberate optimization choice), which protects against node-splitting attacks.

Proxies have been used to introduce new services between Web clients and servers. For example, they have been used to provide Web caching [5,6], and gateway services for onion-routing anonymizers [7]. In this paper, we propose to use proxy as a combination of blacklisting, whitelisting javascript filter and heuristics to identify potentially malicious Web content.

Several pieces of previous work [8,9], have used rewriting at the Java Virtual Machine bytecode interface [10]. This interface is type-safe, and provides good support for reasoning about application-internal abstractions.

In this paper, we use the web crawler to fetch some popular web sites and analyze the detailed information of some JavaScript fragments. With the knowledge of JavaScript codes

This work is supported by Enterprise-Ireland.

fragment distribution of some popular websites, we further propose to use whitelist and blacklist to help the filter the potential malicious html pages.

III. METHODOLOGY

Traditionally a web page was loaded once and when the content of page was to be updated, the whole page had to be loaded again. Asynchronous JavaScript + XML (Ajax) is a technology that allows content being updated asynchronously without loading the whole page. XmlHTTPRequest is an API that enables connections to remote sources via HTTP from client side. It is a key part of Ajax. Usually the transfer format used is XML, JavaScript Object Notation (JSON), HTML or plain text. In Ajax-applications JavaScript is used on client side to make connections and gather data by XMLHTTPRequest and then to modify the page by accessing the Document Object Model and CSS style sheets of the page. By using Ajax the data can be exchanged in small amounts with server and the user is provided an experience more and more like a desktop application without loading the whole page again. These kinds of RIAs seem to be an essential part of growing amount of Web2.0 applications.

JavaScript is a relatively simple but powerful programming language that can be easily used to extend web interfaces in ways that are not possible using HTML alone. It is commonly used to perform the following tasks:

- Validating user-entered data before it is submitted to the server, to avoid unnecessary requests if the data contains errors.
- Dynamically modifying the user interface in response to user actions; for example, to implement drop-down menus and other controls similar as non-web interface.
- Querying and updating the document object model within the browser to control the browser`s behavior.

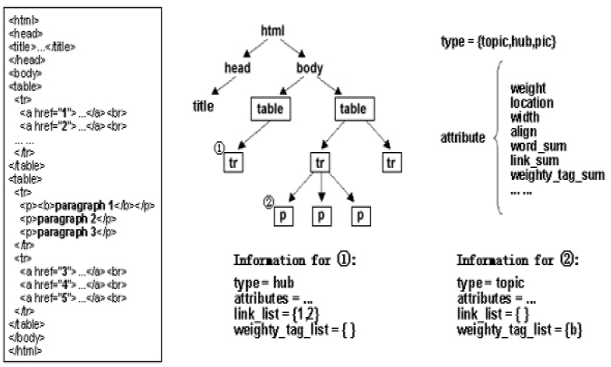

Figure 1 HTML tree generation

Figure 1 shows how html parser generates a HTML tree. When user sends a request to server with specific activities such as opening a url and clicking some hyperlinks, the browser will download the corresponding codes of web page. Then html parser of browser will analyze the html codes and generate DOM tree. Render tree will be built in the next step according to the above DOM tree.

Figure 2 shows how JavaScript can be interpreted in practice. When a HTML DOM tree is generated, the JavaScript code fragment will be sent to a JavaScript Parser to interpret the JavaScript codes and build a JS parse tree if there is an occurrence of JavaScript code in the HTML DOM tree. After the execution in client side or communication with remote server side via Ajax in JavaScript Runtime Environment, a render tree is generated as the basic of web view. If the JavaScript is too complicated, the browser could not display the whole page before all the JavaScript has been executed. Obviously if two web pages contain a slice of same JavaScript fragment, we could reuse them after download the JavaScript fragment first time so as to save time.

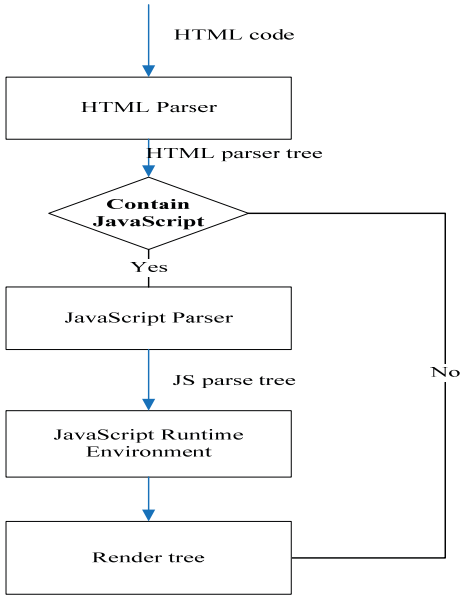

Figure 2 Generalized functional diagram of existing browsers' HTML interpretation process.

The web crawler Larbin is used to fetch web pages from Cable News Network (CNN.com) which is one of the most famous news websites. We fetched huge number of web pages without considering files extension of .pdf, .tar, .mp3, etc. After fetching web pages of CNN from March 1st to March 6th, we got approximate 102,859 files of 52 folders. Then we calculated the percentage of two popular kinds of JavaScript code fragments, "*<script.*?</script>*" and "*javascript:*".

Table 1 Statistic of tow popular JavaScript code fragments

Code types	Line No.	Fragments No	Multiple No
All the codes	93,116,339		
<script.?</script>*	22,478,162	3,320,519	3,164,104 （95.2%）
javascript:	640,761	526,363	496,716 (94.3%)

As shown in the Table 1, there are 95.2% multiple JavaScript fragments like *<script.*?</script>*. Such as:

```
<script type="text/javascript"
    src="http://i.cdn.turner.com/cnn/.element/js/2.0/ad_head0.js">
</script>
```

The external JavaScript itself, which is simply a text file with the containing JavaScript code, saved as a *.js* file.

```
<script type="text/javascript">
  if(cnnShow_setPref && (location.hostname.indexOf('.cnn.com') > -1))
      { cnnSetEditionBox(); }
</script>
```

A <script> tag refers to the external JavaScript file and is defined on the pages that use the library.

Similarly fragment "*javascript:*" also has high percentage of multiple codes. So we can draw the following conclusions according to the statistics:

1. Unique script code segment is far less than the script code segments. So website could reuse script code in the proxy client so as to download the same JavaScript fragment in different web pages.

2. JavaScript codes do not change frequently even if the web pages are dynamically changed, such as the index page of CNN and some portal pages.

3. JavaScript code of big size has less modification probability. Actually the editor seldom updates the JavaScript codes after they submit them into the server.

Most programming languages provide libraries, such as C or Java support "code libraries", where a programmer can save a commonly used piece of code as a library file and refer to it from the main program. For example, Software developers generally use *.jar* files to distribute Java classes and associated metadata. JavaScript supports external libraries too, in the form of the *.js* file.

While obviously the main reason for using JavaScript libraries is that it allows you to easily distribute one code for users on many pages, a secondary reason is not. A JavaScript library, when used on multiple pages, is actually more efficient than directly embedding the code inside the library on each page. Once the browser in client side encounters the library the first time around, it saves the containing code in cache. Subsequent requests for the library on other pages will result in the library being loaded from cache, or the speed demon.

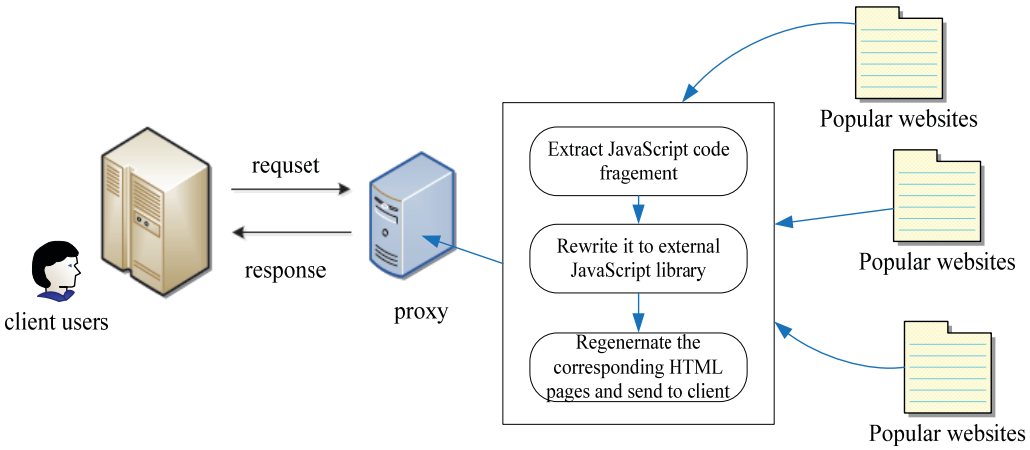

Figure 3 Cache server-side proxy for popular websites

As shown in Figure 3, we use a proxy server to extract the JavaScript code fragment, rewrite to a library out of it, so multiple pages can share a same JavaScript code library without physically including the original code on those pages.

By including the above reference, the client side browser will now download the code stored inside external *.js* file, and run it as if the code was physically typed onto the original web page.

At the same time, in our proxy engine, we detect the JavaScript library to see whether there are malicious codes in it. Since the JavaScript library does not often change, we can easily create a Black-list for the malicious libraries. If virus codes have been found, the proxy engine will stop parse the JavaScript codes and alert to the client users.

IV. Conclusion

In this paper, we analyze the percentage of two popular kinds of JavaScript code fragments of popular website. We found that there are approximate 95.2% multiple JavaScript code fragment according to the statistics. A cache proxy is proposed to extract the same JavaScript fragments to external *.js* JavaScript code libraries to save the expensive runtime waste.

V. Future Work

As an on-going research, we plan to make the proxy work as a special sand-box which execute the JavaScript instead of client side and send back the result codes to client browser. The proxy must be authenticated by client user to get the sensitive information, such as cookies.

References

[1] http://larbin.sourceforge.net/index-eng.html

[2] Emre Kıcıman, "AjaxScope: A Platform for Remotely Monitoring the Client-Side Behavior of Web 2.0 Applications", Oct. 2007, SOSP`07

[3] D. Brettle, "NeatHtml: Displaying untrusted content securely, efficiently, and accessibly," Jun. 2008, white

paper. [Online]. Available: http://www.brettle.com/NeatHtml/docs/Fighting_XSS_with_JavaScript_Judo.html

[4] Google Caja, “A source-to-source translator for securing JavaScript-based web content.” [Online]. Available: http://code.google.com/p/google-caja/

[5] Alec Wolman, Geoff Voelker, Nitin Sharma, Neal Cardwell, Anna Karlin, and Henry Levy. On the scale and performance of cooperative Web proxy caching. In Proceedings of the 17th ACM Symposium on Operating Systems Principles (SOSP ’99), Kiawah Island, SC, December 1999

[6] Brian Duska, David Marwood, and Michael J. Feeley. The measured access characteristics of World Wide Web client proxy caches. In Proceedings of the 1st USENIX Symposium on Internet Technologies and Systems (USITS 97), Monterey, CA, December 1997.

[7] Roger Dingledine, Nick Mathewson, and Paul Syverson. Tor: The second-generation onion router. In Proceedings of the 13th USENIX Security Symposium, San Diego, CA, August 2004.

[8] U. Erlingsson and F. B. Schneider. IRM Enforcement of Java Stack Inspection. In IEEE Symposium on Security and Privacy, 2000.

[9] U. Erlingsson and F. B. Schneider. SASI Enforcement of Security Policies: A Retrospective. In WNSP: New Security Paradigms Workshop, 2000.

[10] T. Lindholm and F. Yellin. The Java Virtual Machine Specification, 2nd edition, 1999.

Section 3A

CHANNELS AND PROPAGATION

Research on the Gain flatness of Fiber-Optic Parametric Amplifier with Periodic Dispersion Compensation

Jing Jin, Qiliang Li
Institute of Communication and Information System, College of Communications, Hangzhou Dianzi University, Hangzhou 310018, China
kimjung2@yahoo.cn

Abstract

We study the gain flatness in a two-pump fiber optical parametric amplifier with periodic dispersion compensation. The results show that the gain fluctuation of the two-pump fiber-optic parametric amplifier have been improved obviously by inserting dispersion compensating fibers at regular intervals in a high-nonlinear fiber. It is found that the gain have a relationship with the length of the high-nonlinear fiber. With the increase of the length of the high-nonlinear fiber, the parametric gain is raised, but the gain flatness is decreased. The parametric gain can be flattened, by inserting more dispersion compensation fiber segments.
Keywords: fiber optical parametric amplifier; high nonlinear fiber; dispersion compensation fiber; gain flatness

1. Introduction

Fiber-optic parametric amplifiers (FOPAs), relying on four-wave mixing (FWM), have attracted considerable attention in recent years. FOPAs offer some unique properties when compared to other traditional amplifiers, such as Erbium-doped fiber amplifier [1], [2], FOPAs amplify at any arbitrary wavelengths in theory and offers high gain, large bandwidth as well as low noise figure [3].

FOPAs can be classified into two categories of one- and two-pump. Owing to the phase-matching condition of the underlying FWM process, single pump FOPAs generally exhibit a lager gain fluctuation in the zero-dispersion wavelength (ZDWL) region of the optical fiber [4]. Based on this limitation, the concept of two-wavelength pumping has been demonstrated theoretically in Ref. [5], and has been shown that the two-pump FOPAs can provide a gain spectrum that is relatively uniform over a bandwidth larger than 100nm.

The phase-matching plays an important role in the FWM process; it is the key to achieve efficiently FWM. Laurent et al. proposed a scheme, based on a multisection dispersion-tailored in-line nonlinear fiber arrangement, allows for the achievement of over 100 nm flat gain bands with a ripple of less than 0.2 dB in the ZDWL region [6]. Marhic et al. suggested a method, in which meltisection dispersion compensating fibers (DCFs) are inserted in highly nonlinear fiber, achieve flat gain over ultrabroad bands with a single pump fiber-optic parametric amplifier operating in the ZDWL region [7].

Pumping in the vicinity of ZDWL or using high-nonlinear fibers (HNLF) has been proposed to enhance the gain [7], [8]. Unfortunately, the unavoidable fluctuation of ZDWL brings to detriment the near-ZDWL pumping scheme [9]. This gain fluctuation can be avoided by increasing the separation between the pump wavelengths and the ZDWL (>10nm) [9], which leads the dispersion to be larger. Therefore the dispersion must be compensated to realize the quasi-phase matching, and obtain flat gains over a wide spectral rang. Marhic et al. have shown that the one-pump FOPA can provide a higher gain and larger bandwidth by inserting meltisection DCFs in Ref. [7]. In this paper we focus on the quasi-phase matching of two-pump FOPAs that flatten efficiently the gain spectrum in the two-pump FOPA.

2. Theoretical model

We consider a length of HNLF L, consisting of $(m+1)$ segments of equal length $l = L/(m+1)$, connected by m pieces of DCF, each of length l', Fig. 1.

The DCF is assumed to have negligible nonlinearity. We also neglect attenuation in both HNLF and DCF; this is a very good approximation for short fiber lengths, as are used for high-power pulsed pumps. The propagation constants in the HNLF and DCF are respectively $\beta(\omega)$ and $\beta'(\omega)$.We consider two pumps, a signal, and an idler, with respective angular frequencies ω_1, ω_2, ω_3, and ω_4, and electric field E_1, E_2, E_3, and E_4; all fields are in the same state of linear polarization. The total electric field $\vec{E}$ can be written as

$$\vec{E} = \frac{1}{2}\hat{x}\sum_{j=1}^{4} E_j \exp(i\omega_j t - k_j z) + c.c, \qquad (1)$$

where $k_j = n_j\omega_j/c$ is propagation constant，where n_j is the index of refraction.

Figure 1. Schematic of high-nonlinear fiber with periodic dispersion compensation.

Using the Maxwell equation, the differential equations governing of pumps, the signal, and idler in the (m+1)th HNLF segment are

$$\frac{dE_{1,m+1}}{dz} = i\gamma\alpha^m\left(P_1 + 2P_2\right)E_{1,m+1} \qquad (2a)$$

$$\frac{dE_{2,m+1}}{dz} = i\gamma\alpha^m\left(2P_1 + P_2\right)E_{2,m+1} \qquad (2b)$$

$$\frac{dE_{3,m+1}}{dz} = 2i\gamma\alpha^m\left(P_1 + P_2\right)E_{3,m+1} + i\gamma E_{1,m+1}E_{2,m+1}E^*_{4,m+1}\exp\left(-i\Delta\beta z\right) \qquad (2c)$$

$$\frac{dE_{4,m+1}}{dz} = 2i\gamma\alpha^m\left(P_1 + P_2\right)E_{4,m+1} + i\gamma E_{1,m+1}E_{2,m+1}E^*_{3,m+1}\exp\left(-i\Delta\beta z\right), \qquad (2d)$$

where: E_j is the envelope of the electric field; z is the distance from the beginning of the first HNLF segment; β_2 is the second-order dispersion coefficient and γ is the nonlinear parameter; $P_j=|E_{j,1}(0)|^2$ is the pump power at z=0; $\alpha=10^{-0.2Ls}$ is the transmittance through two splices; L_S is the power loss, in dB, of a single splice. We can expand the linear phase mismatch $\Delta\beta=\beta(\omega_3)+\beta(\omega_4)-\beta(\omega_1)-\beta(\omega_2)$ in a Taylor series [10]

$$\begin{aligned}\Delta\beta &= 2\sum_{m=1}^{\infty}\frac{1}{(2m)!}\left(\frac{d^{2m}\beta}{d\omega^{2m}}\right)_{\omega=\omega_c}\left[\left(\omega_3-\omega_c\right)^{2m}-\omega_d^{2m}\right]\\ &\approx \beta_2(\omega_c)\left[\left(\omega_3-\omega_c\right)^2-\omega_d^2\right]+\frac{\beta_4(\omega_c)}{12}\left[\left(\omega_3-\omega_c\right)^4-\omega_d^4\right]\\ &= \beta_2(\omega_c)\left(2\pi c/\lambda_0^2\right)^2\left[\left(\lambda_3-\lambda_c\right)^2-\lambda_d^2\right]\\ &\quad+\beta_4(\omega_c)\left(2\pi c/\lambda_0^2\right)^4\left[\left(\lambda_3-\lambda_c\right)^4-\lambda_d^4\right]/12,\end{aligned} \qquad (3)$$

here: $\omega_c=(\omega_1+\omega_2)/2$ is the mean frequency of the two pumps and $\omega_d=(\omega_1-\omega_2)/2$ is half their difference; ω_1 and ω_2 are the two pump frequencies, ω_3 is the signal frequency; $\beta_2(\omega_c)$ and $\beta_4(\omega_c)$ are respectively the second-, fourth-order dispersion coefficient at ω_c, where $\beta_2(\omega_c)=\beta_2(\omega_0)(\omega_c-\omega_0)+\beta_4(\omega_0)(\omega_c-\omega_0)^2/2$, $\beta_4(\omega_c)\approx\beta_4(\omega_0)$, ω_0 is the zero-dispersion frequency; λ_0 is the zero-dispersion wavelength; λ_3 is signal wavelength; $\lambda_c=(\lambda_1+\lambda_2)/2$, $\lambda_d=(\lambda_1-\lambda_2)/2$, where λ_1 and λ_2 are the pump wavelengths.

3. Gain of fiber-optic parametric amplifiers

We assume that the pumps are not depleted by the nonlinear process, thus the solutions of (2a) and (2b) are

$$\begin{cases}E_{1,m+1} = E'_{1,m}\exp\left[i\gamma\alpha^m\left(P_1+2P_2\right)z\right],\\ E_{2,m+1} = E'_{2,m}\exp\left[i\gamma\alpha^m\left(2P_1+P_2\right)z\right],\end{cases} \qquad (4)$$

where, $E'_{1,\mathrm{m}}$ and $E'_{2,\mathrm{m}}$ are the pump field phasors at the output of the mth DCF segment. (4) have included the contribution of self-phase modulation (SPM) and cross-phase modulation (XPM) induced by the two pumps.

The optical field amplitudes for the signal and idler waves, E_j, are related to H_j by a phase factor through $E_j = H_j\exp\left[2i\gamma\alpha^m\left(P_1+P_2\right)z\right]$. (2c) and (2d) can be written as

$$\frac{dH_{j,m+1}}{dz} = i\gamma\alpha^m\sqrt{P_1P_2}\exp\left(-i\kappa_m z\right)\exp\left(i\Phi_m\right)H^*_{7-j,m+1}, \quad j=3,4\ \ m=1,2\ldots \qquad (5)$$

where, $\Phi_m = 3\gamma\left(P_1+P_2\right)\sum_{p=0}^{m-1}\alpha^p l = 3\gamma\left(P_1+P_2\right)\frac{1-\alpha^m}{1-\alpha}l$, $\kappa_m = \Delta\beta+\gamma\alpha^m(P_1+P_2)$ describes the total phase mismatch. Using the boundary conditions, we can obtain the solution of (5), which can be written in the form of matrix

$$\begin{pmatrix}H_{3,m+1}(l)\\ H^*_{4,m+1}(l)\end{pmatrix} = \alpha^{1/2}M_m\begin{pmatrix}H_{3,m}(l)\\ H^*_{4,m}(l)\end{pmatrix}, \qquad (6)$$

where, M_m is the transfer matrix of the (m+1)th HNLF segment,

$$M_m = \begin{pmatrix}m_{33} & m_{34}\\ m_{43} & m_{44}\end{pmatrix}, \qquad (7)$$

where,

$$m_{33} = e^{-\frac{i\kappa_m l}{2}}e^{i\psi_m}\left(\cosh\left(g_m l\right)+\frac{i\kappa_m}{2g_m}\sinh\left(g_m l\right)\right),$$

$$m_{34} = e^{-\frac{i\kappa_m l}{2}}e^{-i\psi_m}\frac{i\gamma\alpha^m\sqrt{P_1P_2}e^{i\Phi_m}}{g_m}\sinh\left(g_m l\right),$$

$$m_{43} = e^{\frac{i\kappa_m l}{2}} e^{i\psi_m} \frac{-i\gamma\alpha^m \sqrt{P_1 P_2} e^{-i\Phi_m}}{g_m} \sinh(g_m l),$$

$$m_{44} = e^{\frac{i\kappa_m l}{2}} e^{-i\psi_m} \left(\cosh(g_m l) - \frac{i\kappa_m}{2g_m} \sinh(g_m l) \right),$$

where, $\psi_m = 2\gamma\alpha^{m-1}(P_1 + P_2)l + \Delta\beta' l'/2$, m=1,2…; g_m is the parametric gain coefficient of the (m+1)th HNLF segment are given by $g_m = \sqrt{\gamma^2 \alpha^m P_1 P_2 - (\kappa_m / 2)^2}$.

The transfer matrix M for the whole arrangement is $M=M_0 M_1 \ldots M_m$. (6) can be written as

$$\begin{pmatrix} H_{3,m+1}(l) \\ H^*_{4,m+1}(l) \end{pmatrix} = \alpha^{m/2} M_0 M_1 \cdots M_m \begin{pmatrix} H_3(0) \\ H^*_4(0) \end{pmatrix} = \alpha^{m/2} M \begin{pmatrix} H_3(0) \\ H^*_4(0) \end{pmatrix}. \quad (8)$$

The total signal gain at the output of the (m+1)th HNLF segment is found to be

$$G_{m+1} = 20\lg\left[\left| H_{3,m+1}(l) \right| / H_3(0) \right]. \quad (9)$$

4. Analysis of gain flatness

The above expression shows that the parametric gain have a relationship with the section numbers of dispersion compensation fibers and the high-nonlinear fiber's length. We will analyze the gain flatness by modifying the inserting number of DCF segments and the HNLF's length.

Fig. 2 shows that the gain value and flatness are influenced by the inserting number of DCF segments. The HNLF have a zero-dispersion wavelength λ_0=1591 nm, which is less than ideal for making FOPA's operating near-1550nm, desirable for optical communication systems. The parameters used correspond to our simulations, namely: pump powers are respectively 0.2W and 0.4W; pump wavelengths are 1542nm and 1560nm; L=300m; γ=20W^{-1}km^{-1}; $\beta_2(\omega_0)$=-0.01ps^2/km, $\beta_4(\omega_0)$=-2.85ps^4/km; $\beta'_2(\omega_0)$=2ps^2/km, $\beta'_4(\omega_0)$=3×10^{-4}ps^4/km.

From Fig. 2, we can see that, with the increase of the DCF segment numbers, the gain fluctuation have been improved obviously. When m=0，there is no inserting DCF segment in a HNLF, the fluctuation is large, about 3.8dB. However, when m=4, inserting four DCF segments periodically in a HNLF, the gain became flatter and wider. But the value of gain is reduced because of inevitable splicing losses.

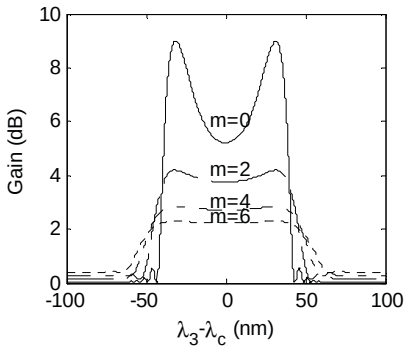

Figure 2. Graph of signal gain with different m versus wavelength. (a) m=4; (b) m=6.

Fig. 3 shows the influence of the length of FOPA on gain value and flatness. In Fig. 3(a): m=4, inserting four DCF segments periodically in a HNLF; Fig. 3(b): m=6, inserting six DCF segments periodically in a HNLF. The parameters are same as the above-mentioned. As shown clearly in Fig. 3, with the increase of the length of HNLF, the value of gain is raised, while the flatness is reduced.

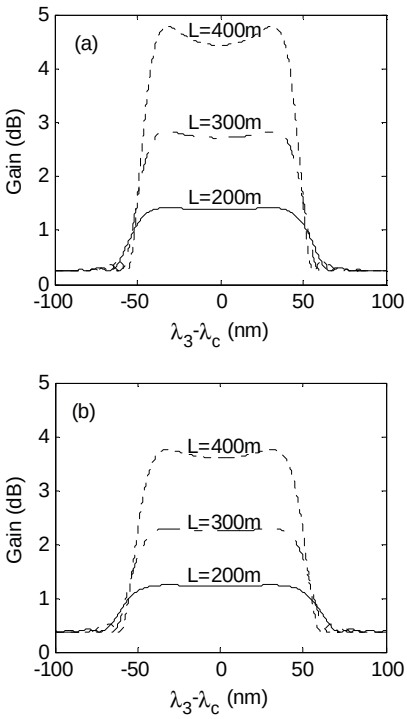

Figure 3. Graph of signal gain with different length of HNLF versus wavelength. (a) m=4; (b) m=6.

From Fig. 3(a), m=4, when L=200m, we can obtain a 1.40dB nearly flat gain bandwidth; when L=400m, the gain value reached to 4.43dB, the bandwidth remained constant, but the fluctuation increased, about 0.35dB, which can be solved by inserting more DCF segments.

When m=6, the fluctuation have been improved obviously, Fig. 3(b).

5. Conclusion

This paper has theoretically investigated a two-pump FOPA realizing quasi-phase matching with periodic dispersion compensation. We have derived the gain expression of FOPA by use of the coupled equations of pumps, signal and idler field, then analyze the gain flatness of two-pump FOPA with periodic dispersion compensation. This study shows that the FOPA's gain depends on the inserting numbers of DCF segments and the HNLF's length.

We have shown that with the increase of the inserting number of DCF segment, the fluctuation of FOPA gain has been improved obviously, which can realize flat gain over a considerable wide spectral rang. However, the value of gain reduces because of inevitable splicing losses, which can be solved by increasing the length of HNLF. The value of gain is increased when the HNLF's length increases, while the flatness is reduced. The parametric gain can be flattened by inserting more DCF segments.

This paper investigate theoretically an approach that realize quasi-phase matching of two-pump FOPAs, which is of practical significance in designing a FOPA that have the function of equalizing amplification over a wide spectral range.

References

[1] J.Hansryd, and P.A. Andrekson, "Broad-band continuous -wave-pumped fiber optical parametric amplifier with 49-dB gain and wavelength conversion efficiency", *IEEE Photon. Technol. Lett.*, vol. 13, no. 3, Mar. 2001, pp. 194–196.

[2] J. Hansryd, P.A. Andrekson, M. Westlund, J. Lie, and P.-O. Hedekvist, "Fiber-based parametric amplifiers and their applications", *IEEE J. Select Topics Quantum Electron.*, vol. 8, no. 3, May/Jun. 2002, pp. 506–520.

[3] J.L. Blows, and S.E. French, ''Low-noise-figure optical parametric amplifier with a continuous-wave frequency modulated pump'', *Opt. Lett.*, vol. 27, 2002, pp. 491–493.

[4] M.E. Marhic, N. Kagi, T.-K. Chiang, and L.G. Kazovsky, ''Broadband fiber optical parametric amplifiers'', *Opt. Lett.*, vol. 21, 1996, pp. 573–575.

[5] Li Qiliang, Li Yuanmin, and Qian Sheng, "Gain of cascaded two-pump fiber-optical parametric amplifier with high order dispersion", *Chinese J. Lasers*, vol. 33, no. 6, 2006, pp. 760-764.

[6] Laurent Provino, Arnaud Mussot, Eric Lantz, Thibaut Sylvestre, and Hervé Maillotte, "Brodband and flat parametric amplifiers with a multisection dispersion-Tailored nonlinear fiber arrangement", *J. Opt. Soc. Am. B.*, vol. 20, no. 7, 2003, pp. 1532-1537.

[7] M.E. Marhic, Frank S. Yang, Min-Chen Ho, and Leonid G. Kazovsky, "High-Nonlinearity Fiber Optical Parametric Amplifier with Periodic Dispersion compensation", *Journal of Lightwave Technology*, vol. 17, no. 2, February 1999, pp. 210-215.

[8] G.A. Nowak, Y.-H. Kao, T.J. Xia, and M.N. Islam, "Low-power high efficiency wavelength conversion based on modulational instability in high nonlinearity fiber", *Opt. Lett.*, vol. 23, Jun. 1998, pp. 936–938.

[9] Jaeyoun Kim, Özdal Boyraz, Jin H. Lim, and Mohammed N. Islam, "Gain enhancement in cascaded fiber parametric amplifier with quasi-phase matching: theory and experiment", *Journal of Lightwave Technology*, vol. 19, no. 2, 2001, pp.247-251.

[10] Ngai Wong, and Kenneth K.Y. Wong, "Gain bandwidth optimization in two-pump fiber optical parametric amplifiers under bounded zero-dispersion wavelength fluctuations", *Optics Communications*, vol. 272, no. 2, 2007, pp. 514-520.

ISIS – Urban Radio plan and time-variant characteristics of mobile vehicular network

Serenus Jeyakumar, David Linton, senior member IEEE
Institute of Electronics, Communications and Information Technology (ECIT)
Queen's University Belfast, BT3 9DT
Fax: +44(0) 28 9097 1702; Tel: +44(0) 28 9097 1808
Email: sjeyakumar01@qub.ac.uk, d.linton@ee.qub.ac.uk

Abstract - Integrated Sensor Information System (ISIS) will detect potential criminal/terrorist threats on the bus public transport network using audio/visual/RF sensors and inform decision makers at a central control point who use this information to decide on the perceived threat level. The ISIS system will also manage its own network so that it is not reliant on commercial mobile phone networks. iBurst technology was proposed to be used for communication between a mobile bus and the Central Control Point. This paper is a study of the radio plan, propagation channel and time variant characteristics of an iBurst system in a vehicular network system.

Keywords: **iBurst, Urban propagation modelling, Vehicular Network, sensor.**

I Introduction

From recent occurrences of crime and terrorist attacks in public transport, it is difficult to guarantee safety of the public on board these transportation units. However, it is possible to record the events and crimes taking place, through CCTV and then analyzing it later to capture the criminal. The problem is that there are no means to prevent the crime from happening and actions are taken against the criminal only after a crime has occurred leaving the victim, if they survive the attack, traumatized for an unknown period of time depending on the crime committed.

Some examples of major crime/terrorist attacks on public transportation in the near past are the 9/11 airplane incidents, 7/7 bombings in London, train Bombings in Madrid, Spain and Mumbai, India. In addition to these, we also have to consider the smaller attacks aimed at the individual person with knives, guns, etc and fraudulent claims on incidents that may not have occurred on buses. In response to this, governments have made a call upon the scientific and engineering research communities to play an important role in the effort to fight crime and terrorism [1].

ISIS aims towards working against these crimes on buses by providing an integrated security system within the platform that communicates with a control centre. ISIS will detect threats and inform decision makers of that threat and manage its own network. The proposed system would have the potential to reduce assaults on public and staff on transport units. Research of a similar nature is being conducted on trains in France under the Celtic-BOSS project [2] but there is almost no research being performed on buses.

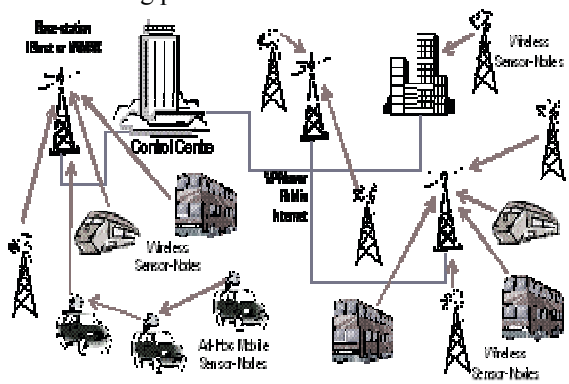

Fig1. Overview of ISIS

This paper associated with ISIS, overviews the wireless and electromagnetic systems. A number of simulations using ray tracing software and electromagnetic simulation tools are used to study the effect of microwaves in a communication channel between a mobile bus and a network operation centre and use this data to build an optimum and robust wireless network. Studies and measurements have been performed on the propagation modelling of populated indoor environments and the effect of human beings on the propagation of microwaves [3].

As the data exchange between the bus and the Network operation centre is crucial, the proposed network should not have significant variation in received power levels during the exchange of data. This variation is due to fading, environmental clutter and other characteristics that affect the propagation of microwaves [4].

II. iBurst technology

iBurst wireless broadband system was initially developed by ArrayComm in 2001 and has been issued under the IEEE 802.20 standard. iBurst is licensed to operate within the frequency range of 1.7 GHz to 2.3 GHz.

Across a 5 MHz spectrum, the maximum data rate reaches up to 1,061 kbps for downlink and 346 kbps for uplink. iBurst can also achieve high data rates, even during the high speed movement of user terminals [5], [6]. The iBurst system uses Asymmetric TDD/TDMA frame designed for 625 kHz channelization and performs Spatial Division Multiple Access (SDMA) by using Adaptive Antenna Array technology and adaptive modulation and coding for efficient use of frequency resources [4]. The Adaptive Antenna Arrays have 12 antenna elements at the Base Station (BS) which enhance signals transmitted to and received from the User Terminal (UT), while suppressing interference signals from other UTs in the same time slot and in the same frequency band, but in different angles of arrival [6], [7]. There have been studies on the outdoor to indoor propagation characteristics of iBurst in an urban and suburban area at stationary UTs. These studies showed an investigation of the temporal signal variation observed by wireless broadband channels in urban and suburban environments [6].

The iBurst base stations in Belfast operating at 1795 MHz to 1800 MHz, are under trial. iBurst technology was proposed to be used with the ISIS project in the vehicular network system for the transfer of data from sensors within the bus to a network operation centre where the data will be monitored.

III Sensors

The data transmitted over the vehicular network system is sourced from sensors such as CCTV cameras, CAN bus sensors and audio sensors to be found in different locations on board the bus. 16 video cameras are located in different positions forming a closed circuit to monitor events and incidents happening on board the bus. The data from the CCTV cameras will be transmitted from the bus through the proposed communications channel to the network operation centre to inform decision makers of the perceived threat level.

Controller Area Network (CAN) bus sensors will be integrated with the system and a combination of data from the CAN bus sensors and the CCTV cameras will provide evidence against fraudulent claims by passengers on buses after an event or incident has occurred. Audio sensors will be used to study and analyze the voice patterns of passengers on board the bus. For this data to be transmitted over a vehicular network system a robust wireless network for live transmission of crucial data is required and hence a radio plan of the city is required to study and analyze the received/transmitted power signals and propagation paths within the network for a moving vehicle. This study is performed using WinProp™, a ray tracing software and is shown below.

IV. Database

A bus route from the Titanic Quarter in Belfast through the City Centre to the South Belfast area was chosen for study. The proposed bus route is approximately 6.5 Km long and comprises of urban (Densely populated) and suburban (Less dense) clutter. Clutter data was obtained by purchasing rooftop outlines from the Ordinance Survey Northern Ireland (OSNI). This data was imported into the ray tracing software (WinProp™) and the approximate height of buildings was entered manually.

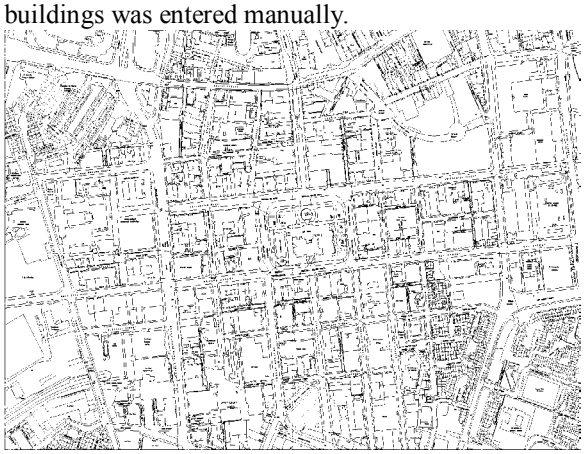

Fig2. OSNI Tiles map of Belfast City Centre

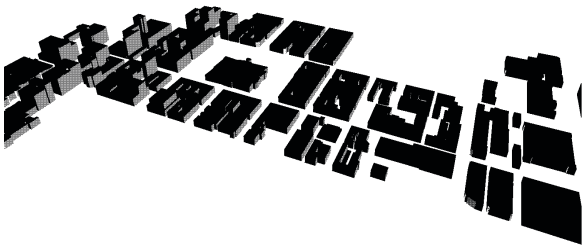

Fig3. 3D view of Belfast City Centre in WinProp

V. Urban Radio plan

WinProp is the Ray tracing software tool used to study the power distribution, propagation paths and time variant properties of signals in an urban or suburban environment. Drawings obtained from WrightBus™ were used to build a model bus into WinProp™. The UT (Bus) is programmed to move along a designated path while the predictions from the BS to the UT are being computed.

Fig 4 shows the propagation paths and received power at the UT from the BS. This is a suburban environment with less clutter and hence there is no critical signal variation with time variance.Fig 5 shows the propagation paths and received power at the UT from the BS in the City Centre (Urban Environment). Due to dense clutter and multipath propagation, there are significant fading effects predicted. Screenshots of the City Centre in Belfast from the simulation and from Google maps are shown for comparison of clutter data.

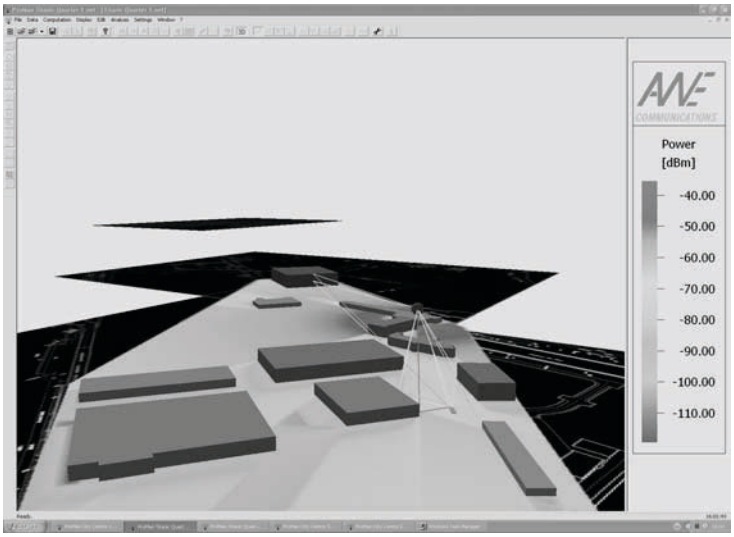

Fig4. Prediction of radio propagation in a less dense urban environment

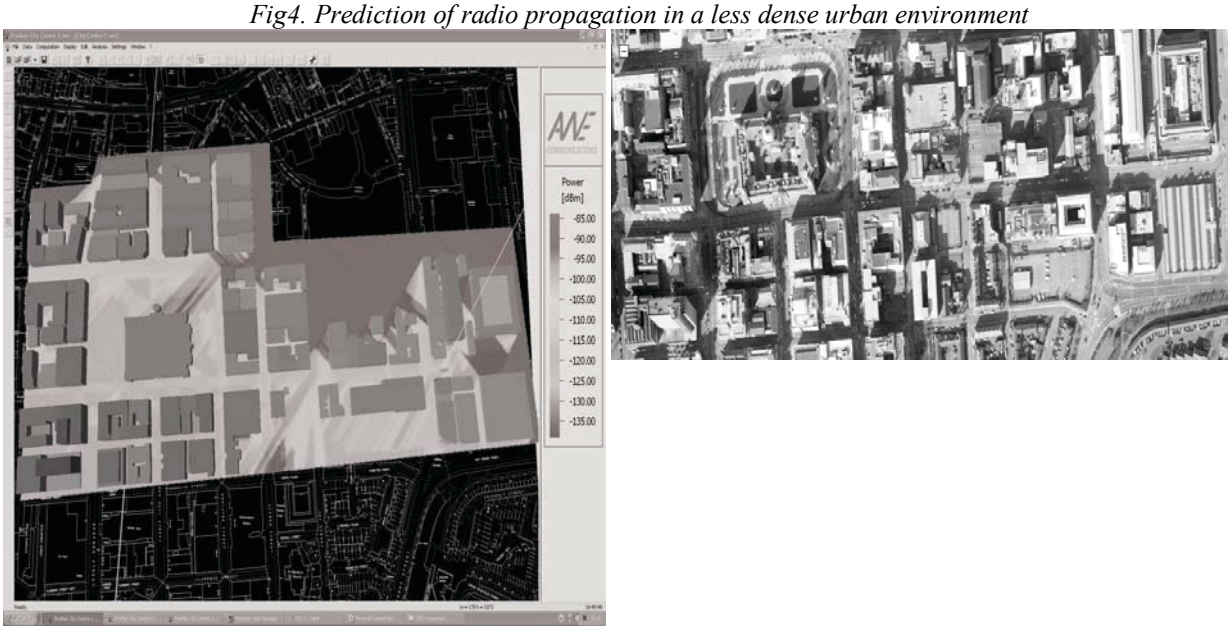

Fig5. Prediction of radio propagation in an urban environment

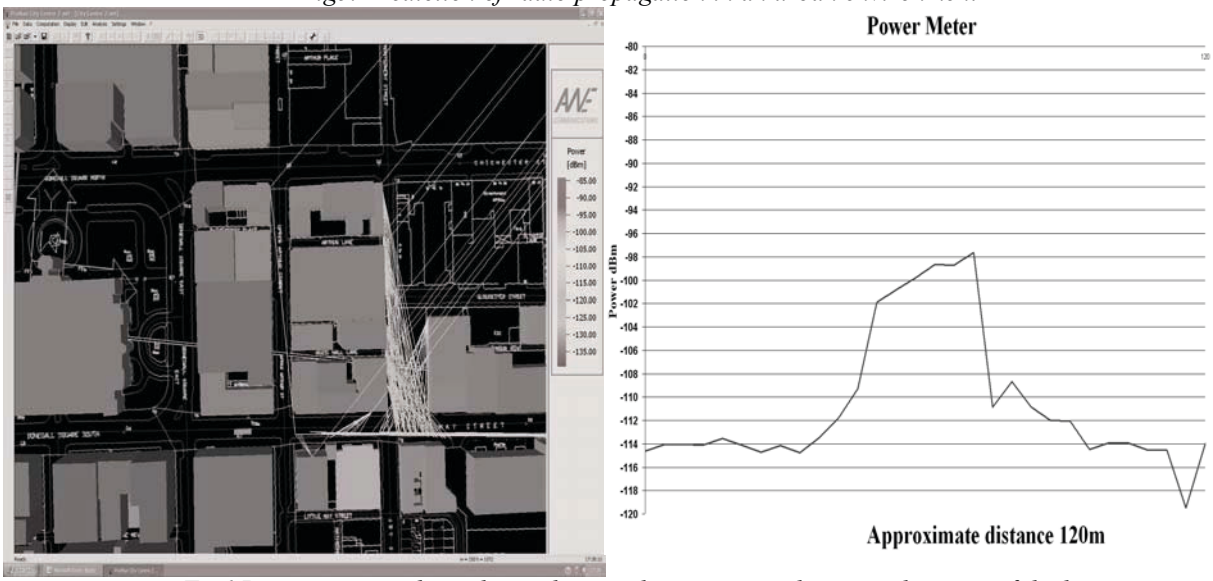

Fig6.Propagation paths and signal strength variation with time and motion of the bus

Fig 6 shows the time variant characteristics of the received signal power and propagation paths from the BS to the mobile UT. In a sample taken approximately 120m long from a random point A to destination B, there is a significant signal strength fluctuation of approximately 23 dBm. Considering the importance of the data being exchanged between the UT and the BS in the ISIS project, such variations in signal strength should be minimised for the transmission of crucial information.

VI Conclusion

A radio plan on two different locations with different clutter data was simulated from a single base station. It was found that there was more scattering, signal loss and signal strength fluctuation in an urban area with dense clutter against a suburban area. This data can be used to create a more robust wireless network. Future works include enhancing the sensor network and a radio plan simulation of the bus route using an iBurst network system with three base stations and carrying out measurements of data transmitted from the sensors on the bus through the iBurst network.

VII Acknowledgements

The authors would like to thank the Engineering and Physical Sciences Research Council (EPSRC) for the funding granted towards the ISIS project and the ISIS Consortium members for their involvement with the ISIS project.

References

[1] Hsinchun Chen, Fei-Yue Wang, Daniel Zeng, ''Intelligence and Security Informatics for Homeland Security: Information, Communication, and Transportation'' IEEE Transactions on Intelligent Transportation Systems, Vol. 5, no. 4, pp. 329 – 341, December 2004.

[2] D. Sanz, V. Delcourt, O. Gatin, M. Berbineau, S. Ambellouis, L. Khoudou, ''BOSS: intelligent embedded video surveillance system with real-time transmission of video to the control centre

[3] K. I. Ziri-Castro, N. E. Evans and W. G. Scanlon, "Propagation Modelling and Measurements in a Populated Indoor Environment at 5.2 GHz" In: Proceedings of the 1st IEEE International Conference on Wireless Broadband and Ultra Wideband Communications, 13-16 March 2006, Sydney, Australia

[4] Shiann-Shiun Jeng, Guanghan Xu, Hsin-Piao Lin, and Wolfhard J. Vogel, "Experimental Studies of Spatial Signature Variation at 900 MHz for Smart Antenna Systems" ,IEEE Transactions on Antennas and Propagation Vol. 46, No. 7, July 1998 pp. 953 – 962

[5]http://global.kyocera.com/prdct/telecom/office/iburst/technicaloverview.pdf

[6] Hajime Suzuki, Carol D. Wilson and Karla Ziri-Castro, "Time variation Characteristics of Wireless Broadband Channel in Urban areas" , 1st European Conference on Antennas and Propagation, 6-10 Nov. 2006, Nice, France.

[7] Martin Cooper, Marc Goldburg, "Intelligent Antennas: Spatial Division Multiple Access" 1996 Annual Review Of Communications, pp. 999 - 1002

Investigation of Dispersive Fading in UWB Over Fiber Systems.

A. Castillo, P. Perry, P. Anandarajah and L.P. Barry

RINCE, Dublin City University, Dublin, Ireland. Antonio.Castillo@eeng.dcu.ie

Abstract

We present an analysis of the response and performance of an optical system for high bit-rate and long-distance RF signal transmission combining the technologies UWB (Ultra-WideBand) and ROF (Radio Over Fibre). We analyse the frequency response of the system and measure the PER obtained at the receiver. This way, we examine the relationship between the main system parameters such as bias current of the laser, frequency response and length of fiber used. We compare the results for two different lasers, obtaining a consistent relationship for a low bandwidth laser, but a more complicated, and inconsistent behaviour in the case that a higher bandwidth laser is used.

I. Introduction

Radio Over Fibre (ROF) is a technology that offers the possibility of transmitting RF signals, in a transparent way, over an optical fibre distribution system. It works for long distances with low latency and attenuation, but with a frequency response that is affected by dispersive fading and nonlinear effects in the laser and fiber.

Ultra Wide Band (UWB) technology, since its regulation by FCC in February 2002, has been developed as a commercially attractive method to implement high speed wireless transmission in different end-user technologies with low power consumption. To achieve this, it uses Multi-Band Orthogonal Frequency Division Multiplexing (MB-OFDM) in 528Mhz sub-bands, with 128 sub-carriers each. It achieves maximum speeds between 320Mbps and 480Mbps, and it is expected that it reaches 1Gbps in the near future with new draft specifications.

In this investigation we use the WiSair 9110 Developers Kit which generates an UWB signal in band group 1, from 3.1 to 4.7Ghz, using three sub-bands. The board directly modulates a laser connected through single mode fibre to a photodetector, which in turn feeds the receiver on the peer WiSair board. This system therefore offers a low cost way to extend the reach of UWB systems, only needing an opto-electrical conversion in the receiver ends to be able to radiate the converted signal through UWB antennas using simple transceivers.

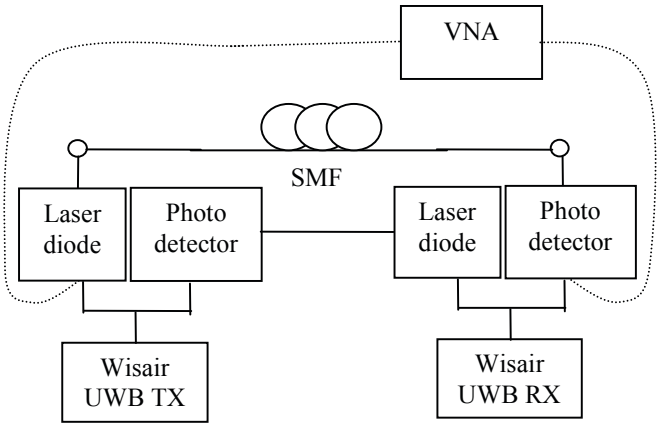

Fig. 1: System setup for dispersive fading test.

In the system, the RF signal is directly modulated onto the optical carrier as a double sideband (where both sidebands are separated by twice the RF carrier frequency), although different methods could be used to improve these results.

Due to fibre dispersion, these sidebands propagate at different speeds, so that the received RF signal experiences fading behaviour [1]. This causes signal strength reduction and inter-symbol interference resulting in errored bits that can often be corrected by Forward Error Correction (FEC). Although, if the level of FEC is not sufficient to overcome the channel degradation, then packet errors will result.

In this paper, we evaluate the frequency dispersion behaviour of the ROF system and compare this with the application layer level performance. Measuring the Packet Error Rate (PER) obtained in the receiver for two different lasers.

We show the relationship between parameters and the importance of adjusting them depending on the optical power, RF power and the length of fiber used in the transmission, given that the frequency response we will obtain from the system depends on them.

II. Dispersive fading

To analyze dispersive fading and the impact it causes on the overall frequency response, a Vector Network Analyzer (VNA) was connected to both the laser and photo-detector at the ends of the optical transmission system, as shown by the dotted lines in figure 1. The frequency response obtained typically shows a transmission notch [3] that at first appears at a higher frequency than the operating band. The measurements done show that increasing transmission length will make it shift down in frequency and interfere with the RF signal. This is a dispersive fading effect which will cause degradation and should be addressed [6].

Thus, the frequency response was measured for different lengths of fiber and laser bias currents using two different lasers. Figure 2 illustrates the frequency response of a commercially available single mode laser used in the RoF system with 37km of Single Mode Fibre (SMF). The laser was a temperature controlled hermetically sealed high-speed butterfly package, with a bandwidth of about 16GHz at a bias current of 30mA. It has a room temperature emission wavelength of 1545nm and a threshold current of 10mA. Tests show that the non linearities in the laser become more pronounced for lower

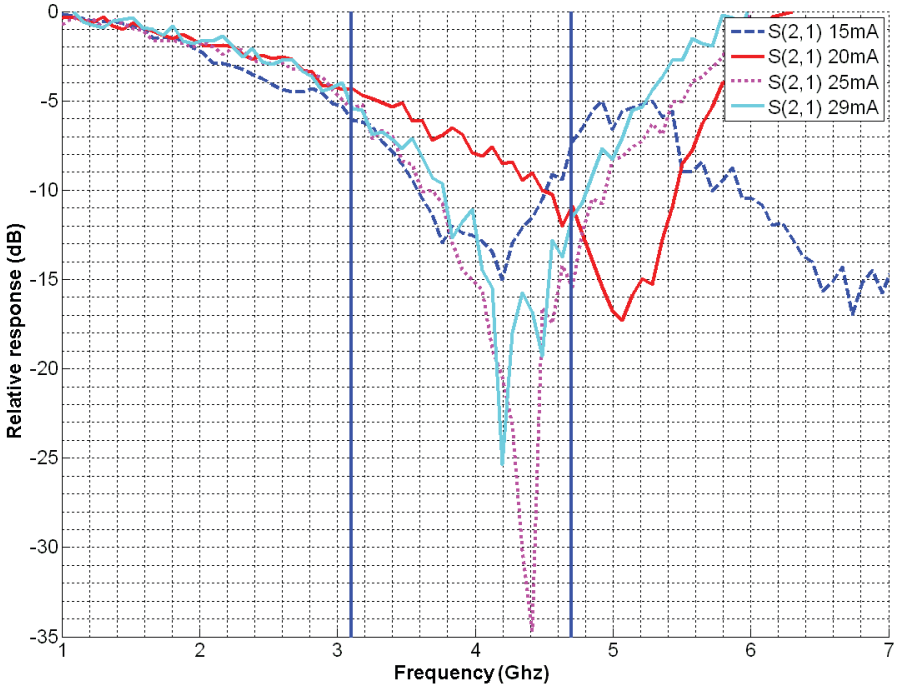

Fig. 2: High bandwidth laser frequency response of the system for a 37km fiber transmission length and different bias currents applied.

bias points and cause the dispersive fading notch to appear at unpredictable frequencies and vary in depth. This is due to the presence of harmonics of the modulating RF signal as multiple sidebands on the optical carrier. It makes the behaviour very complex and system performance difficult to predict, as can be noticed in the graph, where a difference of some milliamps in bias current can make the notch change from a 5dB to a 30dB depth and shift in frequency position. These results show that further investigation would be needed to understand these effects and obtain an adequate response and integrate this type of laser in an UWB ROF system.

The solution chosen to overcome this unpredictable behaviour was the use of a lower bandwidth laser so that higher order harmonics could not be generated. This way, the negative effects affecting our system response would be avoided. As expected in this case, the dispersive fading notches appeared at the expected frequencies and did not shift with changing laser diode bias current, making the system behaviour much more stable and easy to study.

Figure 3, shows the frequency response of this commercially available single mode laser in a hermetically sealed TO-can. It has an emission wavelength of 1540nm and a threshold current of 14mA. Results indicate that the laser has an inherent resonance around 2GHz in its back to back performance due to packaging parasitics, but has reasonably flat response at the Band Group 3 frequencies that we will use. The dispersive fading behaviour is also clearly shown here as the notch appears at 7GHz for 14km, 4.5GHz at 37km and 3.8GHz at 51km. These curves are not bias dependent, which indicates a high degree of linearity in the system. Using this laser, it will be easier to predict system performance and tune parameters to obtain the better possible PER, as opposed to the system behaviour for the high bandwidth laser.

Both results shown in figure 2 and 3 have the working band of our system, between 3.1 and 4.7 GHz, highlighted.

III. Packet error rate (PER)

To characterize the achievable PER, a bidirectional system was set up, because of the requirement of the Wisair boards to see each other to establish transmission, as indicated by the solid lines in figure 1. As shown there, the uplink optical connection was done back to back, instead of over the fiber reel, to avoid using multiple optical amplifiers and to isolate the performance of a single transmitting path. The transmission parameters changed for the tests were the bias current of the laser, the fiber length and the bitrate of the transmission, using most

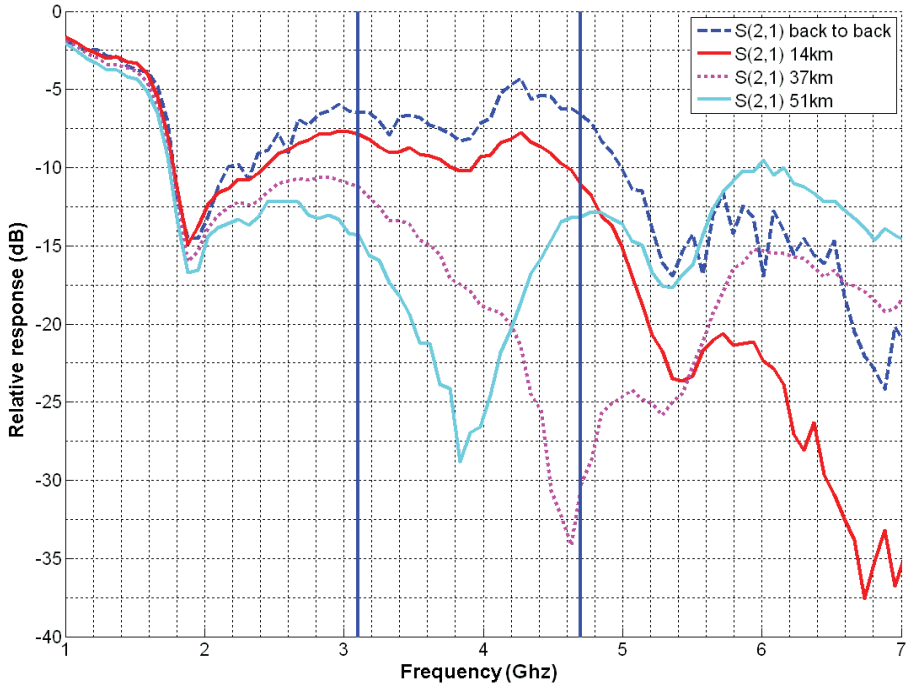

Fig. 3: Low bandwidth laser frequency response of the system for different fiber transmission lengths and a 25mA bias current applied.

of the different speeds UWB standard supports: 53.3Mbps, 80Mbps, 160Mbps, 320Mbps and 480Mbps. PER was measured from the receiver Wisair board application software for the different scenarios [2], [5].

The PER graphs for the high bandwidth laser are shown in figure 4 and indicate rather peculiar behaviour which seems to be a result of the complex interaction of the laser nonlinearities and the fibre dispersion, so that the effective channel the Wisair Radio is experiencing is unpredictable. However, the results in figure 5 showing the performance for the low bandwidth laser correlate well

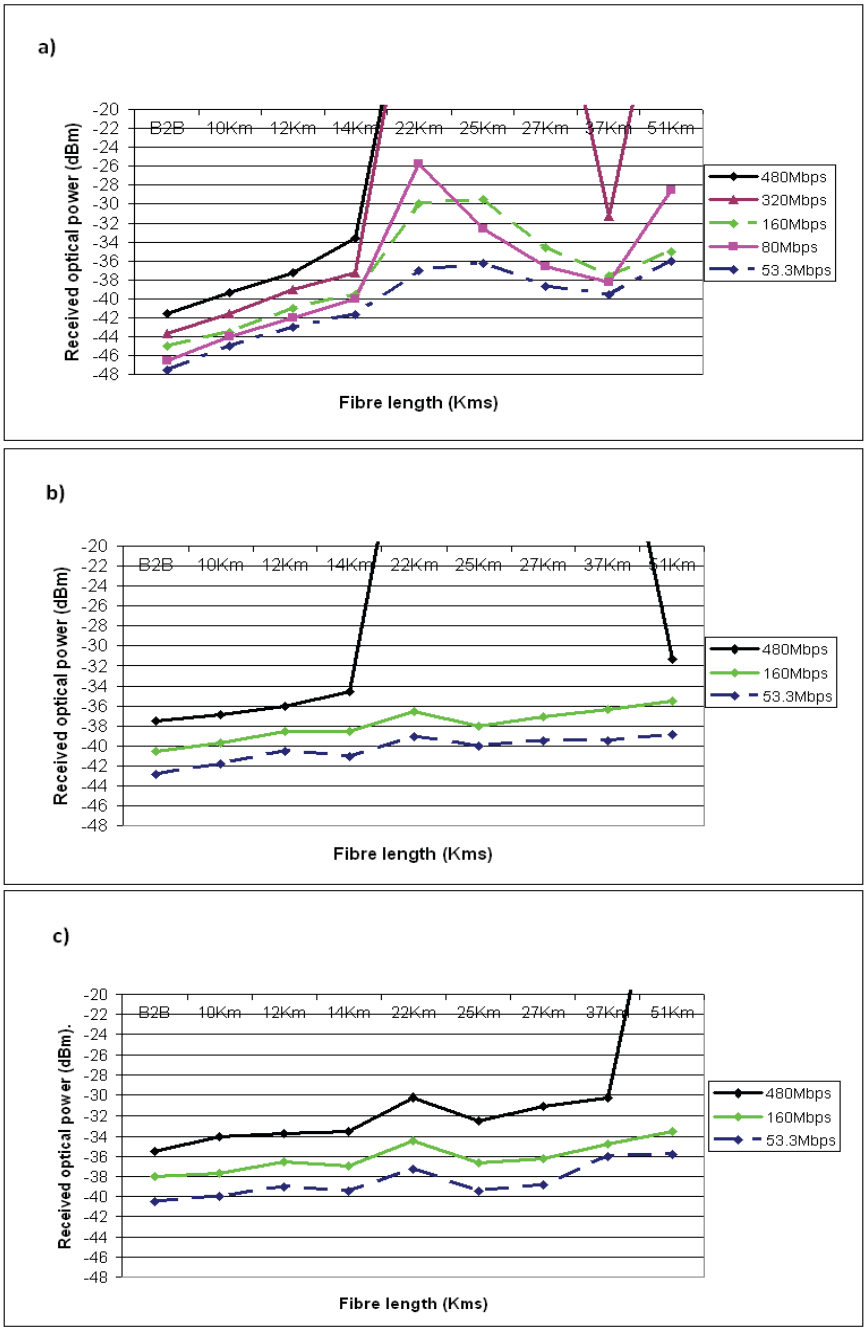

Fig. 4: High bandwidth laser 10% PER points for different transmission bitrates and fiber lengths with: a) 15mA, b) 20mA and c) 25mA bias currents applied to the laser.

with the frequency response graphs seen before in figure 3. It can be seen from these graphs that transmission cannot be established for distances greater than 14km for the 480Mbps case as this scheme uses no FEC. By contrast, reduced bit rates use higher levels of FEC and are capable of overcoming the channel degradations caused by dispersive fading.

Moreover, for the low bandwidth laser, Dispersion Compensating Fiber (DCF) could be used to improve PER and obtain at 37km a similar performance to the one at 12km. By contrast using DCF did not improve system performance when using the higher bandwidth laser. This is explained by the fact that the main phenomenon affecting performance for the low bandwidth laser is dispersion. But additional effects occur in the system for the higher bandwidth laser, keeping the performance low.

It is also interesting to note that the received optical power to achieve 10% PER needs to be approximately

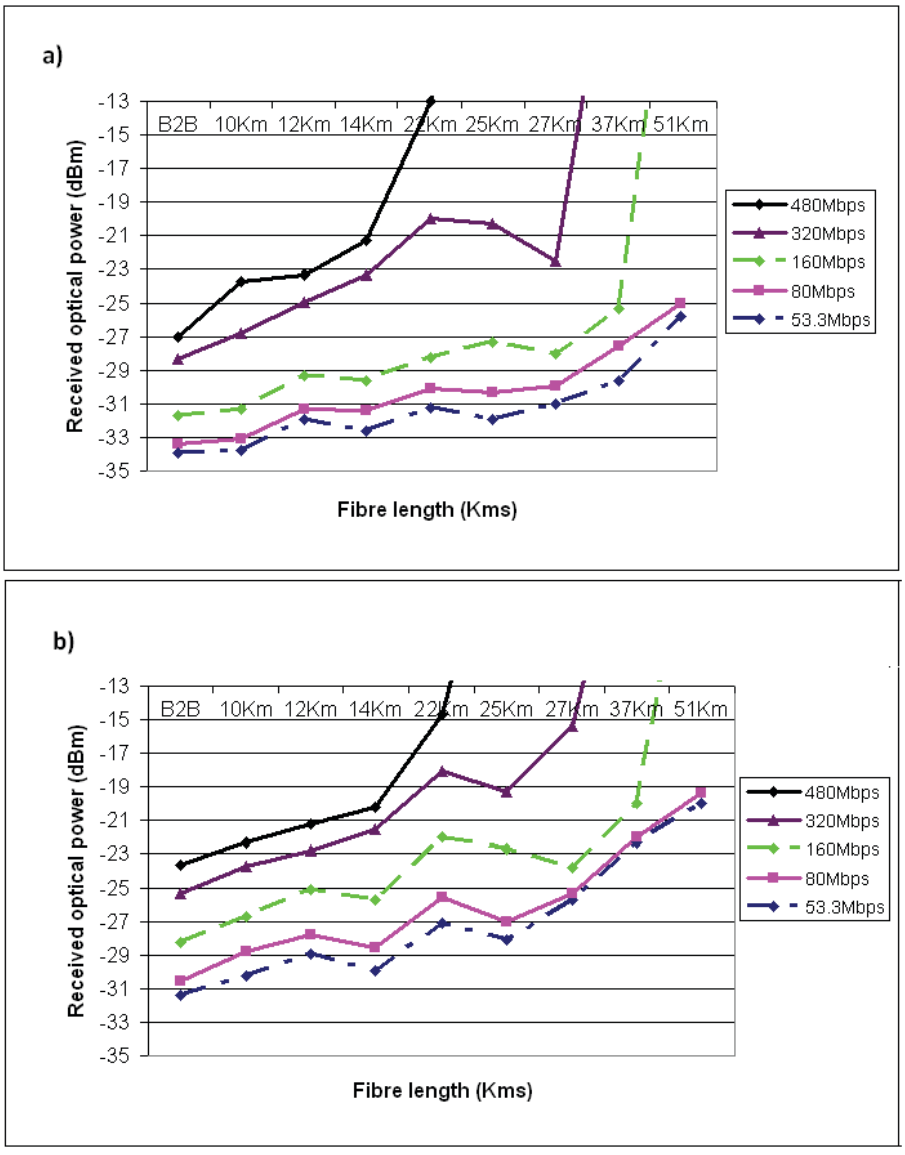

Fig. 5: Low bandwidth laser 10% PER points for different transmission bitrates and fiber lengths with: a) 20mA and b) 25mA bias currents applied to the laser.

3dB higher for the laser biased at 25mA than that at 20mA for a given distance. This is due to the reduction in modulation depth and the associated increase in carrier power when bias current is increased.

IV. Conclusions

In this paper we have shown that the simple dispersive fading model is insufficient for explaining the behaviour of UWBoF systems when the directly modulated lasers have a high bandwidth. By contrast, a low cost laser with restricted bandwidth offers improved system performance that is predictable and could be integrated in commercial systems.

Furthermore, the increased receiver sensitivity that can be gained by using a low bias current will give benefits for short lengths of fibre, needing less power to obtain similar error rates.

To summarize, it is shown that these systems have a clear practical application and could be used to distribute UWB signals with many advantages over other approaches. It could be done using optical fiber for a long distance with low attenuation and with a good frequency behaviour, taking into account the relationship between the different parameters involved and studied in this paper.

Acknowledgements

We would like to thank Linda Doyle of Trinity College Dublin for the loan of the Wisair boards used in this work and the company Wisair for the technical support.

References

1. *S. Yaakobl, W. R. Wan Abdullahl, Effect of Laser Bias Current to the Third Order Intermodulation in the Radio over Fibre System, International RF and Microwave Conference Proceedings (2006)*

2. *M.L. Yee, V.H. Pham, Performance Evaluation of MB-OFDM Ultra-Wideband Signals over Single mode Fiber, IEEE International Conference on Ultra-Wideband ICUWB (2007)*

3. *F. Ramos, J. Martí, Frequency Transfer Function of Dispersive and Nonlinear Single-Mode Optical Fibers in Microwave Optical Systems, IEEE Photonics Technology Letters (2000)*

4. *T. Alves, A. Cartaxo, Performance Degradation Due to OFDM-UWB Radio Signal Transmission Along Dispersive Single-Mode Fiber, IEEE Photonics Technology Letters (2009)*

5. *A. Pizzinat, P. Urvoas, 1.92Gbit/s MB-OFDM Ultra Wide Band Radio Transmission over Low Bandwidth Multimode Fiber, OFC/NFOEC (2007)*

6. *Y. Ben-Ezra, M. Ran, Wimedia-Defined, Ultra-Wideband Radio Transmission over Optical Fibre, OFC/NFOEC (2008)*

7. *A.J.Lowery, Fiber nonlinearity pre- and post-compensation for long-haul optical links using OFDM, vol 15, no 20, Optics Express (2007)*

An Efficient Consolidated Authentication Scheme for the Handover Process in Heterogeneous Networks

Mei Song[1], Li Wang[1], Xiaojun Wang[2], Lei Wang[1], Junde Song[1]
[1]School of Electronic Engineering,
Beijing University of Posts and Telecommunications, Beijing, P.R. China
songgm@bupt.edu.cn
[2]School of Electronic Engineering, Dublin City University, Ireland,
xiaojun.wang@dcu.ie

Abstract*—In order to reduce the authentication latency during handover process between different wireless networks, this paper proposes a novel consolidated authentication scheme, in which the re-authentication and the pre-authentication are performed. When a mobile node (MN) moves into a new domain, its identity must be verified by the EAP (Extensible Authentication Protocol) server. In this paper, EAP-MD5 method is adopted for the authentication process. After the first authentication, the re-authentication method is executed to reduce the time required for producing master key (MSK) between the MN and the EAP server before the MN leaves the domain. If MN moves into a new domain, the pre-authentication method will be carried out to reduce the required authentication time. Theoretical analysis and performance evaluation of the proposed scheme are presented, demonstrating the scheme's efficiency. Finally, the detailed implementation of the EAP-MD5 by using Open Diameter is given.

Keywords-consolidated authentication; Open Diameter; pre-authentication; re-authentication

I. INTRODUCTION

Driven by increasing user demand, an integrated access technology for seamless wireless communication mobility is becoming one of the objectives of next generation wireless communication technologies. When the mobile equipment changes its access point, the continuity of service will be affected by the relevant handover process. During the handover, it is necessary to provide some authentication mechanisms to guarantee the security of resource configuration and distribution. The latency of authentication is becoming the bottleneck of fast handover. Many research groups focus on the fast authentication during the handover process. Document [1] gives a description of the EAP fast re-authentication method and related key management framework. However, it is only suitable for intra domain handover. The EAP pre-authentication problem statement and related thought are presented in [2], while the discussion of extending PANA (Protocol for Carrying Authentication for Network Access) for pre-authentication is documented in [3]. All the references mentioned above have considered different scenarios but none of them provide a cooperative mechanism to perform the consolidated intra domain handover and inter domain handover.

Through analyzing the statement of authentication mechanism during handover process, this paper proposes a novel consolidated authentication scheme, in which the EAP pre-authentication (PA) and EAP re-authentication (RA) are adopted, and a central authentication server is defined to manage the detailed pre-authentication between different domain and re-authentication in the same domain, so as to reduce the authentication latency further.

II. PROPOSED CONSOLIDATED AUTHENTICATION SCHEME

A. Hierarchical Authentication Architecture

In order to reduce the time for signaling so as to reduce the handover latency, this section firstly proposes a hierarchical authentication architecture (HAA), which can be divided into two layers, home EAP server and local RA servers. From figure 1, it can be seen that HAA is composed of several authentication domains. There are many Intra domain RA authenticators and Inter domain RA authenticators in each authentication domain, and a local RA server is deployed in the center of the domain.

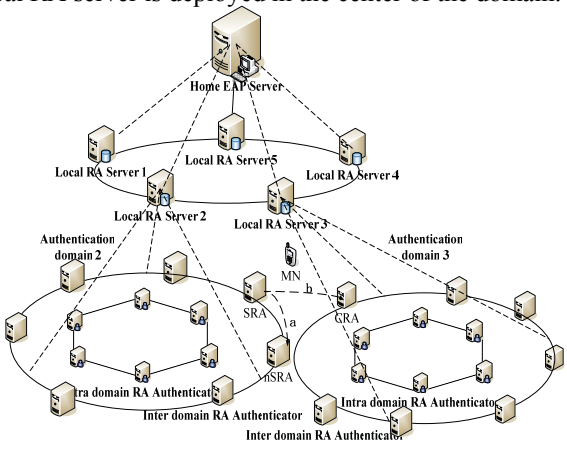

Figure 1. The hierarchical authentication architecture

In order to describe the problem clearly, figure 1 only gives a detailed description of two authentication domains, which are authentication domain 2 and authentication domain 3. In each domain, a local RA server will perform the re-authentication process for the mobile peer. The local RA server is also responsible for requesting the key

information for inter domain pre-authentication, and for collecting and saving the information of neighbors for the inter domain RA authenticators.

This scheme is proposed based on the EAP framework, which relies on the EAP method layer to perform the specific authentication process. The pass-through authentication model can be seen from figure 2. In addition, the key material, including Master Session Key (MSK) and extended Master Session Key (EMSK), will be produced by the EAP methods, such as EAP-MD5.

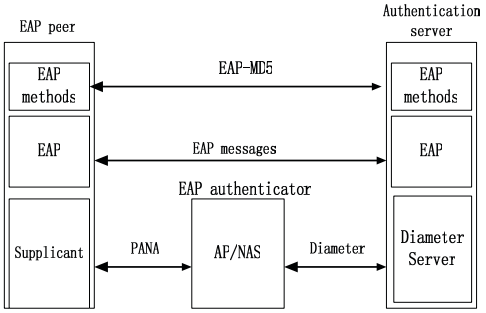

Figure 2. The pass-through authentication model

Before taking the inter domain pre-authentication, it should be assumed that the serving authenticator could detect the information of neighboring candidate authenticators (CA), including the authentication domain name and the name of the local RA server. However, the neighbor information discovered should be stored in the local RA server. The detailed topology of neighbors is defined when each domain is deployed and could be adjusted dynamically.

Generally speaking, pre-authentication requires an address of a RA candidate authenticator (CRA) to be discovered either by a peer or by a serving RA authenticator (SRA) or by some other entities before handover. In this paper, the authenticator discovery protocol, which is typically defined as a separate protocol, is not considered. For both intra-domain and inter-domain handover, the IP address of a candidate authenticator must be reachable by the peer or the SRA that is performing the pre-authentication. Note that, an authenticator discovery requires a database of the neighboring network information.

B. EAP Re-authentication for Intra Handover

Figure 1 illustrates the EAP re-authentication procedures when a mobile peer moves between different authenticators within a same authentication domain. Then figure 3 and figure 4 show the initialization process and the EAP re-authentication procedure respectively.

In authentication domain 2, the mobile peer needs to know the name of the local authentication domain or the name of local RA server when it first enters the domain. As is shown in figure 3, the normal EAP process will be performed first, including EAP request and EAP response messages. Between the mobile peer and the EAP server, a MSK will be produced and sent to the authenticator (SRA), used for making the secure connection subsequently. During the process of EAP exchange, the EMSK is produced between the mobile peer and the EAP server.

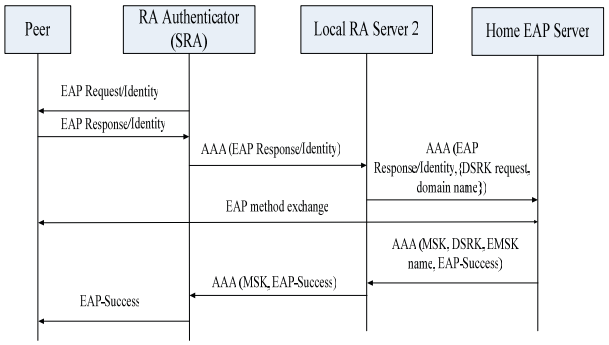

Figure 3. Initialization process for the re-authentication procedure

During the EAP re-authentication process, the local RA server will request a Domain Specific Root Key (DSRK) for the home EAP server by sending its own domain name. Then the home EAP server will calculate the DSRK based on the EMSK，and send the DSRK and its EMSK name to the local RA server. On receiving the related messages, the re-authentication Root Key（DS-rRK）and re-authentication Integrity Key（DS-rIK）will be calculated using DSRK, meanwhile, DS-rRK and DS-rIK are gotten by the mobile peer. When the mobile peer moves from the SRA to the nSRA (next SRA), the EAP re-authentication will be triggered. nSRA will send EAP-Initiate/Re-auth-Start message to indicate the start of EAP re-authentication. After receiving the EAP Initiate/Re-auth message, the local RA server uses the still valid DS-rRK to produce a re-authentication MSK (rMSK), and send it to nSRA, as shown in figure 4. Similarly, based on DS-rRK the mobile peer can also generate rMSK which can be used as Master Session Key (MSK) for secure connection. Here, it is unnecessary to retrieve the MSK from home EAP server, and the multiple information exchange operations between the peer and the EAP server could be omitted. The proposed scheme can thus significantly reduce the handover latency, especially in the roaming mode when the mobile peer is far away from the home EAP server with longer signal round trips.

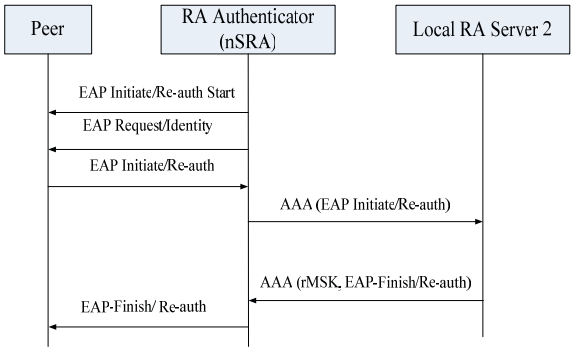

Figure 4. Re-authentication procedure

C. EAP Pre-authentication for Inter Handover

From figure 1, we can see that when the mobile peer moves along route b, it crosses the boundaries of the authentication domain 2 and domain 3. The intra domain re-authentication scheme devised in the above section is

not applicable here, because the authenticator SRA and authenticator CRA are located in different authentication domains. The key material (DS-rRK and DS-rIK) from authentication domain 2 is not allowed to be used in authentication domain 3. Therefore, we propose a novel consolidated inter domain authentication scheme. Figure 5 shows the detailed procedure of pre-authentication between SRA and CRA.

In figure 5, when a mobile peer moves to the SRA, which stands at the border of authentication domain 2, the SRA first carries out the re-authentication process, and then it starts the pre-authentication process. The detailed message flow is as follows.

When a mobile peer makes its authentication through SRA, the local RA server 2 will choose its CA and start the pre-authentication process by sending EAP Pre-auth Request/Identity from SRA to CRA. On receiving the EAP Pre-auth Response/Identity message from the peer, the SRA requests its neighbor information from local RA server 2. The mapping information of SRA-CRA stored in local RA server 2 will be sent to SRA, and related information of CRA will be sent to the mobile peer, such as the domain name of CRA. After receiving its neighbor information, the SRA sends the received EAP Pre-auth Response/Identity message to local RA server 3 through CRA. Subsequently, local RA server 3 will request the valid key material, such as DSRK, and EMSK name. Then, DS-rRK and DS-rIK will be calculated and stored.

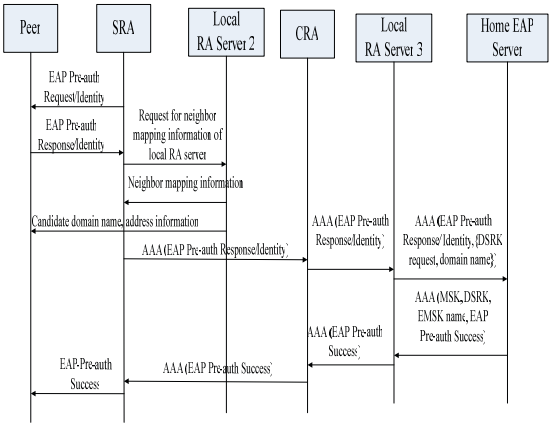

Figure 5. Pre-authentication procedure

When the mobile peer moves into domain 3, the rMSK generated in domain 2 could be sent to CRA. In addition, the new access domain name obtained by the mobile peer can be used to produce new rMSK. Thus, a secure connection could be established. In the pre-authentication mode, the signaling operations are restricted between the RA server and the mobile peer. It does not need to contact the home EAP server.

III. PERFORMANCE EVALUATION AND IMPLEMENTATION

In order to reduce the system cost and to reduce the handover delay further, we proposed a consolidated authentication scheme in section II. In this section, a detailed implementation and a performance analysis of the proposed scheme will be given.

A. Implementation

The software used in this paper is open source. For the AAA architecture and the Diameter protocol, the opendiameter implementation is used. It supports different Diameter applications such as EAP, PANA and NASREQ. Opendiameter-1.0.7-i is used in this paper. The base protocol implementation is available as a C++ library and currently supports Linux, BSD and Windows systems. An implementation of EAP and PANA for client/user network access is also available under the Open Diameter project. Currently, the EAP stack can already support methods including EAP-MD5, EAP-TLS, EAP-AKA and EAP-GPSK. Note that, this section will take EAP-MD5 for example. By using of EAP-MD5, the whole PANA latency between PAC and PAA is about 2.43 seconds, when the MN first moves into a new domain to make its first authentication.

In summary, the state machine of pass through authentication model can be seen in figure 6. When the pass-through authenticator receives a message, it will change from the "IDLE" state to the "Received" state. Authenticator starts to process the received message. If the message is the authentication request sent from the backend server, the authenticator gets into "SendRequest" state, and forwards the request to the peer. If the message is the authentication response sent from the peer, the authenticator gets into "SendResponse" state, and forwards the response to the backend authentication server. If the message is invalid, the authenticator discards the message, and returns to the IDLE state unconditionally. After each sending action (sending request/response), the authenticator will return to the IDLE state.

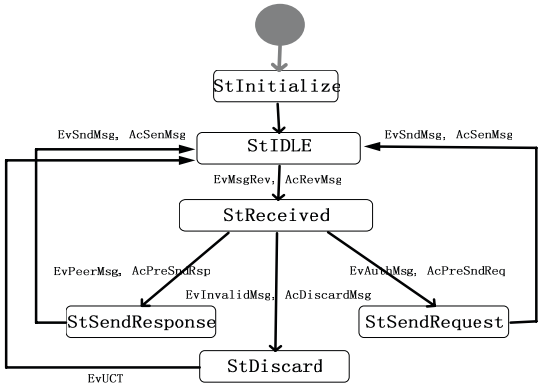

Figure 6. State machine for pass through authentication model

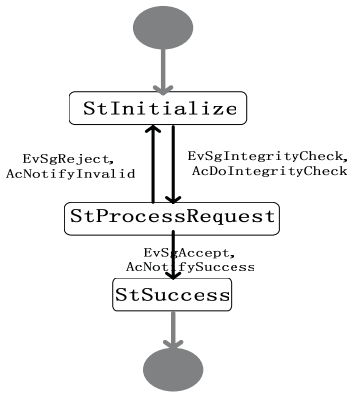

Figure 7. EAP-MD5 state machine on the MN

In addition, the opendiameter implementation uses different state machines to model the different EAP methods. In this section, we take EAP-MD5 as an example. Figure 7 shows the state machine for the EAP-MD5 method that is used on the MN [7]. StInitialize is the initial state and StSuccess is the final state. The events that trigger the transitions are named as `EvSgIntegrityCheck`, `EvSgReject` and `EvSgAccept` respectively. The actions that get started for every transition could be named as `AcDoIntegrityCheck`, `AcNotifyInvalid` and `AcNotifySuccess`. Figure 8 shows the state machine for the EAP-MD5 method that is used on the AAAH.

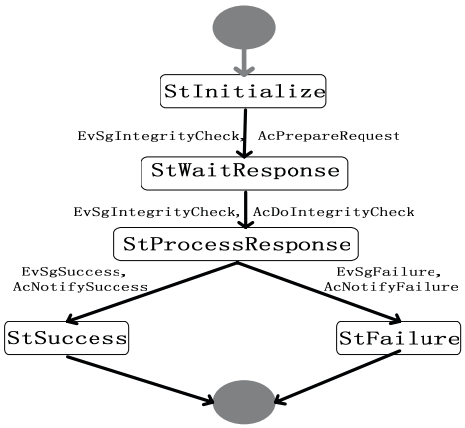

Figure 8. EAP-MD5 state machine on the AAAH

B. Performance Analysis

In this paper, EAP framework is used for guaranteeing the heterogeneous requirements of future interworking networks. When handover process occurs, the normal EAP authentication process will be triggered. It should be noted that, after sending EAP Response/Identity message by MN, at least one interactive operation is needed to produce MSK, the time required for the operations depends on the EAP methods used. The process of producing MSK will incur additional cost, in terms of delay which is undesirable, especially in the roaming case.

In this proposed scheme, when a MN enters into a new domain, it will perform its first authentication process, in which the normal EAP methods are used, such as EAP-MD5 and EAP-TLS [8]. Then, before the MN moves out to another new domain, the re-authentication mode can be used to make the following authentication. On the other hand, when the MN leaves its current domain, the pre-authentication mode will be adopted. The detailed authentication signaling operation time comparison can be seen from the following table.

Table 1. Performance comparison

EAP method (proposed)	Authentication signaling operation time
EAP-MD5	1.5 round trips (Peer-EAP server)
EAP-TLS	3 round trips (Peer-EAP server)
Re-auth	1 round trip (Peer-local RA server)
Pre-auth	1 round trip (Peer-local RA server)

Each RA server in each authentication domain will play a critical role. It not only performs re-authentication in its own local domain, but also collects and manages the neighbor information during the pre-authentication process. Before the intra domain handover, the initialization of intra domain authentication is executed in advance, with an aim to establish secure connection by using the obtained DS-rRK and DS-rIK etc. Then the remaining authentication process needs not to contact the EAP server. And only one round trip is necessary between the peer and the local RA server, as can be seen in table 1. In summary, the proposed scheme can significantly reduce the total authentication cost in terms of both the number of authentication signals and the distances of the authentication signals have to travel.

IV. CONCLUSIONS

Based on the EAP framework, this paper proposes a consolidated authentication scheme, in which re-authentication is used in intra domain handover process, and pre-authentication is adopted in inter domain handover process. The performance analysis demonstrates that the proposed scheme reduces the authentication cost. Moreover, if the movement of a mobile peer could be tracked, then the number of candidate authenticators can be reduced, so as to reduce the additional cost for the pre-authentication initialization process. The authors will conduct further research in this area.

ACKNOWLEDGMENT

This work was supported by the National High-Tech Research and Development Plan of China (No. 2007AA01Z226).

REFERENCES

[1] B.Aboba, D.Simon and P. Eronen. "Extensible Authentication Protocol (EAP) Key Management Framework", IETF RFC 5247, August 2008.

[2] V.Narayanan and L. Dondeti. "EAP Extensions for EAP Re-authentication Protocol (ERP)", RFC 5296, August 2008.

[3] Q.Wu and Y.Ohba,"EAP Pre-authentication Problem Statement", IETF draft-ietf-hokey-preauth-ps-06, March 8,2009.

[4] J.Salowey, L.Dondeti, V.Narayanan and M.Nakhjiri,"Specification for the Derivation of Root Keys from an Extended Master Session Key (EMSK)",IETF RFC 5295, August 2008.

[5] B.Aboba, L.Blunk, J.Vollbrecht,et al."Extensible Authentication Protocol (EAP)", IETF RFC 3748, June 2004.

[6] M. Parthasarathy. "Protocol for carrying Authentication for Network Access (PANA) Threat Analysis and Security Requirements", IETF RFC 4016, March 2005.

[7] Elias Diem."An Authentication Architecture for Network Access in Multi-Domain Mobile IPv6 Networks", Diploma Thesis, University of Zurich, Switzerland, March 2007.

[8] B.Aboba and D. Simon. "PPP EAP TLS Authentication Protocol", IETF RFC 2716, October 1999.

Section 3B

COMPUTER VISION

A new algorithm of edge detection based on soft morphology

Shang Junna, Jiang Feng

（Hangzhou Dianzi University，Hangzhou Zhejiang 310037）

Abstract: An algorithm of edge detection based on mathematical morphology is discussed in the paper. Due to the characteristics of the basic morphology algorithm of image processing，the common edge detection algorithms with traditional morphological edge detection algorithm is analyzed and compared, and the characteristics of each, as well as inadequateness are given here. Combined with the geometric algorithms, applied to binary gray scale image edge detection, based on the classic edge detection algorithms and soft filtering properties, the morphology of the soft edge detection algorithm and optimization algorithm is put forward for the edge detection and image de-noising processing.

Key words: mathematical morphology;　binary gray scale image;　edge detection;　soft morphology

1. Introduction

Mathematical Morphology is a new kind of nonlinear algorithm, using a certain form of structural elements to measure and extract the shape of the corresponding image in order to achieve the image analysis and identification purposes. It is more suitable for visual information processing and analysis, and the type of interaction are completed by the basic operations of Erosion and Dilation as well as Open and Closed operations. Edge detection in image processing and computer vision occupies a special status, a large number of image information contained, to reflect the main features of the object. Therefore, the extraction of edge information for image processing is very important.

2. Morphological edge detection of gray image

The edge of the gray-scale images or structure where own more or less mutations, indicating that the end of a region and the beginning of another regional location. Classical edge detection method is based on space operations, these methods sensitive to noise, poor anti-noise performance, and the edge of the detection noise is strengthened. For the noise pollution, the general approach is to filter, and then detect the edge by differential coefficient. However, the filter smoothes the image at the same time, the edge will inevitably be fuzzy, and the test results will be affected, is not conducive to the image feature extraction, such as follow-up treatment; the number of links increasing, extend the time of image processing, it is not fit for the high real-time requirement occasions.

2.1 Commonly used edge detection algorithm

Edge extraction usually based on a variety of differential algorithm combined use of templates, threshold, smooth and other means. Commonly used edge detection algorithms are Robert, Sobel, Prewitt, Laplacian, LOG and Canny algorithm.

Robot is the First-order differential algorithm which uses the difference between adjacent pixels to detect edge. This measure has high positioning accuracy, but the noise with bad robustness can't be suppressed.

Prewitt is a model algorithm for edge detection which uses the same measure as Sobel Algorithm. This arithmetic detect edge with the pixels' upper, lower, left and right of gray-weighted neighborhood algorithm that these pixels reach the extremum of principle. This measure can smooth the noise but with huge amount of calculation and its position accuracy is not well.

LOG is the Second-order differential algorithm which uses pre-smoothing with Gaussian low-pass filter on the image first. Then this arithmetic identifies the image edge of the steep with Laplacian algorithm. At last it generates closed and connected contours with zero-gray value by elimination of all internal points. It could filter the noise and also smooth the edge.

Canny is a kind of filtering method which is a compromise method between smoothing and filtering through Gaussian smoothing filter. This measure has high de-noising. The real weak-edge can be detected and the interference noise will be less susceptible. But some edge information also be smoothed. In

practical application work, it is a complex programming and slower computing work.

Commonly used edge detection algorithm MATLAB simulation:

Figure 1 Prewitt algorithm

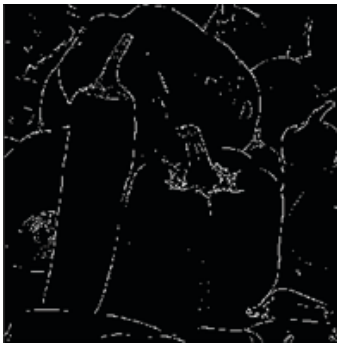

Figure 2 Rober algorithm

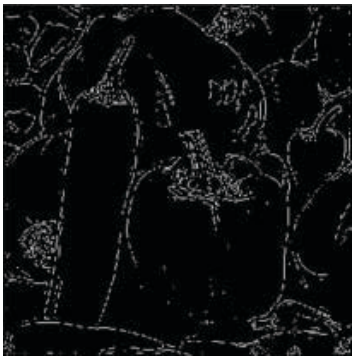

Figure 3 LoG algorithm

Figure 4 Canny algorithm

2.2 Soft morphology

Through the edge detection algorithm on the summary can be seen in the image edge detection in some of the requirements are as follows：

1 First of all, it is able to detect the right edge of the effective;

2 Edge positioning must be high accuracy；

3 The best response to detection is a single pixel;

4 For the edge of different scales are better able to respond and to minimize missed;

5 Unsensitive to noise;

6 The sensitivity of detection by the edge of the direction of the impact should be small.

These requirements are often contradictory, and it is difficult to be completely unified in one edge detector. Based on these classical algorithms, a new optimization algorithm was put forward, such as soft morphological edge detection method, using mathematical morphology method to sort the well-weighted expansion, corrosion algorithms have been based on the gray image edge detection algorithm.

Based on soft forms of edge detection algorithm and using the characters of soft transformation, the edge information can be attained by the difference of the transformed image. Soft form as a result of transformation can be determined by three parameters, namely, B, A, k, so the three parameters become the basis of edge detection as a result of the different transformation monotonicity, scalability, and anti-expansion. Taking $f \oplus [B, A, k] - f$ for example, Figure 5 is used to explain the geometric significance of edge detection.B, A as the soft elements form the structure of transformation，when in flat areas, due to fall on "the structure of the window" within the gray value of the points are similar, so even after the transformation of regional, output and input is not much difference. Once hopping into the gray area, gray value due to relatively are largely different, so the output of the transformed image near the gray-scale structural elements in the transition region where there is a "higher" than the original image. According to the expansion of soft forms of transformation, there is $f \oplus [B, A, k] \geq f$ .If an image subtraction between $f \oplus [B, A, k]$ and the input the image is taken, then $f \oplus [B, A, k] - f$ reflects the image of the edge information. This is because when in flat areas, $f \oplus [B, A, k]$ and f close to the zero difference. In the hopping gray area, there are much difference between them.

Control structure elements of shape and size, the impact of extraction on the edge of their predecessors have been devoted, and here only to discuss the selection of k value of the impact on the Edge.

As Figure 6 shows: To $f \oplus [B, A, k]$,

when k<k1, $f \oplus [B, A, k] > f \oplus [B, A, k_1]$.

In this way, for the case of noise, the algorithm can be constructed by $f \oplus [B, A, k] - f \oplus [B, A, k_1]$, in order to extracting the edge an erasing the noise can be done at the same time.

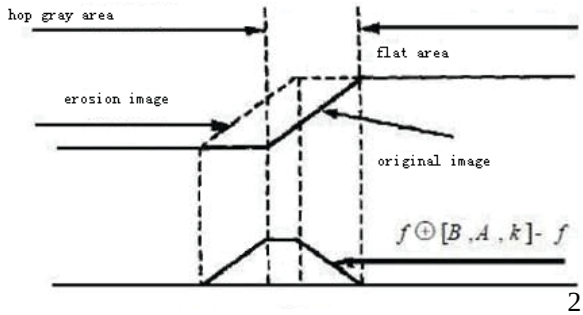

Figure 5 Geometric significance of edge detection schematic

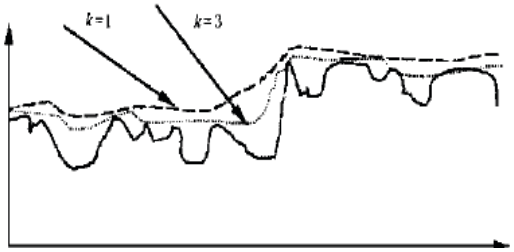

Figure 6 Figure of different K value

So the soft algorithm is following: Select the structural element -> Define hardcore element -> Determine K value -> Traverse the image by structural elements ->Hardcore loops K times and traverse image points, while stores the remained points in array -> Sort the array and select the small value of the first K -> Subtract with the original image.

In the simulation, the structure elements(SE) is selected as

SE=[1 1 1 1 1;

1 1 1 1 1;

1 1 1 1 1]*180

The shape of SE is picked as a convexity, so that more useful information can be got.

Hardcore is selected as

Hardcore =[1 3;

2 1;

2 2;

2 3;

2 4;

2 5;

3 3];

Saving all the point covered by hardcore, and loop k times.

According the basic algorithm of soft morphology:

$$f \oplus [B, A, k] - f \quad \text{for any A,B,k,}$$

The simulation result is given as figure 7.

Figure 7 Algorithm of gray soft morphology

2.3 The modified algorithm of edge detection based on soft morphology

The original algorithm is:

$$f \oplus [B, A, k] - f$$

The image will be inflated at first and then get a difference between the new inflated and the raw image.

The modified algorithm is:

$$f \oplus [B, A, k] - f \oplus [B, A, k] \Theta [B_1, A_1, k_1],$$

for any A，B，k，A1，B1，k1

The image will be inflated at first also, but then get a difference with opening operation of the raw image. The simulation result is given as figure 8.

Figure 8 Modified algorithm of edge detection based on soft morphology

It is indicated in the figure that the soft morphology exchange can restrain the image noise efficiently and detect the edge of the image under strong noise condition. But when the

edge is complex, the edge detected by simple soft morphology will be coarser, and the new algorithm of this paper can attain a single pixel wide edge.

3. Conclusion

Mathematical morphology as an effective non-linear image processing methods and theory, in the image processing, pattern recognition and computer vision and other fields, the application are very important. Based on mathematical morphology edge detection algorithm, it can overcome the shortcomings of the traditional edge detection algorithm, but at the same time as a result of a morphological filter characteristics, the use of morphological transformation, the edge detected relatively wide. This paper focuses on the image edge detection algorithm based on mathematical morphology

In this paper, the commonly used edge detection algorithm as well as traditional morphological edge detection algorithm are analyzed and compared，pointing out that the characteristics of each, as well as inadequate, put forward a soft morphological edge detection algorithm on the basis, in turn to improve the above algorithms, and put forward a modified soft morphological edge detection algorithm, which can effectively detect image edge, while restrain the impact of noise, which has strong robustness. Additionally based on actual requirements, choose different structural elements to achieve detection of different purposes with flexibility. It should be pointed out, however, for the edge detection of image noise, performance enhancement based on the cost of complexity, how to reduce the amount calculated to meet the requirements of real-time while effectively suppressing noise and edge detection, will to be in further study.

Reference

[1] Ruan Qiu-qi, Digital Image Processing [M]. Beijing: Electronic Industry Press, 2001.

[2] FU Yong-qing, WANG Yong-sheng. A mathematical morphology-based edge detection algorithm for gray-scale images [J]. Journal of Harbin Engineering University, 2005,26 (5) :685 - 687.

[3] Chen Yang and other 《graphics programming and image processing》, Xidian University Press, 2003.

[4] Gong Wei. Figures space mathematical morphology - theory and application [M]. Beijing: Science Press, 1997.

[5] Huang Feng-gang ,Yang Guo, Song Ke-ou. Flexible Morphology in Image Edge Detection [J]. Chinese Journal of Image and Graphics, 2000, 5A (4): 284 - 287.

[6] Wei Gong, Shi Qing-yun, Cheng Ming-de Tak. The number of space in the mathematical morphology - theory and application [J]. Beijing: Science Press, 1997,429 - 445.

[7] ZHAO Chun—hui, SUN Sheng-he, HUI Jun-ying.《Optimization of soft morphological filters by simulated annealing[C]》. Beijing：Proceedings of ICSP．2000.

[8] T.Chen,Q.H.Wu, R.Rahmani-Torkaman, J.Hughes. A pseudo top-hat mathematical morphological approach to edge detection in dark regions[J]. Pattern Recognition,2002,35: 199 - 210.

[9] Cenzo A D, Strip mode processing of spotlight synthetic aperture radar data[J]. IEEE Trans on Aerospace and Electronic Systems, 1988, 24(3): 225-230.

3D TOOTH RECONSTRUCTION WITH MULTIPLE B-SPLINE SURFACES THROUGH LINEAR LEAST-SQUARES FITTING

Nailiang Zhao[†] and Weiyin Ma[‡]

[†] Institute of Graphics and Image, Hangzhou Dianzi University,
Hangzhou, Zhejiang, P.R. China 310018
znl@hdu.edu.cn
[‡] Department of Manufacturing Engineering and Engineering Management, City University of Hong Kong,
Kowloon, Hong Kong SAR, China
mewma@cityu.edu.hk

Abstract

Geometric modelling of tooth has a great value in medical applications. Common 3D models of tooth are usually discrete grid meshes based on the image slice sequence, which is not convenient for further mathematical processing. In this paper, based on the unorganized points from a tooth, we obtain a 3D model of G1-connected B-spline surfaces through data segmentation and parameterization. The equations of multiple B-spline surfaces fitting are solved by least-squares (LSQ) method. Finally, some examples of tooth surface reconstruction are provided.

Keywords: Tooth reconstruction; B-spline surface; G1 continuity; Linear least-squares fitting

1 Introduction

Advanced computer technology has been widely used in medical treatment. Various medical equipments, such as CT and MRI, have limitations in using 2D planar images for disease diagnosis and treatment. 3D reconstruction of human organ has been developed rapidly in recent years, including education, simulations and treatment [1]. The morphological characteristics and physiological functions of teeth are very important in dental sciences. In practice, doctors may suffer from somewhat inconvenience on dental treatment, plastic and even communication with patients if only documents and pictures are used [2]. Therefore, it is an urgent requirement to reconstruct virtual 3D teeth from human teeth.

Buchaillard *et al*. presented a method to reconstruct the 3D shape of a tooth based on statistical models [3]. Liao *et al*. use the patient CT volume and a 3D geometric prior model to produce a "best-fit" patient specific 3D model of the whole tooth using thin-plate splines warp [4]. Wang *et al*. proposed a Special Marching Cubes (SMC) algorithm to construct 3D tooth based on isosurface construction [5]. Bors *et al*. proposed a binary morphological morphing algorithm of reconstructing the shape of various teeth from slices [6]. To our knowledge, little work focuses on multiple B-spline surfaces for reconstruction 3D tooth.

Among the publications in multiple B-spline surface modelling, Milroy *et al*. proposed a procedure for achieving approximate global G1 continuity [7]. Another approach was developed by Eck and Hoppe for automatic construction of B-spline surfaces from unorganized points with exact G1 continuity [8]. However, the surfaces model therein is actually composed of Bézier patches rather than B-splines. Ma and Zhao present a method for fitting multiple B-spline surfaces with Catmull-Clark subdivision surfaces for extraordinary corner patches using pure linear least squares fitting [9]. Based on the G1 continuity of two adjacent bicubic B-spline surfaces with single interior knots, Shi *et al*. discussed the reconstruction of convergent G1 smooth B-spline surfaces [10].

This paper develops an approach to reconstruction 3D tooth from a set of measured points. The principal contributions of the paper and major differences between our approach and others are summarized as follows:

- B-spline surfaces: they are widely used by most of the commercial medical software systems and are the de-facto standards in the CAD/CAM industry.
- Unorganized points: it is easy to construct arbitrary topology from either 2D slice images or 3D laser measured data.
- Efficiency: the final observation system of multiple surface fitting can be represented as a linear LSQ procedure.
- Continuity: perfect G1 can be achieved by using linear connecting functions.

2 Theory of G1 continuity conditions for multiple connected B-spline surfaces

We first define two B-spline surfaces $\mathbf{P}(u,v)$ and $\mathbf{Q}(u,v)$

$$\begin{cases} \mathbf{P}(u,v) = \sum_{i=1}^{n}\sum_{j=1}^{n} B_{i,k}(u)\cdot B_{j,k}(v)\cdot \mathbf{P}_{ij} \\ \mathbf{Q}(u,v) = \sum_{i=1}^{n}\sum_{j=1}^{n} B_{i,k}(u)\cdot B_{j,k}(v)\cdot \mathbf{Q}_{ij} \end{cases} \quad (1)$$

Without lost of generality, we assume that the two surfaces share the same order and the same set of knots for the u-directions and v-directions. For $\mathbf{P}(u,v)$, k is the order of the surface along two directions, and $\mathbf{P}_{ij} \in \mathbf{R}^3$ are the $n \times n$ control points. $\{u_i\}$ and $\{v_i\}$ $i = 1,2,\cdots,n+k$ are the two sequences of knots with $u_k = v_k = 0$, and $u_{n+1} = v_{n+1} = 1$. The parameters for $\mathbf{Q}(u,v)$ are defined in a similar way.

We further assume that the two surfaces will be connected side by side along the v-directions with $\mathbf{P}(1,v)$ and $\mathbf{Q}(0,v)$ being the two boundaries for G^1 connection. It is easy to verify that the sufficient and necessary conditions of G^0 continuity between $\mathbf{P}(u,v)$ and $\mathbf{Q}(u,v)$ is

$$\sum_{i=n-k+2}^{n} B_{i,k}(1)\cdot \mathbf{P}_{ij} = \sum_{i=1}^{k-1} B_{i,k}(0)\cdot \mathbf{Q}_{ij},\ j = 1,2,\cdots,n \quad (2)$$

$\mathbf{P}_u'(1,v)$, $\mathbf{Q}_u'(0,v)$ and $\mathbf{Q}_v'(0,v)$ denote three tangent vector functions respectively along the common boundary $\mathbf{P}(1,v) = \mathbf{Q}(0,v)$. One of the sufficient conditions of G^1 continuity between $\mathbf{P}(u,v)$ and $\mathbf{Q}(u,v)$ is

$$\mathbf{P}_u'(1,v) = \alpha\cdot \mathbf{Q}_u'(0,v) + (\beta v + \gamma)\cdot \mathbf{Q}_v'(0,v) \quad (3)$$

where $\alpha > 0$ and $\beta^2 + \gamma^2 \neq 0$. We call $f(v) = \alpha$ and $g(v) = \beta v + \gamma$ of equation (3) linear connecting functions.

When constructing the topological structure for smooth multiple surface modelling, we adopt a boundary representation (B-rep) with quadrilateral domains. Each of the domains is filled with a B-spline surface defined by equation (1). Each surface boundary or domain boundary may be shared by at most two adjacent surfaces. Any number of boundaries may however meet at a common corner, as illustrated in Figure 1.

To determine the blending functions, we proceed corner by corner similar to Bézier surfaces widely accepted in literature, called umbrella-shaped configuration. Actually, the common boundary will degenerate as a Bézier curve under the linear connecting functions [11]. Let $\{\mathbf{T}_i\}_{i=1}^N$ be a set of outwards oriented and anti-clockwise unit tangent vectors at a common corner $\mathbf{P}$ in Figure 1. The valence N is the number of boundaries (or surfaces) that meet at the corner $\mathbf{P}$. Any control point with valence $N \neq 4$, i.e., its valence is three or larger than four, is called an extraordinary corner. Otherwise, it is called a regular corner.

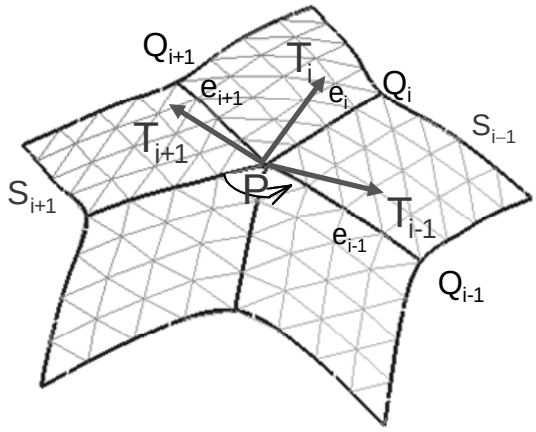

Figure 1: Configuration of multiple B-spline surfaces.

A set of parameters $\{\alpha_i > 0, \beta_i\}_{i=1}^N$ should be assigned to each of the common corners such that

$$\mathbf{T}_{i+1} = -\alpha_i \mathbf{T}_{i-1} + \beta_i \mathbf{T}_i \quad i = 1,2,...,N \quad \text{mod } with\ N \quad (4)$$

For the i-th common boundary, the γ_i parameter at one end is actually the β_i parameter at the other end and, therefore, needs not be addressed separately. Similar to the construction of multiple Bézier patches, we should carefully define the parameters $\{\alpha_i > 0, \beta_i\}_{i=1}^N$ for all common corners without conflict and degeneracy at each corner and with twist compatibility for all corners. In this paper, we adopt a symmetrical solution at internal extraordinary corners and an unsymmetrical solution at internal regular corners [12].

$$\begin{cases} \alpha_i = 1, \beta_i = \lambda = 2\cos(2\pi/N) \\ \quad i = 1,2,\cdots,N \quad \text{when } N \neq 4 \\ \alpha_1 = \alpha_2 = \alpha_3 = \alpha_4 = 1, \\ \beta_1 = \beta_3 = 0, \beta_2 = -\beta_4 = \lambda \\ \quad \lambda \neq 0 \quad \text{when } N = 4 \end{cases} \quad (5)$$

Once the parameters $\{\alpha_i > 0, \beta_i\}_{i=1}^N$ of all corners have been defined, the parameters of linear connecting functions in equation (3) of all common boundaries are also determined.

3 Strategies for tooth reconstruction with multiple B-spline surfaces

A set of unorganized points $\{\overline{\mathbf{P}}_i \in R^3\}_{i=1}^m$ are measured from the continuous surface area of a human tooth, and $\{\mathbf{S}_j(u,v)\}_{j=1}^s$ is a set of smooth connected B-spline surfaces that we will approximate the tooth shape. Generally three steps are needed to obtain the fitted B-spline surfaces.

3.1 Topological structure and base surface definition

A quadrilateral topological structure of the tooth is first interactively defined from the point clouds $\{\overline{\mathbf{P}}_i \in R^3\}_{i=1}^{m}$, as illustrated in Figure 2. The four boundaries of each quadrilateral domain are represented as B-spline curves and are defined by fitting through a limited number of interactively selected sample points.

After topological structure modelling, a set of approximate B-spline surfaces $\{\overline{\mathbf{S}}_j(u,v)\}_{j=1}^{s}$ are created as base surfaces for the partition and parameterization of the measured points, as illustrated in Figure 3. The base surfaces are actually the initial approximation of the final fitted B-spline surfaces. These base surfaces are easily created from the four boundary curves with or without additional uni-directional interior curves for accurate approximation.

3.2 Data partition and parameterization

Data partition and parameterization are realized through a projection process using the base surfaces approach reported in [9]. After projecting all measured points $\{\overline{\mathbf{P}}_i \in R^3\}_{i=1}^{m}$ onto the multiple base surfaces $\{\overline{\mathbf{S}}_j(u,v)\}_{j=1}^{s}$, each point $\overline{\mathbf{P}}_i$ in the point clouds will be distributed to an individual topological domain and associated with an index j of a base surface with $\{j \mid 1 \le j \le s\}$. Two location parameters (u_i, v_i) of $\overline{\mathbf{P}}_i$ relative to the corresponding base surface are also simultaneously obtained. After all the measured data are processed, one obtains a set of location parameters $\{\{(u_{ij}, v_{ij})\}_{i=1}^{m_j}\}_{j=1}^{s}$ corresponding to the partitioned data point $\{\{\overline{\mathbf{P}}_{ij}\}_{i=1}^{m_j}\}_{j=1}^{s}$, where m_j is the number of measured points which belong to base surface $\overline{\mathbf{S}}_j$ with $\sum_{j=1}^{s} m_j = m$.

3.3 Linear least-squares fitting

After introducing the measured data $\{\{\overline{\mathbf{P}}_{ij}\}_{i=1}^{m_j}\}_{j=1}^{s}$ and the location parameters $\{\{(u_{ij}, v_{ij})\}_{i=1}^{m_j}\}_{j=1}^{s}$ into the multiple B-spline surfaces $\{\mathbf{S}_j(u,v)\}_{j=1}^{s}$ defined similar to equation (1), one obtains the following sets of observation equation

$$\mathbf{B}_j\mathbf{X}_j = \overline{\mathbf{X}}_j, \mathbf{B}_j\mathbf{Y}_j = \overline{\mathbf{Y}}_j, \mathbf{B}_j\mathbf{Z}_j = \overline{\mathbf{Z}}_j \qquad (6)$$

$\mathbf{X}_j$, $\mathbf{Y}_j$ and $\mathbf{Z}_j$ represent the collection of x-, y- and z-coordinates of control points of the j-th surface, $\overline{\mathbf{X}}_j$, $\overline{\mathbf{Y}}_j$ and $\overline{\mathbf{Z}}_j$ represent the coordinates of the measured points falling on the j-th surface, and $\mathbf{B}_j$ is the j-th matrix defined by

$$\mathbf{B}_j = \begin{bmatrix} B_{1j}(\cdot_{1j}) & B_{2j}(\cdot_{1j}) & \cdots & B_{nj}(\cdot_{1j}) \\ B_{1j}(\cdot_{2j}) & B_{2j}(\cdot_{2j}) & \cdots & B_{nj}(\cdot_{2j}) \\ & \vdots & & \\ B_{1j}(\cdot_{m_j j}) & B_{2j}(\cdot_{m_j j}) & \cdots & B_{nj}(\cdot_{m_j j}) \end{bmatrix} \qquad (7)$$

where $(\cdot_{ij}) = (u_{ij}, v_{ij})$ for $i = 1,2,...,m_j$, $j = 1,2,...,s$.

The s observation system of equation (6) can be collectively represented by the following general observation equations

$$\mathbf{BX} = \overline{\mathbf{X}}, \mathbf{BY} = \overline{\mathbf{Y}}, \mathbf{BZ} = \overline{\mathbf{Z}} \qquad (8)$$

where $\mathbf{B} = diag\{\mathbf{B}_1, \mathbf{B}_2, \cdots, \mathbf{B}_s\}$, and $\mathbf{X}$, $\mathbf{Y}$ and $\mathbf{Z}$ represent the coordinates of control points of all B-spline surfaces, $\overline{\mathbf{X}}$, $\overline{\mathbf{Y}}$ and $\overline{\mathbf{Z}}$ represent the coordinates of all points measured from tooth.

For x-component, the integrated observation equations are

$$LSQ: \mathbf{BX} = \overline{\mathbf{X}} \qquad S.T.: \mathbf{AX} = \mathbf{0} \qquad (9)$$

where $\mathbf{AX} = \mathbf{0}$ is the collection of all G^0 and G^1 continuity conditions in equations (2) and (3). After eliminating some variables of control points $\mathbf{X}$ through the variable substitution with $\mathbf{AX} = \mathbf{0}$. One obtains the following simplified observation system for smooth multiple surface fitting.

$$\tilde{\mathbf{B}}\tilde{\mathbf{X}} = \overline{\mathbf{X}} \qquad (10)$$

and $\tilde{\mathbf{X}}$ can be solved by linear least-squares method without any constrains.

$$\tilde{\mathbf{X}} = \left(\tilde{\mathbf{B}}^T\tilde{\mathbf{B}}\right)^{-1}\left(\tilde{\mathbf{B}}^T\overline{\mathbf{X}}\right) \qquad (11)$$

Then all $\mathbf{X}$ can be obtained through the reverse variable substitution with $\mathbf{AX} = \mathbf{0}$.

4 Results and discussions

The algorithms discussed in this paper are implemented in an in-house developed modelling environment built upon OpenGL on Windows XP (Pentium IV 1.7GHz, 512MB RAM). The final fitted 3D tooth is represented as a B-rep surface/solid model.

The original measured data of the tooth in this paper include 9337 unorganized points in Figure 2. The topological model of the tooth contains 11 inter-connected quadrilateral surface domains as shown in Figure 2. All initial base surfaces are shown in Figure 3 with G^0 continuity. There are in total 11 common corner with 8 extraordinary corners of valence $N = 3$ and 4 regular corners of valence $N = 4$.

The matrix $\left(\tilde{\mathbf{B}}^T\tilde{\mathbf{B}}\right)$ in equation (11) should be orthogonal and invertible if there are sufficient numbers of samples points are used. Precisely, it requires that there should be at least one sample point located within the definition domain for each of

the basis functions of B-spline. With too less number of sample points, there might be a danger of unstable solution (almost not invertible), while with too many points, the computing time will be longer. For practical fitting, we need to use "just enough points" for achieving stable and representative results. After data partition and parameterization, we only adopt 2816 points to fit the final surfaces for this example.

All B-spline surfaces shown in the Figure 4 and 5 are defined with bi-quartic splines and uniform knots with $k = 5$, and the number of control points for each surface is $n \times n = 8 \times 8 = 64$ in Figure 4. Each surface has $4 \times 4 = 16$ patches. We resize all measured points into the interval [-1,1] before processing, then, the maximum, average, minimum and standard deviations of the fitting errors of reconstructed 3D tooth are 0.0722, 0.0158, 0.0003 and 0.0002, respectively.

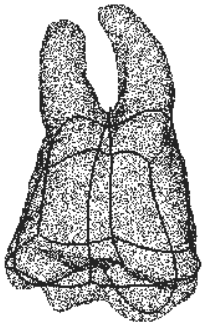

Figure 2: Measured points and quadrilateral topological structure.

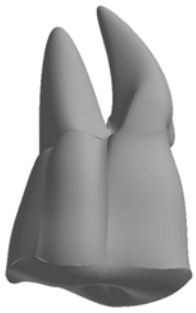

Figure 3: Base surfaces for data partition and parameterization.

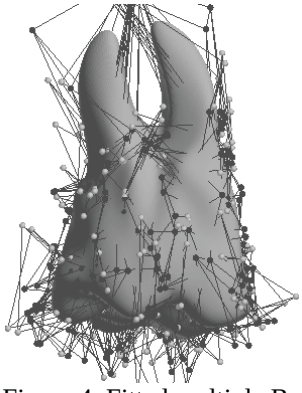

Figure 4: Fitted multiple B-spline surfaces with their control points.

Figure 5: Reconstructed 3D tooth with smooth connected B-spline surfaces.

5 Conclusions

This paper presents a method for reconstructing 3D tooth with smoothly connected multiple B-spline surfaces through linear least-squares fitting. A quadrilateral topological structure is first defined. The control mesh of the multiple surfaces is then automatically constructed through linear least squares fitting. The final fitted surfaces are smoothly connected with perfect G1, it is easy to process, such as prototype of artificial tooth in advance. Because the topological structures of one kind of tooth are similar, this method is quite effective and suitable for medical applications.

Acknowledgements

The work presented in this paper is sponsored by City University of Hong Kong through a Strategic Research Grant (#7001928) and Qianjiang Talent Project of Zhejiang Province, China (#2007R10011).

References

[1] Muraki Shigeru and Kita Yasuyo. “A survey of medical applications of 3D image analysis and computer graphics”, *Systems and Computers in Japan*, vol. 37(1), pp. 13-46, January (2006).

[2] El-Bialy and Ahmed. “Towards a complete computer dental treatment system”, *Proceedings of the Cairo International Biomedical Engineering Conference*, pp. 1-8, (2008).

[3] Stéphanie I. Buchaillard *et al*. “3D statistical models for tooth surface reconstruction”, *Computers in Biology and Medicine*, vol. 37(10), pp. 1461-1471, October (2007).

[4] Sheng-hui Liao, Ruo-feng Tong and Jin-xiang Dong. “3D Whole Tooth Model from CT Volume using Thin-Plate Splines”, *Proceedings of the Ninth International Conference on Computer Supported Cooperative Work in Design*, vol. 1, pp. 600- 604, (2005).

[5] Hongjian Wang, Fen Luo and Jianshan Jiang. “3D Reconstruction of CT Images Based on Isosurface Construction”, *Proceedings of the International Conference on Intelligent Computation Technology and Automation*, vol. 2, pp. 55 - 59, October, (2008).

[6] A. G. Bors, L. Kechagias and I. Pitas. “Binary morphological shape-based interpolation applied to 3-D tooth reconstruction”, *IEEE Transactions on Medical Imaging*, vol. 21(2), pp. 100-108, (2002).

[7] M. J. Milroy *et al*. “G1 continuity of B-spline surface patches in reverse engineering”, *Computer Aided Design*, vol. 27, pp. 471-478, (1995).

[8] M. Eck, and H. Hoppe. “Automatic reconstruction of B-spline surfaces of arbitrary topology type”, *Computer Graphics*, vol. 30, pp. 325-334, (1996).

[9] Weiyin Ma, Nailiang Zhao. “Smooth multiple B-spline surface fitting with Catmull–Clark surfaces for extraordinary corner patches”, *The Visual Computer*, vol. 18(7), pp. 415-436 (2002).

[10] Xiquan Shi, Tianjun Wang and Piqiang Yu. “A practical construction of G1 smooth biquintic B-spline surfaces over arbitrary topology”, *Computer Aided Design*, vol. 36, pp. 413-424, (2004).

[11] Nailiang Zhao and Weiyin Ma. “Properties of G1 continuity conditions between two B-spline surfaces”, *Advances in Computer Graphics, in Lecture Notes on Computer Science*, vol. 4035, pp. 743-752, (2006).

[12] Weiyin Ma and Nailiang Zhao. “Exact G1 Continuity Conditions for B-Spline Surfaces with Applications for Multiple Surface Fitting”, *Proceedings of the International Conference on Manufacturing Automation*, pp. 47-56, December, (2002).

Automatic Recognition of Head Movement Gestures in Sign Language Sentences

Daniel Kelly, Jane Reilly Delannoy, John Mc Donald, Charles Markham
Computer Science Department, National University of Ireland, Maynooth, Ireland
dankelly@cs.nuim.ie

***Abstract*—A novel system for the recognition of head movement gestures used to convey non-manual information in sign language is presented. We propose a framework for recognizing a set of head movement gestures and identifying head movements outside of this set. Experiments show our proposed system is capable of classifying three different head movement gestures and identifying 15 other head movements as movements which are outside of the training set. In this paper we perform experiments to investigate the best feature vectors for discriminating between positive a negative head movement gestures and a ROC analysis of the systems classifications performance showed an area under the curve measurement of 0.936 for the best performing feature vector.**

***Keywords*-Sign Language, Non Manual Signals, HMM**

I. Introduction

Sign Language is a form of non-verbal communication where information is mainly conveyed through hand gestures. Since sign language communication is multimodal, it involves not only hand gestures (i.e., manual signing) but also non-manual signals. Non-manual signal are conveyed through facial expressions, head movements, body postures and torso movements. Recognizing Sign Language communication therefore requires simultaneous observation of manual and non-manual signals and their precise synchronization and signal integration. Thus understanding sign language involves research in areas of face tracking, facial expression recognition, human motion analysis and gesture recognition.

Over the past number of years there has been a significant amount of research investigating each of these non-manual signals attempting to quantify their individual importance. Works such as [1], [2], [3] focused on the role of head pose and body movement in sign language. These researchers found evidence which strongly linked head tilts and forwards movements to questions, or affirmations. The analysis of facial expressions for the interpretation of sign language has also received a significant amount of interest [4], [5]. Computer-based approaches which model facial movement using *Active Appearance Models* (AAMs) have been proposed [6], [7], [8].

The development of a system combining manual and non-manual signals is a non-trivial task [9]. This is demonstrated by the limited amount of work dealing with the recognition of multimodal communication channels in sign language. Ma et al [10] used Hidden Markov Models (HMMs) to model multimodal information in sign language, but lip motion was the only non-manual signal used. Their work was based on the assumption that the information portrayed by the lip movement directly coincided with that of the manual signs. While this is a valid assumption for mouthing, it cannot be generalised to other non-manual signals as they often span multiple manual signs and thus should be treated independently.

In this paper we evaluate techniques for the automatic recognition head movement gestures used to convey non-manual information in Irish Sign Language (ISL) sentences. We propose a framework for the automatic recognition of head movement gestures, building on the techniques proposed by Kelly et al [11] who use a HMM threshold model system to recognize manual signals.

II. Feature Extraction

The focus of this work is to evaluate the HMM threshold model framework as a system for recognizing head movement gestures. For completeness, we briefly describe the feature tracking techniques used, though we do not consider it to be the novel part of our work.

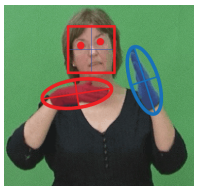

Figure 1. Extracted Features from Image

Face and eye positions are used as features for head movement recognition. Face and eye detection is carried out using a cascade of boosted classifiers working with haar-like features proposed by Viola and Jones [12]. A set of public domain classifiers [13], for the face, left eye and right eye, are used in conjunction with the OpenCV implementation of the haar cascade object detection algorithm. We define the raw features extracted from each image as follows; face position (FC_x, FC_y), left eye position (LE_x, LE_y) and right eye position (RE_x, RE_y).

III. Hidden Markov Models

Hidden Markov Models (HMMs) are a type of statistical model and can model spatiotemporal information in a natural way. HMMs have efficient algorithms for learning and recognition, such as the Baum-Welch algorithm and Viterbi

search algorithm [14]. A HMM is a collection of states connected by transitions. Each transition (or time step) has a pair of probabilities: a transition probability (the probability of taking a particular transition to a particular state) and an output probability (the probability of emitting a particular output symbol from a given state). We use the compact notation $\lambda = \{A, B, \pi\}$ to indicate the complete parameter set of the model where A is a matrix storing transitions probabilities and a_{ij} denotes the probability of making a transition between states s_i and s_j. B is a matrix storing output probabilities for each state and π is a vector storing initial state probabilities. HMMs can use either a set of discrete observation symbols or they can be extended for continuous observations signals. In this work we use continuous multidimensional observation probabilities calculated from a multivariate probability density function.

To represent a gesture sequence such that it can be modeled by a HMM, the gesture sequence must be defined as a set of observations. An observation O_t, is defined as an observation vector made at time t, where $O_t = \{o_1, o_2, ..., o_M\}$ and M is the dimension of the observation vector. A particular gesture sequence is then defined as $\Theta = \{O_1, O_2, ..., O_T\}$. To calculate the probability of a specific observation O_t, we implement probability density function of an M-dimensional multivariate gaussian (see Equation 1). Where μ is the mean vector and Σ is the covariance matrix.

$$\aleph(O_t; \mu, \Sigma) = (2\pi)^{-\frac{N}{2}} |\Sigma|^{-\frac{1}{2}} exp\big(-\tfrac{1}{2}(O_t-\mu)^T \Sigma^{-1}(O_t-\mu)\big) \quad (1)$$

A. HMM Threshold Model

Lee and Kim [15] proposed a HMM threshold model to handle non-gesture patterns. The threshold model was implemented to calculate the likelihood threshold of an input pattern and provide a confirmation mechanism for provisionally matched gesture patterns. We build on this work carried out by Lee and Kim to create a framework for calculating a probability distribution of head movement input gesture using continuous multidimensional observations. The computed probability distribution will include probability estimates for each pre-trained sign as well as a probability estimate that the input sign is a non head movement gesture.

In general, a HMM recognition system will choose a model with the best likelihood as the recognized gesture if the likelihood is higher than a predefined threshold. However, this simple likelihood threshold often does not work, thus, Lee and Kim proposed a dynamic threshold model to define the threshold of a given gesture sequence.

A property of the left-right HMM model implies that a self transition of a state represents a particular segment of a target gesture and the outgoing state transition represents a sequential progression of the segments within a gesture sequence. With this property in mind, an ergodic model, with the states copied from all gesture models in the system, can be constructed as shown in Figure III-A and III-A, where dotted lines in Figure III-A denote null transitions (i.e. no observations occur between transitions).

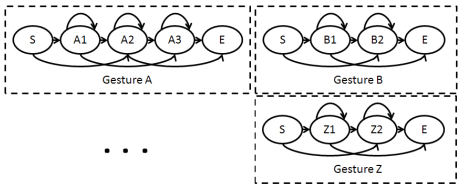

Figure 2. Dedicated Gesture Models

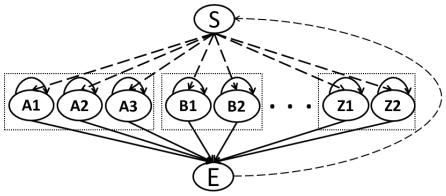

Figure 3. Threshold Model

States are copied such that output observation probabilities and self transition probabilities are kept the same, but all outgoing transition probabilities are equally assigned as defined in Equation 2 where N is the number of states excluding the start and end states (The start and end states produce no observations).

$$a_{ij} = \frac{1 - a_{ij}}{N - 1}, \quad \forall j, i \neq j, \quad (2)$$

As each state represents a subpattern of a pre-trained gesture, constructing the threshold model as an ergodic structure makes it match well with all patterns generated by combining any of the gesture sub-patterns in any order. The likelihood of the threshold model, given a valid gesture pattern, would be smaller than that of the dedicated gesture model because of the reduced outgoing transition probabilities. However, the likelihood of the threshold model, given an arbitrary combination of gesture sub-patterns, would be higher than that of any of the gesture models, thus the threshold model, denoted as $\overline{\lambda}$, can be used as a non head movement gesture measure.

B. HMM Threshold Model & Gesture Recognition

Kelly et al [11] expand on the work of Lee and Kim [15] to develop a HMM threshold model system which models continuous multidimensional sign language observations within a parallel HMM network to recognize two hand signs and identify movement epenthesis. In this paper, we expand on the work of Kelly et al to create a framework for recognizing head movement gestures.

For a network of HMMs $\Lambda = \{\lambda_1, \lambda_2, ..., \lambda_C\}$, where λ_c is a dedicated gesture HMM used to calculate the likelihood that the input gesture is belonging to gesture class c, a single

threshold model $\overline{\lambda}$ is created to calculate the likelihood threshold for each of the dedicated gesture HMMs.

IV. Non Manual Signal Recognition

While hand gestures do play central grammatical roles, movements of the head, torso and face are used to express certain aspects of ISL. In this work we will focus on a single non-manual signal, the head movement, to evaluate our techniques when recognizing non-manual features.

A. Model Training

Our system initializes and trains a dedicated HMM for each head movement gesture to be recognized. In this work we evaluate our techniques using three different head movement gestures; a left head movement, a right head movement and a left-forward movement. A visual example of a signer performing each of the three different head movement gesture is in shown in Figure IV-A.

Figure 4. Example of the three different head movement gestures the system was tested on (a) Right Movement (b) Left Movement (c) Left Forward Movement

To train the head movement HMMs, we recorded 18 different videos of a fluent ISL signer performing the head movements naturally within full sign language sentences. Six videos where recorded for each head movement gesture. Each head movement HMM λ_i^H (where $0 < i < I$ and I is the total number of head gestures) was then trained on the observation sequences extracted from the corresponding videos.

The start and end point of each of the head movement gestures were labeled, the observation sequences Θ_i were extracted and each HMM was then trained using the iterative HMM training model proposed by Kelly et al [11]. A HMM threshold model, $\overline{\lambda^H}$ is then created using the network of trained HMMs λ_i^H (where $0 < i < I$). The set of HMMs, to recognize the I pre-trained head movement gestures, is then denoted as $\Lambda^H = \{\lambda_1^H, \lambda_2^H, ..., \lambda_I^H, \overline{\lambda^H}\}$.

B. Head Movement Recognition

Given an unknown sequence of head movement observations Θ^H, the goal is to accurately classify the head movement as one of the I trained gestures or as a movement which is not a trained gesture. To classify the observations, the Viterbi algorithm is run on each model given the unknown observation sequences Θ^H, calculating the most likely state paths through each model i. The likelihoods of each state path, which we denote as $P(\Theta^H|\lambda_i^H)$, are also calculated. The sequence of observations can then be classified as i if Equation 3 evaluates to be true.

$$P(\Theta^H|\lambda_i^H) \geq \Psi_i^H \tag{3}$$

$$\Psi_i^H = P(\Theta^H|\overline{\lambda^H})\Gamma_i^H \tag{4}$$

Where Γ_i^H is a constant scalar value used to tune the sensitivity of the system to head movement which the system was not trained on.

C. Experiments

An accurate head movement gesture recognition system must be able to discriminate between positive and negative head movement gesture samples, therefore, we perform a set of experiments to find the best feature set when discriminating between isolated positive and negative head gestures.

To test the discriminative performance of different feature vectors, we recorded an additional 7 videos for each head gesture (21 in total), where a fluent ISL signer performed the head movement gestures within different sign language sentences. The start and end points of the head gestures were then labeled and isolated observation sequences Θ_i^τ were extracted. An additional set of 15 other head gesture sequence, outside of the training set, were also labeled in the video sequences to test the performance of the system when identifying negative gestures.

The classification of a gesture is based on a comparison of a weighted threshold model likelihood with the weight denoted as Γ_i^H. In our ROC analysis of the system, we vary the weight, Γ_i^H, over the range $0 \leq \Gamma_i^H \leq 1$ and then create a confusion matrix for each of the weights.

To evaluate the performance of different features, we performed a ROC analysis on the models generated from the different feature combinations and calculated the area under the curve (AUC) for each feature vector model. Table I shows the AUC measurement of four different features which were evaluated during our experiments. To calculate the directional vector of the head, (V_x^H, V_y^H), we used the mid point between the eyes and calculated the direction the midpoint moved from frame to frame. We used a sliding window to average the directional vector and in our experiments we evaluated the best performing window size for each feature vector. Although we evaluated each feature

vector with a range of different window sizes, we report only the best performing window sizes for each feature vector in Table I.

Table I
AUC MEASUREMENTS FOR DIFFERENT FEATURE COMBINATIONS

Features	Window Size	ROC AUC
F_1 - Unit Direction Vector $(\hat{V}_x^H, \hat{V}_y^H)$	6	0.821
F_2 **- Direction Vector** (V_x^H, V_y^H)	**12**	**0.936**
F_3 - Unit Direction Vector $(\hat{V}_x^H, \hat{V}_y^H)$ + Angle Eyes (θ_{eyes})	6	0.863
F_4 - Direction Vector (V_x^H, V_y^H) + Angle Eyes (θ_{eyes})	6	0.868

V. CONCLUSION

In this paper we have discussed current research in the area of automatic recognition of non-manual signals used in sign language. The development of a system to recognize non-manual signals is a non-trivial task and this is demonstrated by the limited number of works dealing with non-manual signals in the context of sign language sentences.

We have presented a framework for recognizing head movement gestures used to convey non-manual information in sign language sentences. We expanded the HMM threshold model technique, proposed by Lee and Kim [15], to develop a system which models continuous multidimensional head movement observations within a HMM network to recognize head movements and identify head movement gestures which the system was not trained on. We perform experiments to investigate possible observation vectors which best discriminate between positive and negative head movement gestures samples. A ROC analysis of different observation vectors showed that the best performing vector, with an AUC measurement of 0.936, was a two dimensional vector describing the movement of the eye midpoint within a sliding window averaged over 12 frames.

The significance of the research presented in this paper is that we have developed a general technique for recognising head movement gestures. With a view to developing an automatic sign language recognition system, identifying non-manual signals such as head movement is an important task. In this paper we have demonstrated that our techniques are capable of identifying typical head movement gestures which occur in sign language sentences, therefore enable us to determine whether or not a question was posed by the signer. Future work will involve incorporating these techniques into a wider framework for automatic recognition of multi-modal continuous sign language.

ACKNOWLEDGMENT

The Authors would like to acknowledge the financial support of the Irish Research Council for Science, Engineering and Technology (IRCSET).

REFERENCES

[1] B. Bahan, "Nonmanual realisation of agreement in american sign language," Ph.D. dissertation, University of California, Berkely, 1996.

[2] E. van der Kooij, O. Crasborn, and W. Emmerik, "Explaining prosodic body leans in sign language of the netherlands: Pragmatics required," *Journal of Pragmatics*, vol. 38, 2006, prosody and Pragmatics.

[3] C. Baker-Shenk, "Factors affecting the form of question signals in asl," *Diversity and Diachrony*, 1986.

[4] R. B. Grossman and J. Kegl, "To capture a face: A novel technique for the analysis and quantification of facial expressions in american sign language," pp. p273–305, 2006.

[5] R. Grossman and J. Kegl, "Moving faces: Categorization of dynamic facial expressions in american sign language by deaf and hearing participants," *Journal of Nonverbal Behavior*, vol. 31, no. 1, pp. 23–38, 2007.

[6] U. von Agris, M. Knorr, and K.-F. Kraiss, "The significance of facial features for automatic sign language recognition," pp. 1–6, 2008.

[7] U. von Agris, J. Zieren, U. Canzler, B. Bauer, and K.-F. Kraiss, "Recent developments in visual sign language recognition," *Universal Access in the Information Society*, vol. 6, no. 4, pp. 323–362, 2008.

[8] C. Vogler and S. Goldenstein, "Facial movement analysis in asl," *Universal Access in the Information Society*, vol. 6, no. 4, pp. 363–374, 2008.

[9] S. C., W. Ong, and S. Ranganath, "Automatic sign language analysis: A survey and the future beyond lexical meaning," *IEEE Trans. PAMI*, vol. 27, no. 6, pp. 873–891, 2005.

[10] J. Ma, W. Gao, and R. Wang, "A parallel multistream model for integration of sign language recognition and lip motion," in *ICMI '00: Proc of the 3rd Intl Conf on Adv in Multimodal Interfaces*, 2000, pp. 582–589.

[11] D. Kelly, J. McDonald, and C. Markham, "Recognizing spatiotemporal gestures and movement epenthesis in sign language," in *IMVIP 2009*, 2009.

[12] P. Viola and M. Jones, "Rapid object detection using a boosted cascade of simple features," *CVPR, IEEE*, vol. 1, p. 511, 2001.

[13] L. A.-C. M. Castrillon-Santana, O. Deniz-Suarez and J. Lorenzo-Navarro, "Performance evaluation of public domain haar detectors for face and facial feature detection," *VISAPP 2008*, 2008.

[14] L. Rabiner, "A tutorial on hidden markov models and selected applications in speech recognition," *Proceedings of the IEEE*, vol. 77, no. 2, pp. 257–286, Feb 1989.

[15] H. K. Lee and J. H. Kim, "An hmm-based threshold model approach for gesture recognition," *IEEE PAMI*, vol. 21, no. 10, pp. 961–973, 1999.

Dirt and Sparkle Detection for Film Sequences

Peter Gaughran, Susan Bergin, Ronan Reilly

Department of Computer Science, National University of Ireland, Maynooth
Maynooth, Co. Kildare, Ireland

peter.gaughran@nuim.ie
susan.bergin@nuim.ie
ronan.reilly@nuim.ie

***Abstract*— Until recently, filming has been an analogue process; it requires a mechanical process to record and view, and the source material itself is prone to decay & abrasion [1]. Film is expensive to store, and prohibitively expensive to restore. All footage - historical, documentary or entertainment – may completely degrade over time. While many archival films stocks are currently being scanned and further damage thus prevented, the digital copies are far from the quality of the original. The types of aberrations found are varied, from frame jitter and line scratches to dirt and sparkle. It is the detection of the latter two (which are frame based abnormalities) that will be examined here.**

***Keywords*— Dirt, sparkle, detection, machine vision, block matching**

I. Motivation

Traditionally, when restoring footage, each frame of a motion picture reel must be cleaned carefully by experts, and, for an average feature length of, for example, 2 hours or 7,200 seconds at 24 frames a second, this results in approximately 172,800 frames that have to be cleaned by hand. Aside from the mechanical method of cleaning, particular areas must also be identified, cleaned if *dirt* is present, or 'filled in' if *sparkle* found. Sparkle occurs when the film surface is scratched or scraped away, usually revealing a light surface (silver nitrate) underneath. It manifests as a small white or lightly coloured blotch in a frame of footage, see *Figure 1*.

Fig. 1. Examples of sparkle encircled in the frame above. Note that in the preceding and following frames, sparkle will not be present in the same locations.

Sparkle can occur either chemically, over time, or mechanically, through wear of repeated viewing. Dirt, however, is simply material that has stuck to the frame, as in *Figure 2*.

Fig. 2. Examples of dirt are circled above. Observe no sparkle is present at the points labeled in Fig. 1.

Both are often referred to simply as *blotches*. Given the time consuming nature of restoration, it is extremely expensive & labour intensive. In the digital era, although requiring less in the way of chemicals and physical storage, restoration is very similar to the traditional means. Once the source material has been scanned (usually using a 4K or 8K scanner) the frames are examined individually and dirt & sparkle identified, before being manually removed. The primary advantage may be said to be convenience. Digital automatic detection has been attempted, however.

II. Previous Dirt and Sparkle Detection

Industrial software exists (such as AlgoSoft, Amped and DIAMANT) – but the means of detection and success rate are unpublished; however, peer assessment & cinematic critique has not been favourable [2]. Previous academic research includes detection of dirt and sparkle by means of motion estimation and 3D autoregressive modelling – in particular, the JOMBADI (Joint Model BAsed Detection and Interpolation) algorithm [3]. The JOMBADI approach attempts to combine blotch detection and repair in a single step; a statistical model of the frame is created and motion vectors randomly adjusted until a predicted (reconstructed)

frame is reached (based on either prediction error or maximum number of iterations). This results in either very high computational loads and/or lack of accuracy. Global Motion Segmentation for blotch detection has also been attempted – using this technique, blotches are detected as 'areas' of pixels that do not adhere to *any* parametric global interframe transformation model [4]. Being exhaustive, the result is also a computational load, and is subject to the accuracies, inaccuracies and possible contradictions of the various transformation models employed. Czúni *et al* have implemented DIMORF - a neural network for semi automatic detection coupled with an XML database to minimise false positives (by meta tagging incorrect finds in a single frame, all other such instances can be ignored if found in subsequent frames) [5]. As such, DIMORF aspires more as a semi-automatic detection and indexing software system. Regardless of the means, all approaches use pixel intensities as the input data, and most of the systems to date (JOMBADI included) use block matching techniques.

III. Block Matching Algorithms

Employed extensively in the domain of video encoding, block matching generally uses motion estimated from the current frame with respect to the previous frame. A motion compensated image is then created from blocks taken from the previous frame. Each frame is divided into 'macro blocks', which are then compared with corresponding block and adjacent neighbours in the previous frame. A vector is then created that stipulates the movement of a given macro block from one location to another. The search area (of where the macro block should be located) is constrained by up to *p* pixels of the previous frame, *see Figure 3*.

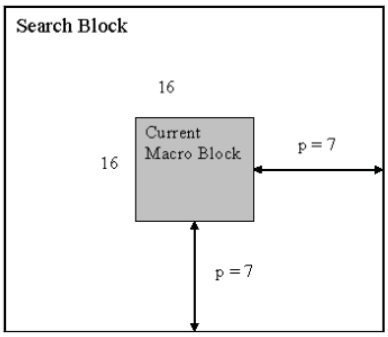

Fig. 3. A sample macroblock search space. The larger *p* becomes, the more computationally expensive the process is.

Usually the macro block is taken as a square of side 16 pixels, and the search parameter p is 7 pixels. Compression is then achieved by means of JPEG encoded difference images - inherently smaller than the full, original frame [6].

A. Implementation

The work completed to date has consisted of implementing several block matching algorithms, in order to assess their suitability for potential use in dirt/sparkle detection – previously, only a modified version of the exhaustive search block matching has been used for blotch detection [2]. These algorithms were fully implemented in Matlab, and include exhaustive search, three step search, simple and efficient three step search, new three step search, four step search, diamond search, and adaptive rood pattern search.

B. Results

As an initial means of comparison, each algorithm and their respective number of computations per frame were plotted, see *Figure 4*. In all cases, the macroblock size was set to 16, and the search parameter *p* was 7, as per the recommended values [7]. Another test was then completed with the presence of an artificial blotch at frame 15. Except for the adaptive rood pattern search, none of the other algorithms' output changed to reflect the presence of a break or discontinuity in motion estimation for a single frame, as can be seen in *Figure 5*. Adaptive rood pattern search assumes that general motion in a frame is usually coherent, *i.e.*, it attempts to anticipate the direction of the motion vectors; as the others do not use this technique, the amount of computation is unaffected. The adaptive rood pattern search alone was then run on a sample 32 frame sequence, with genuine examples of dirt & sparkle digitally copied and placed at frames 5, 10, 15 and 20. However, the resultant graphs from both runs were identical, as in *Figure 6*. Only when the macroblock size was altered (to 8) and the search parameter *p* dropped to 4 were useful results obtained, thus indicating that the detection is size and therefore parameter dependent, see *Figure 7*. The encircled plateaus in *Figure 7* that do not exist in *Figure 6* represent the adaptive rood's attempt to find the closest match; finding such plateaus indicates the location of a potential blotch.

IV. Future Work

Further analysis and alteration of adaptive rood pattern search is required - in particular macroblock & search parameter size - as well as the potential for implementing detection and eventual reconstruction of the frames via parallel means. Statistical or machine learning classifiers may be applied to suspected blotches to improve classification.

Acknowledgment

Thanks to all at the Department of Computer Science, and the Systems & Networks Department in the Computer Centre in the National University of Ireland, Maynooth.

References

[1] R.A. Harris, "Preservation: Why Are Films and Videos Disappearing?", *American Film Institute*, Washington, D.C. Public Hearing, February 1993.

[2] J. Krebs, "Creating the Video Future", Sound & Vision Magazine, Nov. 2004.

[3] A. C. Kokaram, "Advances in the detection and reconstruction of blotches in archived film and video", *Digital Restoration of Film and Video Archives* (Ref. No. 2001/049), IEE pages: 71-76

[4] T. Komatsu, T. Saito, “Detection and Restoration of Film Blotches Using Global motion Segementation,” *ICIP99* (Vol III, pages: 479-483)

[5] L. Czúni, A. Hanis, L Kovács, B. Kránicz, A. Licsár, T. Szirányi, I. Kas, Gy. Kovács, S. Manno, “Digital Motion Picture Restoration System for Film Archives (DIMORF)”, *SMPTE Motion Imaging Journal*, Vol. 113, pp. 170-176, May-June 2004.

[6] I.E.G. Richardson, “Video Codec Design”, Ch. 4-6. West Sussex John Wiley & Sons, Ltd., 2002.

[7] Y. Tu, J. Yang, Y. Shen, M. Sun, “Fast variable-size block motion estimation using merging procedure with an adaptive threshold”, ICME Vol. 2 pages: 789-792, July 2003.

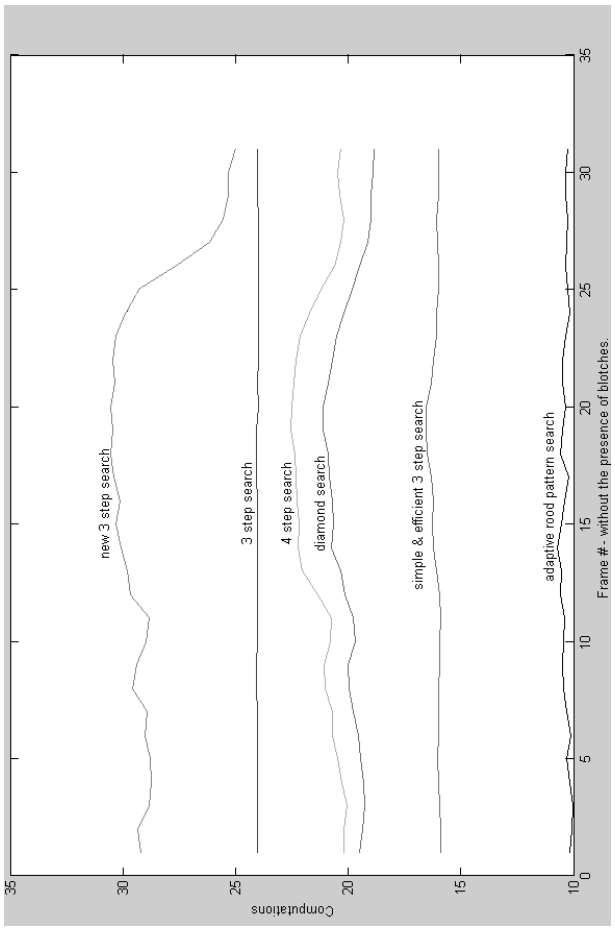

Fig. 4 - A measure of various block matching techniques, compared on the basis of number of computations per frame. The sequence was 32 black and white frames long

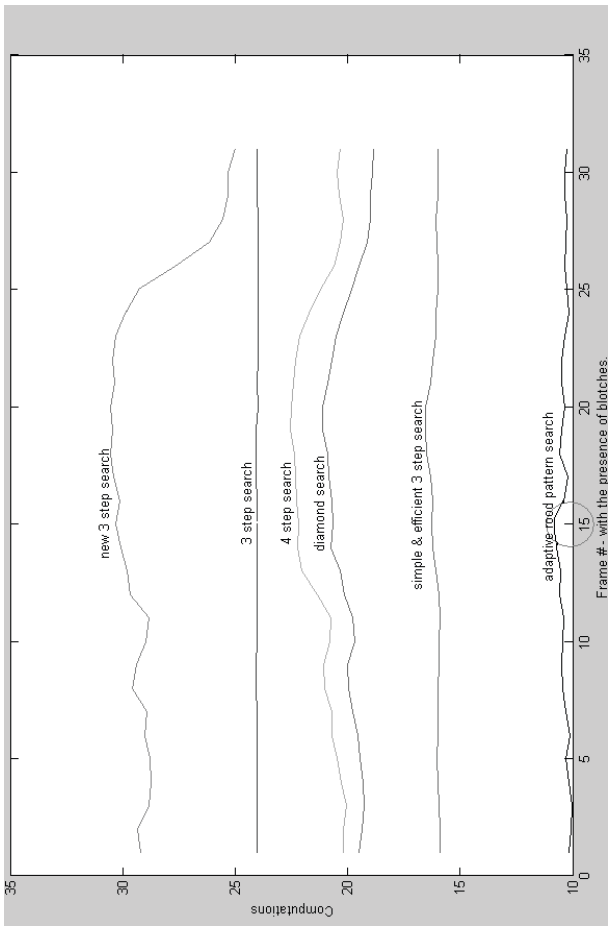

Fig. 5 - Note the change in adaptive rood at the presence of the blotch

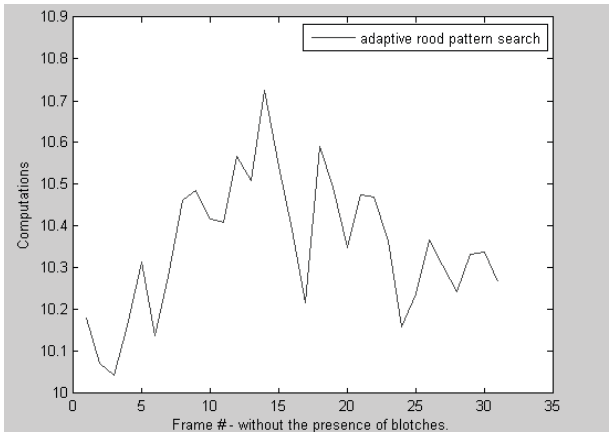

Fig. 6 - 32 frame sequence output, with macroblock and p size altered.

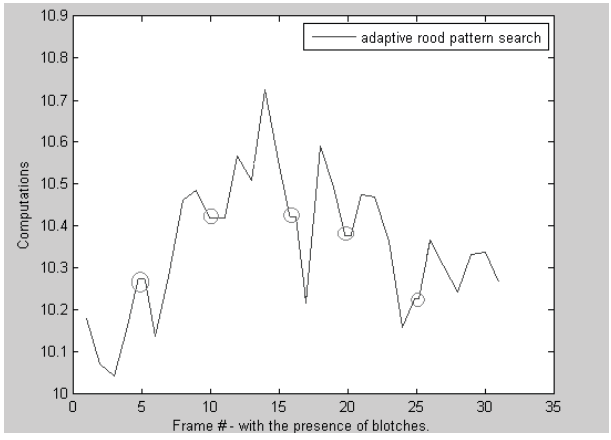

Fig. 7 - 32 frame sequence output, with blotches at the indicated frames

Section 3C

GEOSENSORS

Lightweight Signal Processing Algorithms for Human Activity Monitoring using Dual PIR-sensor Nodes

Muhammad Tahir*, Peter Hung*, Ronan Farrell*, Seán Mcloone* and Tim McCarthy†
*Institute of Microelectronics and Wireless Systems
†National Centre for Geocomputation
National University of Ireland Maynooth, Maynooth, Co. Kildare, Ireland
Email: {mtahir, phung, rfarrell, sean.mcloone}@eeng.nuim.ie, tim.mccarthy@nuim.ie

***Abstract*—A dual Pyroelectric InfraRed (PIR) sensor node is used for human activity monitoring by using simple data processing techniques. We first point out the limitations of existing approaches, employing PIR sensors, for activity monitoring. We study the spectral characteristics of the sensor data for the cases of varying distance between the sensor and moving object as well as the speed of the object under observation. The sampled data from two PIR sensors, is first processed individually to determine the activity window size, which is then fed to a simple algorithm to determine direction of motion. We also claim that human count can be obtained for special scenarios. Preliminary results of our experimentation show the effectiveness of the simple algorithm proposed and give us an avenue for estimating more involved parameters used for speed and localization.**

***Index Terms*—Multi-sensor, activity monitoring, data fusion, pyroelectric IR.**

I. Introduction

Human activity monitoring has always been of much importance, because of a large class of applications, ranging from surveillance to tracking and from smart environments to navigation. Traditionally, human activity monitoring is performed using image sensors producing large data volumes resulting in huge data processing overheads. This may be required to extract certain features of interest, for instance, number of people, position, direction and speed of motion [1] to name a few. Although activity monitoring approaches based on visual sensor solutions provide accurate results, they require large investment and significant infrastructure deployment. Contrary to that, a system based on pyroelectric infrared (PIR) sensors exploit pyroelectricity to detect an object, which is not at thermal equilibrium with its environment [2]. PIR sensors have seen wide deployments in commercial applications, to detect human presence, to trigger security alarms, to control lighting. In addition, these sensors have also found applications in thermal imaging, radiometry, thermometry as well as biometry [3], [4].

While a single PIR sensor is widely used for each surveillance region in security related applications to detect an intruder [5], multiple PIR sensors are needed for more advanced applications such as to achieve coverage [6], assist video surveillance [7] as well as perform tracking [8]. PIR sensors has been used to differentiate a still person from its background [5]. The authors in [6] have employed four PIR sensors to achieve 360° coverage while performing human detection. Since the outputs from all four PIR sensors are fed to the summing amplifier before feeding to the analog-to-digital converter (ADC), this results in inaccessibility of individual sensor outputs to the algorithm. Doing so limits the performance of the sensor node to only human detection. A video surveillance system using multi-modal sensor integration is proposed in [7], where a camera-based tracking system is integrated with a wireless PIR sensor network.

PIR sensors have also been integrated with other sensing modalities to achieve lightweight processing. The problem of localization in a dynamic environment is considered in [9] by using PIR and ultrasonic sensors simultaneously. Linear regression along with smoothing is used for distance correction leading to accurate localization. The multi-modal sensor node design in [6] integrates PIR sensors with acoustic and magnetic sensors to differentiate among humans, soldiers and vehicles. The idea is based on exploiting multiple sensor modalities to achieve the objective.

The task of human monitoring and tracking using PIR sensors can also be implemented in a hierarchical network. This involves the collective actions of sensing modules acting as slaves, a synchronization and error rejection module as a master and a data fusion module termed as a host, as discussed in [8]. In this particular implementation, the geometric sensor module is designed with multiple PIR sensors, each equipped with a Fresnel lens array to obtain a spatially modulated field of view. In addition to tracking, PIR sensors can also be used to detect, differentiate and describe human activity. A multimodal system using a dual PIR sensor node for direction of motion detection using a sensor activation sequence is presented in [7] [10]. The usage of the polarity of the first pulse produced by the sensor for determining the direction of motion limits the applicability of this approach. In [11] the authors have used PIR enabled sensor nodes with information exchange with a base station to determine the direction and number of people. However, this approach is limited due to the requirement for accurate time synchronization across the sensor nodes and

communication overhead involved. Our proposed approach partially addresses these issues by integrating two PIR sensors at each sensor node providing accurate timing for the sampled data from the two PIR sensors and eliminating associated communication overhead.

Rest of the paper is organized as follows. In Section II we discuss the approaches taken in literature to obtain the basic set of parameters, leading to an effective human activity monitoring system. Section III outlines the procedure for data acquisition and the simple algorithms used for processing that data. In Section IV we provide the results for different parameters of interest obtained using simple processing techniques discussed in Section III. Finally, we conclude in Section V with some future directions.

II. Human Activity Monitoring

Usually PIR sensors are designed as part of an overall intrusion detection system, where alarms are activated whenever a PIR output exceeds a predefined threshold. Multiple PIR sensors along with simple signal processing algorithms can be used to obtain parameters of interest for human activity monitoring (e.g. direction of motion, speed and distance of the object and counting these objects to name a few). The first step towards this objective involves distinguishing each individual object and determining its direction of motion as it enters the field-of-view (FOV) of the sensor. The next step involves counting the number of human beings passing through the sensor FOV and estimating the speed of motion. However, there are two key issues in counting the objects, passing by, and measuring their speed of motion.

The first issue is related to counting the number of people passing through the area under observation. There are situations where more than one human being, for instance multiple persons having a conversation and walking parallel to each other are passing through the FOV of the sensor and are close enough to one another that their collective PIR sensor output is almost similar to the case of one person passing. This is because the excitation duration and as a result the size of event window are proportional to human body 'thickness, which appears to be the same for the two scenarios. The second issue is related to speed measurement. Different approaches from the literature, discussed below are limited in their applicability due to the following key features of the sensor response:

- Signal strength at the output of the sensor is not only a function of distance but also speed of the moving object. For instance a relatively slow moving object at the same distance will produce a weaker signal compared to an object moving at a higher speed. This is can be seen from our experimental results shown in Fig. 1. The results in Fig. 1 also show the effect of speed on the spectral characteristics of the output signal.
- The other key aspect of the sensor signal response is the effect of the distance between the sensor and the moving object. The change in distance not only affects the signal strength, but also the spectral characteristics of the sensor response. This can be seen from the experimental results in Fig. 2, where a change in distance from 1 m to 2 m results in a frequency change from 1.2 Hz to 0.55 Hz corresponding to the strongest frequency component.

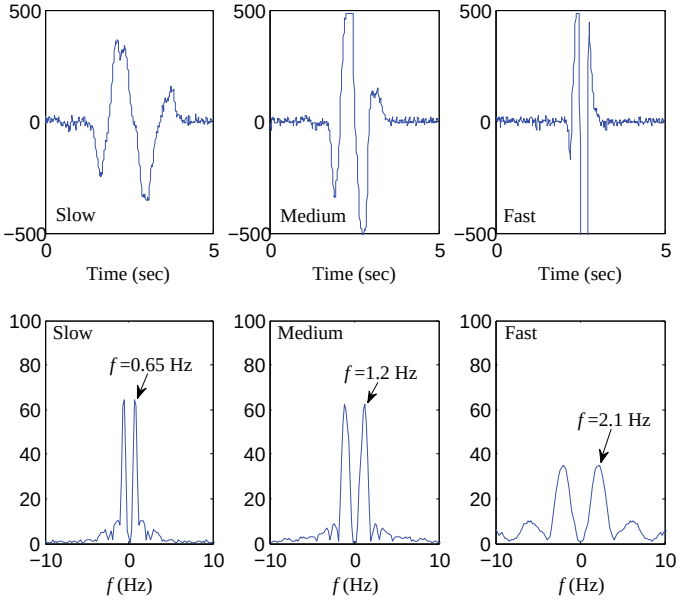

Fig. 1. Experimental results for three different speeds and the corresponding spectrum at a fixed distance form the PIR sensor.

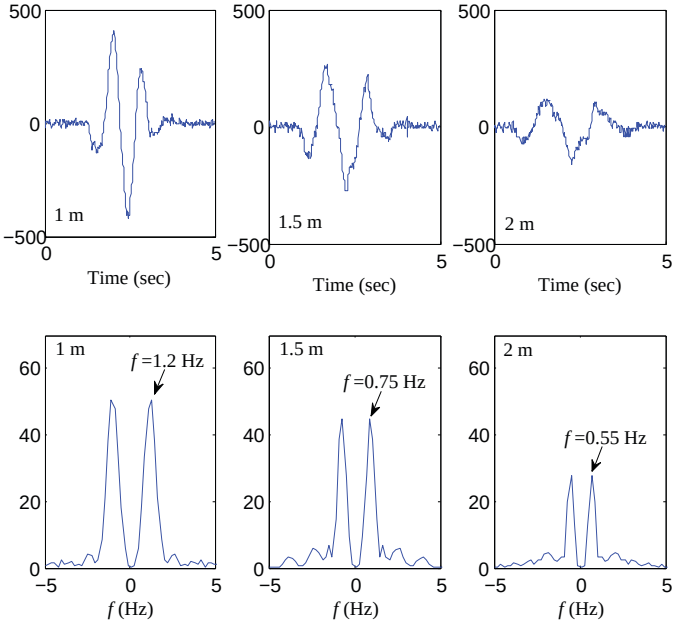

Fig. 2. Spectral characteristics as a function of varying distance between the moving human object and the PIR sensor at a fixed speed.

A. Direction of Motion

A specialized lens arrangement is used in [11] for determining the direction of motion. Specifically, the authors reduced the Fresnel lens horizontal span to a minimum, and choose

a two element PIR sensor, to obtain a phase shift of 180° in the sensor response for the opposite direction. This approach is limited, since using a different lens arrangement or a PIR sensor with an arbitrary number of elements may not give the same response. A multimodal system using a dual PIR sensor node for direction of motion detection using the sensor activation sequence is presented in [7] [10]. Our approach to the problem of direction of motion is somewhat similar to the one in [7], but we measure the phase delay in the responses from the two PIR sensors. The phase delay not only provides an accurate direction detection but also helps in estimating the speed of the moving object.

B. Human Counting

An automated people counting system using low resolution cameras along with a thermal imagery sensor is discussed in [12]. The two imaging systems complement each other in counting people for the low and high density cases. A PIR based direction of motion detection as well as counting of humans, using a specialized Fresnel lens is proposed in [13]. Three physically distributed sensor nodes along the hallway are used for counting people. Two different cases of people walking in line and walking side by side are considered and same direction of motion, for all the objects in the group, is assumed. An accuracy of 75% is claimed for the case when multiple persons are walking side by side.

C. Speed Measurement

The authors in [14] have used the frequency variations as a raw indicator of speed. Twenty repetitive independent back and forth walks are performed for three different speeds namely fast, moderate and slow, along a fixed-path (hence at same distance from the sensor). The authors do not consider the variation in the spectral characteristics as a result of varying the gap between the sensor and the walking person. As we will observe from the empirical results, there is a considerable difference in spectral characteristics due to the varying distance. Hence spectral variations alone can not be used as a measure of speed and it is necessary to take into account the effect of distance.

Another approach used for vehicular traffic speed measurement employing PIR sensors is discussed in [15]. The proposed method is based on measuring the time, the vehicle takes to traverse a fixed distance, between the footprints of the FOVs of the two sensors on the roadway. Consider an object moving at constant speed v and being detected by a PIR sensor for the time interval t. If there are two sensors placed close to each other, such that the midpoints of their FOVs are separated by a distance d, as shown in Fig. 3, then

$$d = \int_{t_1}^{t_2} v dt, \tag{1}$$

where t_1 and t_2 correspond to the time instances when the moving object reaches the sensor FOV midpoints corresponding to the center of the event window. The assumption here is that the object is moving in a narrow pathway (of width c as depicted in Fig. 3) to approximate the distance d as a constant. This results in two sensors producing approximately similar output regardless of how the moving object approaches the detector. For this fixed value of d as depicted in Fig. 3, the expression in (1) can be rewritten as

$$v = \frac{d}{t_2 - t_1} \tag{2}$$

which is used in [14] for speed measurement. The result in (2) can be used to estimate the speed of moving objects only for constant d. This result will not be valid for human activity monitoring, where the distance between the sensor and the moving object changes considerably.

D. Distance Measurement

Distance estimation using two sensor nodes is discussed in [13], where the wireless sensor nodes are installed on the opposite sides of the hallway. They use two different features, the relative amplitude and signal duration from two different sensors, for distance estimation. The results in [13] show that only region based approximate distance classification is possible using this arrangement.

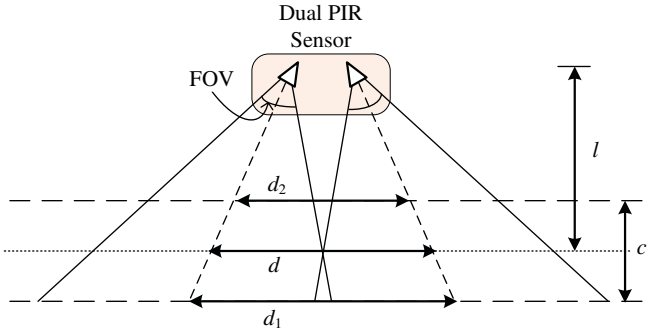

Fig. 3. Physical arrangement of two PIR sensors and their FOV. To limit the error due to relative proximity of the human object to the sensor we assume that $c/l \ll 1$ leading to $d \approx d_1$ and $d \approx d_2$.

III. Data Acquisition and Processing

The data is either sampled directly or amplified before sampling depending on the signal magnitude at the sensor output. Digital potentiometers are used for dynamic amplifier gain control to improve performance range. We have used periodic sampling at a rate of 0.1 kHz for data sampling from two PIR sensors simultaneously. The choice of the sampling rate is to cover a wide range of pedestrian walking speeds. The experiments are performed indoors under bright light conditions.

Data from two PIR sensors mounted on a single node, for distance and speed variation of a single moving object, is analyzed for the spectral characteristics. Zero padding was used to improve the resolution of our small size data set. The frequency components corresponding to peak amplitude at different distances and moving speeds are shown in Fig. 4 and Fig. 5 respectively. As can be seen from the results, an increase

in the distance results in a decrease in the frequency of the strongest spectral component. On the other hand, increasing speed leads to an increase in the frequency as expected.

A. Event Window Calculation

To facilitate human detection and motion tracking, the following data processing is proposed. The duration of each sensor excitation, including the start and end times, should first be found. Then, the number of people as well as their direction of passage through the sensor node viewpoint at a given time interval can be deduced. The RMS values of sensor outputs at event windows are recorded in an attempt to observe its relationship with distance l from the sensor as well as the speed of the moving object. Correlation analysis of delayed sensor outputs is employed to calculate the relative phase delay of both signals, one of the parameters that relates to the speed of object passage.

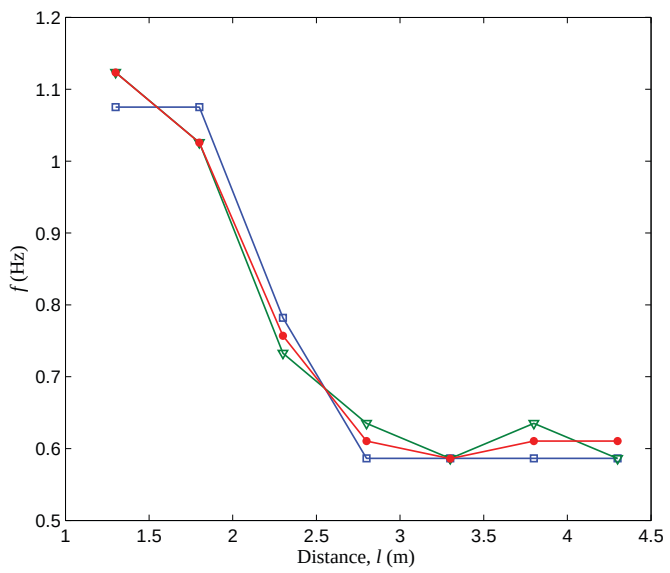

Fig. 4. Spectral characteristics as a function of distance variation between the moving human object and PIR sensor for an approximate fixed speed of 5 km/h.

The general steps used to find the duration of sensor excitation in the form of event window w is illustrated in Fig. 6. As can be seen from Fig. 6, the first low-pass filter is responsible for removing the background noise inherited in the sensor signals and can be different for indoor and outdoor situations. Currently, a third-order Butterworth filter with a cut-off frequency of 5 Hz is employed. The filtered and full-wave rectified signal is then quantized prior to the application to second low-pass filtering. Each individual temporal sensor excitation is segmented by the second first-order Butterworth low-pass filtering with a 0.5 Hz cut-off, which creates an 'enclosure' envelope for each excitation. Finally, a gradient search on the binary signal is performed in each enclosure to detect the event window start and end times, and hence the duration of sensor excitation.

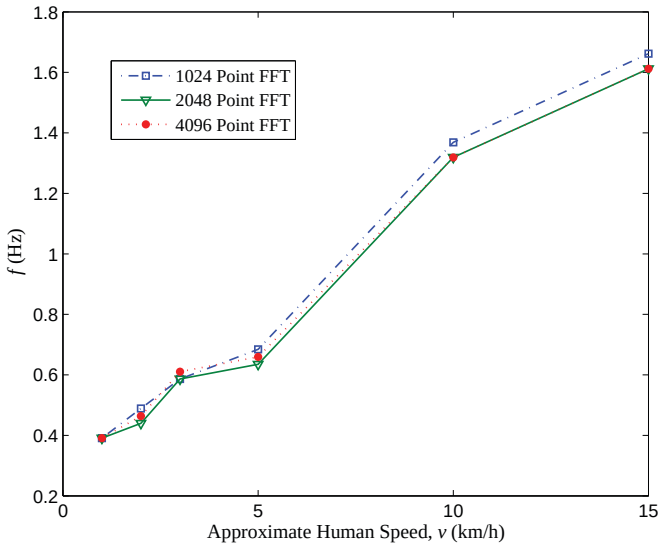

Fig. 5. Variation of spectral characteristics as a function of human speed at a fixed distance of 2.8 m. Experiments for speeds ranging from "slow walking" to "running" are performed.

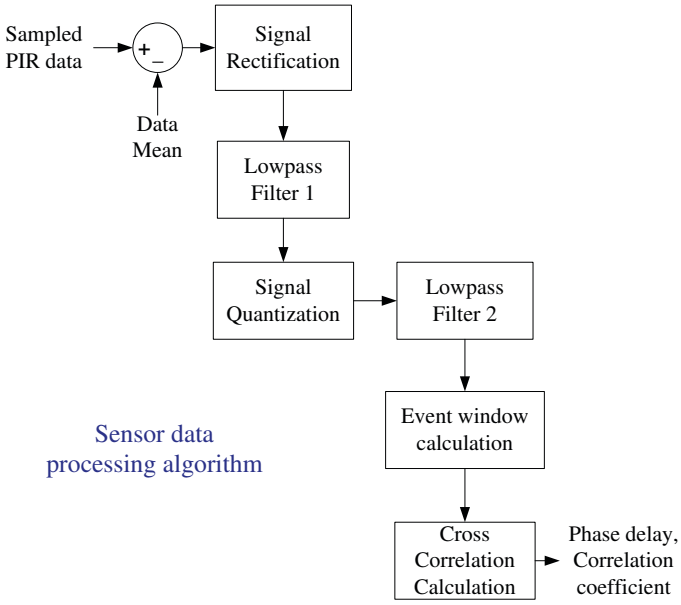

Fig. 6. Block diagram of data processing from single PIR sensor sampled at 10 msec.

During testing, a minimum distance of l (Fig. 3), currently set at 2 m, is used to prevent saturated sensor excitation. Also, it is found that the absolute mean sensor outputs provides more accurate timing information of node excitation compared to zero-mean outputs. This is because a more effective low-pass filtering is possible for non-negative signals compared to the ones with fluctuations above and below the mean value.

B. Human Counting

Due to the incorporation of two PIR sensors in a sensor node, the approaching direction of a human with respect to

the sensor node can readily be checked by comparing the sign of the phase delay between the two sensor outputs. The phase delay can be readily computed as

$$\phi_{delay} = \arg \max_{\phi}[C(y_1(t_{s_1}, t_{e_1}), -y_2(t_{s_2} + \phi, t_{e_2} + \phi))] \quad (3)$$

where ϕ is the relative phase delay in the output from sensor 2 with respect to the sensor 1 output, C denotes the cross-correlation between two signals, $y(a, b)$ represents the sensor output within interval a and b while t_s and t_e are the start and end times of an event window, respectively. Note that the negative polarity in y_2 is to account for the physical arrangement of the two PIR sensors, which are mounted $180°$ phase shifted on the sensor board. Taking this into account would produce a higher average C_{max} than performing cross-correlation analysis for the two sensor outputs with the same polarity. The magnitude of the phase delay is also related to the speed v of human motion, while the magnitude of maximum correlation,

$$C_{max} = C(y_1(t_{s_1}, t_{e_1}), -y_2(t_{s_2} + \phi_{delay}, t_{e_2} + \phi_{delay})) \quad (4)$$

indicates the accuracy of phase delay matching. A value of C_{max} approaching unity suggests near perfect matching. In practice, a maximum absolute phase delay threshold $|\phi_{max}|$ should be included in the data processing to prevent matching with sensor excitations from the previous or the following event windows.

C. Speed and Distance Measurement

Since the speed and distance affect the signal amplitude as well as frequency, it becomes a non-trivial task to measure both parameters simultaneously. One possible approach is to employ multiple sensor nodes and combined their relative position information to estimate these parameters. Alternatively, we can fix one of the parameters to estimate the other, although this leads to a solution with limited practicality. Another possible solution is to consider using multiple sensor modalities to resolve for one parameter. For instance using an ultrasonic sensor we can estimate the distance fairly accurately [9], which can be used to extract the speed from frequency.

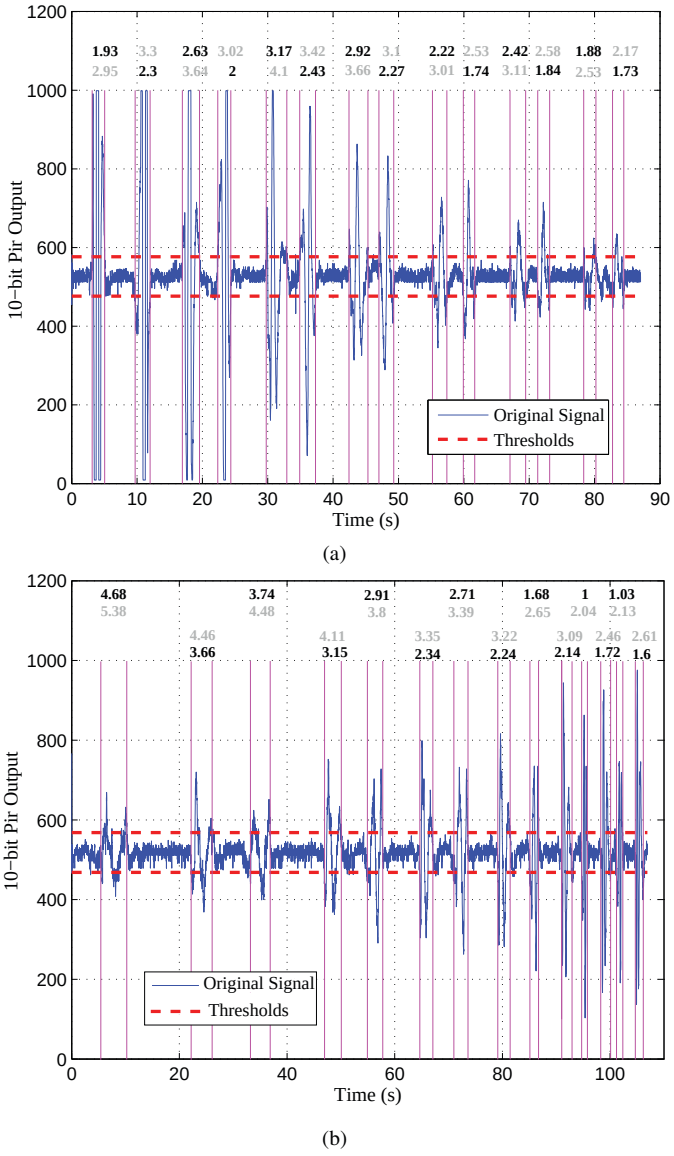

Fig. 7. The raw sensor signal for a moving object and the resulting windowed output for a given threshold level for (a) increasing distance at an approximate speed of 5 km/h, (b) increasing speed at a fixed distance of 2.8 m. The raw signal is obtained from a 10-bit ADC with thresholds at 10 and 1000 to avoid saturation.

IV. Experimental Results

This Section presents some preliminary results on human activity monitoring. Fig. 7(a) shows the raw output of one of the sensors and the event window duration (marked as vertical solid lines with their equivalent numerical values shown in black above the event window) corresponding to the variation in the distance. The numerical values in grey represent the envelop of the filtered signal. The result in Fig. 7(b) shows the results for the variation in speed. As can be observed from Fig. 7(a) that event window duration varies between 3.17s and 1.73s for different distances while for the case of speed variation the event window varies between 4.68s and 1s. By minimizing the event window variation for the case of different distances, it can be used for differentiating the signal spectral changes due to varying speed from those due to varying distance.

The data from two sensors is processed and the maximum cross correlation is computed in order to obtain the phase delay. Table I gives the phase delay corresponding to different distances. Since the person was walking back and forth in front of the two PIR sensors, the resulting phase delay has corresponding sign reversals to show the direction of motion. Table I also gives the cross-correlation coefficients at different distances. This approach for determining the direction of motion is more robust and generalized compared to the polarity based special case. An increase in the phase delay due to increasing distance is because of larger separation between

TABLE I
CROSS-CORRELATION BASED PHASE DELAY VARIATION AS A FUNCTION OF DISTANCE FOR $v = 5$ km/h.

Distance (m)	Phase Delay	Cross-correlation Coefficient
1.3	0.5100	0.7012
1.3	-0.4300	0.8341
1.8	0.7700	0.8980
1.8	-0.6300	0.8694
2.3	0.8300	0.9224
2.3	-0.8300	0.8608
2.8	1.0600	0.8730
2.8	-1.0000	0.6667
3.3	1.1200	0.7927
3.3	-1.0100	0.6537
3.8	1.3600	0.6677
3.8	-1.0900	0.5324

TABLE II
CROSS-CORRELATION BASED PHASE DELAY VARIATION AS A FUNCTION OF SPEED FOR $l = 2.8$ m.

Speed (Kmph)	Phase Delay	Cross-correlation Coefficient
1	2.6900	0.7116
1	-2.0900	0.7878
2	2.0500	0.8217
2	-1.6200	0.7995
3	1.1400	0.8341
3	-1.0800	0.8067
5	1.1000	0.8635
5	-0.9800	0.8171
10	0.6400	0.9130
10	-0.6200	0.8372
15	0.3700	0.8399
15	-0.4200	0.7909

the mid points of the FOVs of the two PIR sensors. The phase delay variation for different speeds and a single object moving back and forth, is provided in Table II. As expected, the phase delay corresponding to higher speed of motion is small, i.e. 0.37 and -0.42 in contrast to the phase delays of 2.69 and -2.09 corresponding to very slow speed.

Using the event window duration and the direction of motion, the objective of counting people can be achieved for the cases: 1) a single person enters or exits at an entrance: 2) multiple people enter or exit in a queue. In the case, where multiple people walking in a queue are close to each other, the sensor excitations do not have any region of inactivity separating the sensor excitations. However, the knowledge of phase delay can be used to get a rough estimate of the speed, which along with event window duration provides the count of the people present in the queue.

We have also studied the effect of distance and speed variations on the received signal strength. Root mean square (RMS) is used as a measure of received signal strength variation. Fig. 8 shows the normalized RMS corresponding to its event window duration as a function of distance. The results show closeness of the RMS values for two opposite directions of motion. The RMS variation as a function of the speed of the moving object is shown in Fig. 9, where the

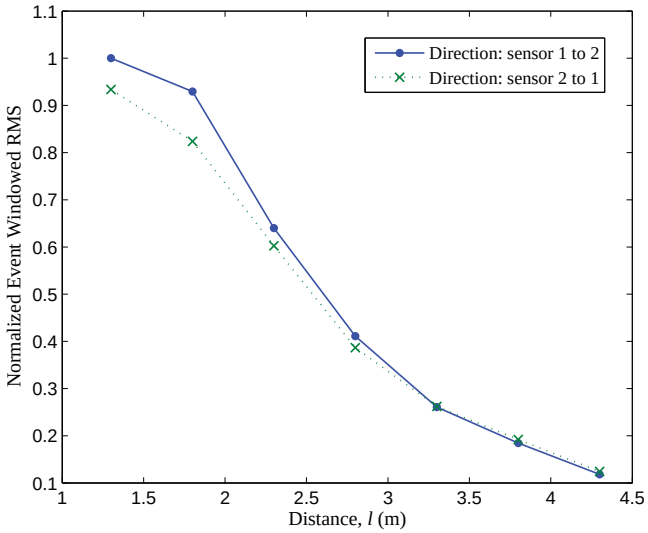

Fig. 8. The Normalized RMS, based on event window duration, as a function of distance variation for $v = 5$ km/h.

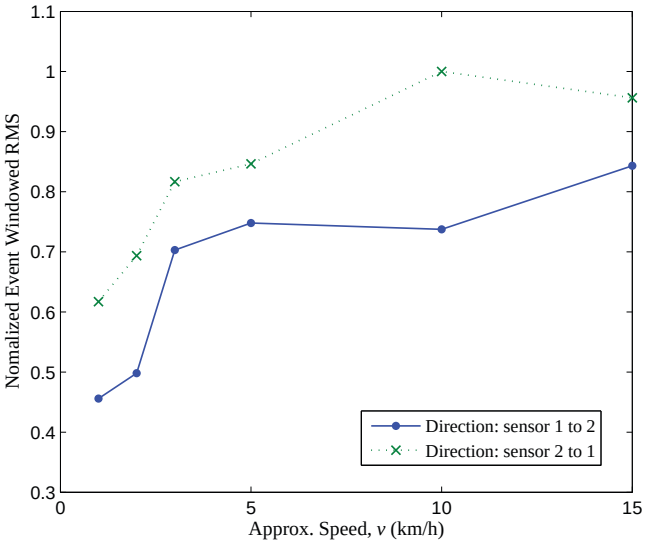

Fig. 9. The Normalized RMS, based on event window duration, as a function of speed variation for $l = 2.8$ m.

responses are different for opposite directions of motion. This is due to the fact that the two sensors had different background views.

To obtain an estimate for the speed a simple algorithm is not possible, because different parameters varying with speed are also affected by distance. For instance, as we observed earlier that the duration of event window changes from 3.17s to 1.73s at different distances for fixed speed v compared to a variation of 4.68s to 1s for the case when the speed is changed for a fixed distance l (Fig. 7). As a result we may not use event window duration for reasonably accurate estimate of distance. This implies that the use of the event window duration along with frequency and amplitude

parameters may not lead to simple algorithms to determine the distance parameter accurately. On the other hand, from Fig. 5, signal frequency changes approximately linearly and is a more reliable parameter for speed estimation by fixing the distance parameter l. Using a curve fit to the speed data in Fig. 5 we obtain the linear relationship of $f = 0.0867v + 0.3$, which can be used to estimate v provided l is fixed. In future we plan to use ultrasonic sensor for estimating the distance along with PIR sensors to develop an improved human activity monitoring system.

V. Discussion and Conclusions

We have developed lightweight signal processing algorithms for sensor nodes equipped with dual Pyroelectric InfraRed (PIR) sensors to achieve the objective of human activity monitoring. First the limitations of the existing approaches for activity monitoring are discussed. Next the spectral characteristics of the sensor data for varying distance and speed of the moving objects are analyzed. Data from dual PIR sensor nodes is first processed individually to determine the activity window size, which is then used to determine direction of motion. Human count for special scenarios can be obtained using the direction of motion and event window durations. Preliminary results of our experimentation show the effectiveness of the simple algorithms proposed. In future, we intend to extend the proposed algorithms for estimating the object speed and localization using distributed algorithms, involving multiple sensor nodes with collaborative sensing, while achieving a real time implementation.

Acknowledgment

Research presented in this paper was funded by a Strategic Research Cluster grant (07/SRC/I1168) by Science Foundation Ireland under the National Development Plan. The authors gratefully acknowledge this support.

References

[1] Q. Cai, J. Aggarwal, R. Inc, and W. Seattle, "Tracking human motion in structured environments using adistributed-camera system," *IEEE Transactions on Pattern Analysis and Machine Intelligence*, vol. 21, no. 11, pp. 1241–1247, 1999.

[2] P. Muralt, "Micromachined infrared detectors based on pyroelectric thin films," *Reports on Progress in Physics*, vol. 64, no. 10, p. 1339, 2001.

[3] C. Tsai and M. Young, "Pyroelectric infrared sensor-based thermometer for monitoring indoor objects," *Review of Scientific Instruments*, vol. 74, p. 5267, 2003.

[4] J. Fang, Q. Hao, D. Brady, M. Shankar, B. Guenther, N. Pitsianis, and K. Hsu, "Path-dependent human identification using a pyroelectric infrared sensor and Fresnel lens arrays," *Optics Express*, vol. 14, no. 2, pp. 609–624, 2006.

[5] D. Karuppiah, P. Deegan, E. Araujo, Y. Yang, G. Holness, Z. Zhu, B. Lerner, R. Grupen, and E. Riseman, "Software mode changes for continuous motion tracking," *Lecture notes in computer science*, pp. 161–180, 2001.

[6] A. Arora, R. Ramnath, E. Ertin, P. Sinha, S. Bapat, V. Naik, V. Kulathumani, H. Zhang, H. Cao, M. Sridharan *et al.*, "Exscal: Elements of an extreme scale wireless sensor network," in *11th IEEE International Conference on Embedded and Real-Time Computing Systems and Applications*, 2005, pp. 102–108.

[7] A. Prati, R. Vezzani, L. Benini, E. Farella, and P. Zappi, "An integrated multi-modal sensor network for video surveillance," in *Proceedings of the third ACM international workshop on Video Surveillance & sensor networks*, 2005, pp. 95–102.

[8] Q. Hao, D. Brady, B. Guenther, J. Burchett, M. Shankar, and S. Feller, "Human tracking with wireless distributed pyroelectric sensors," *IEEE Sensors Journal*, vol. 6, no. 6, pp. 1683–1696, 2006.

[9] D. Kim, J. Choi, M. Lim, and S. Park, "Distance correction system for localization based on linear regression and smoothing in ambient intelligence display," in *Proceedings of Annual International Conference of the IEEE Engineering in Medicine and Biology Society*, 2008, pp. 1443–1446.

[10] R. Cucchiara, A. Prati, R. Vezzani, L. Benini, E. Farella, and P. Zappi, "Using a wireless sensor network to enhance video surveillance," *Journal of Ubiquitous Computing Intelligence*, vol. 1, pp. 1–11, 2006.

[11] P. Zappi, E. Farella, and L. Benini, "Enhancing the spatial resolution of presence detection in a PIR based wireless surveillance network," in *IEEE Conference on Advanced Video and Signal Based Surveillance*, 2007, pp. 295–300.

[12] I. Amin, A. Taylor, F. Junejo, A. Al-Habaibeh, and R. Parkin, "Automated people-counting by using low-resolution infrared and visual cameras," *Measurement*, vol. 41, no. 6, pp. 589–599, 2008.

[13] P. Zappi, E. Farella, and L. Benini, "Pyroelectric InfraRed sensors based distance estimation," in *IEEE Sensors*, 2008, pp. 716–719.

[14] J. Fang, Q. Hao, D. Brady, B. Guenther, and K. Hsu, "A pyroelectric infrared biometric system for real-time walker recognition by use of a maximum likelihood principal components estimation (MLPCE) method," *Optics Express*, vol. 15, no. 6, pp. 3271–3284, 2007.

[15] T. Hussain, A. Baig, T. Saadawi, and S. Ahmed, "Infrared pyroelectric sensor for detection of vehicular traffic using digital signal processing techniques," *IEEE transactions on vehicular technology*, vol. 44, no. 3, pp. 683–689, 1995.

Wavelength modulated off-axis integrated cavity system for trace H_2S measurements

Haitao Gu[1,2], Dahai Yu[3], Xia Li[3], Xiumin Gao[2], Wei Huang[3], Stephen Daniels[1], Jian Wang[3]
1. Dublin City University, Dublin 9, Irland
2. School of Electronics and Information, Hangzhou Dianzi University, Hangzhou 310018
3. Focused Photonics (Hangzhou) Inc. Hangzhou 310052
E-mail: jian_wang@fpi-inc.com

Abstract

Trace level measurements of gases play important roles in many fields, especially in industrial process control for purpose of optimizing the process, reducing the energy consumption, improving the production efficiency and safety. In this article as example, 0-20ppm trace H_2S in natural gas has been measured by means of off-axis integrated cavity output spectroscopy (OA-ICOS) technology. The off-axis alignment geometry was used to eliminate the problem of mode matching between laser and optical resonant cavity. And in order to gain higher measurement resolution, the wavelength modulation technique was also employed in the system. Experiments demonstrated that the repeatability of instrument in H_2S measurement was 0.30ppm (3σ) and the linearity was less than 3% F.S., which met the requirement of trace H_2S measurements in petrochemical or natural gas industry.

Keyword: *OA-ICOS, DLAS, wavelength modulation, H_2S*

1. Introduction

Accurate measurement for trace H_2S is much significant to petrochemical process analysis, natural gas storage and transportation security, environmental monitoring and health care. For instance, purification plant, gas transport stations and CNG (compressed natural gas) stations need to measure the trace H_2S in range of 0-20ppm in order to prevent corrosion of pipelines. Traditional methods for H_2S measurement include lead acetate strips, gas chromatography and electrochemical technology. But the disadvantages of these methods are high drift, slow response, etc. In addition, lead acetate strips and gas chromatography will consume a large amount of materials and high maintaining costs. Diode laser absorption spectroscopy (DLAS) can solve above problems, however, DLAS can not detect such a low concentration of H_2S [1].

Various methods and techniques based on DLAS have been developed, which include direct absorption spectroscopy[2], wavelength modulation (WM) spectroscopy and frequency modulation (FM) spectroscopy[3], photo-acoustic spectroscopy[4], cavity ring-down spectroscopy (CRDS)[5], cavity enhanced absorption spectroscopy (CEAS)[6] and integrated cavity output spectroscopy (ICOS)[7], etc. They all show different sensitivity and accuracy in trace gas measurement. In 2001, J. B. Paul[8] proposed the off-axis integrated cavity output spectroscopy, which had simple structure and it was a great improvement for high finesse optical cavity spectroscopy.

Combining the advantages of OA-ICOS and WM-DLAS, this paper has developed a gas analysis instrument with simple structure. This instrument uses diode laser and photoelectric detector without piezoelectric transducer, chopper, APD, and other complex and expensive devices which makes the instrument more stable and cheaper. Meanwhile, the instrument uses wavelength modulation methods, which compress the noise and achieve the higher detection sensitivity. In this article, the trace H_2S in range of 0-20ppm is accurately and sensitively measured using OA-ICOS in near infrared wavelength.

2. OA-ICOS principle

2.1. The cavity mode matching

From the Fabry-Perot theory, the stability condition of optical resonator defined by the inequality:

$$0 < (1 - \frac{d}{R_1})(1 - \frac{d}{R_2}) < 1 \qquad [1]$$

where d is the cavity length, R_1 and R_2 are the mirror curvatures. In the resonant cavity, the light beam can reflect multiple times between high reflectivity mirrors for tens of thousands of times. However, the interference of cavity resonances arises because of the periodic boundary condition imposed by the mirror surfaces. Only the light which frequency matches the resonance transmission spectrum can pass through the cavity and the other beams will be compressed. In the case of coaxial, the FSR (free spectral range) of the cavity is directly determined by the cavity length. In the coaxial cavity ring-down cavity and coaxial ICOS, piezoelectric transducer is often used to change the cavity length, so that the single-frequency laser can be locked to a separate single resonance mode of the cavity. It is therefore complex and expensive.

In the 1960s, Herriott and others first investigated the off-axis coupling into the optical cavity [9, 10] and the OA-ICOS was developed based on Herriott's off-axis aligning[8]. In the off-axis aligning case, the laser beam makes multiple reflections within the cavity before two light spots overlap on one mirror surface. The resonance distance increases remarkably, and the FSR therefore reduces. If the number of optical round-trip passes is much enough and FSR will small enough, and the cavity transmission will be averaged versus frequency. That means the light beam can pass through the cavity without mode matching between single frequency laser and resonance mode of cavity. For example, 0.5 m length cavity has the FSR of 300MHz, if the beam passes 100 round trips, the cavity resonance distance will be 200 times of cavity length, the FSR at this time reduced to only 1.5MHz, but the line-width of diode laser used in spectroscopy is about 10 ~ 100MHz, and the FWHM of the gas absorption lines in near-infrared wavelength is in the 1GHz magnitude. In this paper, the number of optical round-trip passes has been increased to 300 times. The mode matching problem has been solved successfully.

2.2. Absorption enhancement

In the OA-ICOS, light transmission also follows the Beer-Lambert Law:

$$I = I_0 e^{-\alpha(v)L} = I_0 e^{-C\sigma(v)L} \qquad [2]$$

where I_0 is the intensity of incident light, $\alpha(v)$ is the absorbance in unit length, C is the concentration of gas, σ is absorption cross-section, L is the effective optical path length, v is the center frequency of absorption line.

Laser beam goes through the gas in cavity many times and the effective optical path length increases remarkably. In OA-ICOS, effective optical path length is related to the reflectivity of the cavity mirrors, cavity length and other parameters, as follows [11]:

$$L = \frac{-1}{\alpha(v)} \ln[\frac{(1-R^2)e^{-\alpha(v)d}}{1-R^2 e^{-2\alpha(v)d}}] \qquad [3]$$

where R is the reflectivity, d is cavity length. If $R = 99.97\%$, $\alpha(v) = 6.5 \times 10^{-8}\, cm^{-1}$ (equivalent to 10ppm H_2S gas absorption in the 1cm length), $d = 0.5m$, the effective optical path length will be $L = 1666m$, which increased of 3333 times of cavity length. Compare to the traditional single path length instrument, absorption has been increased remarkable and much lower minimum detection limit is achieved.

2.3. WM-DLAS

OA-ICOS is combined with the high sensitivity WM-DLAS technology. The diode laser is tuned by a modulation signal, which combines sinusoidal wave signal and triangle wave signal. Laser wavelength tuned by the triangle wave signal scans the absorption line of measured gas. And the wavelength is modulated by sinusoidal wave signal simultaneously. The transmission signals are received by photo-electronic detector and passed through the high-pass filter, then a phase-sensitive detector "locks in" and amplifies the second harmonic signals. The signals are proportional to the concentration of gas [12], as follows:

$$\begin{aligned} S_{2f} &\propto I_0 H_2(v,a) \\ &= I_0 \{\frac{S(T)PCL}{\pi} \int_{-\pi}^{\pi} g[\bar{v} - v_0 + a\cos(u)] \times \cos(2u) du\} \end{aligned} \qquad [4]$$

where $S(T)$ is the absorption intensity of the absorption lines, the linear function $g[\bar{v} - v_0 + a\cos(u)]$ represents the shape of the absorption lines, P is the pressure. At the same time, the photo-electronic detector signals pass through the low-pass filter, so we can get DC components:

$$DC = I_0 \qquad [5]$$

From equation 4 and 5, the gas concentration can be solved:

$$C = \frac{S_{2f} / DC}{KPLS(T)B(P,T)} \qquad [6]$$

where $B(P,T)=\int_{-\pi}^{\pi} g[\bar{v}-v_0+a\cos(u)]\times\cos(2u)du$ is the compensation matrix which is related to the shape of absorption lines, K is calibration factor, and b_0 is zero factor.

3. Experimental

The experimental setup employed in the present work is depicted in figure 1. Highly reflective 25.4 mm diameter concave mirrors (1 m radius of curvature) separated by a 50 cm stainless steel spacer formed the optical OA-ICOS cavity. The reflection coefficient for the ultra-low-loss mirror was estimated to be $R \geq$ 99.95% using a CDRS approach. After focused by a small aperture convex lens, the laser beam was collimated. Collimated light was injected into the cavity through one mirror. And the angle between light and cavity axis was about 1º. At the other side of the cavity, a convex lens was used to collect emission beam from cavity, and a photoelectric detector was placed at the focal point of the lens. After processed by circuit, the DC signal and second harmonic signals (S_{2f}) were derived from the signals received by photoelectric detector. Then the gas concentration can be solved by equation 6.

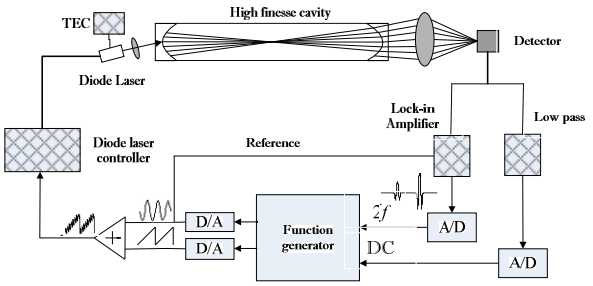

Figure 1. The schematic diagram of the instrument

A DFB laser was used as light source operating in the near infrared. Frequency turning of the single mode diode laser can be carried out by the current (over more than 1 cm^{-1}). Laser modulation signals were generated by a function generator. The frequency of sinusoidal wave was 15 kHz, frequency of triangle wave was 100Hz, and triangle-wave range determined the scan range of laser wavelength.

In this article, the measured absorption line of H_2S was in 1.55μm wavelength region[1]. Under the normal pressure and room temperature, the absorbance of 1% H_2S in 1 cm path length is 6.5×10^{-5} cm^{-1}. The following diagram is the absorption spectrum of H_2S in near infrared region:

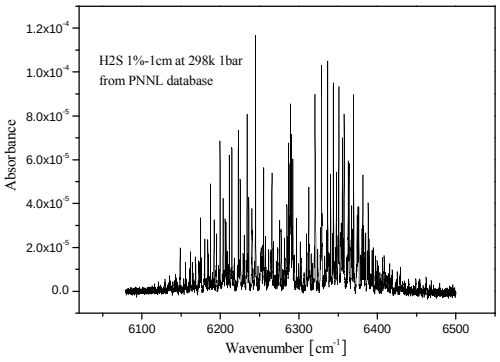

Figure 2. Absorption spectrum of H_2S in 1% concentration and 1 cm path length under normal pressure and room temperature.

4. Results and discussion

4.1. Linearity

The full measurement range of the H_2S was 20ppm. after zero calibration, 35% F.S. (7ppm), 50% F.S. (10ppm), and 70% F.S. (14ppm) of standard gas were separately flowed through cavity. Second harmonic signals are showed as following figure 3, as well as the figure which shows the relationship between signal intensity and the concentration in the upper right corner of figure 3. The linearity is less than 3% F.S. .

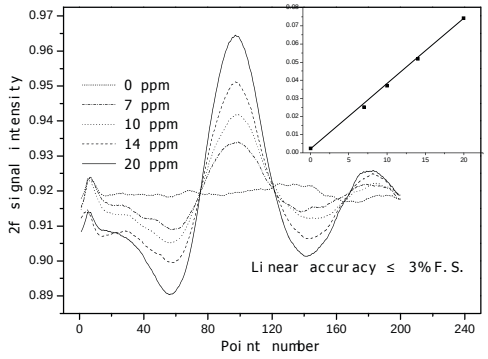

Figure 3. Linearity of the instrument in H_2S measurement

4.2. Repeatability

With different concentrations of H_2S standard gas, the measurement results are shows in the figure 4. The peak-to-peak deviations of output with constant input can be calculated from figure 4. The measurement

repeatability is normally defined as 3 times of statistical standard deviation, $3\sigma = 0.30\text{ppm}$.

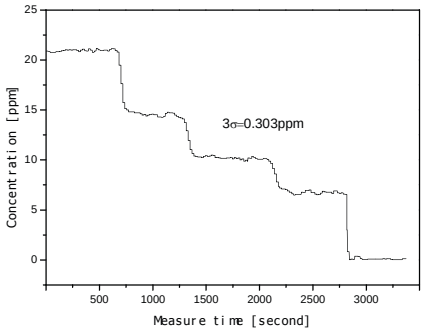

Figure 4. The measurement repeatability of the instrument in H_2S measurement

4.3. H_2S measurements in natural gas

When measuring natural gas, methane absorption lines are common. Methane has several overtone and combination absorption bands in the near-infrared wavelength range. At a wavelength of 1.56~1.63μm, H_2S has strong absorption lines, but methane is still absorbing light at a low level. The situation is fairly similar in the case of other hydrocarbons, too. Due to the lack of rotationally resolved absorption lines these molecules have broad background-like absorption, which varies slowly within the wavelength-tuning range of the diode laser. It became obvious that reliable measurement of H_2S in nature gas was only possible if a reference gas that had the H_2S removed was used to determine and subtract the methane content from the H_2S measurement. Figure 5. shows the spectral response of the H_2S analyser using this differential method. Figure 6. illustrates the linearity of the system. The reference gas was generated by letting the natural gas flow through an absorbing cell that contained Fe_2O_3 and FeO as a H_2S scrubber.

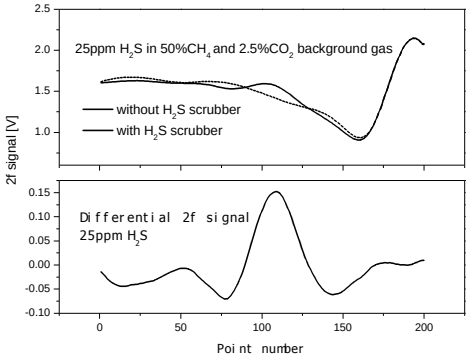

Figure 5. Spectral response to H_2S using a differential method

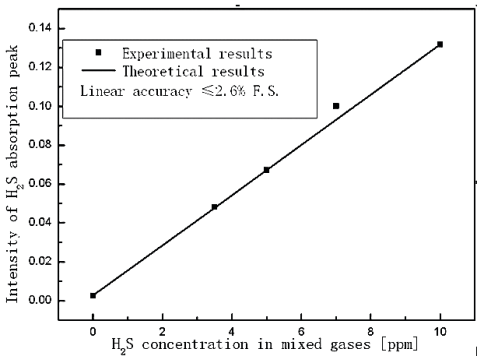

Figure 6. The linearity of 0~10ppm H_2S

5. Conclusion

In this article, we have measured trace H_2S by a combination of OA-ICOS and WM-DLAS. Laser beam is injected into the high finesse resonant cavity by off-axis aligning methods. It resolves the mode matching problem between laser frequency and mode of resonant cavity, and simplifies the structure of instrument. By combined with WM-DLAS technology, it improves the detection sensitivity of the instrument. By making light beam multiple reflect in high finesse resonant cavity, it increases the effective optical path length significantly, so that lower minimum detection limit. Experiments demonstrate that the measurement repeatability of instrument is 0.303ppm (3σ), linearity is less than ± 3% in range of 0-20ppm. The instrument meets the trace H_2S measurement requirement in petrochemical and natural gas industry.

Acknowledgement: This work was supported by National Natural Science Foundation of China (50574035) and National 863 Project of China (2006AA040310, 2007AA04Z196).

10. References

[1] Weldon, V., Gorman, J.O', Phelan, P., Hegarty, J., Tanbun-Ek, T., "H_2S and CO_2 gas sensing using DFB laser diodes emitting at 1.57μm," *Sensors and Actuators B*., 29,1995, pp.101-107.

[2] Allen, M.G., "Diode laser absorption sensors for gas-dynamic and combustion flows," *Meas. Sci. Technol.*, 9, 1998, pp.545-562.

[3] Bomse, D.S., Stanton, A.C., Silver, J.A., "Frequency modulation and wavelength modulation spectroscopies comparison of experimental methods using a lead salt diode," *Appl. Opt.*, 31, 1992, pp. 718-731.

[4] Varga, A., Bozoki, Z., Szakall, M., Szabo, G., "Photoacoustic system for on-line process monitoring of hydrogen sulfide (H_2S) concentration in natural gas streams," *Appl. Phys. B*, 85, 2006, pp. 315-321.

[5] Keefe, A.O', Deacon, D.A.G., "Cavity ring-down optical spectrometer for absorption measurement using pulsed laser sources," *Rev. Sci. Instrum.*, 59(12), 1988, pp. 2544-2551.
[6] Engeln, R., Berden, G., Peeters, R., Meijer, G., "Cavity enhanced absorption and cavity enhanced magnetic rotation spectroscopy," *Rev. Sci. Instrum.*, 69, 1998, pp. 3763-3769.
[7] Keefe, A.O', "Integrated cavity output analysis of ultra-weak absorption," *Chem. Phys. Lett.*, 293, 1998, pp. 331-336.
[8] Paul, J.B., Lapson, L., Anderson, J.G., "Ultra sensitive absorption spectroscopy with a high-finesse optical cavity and off-axis alignment," *Appl. Opt.*, 40(27), 2001, 4904-4910.
[9] Herriott, D.R., Kogelnik, H., Kompfner, R., "Off-axis paths in spherical mirror interferometers," *Appl. Opt.*, 3, 1964, pp. 523-526.
[10] Herriott, D.R., Schulte, H.J., "Folded optical delay lines," *Appl. Opt.*, 4,1965, pp. 883-889.
[11] Fiedler, S.E., Hese, A., Ruth, A.A., "Incoherent broad band cavity-enhanced absorption spectroscopy," *Chem. Phys. Lett.*, 371, 2003, pp. 284-294.
[12] Wang, J., Maiorov, M., Baer, D., et al., "In situ combustion measurements of CO with diode-laser absorption near 2.3um," *Appl. Optics.*, 39(30), 2000, pp. 5579-5589.

Integrated air quality monitoring: applications of geosensor networks

Jer Hayes[¥], King-Tong Lau*, Roberty J. McCarhty[¥], Dermot Diamond*
*Clarity – centre for sensor web technologies, Dublin City University, Glasnevin, Dublin 9, Ireland
[¥]IBM, Innovative environmental solutions, Mulhuddart, Dublin 15, Ireland
E-mail: hayesjer@ie.ibm.com; kim.lau@dcu.ie; rjmccarthy@ie.ibm.com; dermot.diamond@dcu.ie

Abstract

Worldwide environmental monitoring has become evermore important due to the increasing pollution caused by human activities and also as a result of climate change. The measurement of a wide spectrum of environmental parameters is very labour intensive and costly using the current conventional sampling methods whereby samples are normally collected and transported to laboratory for analysis or hand held devices are used for on-the-spot measurements. These approaches are expensive and result in very low measurement frequency. To increase temporal and spatial resolution, geosensor networks using various techniques including wireless autonomous sensing, low cost sensor networks and information extraction from web available satellite remote sensing data are required. We describe and demonstrate on-going work on using remote sensing to monitor atmospheric NO_2 levels in Ireland and novel in-situ gas sensing. .

1. Introduction

Human activities are the main source of pollution in modern day society. Agricultural wastes leached out from farm land, toxic wastes emitted from various industries and commuter cars that are pumping out toxic chemicals have numerous impacts in our daily lives. It is changing the weather, affecting our health and also changes our lifestyle. Modern lifestyle is a double blade sword – it makes life more comfortable but also known to contribute greatly to environmental destruction and pollution. It was unthinkable for people in the eighties of the last century to carry with them a bottle of water whenever they went out and that the water could come from many thousand miles away. Combined with the disposable culture that was created by high through put and mass production, driven by consumer market, the level of pollution and destruction of our environment escalated at a pace the earth has never seen before.

Environmental monitoring and pollution control are becoming urgent tasks in light of the climate change we experience in recent years. As a result, water resources in some area have become less available whereas in other places, flooding and related water pollutions are occurring in higher frequency and severity. On the other hands, the ever-increasingly dependency on fossil fuels of our society, contributes to the pollution in air, land and water bodies. Consequently, environmental protection is much needed to safeguard our very own existence in this increasingly hostile world. Facing such huge scale of pollution and environmental change that affects all human lives, the task of monitoring water, soil and atmosphere parameters is also a global challenge that all countries are obliged to take considerable effort in monitoring and controlling the pollution level.

Geosensor networks are being deployed which use various techniques including wireless autonomous sensing, low cost sensor networks and information extraction from web available satellite remote sensing data to increase the temporal and spatial resolution of environmental monitoring. The adaptive sensors group [1] are involved in the development of sensors and sensor networks for air and water quality monitoring (e.g. [2,3]) as part of the Clarity, centre for sensor web technologies [4]. In-situ sensors can give precise information for particular points; they do not have sufficient coverage to give information even on regional level. Remote sensing is used to provide a more complete picture of pollutant dispersion at a much larger scale. To support in-situ sensing, remote sensing which covers larger spatial areas are required, e.g. satellite-based systems can gather data for the whole globe. We will describe and demonstrate on-going work on NO_2 levels in Ireland using remote sensing data from satellites. This includes developing visualisation techniques to automatically process and present data in a useful manner.

One example of a remote sensing satellite is the Environmental Satellite (ENVISAT) built by the European space agency (ESA). The satellite hosts a suite of instruments which can be used for measuring ocean currents and ocean topography; landscape topography and the presence of snow and ice; measuring ocean colour and biology (e.g. algal blooms); vegetation types; presence of clouds; precipitation; sea surface temperature; and atmospheric chemistry. One instrument on onboard ENVISAT is the Scanning Imaging Absorption SpectroMeter for Atmospheric CartograpHY (SCIAMACHY) instrument which is a satellite spectrometer designed to measure solar radiation transmitted, backscattered and reflected from the atmosphere. The data is recorded at relatively high resolution in the ultraviolet, visible and near infrared wavelength region. This system produces valuable raw data which are made available online in their web site. However, useful information can only be obtained after complicated data extraction and processing.

There are two basic reasons for using SCIAMACHY: (1) Pollution does not respect borders – we need to examine the trans-boundary transport of pollution. (2) There has been a worldwide increase in tropospheric green-house gases. Therefore we need to determine the situation in Ireland with respect to the rest of Europe and the World.

How do we show that pollution moves across borders? Examining the accumulation of NO_2 over long periods can reveal the location of NO_2 sources and also indicate the typical movements of this gas. In the context of Europe, Ireland has relatively low NO_2 rating (which reflects the low population).

It is often a cumbersome task to extract useful information from the vast sea of data collected by satellite-based instruments. Huge amounts of raw data are downloaded from which selected data from the geographical zone of interest are then extracted and classified. From the processed data, we apply a simple visualisation technique that allow users to browse the overall results and to find data of interest (see section II). This work is being done to complement work in wireless chemical sensors which is highlighted in section III. A complete picture outdoor air quality monitoring requires the integration of in-situ and remote sensing data.

2. Visualising data

Online web based data browsers from SCIAMACHY already exist, e.g. the SCIAMACHY tropospheric DOAS nadir data browser [5]. However, a general, low-resolution visual data are presented which falls into a number of views with the one giving the most coverage of Ireland being a European-wide view. Although such views are useful, a European-wide view will likely show the highest levels of NO_2 over parts of the UK and the Benelux countries and are not useful for in-depth analysis of individual countries such as Ireland.

For the purposes of clarity we would like to present users with a visualization of location-specific NO_2 levels with respect to a particular period such as that shown in Figure 1, which highlights Ireland and part of UK. Ideally, images of NO_2 levels are made available online where raw data from which these images are created can be accessed through the browser. Because these images are made up of boxes covering areas where average values of gas concentration are represented by a colour scheme. We consider these images as only an approximate representation of the data; especially when a long time frame is selected. These images are best used to give an overview of the gas dispersion and raw data are available when requested.

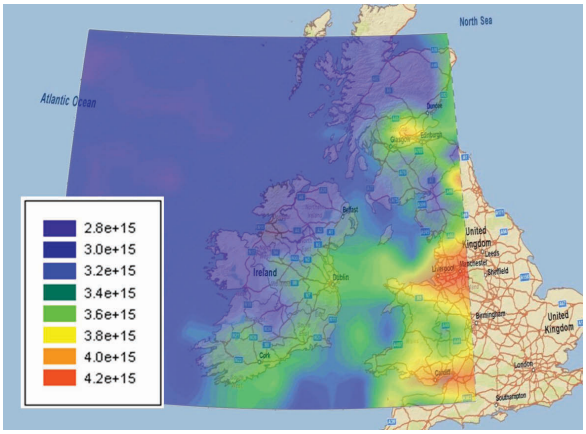

Figure 1: The NO_2 levels are measured by the SCIAMACHY instrument on the Envisat satellite. In this example the atmospheric volume directly under the satellite is observed (nadir). Each scan covers an area on the ground of up to 960 km across track with a maximum resolution of 26 km x 15 km.

In this work we use a collection of applications (including VISAN [6]) and scripts to create the images similar to that in Fig. 1. The images are represented by contour plots of NO_2 vertical column densities with geo- referencing information that can be displayed and interacted through programs such as ArcGIS explorer and Google Earth. These programs are preferred to Google Maps (see Fig. 2) as they can display more data points. These images are automatically generated from data made available by the ESA. The process of creating the contour plots works as follows: (1) Satellite data products in N1 format are converted to ASCII format using VISAN [5]; (2) the data is smoothed using inverse squares (Cauchy weight function); (3) the contour plots are created from this smoothed data (see Fig. 3). Currently contour plots are made for monthly data sets. The

colour coded data that are used to create the data plots are shown in Fig. 2, where a map-based interface is used to indicate the locations from which the data are collected.

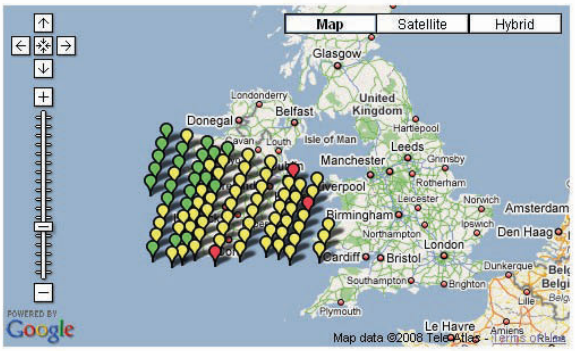

Figure 2: The SCIAMACHY instrument operates in three modes Nadir, Limb, and Occultation. For a single day the Nadir measurements do not cover all of Ireland (and the UK) and so data is typically built up over several weeks. For example, on this day although most of northern Ireland was not covered by the nadir measurement.

Monthly plots are chosen as the SCIAMACHY may pass over parts of Ireland every 1 to 3 days and measures in three viewing geometries: Nadir, Limb, and Occultation. In Nadir mode the atmospheric volume directly under the instrument (i.e. the spacecraft) is observed. In Limb mode the instrument looks at the edge of the atmosphere. Using only Nadir or Limb modes global coverage is achieved within 3 days (for 960 km swath width). So for any individual day there are blank areas where no data is available (see Fig. 2).

3. Chemical sensor networks

Yearly NO_2 data from SCHIAMACHY over the Dublin region in Ireland is presented in Fig. 4. Remote sensing data can provide background level information for parameters of interest over very large areas. However, the resolution of these sensors means that we still need in-situ sensors to provide a more accurate local pollution level to complete the picture.

Commercial gas sensors generally lack selectivity, require high operation voltage and have high power consumption. This demands the development of new low-powered novel sensing techniques that can measure gas concentrations required by the atmospheric pollution control [7]. The adoption of wireless sensor networks adds another parameter to using gas sensors; namely that they should be relatively cost effective to ensure affordability.

One interesting area is the use of colorimetric sensors whereby a colour change indicates the presence (and amount) of a chemical species. A simple polymer based colorimetric sensor can be fabricated by dissolving the pH indicator dye into a polymer solution [8]. This polymer formulation can be coated onto to the surface of low-cost optical sensor component such as LEDs. Thus a low-cost low-power wireless sensor networks based on optical sensing system can be realized (see Fig. 5). The current focus of WSN research tends to be on hardware, communication protocols and power management and also on simulation/modelling of these networks. Clearly research has to be carried out on these areas to solve fundamental issues concerned. However, sensor nodes are platforms for hosting (chemical, biochemical) sensors and, as such, consideration must also be given to the sensor development and integration as they provide the vital information on the environment.

There is still a large gap between the development of wireless sensors networks and the development of chemical sensors as research into both are still essentially discrete fields despite the growing interest in merging these two disciplines. However, Wireless chemical sensor networks have been deployed in controlled environments [3,8] but these could easily be modified to use in outdoor scenarios. These wireless chemical sensors networks can be used to compliment the remote sensing technique to provide a more complete picture of the environment.

4. Conclusions

To increase the temporal and spatial resolution of environmental monitoring, Geosensor networks are being developed. These networks use various techniques including wireless autonomous sensing, low cost sensor networks and information extraction from web available satellite remote sensing data to monitor the environment.

We described on-going work on NO_2 levels in Ireland using data from SCIAMACHY and also outlined ongoing work on wireless chemical sensor networks. Currently the satellite data is being used to provide information background levels of various tropospheric gases.

Acknowledgements

The authors wish to thank the following for their support: Science Foundation Ireland (SFI 07/CE/I1147, “Clarity: centre for sensor web technologies”), Barry Fennell of Enterprise Ireland and the European Space Agency.

5. References

[1] The Adaptive Sensors Group, http://www.dcu.ie/chemistry/asg/

[2] Christina M. McGraw, Shannon E. Stitzel, John Cleary, Conor Slater, Dermot Diamond, (2007) Autonomous microfluidic system for phosphate detection, TalantaVolume 71, Issue 3, 28, pages 1180-1185.

[3] Roderick Shepherd, Stephen Beirne, King Tong Lau, Brian Corcoran, Dermot Diamond, (2007) Monitoring chemical plumes in an environmental sensing chamber with a wireless chemical sensor network, Sensors and Actuators B: ChemicalVolume 121, Issue 1, Special Issue: 25th Anniversary of Sensors and Actuators B: Chemical, 30, Pages 142-149.

[4] CLARITY: centre for sensor web technologies, http://www.clarity-centre.org/

[5] SCIAMACHY Data Browser, http://www.iup.uni-bremen.de/doas/scia_data_browser.htm

[6] VISAN documentation, http://www.stcorp.nl/beat/documentation/visan.html

[7] A. Martin, J.P. Santos, H. Vasquez and J.A. Agapito, Study of interferences of NO2 and CO in solid state commercial sensors. Sens. Actuators B 58 (1999), pp. 469–473.

[8] Jer Hayes, Stephen Beirne, Breda M. Kiernan, Conor Slater, King-Tong Lau and Dermot Diamond (2008). Chemical Species Concentration Measurement via Wireless Sensors. In the proceedings of World Academy of Science, Engineering and Technology, Venice, Italy (2008).A.B. Smith, C.D. Jones, and E.F. Roberts, "Article Title", *Journal*, Publisher, Location, Date, pp. 1-10.

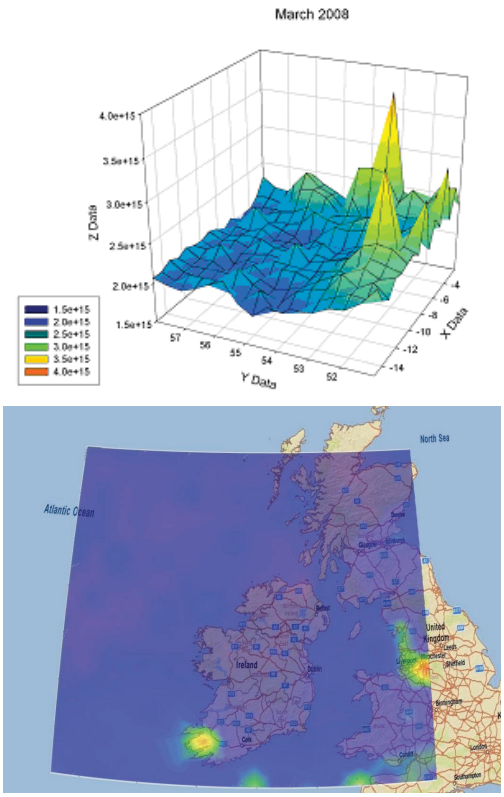

Figure 4: An image of a contour plot of NO2 vertical column densities with geo-referencing information that can be displayed and interacted with through programs such as ArcGIS explorer and Google Earth. These images are automatically generated from data made available by the European Space Agency.

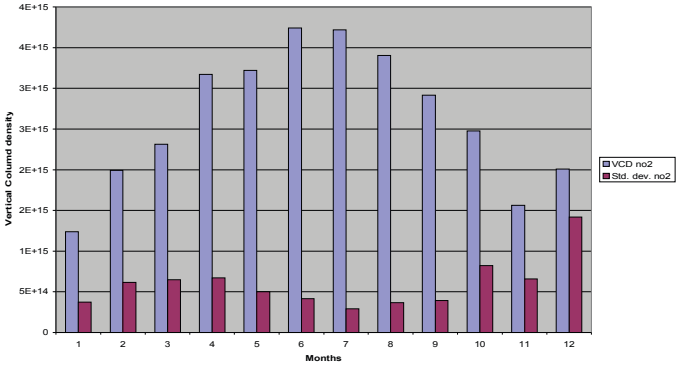

Figure 3: Monthly averages of NO_2 levels over the Dublin area for 2007. The data was derived from SCIAMACHY data products provided by the European Space Agency. Remote sensing data can provide background level information for parameters of interest over very large areas. However, the resolution of these sensors means that we still need in-situ sensors to provide a complete picture.

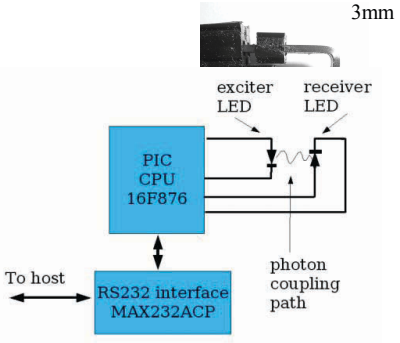

Figure 5. An example of LED based optical sensor platform.

Approximate Analysis of Fibre Delay Lines and Wavelength Converters in an Optical Burst Switch

Daniele Tafani and Conor McArdle
Research Institute for Networks & Communications Engineering,
School of Electronic Engineering, Dublin City University, Ireland
E-mail: tafanid@eeng.dcu.ie

***Abstract*—We consider an optical burst switch with and without tuneable wavelength converters and with varying numbers of fibre delay lines. We propose a virtual flow model of traffic within the switch and apply the Equivalent Random Method to resolve blocking probability analytically. Our emphasis is on approximate models with good numerical efficiency in the solution. Analytic results are compared to results from discrete-event simulations.**

I. Introduction

In recent years, Optical Burst Switching (OBS) [1] has been proposed as a possible near-term solution to utilise the capacity of deployed optical fibre efficiently. In an optical burst switch, contention occurs when two or more incoming bursts are directed to the same output channel at the same time. When this happens, a contention resolution startegy may be applied to prevent burst loss. The most common strategies involve the use of Fibre Delay Lines (FDLs) and Wavelength Converters.

There are several existing approaches to performance evaluation of OBS nodes equipped with FDLs or wavelength converters. In [2], Callegati evaluates burst blocking probability, modelling a single FDL as a queue with balking. An exact Markov chain analysis of an FDL, for correlated arrivals, is considered in [3]. An analysis of limited numbers of wavelength converters has been developed in [4] while converters with a limited conversion range are considered in [5]. Gauger [6] investigates the performance of the combination of wavelength converters and FDL buffers, through simulations.

The approach in the current paper is based on resolving a network of relatively simple queuing systems, representing virtual traffic flows within the node. This differs from previous work, which has focused mainly on detailed evaluation of single queueing system models. We apply Equivalent Random Theory (ERT) [8] to resolve blocking probability of an OBS switch equipped with both FDLs and wavelength converters. Our work most closely relates to [4] where ERT has been applied to approximate analysis of shared wavelength converters in an OBS node without FDLs.

II. Model Description

We focus on the analysis of burst blocking probability in an optical burst switch having N wavelength channels in each of P input/output ports and a bank of K fibre delay lines, which are shared by all ports (Fig. 1). Additionally, we will consider the cases of (a) full wavelength conversion, where tuneable converters at the input ports allow a burst on any incoming wavelength channel to be switched to any outgoing channel or to any channel in an FDL, where each FDL can carry up to R burst simultaneously, $R \leq N$, and (b) no wavelength conversion, where there are no converters present and an incoming burst must exit on the same wavelength as it has arrived or be delayed in one of K single-channel FDLs. We next describe the combined behaviour of the output channels, FDLs and wavelength converters, which determines how we model the overall switch behaviour.

Each FDL unit is a single fibre offering a constant delay time of D_k seconds, $k \in \{0, 1, 2, \ldots, K\}$. Delay times of the units are each a multiple of a base delay time C such that $D_k = kC$. A controller coordinates scheduling of the output channels, FDLs and wavelength converters. The controller aims to resolve contention between bursts arriving from different input ports that are destined for the same output channel. If wavelength converters are present in the switch and none of the N output channels is available for the duration of a burst arriving at a time t, an attempt is made to simultaneously schedule a free FDL channel (with delay length D_k) and any outgoing channel that will become free

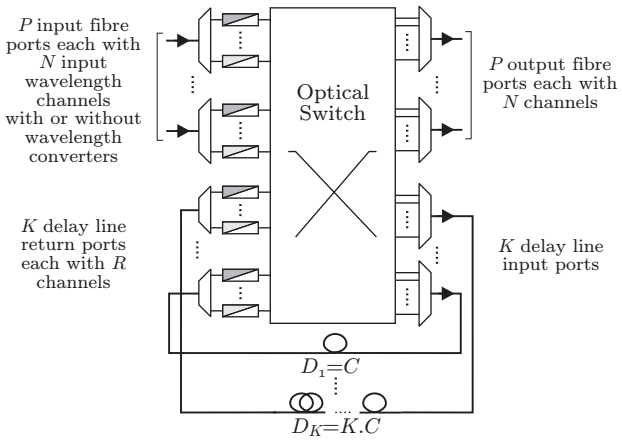

Fig. 1. Optical Burst Switch Under Study

This material is based on research supported by Science Foundation Ireland (SFI) under the Research Frontiers Programme Grant No. [08/RFP/CMS1402].

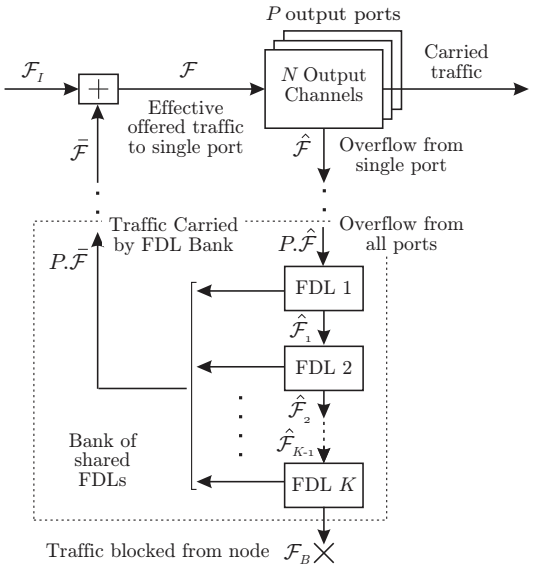

Fig. 2. Virtual Flow Model of Switch Output Port with FDLs

at time $t + D_k$. For the case of no wavelength conversion, if the burst's wavelength channel is busy, an FDL is sought that delays the burst sufficiently until that same wavelength channel becomes free. In either case, the scheduler first attempts the procedure using FDL unit 1, offering delay D_1, and iterates in sequence through successively longer FDLs until a feasible schedule is found. If none of the available FDL delay times can resolve the schedule, then the burst is blocked (lost).

A queueing model, that approximates this behaviour, is proposed in (Fig. 2). In the case of full wavelength conversion, the combined action of the output channels in an output port and the input wavelength converters is modelled as a fully accessible blocking system with N channels [9] (an $M/M/N/N$ system). In the case of no wavelength conversion, the output channels are modeled as N independent single-server blocking systems ($M/M/1/1$ systems). In either case, we may consider bursts, that would be immediately blocked at an output port if there were no FDLs present, as forming an *imaginary* overflow traffic that is offered as an input traffic flow to the bank of FDLs. This flow is indicated as $\hat{\mathcal{F}}$ in Fig. 2. The combined overflow from all P output ports, offered to the shared FDL bank, is indicated as $P \cdot \hat{\mathcal{F}}$.

The bank of FDLs is modelled as a sequence of overflowing blocking systems, with overflowing (blocked) traffic $\hat{\mathcal{F}}_k$ from FDL k feeding FDL $k+1$. The aggregate traffic carried by all FDLs, $P \cdot \bar{\mathcal{F}}$, is additional traffic that, having exited the FDL units, must then be carried by the output ports. We assume, without loss of generality, that loading across output ports is evenly distributed, as are overflow volumes from each output port, so carried traffic from the FDL bank is also evenly distributed to the P output ports, with each port receiving flow $\bar{\mathcal{F}}$.

The combination of this FDL carried traffic and the actual offered flow to each port, $\mathcal{F}_I$, is denoted $\mathcal{F}$, which we call the effective offered traffic. We assume that the actual offered traffic to the port is Poisson in nature and we assume that the feedback flow ($\bar{\mathcal{F}}$) is small in comparison with this. Thus, neglecting any traffic correlations, we assume the effective input traffic $\mathcal{F}$ is also Poisson.

Traffic which overflows from the FDL bank ($\hat{\mathcal{F}}_B$) is lost from the system. In the next section, we resolve the mean of the effective input flow $\mathcal{F}$ and, from this, the mean of the blocked traffic $\hat{\mathcal{F}}_B$, from which we may calculate the blocking probability. In developing our queuing analysis, we assume that the burst durations are exponentially distributed. We note that the validity of assuming exponentially distributed burst lengths is supported by OBS performance studies in [6] and [7].

III. Model Analysis

We first note that the traffic overflowing from the ports, subsequently offered to the bank of FDLs, is not Poisson. Thus, each FDL could be described by a $GI/M/R/R$ system, where GI denotes independent arrivals of a general distribution and R is the number of channels an FDL may carry. We also note that, alternatively to an individual $GI/M/R/R$ model for each FDL, we may model the combined chain of K FDLs as a single $GI/M/L/L$ system, where $L = K.R$ is the total number of FDLs channels in the bank, because the overflows are renewal streams under the current assumptions. This $GI/M/L/L$ model directly relates the traffic offered to the FDLs, $P \cdot \hat{\mathcal{F}}$, to the carried and overflow traffics, $P \cdot \bar{\mathcal{F}}$ and $\hat{\mathcal{F}}_B$ respectively. We treat the case of no wavelength conversion first (where $R = 1$ and $L = K$) and then extend to the case of full wavelength conversion.

A. No Wavelength Conversion

In this case, each output channel is modeled as an independent $M/M/1/1$ system and so an output port corresponds to a set of N independent $M/M/1/1$ queues. The effective offered input traffic to a port, $\mathcal{F}$ with mean intensity M, is split into N input subflows with the same mean intensity $m = M/N$, being offered to each one of the N independent $M/M/1/1$ queues. Therefore, the probability of blocking in the output port is equivalent to the probability of having one output channel busy when the mean intensity of the offered traffic is m. This probability is given by the well known Erlang B formula, of the form

$$E(A, N) = \frac{A^N}{N!} \Big/ \sum_{k=0}^{N} \frac{A^k}{k!}, \tag{1}$$

where A is the arrival intensity of the offered traffic in units of Erlangs and N is the group size (number of output channels) [10]. The arrival intensity A is given as the product of the mean arrival rate λ and the mean channel holding time $1/\mu$, where μ is the mean burst transmission rate. In our case, for one output channel the blocking probability given by (1) is simply $E(m, 1) = m/(1 + m)$.

We now wish to calculate the mean ($\hat{m}$) and variance ($\hat{v}$) of the overflow traffic from one of the N independent $M/M/1/1$ systems.

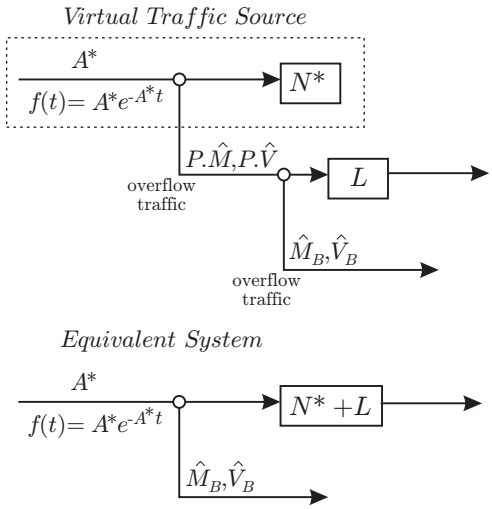

Fig. 3. Overflow System and its Equivalent for N Output Channels and L Total Channels in FDL Bank

According to the Kosten overflow equations [8], we have

$$\hat{m} = m \cdot E(m, 1) \tag{2}$$

$$\hat{v} = \hat{m}\left(1 - \hat{m} + \frac{m}{2 + \hat{m} - m}\right). \tag{3}$$

Therefore, the mean of the overflow traffic from an output port (denoted $\hat{M}$) will be given by $\hat{M} = N \cdot \hat{m}$ and, since we are assuming independence between the output channels, the overflow variance (denoted $\hat{V}$) is given by $\hat{V} = N \cdot \hat{v}$. Again, assuming independence between output ports, the total overflow traffic from all ports is described by $P \cdot \hat{M}$, $P \cdot \hat{V}$. This traffic is offered traffic to the FDL bank.

We note that the overflow traffic is "peaked" (the variance $\hat{V}$ of the traffic intensity is greater than the mean $\hat{M}$) and not Poisson. To evaluate the overflow mean from the bank of FDLs we employ Equivalent Random Theory [8]. Particularly, we introduce a virtual equivalent system with a primary group of N^* number of channels being offered Poisson traffic with mean intensity A^* (Fig. 3). We then match the overflow of this system with the offered traffic to the FDL bank. This means that the mean A^* of the equivalent Poisson offered traffic and the equivalent number of channels N^* must both satisfy the Kosten overflow system of equations,

$$P \cdot \hat{M} = A^* \cdot E(A^*, N^*) \tag{4}$$

$$P \cdot \hat{V} = P \cdot \hat{M}\left(1 - P \cdot \hat{M} + \frac{A^*}{N^* + 1 - A^* + P \cdot \hat{M}}\right). \tag{5}$$

which may be solved for A^* as a numerical root finding problem. We may choose an initial solution for the numerical solution from Rapp's approximation [9] for an overflow system:

$$A^* \approx P \cdot \hat{V} + 3\hat{Z}(\hat{Z} - 1)$$

$$N^* \approx \frac{A^*(P \cdot \hat{M} + Z)}{P \cdot \hat{M} + \hat{Z} - 1} - P \cdot \hat{M} - 1$$

where $\hat{Z}$ is the "peakedness" factor $P \cdot \hat{V}/P \cdot \hat{M}$.

In this way, we can calculate the mean ($\hat{M}_B$) and the variance ($\hat{V}_B$) of the overflow traffic from the FDLs bank employing the Brockmeyer overflow system of equations,

$$\hat{M}_B = A^* \cdot E(A^*, N^* + L) \tag{6}$$

$$\hat{V}_B = \hat{M}_B\left(1 - \hat{M}_B + \frac{A^*}{N^* + L + 1 - A^* + \hat{M}_B}\right). \tag{7}$$

Consequently, the mean of the FDLs carried traffic is given by

$$P \cdot \bar{M} = P \cdot \hat{M} - \hat{M}_B \tag{8}$$

Now, considering the feedback connection at the input, the aggregation of the actual input flow $\mathcal{F}_I$ at a single port, of mean M_I, and the carried traffic flow $\bar{\mathcal{F}}$ gives

$$M = M_I + \bar{M}, \tag{9}$$

where M, M_I and $\bar{M}$ are means of flows $\mathcal{F}$, $\mathcal{F}_I$ and $\bar{\mathcal{F}}$ respectively. We solve equation (9) numerically using a simple bisection method with initial bounds determined as follows. The lower bound on M is taken as M_I, as we are assured that the feedback flow $\bar{M}$ makes $M > M_I$. The upper bound on M is taken as $2M_I$ as the feedback flow intensity cannot be greater than M_I. Finally, having computed the FDLs overflow intensity mean, we calculate the node blocking probability as

$$\boxed{B = \hat{M}_B\,/(P \cdot\ M_I).} \tag{10}$$

B. Full Wavelength Conversion

We are now assuming that the optical switch of Fig. 1 has full wavelength conversion capability. In this case, a burst will be blocked if and only if all output channels are busy, therefore the output port can be modeled as an $M/M/N/N$ queue. The analysis follows the above approach but with overflow from one output port now given by

$$\hat{M} = M \cdot E(M, N) \tag{11}$$

$$\hat{V} = \hat{M}\left(1 - \hat{M} + \frac{M}{N + 1 + \hat{M} - M}\right). \tag{12}$$

The remainder of the analysis is the same. Given $\hat{M}$ and $\hat{V}$, the overflow from the FDL bank is calculated by (4), (5), (6) and (7). Finally equation (9) is iterated to the solution and the blocking probability calculated with Equation (10).

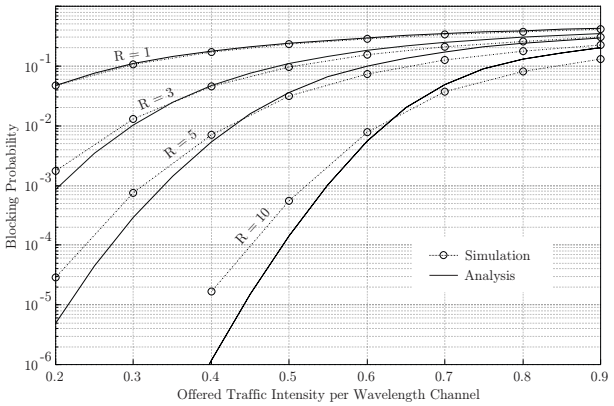

Fig. 4. Blocking Probability - 10 Channels per Output Port - 1,3,5 & 10 FDLs each with one Channel - No Wavelength Conversion

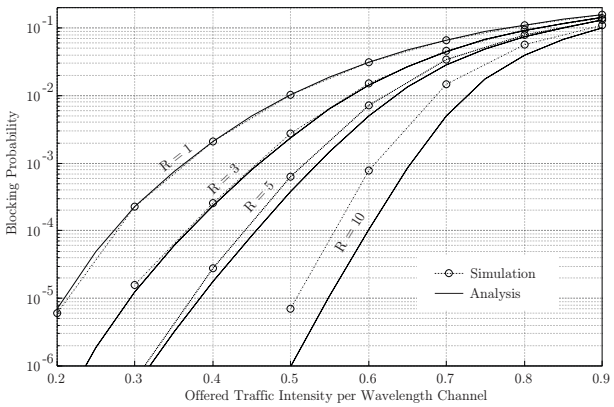

Fig. 5. Blocking Probabilit4 - 10 Channels per Output Port - 1,3,5 & 10 Channels on single FDL - Full Wavelength Conversion

IV. Results and Analysis

We compare analytic results for blocking B with results from a discrete-event simulation of an OBS node implemented in Opnet Modeler^{TM}. We consider a node with four ports and three different node configurations, (i) a node with 10 output channels with no wavelength conversion (Fig. 4), (ii) a node with 10 output channels and full conversion (Fig. 5) and (iii) a node with 40 output channels and full conversion (Fig. 6). For case (i) we compare results for different numbers of single-channel FDLs. For cases (ii) and (iii) we compare results for different numbers of channels in a single FDL.

We can observe that the values of blocking probability calculated through analysis for a small number of total FDL channels are in good agreement with the results obtained from simulation. For larger numbers of FDL channels the results provide an approximate lower bound for the full wavelength conversion case. The inaccuracy can be, at least partly, attributed to the fact that as the number of FDL channels increases the proportion of the non-Poisson traffic offered to the output channels (which we have assumed Poisson) will increase. Additionally, this traffic tends to be peaked as it is mainly characterised by the overflow traffic from the output port, and peaked traffic will result in higher actual blocking probability. For the case of no wavelength conversion and high offered load, the opposite occurs with the blocking probability being over estimated. In this case, the carried traffic from the FDLs is in reality smoother than Poisson due to the single-channel FDLs being heavily loaded enough to smooth the peaked offered traffic from the output ports.

V. Conclusions

In this paper we have proposed an approximate analysis for calculating the blocking probability in an OBS switch equipped with FDLs and wavelength converters using Equivalent Random Theory and assuming Poisson input traffic. The accuracy of the proposed analysis may be further improved if the input traffic were modelled by two moments, which is possible with ERT. This will be a topic for future work.

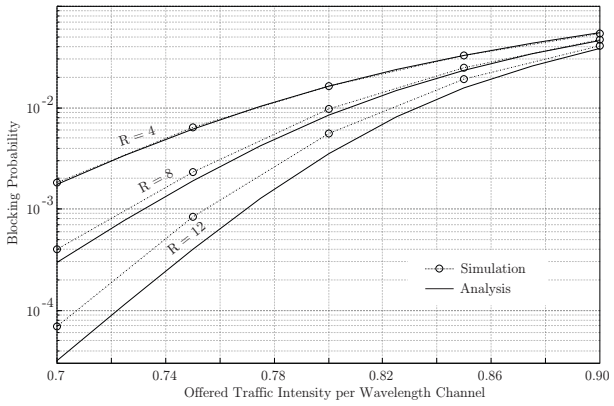

Fig. 6. Blocking Probability - 40 Channels per Output Port - 4,8 & 12 Channels on single FDL - Full Wavelength Conversion

References

[1] C. Qiao, M. Yoo, "Optical burst switching (OBS) - a new paradigm for an optical Internet," *Journal of High Speed Networks*, vol. 8, no. 1, pp. 69-84, January 1999.

[2] F. Callegati, "Optical Buffers for Variable Length Packets," *IEEE Communications Letters*, Vol.4, n.9, September 2000.

[3] W. Rogiest, D. Fiems, K. Laevens, H. Bruneel, "Exact Performance Analysis of FDL Buffers with Correlated Arrivals," *IFIP International Conference on Wireless and Optical Communications Networks*, 2007.

[4] P. Reviriego, A. M. Guidotti, C. Raffaelli, J. Aracil, "Blocking models of optical burst switches with shared wavelength converters: exact formulations and analytical approximations," *Photonic Network Communications*, vol.16, issue 1, 2008.

[5] Z. Rosberg, A. Zalesky, H. L. Vu, M. Zukerman, "Analysis of OBS Networks With Limited Wavelength Conversion," *IEEE/ACM Transactions on Networking*, vol. 14, no.5, pp. 1118-1127, October 2006.

[6] C. M. Gauger, H. Buchta, E Patzak, "Integrated Evaluation of Performance and TechnologyThroughput of Optical Burst Switching Nodes Under Dynamic Traffic," *Journal of Lightwave Technology*, vol. 26, n. 13, pp. 1969-1979, July 2008.

[7] A. Rostami, A. Wolisz, "Modeling and Synthesis of Traffic in Optical Burst-Switched Networks," *Journal of Lightwave Technology*, vol. 25, n. 10, pp. 2942-2952, October 2007.

[8] A. Girard, *Routing and Dimensioning in Circuit-Switched Networks*, Addison-Wesley Longman Publishing Company, 1990.

[9] ITU-D, Study Group 2, *Teletraffic Engineering Handbook*, URL:http://www.itu.int/ITU-D, last visited May 2009.

[10] L. Kleinrock, *Queueing Systems Volume I:Theory*, John Wiley & Sons Inc, 1975.

Section 4A

ANTENNAS AND CIRCUITS 2

Design of Integrated Stacked Spiral Thin-Film Transformer

Based on Silicon Substrate

Liang Zheng[1,2], Huibin Qin[2], Stephen Daniels[1]
1.National Centre for Plasma Science and Technology,Dublin City University,Dublin, Ireland
2. Institute of Electron Device & Application,Hangzhou Dianzi University,Hangzhou, China
E-mail:zhlbsbx@hotmail.com

Abstract

In this paper, a kind of integrated stacked Spiral thin-film transformer is presented. A lumped model is used to simulate the characteristic of the integrated transformer. The structure and manufacture process of transformer are shown based on IC technology. S-parameters are measured at 10MHz-20GHz. The result shows that the transmission efficiency of air core thin-film transformer more than 50% at 1GHz-20GHz, and the maximum is 89% at 20GHz.

1. Introduction

In the past several decades, because of the rapid development of electronic technology, high-speed electronic devices get wide spread use in radio frequency circuits and other systems, such as Bluetooth, GSM Mobile, WLAN, UWB, etc. At the same time, people need smaller electronic aid for more convenient living, it means the modern electron devices should being miniaturized, integrated and used in higher operating frequency. Now the transistor, resistor, capacitance and inductance at nH level have been integrated on chip successfully. However, the integrated technology of transformer has not well studied, which limits the development of electronic systems.

As indispensable passive components, transformer has intrinsic advantages relative to active devices on signals insulation and transmission, signals synthesis and conversion. The size of transformer is being reduced; miniature transformers like planar transformer and thin-film transformer are presented in 90's of last century. In 1993, Japanese K.Yamaguchi[1] presented a spiral coil type thin film microtransformer with the size of 2.4*3.1 mm^2 fabricated using photolithography techniques. An amorphous magnetic film of a multilayered CoNbZr/Si02 was used as magnetic core. In 2004, Irish Terence O'Donnell[2] designed a transformer having 80 μm thick copper conductors and a two-layer laminated magnetic core. The transformer had an efficiency of 78% at an output power of 3.5W in 5MHz-10MHz. In addition, people used other technologies to fabricate thin film transformer [3, 4].

However, these miniature transformers has disadvantages such as chip areas of transformer fabricated by multilayer printed technology are still too large compare with size of RFIC chip, technique of transformer using MEMS technology is complexity, etc. The most difficulty is the transmission efficiency isn't high enough in particular at high frequency. In this paper, a stacked spiral thin-film transformer working on high frequency based on IC technology is designed and prepared.

2. Equivalent circuit model of Thin-film Transformer

There are a number of parasitic effects on thin-film transformer at high frequency, such as the capacitive coupling between primary inductance spiral and secondary inductance spiral, the eddy loss of substrate, and so on. Stacked transformer, which has two overlapped spiral with same shape, can provide high self-inductance and high coupling because of its vertical and lateral magnetic coupling. A simply lumped circuit model can simulate the characteristic of transformer, and describe physical significance of the parasitic effects intuitively. The equivalent circuit model [5] is showed in figure 1.

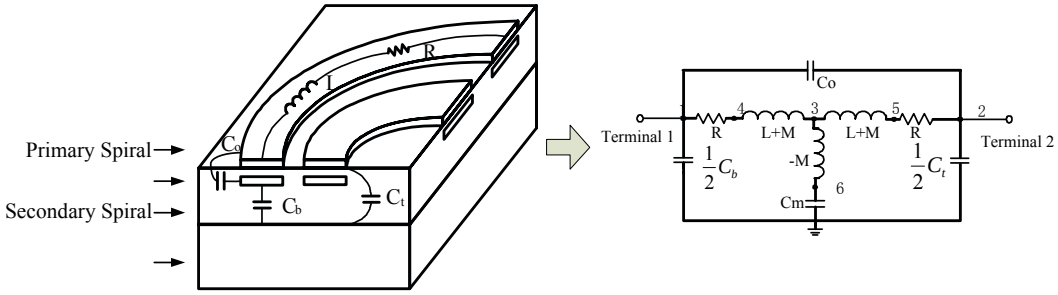

(a) (b)

Figure1. Simply lumped equivalent circuit model of thin-film transformer

In this equivalent circuit model, L models the self inductance of the primary spiral and secondary spiral, M is the mutual coupling coefficient, C_O is coupling capacity between two spirals, C_b is coupling capacity between primary spiral and substrate, C_t is coupling capacity between secondary spiral and substrate. The computing formula is showed below:

$$C_b = \frac{\varepsilon}{2t_b} lw \quad (1)$$

$$C_t = \frac{\varepsilon}{2t_t} lw \frac{A - A_{ov}}{A} \quad (2)$$

$$C_m = C_t + C_b \quad (3)$$

$$C_o = \frac{\varepsilon}{t_{t-b}} lw \frac{A_{ov}}{A} \quad (4)$$

$$R = \frac{\rho l}{\delta w(1 - e^{-t/\delta})} \quad (5)$$

$$M = kL \quad (6)$$

$$L = \frac{\mu n^2 d_{avg}}{2} \left[\ln(2.46/\rho) + 0.2\rho^2\right] \quad (7)$$

In these formulas, l is the length of the spiral, μ is permeability, ε is dielectric constant, ρ is metal resistivity, W is width of the spiral, δ is skin depth, k is mutual coupling coefficient (k of stacked transformer is about 0.7-0.9), R is series resistance, A is chip area of inductor spiral, A_{ov} is overlapped area of two spirals.

From the equivalent circuit model, it is easy to find that reduce the parasitic capacity, which is caused by spirals and substrate at high frequency, is the key point to improve the transmission efficiency of transformer.

3.Structure and Fabrication sequences of Thin-film Transformer

There are good experiences to reduce the parasitic capacity in preparation technology of integrated inductor [6, 7]. High-resistance substrate and thick substrate are adopted to reduce parasitic capacitor due to substrate loss of transformer. In this paper, an air-core stacked thin-film transformer is designed. The primary coil and secondary coil are overlapped completely. Overlapping coils has high magnetic coupling which can transmit energy more effective, the structure is showed in fig.2.

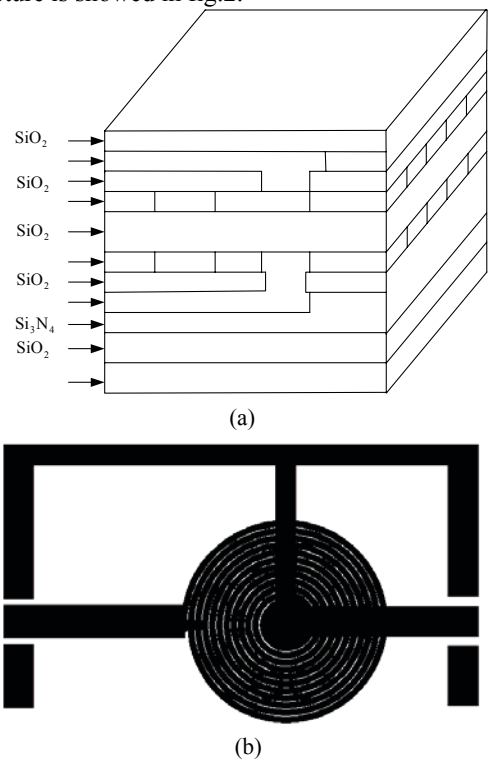

(a)

(b)

Fig. 2 Structure of thin-film transformer(a)cross-section view, (b)topview

The whole structure consists of 10 layers besides the Silicon substrate.

1) Layer 1 is SiO_2. It supplies the whole device and isolates Si substrate. Thermal oxidation is used to fabricate SiO_2 .The thickness of SiO_2 layer is 1μm, thick oxide can reduce the parasitical capacitor.

2) Layer 2 is Si_3N_4. PECVD is used to fabricate. The thickness of Si_3N_4 layer is 120 nm. The electrical resistivity of Si_3N_4 is $10^{15}\Omega$•cm, substrate with highly electrical resistivity can reduce substrate loss. Furthermore, Si_3N_4 has low-fluidity and difficult to corrupt, these characteristics can improve the compatibility of subsequent etching process.

3) Layer 3 is Metal1. Metal1 is lead wire using aluminum. DC magnetron sputtering is used to fabricate Al. Two lead terminals of primary spiral are prepared. The thickness of Al layer is 0.7 μm.

4) Layer 4 is SiO_2. SiO_2 with 1μm thickness isolate lead wire and primary spiral and fabricated by PECVD.

5) Layer 5 is primary spiral. DC magnetron sputtering is used to fabricate Al with 1μm thick.

6) Layer 6 is SiO_2. PECVD is used to prepare SiO_2. The thickness is 1μm.

7) Layer 7 is second spiral. DC magnetron sputtering is used to fabricate Al with 1μm thick.

8) Layer 8 is insulation layer. PECVD is used to fabricate SiO_2 layer with 1.2 μm thickness.

9) Layer 9 Metal4 is also lead wire using aluminum. DC magnetron sputtering is used to fabricate Al. Two lead terminals of primary spiral are prepared. The thickness of Al layer is 1.2 μm.

10) Layer 10 is passivation layer. PECVD is used to fabricate SiO2 layer with 1.2 μm thickness.

Fabrication sequence is showed in figure3.

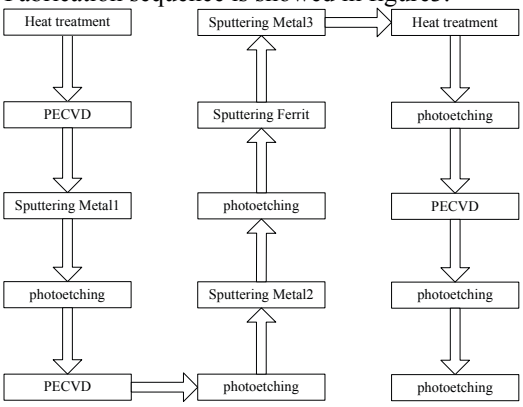

Figure3. Fabrication sequences of the thin-film transformer

4. Measurement results

A kind of thin-film transformers is measured,. The turn numbers of two spirals are all 5, the spiral width line is 12μm, the spiral distance line is 3μm, the thickness of Al layer is 1μm, and the spiral area are $0.5*0.5mm^2$. The transmission characteristics are measured at 10MHz-20GHz by vector network analyser Agilent PNA E8363B and probe Cascade Microtech ACP GSG. The measured results are showed in Fig.4.

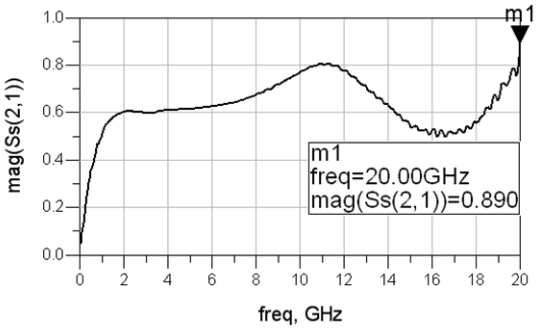

Figure 4. 5:5 transformer's S(2,1) curve

5. Conclusions

A thin-film transformer based on Si IC technology was presented. High-resistance substrate and thick substrate are adopted to reduce substrate loss. Test result shows the transformer can obtain the maximal transmission efficiency 89% at 20GHz. The thin-film transformer has advantages like small in size, operating at high frequency, suitable for mass production, and so on. It can be used in RFIC hopefully.

6. Acknowledgement

This paper is supported by National Nature Science Foundation of China (No.60601022, NO.60671024) and Natural Science Foundation of Zhejiang Province of China (No. Y107205 and No. Y407133).

7. References

[1] Yamaguchi K, Sugawara E, Nakajima O. "Load characteristics of a spiral coil type thin film microtransformer". *IEEE Transactions on Magnetics*.vol. 29, pp. 3207-3209. Nov.1993.

[2] Terence O'Donnell, Ningning Wang, Magali Brunet, Saibal Roy, et al. "Thin film micro-transformers for future power conversion". *APEC '04. Nineteenth Annual IEEE*, vol. 2, pp. 939-944. 2004.

[3] Hiroaki Tsujimoto, Ieyasu O. "High frequency transmission characteristic of co-planar film transformer fabricated on flexible polyamide film". *IEEE transactions on magnetics*, vol. 31, pp. 4232-4234. Nov. 1995.

[4] A H Miklich, J X Przybysz, T J Smith. “Superconducting thin-film transformers at microwave frequencies”. *IEEE transactions on applied superconductivity*, vol.9, pp. 3062-3065. Jun. 1999.

[5] Mohan S S The design, *modeling and optimization of on-chip inductor and transformer circuits*[D].Stanford University. 1999 : 128-129.

[6] Kirk B Ashby, Ico A Koullias, William C, et al. “High Q inductors for wireless applications in a complementary silicon bipolar process”. *IEEE Joural of solid-state circuits*, vol. 31,pp. 4-9. Jan. 1996.

[7] H B Erzgraber, Th Grabolla, H H Richter, et al. “A novel buried oxide isolation for monolithic RF inductors on silicon”. *IEDM ’98 Technical Digest*: 535-539.Dec.1998.

Equivalent Circuit Modeling for On-Wafer Interconnects on SiO_2-Si Substrate

Jun Liu[1,2], Lingling Sun[1], Huang Wang[1], Liheng Lou[1], Charles McCorkell[2]
[1] *Key Laboratory of RF Circuits and Systems, Ministry of Education, Hangzhou Dianzi University, Hangzhou, China*
[2] *School of Electronic Engineering, Dublin City University, Dublin 9, Ireland*
ljun77@163.com

Abstract

A new equivalent circuit for on-wafer interconnects modeling is presented. The skin effect, fringing effect, and substrate losses have been considered. An additional element is introduced to predict the substrate capacitive couple effect smartly. Besides, an enhanced de-embedding method was introduced to remove the parasitics from other test structures, and de-embedded measured data are used to analytically extract the associated model parameters. The accuracy was demonstrated by the on-wafer Y-parameter measurements of interconnects up to 40GHz, fabricated on the top-metal layer employing SMIC 0.18μm RF-CMOS technology.

1. Introduction

Due to the combination of the increased circuit complexity and higher frequencies, modern integrated circuit (IC) performance becomes more and more subjected to the interconnect behaviors [1-3]. Accurate modeling and analysis of the interconnect structure are essential to the realization of the next generation of high performance IC's. Many interconnect modeling methods such as electromagnetic (EM) based modeling approach [4-6], measurement based modeling approach (i.e. Lumped equivalent circuit modeling method) [7-9] have been developed in literature. Compared with the EM-based modeling approach, the measurement based modeling approach has more silicon-verified accuracy and more computational efficiency [10]. When a shorter subsection model is well established, equivalent circuit model of longer wires can be obtained by cascading shorter subsections together conveniently.

Several equivalent models of interconnects have been reported [7-9], part of them were so simple that many effects such as fringing, skin, loss of substrate have not be described, these models can not be used in RF/ mm-wave region [7, 8]. The extraction of associated parameters of some reported models [9] have to be performed using optimization and fitting procedures, which may result in nonphysical extracted values. Besides, since the accuracy of measurements can affect the accuracy of extracted model parameters seriously, traditional de-embedding methods such as OSD (open-short-de-embedding), POSD (pad-open-short-de-embedding), OTD (open-through-de-embedding), OSTD (open-short-through-de-embedding) can not remove all the test structures parasitics, especially the pad-stub-line discontinuities.

In this paper, a more accurate equivalent circuit model for interconnects was presented with analytical parameters extraction method. A novel component was introduced to characterize the substrate capacitive couple effect along with the line at high frequency. Besides, an enhanced de-embedding method based on transmission line theory [11] was developed to remove parasitic from the pads and other test structures. In order to substantiate the proposed modeling method, two test structures are designed and fabricated using a 0.18um RF CMOS process by Semiconductor Manufacture International Corporation (SMIC) and characterized up to 40GHz.

2. De-embedding Method Description

By simply modeling the left and right pads solely as lumped admittances YL and YR (YR=YL, for the reason of symmetric), and lumping pad-line discontinuities together with the pads, Alain M. Mangan et al. developed a novel de-embed the contributions of parasitic structures from interconnect/transmission line measurements technique

based on the *ABCD* transmission matrix theory [11]. In actual application instances, when the length of measured interconnect line is much longer than the size of pads structure, [11] can be accurately implemented to high frequency. But, when one's length become comparable to the size of the pads, solely modeling the left or right pad structure as a lumped Y-admittance will introduce error in the interconnect line parameters extraction, because of the existence of parasitic between the two pads.

In fact, consider a real-world test structure of a interconnect line, Fig. 1 reveals that the transmission matrix of either test structure can be decomposed into a cascade of 6 two-port networks (but not 5 two-port networks introduced in [11]) consisting of the two pads (modeled by YL and YR), parasitic between the two pads (modeled by YF), the intrinsic device, and the associated pad-line discontinuities. Assuming that the pad-line junctions can be modeled by lumped admittances, parasitic introduced by the two pads can be removed by a pad-open structure using traditional de-embedding theory, a more accurate de-embedding method similar to [11] can be derived as follows:

Consider two interconnect line test structures of length ℓ_1 and ℓ_2 ($\ell_1 > \ell_2$) with pad-open structure respectively (Fig.2), implement a de-open procedure to remove the pads parasitics (e.g. YL, YR and YF in Fig.1.(b)) from the measurements at first, then transform the de-embedded measurements to *ABCD* matrix:

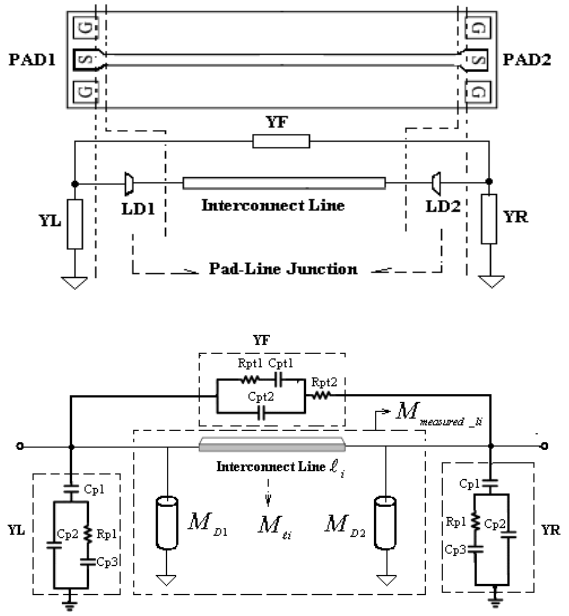

Fig. 1 (a) Composition of a interconnect line test structure and (b) a possible equivalent representation for the two pads.

$$Y_{measured\_\ell i} = stoy[S_{measured\_\ell i}] - stoy[S_{measured\_openi}] \quad (1)$$

$$M_{measured\_\ell i} = ytoabcd[Y_{measured\_\ell i}],\ (i = 1,2) \quad (2)$$

The *ABCD* transmission matrix of test structure ℓ_i , $M_{measured\_\ell i}$ can be represented as the following product:

$$M_{measured\_\ell i} = M_{D1} \times M_{\ell i} \times M_{D2} \quad (3)$$

where

$M_{\ell i}$ *ABCD* matrix represents the intrinsic line segment of structure;

M_{D1} *ABCD* matrix represents, the left pad-line junction;

M_{D2} *ABCD* matrix represents the right pad-line junction.

Consider $M_{\ell 1}$ multiplying with the inverse of $M_{\ell 2}$, define $M_{measured\_\ell i}$ as the hybrid "structure" $M_{measured\_\ell 1} \times Inverse[M_{measured\_\ell 2}]$ and $M_{\ell 1-\ell 2}$ as a line segment of length $\ell_1 - \ell_2$:

$$\begin{aligned} M_{measured\_\ell 1-\ell 2} &= M_{measured\_\ell 1} \times Inverse[M_{measured\_\ell 2}] \\ &= M_{D1} \times M_{\ell 1-\ell 2} \times Inverse[M_{D1}] \end{aligned} \quad (4)$$

Assuming that the left pad-line discontinuity can be modeled solely by a lumped admittance *YD*, then:

$$M_{D1} = \left(\begin{bmatrix} 1 & 0 \\ YD & 1 \end{bmatrix} \right) \quad (5)$$

$$M_{measured\_\ell 1-\ell 2} = \left(\begin{bmatrix} 1 & 0 \\ YD & 1 \end{bmatrix} \right) \times M_{\ell 1-\ell 2} \times \left(\begin{bmatrix} 1 & 0 \\ -YD & 1 \end{bmatrix} \right) \quad (6)$$

Under the lumped pad assumption, the hybrid "structure" can be expressed in terms of parameters, as a parallel combination of the intrinsic transmission line and the parasitic lumped pads:

$$Y_{measured\_\ell 1-\ell 2} = Y_{\ell 1-\ell 2} + \begin{bmatrix} YD & 0 \\ 0 & -YD \end{bmatrix} \quad (7)$$

where $Y_{measured\_\ell 1-\ell 2}$ is the *Y*-parameter representation of $M_{measured\_\ell 1-\ell 2}$, $Y_{\ell 1-\ell 2}$ is the *Y*-parameter representation of $M_{\ell 1-\ell 2}$.

Since the intrinsic device is symmetric, its *Y*-parameters can be isolated by connecting $Y_{measured\_\ell 1-\ell 2}$ in parallel with a port-swapped version of itself, thus canceling out the effects of the pads:

$$Y_{\ell 1-\ell 2} = \frac{Y_{measured\_\ell 1-\ell 2} + Swap[Y_{measured\_\ell 1-\ell 2}]}{2} \quad (8)$$

where

$$Swap\left(\begin{bmatrix} a_{11} & a_{12} \\ a_{21} & a_{22} \end{bmatrix} \right) = Swap\left(\begin{bmatrix} a_{22} & a_{21} \\ a_{12} & a_{11} \end{bmatrix} \right) \quad (9)$$

3. Interconnect Modeling

A. Equivalent Circuit Model

With frequency increasing, the frequency dependent effects of the interconnect line, such as skin effect,

substrate effect and distributed effect begin to impact the performance. In anther words, characteristics of interconnects in RF/mm-wave region are frequency-variant. Unfortunately, the current commercial circuit simulators (such as H/P-SPICE, Agilent Advanced Design System, Cadence) do not support simulations of the frequency-variant parameters. And the distributed nature of the component is easily accommodated so that the compact model can operate over an extended frequency range (i.e., into the mm-wave region)[12]. Thus, employing equivalent circuit model to characterize these effects with frequency-independent components becomes a technology of more importance.

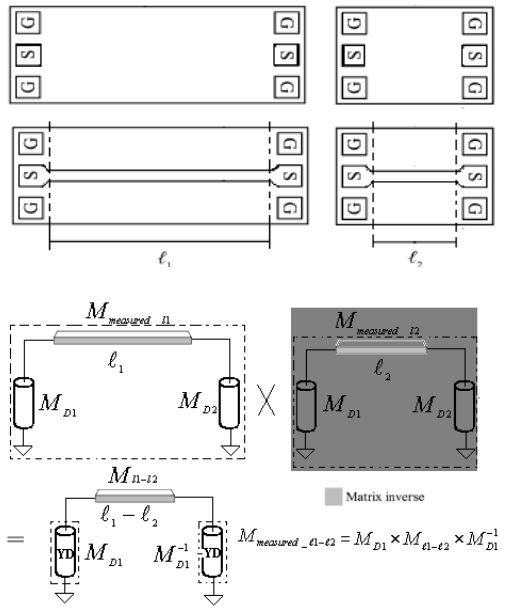

Fig. 2 (a) Two interconnect line test structures with pad-open structures respectively and (b) multiplying the transmission matrix of line 1 with the matrix inverse of line 2 after removing the pad-open parasitics.

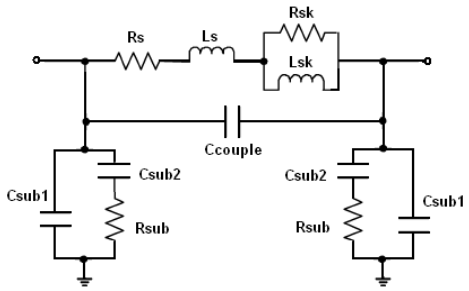

Fig. 3 Equivalent circuit model.

Because the lengths ($\ell_1 - \ell_2$) of interconnect line we researched here is less than 174um, according to [13], the one- Π model should be capable of precisely characterizing the high frequency behaviors of interconnects. Fig. 3 shows the equivalent circuit model proposed for interconnect lines fabricated in silicon technology. A novel component "C_{couple}" was brought in to predict the substrate capacitive couple effect and power storage in the substrate below interconnect line at high frequency. The parallel components R_{sk} and L_{sk} are introduced to characterize the skin effect reference to [9]. The series components C_{sub2}, and R_{sub} combined with C_{sub1} are used to characterize the parasitic of substrate such as loss effect, couple effect and others.

B. Calculation of the Model Parameters

Assuming that the parasitics of the pads and the pad-line junctions have been removed using the de-embedding method proposed in section II. Then the equivalent circuit illustrated by Fig. 3 can be characterized as three admittances, these can be determined from:

$$Y1 = Y_{\ell1-\ell2}.11 + Y_{\ell1-\ell2}.12 \tag{10}$$

$$Y2 = Y_{\ell1-\ell2}.22 + Y_{\ell1-\ell2}.21 \tag{11}$$

$$Y3 = -Y_{\ell1-\ell2}.12 \tag{12}$$

where $Y_{\ell1-\ell2}$ is the *Y*-parameter of intrinsic line $\ell_1 - \ell_2$ mentioned in section II.

Furthermore, from *Y*-parameters of the equivalent circuit in Fig. 3, the following equations can be derived:

$$Y1 = Y2 = \mathrm{Real}(Y1) + j \cdot \mathrm{Imag}(Y1) \tag{13}$$

where

$$\mathrm{Real}(Y1) = \frac{R_{sub}}{R_{sub}^2 + (\frac{1}{\omega C_{sub2}})^2} \tag{14}$$

$$\mathrm{Imag}(Y1) = \omega C_{sub1} + \frac{\frac{1}{\omega C_{sub2}}}{R_{sub}^2 + (\frac{1}{\omega C_{sub2}})^2} \tag{15}$$

As seen from Fig. 3, follow equations can be derived:

$$Y3 = [-Y_{\ell1-\ell2}.12] = j\omega C_{couple} + [\mathrm{Re}al(Z3) + j\,\mathrm{Im}ag(Z3)]^{-1} \tag{16}$$

where

$$\mathrm{Re}(Z3) = R_s + \frac{\omega^2 L_{sk}^2 R_{sk}}{R_{sk}^2 + \omega^2 L_{sk}^2} \tag{17}$$

$$\mathrm{Im}(Z3) = \omega L_s + \frac{\omega^2 L_{sk} R_{sk}^2}{R_{sk}^2 + \omega^2 L_{sk}^2} \tag{18}$$

At low frequency, skin effect is not significant, below a given frequency (10GHz, in our work), the parallel components R_{sk} and L_{sk} in Fig. 3 can be neglected, and thus, real and imaginary parts of *Y*3 can be derived as follows:

$$\mathrm{Re}(Y3\_LowFreq) = \frac{R_s}{R_s^2 + \omega^2 L_s^2} \tag{19}$$

$$\mathrm{Im}(Y3\_LowFreq) = \omega C_{couple} - \frac{\omega L_s}{R_s^2 + \omega^2 L_s^2} \tag{20}$$

The above expressions for *Y*1, *Y*2 and *Y*3/*Z*3 contain all the information required for extracting all the parameters of the model. Taking the related *Y*-parameters into account, the extracted values are determined as:

1) Rearrange (14) as follows:

$$\frac{\omega^2}{\mathrm{Real}(Y_i)} = \omega^2 K_1 + H \tag{21}$$

where

$$K_1 = R_{sub} \tag{22}$$

$$H = \frac{1}{R_{sub} C_{sub2}^2} \tag{23}$$

Using (21), R_{sub} can be extracted from the slope of the linear regression of the experimental $\omega^2 / \mathrm{Real}(Y_i)$ versus ω^2. After subtracting R_{sub}, (23) gives C_{sub2}. Thus, C_{sub1} can be calculated as follows:

$$C_{sub1} = \omega^{-1} \cdot \left(\mathrm{Im}ag(Y1) - \frac{\frac{1}{\omega C_{sub2}}}{R_{sub}^2 + (\frac{1}{\omega C_{sub2}})^2} \right) \tag{24}$$

2) Rearrange (19) as follows:

$$\frac{1}{\mathrm{Re}(Y3\_LowFreq)} = R_s + \omega^2 \frac{L_s^2}{R_s} \tag{25}$$

Using (25), R_s can be extracted from the intercept of the linear regression of the experimental $\frac{1}{\mathrm{Re}(Y3\_LowFreq)}$ versus ω^2. After subtracting R_s, L_s can be calculated from the slope. Once Ls and R_s are subtracted, C_{couple} can be determined by using (20).

The elements (R_{sk} and L_{sk}) introduced to represent the skin effects are extracted from *Y*-parameters at high frequency. As C_{couple}, R_s and Ls has been subtracted, by using (18), Real(*Y*3) can be rearranged as follows:

$$Y3 = \left[-Y_{\ell 1-\ell 2}.12\right] = j\omega C_{couple} + \left[\mathrm{Re}al(Z3) + j\,\mathrm{Im}ag(Z3)\right]^{-1} \tag{26}$$

$$\left[\mathrm{Re}al(Z3) - R_s\right]^{-1} = \frac{R_{sk}}{\omega^2 L_{sk}^2} + \frac{1}{R_{sk}} \tag{27}$$

Thus, R_{sk} can be extracted from the intercept of the linear regression of the experimental $\left[\mathrm{Re}al(Z3) - R_s\right]^{-1}$ versus ω^{-2}, and after subtracting R_{sk}, L_{sk} can be calculated from the slope.

4. Measurements and Verification

Two interconnect test structures are fabricated employing a SMIC 0.18μm 1P6M RF CMOS technology. The width of the two lines is fixed at 10μm, and the length is 150μm (ℓ_1) and 50μm (ℓ_2), respectively. Two-port measurements were performed with the Agilent E8363B Network Analyzer and a CASCADE Summit probe station. The measurements were calibrated using the short-load-open-through (SLOT) algorithm provided with the VNA. The de-embedding and parameters extraction procedure is carried out as described above. The extracted parameter values are summarized in Table 1.

Simulations of the proposed equivalent circuit model based on the extracted parameter values are performed in ADS2005A. The simulated *Y*-parameters are compared with the corresponding measured ones and the plots are presented from Fig. 4 to Fig. 7. Considering the symmetry of the physical structure, *Y*-parameters are thus symmetrical, i.e. *Y*11=*Y*22 and *Y*12=*Y*21 [14]. Therefore, only *Y*11 and *Y*12 are compared, and Real(*Y*ij) and Imag(*Y*ij) are plotted separately.

5. Conclusion

An improved de-embedding methodology which can accurately remove pad parasitics and pad-line discontinuities is presented for lossy RF-CMOS interconnects modeling. A novel one-Π equivalent circuit model for RF on-wafer interconnects is proposed. Based on the *S*-parameter measurements and with an analytical parameter extraction procedure, the model is constructed and element parameters are extracted efficiently. The accuracy of the model based on the extracted parameter values has been verified by the excellent agreement between the simulated results and the measurement data. It demonstrates that the improved de-embedding method and the proposed equivalent circuit model are capable of accurately characterizing the behaviors of RF-CMOS interconnects.

Table 1 Extracted values for the $\ell_1 - \ell_2$ segment model

L_s	79pH	C_{sub1}	2fF
R_s	0.285 Ω	C_{sub2}	5.7fF
L_{sk}	13.7pH	C_{couple}	3.405fF
R_{sk}	1.52 Ω	R_{sub}	2.089k Ω

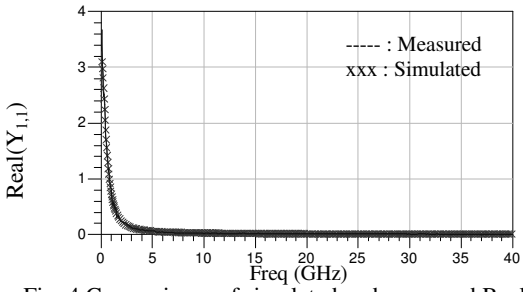

Fig. 4 Comparisons of simulated and measured Real($Y_{1,1}$)

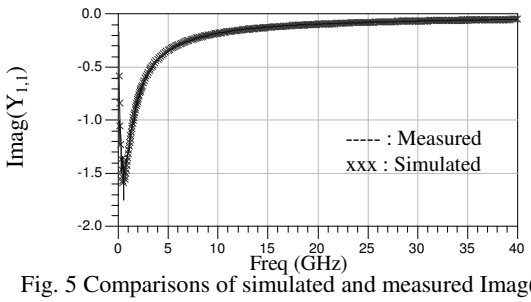

Fig. 5 Comparisons of simulated and measured Imag($Y_{1,1}$)

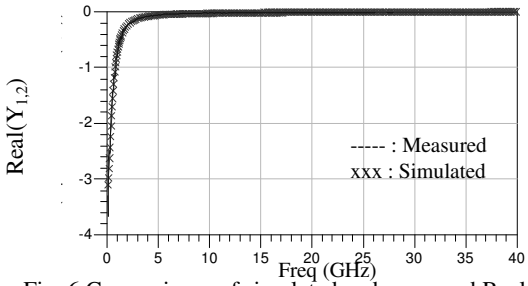

Fig. 6 Comparisons of simulated and measured Real($Y_{1,2}$)

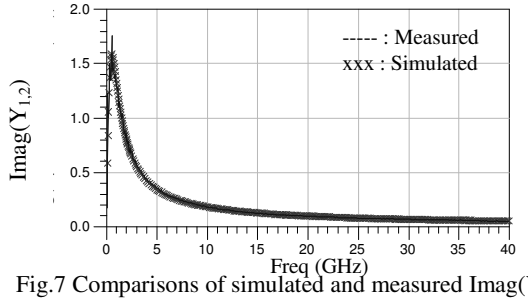

Fig.7 Comparisons of simulated and measured Imag($Y_{1,2}$)

References

[1] R. Hossain, F. Viglione, M. Cavalli, "Designing fast on-chip interconnects for deep submicrometer technologies," *IEEE Trans. Very LargeScale Integr. (VLSI) Syst*, 2003, 11:276.

[2] Q. Xu, P. Mazumder, "The fifth-order differential quadrature methods," *IEEE Trans. Very Large Scale Integr. (VLSI) Syst*, 2003, 11: 1068.

[3] W. Sun, W. Dai, W. Hong, "Fast parameter extraction of general interconnects using geometry independent measured equation of invariance," *IEEE Trans. MTT*, 1997,45(5):827.

[4] F. Alimenti, V. Palazzari, P. Placidi, G. Stopponi, A. Scorzoni, and L.Roselli, "Analysis of CMOS interconnects combining Le-FDTD method and SoC procedure," *IEEE MTT-S Dig*, Seattle, WA, 2002, 2:879.

[5] R. H. Havemann, J. A. Hutchby, "High-performance interconnects: An integration overview," *Proceedings of the IEEE*, 2001, 89(5):586.

[6] D. A. White, M. Stowell, "Full-wave simulation of electromagnetic coupling effects in RF and mixed-signal IC's using a time-domain fi- nite-element method," *IEEE Trans. MTT*, 2004, 52(5):1404.

[7] B. Kleveland, X. Qi, L. Madden, "High-frequency characterization of on-chip digital interconnects," *IEEE Trans. Solid-State Circuits*, 2002,37:716.

[8] B. Kleveland, C. H. Diaz, L. Madden, et al. "Exploiting CMOS reverse interconnect scaling in multigigahertz amplifier and osillator design," *IEEE Trans. Solid-State Circuits*, 2001,36:1480.

[9] Xiaomeng Shi, Jian-Guo Ma,et.al."Equivalent Circuit Model of On-Wafer CMOS Interconnects for RFICs", *IEEE Trans. Very Large Scale Integr. (VLSI) Syst*, 2005, 13(9):1060.

[10] X. Shi, J. Ma, B. H. Ong, K. S.Yeo, M. A. Do, and E. Li, "Equivalent circuit model of on-wafer interconnects for CMOS RFICs," *Radio and Wireless Conference*, 2004: 95.

[11] Alain M. Mangan, Sorin P. Voinigescu, " De-Embedding Transmission Line Measurements for Accurate Modeling of IC Designs", *IEEE Trans. Electron Devices*, 2006, 53(2):235.

Section 4B

eLearning

Assessing Power Saving Techniques and Their Impact on E-learning Users

Arghir-Nicolae Moldovan
School of Computing
National College of Ireland
Mayor Street, Dublin 1, Ireland
E-mail: amoldovan@student.ncirl.ie

Cristina Hava Muntean
School of Computing
National College of Ireland
Mayor Street, Dublin 1, Ireland
E-mail: cmuntean@ncirl.ie

Abstract—**As mobile devices are constantly improving, they have started to be used for online learning. If the delivery of educational content involves multimedia streaming, additional pressure is put on the battery life, causing it to discharge faster. Running out of battery life during a learning session can have a negative impact on the learner's Quality of Experience. This paper suggests the fact that adaptive e-learning environments should become energy-aware and power saving techniques should be considered in order to assist the learner in a low power situation. The impact of various factors on the battery life was analysed and the results show that significant power saving can be achieved by applying different techniques during the multimedia streaming process. However, subjective tests conducted on a small group of participants show that some of these techniques have a negative impact on end-user perceived quality and may not be suitable for an e-learning environment.**

Keywords—***power saving; e-learning; multimedia content adaptation; subjective quality evaluation***

I. INTRODUCTION

Over the past few years, technology has become a part of our life like never before. More and more people use it as a way to stay in touch with friends, to access information, to work, to study, or for entertainment. With the help of the new technologies, e-learning has become an increasingly important form of education, and many educational institutions have extended their activity on the Internet.

At the same time, users in general, learners in particular, have already become more oriented through mobility. A recent study report published by the Educause Centre for Applied Research shows that laptop ownership increased among undergraduate students from 65.9% in 2006 to 82.2% in 2008 [1]. The study was conducted in 44 universities and colleges in the USA.

Mobility comes with a lot of advantages for the learners but also with a number of limitations. A major limitation is that, while on the move, learners rely mainly on the mobile device battery power supply. Given the fact that an increasing number of e-learning environments have included multimedia content in their applications, accessing a course over the wireless network can quickly drain the power from the battery. If learners have to stop their activities due to low power situations, not only their Quality of Experience (QoE) is affected, but also the learning outcome may be significantly reduced.

In this context, e-learning environments have to become energy aware and to assist the learners in maximising their learning outcome. Therefore, power saving techniques must be integrated with the e-learning applications. Battery life will be extended by personalising the educational multimedia content depending on the available power resources of each particular mobile device that is used.

This paper presents an experimental evaluation of some of the factors that have an impact on the battery power consumption when multimedia content is delivered to mobile devices. It also looks at different actions that can be taken in order to reduce the power consumption. These actions can be integrated into a power saving mechanism which will extend the functionality of the adaptive e-learning systems.

Considering the fact that users are becoming increasingly quality-aware, a subjective testing was conducted on a group of participants in order to assess how their perceived quality is impacted when power saving actions are applied.

The paper is structured as follows. Section two consists of a literature review of the existing power saving techniques in the wireless communication area and previous research in the area of adaptive learning. The paper continues with experimental results assessing the impact of various factors on battery power consumption, but also with the results of the subjective evaluation. In the end conclusions are drawn and future directions are presented.

II. RELATED WORK

In the last decade, adaptation and personalisation have gradually been brought to the forefront of research and as a result a large number of applications in the technology-enhanced learning area have been proposed. Various aspects

were investigated as important input in the personalisation of the course material and learning process.

Content personalisation may be driven by the needs of individual learners, their preferences, goals [2], knowledge level [3] or cognitive preferences [4]. Personalisation of the learning process may be driven by the user's abilities, motivation and their previous interaction with e-learning environment, as well as by the learner's concentration level and frequency of disruptions [5].

Most of the research in the area of adaptive e-learning has concentrated on delivering personalised educational content based on learner characteristics. More recently research focused on proposing solutions for multimedia content adaptation according to learner device type and characteristics [6], [7], network type and conditions [8] and user Quality of Experience (QoE) [9].

Although much research was performed in this area and there are clear evidences that the available power of the mobile device could affect the learning process, no study has considered the learner device battery level in the personalisation process of the multimedia content, apart of other characteristics.

Batteries have improved over the last few years, but still a combination of multimedia tasks that are using at the same time multiple components simultaneously (such as screen and speakers, CPU, memory and the Wireless Network Interface Card (WNIC)) may drain the battery power quickly.

However, battery life is not a new issue and many power saving techniques in wireless communications have been proposed over the time. For the particular case of multimedia streaming, the proposed solutions can be classified in the following categories:

1) *Power saving in the reception stage* of the multimedia stream. These solutions look at sending and receiving data and mainly focus on maintaining WNIC in a low power state for a longer period. A proposed solution is to send video frames in a bulk based on the network traffic shape instead of sending them individually. Thus data waiting time for the device is reduced [10]. Another proposed solution uses periodic bulk transfer of the video data in order to reduce the working time of the wireless card, combined with a decrease of the video quality at an intermediate proxy node [11]. Existing research shows that significant improvements in the battery life can also be achieved by extending the power saving mechanism, already built in the IEEE 802.11 standard [12]. This solution uses an additional buffer to hide the data corresponding to several beacon intervals, from the station it is intended for, and forcing it to return to sleep. The buffered data is finally released at once to the mobile station after several attempts to receive it.

2) *Power saving in the decoding stage*. A study [13] has proposed to use dynamic online feedback for setting the average frame decode rate to the same value as the display rate in order to save power in the decoding stage.

3) *Power saving in the playing stage*. The majority of the solutions that have been proposed for saving power in the reception stage have focused on the device screen. Battery power consumption can be reduced by optimising the backlight power consumption [14], or by extending the Dynamic Luminance Scaling (DLS) to cope with transflective LCD panels that can operate with or without backlight [15] depending on the battery level and ambient luminance. Power save can also be achieved by adjusting screen brightness and volume level but since the user has control on these settings, little research has been performed in this area.

Literature review shows that numerous power saving techniques with good results have already been proposed. The novelty of this research consists of the fact that it will bridge the well researched area of personalised e-learning with the power saving in the wireless communications and will look not only to increase the battery life, but also to improve the learning process.

III. Factors That Influence Battery Power Consumption of The Mobile Devices

Playing multimedia educational content on a mobile device is an energy intensive task, especially when this is streamed over a wireless network. In this situation significant power is consumed by the WNIC for retrieving and processing the multimedia stream, in addition to the power consumed by other components for decoding and playing the audio-video sequence. The multimedia streaming process can be seen as consisting of three different stages: data reception, decoding and playing. Each of them contributes more or less to the overall battery consumption of the mobile device.

Various experimental tests (see Table I) were conducted in order to investigate the impact of each of the three stages on the battery power consumption. Different factors specific to each stage were also considered. For testing purposes, a video clip with a reduced degree of motion content, was used. Various versions of the studied video clip that have different values of the encoding parameters were created. This set of videos can be classified according to the encoding parameter that is studied. Any two videos corresponding to a specific encoding parameter have different values for that parameter. The rest of the encoding parameters are constant and their values are in the following groups: video compression - H.264 encapsulated in the MP4 multimedia container, resolution - 320 x 240 pixels, frame rate - 24 fps and average video bit rate - 384 Kbps.

Depending on the performed test, each video was streamed to the mobile device and/or played locally in a loop until the battery was completely discharged. To

TABLE I
EXPERIMENTAL TESTS PERFORMED

Test	*Stages Involved*	*Parameter Category*	*Studied Parameters*	*Parameter's Values*
Streaming and Local Playback	Reception, Decoding, Playing	Encoding Parameters	Video Compression	H.264, WMV 9, MPEG4 Part2, H.263
			Video Resolution	480 x 360, 320 x 240, 240 x 180
			Video Frame Rate	24 fps, 20 fps, 16 fps
			Average Video Bitrate	512 Kbps, 384 Kbps, 192 Kbps
Local Playback	Decoding, Playing	Device Settings	Volume Level	100%, 50%, 0%
			Screen Brightness	100%, 50%
			CPU Clock Speed	520 MHz, Auto Speed, 208 MHz

maximize the accuracy of the results, similar conditions were kept between any two different tests. The only applications running on the mobile device were the media player and the program used for tracing information on the battery power consumption. For the case when a video was streamed, the mobile device was maintained in a fixed position where the wireless signal strength was high and constant. For the case when the video was played locally the WNIC was switched-off. To ensure that the battery degradation in time has a minimum impact on the results, the tests corresponding to the same parameter were performed consecutively with a minimum time necessary to charge the battery between them. All the tests were performed in a laboratory where the temperature was constant.

The mobile device consisted of a Dell Axim PDA with an IEEE 802.11b wireless card and a 520 MHz ARM processor, running Microsoft Windows Mobile. Additionally, a laptop with 2 GHz Intel Core 2 Duo processor and 2 GB of RAM memory, running Microsoft Windows Vista was used as a streaming server when the videos were streamed to the mobile device. Additional details on the test setup can be found in [16].

A. The Impact of WNIC on the Battery Life

In the reception stage, most of the power is consumed by the for network related tasks, such as receiving the data packets and processing them. In order to assess WNIC's effect on the battery power consumption, a number of comparative tests were performed when the same versions of the multimedia clip were first streamed from the server to the mobile device via an Access Point (AP), and then stored and played locally on the PDA.

The results presented in Fig. 1.a-d show that when the multimedia clips were streamed, the battery discharged in half of the time required when the same clips were played locally. Only the times needed to discharge the battery from 50% battery charge to 1% battery charge were considered in the comparison. For example, in the case of the H.264 video with a frame rate of 16 fps, the battery life was reduced by 52%, from 84.22 minutes when the video was played locally to 40.4 minutes when it was streamed and played in real time (see Fig. 1.c).

The conclusion that can be raised is that WNIC is responsible for approximately 50% of the total battery consumption when retrieving the streamed multimedia clip and the reception stage is where significant power can be saved, by applying different techniques.

B. The Impact of Encoding Parameters on Battery Life

Before it can be played, a multimedia clip has to be decoded according to the encoding scheme used. CPU and memory are the main components responsible for the power consumption at this stage. In order to assess the effect of the encoding scheme on battery power consumption, following multimedia clip parameters were considered: video compression technique, video resolution, frame rate and bitrate. Comparative results (see Fig. 1.a-d) show that the battery life can be increased by changing the video compression technique to a more energy efficient one or by reducing the values of other encoding parameters.

Fig. 1.a shows that an increase in battery life of 21.53% can be achieved, by changing the video compression technique from H.264 to H.263 (encapsulated as a Flash video), when the videos were played locally on the device. The improvement was even higher when the same videos were streamed to the mobile device (27.6%).

As opposed to the video compression technique, reducing the quantitative encoding parameters will have a higher impact on the battery life if the videos are played locally, rather than streaming them. For example, by reducing the resolution from 480 x 360 pixels to 240 x 180 pixels, the frame rate from 24 fps to 16 fps and the average video bitrate from 512 Kbps to 192 Kbps, the battery life increased with 25.66%, 15.31% and 14.67% respectively, when the videos were played locally, and with 15.93%, 10.94% and 7.27% respectively, when the videos were streamed to the PDA (see Fig. 1.b-d).

Concluding this, one can say that battery power can be saved by varying the encoding parameters of the multimedia clip being delivered, but the amount of power saved is significantly smaller than that in the reception stage of the multimedia streaming process.

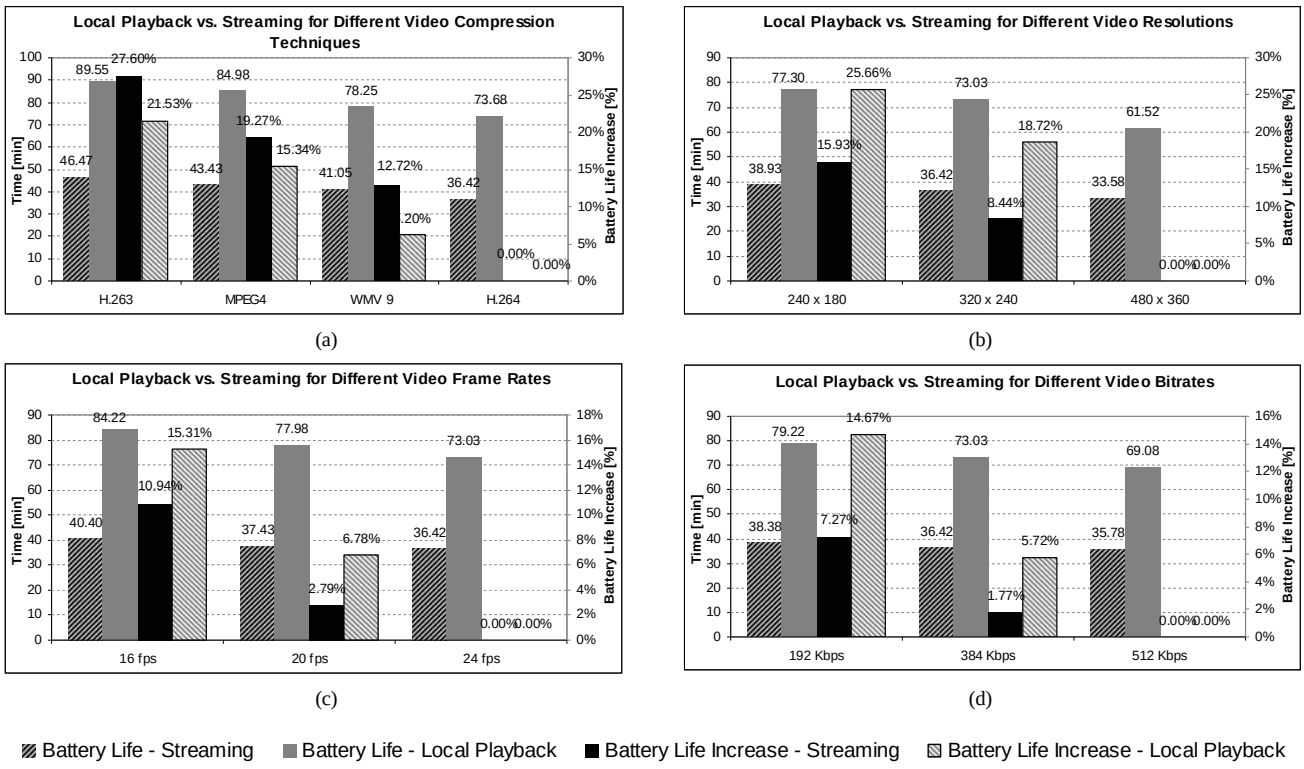

Fig. 1. Battery life and battery life increase (comparing with the less energy efficient case from the group), when videos with different encoding parameters are streamed and played locally on the mobile device: (a) the effect of video compression technique on battery life; (b) the effect of video resolution on battery life; (c) the effect of video frame rate on battery life; (d) the effect of average video bitrate on battery life.

C. The Impact of Device Settings on the Battery Life

Depending on the type of multimedia content, the device screen and speakers are the main components responsible for the power consumed when the multimedia clip, previously decoded, is played to the user. A new set of tests were carried out in order to assess the effect of device components and especially their settings on the battery life. Each test consisted of playing locally the same video file until the battery was completely discharged. The WNIC was switched-off to eliminate its effect on power consumption and to increase the contribution of the component whose settings were changed.

To assess the effect of the speakers on the battery life, the volume was set to three different levels and the time needed to discharge the battery was measured. The levels considered were 0%, 50% and 100%. Fig. 2.a shows that if the media clip that is being played consists in an audio-video sequence, the sound playback by the speaker has a small contribution to the overall power consumption of the mobile device. Turning the sound OFF will increase the battery life only with 9% comparing with the case when the volume is set to 100% both in the media player and in the Operating System. Since no important benefit was noticed when the volume level was set to 50%, the case was not plotted on the graph.

To investigate the effect of the device screen, on the battery consumption, two levels were considered for the screen brightness: 100% and 50%. Fig. 2.b shows that in comparison with the sound volume, screen brightness has a higher impact on power consumption. An increase in battery life of approximately 31% is achieved when the screen brightness is reduced to half of its maximum level.

A last set of experimental tests was conducted in order to investigate the effect of CPU on the battery power consumption. For this, the CPU clock speed was set to three different values: 520 MHz, auto speed and 208 MHz. Fig. 2.c shows that comparing with the case when the clock speed is set at 208 MHz, changing this speed to 520 MHz will increase the battery consumption by 25%, while letting the system to choose the optimum speed, reduces the battery life by 17%.

D. Reflections on the Results

The experimental results presented above show that during the streaming process of a multimedia clip, there are multiple options for extending the battery life. By turning ON the WNIC to retrieve the multimedia content from the network, the battery consumption increases with up to 50%. So is at this stage where significant battery power can be saved. The longer the time that WNIC spends in a low power state before retrieving data, the higher the amount of

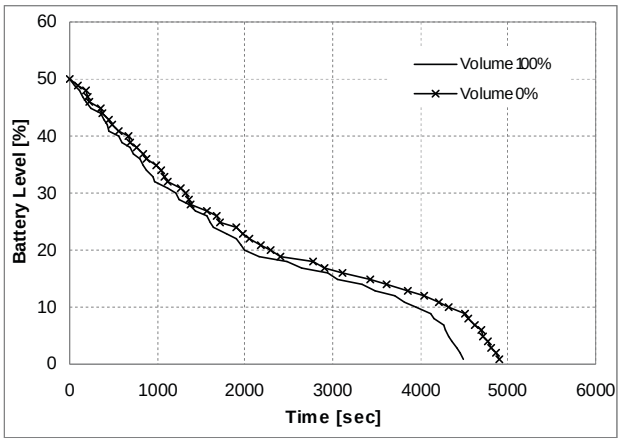

(a)

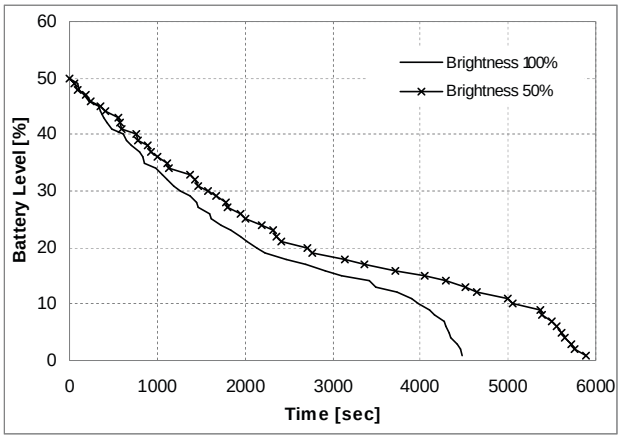

(b)

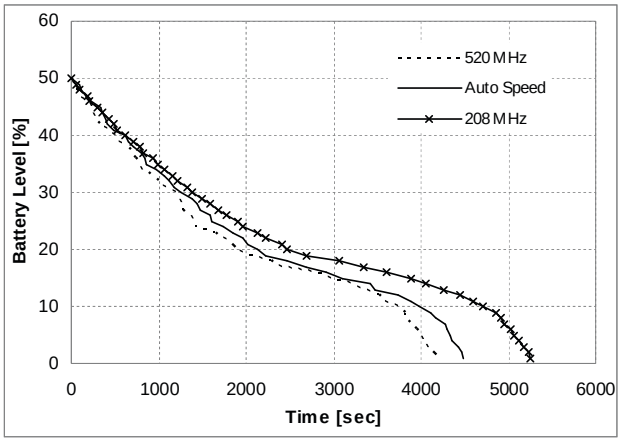

(c)

Fig. 2. Battery life when changing different settings of the mobile device: (a) the sound volume level; (b) the screen brightness; (c) the CPU clock speed.

power that is saved. Solutions for extending this time must be found without introducing delays that can impact negatively the learning process.

By changing the encoding parameters of the streamed multimedia clip, additional power can be saved. There are two possible options to do this. First, advance creation of multiple versions of the multimedia content which differs in terms of encoding parameters. This method requires more storage space on the server side, but this is not a serious issue as over the last years, the storage devices have exponentially increased in capacity and their price has drastically dropped. A second option makes use of transcoding, reducing the required storage space and enabling real time modifications of the encoding parameters to be performed easier. The disadvantage of this solution is that requires high processing power on the server side, especially when a high number of users are accessing the application at the same time.

The power saving techniques related to the reception and the decoding of the multimedia stream can be implemented on the server side, or between the server and the client. The users have reduced control on how data is received and on the amount of resources necessary to decode and play the multimedia content that is being sent. If the e-learning environment allows them, they have the option to download the multimedia content and view it afterwards, saving power at the same time. In this case the reception is controlled by the users but is efficient only if there is enough network bandwidth available to allow them to download a clip in a much shorter time then needed to stream it. On the other hand, the users have a high level of control on the device settings. Changing these settings in order to save power can have a negative impact on users' satisfaction.

It is worth mentioning that in the case of this particular device, the battery has a nonlinear discharge characteristic (see Fig. 2.a-c), but with several sections approximately linear (50% to 20%, 20% to 10% and 10% to 1%). Also a significant interval from the total battery life increase, achieved by changing a specific parameter, corresponds to the section when the battery life decreases from 10% to 1%. A power saving algorithm must consider the discharge characteristic of the battery model corresponding to the mobile device that is being used to access the multimedia content, but also the battery level at which the device is set to turn off, usually between 5% and 10% for laptops or PDAs.

IV. Preliminary Subjective Evaluation

This section presents preliminary results of subjective tests that have been carried out in order to assess the impact of some of the actions that can be taken to increase the battery life, on end-user perceived quality of the multimedia clip. A small number of participants have attended and further tests are ongoing. The evaluation addressed only the encoding parameters because their variation is easier to be controlled and is directly reflected in the final quality of the multimedia clip.

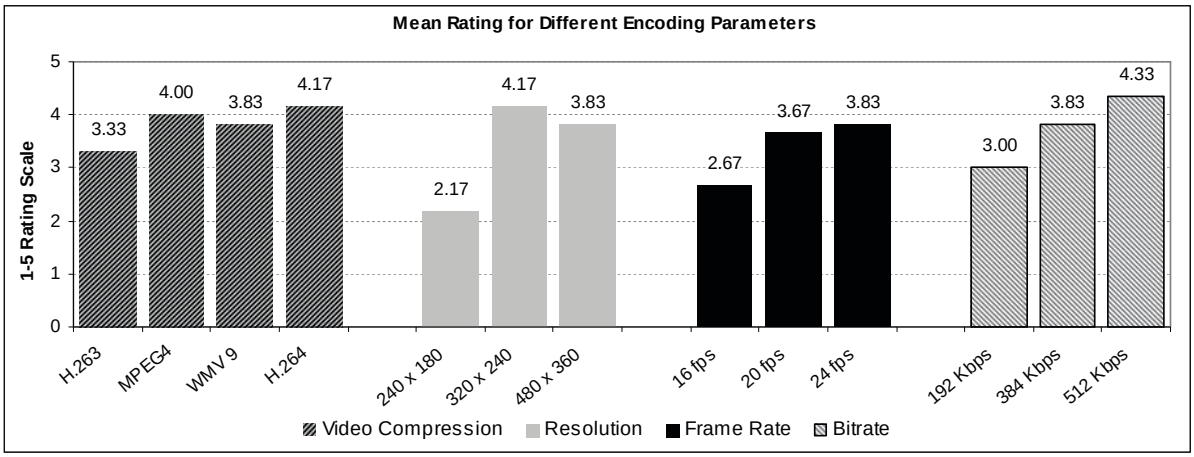

Fig. 3. End-user perceived quality when varying the encoding parameters.

A. Evaluation Setup

Four sets of short video sequences were created, one for each of the encoding parameters whose impact on battery life was previously studied. In particular, each set consisted in a number of three or four video sequences with different values for the parameter associated with that set, and constant values for the rest of the parameters.

To eliminate the influence of other factors, such as fluctuations in the available network bandwidth, on the final perceived quality, the video sequences were stored and played locally on the mobile device. Also, to keep a uniform testing environment, all the participants used the same PDA device for viewing the video sequences. The screen brightness was set to 100% and the volume level was set at an adequate level for the laboratory environment where the testing was conducted. None of the participants changed the mobile device settings, even if they were allowed to do so.

The subjective tests were performed with one participant at a time and before starting, he/she was introduced to the test environment and to the method of assessment. A five-grade quality scale (i.e. 1 - Bad, 5 - Excellent) was used for this purpose. The participant was asked to rate his/her overall impression given by each sequence in part, and to mark the corresponding checkbox on a form that was provided. Code names were associated with the video sequences so that the viewers were not aware of the parameters being analysed. The overall duration of the test session, including introduction, viewing and rating, was planned to last less than 20 minutes. A different order of displaying the video sequences was chosen for each participant to the subjective test.

B. Preliminary Results

Fig. 3 presents the mean scores, achieved by each particular sequence. Preliminary results show that, changing the video compression technique has a lower impact on end-user perceived quality, than decreasing the resolution, the frame rate or the bitrate. Significant battery power can be saved by changing the video compression, while maintaining a good quality level. For example by changing the video compression from H.264 to MPEG4 Part 2, there is an improvement in battery life of 19.27% when the video is streamed to the mobile device and 15.35% when the video is played locally (see Fig. 1.a). At the same time a good level of quality was maintained, the sequence encoded using MPEG4 scored an average rating of 4 out of 5, whereas the sequence encoded using H.264 scored an average of 4.17 out of 5.

Results also show that by reducing other encoding parameters to levels that offer a good energy saving, the user perceived quality is significantly reduced. At the same time, a slight decrease which maintains a good level of quality, may not have real benefits in terms of power saving. For example by reducing the frame rate from 24 fps to 16 fps, an increase in battery life of 10.94% could be achieved for the case when the videos are streamed, but the quality was significantly reduced, the corresponding video sequence scored an average of 2.67 out of 5. Reducing the frame rate to 20 fps, the quality is still good, but the increase in battery life that can be achieved is only 2.79%.

As it can be seen in Fig. 3, the video sequence with a resolution of 320 x 240 pixels, achieved a higher score than that with a resolution of 480 x 360 pixels, when the contrary was expected. This is explained by the fact that device screen had a resolution of 320 x 240 pixels and additional tasks were required for scaling down the video, negatively influencing the user perceived quality.

If e-learning users are in the middle of a learning activity and an interruption occurs due to insufficient battery power, their QoE can be negatively impacted. This can also happen if the quality of the multimedia content is reduced too much, even if by doing this sufficient power is saved to allow them to complete the learning activity. To maximise the learning outcome, a power saving solution for e-learning environments must find the right balance between the amount of power saved and the user QoE.

V. Conclusion and Future Work

The goal of this paper was to assess the factors behind the battery power consumption when multimedia content is streamed and played on a mobile device. A number of experimental tests were carried out, which have shown that during the multimedia streaming process, data reception accounts for half of the total power consumption of the mobile device. Results have also shown that battery power consumption is influenced by the encoding parameters of the multimedia clip and by the settings of the mobile device. However, their contribution is found to be significantly smaller than that of WNIC.

Preliminary subjective testing was conducted in order to assess the impact of encoding related to the power saving actions on the end-user perceived quality. The conclusion drawn from these tests was that changing the encoding parameters, while at the same time maintaining a good quality, may not save enough power to improve the learning process. Therefore most of the effort must be concentrated to save power in the reception stage of the multimedia streaming. Encoding related techniques should be used when the power saved in the reception stage is still not enough to maximise the learning outcome.

Future work will address the deployment of a power save mechanism that will incorporate various techniques specific to different stages of the multimedia streaming process. Further experimental testing will be conducted on various mobile devices, in order to propose a battery independent discharge model that estimates with accuracy the remaining battery life.

Elaborate subjective testing will also be conducted on a large number of participants in order to assess the benefits of the proposed solution in terms of battery power save, end-user satisfaction and learning improvement.

Acknowledgment

The support of Science Foundation Ireland is gratefully acknowledged.

References

[1] G. Salaway, J.B. Caruso, and M.R. Nelson, "ECAR Study of Undergraduate Students and Information Technology, 2008," *EDUCAUSE Center for Applied Research*, vol. 8, Oct. 2008, p. 10.

[2] R. Clifford, "Adaptive Hypermedia for Music Instruction", *7th International Technological Directions in Music Learning Conference*, 2000.

[3] P. De Bra, A. Aerts, B. Berden, B. de Lange, B. Rousseau, T. Santic, D. Smits, and N. Stash, "AHA! The adaptive hypermedia architecture," *Proceedings of the fourteenth ACM conference on Hypertext and hypermedia*, ACM Press New York, NY, USA, 2003, pp. 81-84.

[4] S.Y. Chen and R.D. Macredie, "Cognitive styles and hypermedia navigation: Development of a learning model," *Journal of the American Society for Information Science and Technology*, vol. 53, 2002, pp. 3-15.

[5] B. Bomsdorf, "Adaptation of Learning Spaces: Supporting Ubiquitous Learning in Higher Distance Education," *Mobile Computing and Ambient Intelligence: The Challenge of Multimedia, Dagstuhl Seminar Proceedings*, 2005.

[6] F. Meawad and G. Stubbs, "A framework for enabling on-demand personalised mobile learning," *International Journal of Mobile Learning and Organisation*, vol. 2, 2008, pp. 133-148.

[7] S.A. Petersen and J.K. Markiewicz, "PALLAS: Personalised Language Learning on Mobile Devices," *Wireless, Mobile, and Ubiquitous Technology in Education,. WMUTE 2008. Fifth IEEE International Conference on*, 2008, pp. 52-59.

[8] C.H. Muntean, "Improving Learner Quality of Experience by Content Adaptation based on Network Conditions," *Computers in Human Behavior Journal, Special issue on "Integration of Human Factors in Networked Computing"*, vol. 24, 2008, pp. 1452-1472.

[9] C.H. Muntean and G.M. Muntean, "End-User Quality of Experience Aware Personalised E-Learning," *Architecture Solutions for E-Learning Systems*, C. Pahl, ed., IGI Global, 2008, pp. 154-174.

[10] F. Zhang, S. Chanson, "Proxy-assisted scheduling for energy-efficient multimedia streaming over wireless LAN", *4th Int. IFIP-TC6 Networking Conference, Lecture Notes in Computer Science*, Vol. 3462, 2005, pp. 980-991.

[11] M. Tamai, T. Sun, K. Yasumoto, N. Shibata, and M. Ito, "Energy-aware video streaming with QoS control for portable computing devices," *Proceedings of the 14th international workshop on Network and operating systems support for digital audio and video*, Cork, Ireland: ACM, 2004, pp. 68-73.

[12] J. Adams and G.M. Muntean, "Adaptive-Buffer Power Save Mechanism for Mobile Multimedia Streaming," *Communications, ICC '07. IEEE International Conference on*, 2007, pp. 4548-4553.

[13] Z. Lu, J. Lach, M. Stan, and K. Skadron, "Reducing multimedia decode power using feedback control," *Computer Design, Proceedings. 21st International Conference on*, 2003, pp. 489-496.

[14] S. Pasricha, S. Mohapatra, M. Luthra, N. Dutt, and N. Venkatasubramanian, "Reducing backlight power consumption for streaming video applications on mobile handheld devices", *In Proc. First Workshop Embedded Systems for Real-Time Multimedia*, pp. 11-17, 2003

[15] H. Shim, N. Chang, and M. Pedram, "A backlight power management framework for battery-operated multimedia systems," *IEEE Design and Test of Computers*, vol. 21, no. 5, 2004, pp. 388 – 396.

[16] A.N. Moldovan and C.H. Muntean, "Personalisation of the multimedia content delivered to mobile device users," *Broadband Multimedia Systems and Broadcasting, BMSB '09. IEEE International Symposium on*, 2009, pp. 1-6.

Billing Issues when Accessing Personalised Educational Content

Andreea Molnar, Cristina Hava Muntean
National College of Ireland, School of Computing, Mayor Street, Dublin 1, Ireland
amolnar@student.ncirl.ie, cmuntean@ncirl.ie

Abstract

The increased affordability of mobile devices combined with the availability of the latest wireless technologies have made mobile devices an attractive tool for learning. Nowadays learners can choose between multiple wireless networks with different characteristics, belonging to the same or to different mobile operators. Unfortunately, the Internet billing plans are still difficult to predict and control by most users. This paper presents an algorithm which aims to determine the best network, from a list of available ones (in terms of price), for delivering the selected educational content.

1. Introduction

Mobile device popularity has increased tremendously in the last years. For example, more than half of the world population has a mobile phone [1]. Mobile devices are present everywhere and they have become more and more accessible. Their prices dropped, their portability has increased and the performance offered by mobile networks has improved a lot. Due to their pervasive presence as well as to the tremendous development of new features and capabilities they have become an attractive tool for education.

Owning a mobile device that has connectivity to one or more wireless networks makes the access to educational content easy at any time and from anywhere. Mobile devices ease the learner's access to information, helping them to have access to the right resource at the right time. In the same time, they are particularly useful for learners that do not have the time to plan a learning session and they are usually studying in unplanned situations. Difficulties due to time constraints have been observed especially for part time students. Becking et al. [2] noted that these phenomena, giving examples of unpredictable situations where learners could benefit from having access to the educational content. Among the examples given is the one of a salesman who travels a lot and may learn while s/he is on train. Another example is of a mother who is waiting for her turn in the doctor waiting room.

Even though mobile devices offer new opportunities for learning, they have some restrictions: small screen size, limited number of buttons, battery life limitations etc. Therefore, offering guidance to the learners and providing them with the adequate educational content suited to their needs is an important issue addressed by learning systems. Adaptive e-learning systems offer solutions to these problems, by providing guidance and personalised material suitable to the learner. Different user's characteristics have been taken into consideration in the adaptation process such as: knowledge [3], goal [4], learning styles [5], prerequisites and experience [6], network performance [7], etc. Lately, learner device characteristics were also considered in the personalisation process [8, 9, 10].

However, to the best of our knowledge, none of these e-learning systems have considered that the learner may choose between different networks, when the mobile device offers access to more than one wireless network. For example a number of mobile devices that include these features are listed below:

- PDA O2 XDA Zinc has access to 3G, WiFi and GPRS;
- HTC TyTN II has access to HSDPA/UMTS, WiFi, GSM, EDGE and GPRS;
- HTC P3300 has access to GSM/GPRS/EDGE and WiFi;
- Mobile Pocket PC-i-mate Jasjar has access to GPRS, WiFi, etc

Each type of wireless network may have both different delivery performance and billing plans. Cheaper alternatives may trigger the learner to switch manually between the networks.

This paper presents a Performance Aware and Cost Oriented e-Learning Framework (PACO-eLF) that supports content personalisation by taking into account

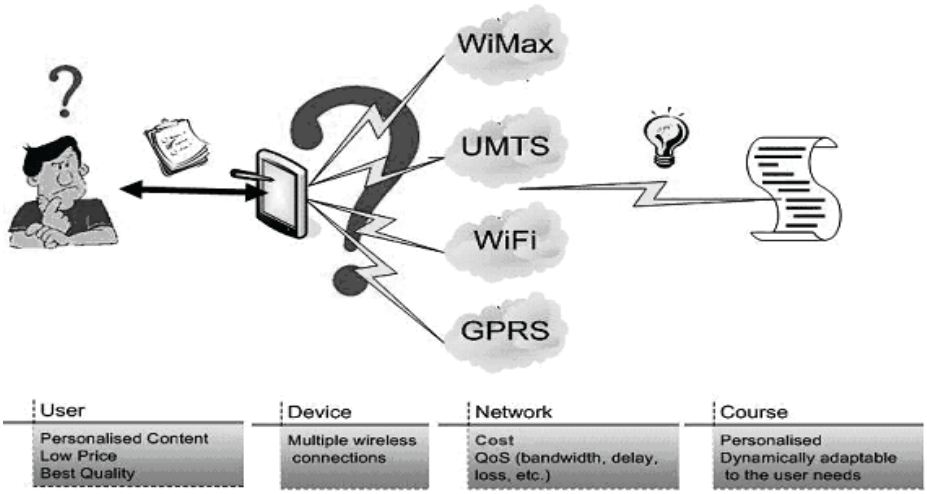

Figure 1 Multiple network selection

learner's profile, the device used, the network characteristics and the cost they have to pay for accessing the content. An algorithm that determines the best network, from a list of available ones (in terms of price), for delivering the personalised educational content is also described.

The rest of the paper is organised as follows. Section 2 presents an overview of the existing billing models for Internet access through mobile devices. Section 3 briefly introduces the PACO-eLF and presents the network selection algorithm. Section 4 presents the conclusions we arrived so far and describes new directions to continue our research work.

2. Billing models for Internet access through mobile devices

Access to multiple networks offers to the learner more possibilities of retrieving the educational content, by choosing a given mobile service (Figure 1). Ideally the learner selects from the available networks, the one which offers him the best price and performance, or at least the best trade off between them. Unfortunately this is not always the case. Mobile data billing systems are still difficult to understand by most users and determining the best network in terms of performance often requires engineering knowledge. This problem becomes even more important in the context of the wireless channel where network resources are limited.

The diversity of billing schemes that currently exists on the market (Table 1) does not help the learner in making a decision. The most common data billing plan in mobile communication is the flat rate bundle [11]. Other billing plans include, but are not limited to:

- Time based billing (paying for the amount of time that is spent using the Internet, for example 0.005€/minute)
- Data based billing (paying for the amount of

Table 1 Mobile billing plans diversity

Operator	Time billing	Data billing	Bundle billing	Monthly flat rate	Other services included
T-mobile(USA)			X	X	X
Meteor(Ireland)			X		
Three(Ireland)			X		
Vodafone(Ireland)			X		
O2(Ireland)			X		
Indosat(Indonesia)	X	X	X	X	
Mobility(Saudi Arabia)		X	X	X	
Vodacom(South Africa)		X	X		

data consumed, for example 0.2€/MB)

- Monthly flat rate (unlimited Internet access, paid monthly)
- Free Internet access

Sometimes billing plans are much more complex. Depending on the carrier policy, a user can pay more by visiting some websites or not pay at all (e.g. when visiting the carrier portal). The price may also depend on the connection speed or on the time of the day when the Internet is accessed. Most of the time, mobile data traffic is charged separately from other services such as SMS (Short Message Service), MMS (Multimedia Messaging Service), calls etc. Each particular service may have a different cost associated. However there are times when they are included in one single package.

Time based billing is relatively easy to understand, but the attention of the user is on optimising his actions in order to spend less time on the Internet when retrieving the actual information s/he is requesting [12].

Data based billing, is not so easy understandable for the users. Most of them do not know how to predict the amount of data downloaded. Sometimes there is no way to find how much the users spend. Even when the mobile operator facilitates this process by providing a counter for the data used so far, some of the users do not know that it exists or how to use it [12].

The data bundle has the advantage of offering data at low price. However when the user passes the data limit the price becomes quite high. Most of the users do not realise when they exhaust the amount of data available in the bundle. This leads to high bills, discouraging users to access the Internet through their mobile devices [12, 13].

Choosing the right network in terms of price and controlling the cost may distract the learner's attention from the educational content he is presented with. Therefore, there is a need for an automatic mechanism that assesses the billing plan. This paper presents an algorithm that aims to help the learners in selecting the right network in term of cost.

3. Cost oriented adaptive e-Learning system

PACO-eLF (Performance Aware and Cost Oriented e-Learning Framework) (Figure 2) aims at offering adaptive educational content to learners by taking into account their profile, the device they are using, the network performance and the cost they have to pay for accessing the content. The classical architecture of an adaptive e-learning system that consists of UM (User Model), DM (Domain Model) and AM (Adaptation Model) has been extended by adding the PM (Performance Model) and CM (Cost Model).

PACO-eLF consists of a *Client Application* and a *Server Application*. The *Client Application* maintains the CM. It stores the billing plans for every network the

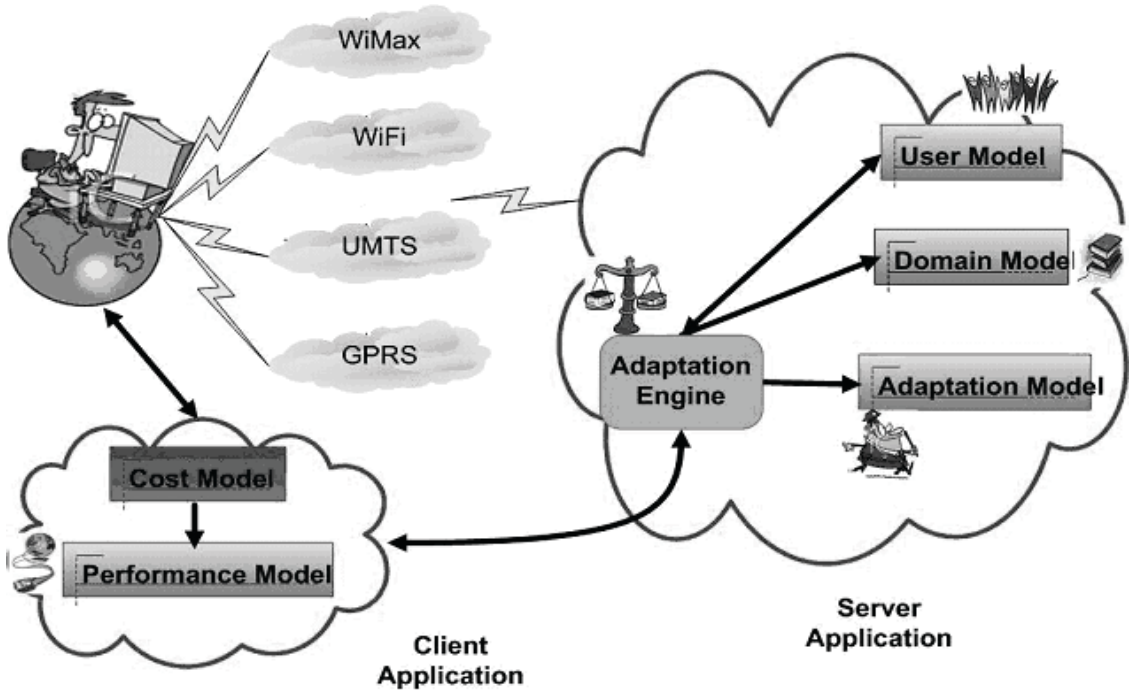

Figure 2 PACO-eLF

learner device has access to. It also estimates the price for each available network when a document is required. It interacts with the *Sever Application* to get information with respect to what changes occur in the characteristics of the network currently in use that may affect the price that will be paid for the data retrieval. If the total price increases over a certain threshold imposed by the learner, the learner is prompted and provided with an alternative network to be used that would offer a better price for retrieving the educational content.

The *Server Application* maintains information about learner profile (UM), available courses (DM), network performance (PM) and adaptation rules that describe how to personalise the educational content based on the user profile and the network conditions (AM). The rules are interpreted by the Adaptation Engine (AE).

User Model (UM) holds the learner profile. It consists of:

- demographic information (e.g. address)
- personal data (e.g. name, password, etc)
- learner preferences
- learner goals
- knowledge about the concepts contained in the DM
- device characteristics
- how much the learner is willing to pay in order to retrieve educational content, etc.

Device characteristics considered by the UM are:

- *Screen size*: width and height in pixels;
- *Screen colour depth*: bits/pixel;
- *Screen mode*: it refers to whether the screen has portrait or landscape mode and if it supports switching between the two modes;
- *Capabilities*: whether the device is capable of displaying video, audio, images, etc;
- *Supported mark-up or scripting language*: e.g. not all mobile devices support all JavaScript functions;
- *Memory*: capacity.

Device Model (DM) stores and organises the educational content, divided into fragments between which relationships exist. For example a *link*: indicates that between two fragments navigation can be done and a *prerequisite* relationship indicates that there is an order in which the fragments should be delivered to the learner (e.g. a learner should not read about a certain concept if s/he has no knowledge or if s/he did not read first about the *prerequisite* concept). The educational content fragments can be grouped together based on these relationships in order to form complex concepts.

Performance Model (PM) contains information about the performance of the different networks that the learner has access to. For every enabled network the device has, performance characteristics are maintained and continuously monitored, in order to determine the quality of the transmitted content. It also provides suggestions on how the educational content should be adopted so that it is suitable for transmission over the active network.

The *Adaptation Model* (AM) holds the adaptation rules based on which the content selection and personalisation is done. The rules combine information on learner profile, device, network conditions and cost.

Adaptation Engine (AE) interprets the rules from the AM and selects the most suitable educational content.

The *Cost Model* (CM) maintains the learner billing plans. It also has the role of suggesting to the learner the best network to be used in terms of cost and performance in order to assure that the threshold imposed by the learner is not surpassed. The based network to be used is determined by an algorithm that is presented in the next section.

4. Cost oriented network selection algorithm

The main goal of the algorithm is to determine the best network, from a list of available ones on the device (in terms of price), for delivering the personalised educational content.

We consider that the learner has one or more mobile network operators and s/he may have one or more billing plans currently in use. The plan types the learner may have are: free Internet access, flat free billing, data bundle billing, data based billing and/or time based billing.

For the data bundle billing the quantity of information contained in the bundle is usually available for a specific period of time. Sometimes, the mobile data operator does not allow a new bundle to be acquired if the learner has a bundle in use for the current time period. For example, if the learner chooses a data bundle over a period of 30 days which contains 500 MB of data, s/he may not choose another data bundle billing plan if the 30 days period has not expired. This leads to the situation in which the other plans are unavailable for the user. Therefore, they should not be considered by the algorithm when the learner is provided with the cheapest alternative to access the educational content. An algorithm for selecting just the available plans for every operator/network the learner has access to is presented in Figure 3. It takes as input all the available operators

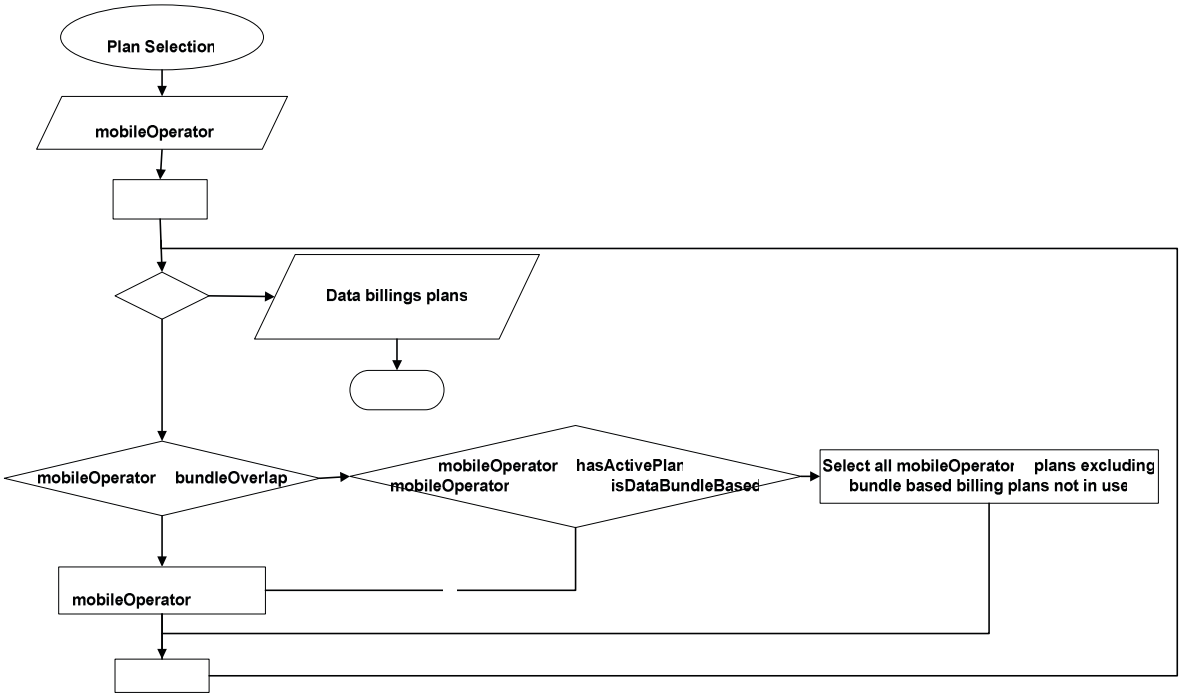

Figure3 Operators Plans Selection

and returns billing plans the learner has currently access to.

Based on the selected plans, on the lecture size and on the network connection speed, the price for accessing the educational content is computed (Figure 4a-d). The lecture size is provided by the AE (Adaptation Engine) after selecting the educational material suitable to the learner profile. The connection speed for each of the available networks is provided by the PM (Performance Model).

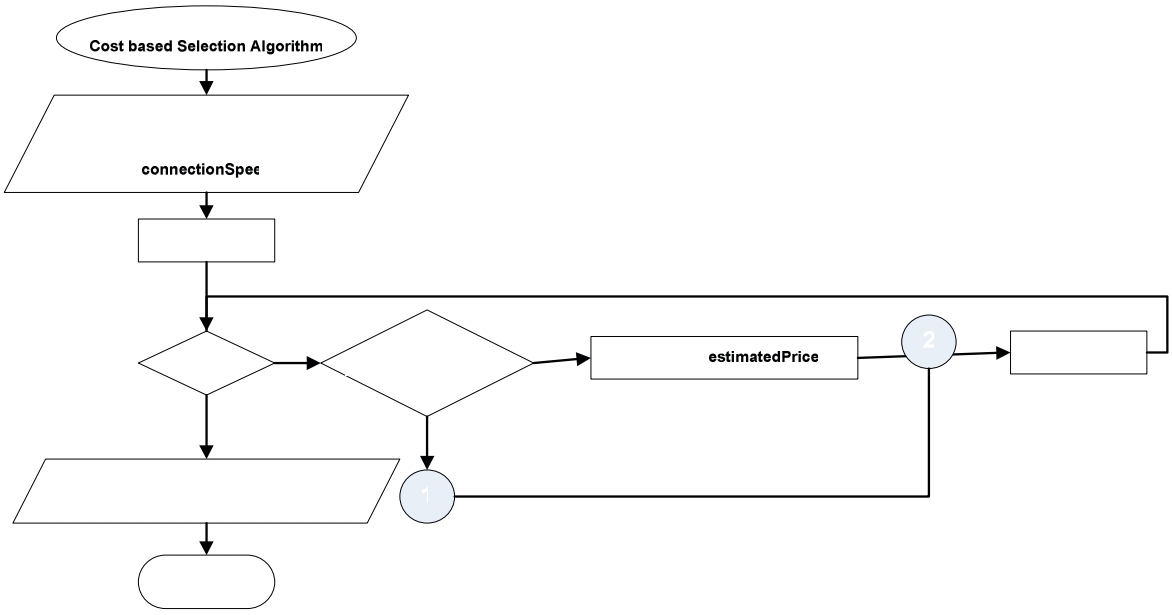

Figure 4a Cheapest algorithm selection3

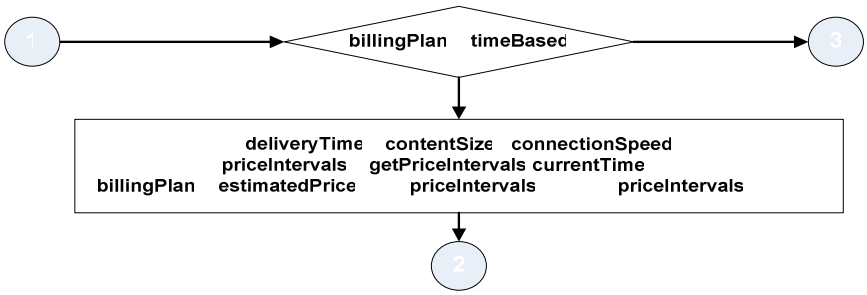

Figure 4b Estimated price for time based plan

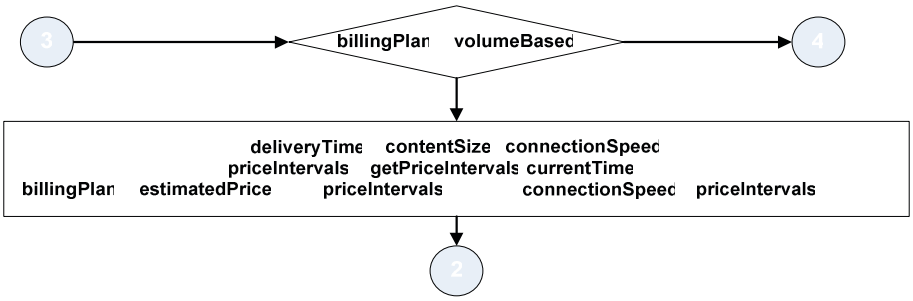

Figure 4c Estimated price for volume based plan

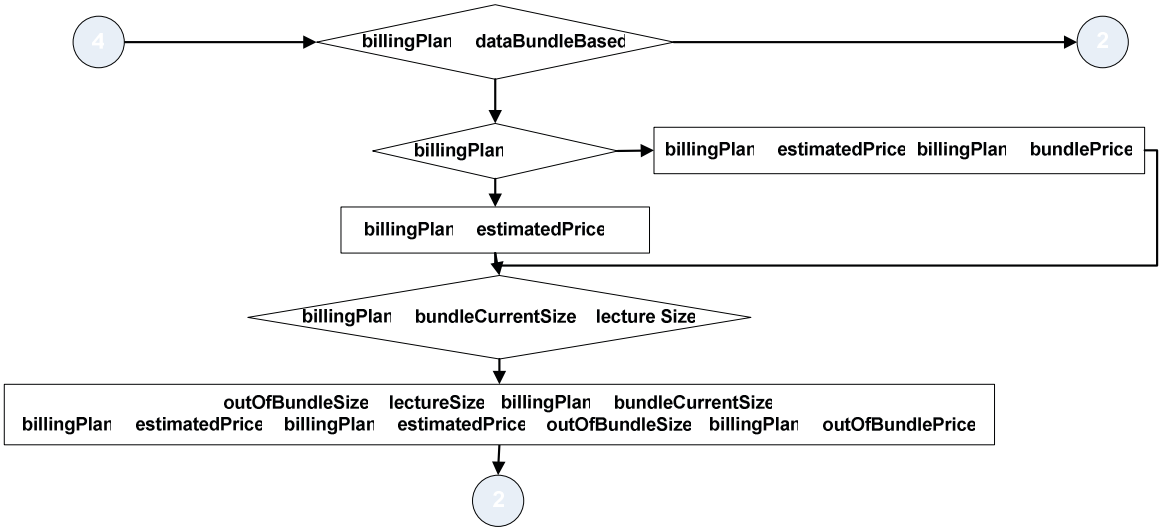

Figure 4d Price estimate for data based bundle plan

The estimated price the learner has to pay may be null in three cases:

- the learner has access to a free network
- the learner has a flat free plan
- the learner has a bundle data plan already in use and the remaining size of the bundle is less than the total size of the requested document.

Otherwise:

- if the learner has a data bundle plan already in use and the size of the lecture exceeds the remaining quantity of data from the bundle, the price for the quantity of information which exceeds the limit. This is calculated and that is considered the estimated price the learner has to pay (Figure 4d).
- if a data bundle plan is available but not in use, the price will include also the price of the bundle (Figure 4d).
- if the learner has a time based plan (Figure 4b), the estimated price will be computed based on the price per time and the average network speed.
- if the learner has a data volume based plan the estimated price is computed based on the

lecture size and the price per quantity of information(Figure 4c).

Having all these prices computed, a ranking can be made based on the amount of money the learner has to pay. Two other cases are taken into account when the data bundle based plans are classified: the expiring date for the data bundle or the quantity of information contained in a bundle. The first case is useful when there are two bundles already in use that have the same price. Probably most learners would choose to use the bundle that is going to expire first. For example if there are two bundles in use, first having a remaining data bundle of 500Mb and expires next day and the second one has 1Gb and expires in a week and the lecture size is less than 500Mb, the first network will be displayed for the learner as the first option. The second case is when the bundles are not in use yet, but two mobile operators offer at the same price data bundles with different limits on the quantity of information to be transferred. In this case the plan which has the bigger quantity of information in the bundle may be chosen. For example if an operator offers a 1Gb data bundle for 15 Euros whereas the second one offers 5Gb for the same price, the most advantageous for the learner would be the plan offered by the second operator.

After ranking the plans the top three plans in terms of cost are displayed to the learner and s/he will choose among them. However, the learner has the option to see the other plans, if s/he wishes to do so.

5. Conclusions and further work

This paper presented and discussed various billing plans that currently exist on the market for accessing the Internet. PACO-eLF – an adaptive e-learning framework was briefly presented and an cost oriented network selection algorithm was described in details. The algorithm assesses the billing plans of the active networks on the learner device and computes the price when downloading a given document, for each network. It provides the learner with information related to how much s/he needs to pay when the educational content is retrieved.

We are currently working on an improved version of the algorithm that provides a better estimation on the price the learner has to pay. We achieve this by taking into account also other messages/information sent over the network that are not included in the lecture size. The algorithm will also take into account network conditions, in order to provide the learner with the best network alternative over which the educational content can be sent. The PACO-eLF framework is currently under implementation. Tests will be performed to see the effects of the algorithm on the learner QoE (Quality of Experience). The results will be presented in another paper.

ACKNOWLEDGEMENT

This research work is supported by IRCSET Embark Postgraduate Scholarship Scheme and SFI Research Frontiers Programme.

References

[1]C. Shuler, “Pockets of Potential: Using Mobile Technologies to Promote Children’s Learning”, *The Joan Ganz Cooney Center at Seasame Workshop*, New York, USA, 2009 Retrieved April 10, 2009, from http://joanganzcooneycenter.org/pdf/pockets_of_potential.pdf

[2] D. Becking, S. Betermieux, B. Bomsdorf, F. Birgit, E. Heuel, P. Langer and G. Schlageter, „Didactic Profiling: Supporting the Mobile Learner” In G. Richards (Ed.), *Proceedings of World Conference on E-Learning in Corporate, Government, Healthcare, and Higher Education*, 2004, pp. 1760-1767.

[3]M. Yudelson, O. Medvedeva and R. Crowley, "A multifactor approach to student model evaluation," *User Modeling and User-Adapted Interaction*, 2008, 18(4), pp. 349-382.

[4]P. Karampiperis and D. Sampson, "Adaptive learning resources sequencing in educational hypermedia systems", *Educational Technology & Society*, 2005, 8(4), pp. 128-147.

[5]E. Brown, T. Brailsford, T. Fisher, A. Moore and H. Ashman, "Reappraising cognitive styles in adaptive web applications", *Proceedings of the 15th International conference on World Wide Web*, ACM Press, New York, USA, 2006, pp. 327-335.

[6]P. De Bra, D. Smits and N. Stash, “Creating and Delivering Adaptive Courses with AHA!”, *Proceedings of the first European Conference on Technology Enhanced Learning*, Springer LNCS 4227, Crete, October 2006, pp. 21-33.

[7]C. H. Muntean, “Improving learner quality of experience by content adaptation based on network conditions”, *Computers in Human Behavior*, 2008, 24(4), pp. 1452-1472.

[8]A. Brady and O. Conlan, V. Wade, “Dynamic Composition and Personalisation of PDA-based eLearning – Personalized mLearning”, *E-Learn’04, World Conference on E-Learning in Corporate, Government, Healthcare and Higher Education, Washington*, D.C, 2004, pp. 234-242.

[9]M. Á. C. González, M. J. C. Guerrero, M. A. Forment and F. J. G. Peñalvo, “Back and Forth: From the LMS to the

Mobile Mobile Device. A SOA Approach" *Proceedings Mobile Learning Conference 2009*, IADIS Press, 2009, pp. 114-120.

[10]D. Keegan, "Mobile Learning: The Next Generation of Learning Distance Education International", 2005, Retrieved April 30, 2009, from http://learning.ericsson.net/mlearning2/files/workpackage5/book.doc

[11]Telecoms Pricing, "Mobile Broadband Pricing Survey 2009", 2008, Retrieved April 10, 2009, from http://www.telecomspricing.com/product.cfm?ds=telecomspricing_content&prod=311&dept=304

[12]V. Roto, R. Geisler, A. Kaikkonen, A. Popescu and E. Vartiainen, "Data Traffic Costs and Mobile Browsing User Experience", *MobEA IV workshop on Empowering the Mobile Web, in conjunction with WWW2006 conference*, 2006, Retrieved April 10, 2009, from http://www.research.att.com/~rjana/MobEA-IV/PAPERS/MobEA_IV-Paper_7.pdf

[13]P. Isomursu, R. Hinman, M. Isomursu and M. Spasojevic, "Metaphors for the Mobile Internet", *Journal on Knowledge, Technology & Policy*, 2007, 20(4), pp. 259-26.

Section 5A

RADIO SYSTEMS 2

A Blind Detection Method of Non-Periodic DSSS Signals at Lower SNR

Junjie Pu
School of Telecommunication
Hangzhou Dianzi University
Hangzhou, 310018, China
gigibest@gmail.com

Zhijin Zhao
School of Telecommunication
Hangzhou Dianzi University
Hangzhou, 310018, China
zhaozj03@hdu.edu.cn

***Abstract*—Because detecting non-periodic direct spread spectrum sequence (DSSS) signals can not make use of periodicity and relevance directly, and the signals always flood in the background noise, the blind detection and parameter estimation is even more difficult. Since the fourth-order moment chip of non-periodic DSSS signals contains the carrier frequency information and has good performance in depressing Gaussian white noise, the detection method based on the quadratic fourth-order moment chip of non-periodic DSSS signals is proposed. Experimental results show that the detection performance of the proposed method is better than that of the double frequency method, spectrum-reprocessing method and cepstrum method. When the false alarm probability is 1%, the detection probability of the method reaches above 90% at SNR -20 dB.**

***Keywords- Non-periodic DSSS** signal; fourth-order moment chip; signal detection; lower SNR*

I. INTRODUCTION

Low probability of interception (LPI) signal detection and parameter estimation has been a hot and difficult research at home and abroad. Since the DSSS signal has been widely used in military communications, satellite communications satellite navigation systems and many other systems because of its secrecy capacity, concealment and anti-interference ability. DSSS signal can be divided into periodic signals and non-periodic signals. A non-periodic DSSS signal also known as long-code signals, which means a spread-spectrum sequences cycle including a number of information symbol cycle. That is, different information symbol code corresponds to different spread-spectrum PN code. Typical applications include JTIDS signal, GPS-P(Y) code signal and so on. WCDMA signals are non-periodic signals.

According to a lot of the current literature, the key of DSSS signal blind detection is generally focused on how to use the characteristics of PN code and the signal correlation, and also use the method of accumulation to depress the noise to achieve the detection and parameter estimation. Generally, DSSS signal is assumed a periodic signal, and some good test results at a low SNR are obtained. However, when the received signal is non-periodic DSSS signal, the blind detection and parameter estimation becomes very difficult at a low SNR. Because non-periodic DSSS signal destroys the characteristics of PN code cycle and its correlation, the signal detection performance degrades. The lower SNR means that signal is very weak and the signal spectrum is entirely submerged in Gaussian white noise spectrum, which brings larger error to the detection and data processing. Energy method [1], double frequency method [2], conventional multiplication delay detection method [3], cumulative method [4], cepstrum method [5] and spectral correlation method [6~8] can detect non-periodic DSSS signal successfully only above the SNR from -8dB. Therefore the non-periodic DSSS signal detection and estimation at a much lower SNR is a problem to be studied in depth.

Because the high-order statistics contains a rich information on the characteristics of signal, basing on the work of the paper [9~10], a blind detection method of non-periodic DSSS signals using the quadratic fourth-order moment chip at lower SNR is proposed in this paper. The detection probability of this method is above 90% at SNR -20dB, and this method doesn't involve extensive matrix operations.

II. SIGNAL MODEL AND THEORETICAL ANALYSIS

Non-periodic DSSS signal (WCDMA signal) is defined as:

$$\begin{aligned} s(t)=\sum_{k=1}^{K}\{&A_k[d_{ki}(t-t_k)G_k c_k(t-t_k)S_{ki}(t-t_k) \\ &-d_{kq}(t-t_k)G_k c_k(t-t_k)S_{kq}(t-t_k)]\cos(2\pi f_c t+\varphi_k) \\ &+A_k[d_{ki}(t-t_k)G_k c_k(t-t_k)S_{kq}(t-t_k) \\ &+d_{kq}(t-t_k)G_k c_k(t-t_k)S_{ki}(t-t_k)]\sin(2\pi f_c t+\varphi_k)\} \end{aligned} \quad (1)$$

where A_k is the kth user's signal amplitude; $d_{ki}(t-t_k)$, $d_{kq}(t-t_k)$ are the kth user's the odd-bit and evenl-bit data; $c_k(t-t_k)\in\{1,-1\}$ is OVSF code; the channel code in the same state varies with each other; $S_{ki}(t-t_k), S_{kq}(t-t_k)$ are the real and imaginary parts of the complex scrambling code. They are independent, and the scrambling code between the different areas is also independent. f_c is carrier frequency; φ_k is a random phase distributed in (0,2π) evenly. t_k is the kth user's random delay

and is uniformly distributed in the range of $[0,T]$; T is the width of the symbol.

The two hypotheses is:

$$H_1 : x(t) = s(t) + n(t) \tag{2}$$

$$H_0 : x(t) = n(t) \tag{3}$$

where $s(t)$ is non-periodic DSSS signal , $n(t)$ is Gaussian white noise with zero mean, and they are independent.

Under the hypothesis of H_0, the fourth-order moment of x(t) is:

$$m_{4x}(\tau_1,\tau_2,\tau_3) = \sigma_n^4[\delta(\tau_1)\delta(\tau_3-\tau_2)+\delta(\tau_2)\delta(\tau_3-\tau_1) + \delta(\tau_3)\delta(\tau_2-\tau_1)] \tag{4}$$

One of the fourth-order moment chip is:

$$m_{4x}(0,0,\tau) = 0 \ , \ \tau \neq 0 \tag{5}$$

Under the hypothesis of H_1, one of the fourth-order moment of x(t) is:

$$m_{4x}(0,0,\tau) = \{\sum_{k=1}^{K} A_k^4[m_{4d}(0,0,2\tau)+m_{4d}(0,1,2\tau+1)$$

$$+ m_{4d}(0,-1,2\tau-1)+\frac{1}{2}m_{4d}(1,1,2\tau)+\frac{1}{2}m_{4d}(-1,-1,2\tau)]$$

$$+ \frac{21}{2}\sum_{k=1}^{K}\sum_{m\neq k}^{K} A_k^2 A_m^2 R_d(0)R_d(2\tau)$$

$$+ 2\sigma_n^2\sum_{m\neq k}^{K} A_k^2 R_d(2\tau)\}R_c(\tau)R_S(\tau)\cos(2\pi f_c\tau)$$

$$+ \{\sum_{k=1}^{K} A_k^4[2m_{4d}(0,0,2\tau+1)-2m_{4d}(0,0,2\tau-1)$$

$$+ m_{4d}(1,1,2\tau+1)-m_{4d}(-1,-1,2\tau-1)]$$

$$+ 6\sum_{k=1}^{K}\sum_{m\neq k}^{K} A_k^2 A_m^2 R_d(0)[R_d(2\tau+1)-R_d(2\tau-1)]$$

$$+ \sigma_n^2\sum_{m\neq k}^{K} A_k^2[R_d(2\tau+1)-R_d(2\tau-1)]\}R_c(\tau)$$

$$R_S(\tau)\sin(2\pi f_c\tau) \tag{6}$$

In Eq.(6), $\tau \neq 0$, $R_c(\tau) = E[c(t)c(t+\tau)]$,

$R_d(\tau) = E[d(t)d(t+\tau)]$,

$R_S(\tau) = E[S(t)S(t+\tau)]$,

$m_{4d}(\tau_1,\tau_2,\tau_3)$ is the fourth-order moment of $d(t)$.

In Eq.(6), the carrier frequency component is contained in the fourth-order moment chip, the existence of non-periodic DSSS signal can be detected through the analysis of received signals in frequency domain. The figure 1 is the spectrum of $m_{4x}(0,0,\tau)$, when the carrier frequency is 10MHz and SNR is -5dB. Form the figure 1, $m_{4x}(0,0,\tau)$ has a clear peak at the carrier frequency. Hence, the fourth -order moment chip can be used as a detection statistics to detect the non-periodic DSSS signal.

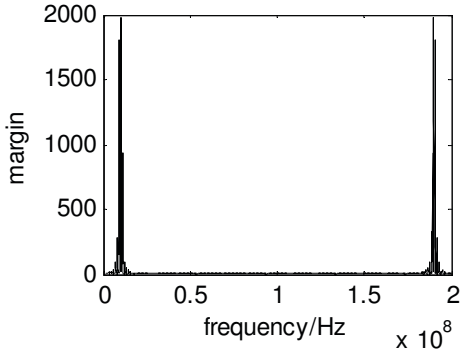

Figure 1. The spectrum of $m_{4x}(0,0,\tau)$ at SNR=-5dB.

III. DETECTION METHOD

A. *Detecting rules*

According to Eq.(5) and (6), under the hypothesis of H_1, the $m_{4x}(0,0,\tau)$ of the mixed-signal noise is not equal to zero; under the hypothesis of H_0, the $m_{4x}(0,0,\tau)$ of the Gaussian white noise is equal to zero, which means $m_{4x}(0,0,\tau)$ can suppress Gaussian white noise well except the point $\tau = 0$. At this point $\tau = 0$, there is information about noise. So $m_{4x}(0,0,\tau)$ at the point $\tau = 0$ is removed in order to reduce the impact of noise. In practice, since the estimation error of higher-order statistics will be increased with the number of the order increasing, higher-order statistics can not suppress Gaussian white noise as well as expected. In order to solve the problem, a new detection method of non-periodic DSSS signal based on the quadratic fourth-order moment chip (QFMC) is proposed, which is described as follows:

(1) The fourth-order moment chip of non-periodic DSSS signal is estimated as $m_{4x}(0,0,\tau)$.

(2) Removing $m_{4x}(0,0,\tau)$ at the point $\tau = 0$, the other $m_{4x}(0,0,\tau)$ is denoted $y(t)$.

(3) The fourth-order moment chip of $y(t)$ is computed and is transformed into frequency domain as $\left|FFT(m_{4y}(0,0,\tau))\right|$.

(4) If $\left|FFT(m_{4y}(0,0,\tau))\right| > T_D$, the non-periodic DSSS signal is existed; instead, the signal does not exist.

The detector structure of this method is shown in Figure 2.

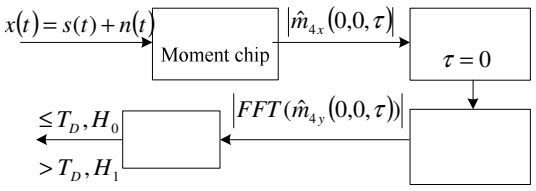

Figure 2. The blind detector structure of non-peridic DSSS signal based on the quadratic fourth-order moment chip.

Because the load of direct computation for $|m_{4x}(0,0,\tau)|$ is too heavy, Eq.(7) is used to reduce the amount of calculation. In the actual calculations, we approximate estimation of $|m_{4x}(0,0,\tau)|$ by omitting the computation of limit and expectation in Eq.(7).

$$|m_{4x}(0,0,\tau)| = IFT\{\lim_{N\to\infty} E\{\frac{1}{2N+1}[\sum_{t=-N}^{N} x(t)e^{-j2\pi ft}]^* \sum_{t=-N}^{N} x^3(t)e^{-j2\pi ft}\}\} \quad (7)$$

B. Simulation and Analysis

In the simulation, chip rate is 2Mbps; information rate is 10kbps; the carrier frequency is 10MHz; A/D sampling frequency is 200MHz, sample number N in one carrier period is 20. The spreading factor of Walsh code is 64, and the length of scrambling code is 2047. Additive noise is Gaussian white noise. A scrambling code contains a maximum of 32 information code. Setting the false alarm probability 1%, and the detection threshold T_D can be determined.

When the SNR is -25dB, the spectrum of $m_{4x}(0,0,\tau)$ is shown in figure 3. As the noise increases, the spectrum peak of signals is not obvious. In theory, the fourth-order moment chip of mixed-signal can effectively suppress Gaussian white noise, but since the estimation error and the noise is not strictly Gaussian white noise in the simulation, noise can not be completely suppressed. When the SNR is -25dB, the spectrum of $m_{4y}(0,0,\tau)$ is shown in figure 4. In this figure, noise has been suppressed and the spectrum peak of the non-periodic DSSS signals is obvious. So the proposed method in this paper not only can effectively reduce both Gaussian white noise and estimation error, but also can improve the detection performance.

If the user number is 2, 4, 8, respectively, the detection performance of proposed QFMC is shown in Figure 5. We can see that with the increase of the number of users K, the probability of detection increases. According to Eq.（6）, if the number of users increases, the value of the fourth-order moment chip will increase. Thus, the simulation results are consistent with the theory analysis.

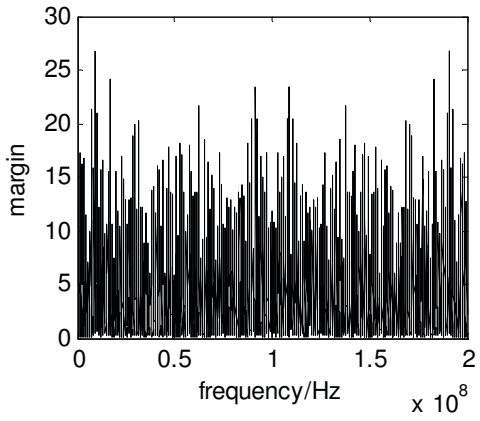

Figure 3. The spectrum of fourth-order moment chip of mixed-noise signal at SNR=-25dB

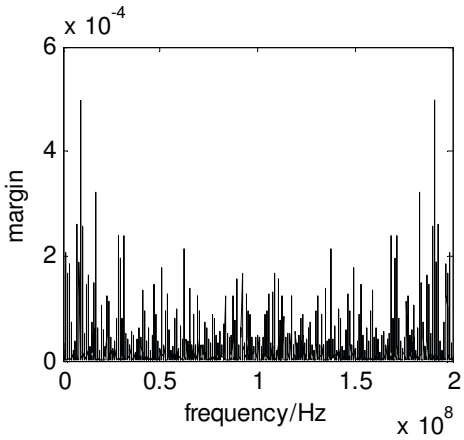

Figure 4. The spectrum of quadratic fourth-order moment chip of mixed-noise signal at SNR=-25dB

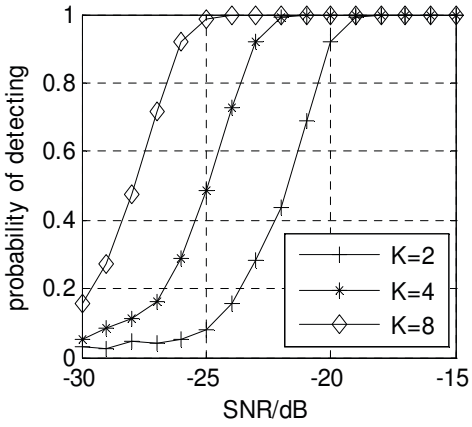

Figure 5. The detection of non-peridic DSSS signal with different number of users

When the number of users is 2, and the detection performances of the double frequency method (DFM), the spectrum-reprocessing method (SRM), cepstrum method (CM) and proposed method QFMC are shown in Figure 6. From the Figure 6, it can be seen that the detection probability of QFMC is above 90% at SNR -20dB. The detection performance of QFMC is much better than that of other methods. The SNR improvement of QFMC method is above 9dB when the detection probability is above 90%.

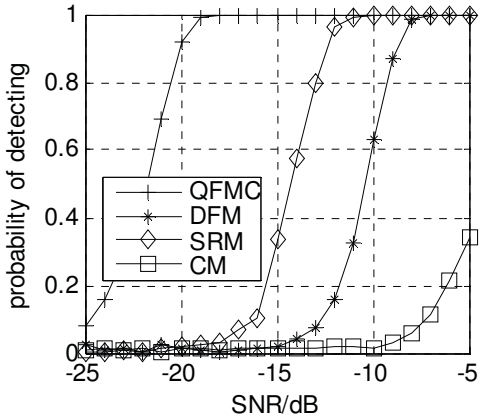

Figure 6. The blind detection of non-peridic DSSS signal with methods.

IV. CONCLUSION

Since the fourth-order moment chip of non-periodic DSSS signals has good performance in depressing Gaussian white noise, the detection method based on the quadratic fourth-order moment chip of non-periodic DSSS signals is proposed. The simulation results show this method' detection probabilities could reach above 90% at SNR -20dB.

REFERENCES

[1] Urkowitz, H. Energy Detection of Unknown Deterministic. Proceeding of IEEE. 1967. 55(4). 523-531.

[2] Hill, D.A. and Bodie, J.B. Carrier Detection of PSK Signals. IEEE Trans on Commun. 2001. 49(3).487-496.

[3] Yuan Liang, Liu Jinan and Wen Zhijin. A Detection Method For DS/SS Signal in the Low SNR Condition. Modern Electronics Technique. 2005.196(5). 50-51.

[4] Reed, D.E. and Wickert, M.A. Spread spectrum signals with low probability of chip rate detection. Selected Areas in Communications, IEEE Journal on. 1989. 7(4).595-601.

[5] Gardner, W.A. and Spooner, C.M.(1992). Signal Interception: Performance Advantages of Cyclic-Feature Detectors. IEEE Trans on Commu.40(1).149-149.

[6] Gardner, W.A. and Spooner, C.M.(1992). Detection and Source Location of Weak Cyclostationary Signals: Simplifications of the Maximum Likelihood Receiver. IEEE Trans on Commu.41(6).905-916.

[7] Zhang Tianqi, Zhou Zhengzhong. A new spectral Method of Periodic Detection of PC sequence in lower SNR DS/SS signals. Chinese Journal of Radio Science. 2001. 16(4).518-521.

[8] Zhang Jianli. DS Signal Detection. Radio Engineering of China. 1994. 24(2).19-21。

[9] Zhao Zhijin, Wu Jia, Xu Chunyun. The Study on the Detection Methods of DSSS/QPSK Signal Based on the Fourth-order Cumulants. Acta Electronica Sinica. 2007. 35(6).1046-1049.

[10] Wu Jia, Zhao Zhijin, Shang Junna, Kong Xianzheng. Detection and Multiple Parameter Estima tion Methods for Direct Sequence Spread Spectrum Signal at Lower SNR. Computer Simulation. 2008.25(2).153-156.

Power Consumption Analysis of Bluetooth in Sniff Mode

Jiangchuan Wen
Electronic and Computer Engineering Department
University of Limerick
Limerick, Ireland
Jiangchuan.Wen@ul.ie

John Nelson
Electronic and Computer Engineering Department
University of Limerick
Limerick, Ireland
John.Nelson@ul.ie

Abstract—**Bluetooth (BT) is a short-range wireless communications system and the key features of BT are robustness, low power, and low cost. In this paper, we focus on the BT power consumption in sniff mode. First of all, we discuss the BT operations and acquire the expression of BT average power in sniff mode. Secondly, we use the current unit (microampere) to scale the BT's average power and calculate it using the acquired expression. Thirdly, the analysis shows significant saving when a BT chip is in the slave role using the sniff mode even when using short sniff intervals, for instance a sniff interval T_{sniff} is 40 ms, the slave role can save 96.6% power, which is in comparison to the master's power consumed when N_{poll}=2 slots on the ACL links. Given that the slave's clock needs re-synchronization and considering the worst case clock drift and the response time, the longest supported T_{sniff} is not recommended. The impacts of the $N_{sniff\_attempt}$ and T_{sniff} parameter and the recent introduction of sniff sub-rating are also considered.**

Keywords-component: Bluetooth, Sniff Mode, Power saving, Power Consumption, Sniff sub-rating;

I. INTRODUCTION

Bluetooth [1] is a popular short-range wireless communications system, operating in the unlicensed 2.4 GHz ISM (Industrial Scientific Medical) band and its key features are robustness, low power, and low cost. Currently, Bluetooth is being applied to more and more applications in diverse fields, for example PC accessories, mobile phone accessories, home and entertainment devices, medical and fitness sensors, automotive industry and automation – factory and industrial sensors etc.

Increase with the Bluetooth application widely, more and more portable devices have a Bluetooth module. These devices have a large battery to supply for up to a week or more. As Bluetooth module is the main data transmission module between devices, its energy consumption problem is gradual emerged. This paper presents the BT power consumption study of the standard specified sniff mode.

The paper is structured as follows. Section II gives a short summary of Bluetooth low power modes. Section III explains the sniff mode operation in detail. In section IV, we discuss the expression of BT average power in sniff mode. Section V we evaluate the BT's power and analyze the results. Finally, section VI presents our conclusion.

This publication has been supported by the Irish Research Council for Science, Engineering and Technology (IRCSET) and the Wireless Access Research Centre, University of Limerick, Ireland.

II. BLUETOOTH LOW POWER OPERATIONS OVERVIEW

Bluetooth provides various low-power operations to manage power consumption. At the microscopic level, the operation of packet handling and slot occupancy must be minimized but in accordance with the core specification. The basic idea is to reduce information exchange between the Bluetooth devices, and allow the transmitter and receiver to return to sleep if possible.

At the macroscopic level, the basic idea which realizes low power is to adopt low power operation that reduces the duty cycle of the Bluetooth devices. It has three low power operation modes: sniff, hold and park, all of which are optional.

In sniff mode, the master and slave agree periodic anchor points where they will communicate. Consequently, the Bluetooth devices negotiate a sniff interval (T_{sniff}) and a sniff offset (D_{sniff}) in the Asynchronous Connectionless Link (ACL) logical transport which is used largely to carry data as opposed to voice. The master shall only start a transmission to the slave in the specified sniff attempt slots and the slave may return to sleep in the remaining slots of the T_{sniff} period. The sniff sub-rating (SSR) allows both the master and slave to increase the time between sniff anchor points, which could further reduce power consumed by link management in sniff mode.

In hold mode, the slave shall not support ACL packets on the piconet's channel. A timer shall be initialized with the timeout value holdTO. When the timer expires, the slave shall wake up, synchronize to the traffic on the channel and will wait for further master transmissions. During sniff and hold mode, the slave device keeps its logical transport address (LT_ADDR).

A slave in Park mode does not need to participate on the piconet's channel, but still needs to remain synchronized to the channel. The slave shall give up its logical transport address LT_ADDR and shall receive two new addresses to be used in the park state.

Most research work focuses on the sniff mode and it is widely recommended for low-power operation. In [2] [3], the authors proposed a sniff scheduling scheme for power saving. In our paper, we will discuss the Bluetooth power consumption in sniff mode within different sniff intervals.

III. BLUETOOTH OPERATIONS IN SNIFF MODE

Sniff mode is the most common and flexible method for reducing Bluetooth's power consumption. The operations are as follows.

A. LMP and HCI Commands Operations

The Bluetooth core system consists of a Host and one or more Controllers [1]. A Host is defined as all of the layers below the profiles and above the Host Controller Interface (HCI). A Controller is defined as all of the layers below the HCI.

The Link Manager (LM) controls how the Bluetooth piconets and scatternets are established and maintained by the Link Control commands. The Host Controller Interface (HCI) provides a uniform command method of accessing controller capabilities.

To enter sniff mode, both the master and slave can start a negotiation through the Link Manager Protocol (LMP) messages, commonly referred to as LMP protocol data units (PDUs). The process is initiated by sending an LMP_sniff_req PDU containing a set of parameters, which includes *timing control flags*, D_{sniff}, T_{sniff}, $N_{sniff\_attempt}$, $N_{sniff\_timeout}$. The receiving LM shall then decide whether to 1) reject the attempt by sending an LMP_not_accepted PDU; 2) suggest different parameters by replying with an LMP_sniff_req PDU; or 3) to accept the request. The negotiation is shown at Fig.1.

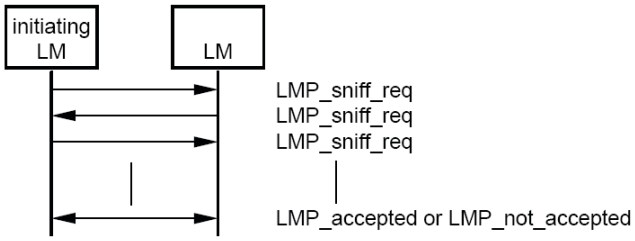

Figure 1. Negotiation for sniff mode [1]

The HCI_Sniff_Mode command is used to alter the behavior of the LM and have it place the ACL baseband connection associated with the specified Connection Handle into the sniff mode. The HCI_Exit_Sniff_Mode command is used to end the sniff mode for a Connection Handle, which is currently in sniff mode.

The HCI_Sniff_Mode command has six command parameters, which are *Connection_Handle, Sniff_Max_Interval, Sniff_Min_Interval, Sniff_Attempt* and *Sniff_Timeout*. Note the HCI_Sniff_Mode parameters include a min and max sniff interval, allowing the LMP a degree of flexibility in selecting the T_{sniff} period.

An example of a sniff mode request which is accepted is shown Fig.2.

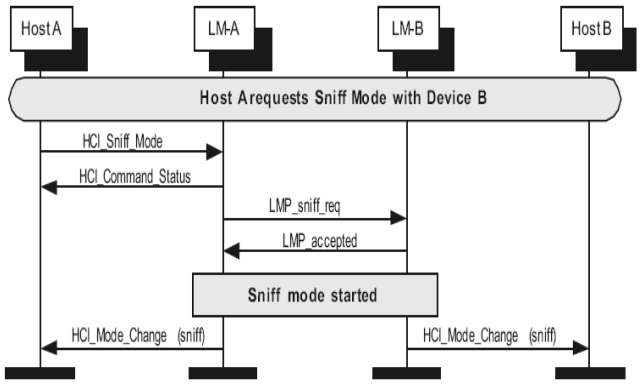

Figure 2. Sniff mode request by LMP and HCI commands [1]

B. Transmitter and Receiver Operations

When a slave enters sniff mode, it needn't listen at every receive slot (Rx) and its receiver may go to sleep until the next anchor point. There are two key parameters in sniff mode: $N_{sniff\_attempt}$ and $N_{sniff\_timeout}$. These parameters specify the number of baseband receive slots for sniff attempt and timeout, respectively. The slave continues to listen from the anchor point for the specified number of sniff attempts, and if it has received a packet addressed to it, then it may continue to listen for more packets up until the specified timeout. The slave's receiver prepares to receive packets from the master at the scheduled sniff receive slots and do some operations based on the content of received packets or pending data for transmission.

Fig.3 gives an overview of the operations of the slave transmitter and receiver.

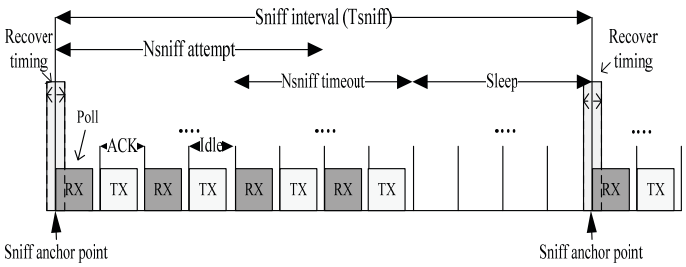

Figure 3. The slave's operations in sniff mode

From Fig.3, we observe that the slave has a recover timing (RT) period at the sniff anchor point. The reason is the slave runs using its native clock (CLKN) in sniff mode and looses synchronization while sleeping. The master clock (CLK) is used for all timing and scheduling activities in the piconet. The slave maintains its own approximation to the master clock, but due to timing jitter and time drift between the respective clocks, it must continuously resynchronize. Hence, an uncertainty window is defined around the exact receive timing. The slave shall not recover the master timing until it receives a packet including the piconet access code from the master at the sniff attempt slots. The slave's recover timing operation is shown in

Fig.4 where the recover timing window is centred around the slaves estimation of the sniff anchor point time.

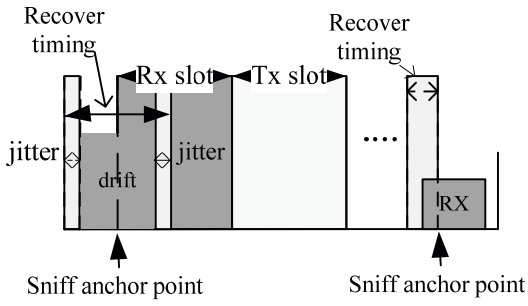

Figure 4. The slave's recover timing operation in sniff anchor point

IV. BT AVERAGE POWER EXPRESSION IN SNIFF MODE

The Bluetooth's power consumption in sniff mode will be scaled by the average power during sniff interval. We analyze the different states when the Bluetooth device is in sniff mode and calculate the time spent in each state (t_i) [4]. Therefore the average power can be expressed by

$$P_{avg} = \frac{\sum P_i * t_i}{\sum t_i} \tag{1}$$

Where P_i represents the power consumption in state i.

A. Slave's Average Power

In sniff mode, the CLKN may be driven by a low power oscillator with worst case timing accuracy (specified in the standard as drift=+/-250ppm and jitter=10μs), the slave's Rx recover timing period (t_{RT}) should be considered. The drift time parameter (t_{drift}) and jitter time parameter (t_{jitter}) will incur power consumption due to resynchronization. The RT power in sniff mode $P_{\mathrm{RT}}(S)$ is the averaged power in a sniff interval, which is as shown in:

$$P_{\mathrm{RT}}(S) = P_{drift}(S) + P_{jitter}(S)$$

$$= \frac{(2 * drift * T_{sniff} + 2 * t_{jitter}) * i_{Rx}}{T_{sniff}} * V \tag{2}$$

S is the slave. T_{sniff} is the sniff mode interval; i_{Rx} is the current of a device in slave role when receiving; V is the voltage for the specific Bluetooth chip.

To simplify the analysis, we set $N_{sniff\_timeout}$=0. The t_{slot}'s length is 625μs. Although it is possible to go to idle after the packet has been received, we will assume that it remains receiving for the full slot. Therefore, from the sniff description of part III, the slave's Rx consumed average power $P_{\mathrm{Rx}}(S)$ in sniff mode is

$$P_{\mathrm{Rx}}(S) = \frac{(N_{sniffattempt} * t_{slot}) * i_{Rx}}{T_{sniff}} * V \tag{3}$$

If the master has no traffic to the slave during the sniff intervals, it is recommended that single slot packets are transmitted by the master during the slave re-synchronization. Therefore the slave should be sent a POLL or NULL packet which includes the piconet access code so that the slave shall keep synchronized to the channel. The slave's transmitter will acknowledge, at the corresponding transmission slot (Tx) e.g. using a NULL packet if no command or data needs to be sent. The slave in the other Tx opportunities typically won't send any packet if it has nothing to send. The slave's Tx consumed average power $P_{\mathrm{Tx}}(S)$ in sniff mode is

$$P_{\mathrm{Tx}}(S) = \frac{i_{Tx} * t_{slot} + ((N_{sniffattempt} - 1) * t_{slot}) * i_{Tx\_idle}}{T_{sniff}} * V \tag{4}$$

After $N_{sniff\_attempt,}$ the slave enters sleep until the next sniff anchor point, which means the lowest power consumption while the slave is in connection state. The sleep consumed average power in sniff mode is

$$t_{sleep} = T_{sniff} - (2 * drift * T_{sniff} + 2 * t_{jitter}) - N_{sniffattempt} * 2 * t_{slot}$$

$$P_{\mathrm{sleep}}(S) = \frac{t_{sleep} * i_{sleep}}{T_{sniff}} * V \tag{5}$$

The average power in sniff mode for the basic scenario considered is the sum of every operations average power, which is given by:

$$P_{avg}(S) = [P_{\mathrm{RT}}(S) + P_{Rx}(S)] + P_{Tx}(S) + P_{Sleep}(S) \tag{6}$$

B. Master's Average Power

The master has three typical operations in sniff mode on the ACL link. The first and worst case power consumption is when the master sends a POLL packet to the slave and receives an NULL packet in return and continues to do so in sniff intervals, which means the effective sniff interval T_{sniff}=1.25ms(2 slots) and the master's slots are always involved (N_{poll}=2 slots) on the ACL links and the average power is

$$P_{avg\_on}(M) = \frac{i_{Tx} * \frac{1}{2} T_{sniff} + i_{Rx} * \frac{1}{2} T_{sniff}}{T_{sniff}} * V$$

$$= \frac{1}{2}(i_{Tx} + i_{Rx}) * V \tag{7}$$

M is the Master.

The second is when the master works as in normal ACL with no data traffic to send in sniff intervals, which means the master only sends POLL or NULL packets within the poll internal N_{poll}, which is default 40 slots. The average power is

$$P_{avg\_poll}(M) = \left(\frac{(i_{Tx} + i_{Rx}) + i_{idle} * (N_{poll} - 2)}{N_{poll}} \right) * V \tag{8}$$

The third typical operation is when the master is on the ACL link only with data transfer e.g. a file transfer, which means the master slots are used for other logical transport

traffic or for POLL and NULL packets to the slave which might be in active mode or sniff mode. The approximate power consumption of this work state is between $P_{avg\_on}(M)$ and $P_{avg\_poll}(M)$.

Fig. 5 illustrates an example of Bluetooth operation during sniff for both master and slave devices. Idle denotes that the receiver attempts to receive but after the short receive window, realizes that there is no packet being transmitted and changes to the idle state.

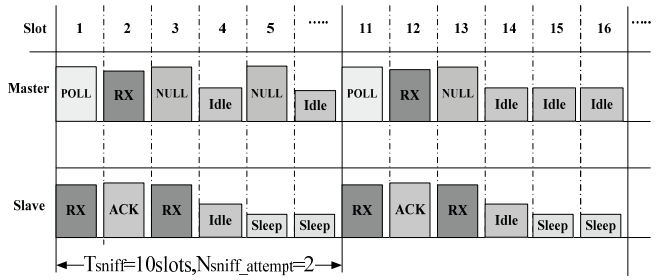

Figure 5. An example of Bluetooth theoretical power in sniff mode

V. POWER CONSUMPTION CALCULATION AND ANALYSIS

A. Calculate Average Power

The power consumption of a Bluetooth module is the sum of that of the BT chip and other parts of the module e.g. microprocessor or wired communication devices. If BT chip works in sniff mode, other parts of module e.g. three-line UARTs could be set to sleep to save power. We only consider the power saving of a BT chip in sniff mode in the paper.

Different Bluetooth chips have different Tx or Rx current and voltage parameters. A simplifying assumption is that voltage parameter is a normalized constant (e.g. V=1) and use the current's unit (microampere) to scale Bluetooth's power.

From [5] [6] [7], we obtain indications of the range of the current parameters of Bluetooth. Therefore we can estimate the values of the parameters, which are representative of real device values. We set the parameters as follows: i_{Tx}=22mA, i_{Rx}=18mA, i_{Tx_idle}=i_{idle}=4mA, i_{sleep}=40μA, $N_{sniff\_attempt}$=1 and $N_{sniff\_timeoutt}$=0. Considering the time drift parameter is variable and isn't always specified at the max value. We set its average value $drift_{avg}$=0.5*$drift_{max}$=125ppm.

Therefore, we can make use of (2)-(8) to calculate average power. The result is as follows:

TABLE I. BT CHIP'S AVERAGE POWER BASED ON CURRENT CONSUMPTION ON ACL LINKS WITH SNIFF MODE

Connection type	Operations Mode (on ACL links)	Average	Unit	$\frac{P(S)}{P(M)}$ (%)
master	N_{poll}= 2 slots	20.0	mA	-
master	N_{poll}= 40 slots(default)	4.80	mA	-
slave	T_{sniff} = 1.25 ms	20.29	mA	101%
slave	T_{sniff} = 40 ms	0.677	mA	3.4%
slave	T_{sniff} = 1.28 s	0.0642	mA	0.32%
slave	T_{sniff} = 40.9 s	0.0454	mA	0.23%

B. Power Consumption Analysis

From Table 1, we observe that if T_{sniff} =1.25ms (2 slots), the BT chip of the slave won't save power in sniff mode and the slave's power will be consumed more than the master's power which in slots are always involved (N_{poll}=2slots) on the ACL links. Fig. 6 compares and analyzes the master and slave's power calculation results for different sniff intervals.

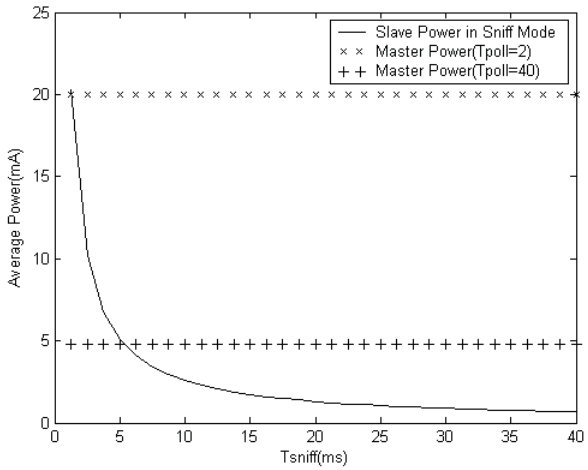

Figure 6. Average power of BT chip in sniff mode, T_{sniff} =[1.25ms,40ms]

If T_{sniff} =40ms, the chip of slave will save 96.6% power consumption, compared to the master's average power consumed using N_{poll}=2slots on the ACL links. The slave's power calculation results for the sniff mode with different sniff intervals are depicted in fig. 7.

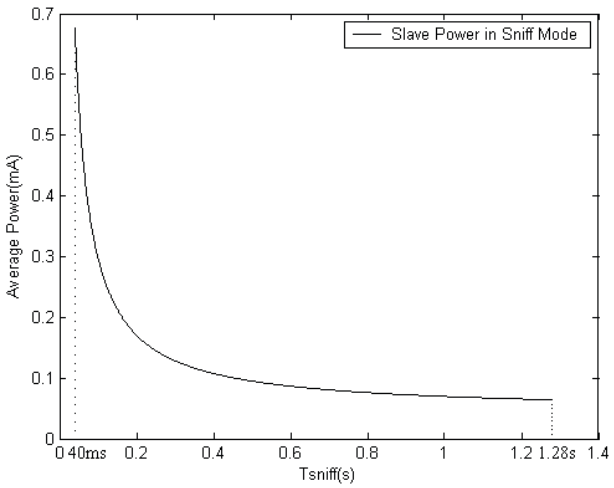

Figure 7. Average power of BT chip in sniff mode, T_{sniff} =[40ms,1.28s]

If T_{sniff} = 40.9s and $N_{sniff\_attempt}$=1, the slave role will save more power in theory. In reality, devices should not adopt the longest T_{sniff} to save power even when the application allows it. There are a few things that must be considered besides power saving.

First of all, we must consider the CLK time drift of slave and the channel conditions. If in perfect synchronization then

the slave device always receive the master to slave transmission at the sniff anchor point. However, the slave CLKN time drift could result in $2*drift*T_{sniff} \approx$10-20ms drift in the case T_{sniff} = 40.9s; whereby the slaves might lose timing and shall require re-synchronization before it may send information. The re-synchronization of the slave consumes power dependent on the length of a single search window and the duration of the search.

Simultaneously, the slave may lose traffic from the master depending on channel conditions. In the worse case channel conditions it is possible that an LMP supervision timeout will be reached (max 40.9s if enabled) causing the ACL connection to be lost. Thus, it is recommended that the parameter $N_{sniff\_attempt} * t_{slot}$ is larger than $2*drift_{max}*T_{sniff}$ in sniff mode to improve the probability that the slave receives a packet scheduling from master during the sniff attempt windows. The slave will consume more power than the above calculation indicates in the longer sniff intervals.

Secondly, for most BT applications it is important that the device has a rapid response time and minimizes latency when communicating to the other device. The longer the sniff interval will incur the longer waiting time when the device needs to transmit data. Some applications will switch between sniff mode and active mode with high frequency. Consequently, if the power saving of BT is only the BT chip in sniff mode, it is meaningless to improve the power saving from 96.6% to 99.9% by using the longest sniff interval.

Last but not least, sniff sub-rating provides a mechanism to increase the time between sniff anchor points. Even if SSR increases the response time in the normal case the advantage of SSR is that when a packet is missed at a SSR anchor point the slave can listen and recover synchronization at the next sniff anchor points.

Finally, there are implications when selecting the value of the $N_{sniff\_attempt}$ parameter. From a power consumption perspective, Fig.8 shows the impact of $N_{sniff\_attempt}$ and T_{sniff}.

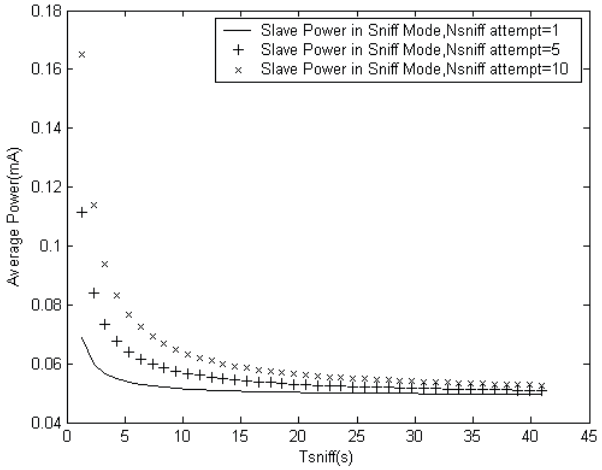

Figure 8. Average power of BT chip in sniff mode, T_{sniff}=[1.28s,40s]

VI. CONCLUSION AND OUTLOOK

This paper introduced the expressions for average BT power consumption through analysis of the BT's operations in sniff mode. We evaluated the BT average power in sniff mode with different sniff intervals. The analysis shows the BT chip in slave mode can save 96.6% of its power consumption while in the sniff mode based on realistic current parameters and setting T_{sniff}=40ms. The saving is in comparison to the master's power consumed when N_{poll}=2slots on the ACL links. The more the slave enters sniff mode with an appropriate T_{sniff}, the more the slave can save power.

In order to reduce the probability of link disconnections, the appropriate value of T_{sniff} and $N_{sniff\_attempt}$ should be determined by the channel conditions. The longest T_{sniff} is not recommended in this paper, its value will be determined by considering the application's required response time and whether sniff sub-rating is available.

Most current BT based devices do not achieve these savings, and the resultant extended battery life, as it requires that other chips in a BT module must also be put into deep sleep during the sniff sleep period e.g. UART devices and microprocessors. This requires cooperation between the host and host controllers, and some of the BT modules do support this.

REFERENCES

[1] Bluetooth SIG, "Specification of the Bluetooth system".21st, April, 2009, Version 3.0+HS;
https://www.bluetooth.org/Technical/Specifications/adopted.htm

[2] Ting-Yu Lin; Yu-Chee Tseng, "An adaptive sniff scheduling scheme for power saving in Bluetooth",Wireless Communications, IEEE [see also IEEE Personal Communications] Volume 9, Issue 6, Dec. 2002 Page(s):92 - 103

[3] Li Xiang, Yang Xiaozong; "A sniff scheduling policy for power saving in Bluetooth piconet", Parallel and Distributed Systems, 2005. Proceedings. 11th International Conference on Volume 1, 20-22 July 2005 Page(s):217 - 222 Vol. 1

[4] Alexandre Lewicki, Javier Del Prado Pavón, Jo Degraef,Jacky Talayssat,and Gilles Jacquemod, "Power Consumption Analysis of a Bluetooth over Ultra Wide Band System", Ultra-Wideband, 2007. ICUWB 2007. IEEE International Conference on, 24-26 Sept. 2007 Page(s):241 - 246

[5] Paul van Zeijl, Jan-Wim Th. Eikenbroek, Peter-Paul Vervoort, Suma Setty, Jurjen Tangenberg, Gary Shipton, Eric Kooistra, Ids C. Keekstra, Didier Belot, Klaas Visser, Erwin Bosma and Stephan C. Blaakmeer. "A Bluetooth radio in 0.18-µm CMOS", Solid-State Circuits, IEEE Journal of Volume 37, Issue 12, Dec. 2002 Page(s):1679 - 1687

[6] BlueCore4-External Data Sheet (BC417143B-ds-001P);
https://www.csrsupport.com/document.php?did=1539

[7] LMX9838 Bluetooth Serial Port Module;
https://www.national.com/ds.cgi/LM/LMX9838.pdf

Necessity for an Intelligent Bandwidth Estimation Technique over Wireless Networks

Zhenhui Yuan, Hrishikesh Venkataraman and Gabriel-Miro Muntean
School of Electronic Engineering, Dublin City University, Dublin, Ireland
E-mail {yuanzh, hrishikesh, munteang}@eeng.dcu.ie

Abstract

With the development of broadband systems, multimedia communication in wireless networks has become very common. However, supporting multimedia applications over multiple users either require high bandwidth or a dynamic bandwidth utilization mechanism. This in turn calls for an efficient technique, that can estimate the available bandwidth in the network accurately over real-time. In this paper, the different estimation algorithms are analyzed and the performance of state-of-the-art estimation algorithm, 'Spruce', is evaluated by comparing with the actual measured bandwidth. The key characteristic found was that the bandwidth estimation technique always produces some error which results in inaccurate estimation. This brings about the necessity for an intelligent estimation technique that would not only offset the inaccuracy resulting from the self-use of the bandwidth, but also minimize the bandwidth used by the estimation algorithm.

I. Introduction

In the recent years, there has been rapid growth of Internet-based services over the wireless network. With this, more and more demands are being placed on the performance of the network. The end-users demand that consistent monitoring of the performance is carried out, in order to both detect faults quickly and also predict and make provision for the growth of the network.

Measuring the performance of the Internet over wireless network is extremely difficult. Even with the complete support of the different Internet service providers (ISP), the complexity of the network means that normally multiple providers are involved in the end-to-end connection between hosts. This situation makes the monitoring of end-to-end performance by any one ISP nearly impossible. In addition, the wireless networks, especially the cellular networks providing both voice and video require accurate bandwidth estimation to optimize the network performance [1]. This puts a great demand for new tools that would enable the end-users and the service providers to assess the performance of the wireless network, especially the network bandwidth, without any external assistance. There are significant constraints in the development of such tools. Importantly, these tools need to rapidly and easily measure the end-to-end performance of the network, while not placing any additional load on the network than is absolutely necessary. It should be noted that any extra load would restrict the times that the measurement could be made, and depending on the topology of the wireless network, it could create large extra traffic charges.

A large amount of time and energy is currently being spent for researching on high speed, next generation networks [2]. These networks are being constructed in-order to support the large growth in the Internet, as well as enabling high bandwidth services to run over the network to more people. There is an increasing demand in the industry to find out whether the performance obtained from these networks is what is expected from them. With this regard, there has been much work on developing techniques for estimating the capacity and available bandwidth of network paths based on end-point measurements. Bandwidth is a key factor in several network technologies. Several applications can benefit from knowing bandwidth characteristics of their network paths. The motivation behind bandwidth estimation has been the potential for applications and end-host-based protocols to take advantage of bandwidth information in making intelligent choices on server selection, TCP ramp-up, streaming media adaptation, etc [3].

In this paper, the different bandwidth estimation techniques that have been proposed and used for wireless networks have been analyzed. Especially, the performance of the state-of-the-art technique, "Spruce" is analyzed in detail, and its advantages and

shortcomings are discussed. In addition, a novel intelligent estimation technique is introduced, especially the characteristics required to make it an efficient method.

The paper is organized as follows. Section II describes the related work, whereas Section III describes the performance of the state-of-the-art bandwidth estimation method, and its characteristics. Section IV describes the experimental set-up that has been built, while Section V describes the simulation results. Section VI introduces a novel intelligent bandwidth estimation technique. Finally, Section VII provides the conclusions and the future work in this direction.

II. Related Work

Recently, bandwidth estimation techniques have drawn widespread interests in network management arena. A couple of bandwidth estimation techniques have been based on the packet-pair principle [4, 5]. However, the initial versions of such techniques did not consider the problem of cross-traffic interference. In order to alleviate this problem, various refinements have been proposed, that includes - sending trains of packets of various sizes (e.g., bprobe [6]) and better filtering techniques to discard incorrect samples: for example, nettimer [7]. However, the filtering technique is made complex by the multi-modality of the distribution of packet-pair spacing [8] and with the observation that the dominant mode might not correspond to the actual network bandwidth [9]. There are several other bandwidth estimation techniques, that were proposed in the early years of research in wireless networks - such as cprobe [6], symptotic dispersion rate [9] etc. Many of the recently proposed techniques fall into two categories: packet rate method (PRM) and packet gap method (PGM). PRM-based tools, such as pathload [10], PTR [11], pathchirp [12], and TOPP [13], are based on the observation that a train of probe packets sent at a rate lower than the available bandwidth

The current research on bandwidth estimation algorithms could be classified into three categories [14], [15]: *packet dispersion measurement* (PDM), *probe gap model* (PGM) and *probe rate model* (PRM). The PDM techniques, such as the packet pair or packet train, estimates network capacity by recording the packet inter-arrival time. However, the main disadvantage of PDM-based technique is that they have very low accuracy when applied to the wireless networks. The basic principle of PGM is that the server sends a probe packet pair with time dispersion, T_{in}, and after successful transmission, the receiver records a changed dispersion time, T_{out}. The value, $T_{out} - T_{in}$ is then the time for transmitting crossing traffics under the condition that a single bottleneck link is assumed. The crossing traffic rate, $BW_{c,}$ could be written as $BW_c = (T_{out} - T_{in}) \times C/T_{in}$, where C is the capacity of the network. Hence, the estimated available bandwidth would be $C - BW_c$. However, the main disadvantage of PGM is that it assumes that the network capacity is known, and that this would supply fast as well as a certain accuracy of estimation. In reality, however, the network capacity is not always known beforehand. The PRM techniques estimate bandwidth using three kinds of traffic rates: sender-side probing rate (C_s), receiver-side probing rate (C_r) and available bandwidth (BW).

III. State-of-the-art Bandwidth Estimation

In terms of measuring the kind of bandwidth in the network, most of the proposed techniques concentrate on measuring one of two values - either the individual link bandwidths of a path, or the capacity of a path. In general, these techniques can be classified into two groups: *Single packet and packet pair techniques*. The names refer to the number of packets that are used in a single probe. A measurement of a link or path will consist of multiple probes, in the case of some implementations [16], this can be in the order of 10MB of data (14400 individual probes) to measure a 10 hop path. The following sections will detail the theory of these techniques, improvements suggested and example implementations.

a. **Single packet techniques:** This method concentrates on estimating the individual link bandwidths as opposed to end-to-end properties. These techniques are based on the observation that slower links will take longer to transmit a packet than faster links. If it is known how long a packet takes to cross each link, the bandwidth of that link can be calculated.
b. **Packet pair technique**: This method attempt to estimate the path capacity not the link capacity discovered by single packet techniques. These techniques have been in use since at least 1993, when Bolot [17] used them to estimate the path capacity between France and the USA. He was able to quite accurately measure the transatlantic capacity, which at that time was 128kbps. Packet pair techniques are often referred to as packet dispersion techniques. This name is perhaps more descriptive. A packet experiences a serialization delay across each link due to the bandwidth of the link. Packet pair techniques send two identically sized packets back-to-back, and measure the difference in the time between the packets when they arrive at the destination.

Spruce: Spruce has been one of the most successful bandwidth estimation techniques under the packet pair technique. Spruce has been found to be significantly superior to other methods like Pathload and IGI [18]. The technique of Spruce is explained, in detail, followed by the experimental results in the next section.

Spruce (Spread Pair Unused Capacity Estimate) is a tool for end hosts to measure available bandwidth. It samples the arrival rate at the bottleneck by sending pairs of packets spaced so that the second probe packet arrives at a bottle-neck queue before the first packet departs the queue. Spruce then calculates the number of bytes that arrived at the queue between the two probes from the inter-probe spacing at the receiver. Spruce computes the available bandwidth as the distance between the path capacity and the arrival rate at the bottleneck. Spruce is based on PGM. Like other PGM tools, Spruce assumes a single bottleneck that is both the narrow and tight link along the path.

Some of the characteristics of Spruce that distinguishes it from other bandwidth estimation tools are explained below.

1. Spruce uses a Poisson process of packet pairs instead of packet trains (or chirps). This form of sampling done by Spruce makes it both non-intrusive and robust.

2. With the help of a careful parameter selection, Spruce ensures that the bottleneck queue is not empties between the two probes in a pair, which is a prerequisite for having the correctness of gap model.

3. Spruce distinguishes capacity measurement clearly from available bandwidth measurement. Spruce considers that the capacity can be measured without any difficulty with one of the capacity measurement tools. In addition, it assumes that the capacity remains stable when measuring the available bandwidth. This assumption holds for all scenarios for which Spruce has been designed for estimating the bandwidth of the paths in overlay networks.

In the next section, the performance of Spruce is analyzed for computing the available bandwidth in real network settings.

IV. Experimental Setup

Fig. 1 shows the simulation topology where multimedia applications send multimedia and crossing traffics to clients via a wired network as well as a last hop WLAN. Traffic servers send crossing traffics to share the bottleneck from AP to clients.

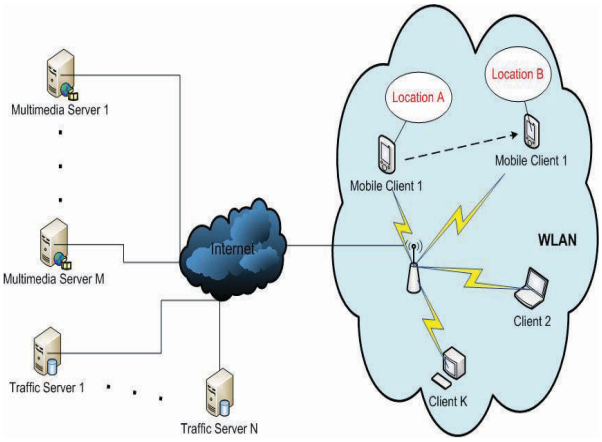

Fig. I Simulation Topology

In the experiment, it is assumed that IEEE 802.11b WLAN is the bottleneck link on the end-to-end path. The WLAN has the smallest available bandwidth which is also the end-to-end available bandwidth.

Table I summarizes the configuration setup in NS. Two additional wireless update package are introduced, NOAH[1] and Marco Fiero Package[2]. NOAH package (No Ad-Hoc) is used for simulating infrastructure WLAN and Marco Fiero Package provides a more realistic wireless network environment. As a result, in our experiment, there are four degrees of bandwidth - 1, 2, 5.5 and 11Mbps, depending on the distance from AP. Fig. 2 shows the characteristic of the real IEEE 802.11b network.

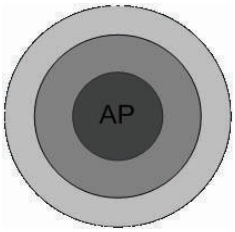

Fig. 2 Signal Strength Around Access Point

W_{min} and W_{max} are the minimum and maximum values of contention window. Basic rate, sending rate of control packets (*ACK*, *RTS*, *CTS*), is set as 1Mbps.

In our experiment, six separate tests were conducted. Each test consists of one to three unicast video traffics and one client starts moving from 5s at the speed of

[1]http://icapeople.epfl.ch/widmer/uwb/ns-2/noah/
[2]http://www.telematica.polito.it/fiore/ns2_wireless_update_patch.tgz

Transport Protocol	UDP
Wireless protocol	802.11b
Routing protocol	NOAH

Error Model	Marco Fiero package
Wired Bandwidth	100Mbps LAN
MAC header	52 bytes
Wmin	31
Wmax	1023
ACK	38 bytes
CTS	38 bytes
RTS	44 bytes
SIFS	10μsec
DIFS	50μsec
Basic rate	1Mbps

Table 1. Simulation Setup in NS-2.29

1m/s. Variable network conditions were also introduced and realized by varying current traffic loads. This is done by generating CBR/UDP crossing traffics using 1500 bytes packet. Additionally, the number of video traffics increases in each separate test. Along with the increasing loads of traffics, the network becomes congested. This set is to verify how the performance of Spruce works under heavy network condition.

V. Experimental Results

This section studies the performance of Spruce by comparing it with *Measured Bandwidth*. *Measured Bandwidth* is based on the concept of maximum throughput that an application can obtain. It depends on the transmission mechanism like TCP, UDP.

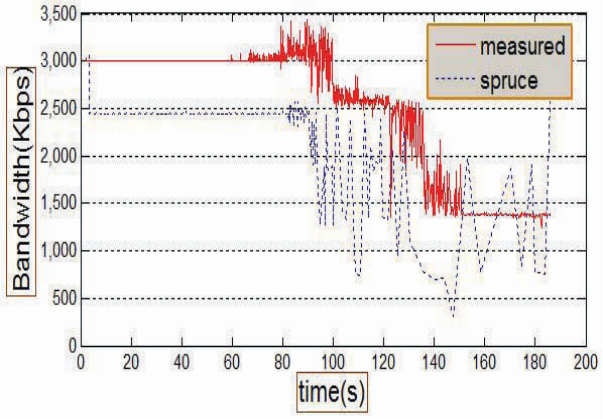

Fig. 3 Comparison of bandwidth calculated from measured and spruce with no crossing traffic. (One server and one client)

Fig. 3 and Fig. 4 show the comparison results of *Measured Bandwidth* (calculated from trace result of NS-2) and *Estimated Bandwidth* (Spruce) for periods of 0 and 200 seconds without cross traffics. The Spruce traffic was started from 3s. Spruce probing traffic used CBR/UDP flow to send packets of 1500 bytes with the rate of 0.15Mbps.

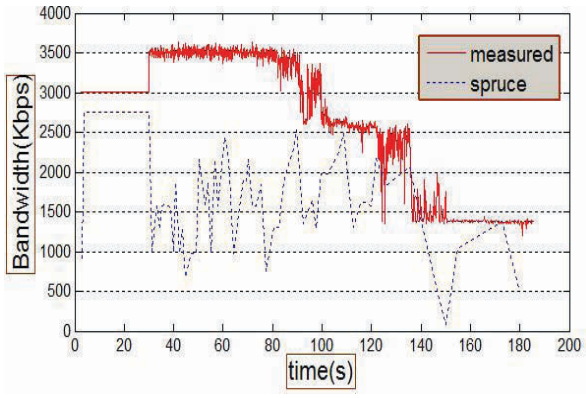

Fig. 4 comparison of bandwidth calculated from measured and spruce without crossing traffic. (One server and two clients)

The first test consisted of one server and one client as provided in Fig. 3. A video clip of two hundred seconds was transmitted to client via high speed (100Mbps) wired network and IEEE 802.11b WLAN. The client started moving away from AP from 2s at the speed of 1m/s. Since Marco Fiero package was implemented, bandwidth dropped when the distance between mobile client and AP increased. As seen in both Fig. 3 and Fig. 4, both the measured and estimated bandwidth fluctuated considerably at around 80s and 130s due to interference of incoming cross traffics. In order to discover the performance of bandwidth estimation, average bandwidth is introduced. In Fig. 3, the average bandwidth estimated by Spruce was 1.51Mbps, notably different from the measured bandwidth of 2.96Mbps. Thus, an error of 1.45 (47%) was observed with Spruce. However, it was observed that Spruce better during the initial time duration (the first 80 seconds). For the same configuration as for Test 1, another multimedia server and client pair were added in Test 2, and the results could be seen in Fig. 4. Two video clips with the same size were transmitted to clients in terms of unicast traffic streams. The error in case of Spruce was 1.63 (25%). Hence, Spruce performed considerably in case of heavy traffic condition (two clients).

Fig. 5, 6, 7, 8 provide the simulation results with the participation of crossing traffics. In order to have fair comparison, the Spruce probing traffic was added as in Test 1 and 2. The results in Fig. 5 were obtained with two video traffics and one crossing traffic. The video traffics were scheduled to start transmission at 2s and 30s, and the crossing traffic began at 50s. The incoming of traffics resulted in changes of estimated bandwidth as shown in the figure. Fig. 6, 7 and 8 show the results when the number of crossing traffic and video traffic increased.

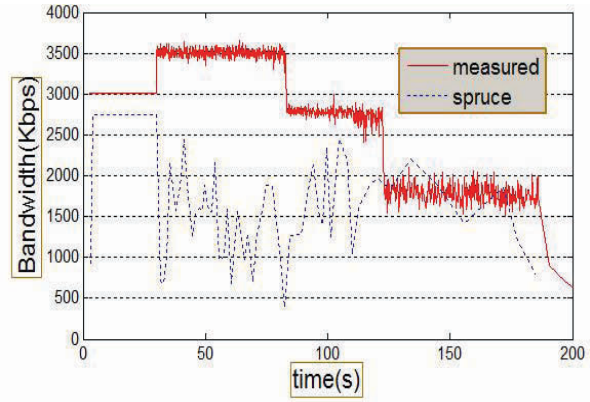

Fig. 5 Comparison of bandwidth calculated from measured and spruce without crossing traffic. (Two clients and one cross traffic)

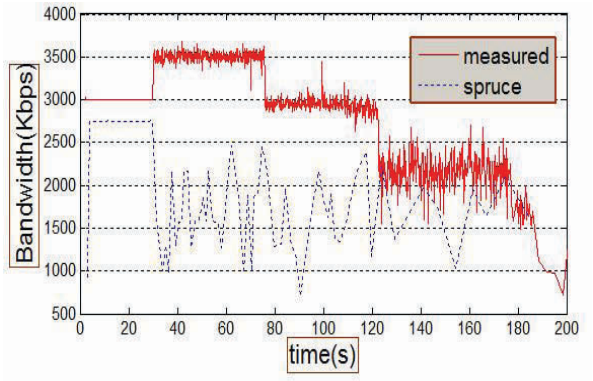

Fig. 6 Comparison of bandwidth calculated from measured and spruce without crossing traffic. (Two clients and three cross traffics)

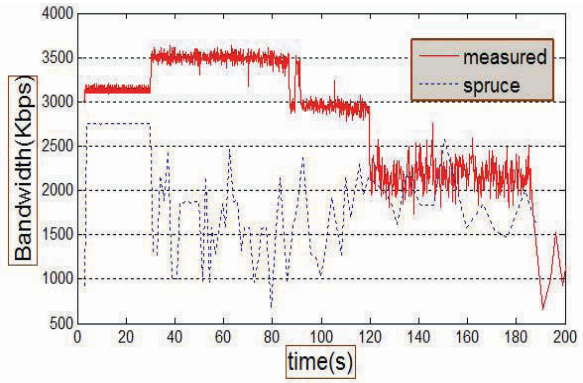

Fig. 7 Comparison of bandwidth calculated from measured and spruce without crossing traffic. (Two clients and two cross traffics)

VI. Necessity for Intelligent Estimation Method

It can be observed from the experimental results in Section V that the performance of Spruce can be offset by up to 50% as compared to the actual measured bandwidth. In practice, on an average, the performance of Spruce is offset by 30%.

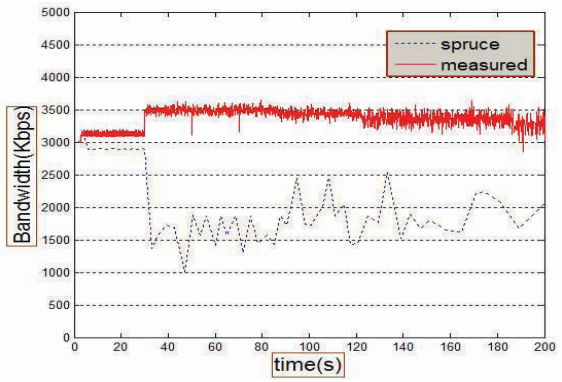

Fig. 8 Comparison of bandwidth calculated from measured and spruce without crossing traffic. (Three clients and three cross traffic)

As the demand for performance on the Internet grows, so does the requirement for tools to accurately measure performance. This growing demand also means that solutions that place a large load on the network would not be able to scale. This in fact creates an urgent need for having tools that can accurately estimate various types of bandwidths. Also, such techniques need to estimate the bandwidth accurately without creating large volumes of traffic.

An intelligent bandwidth estimation (iBE) technique is being researched by our team that would reduce the error between the measured and the estimated bandwidth. The basic idea of iBE is to use the difference between the packet's transmission time and reception time at MAC layer. The actual algorithm and the mechanism of iBE are not explained here completely; as it is still under research. The initial results are shown in Table II. It can be observed from Table II that for CBR/UDP traffic of 0.5 and 1.0 Mbps data rate for different video clients, the iBE shows significantly less error with respect to the actual measured bandwidth, as compared to Spruce.

VII. Conclusion and Future Work

This paper reviews the different categories of bandwidth estimation techniques for wireless networks. Single pair and packet pair were the two prominent kinds of estimating bandwidth for such networks. A state-of-the-art packet-pair estimation technique, "Spruce" was described and analyzed for different kinds of Internet-based multimedia traffics. It was found over different conditions that "Spruce" though satisfactory most of the times, was found to give errors, as much as up to 50%.

A new intelligent bandwidth estimation algorithm for multimedia delivery over wireless networks has been researched in the recent years. The initial results have shown 'intelligent technique' to give results much

#	Video clients	Cross Traffic	Bandwidth (median, Mbps)				
			measured	iBE	Spruce	error	
						iBE	Spruce
1	1	None	2.96	3.52	1.51	0.56	1.45
2	2	None	3.12	3.41	1.49	0.29	1.63
3	2	CBR/UDP 0.5Mb/s	2.72	2.67	1.62	0.05	1.1
4	2	CBR/UDP 0.5Mb/s CBR/UDP 1.0Mb/s	2.63	2.25	1.58	0.38	1.05
5	2	CBR/UDP 0.5Mb/s CBR/UDP 1.0Mb/s CBR/UDP 1.0Mb/s	2.48	2.23	1.51	0.25	0.97
6	3	CBR/UDP 1.0Mb/s CBR/UDP 1.0Mb/s CBR/UDP 1.0Mb/s	2.45	2.31	1.26	0.14	1.19

Table II. Bandwidth Estimation Performance of iBE, Spruce and comparison with actual Measurement

closer to the actual measured bandwidth. Further work in this direction is to fully develop the intelligent bandwidth estimation method, and to test its performance against different multimedia based applications.

Acknowledgments

The authors would like to acknowledge the support of China Scholarship Council.

References

[1] H. Venkataraman, S. Sinanovic and H. Haas, "*Performance Analysis of Hybrid Cellular Networks*", In Proc. of IEEE PIMRC, Berlin, Germany, September, 2005.

[2] J.Curtis**,** T.McGregor**,** "*Review of Bandwidth Estimation Techniques*", Department of Computer Science, University of Waikato, Hamilton, New Zealand, 2001.

[3] M. Jain and C. Dovrolis, "*End-to-End Available Bandwidth: Measurement Methodology, Dynamics, and Relation with TCP Throughput*", In Proc. of ACM SIGCOMM, Pittsburgh, PA, USA, August 2002.

[4] V. Jacobson and M. J. Karels. "*Congestion Avoidance and Control*", In Proc. of ACM SIGCOMM, Stanford, CA, USA, August 1988.

[5] S. Keshav, "*A Control-Theoretic Approach to Flow Control*", In Proc. of ACM SIGCOMM, Zurich, Switzerland, September 1991.

[6] R. L. Carter and M. E. Crovella, "*Measuring Bottleneck Link Speed in Packet Switched Networks*", Performance Evaluation, Elsevier, Vol. 27-28, pp. 297-318, October, 1996.

[7] K. Lai and M. Baker, "*Measuring Link Bandwidths Using a Deterministic Model of Packet Delay*", In Proc. of ACM SIGCOMM, Stockholm, Sweden, August 2000.

[8] V. Paxson, "*Measurement and Analysis of End-to-End Internet Dynamics*", PhD Thesis, University of California at Berkeley, 1997.

[9] C. Dovrolis, D.Moore, and P. Ramanathan, "*What Do Packet Dispersion Techniques Measure?*" In Proc. of IEEE INFOCOM, Anchorage, Alaska, USA, April, 2001.

[10] G. U. Keller, T.E. Najjary and A. Sorniotti, "*Operational Comparison of Available Bandwidth Estimation Tool",* ACM SIGCOMM Computer Communications, Vol. 38, No. 1, January 2008.

[11] N. Hu and P. Steenkiste, "*Evaluation and Characterization of Available Bandwidth Techniques*",.IEEE Journal of Selected Areas in Communications (JSAC), Special Issue in Internet and WWW Measurement, Mapping and Modeling, Vol. 21, No. 6, pp. 879-894, August 2003.

[12] V. J. Ribeiro, R. H. Riedi, R. G. Baraniuk, J. Navratil, and L. Cottrell, "*PathChirp: Efficient Available Bandwidth Estimation for Network Paths*", In Proc. of (Passive and Active Measurements Workshop, Ohio, USA, April 2003.

[13] B. Melander, M. Bjorkman, and P. Gunningberg, "*A New End-to-End Probing and Analysis Method for Estimating Bandwidth Bottlenecks*", In Proc. of IEEE Global Internet Symposium, SanFrancisco, USA, November, 2000.

[14] T. Sun, G. Yang, L. J. Chen, M.Y. Sanadidi, and M. Gerla, "*A Measurement Study of Path Capacity in 802.11b based wireless network*," in Wireless Traffic Measurement and Modeling (*WiTMeMo)*, Seattle, USA, June 2005.

[15] L. Angrisani, A. Botta, A. Pescape, and M. Vadursi, "*Measuring Wireless Links Capacity*," 1st International Symposium on Wireless Pervasive Computing, Phuket, Thailand, January 2006.

[16] V. Jacobson, "*pathchar - A Tool to Infer Characteristics of Internet Paths*", Presented at the Mathmatical Sciences Research Institute, December, 1997.

[17] J.C. Bolot, "*End-to-End Packet Delay and Loss Behaviour in the Internet*", in Proceedings of ACM SIGCOMM, SanFrancisco, USA, September, 1993.

[18] J. Strauss, D. Katabi and F. Kaashoek, "*A Measurement Study of Available Bandwidth Estimation Tools*", Internet Measurement Conference, Proceedings of the 3rd ACM SIGCOMM conference on Internet measurement, Miami Beach, FL, USA, pp. 39-44, 2003.

Section 5B

COMPUTER NETWORKS 2

Quality of Service in IMS based Content networking

Dalton Li, Jonathan Lv

dakeli@alcatel-lucent.com; lv@alcatel-lucent.com
Alcatel-Lucent Qingdao R&D Center, China Qingdao 266101

Abstract

This paper introduces IP Multimedia Subsystem (IMS) as the infrastructure of content networking. The proposed IMS based content networking architecture is enhanced by interaction between bearer gateway and signaling layer to guarantee the Quality of Service (QoS) of the traffic. A new IMS component - Content Navigating Function (CNF) is also introduced to provide content service to the end user. With its well-designed architecture and maturing specifications, the QoS mechanism of IMS does contribute to traffic management in the content network. The typical scenario description and high level call flow of content sharing sessions are also provided.

Keywords: QoS; IMS; Content network.

1 Introduction

People in large and rapidly growing numbers are creating and sharing their content or commercial content products with each other through networks. Traffic generated from this sharing represents a significant component of today's communication networks traffic. Needless to say, content networking providers concern more and more about how to guarantee Quality of Service (QoS) for this kind of traffic, especially for bandwidth hungry traffic, like multimedia stream. Content caching and server clustering have been using for web content delivery [1]. And the Content Delivery Network (CDN) [2, 3, 4] has been proposed to improve end-user Quality of Experience (QoE) by replicating content in a network of geographically distributed surrogate servers. Request-routing mechanisms [5], content replication techniques [6], load balancing and cache management [7] have also been studied. To efficiently implement CDN, the IETF CDI group has proposed Content Distribution Internetworking (CDI) concept to enhance the CDN by aggregating separate CDNs into an integrated one. As the result, several Request For Comments (RFC) have been published, such as CDI architecture overview [8], its models and usage scenarios [9], terminologies and requirements [10].

CDN currently focuses on how to distribute the content on the network and how to redirect the request, as well as how to account. But it doesn't consider Service Level Agreement (SLA) that describes the subscription between the end user and the service provider. On the other hand, IP Multimedia Subsystem (IMS) [11, 12], as a standardized Next Generation Networking (NGN) architecture and the industry's great unifying technology, provides a good solution for this.

This paper proposes an IMS based architecture for both centralized and Peer-to-Peer content network and a new IMS Application Server (AS) [11] - Content Navigating Function (CNF) dedicated for the content network to guarantee the QoS of the traffic. With its well-designed architecture and maturing specifications, the IMS QoS mechanism [13, 14, 15, 16, 17] does contribute to traffic management in the content network. The typical scenario description and high level call flow of content sharing sessions are also provided.

2 IMS based content network architecture

Figure 1 illustrates the IMS based content network architecture, which mainly takes specifications from 3rd Generation Partnership Project (3GPP) [12, 13, 14] and Telecommunication and Internet converged Services and Protocols for Advanced Networks (TISPAN) [15] as the reference.

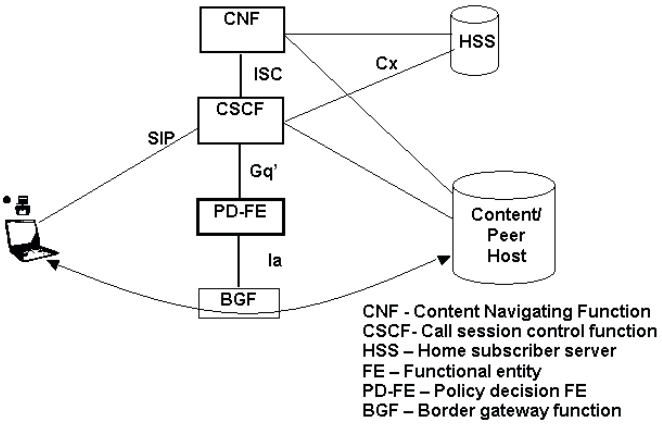

Figure 1. IMS based content networking architecture

2.1 CNF

The Content Navigating Function (CNF) provides information necessary to the user to select a content service. The functionalities of CNF are:

1. Collecting the available content service information that the client can select.
2. Providing UI functionality for the end user to query the content service information.
3. Present the content service information according to the user preference.
4. Navigate the address of content host or peer host in the form of Uniform Resource Identifiers (URIs) or IP addresses.
5. Provide other useful data of the content service.

The CNF is a kind of SIP Application Server (AS) [11].

2.2 CSCF

The Call Session Control Functions (CSCFs) [11, 12] are the core elements to perform the session control in the IMS architecture. It can act as Proxy CSCF (P-CSCF), Serving CSCF (S-CSCF) or Interrogating CSCF (I-CSCF). The P-CSCF is the first contact point for the UE within the IMS; the S-CSCF actually handles the session states in the network; the I-CSCF is mainly the contact point within an operator's network for all IMS connections destined to a subscriber of that network operator, or a roaming subscriber currently located within that network operator's service area [12].

In IMS based content network, CSCFs also provide session control functionalities, such as session establishment, modification, termination for content sharing sessions.

2.3 PD-FE

The Policy Decision Function Entity (PD-FE) [16] is a logical policy decision element for service-based policy control. It makes policy decisions using policy rules defined by the network operator according to the user's subscription or request, and then maps the local policy into the parameters to be sent to the Border Gateway Function (BGF). The PD-FE hides the underlying network topology from applications, which allows the PD-FE to offer a common view to the CSCF regardless of the underlying network topology and particular access technology in use.

In IMS based content network, PD-FE makes policy decisions for content sharing sessions according to user's subscription or request and asks BGF to enforce them.

2.4 BGF

The Border Gateway Function (BGF) is a packet-to-packet gateway for user plane media traffic. The BGF performs both policy enforcement functions and NAT functions under the control of the PD-FE in each of the network segments: access, aggregation and core [15]. The BGF has a policy enforcement function that interacts through the Ia reference point with the PD-FE and is under the control of the PD-FE. The BGF operates on micro-flows, i.e. on individual flows of packets belonging to a particular application session. The BGF's policy enforcement function is a dynamic gate that can block individual flows or allow authorized flows to pass. The PD-FE instructs the BGF to open/close its gate for the particular flow, i.e. to allow the admitted flow to pass through the BGF. Possible resources that are managed by the BGF include the handling of a pool of IP addresses/ports and bit rate on the BGF interfaces.

In IMS based content network, BGF enforces the policy from PD-FE, i.e. allocate bandwidth needed for allowed media flows of content sharing sessions and block unauthorized flows. Furthermore, BGF will report the bandwidth usage status to PD-FE. Essentially, QoS is guaranteed from this.

2.5 HSS

The Home Subscriber Server (HSS) [12] is the main data storage for all subscriber and service-related data of the IMS. The main data stored in the HSS include user identities, registration information, access parameters and service-triggering information. In addition to functions related to IMS functionality, the HSS contains the subset of Home Location Register and Authentication Center (HLR/AUC) functionality required by the packet service domain and the circuit service domain.

In IMS based content network, HSS stores the profile of content network users, such as QoS parameters, service-triggering information, etc.

2.6 Content/Peer Host

Content/Peer Host [1] stores media content or other service information. Content/peer Host is responsible for delivering content data to the client. The difference between content host and peer host is that content hosts are several stable, reliable and powerful servers with large storage provided and maintained by the service provider in some relatively centralized sites, while peer hosts are mainly highly distributed low performance personal computers.

3 CNF communication mechanism

3.1 CNF and Content/Peer host

When the Content/Peer host is online, it contacts CNF and reports its status and the information of services it can provide. The CNF will save the information and response an OK as the acknowledgement. SIP [18] can be used as the communication protocol. Peer hosts communicate with CNF more frequently than content hosts since peers join and leave the network randomly.

3.2 CNF and CSCF

CNF is an Application Server (AS) to CSCF. When requested by the user, CSCF will query CNF for available content service information or available peer host information. CNF sends back information requested back to CSCF. They can use SIP [18] protocol to communicate as defined in [11].

4 Typical scenarios and Call Flows

4.1 Peer-to-Peer content network

Figure 2 depicts the call flow of P2P IMS based content network. In P2P content network, since peers can start sessions directly without CSCF awareness, the CSCF can't control every session in signaling level. It's transport layer entity, like BGF, to take the responsibility to manage the traffic. When the user registers to the network, the BGF will allocate an amount of bandwidth for the user according to the user's subscription. The BGF will perform Deep Packet Investigation (DPI) to guarantee the bandwidth allocated for the user and make sure the bandwidth used by every user can't exceed the assigned value. This resource ration strategy will eliminate the unfairness that some hungry users consume lots of bandwidth, so that other users can only get service with poor quality or even get starved.

1. When a peer host starts up, it will report to CNF its status and the information of service it can provide.
2. CNF responses OK and save this information into its local memory. Here CNF has similar functionality as Gnutella Host-Cache Server [1].
3. The user equipment registers to the CSCF.
4. CSCF queries Home subscriber server (HSS) to get the user's profile, which includes QoS parameters, such as bandwidth subscription, etc.
5. HSS sends the profile to CSCF as requested.
6. CSCF asks PD-FE to authorize bandwidth for the user as subscribed.
7. PD-FE indicates the BGF to enforce the QoS policy for the user.
8. BGF reports the result of policy enforcement to PD-FE.
9. PD-FE reports the result of policy enforcement to CSCF.
10. CSCF sends the registration response to the user.
11. The user asks CSCF to get prospective peer address and related information.
12. CSCF queries CNF for this.
13. CNF sends the information to CSCF as requested.
14. CSCF sends back the requested information to the user.
15. The user contacts peer hosts to get services wanted.
16. The peer hosts response and provide services to the user, like content sharing.

During the content sharing session, the BGF will perform Deep Packet Investigation (DPI) to guarantee the bandwidth allocated for the user and make sure the bandwidth used by the user within the value assigned.

17. If BGF finds that the user is trying to use more bandwidth than assigned value, it will report this to PD-FE.
18. PDFE reports to CSCF that the user is trying to use more bandwidth.
19. CSCF prompts the user to buy more bandwidth.

4.2 Centralized content network

Figure 3 depicts the call flow of IMS based centralized content network. In IMS based content centralized network, every session establishment must pass through CSCF. So CSCF can control all sessions. When the user initiates the session, CSCF will indicate PD-FE/BGF to allocate requested bandwidth for the session. This QoS policy will override the policy enforced in user registration stage. Thus per-session based dynamic QoS policy enforcement can be realized. It's different than P2P content network.
Step 1~10 are similar as P2P content network. Following is the description from step 11:

11. The user asks CSCF for currently available content service information.
12. CSCF query CNF for this.
13. CNF sends back the information to CSCF as requested.
14. CSCF sends back available content service information to the user.
15. The user picks up a service and sends a session initiation request to CSCF. It's usually by a SIP [8] INVITE message.
16. CSCF sends the session initiation request to content host that can provide the service requested by the user.
17. The content host responses CSCF the service request.
18. CSCF asks PD-FE to authorize bandwidth for the session.
19. PD-FE indicates the BGF to enforce the new QoS policy for this session.
20. BGF reports the result of policy enforcement to PD-FE.
21. PD-FE reports result of policy enforcement to CSCF.
22. CSCF sends the session initiation response to the user.

Then the content host can start the content delivery to the user. By enforcing QoS policy in step 19, BGF guarantee the bandwidth allocated for the session and can't exceed it.

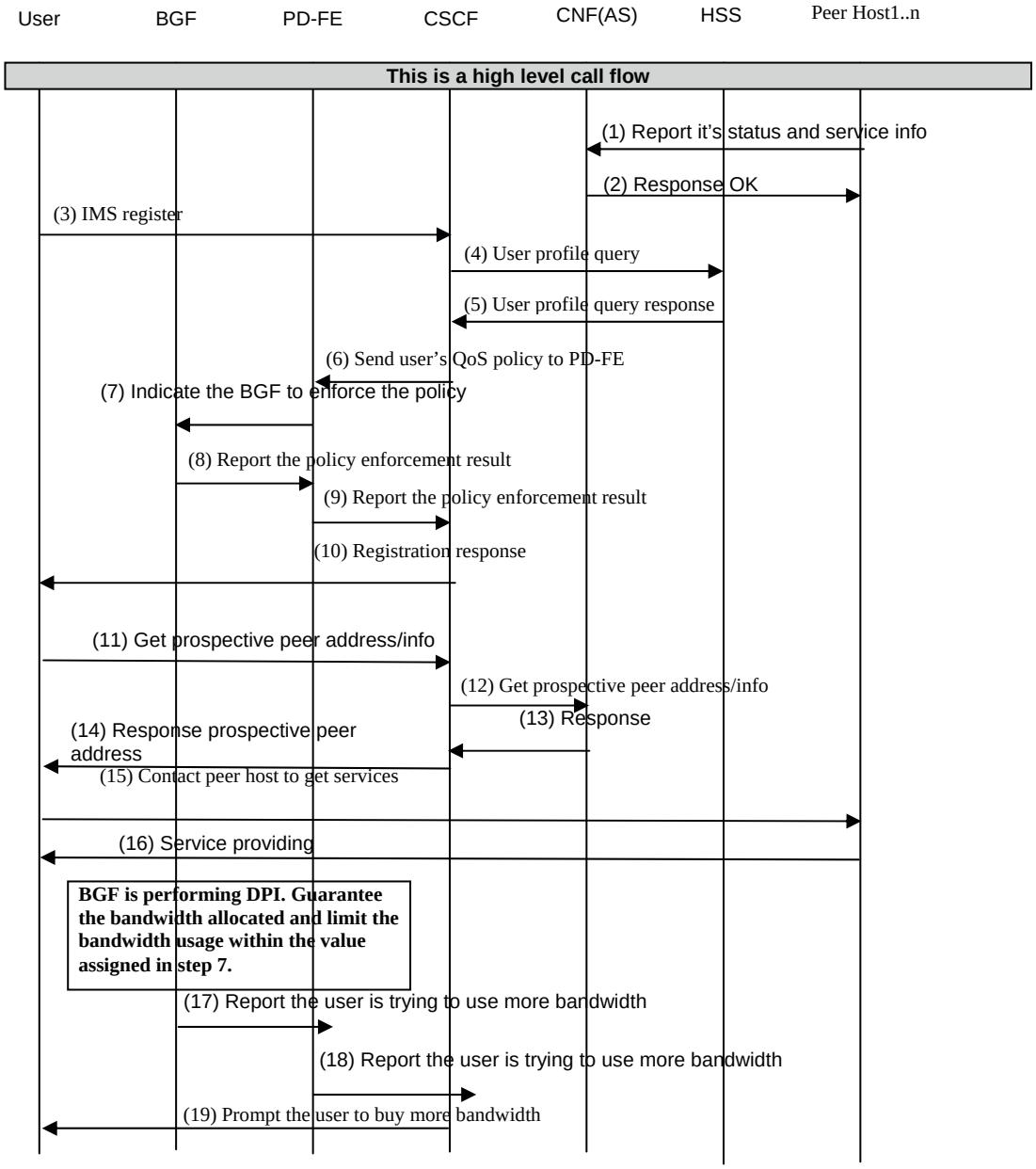

Figure 2. Call flows of IMS based P2P content network

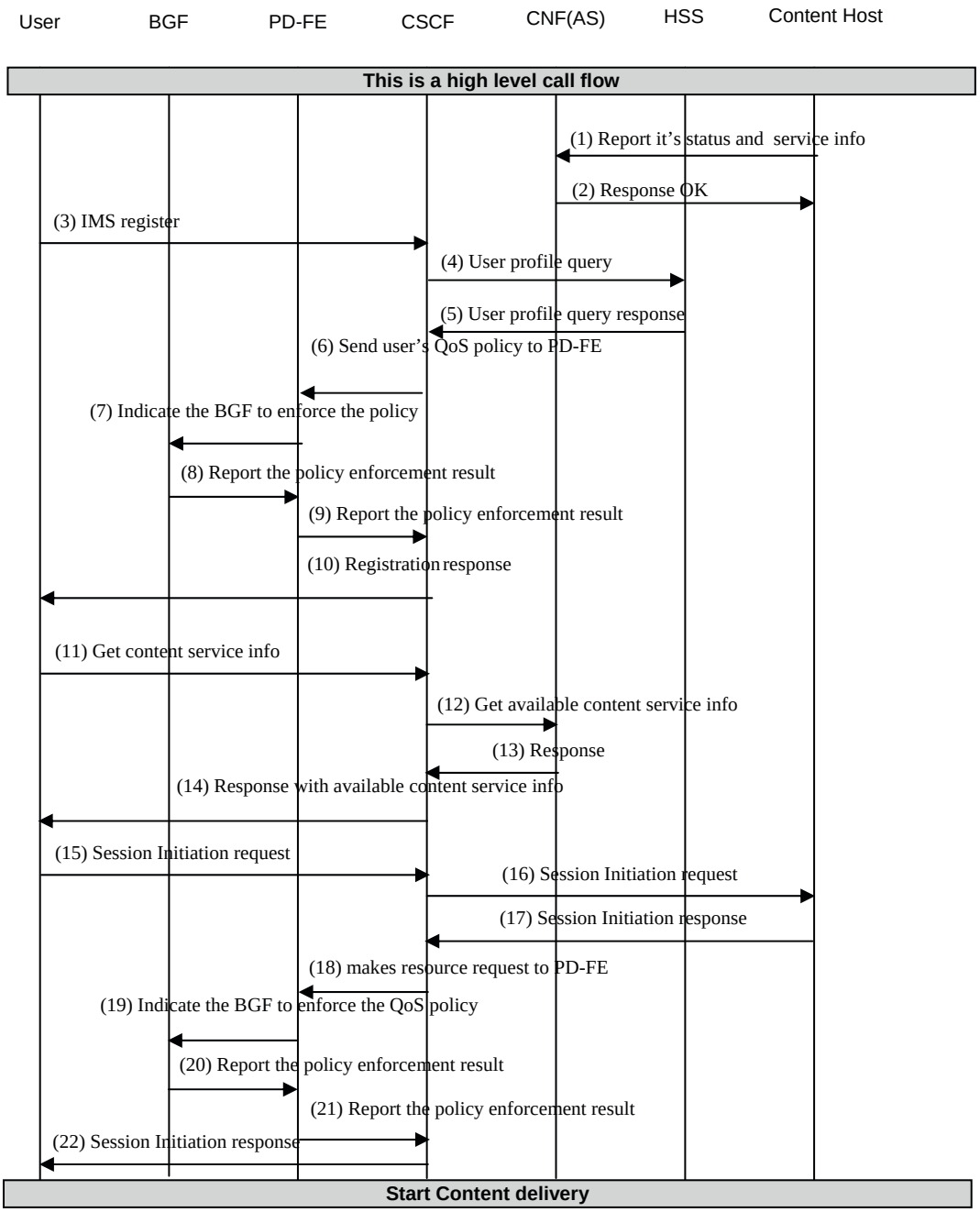

Figure 3. Call flows of IMS based centralized content network

5 Conclusion

This paper proposed an IMS based content network architecture and a new IMS Application Server (AS) - Content Navigating Function (CNF) dedicated for the content networking to guarantee the QoS of the traffic. Mature IMS QoS mechanism can provide solid QoS assurance for content networks. The typical scenario description and high level call flow of content sharing sessions are also provided.

References

[1] Markus Hofmann and Leland R. Beaumont.: "Content Networking: Architecture, Protocols, and Practice", Morgan Kaufmann Publishers, 2005

[2] Vakali, A. and Pallis, G. "Content delivery networks: Status and trends". IEEE Internet Computing 7, 6 (Nov./Dec. 2003), 68–74.

[3] G. Pallis, and A. Vakali, "Insight and Perspectives for Content Delivery Networks," Communications of the ACM, Vol. 49, No. 1, ACM Press, NY, USA, pp. 101-106, January 2006.

[4] Al-Mukaddim Khan Pathan and Rajkumar Buyya - "A Taxonomy and Survey of Content Delivery Networks", Technical Report, GRIDS-TR-2007-4, Grid Computing and Distributed Systems Laboratory, The University of Melbourne, Australia. 12 February, 2007,

[5] Barbir, A., Cain, B., Nair, R., Spatscheck, O.: "Known Content Network (CN) Request-Routing Mechanisms," RFC 3568, July 2003. http://www.ietf.org/rfc/rfc3568.txt?number=3568

[6] J. Kangasharju, J Roberts, and K. W. Ross, "Object Replication Strategies in Content Distribution Networks," Computer Communications, Vol. 25, No. 4, pp. 367-383, March 2002.

[7] M Cieslak, D Foster, G Tiwana, and R Wilson, "Web Cache Coordination Protocol Version 2," http://www.web-cache.com/Writings/Internet-Drafts/draft-wilson-wrec-wccp-v2-00.txt

[8] Green, M., Cain, B., Tomlinson, G., Thomas, S., and Rzewski, P. (2002). Internet Draft: Content Internet Working Architectural Overview, IETF CDI Working Group.

[9] Rzewski, P., Day, M., and Gilletti, D. (2003).: "Content Internetworking (CDI) Scenarios" IETF CDI Working Group, RFC 3570, July 2003. http://www.ietf.org/rfc/rfc3570.txt?number=3570

[10] Day, M., Cain, B., Tomlinson, G., Rzewski, P.: "A Model for Content Internetworking (CDI)," RFC 3466, February 2003. http://www.ietf.org/rfc/rfc3466.txt?number=3466

[11] 3rd Generation Partnership Project, "IP Multimedia Subsystem (IMS); Stage 2" 3GPP TS 23.228, http://www.3gpp.org/ftp/Specs/html-info/23228.htm

[12] 3rd Generation Partnership Project, "Network Architecture" 3GPP TS 23.002, http://www.3gpp.org/ftp/Specs/html-info/23002.htm

[13] 3rd Generation Partnership Project, "End-to-end Quality of Service (QoS) concept and architecture", 3GPP TS 23.207, http://www.3gpp.org/ftp/Specs/html-info/23207.htm

[14] 3rd Generation Partnership Project, 3GPP TS 23.107: "Quality of Service (QoS) concept and architecture", 3GPP TS 23.107, http://www.3gpp.org/ftp/Specs/html-info/23107.htm

[15] European Telecommunications Standards Institute, "Resource and Admission Control Sub-System (RACS) – Functional Architecture," ETSI ES 282 003, http://www.etsi.org

[16] International Telecommunication Union, Telecommunication Standardization Sector, "Functional Architecture and Requirements for Resource and Admission Control Functions in Next Generation Networks," ITU Y.RACF, http://www.itu.org

[17] 3rd Generation Partnership Project, "End-to-End Quality of Service (QoS) Signalling Flows," 3GPP TS 29.208, http://www.3gpp.org/ftp/Specs/html-info/29208.htm

[18] Rosenberg, J., Schulzrinne, H., Camarillo, G., Johnston, A., Peterson, J., Sparks, R., Handley, M., and E. Schooler.: "SIP: Session Initiation Protocol", RFC 3261, June 2002. http://www.ietf.org/rfc/rfc3261.txt?number=3261

Abbreviations, Acronyms, and Terms

3GPP*—3rd Generation Partnership Project
AS— Application server
BGF— Border gateway function
CDI — Content distribution internetworking
CDN — Content delivery network
CNF— Content navigating function
CSCF—Call session control function
DPI— Deep packet investigation
ETSI—European telecommunications standards institute
HLR/AUC—Home location register and authentication center
HSS — Home subscriber server
IMS—IP multimedia subsystem
IP—Internet protocol
ITU—International telecommunication union
P2P—Peer-to-peer
PD-FE—Policy decision functional entity
PDF—Policy decision function
QoE — Quality of experience
QoS — Quality of service
RFC — Request For Comments
SDP—Session description protocol
SIP—Session initiation protocol
SLA— Service level agreement
TISPAN—Telecommunication and Internet converged Services and Protocols for Advanced Networks
UE — User equipment
URI—Uniform resource identifier

The Enhanced Dv-Hop Algorithm in Ad Hoc Network

Zhang Pin, Xu Zhifu
School of Communication Engineering, Hangzhou dianzi University
Hang Zhou, China
zhangpin@hdu.edu.cn qzxuzhifu@163.com

Abstract: **Dv-Hop is one of the Range-Free Algorithms for Wireless Sensor Networks. While lanchor nodes density is low Dv-Hop shows bad average error and poor Stability. This paper proposes an Enhanced Dv-Hop Algorithm(EDVA) in order to improve the performance with low anchor nodes density. The main idea of EDVA is setting anchor nodes at the boundary to reduce the average error. Through simulation, the EDVA has better performance in average error and stability than Dv-Hop.**

Keywords: WSN; Dv-Hop; Average error; Improved; Density

I. INTRODUCTION

Ad-hoc wireless sensor networks have many attractive applications. While located in different environment, to determine the node location is fundamental to these applications. Although the location information can be obtained by GPS system with a good precision, it is obviously not a scalable solution because it is very expensive to implement GPS for a large number of nodes[1].

In an ad-hoc localization system, nodes determine their position in a common coordinate system using a number of anchor nodes that already know their location (through some external means, such as GPS in that coordinate system). These systems assume all nodes possess a ranging capability (the ability to estimate distances to other nodes). Using their range estimates and several distributed position fixing techniques to determine their positions in the coordinate system[2].

Usually radiolocation approaches are applied to ad-hoc sensor networks. it face several challenges[3]: sparse reference points, limited ranging accuracy, and the need for low-power consumption. The number of anchor nodes, or nodes with a prior knowledge of their locations relative to a global coordinate system, are assumed to be limited. The other nodes, their communication range is limited to their immediate neighborhood, have to connect to the anchor nodes hop by hop and estimate the distance to it, and then calculate the coordinates by performing traditional triangulation algorithms. So the place of anchor nodes is important to reduce the error distant estimation.

I. II. DV-HOP ALGORITHM

Dv-Hop algorithm[4-5] is one of the APS distributed localization algorithms which mainly relies on the distance vector routing between the unknown nodes and anchor nodes, it is easy to be achieved. With moderate accuracy, it is a good choose for Wireless Sensor Network that have a limited hardware support.

Dv-Hop algorithm can be divided into three phases:

computing the smallest hop between unknown node with each anchor node.

First , using a typical distance vector exchange protocol to get hops between all nodes with anchor nodes. Anchor nodes broadcast the packet which including hops information to neighbor nodes, and the receive nodes record the smallest hop to every anchor node, ignoring the more large hops from the same anchor node, then increase 1 hop and transmit to neighbor node., so each node can get path with minimal hops to each anchor node.

Then computing the true distance between unknown node with anchor node based on the hops and path length from this node to anchor nodes.

Based on the anchor node location information recorded by the first phase, using formula (1) to estimate the average distance of each hop.

The study is sponsored by Nature Science Foundation of Zhejiang Province (R105473)

$$d = \frac{\sum \sqrt{(X_i - X_j)^2 + (Y_i - Y_j)^2}}{\sum h_{ij}} \quad i \neq j \qquad (1)$$

Where d is the average distance of each jump, (X_i, Y_i) is the true coordinate of anchor node i, h_{ij} is length of the hop between node i with node j, while link (*i*, *j*) belongs to the path with minimal hops between ordinary node and an anchor node. We get,

$$D_i = d * h_i \qquad (2)$$

Where D_i is the estimated distance from unknown node to anchor node, d is the average distance of each jump, h_i is the hops of all unknown node to anchor node i.

Finally, By using maximum likelihood principle estimation when the unknown nodes get three or more anchor nodes, such as formula (3), we can fix node location.

$$\begin{cases} (X - X_1)^2 + (Y - Y_1)^2 = D_1^2 \\ (X - X_2)^2 + (Y - Y_2)^2 = D_2^2 \\ \vdots \\ (X - X_n)^2 + (Y - Y_n)^2 = D_n^2 \end{cases} \qquad (3)$$

Where (X, Y) is the coordinate of unknown node, (X_i, Y_i) is the true coordinate of anchor node i, D_i is the estimated distance from unknown node to anchor node. We write it in the form of matrix.

$$AX = b \qquad (4)$$

Where

$$A = 2 * \begin{Bmatrix} X_1 - X_n & Y_1 - Y_n \\ \vdots & \vdots \\ X_{n-1} - X_n & Y_{n-1} - Y_n \end{Bmatrix} \qquad (5)$$

$$b = \begin{pmatrix} X_1^2 - X_n^2 + Y_1^2 - Y_n^2 + D_n^2 - D_1^2 \\ \vdots \\ X_{n-1}^2 - X_n^2 + Y_{n-1}^2 - Y_n^2 + D_n^2 - D_{n-1}^2 \end{pmatrix} \qquad (6)$$

By using MMSE we can get the unknown nodes coordinates,

$$\widehat{X} = (A^T A)^{-1} A^T b \qquad (7)$$

Anchor nodes are randomly generated in the first phase of DV-Hop algorithm . Through simulation, we find that when the anchor node density reach 10% (random arrangement 100 nodes which including 10 anchor nodes in a 100*100 regional network) in a network, positioning error accuracy can achieve 30%. Although DV-Hop is easy to implement, it has the disadvantage that the positioning accuracy will decrease quickly when the anchor node density or network connectivity drops.

III **An Enhanced Dv-Hop algorithm**

Dv-Hop generates anchor nodes randomly in the first phase of DV-Hop. If the distribution of Anchor nodes is not even, some nodes will suffer from bad accuracy. That means Dv-Hop is not stable just as that the simulation has proved. This paper proposes Enhanced Dv-Hop algorithm that sets anchor nodes at the boundary. EDVA has two advantages:(1)it reduces the hops variance of whole network that finally reduce the error of estimated distance efficiently and improve the accuracy stablity; (2) It reduces the ranging times so as to reduce the power consumption. EDVA is divided into three phase:(1)select four border anchor nodes, computing the smallest hop between unknown node to each anchor node; (2)computing average per hop distance for anchor node;(3)After unknown node get distance to each anchor node, then using maximum likelihood principle to calculate coordinates.

We use Matlab to make simulation on EDVA. At the 100x100 square, randomly set 100 nodes which including five anchor nodes, ranging field is 50, Figure 1 shows the node distribution. The stars are anchor nodes and the others are ordinary nodes.

When simulating EDVA, we set five anchor nodes in the 100x100 square region, and randomly set 92 unknown nodes. Anchor nodes located at center and four corners. Figure 2 shows the node distribution.

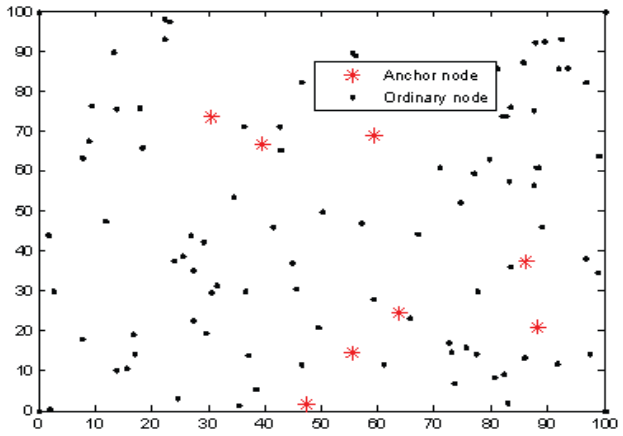

Figure 1: Node distribution for Dv-Hop Algorithm

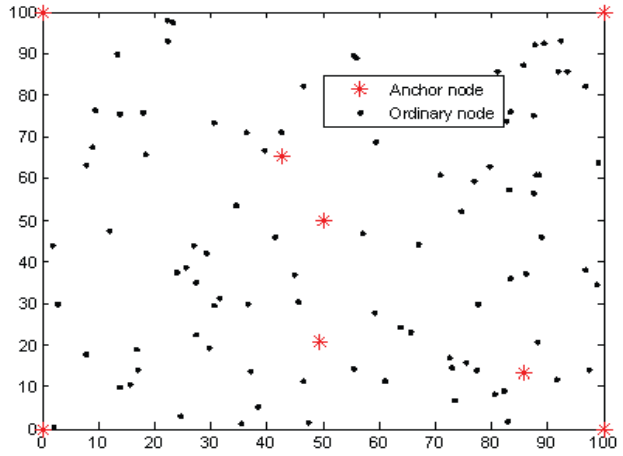

Figure 2: Node distribution for improved Dv-Hop Algorithm

IV. **Simulation Analysis**

We compares average error between the traditional Dv-Hop and the improved Dv-Hop algorithm. The average error is defined as

$$average \quad error = \frac{\sum_{i=1}^{n} \sqrt{(\hat{X}_i - X)^2 + (\hat{Y}_i - Y)^2}}{n}$$

Where n is the number of unknown nodes, $\hat{X}_i$、$\hat{Y}_i$ are the estimated coordinates of unknown node, X_i、Y_i are the true coordinates of unknown node.

We carried out 20 tests for each algorithm. Figure 3 shows results of Dv-Hop algorithm and EDVA.. The line with stars is DV-Hop and the line with Diamonds is EDVA.

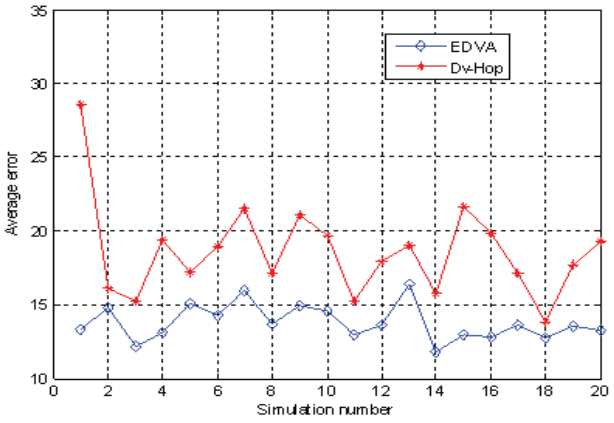

Figure3: Comparison between Dv-Hop algorithm and EDVA

The figure 3 shows the error ranges of DV-Hops is about 15%-30% while EDVA shows better error ranging from 12%-15%. EDVA can achieve better accuracy even with lower anchor density which means less power consumption. On the other hand, setting the anchor at the boundary will reduce the variance the hops of ordinary nodes to the anchor nodes, and finally achieve better accuracy, stability.

V. **Conclusion**

The Dv-Hop algorithm has good scalability and moderate positioning accuracy, but in the low anchor node density network, it shows poor stability and position accuracy. This paper proposes Enhanced Dv-Hop algorithm which can achieve better positioning accuracy and better stability even with lower anchor node density.

REFERENCE

[1] N. Bulusu, J. Heidemann, D. Estrin, “GPS-less low cost outdoor localization for very small devices”, IEEE Personal Communications Magazine, 7(5)(2000): 28–34.

[2] We T, Huang C. “Range-free localization schemes for large scale sensor networks” [C].Proceedings of the ninth Annual International conference on mobile computing and networking. San Diego, california, September 2003:81-95.

[3] N. Patwari , J.N.Ash , S. Kyperountas etc. “Locating the Nodes: Cooperative localization in wireless sensor networks”. IEEE Signal Processing Magazine, Vol 22, 2005

[4] D. Niculescu and B. Nath, "Ad hoc positioning system (APS)," Proc. Of GLOBECOM '01. IEEE, San Antonio, TX USA, 2001: 2926-2931.

[5] Niculescu D, Narh B. “DV-based positioning in ad hoc network”. Telecomm. Systems, 2003, 22(1): 267~280.

Program Dependence Graph Generation and Its Use in Network Applications Analysis

Jing Huang, Xiaojun Wang
School of Electronic Engineering
Dublin City University
Ireland
jing@eeng.dcu.ie, xiaojun.wang@dcu.ie

***Abstract*—Program Dependence Graph (PDG) is an Intermediate Representation used by compilers to characterize the control-flow and data-flow dependences. It is widely used in optimizations for parallel processors systems. This paper demonstrates an implementation of the PDG generation as a compiler pass and the use of PDG in profiling network applications. The paper also introduces our ongoing and future work on using PDG in the research of application partitioning and mapping problem.**

Keywords-Program Dependence Graph; Dependence Analysis; Network Application

I. INTRODUCTION

In the internal work flow of compilers, an *Intermediate Representation* (IR) is a data structure used to collect the input information, e.g. the semantics of C code. Most of the compiler optimizations would conduct upon a specific kind of IR. Classical examples of IRs include the *Control Flow Graph* (CFG) built for flow analysis, *Abstract Syntax Tree* (AST) employed in syntax-directed translation etc. Particularly in our interest of task allocation problem for network processor systems [1], the compiler needs to characterize the dependence profile of an application. Previous researches have employed *Annotated Directed Acyclic Graph* (ADAG) [2], basic-block based task graphs [3], general analytical model [4], etc. to represent the applications. However, these representations are generally derived from runtime traces of the network applications. From the compilers' perspective, they are not directly applicable. Rather, efficient representations of static profiling results are required during compilation. In [5], *Program Dependence Graph* (PDG) was used as the IR to statically characterize the applications and was fed into the task partitioning algorithm. The PDG explicitly expresses the dependences of a given program in a graph, and implicitly indicates the opportunities for code parallelization. Given its great features as an IR, it can be used extensively in compiler optimizations for parallel systems like network processors systems. Hence, we implemented a compiler pass that efficiently generates the PDG in Machine SUIF [6] compiler infrastructure. This paper summarizes the work of the PDG pass implementation and demonstrates its use in network applications analysis.

II. DESIGN AND IMPLEMENTATION

The PDG consists of two sub-graphs, i.e. *Control Dependence Graph* (CDG) and *Data Dependence Graph* (DDG). CDG expresses the *Control Dependence* while DDG depicts the *Data Dependence*. We give the terminologies of the graphs and the implementation issues respectively.

A. Terminologies of PDG

PDG is a graph IR that is strongly related to the concept of Control Flow Graph (CFG), the classical graph IR. As the same in CFG, the instructions are grouped together at the Basic-Block (BB) level. In a BB, the first instruction is the only entry point in the control flow, while the last instruction is the only exit point. Thus CFG represents the control flow with its nodes being BBs and its edges being the path of the control flow.

The very basic kind of CDG is also composed of BBs. However, its edges now represent the *Control Dependences* (CD). CD is an abstraction of the execution order. For example, node *x* in the CFG (i.e. Basic Block *x*) ends with a branch instruction and hence has two paths at the exit point of the node. If node *y* (i.e. Basic Block *y*) will be executed only when the control flow goes through the true path at the exit of node *x*, we say the node *y* is Control Dependent on node *x* on the true edge. Correspondingly in the CDG, a directed edge is added from node *x* to *y*, labeled with a control condition, e.g. *true* in this example. After this initial generation of CDG, the so-called *region nodes* are inserted in the second phase to represent a set of control dependences. For instance, if node *y* is control-dependent on the node *a* on the true edge and on the node *b* on the false edge, we create a region node *R1* to hold the control dependences of <*a*T, *b*F>. The node *y* is made to be control dependent on the newly created region node *R1* only.

As for the DDG, its nodes are still BBs. The edges now represent the data dependences. If an instruction in basic block *y* uses a variable that is defined in basic block *x* (i.e. a def-use chain exists between different basic blocks), we define that there is a data dependence edge between *x* and *y*. It is also assumed that the weight of the edge is same with the number of such def-use chains across two basic blocks. In the DDG, the edges are labeled with the weight.

The PDG then can be easily constructed by combining the CDG and DDG together. Since the nodes of both graphs

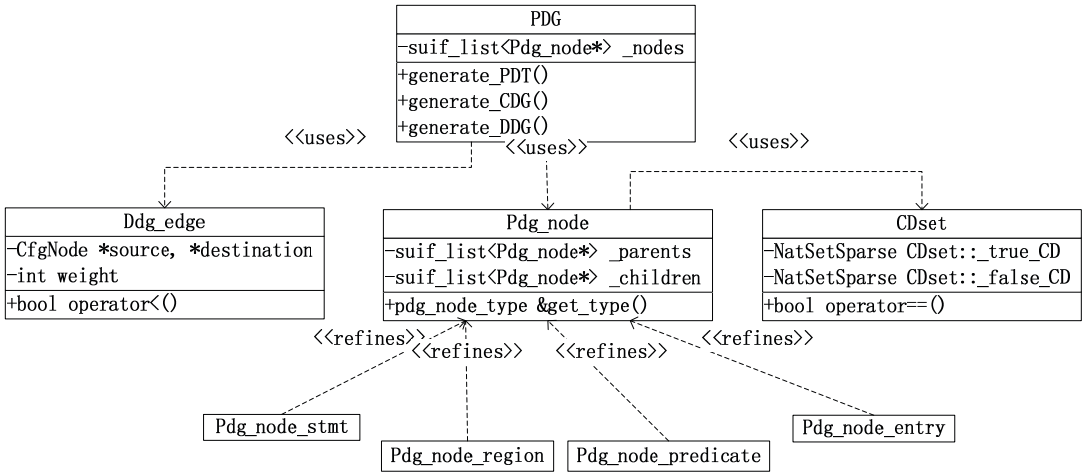

Figure 1. Class Design of PDG Pass

are largely the same (i.e. BBs), with a few additional region nodes in CDG, the merge process is straightforward.

B. Implementation of the PDG Pass

The algorithm of PDG generation is adopted from [7] and was implemented in Machine SUIF compiler infrastructure.

Consistent with other built-in SUIF passes, PDG pass is designed in an object-oriented pattern. The design model of the classes is given by Fig. 1. By construction, the PDG nodes could be classified further into types of entry node, statement node, predicate node and region node. We modelled each of them in an inherited sub-class of the parent class, i.e. `Pdg_node`. The dashed lines labelled with "refines" in the figure represent this relationship. The `CDset` class models an arbitrary set of control dependences and is used by the `Pdg_node` class to represent the control dependences of a given node. Finally the `Ddg_edge` class gives the data dependence information between PDG nodes. It has a weight property to indicate the number of def-use chains, as explained earlier. We do not need a class to model the CDG edges since the control dependences are implicitly included in the `Pdg_node` class, specifically by the properties of `_parents` and `_children` in the class.

The class methods of PDG, namely `generate_CDG` and `generate_DDG`, output the graph results both in a pure text and in graph description formats (i.e. .dot files). The description formats files can be fed into *Graphviz* [12] to generate the actual image files, e.g in JPEG or GIF format.

C. Lessens Learned

SUIF defines an Optimization Programming Interface (OPI) for developers to add their own passes. Abiding by these OPI, we are able to separate the algorithm details from the substrate IR (i.e. SUIF IR); thus the portability of code and productivity of coding are both enhanced. SUIF is also packaged with several built-in libraries facilitating control-flow and data-flow analysis. Making use of these library functions greatly reduced the workload of trivial implementations. For example in data-dependence analysis, the Single Static Form (SSA) library was hired to directly give the def-use chains and we are only left with the work of assembling that information in the PDG form.

III. RESULTS

The PDG generator pass was run on a set of network application benchmarks to testify the validity of the pass and to collect the program dependence information.

Firstly we look at a code segment for checking the packets' integrity, namely the `check_sum` function. It is one of the most common operations in packet processing systems. The procedure of `check_sum` is to calculate the 1's complement sum over the packet header octets. It returns true if the results is all 1 bits. The CFG of the function and its corresponding CDG and PDG output by our generator are given in Fig. 2. In the PDG, the edges in solid lines are CDG edges while those dashed lines are DDG edges. The round vertices represent the statement nodes and diamonds stand for predicate nodes. These two types of nodes are also the BBs derived from CFG nodes containing instructions. The pentagonal vertices are region nodes that summarize a set of control dependences as explained earlier. By the nature of CDG, the set of nodes that are control-dependent on the same node, such as node 1 and node 6 in the Fig. 2, could be executed in parallel, as long as they do not entail any data dependences.

A set of tests consisting of several sample code snippets were also conducted. The results were validated by comparing the generated PDG against those reported in [5] [7] and some in compiler textbooks. These tests are not necessarily all relevant to the network applications, but the comparison results ensured the validity of our PDG pass in general.

A. An Example

We demonstrate a concrete example by running the pass on a trie-based ipv4-packet forwarding application. The IPv4

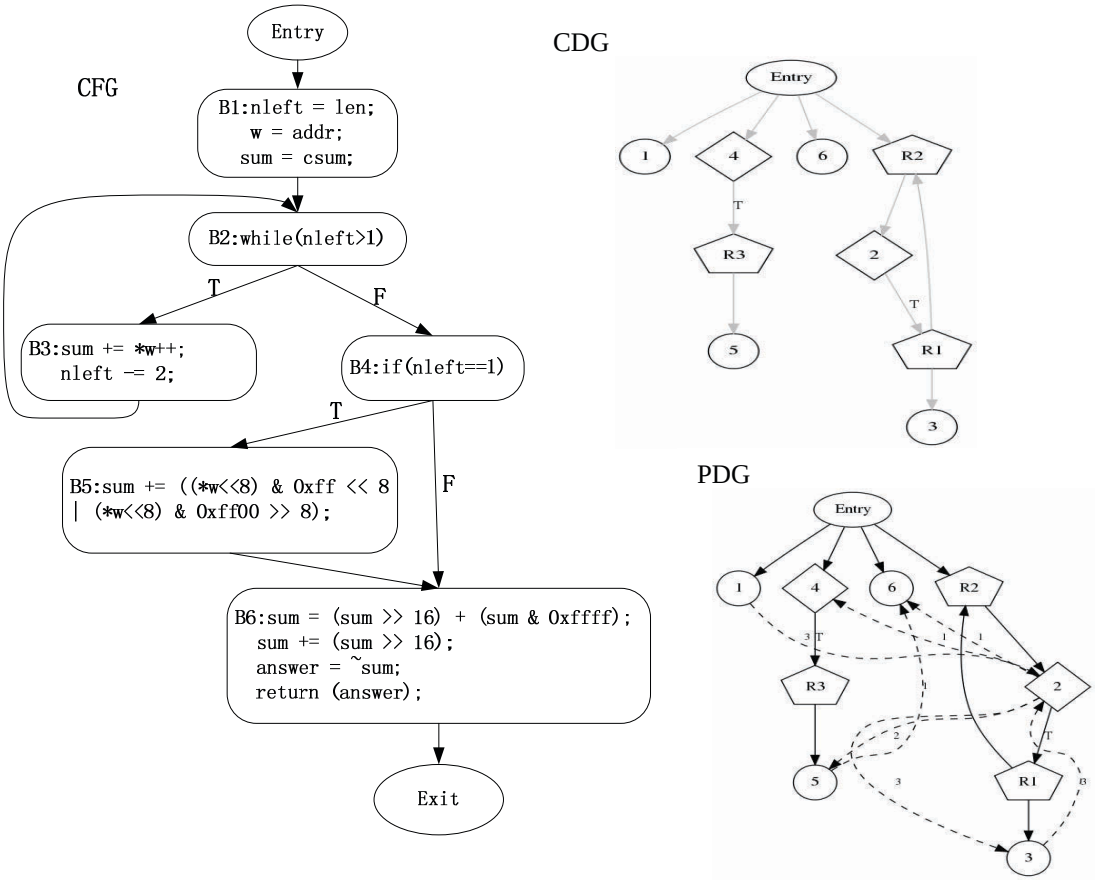

Figure 2. Program Dependence Graph Example

forwarding code was adopted from Packetbench [9]. In order to generate the PDG of the whole ipv4-packet forwarding application, we inlined all the functions. It is common to do so for network applications, since the applications themselves are usually small in C code size.

The major procedures of IPv4 forwarding include building a route table during system initialization; checking the packet type (dropping non-IP packet); validating the integrity of the packet; checking *Time To Live* (TTL) field and decrementing it; updating the checksum; and finally looking up the destination address in the route table to determine the next-hop port. In our experiment, after inlining all the major functions, the C code is lowered down to SUIF IR and then transformed to CFG IR. And then our generator pass takes the CFG IR as the input and generate the PDG of the whole application as the output. Fig. 3 captures the snapshot of running these steps in a Linux box.

```
$ c2suif -o ipv4.suif ipv4.c
$ do_lower ipv4.suif ipv4.lsf
$ do_s2m ipv4.lsf ipv4.svm
$ do_il2cfg ipv4.svm ipv4.afg
$ do_pdg ipv4.afg &>output3.txt
```

Figure 3. Steps of Running PDG Pass

Fig. 4 illustrates the generated PDG of the whole packet forwarding application. The graph exposes clear hierarchy of control dependences. For example, predicate nodes 4, 6, 9, 12, 15, 18, 21, 24 and their respective children nodes are all control-dependent on entry node, and have no remaining entangling control dependence edges among each other. It means the paths (e.g. from node 9 down to node 11 in the figure) could be well grouped together and run independently on one processor. The communication cost, though, is given by the data dependences edges (i.e. the dashed lines) that connecting any node on the path.

IV. Related and Future Work

Previous researchers have employed PDG in various ways in static program analysis. In [10], Gong et al. also constructed PDG in SUIF compiler to facilitate the logic synthesis. Due to their special application domain, their PDG data structure was different, with the SSA form incorporated. Rather in our approach, we directly made use of SSA to collect data dependences. The Linda Compiler, a precursor in developing language support for parallel systems, also explored SUIF to generate PDG for its internal work flow [11]. Their approach is close to ours except that their intended use of PDG was for message communication in distributed-memory systems. Moreover, the Linda Compiler was based on the old SUIF1 that is superseded by the newer

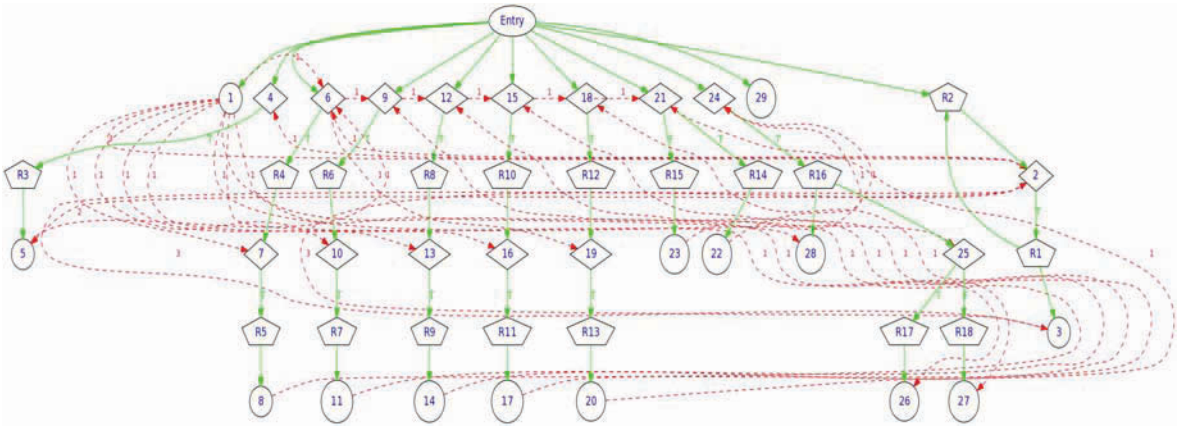

Figure 4. PDG of IPv4 Packet Forwarding

SUIF2 we employed. The two compiler frameworks are not compatible and according to SUIF group's documentation [8], SUIF1 is less flexible in modular design and code-reuse etc. We believe our contribution is more applicable for today's use.

Our ongoing work on network application partitioning and mapping for the network processors systems will make extensive use of the PDG generated by this SUIF pass. In [5] an algorithm adopted from Min-Cut Max-Flow problem was implemented to take the PDG as the input graph and regard the weight of the edges as the flow capacities in the Max-Flow problem. It aimed to minimize the communication cost (including both control dependence and data dependence) among the partitions and balance the resource utilization of the network processors. We plan to investigate other heuristics solving the partitioning and mapping problem for the network applications, and take other performance metrics into consideration.

Besides, the PDG could be used in other compiler optimizations such as efficient data mapping in presence of cache system, branch speculation and loops optimizations. We will experiment to verify their validity in network processors systems.

V. CONCLUSION

In order to perform certain analysis and optimizations in compilers, an efficient representation that explicitly captures the control-flow and data-flow dependence information of the source code is well needed. *Program Dependence Graph* is an example of such representation. In this work, we designed and implemented a compiler pass in Machine SUIF infrastructure that generates the *Program Dependence Graph* IR. The generated PDG was used to analyze the dependence hierarchy of network application benchmarks. The output of our pass could also be fed into *Graphviz* to get visualized image. In the future, the PDG will be input into the application partitioning and mapping algorithms to evaluate the performance of different partitioning and mapping heuristics.

ACKNOWLEDGMENT

This work was funded by the Irish Research Council for Science, Engineering and Technology (IRCSET) under the Postgraduate Scholarship Scheme.

REFERENCES

[1] Q. Wu and T. Wolf, "On runtime management in multi-core packet processing systems," *Proceedings of the 4th ACM/IEEE Symposium on Architectures for Networking and Communications Systems*, ACM New York, NY, USA, 2008, pp. 69-78.

[2] R. Ramaswamy, N. Weng, and T. Wolf, "Application analysis and resource mapping for heterogeneous network processor architectures," *Network Processor Design: Issues and Practices, vol. 3*, 2005, pp. 277–306.

[3] J. Yao, Y. Luo, L. Bhuyan, and R. Iyer, "Optimal network processor topologies for efficient packet processing," *IEEE Global Telecommunications Conference, 2005. GLOBECOM'05.*

[4] X. Huang and T. Wolf, "Evaluating Dynamic Task Mapping in Network Processor Runtime Systems," *IEEE Transactions on Parallel and Distributed Systems*, vol. 19, 2008, pp. 1086-1098.

[5] J. Yu, J. Yao, L. Bhuyan, and J. Yang, "Program mapping onto network processors by recursive bipartitioning and refining," *Proceedings of the 44th annual conference on Design automation*, San Diego, California: ACM, 2007, pp. 805-810.

[6] M.D. Smith and G. Holloway, "An introduction to Machine SUIF and its portable libraries for analysis and optimization," Division of Engineering and Applied Sciences, Harvard University, 2002.

[7] J. Ferrante, K.J. Ottenstein, and J.D. Warren, "The program dependence graph and its use in optimization," *ACM Trans. Program. Lang. Syst.*, vol. 9, 1987, pp. 319-349.

[8] http://suif.stanford.edu/suif/suif2/doc-2.2.0-4

[9] R. Ramaswamy and T. Wolf, "PacketBench: a tool for workload characterization of network processing," *Workload Characterization, 2003. WWC-6. 2003 IEEE International Workshop on*, 2003, pp. 42-50.

[10] W. Gong, G. Wang, and R. Kastner, "A High Performance Application Representation for Reconfigurable Systems," *Intl. Conf. on Engineering of Reconfigurable Systems and Algorithms (ERSA), Las Vegas, NEV, USA*, 2004.

[11] J. Fenwick and L. Pollock, *Implementing an optimizing linda compiler using suif*, 1996.

[12] http://www.graphviz.org

Section 6A

DIGITAL HOLOGRAPHY

Segmentation and three-dimensional visualisation of digital in-line holographic microscopy data

Karen M. Molony
Department of Computer Science
National University of Ireland Maynooth
Maynooth, Co. Kildare, Ireland
kmolony@cs.nuim.ie

Thomas J. Naughton
Department of Computer Science
National University of Ireland Maynooth
Maynooth, Co. Kildare, Ireland
and
University of Oulu
RFMedia Laboratory
Oulu Southern Institute, Vierimaantie 5, 84100 Ylivieska, Finland
tomn@cs.nuim.ie

Abstract

This paper demonstrates that transmissive or partially transmissive scenes imaged by digital in-line holographic microscopy (DIHM) can be reconstructed as a three-dimensional (3-D) model of the imaged volume from a single capture. This process entails numerical reconstruction, segmentation and polygonisation. Numerical reconstruction of a digital hologram captured using a DIHM set up is performed at equally spaced depths within a range. In the case of intensity modulating objects, segmentation of each of the reconstructed intensity images produces a contour slice of the scene by applying an adaptive threshold and border following. These slices are visualised in 3-D by polygonising the data using the marching cubes algorithm. We present experimental results for a real world DIHM capture of a partially transmissive scene that demonstrates the steps in this process.

Keywords: Digital in-line holographic mircroscopy, segmentation, three-dimensional visualisation

1. Introduction

Holography [1, 2] is an imaging science made up of two parts, recording and replay. Traditionally, photographic films were used to record holograms. A hologram encodes 3-D information; intensity and directional information of the optical wave-front. Digital holography is derived from conventional holography but uses a digital area sensor instead of a photographic medium in order to capture the holograms, and reconstruction is performed on a computer numerically [3, 4]. This has only recently become feasible due to advances in computer technology and CCD sensors with high spatial resolution and high dynamic range. The microscopic principle originally proposed by Gabor [1] is the simplest realization of holography and has been coined digital in-line holographic microscopy (DIHM) [5]. It is this optical recording set up that we use in this paper.

Typical microscopy approaches, e.g. confocal microscopy, require dyes to make (quasi-)transparent biological samples, which are compressed between glass slides, visible. DIHM enables biological specimens to be analyzed at a cellular level in a completely unaltered environment in 3-D. Manual analysis of this data by a biologist is a tedious process. A further difficulty is introduced when using DIHM data as DIHM is an emerging technology with which biologists are not yet familiar. This is compounded by the

fact that the DIHM data is 3-D data. Extraction of 3-D data from DIHM data and subsequent analysis is an unsolved problem.

In this paper we focus on visualising 3-D features of scenes imaged by DIHM. In order to achieve this, reconstructions at various depths are obtained. A two part segmentation process is applied. An adaptive thresholding step, and then a border following step comprises the two-dimensional (2-D) segmentation that is applied to each of these reconstructions. The marching cubes algorithm is then implemented on the multiple segmented images to polygonise the dataset. This renders the surface of the volume that was imaged and so a 3-D segmentation and visualisation technique for DIHM is presented.

In section (2) an overview of the DIHM set up and reconstruction process is described. Further explanation of this type of optical setup can be found in [6]. The segmentation approach used is detailed in section (3). In section (4) a description of the marching cubes algorithm is provided. We present some experimental results in section (5) and we conclude in section (6).

2. Digital In-Line Holographic Microscopy

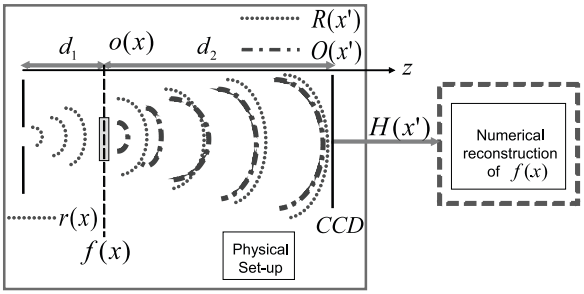

Figure 1. DIHM set up is physically comprised of a light source, pinhole, sample, CCD and a computer for numerical processing.

The first of the two stages of holography involves the recording of an interference pattern from an object beam and a reference beam. The second stage is replaying the wavefront of the original object from this recording. The output of the numerical reconstruction is typically a 2-D description of the wavefront at a single distance from the camera. The DIHM set up requires only a point light source, a pinhole, a transmissive or partially transmissive scene to be imaged, and an intensity recording device. This is suitable for biological samples [5] which are (quasi-)transmissive.

As shown in Fig.1, a spherical diverging beam $r(x)$ emerges from a pinhole illuminating an object, $f(x)$, a distance d_1 away. Immediately behind this plane there is an object wave, $o(x) = f(x)r(x)$. The interference pattern, $H(x')$, between the propagated reference wave, $R(x')$, and the propagated object wave, $O(x')$, is captured on a CCD a further distance d_2 away. This capture is the input to the numerical reconstruction part of the imaging system.

Reconstruction of a capture obtained by this set up is possible on a computer by numerically calculating a diffraction integral that describes the diffraction in free space by the recorded hologram [7]. The sampling conditions for the Fresnel integral have been formalised [8, 9] and numerical approximations of the Fresnel transform (FST) have been applied successfully for digital hologram reconstruction [9, 10, 11]. Some fast algorithms for calculating free space Fresnel diffraction patterns have been developed [12, 13] and are applied for reconstructing the DIHM holograms in the experiments described.

3. Segmentation

In image processing, segmentation subdivides an image into regions. In digital holography, not all parts of a 3-D imaged object will necessarily be in-focus in a given 2-D reconstruction at a specific depth. Segmentation can be performed on a single reconstruction at a specific depth, or on multiple independently focused reconstructions at different depths [14], which, when combined can be considered a topography of the scene. In conventional digital holography a range of perspectives allow manipulation of the scene to overcome occlusions [15]. In DIHM such a range is not available due to the proximity of the components in the set-up. However, as DIHM is applied to transparent objects, retrieving segmentations at multiple depths can be achieved without the obstruction of occluding features. At any given depth, a reconstruction will show features in-focus at that depth and all out-of-focus features with reduced clarity [14]. Applying an adaptive threshold to filter out-of-focus features in an intensity reconstruction of a DIHM capture allows a successful application of border following.

3.1. Adaptive Threshold

In order to remove out-of-focus background features from a reconstructed intensity image a threshold can be applied. It is assumed that the in-focus features are brighter with respect the background than out-of-focus features. A straightforward threshold is not as applicable if the background is not even. There is ample opportunity for noise to enhance an uneven background in a DIHM reconstruction, for example the DC term and twin image [16], speckle noise

[17], and out-of-focus features themselves can influence the background. Therefore an adaptive threshold [18] is applicable. An example of adaptive thresholding is shown in Fig.2. OpenCV [19] provides an implementation of this

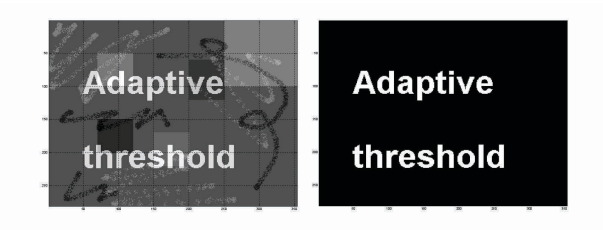

Figure 2. Adaptive thresholding applied to the text on the left with an inconsistent background produces the binary result on the right hand side.

which we apply in the grayscale region $\{0\text{-}255\}$ on block sizes $\approx 2\%$ of our image using mean weighting of pixels. The variable threshold is the weighted average of pixels within a block minus an offset. This provides a binary image of foreground and background features.

3.2. Border following

Border following is an algorithm that takes a binary image as input and outputs the borders of the objects and holes within those objects in the image. By indexing into the 2D raster, each pixel is checked to see if it is a foreground pixel. Once such a boundary pixel is found, i.e. the previous pixel was a background pixel, its connected pixels are examined. Usually the next pixel to be checked is in the same direction that has just been found. This process is repeated for each subsequent connected neighbour pixel, tracing the boundary until no more connected border pixels are found. Typically boundaries of the object are assumed to be in 8-connectivity and boundaries of holes to be in 4-connectivity [20] and so can be treated disinctly in the output. An example of border following is shown in Fig.3.

OpenCV provides an implementation of this based on [20]. The output is a contour, or a list of points that comprise a curve in an image [19]. This list can be manipulated to only consider contours in a given range of lengths, using a-priori knowledge of saught features to limit the number of false feature boundaries isolated.

4. 3-D visualisation

As segmentation is applied at a range of depths, a stack of binary contour images can be obtained and a volume

Figure 3. Border following applied to the binary input on the left with a size restrucution results in the image on the right.

is constructed from these. The data is now represented by slice segmentations through the scene. There are various scanning technologies that obtain data which is stored in a similar manner, e.g. confocal miscroscopy and magnetic resonanace imaging (MRI). The significant difference with DIHM data is that the slices are all obtained from a single capture and the volume is not physically scanned. Therefore movement of a sample is not a consideration. Furthermore no alteration of the sample is required, e.g. in confocal microscopy fluroescence or chemical dyes are required. Some 3D visualisation techniques of data stored in this way been explored [21]. Marching cubes [22] is an algorithm that was developed specifically for visualising this type of data and has proved effective for the polygonisation of similar scalar data [23].

4.1. Marching Cubes

Marching cubes [22] is an algorithm that generates triangles to represent surfaces. A 3D raster is subdivided into cubes. Each vertex of the cube is numbered $0-7$ as shown in Fig.4.

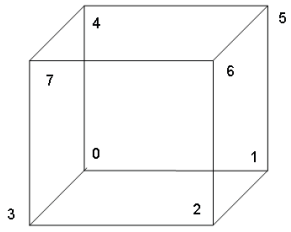

Figure 4. A volume is subdivided into cubes. The vertices of such a cube are numbered $0-7$

Based on the values of the vertices of the cube with respect to an isosurface value, that cube is considered to be wholly inside or outside of a surface, or intersected by a surface. If some vertices are higher than the isosurface value and some are lower then trangles are drawn on the edges of the cube to

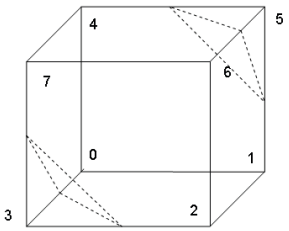

Figure 5. Triangles drawn for a cube where only vertex 3 and vertex 5 are below the isosurface

demonstrate the intersections. There are 2^8 possiblities and so a known look up table is used which returns a twelve bit result, one for each edge of the cube, to show intersections on this cube. A look up table of corresponding triangles is also provided for computational efficiency. An example is shown in Fig.5 where vertex 3 and 5 are below the isosurface and the resulting intersecting triangles are drawn.

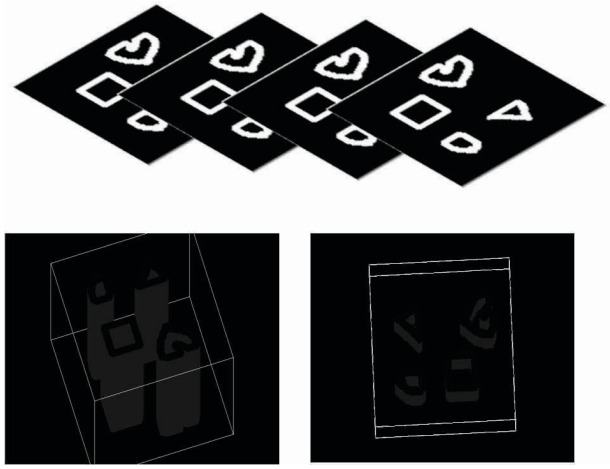

Figure 6. For a stack of a repeated contour image, above, a 3-D rendering can be constructed of the surfaces and viewed from different perspectives, below.

An example of marching cubes applied to a stack of the same input binary image is shown from two different perspectives in Fig.6.

5. Experimental Results

In this paper we detail the steps involved in the segmentation and visualisation of transmissive or partially transmissive scenes. These steps are illustrated here using a hologram of a cross hair sample captured using a DIHM set up. While this is not ideal as hair is opaque, this hologram does allow for the demonstration of the process as the opaque sample is small with respect to the imaged scene.

A digital hologram of two hairs at one depth from the camera, and a single hair at a different depth were imaged by the DIHM process decribed previously as shown in Fig. 7. The scene can be reconstructed numerically from this sin-

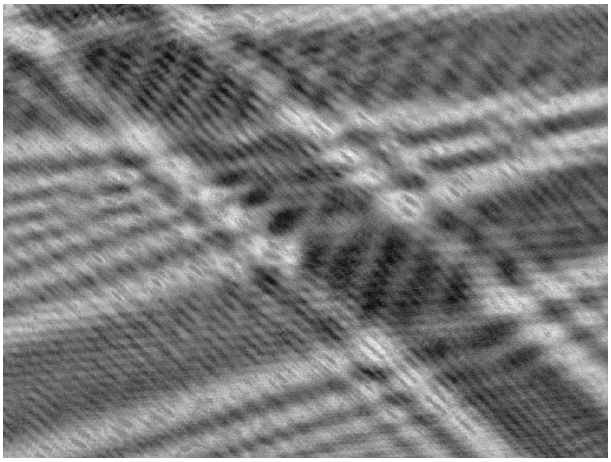

Figure 7. Hair hologram captured using a DIHM set up

gle capture so that the foreground cross hairs and the single background hair can be displayed in focus seperately. In Fig. 8.A and 8.B numerical reconstructions of the scene are presented at a reconstruction depth of 235 mm and 300 mm respectively. Note that the reconstruction distances are the physical distances magnified. A human hair is ≈ 100 μm thick. Reconstructions for depths ranging from $\{200-335\}$

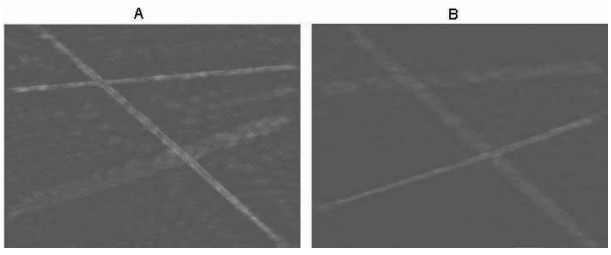

Figure 8. A. Reconstruction at depth = 235 mm, B. reconstruction at depth = 300 mm

mm in steps of 5 mm were computed. the results of applying an adaptive threshold to the images shown in Fig.8 are shown in Fig.9. Following on from this, border following was applied for each thresholded result and the resulting contours were saved individually for further processing where each result represents a contour slice through the scene at that reconstruction depth. Examples of con-

Figure 9. A,B are thresholds of Fig.8.A,B

tour slices corresponding to the reconstructions shown in Fig.8 are shown in Fig.10. Since we only consider contours $\geq$ 1000 pixels, noise arising from out-of-focus features is omitted from the contour slice.

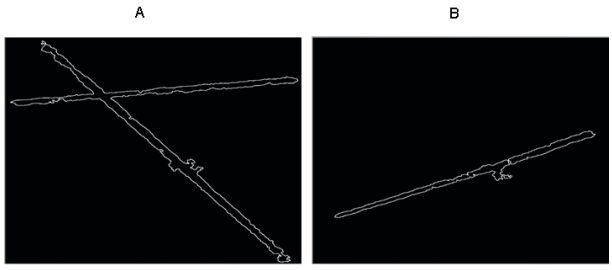

Figure 10. A,B are contours of Fig.9.A,B

The previously computed stack of contour slices comprises the 3-D input raster for the marching cubes algorithm. As the experimental sample is non-transmissive, contours are of the hairs in-focus and nearly in-focus, and so a 3-D type representation can be made. However, for a transmissive sample contour slices are of in-focus features only through the scene so a 3-D model representative of the volume can be obtained. As can be seen in Fig.11 the polygonsied surface of the scene can be viewed from any angle. The cross hairs at one plane, intersecting on the left hand side in both views in Fig.11, can be seen at a different depth than the single hair by looking at the z-axis shown.

As mentioned, the contour slices here are for the in-focus and nearly in-focus hairs and so the 3-D representation is not showing a 3-D model of the hair but rather the outline of those in the x-y plane at a range of depths. It is expected that a 3-D visualisation of a transmissive biological sample would appear more like the test example shown in Fig. 12 where each contour slice represents the exact boundaries of in focus features at that depth. The test sample is constructed from a stack of the same 2-D segmentation of a hologram of a 2-D sample of mammalian cells on a glass slide which is shown in the top left corner.

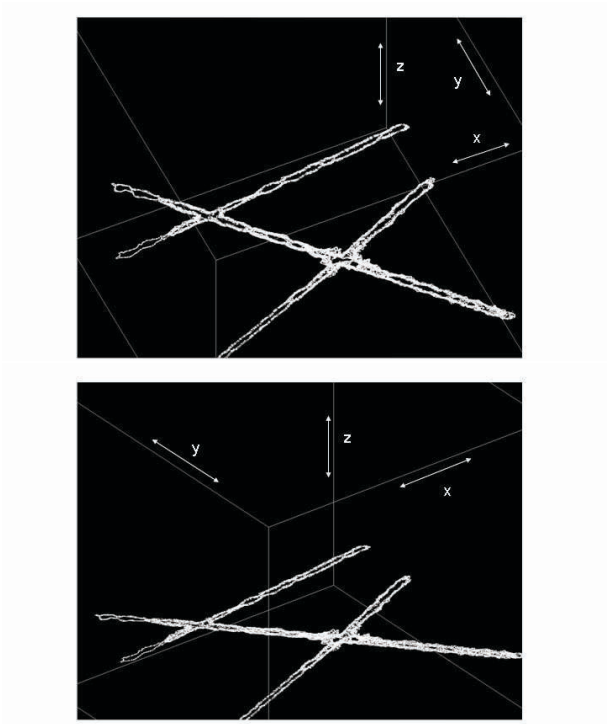

Figure 11. Two different perspectives of a 3-D visualisation of contour slices

6. Conclusions

We have shown that multiple 2-D segmentations of a scene at different depths can be obtained from a single hologram of a transmissive or partially transmissive scene. These 2-D segmentations can be used to then model a 3-D surface of the imaged sample. This is achieved by first applying an adaptive threshold to numerical reconstructions for a range of depths of a single digital hologram captured using a DIHM set up. Then border following is applied to the resulting binary image which produces a list of contours. Only contours within a specified range of lenghts are selected. These lists are segmented slices, or contour slices, of the in-focus features at the corresponding reconstruction depth. Finally these contour slices are input to the marching cubes algorithm in order to polygonise the surface. This allows a 3-D visualisation of the imaged sample. The steps involved in this process were demonstrated using a test case of a real world hologram of hair. Future work on this topic requires DIHM captures of volumes of transmissive samples.

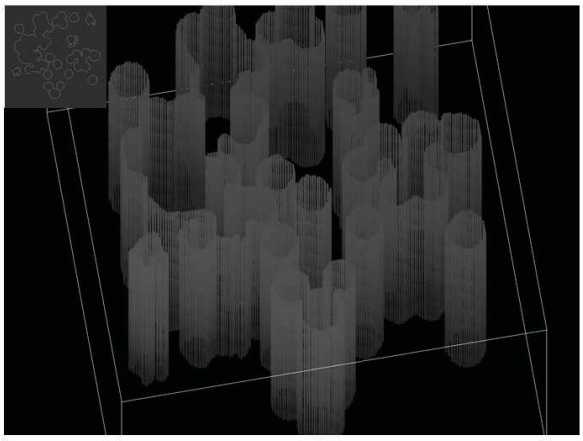

Figure 12. 3-D visualisation of 200 repeated 2-D contour slices, shown at the top left corner, of a transmissive sample

References

[1] D. Gabor, "A new microscopic principle," *Nature*, vol. 161, pp. 777–778, 1948.

[2] E. N. Leith and J. Upatnieks, "Wavefront reconstruction with diffused illumination and three-dimensional objects," *J. Opt. Soc. Am.*, vol. 54, pp. 1295–1301, 1964.

[3] T. M. Kreis, *Handbook of Holographic Interferometry*. Wiley-VCH, 2005.

[4] U. Schnars and W. P. O. Jüptner, *Digital Holography*. Springer, 2004.

[5] J. Garcia-Sucerquia, W. Xu, S. K. Jericho, P. Klages, M. H. Jericho, and H. J. Kreuzer, "Digital in-line holographic microscopy," *Appl. Opt.*, vol. 45, pp. 836–850, 2006.

[6] K. M. Molony, B. M. Hennelly, D. P. Kelly, and T. J. Naughton, "Reconstruction algorithms applied to in-line gabor digital holographic microscopy," in preperation.

[7] G. Pedrini, P. Frning, H. Fessler, and H. J. Tiziani, "Inline digital holographic interferometry," *Appl. Opt.*, vol. 37, pp. 6262–6269, 1998.

[8] F. Gori, "Fresnel transform and sampling theorem," *Opt. Eng.*, vol. 39, pp. 293–297, 1981.

[9] A. Stern and B. Javidi, "Analysis of practical sampling and reconstruction from fresnel fields," *Opt. Eng.*, vol. 43, pp. 239–250, 2004.

[10] Y. Zhang, G. Pedrini, W. Osten, and H. J. Tiziani, "Reconstruction of in-line digital holograms from two intensity measurements," *Opt. Lett.*, vol. 29, pp. 1287–1789, 2004.

[11] Y. Frauel, T. J. Naughton, O. Matoba, E. Tajahuerce, and B. Javidi, "Three-dimensional imaging and processing using computational holographic imaging," *Proc. IEEE*, vol. 94, pp. 636–653, 2006.

[12] D. Mas, J. Garcia, C. Ferreira, L. M. Bernardo, and F. Marinho, "Fast algorithms for free-space diffraction patters calculation," *Opt. Commun.*, vol. 164, pp. 233–245, 1999.

[13] D. Mas, J. Prez, C. Hernndez, C. Vzquez, J. Miret, and C. Illueca, "Fast algorithms for free-space diffraction patters calculation," *Opt. Commun.*, vol. 227, pp. 245–258, 2003.

[14] C. P. McElhinney, J. B. McDonald, A. Castro, Y. Frauel, B. Javidi, and T. J. Naughton, "Depth-independent segmentation of macroscopic three-dimensional objects encoded in single perspectives of digital holograms," *Optics Letters*, vol. 32, pp. 1229–1231, 2007.

[15] J. Maycock, C. P. M. Elhinney, B. M. Hennelly, T. J. Naughton, J. B. M. Donald, and B. Javidi, "Reconstruction of partially occluded objects encoded in three-dimensional scenes using digital holograms," *Applied Optics*, vol. 45, pp. 2975–2985, 2006.

[16] J. W. Goodman, *Introduction to Fourier Optics*. Roberts & Company Publishers, 2004.

[17] J. Maycock, B. M. Hennelly, J. B. McDonald, Y. Frauel, A. Castro, B. Javidi, and T. J. Naughton, "Reduction of speckle in digital holography by discrete fourier filtering," *Journal of Optical Society of America A*, vol. 24, no. 6, pp. 1617–1622, 2007.

[18] F. H. Y. Chan, F. K. Lam, and H. Zhu, "Adaptive thresholding by variational method," *IEEE TRANSACTIONS ON IMAGE PROCESSING*, vol. 7, pp. 468–473, 1998.

[19] G. Bradski and A. Kaehler, *Learning OpenCV Computer Vision with the OpenCV Library*. O'Reilly Media, Inc, 2008.

[20] S. Suzuki and K. Be, "Topological structural analysis of digitized binary images by border following," *Computer Vision, Graphics, and Image Processing*, vol. 30, pp. 32–46, 1985.

[21] K. OConor, H. P. Voorheis, and C. OSullivan, "3d visualisation of confocal fluorescence microscopy data," *Eurographics Ireland Workshop*, pp. 49–54, 2004.

[22] W. E. Lorensen and H. W. Cline, “Marching cubes a high resolution 3d surface construction algorithm,” *Computer Graphics*, vol. 21, pp. 163–169, 1987.

[23] U. Tiede, K. H. Hoene, M. Bomans, A. Pommert, M. Riemer, and G. Wiebecke, “Investigation of medical 3d-rendering algorithms,” *Computer Graphics and Applications, IEEE*, vol. 10, pp. 41–52, 1990.

Speed up of Fresnel transforms for Digital holography using pre-computed chirp and GPU processing.

Nitesh Pandey, Bryan M. Hennelly, Damien P. Kelly and Thomas J. Naughton

***Abstract*— We show how the common Fresnel reconstruction of digital holograms can be speeded up on ordinary computers by precomputing the two chirp factors for a given detector array size and then calling these values from memory during the reconstruction. The speedup in time is shown for various hologram sizes. We also run the same algorithm on Nvidia GPU using Matlab.**

***Index Terms*—Digital holography, Optics, imaging , FFT**

I. INTRODUCTION

Digital holography[1] is a fast growing field with applications in Microscopy[2], Metrology[3] and 3-D information processing[4,5] and display[6] to name a few. In digital holography, the holograms are recorded electronically by a CCD target. The real image can be reconstructed from the digitally sampled hologram by numerically propagating the wavefield back to the plane of the object using the theory of Fresnel diffraction. Reconstructions based on the Fresnel transform are widely used for objects for large hologram sizes because they traditionally employ the fast Fourier Transform (FFT) algorithm [7] which reduces the computations required for a *N*x*N* matrix from O(N^2) to O(*N*log*N*) steps. The memory consumption and the speed of the FFT makes it a highly important and useful algorithm. As CCD sensor sizes increase in terms of pixel numbers and density, the computational complexity of the reconstruction also increases. Here we aim to show how the reconstruction using the Fresnel transform can be simplified using pre computed chirp and phase factors.

Manuscript received May 29th, 2009. The research leading to these results has received funding from the European Community's Seventh Framework Programme FP7/2007-2013 under grant agreement no. 216105

N.Pandey, B.Hennelly and D.kelly are with Dept of computer science, NUI Maynooth e-mail: npandey@cs.nuim.ie).

T.Naughton is with Dept of Computer sciene, NUI Maynooth and with [2]*University of Oulu, RFMedia Laboratory*

II. FRESNEL TRANSFORM

Consider the Fresnel transform below which describes the relationship between the wavefield at 2 planes $h(x,y)$ and $\Gamma(\xi,\eta)$ separated by a distance d

$$\Gamma(\xi,\eta)=\frac{ia}{\lambda d}\exp\left[-i\frac{\pi}{\lambda d}\left(\xi^2+\eta^2\right)\right]\int_{-\infty}^{\infty}\int h(x,y)\times\exp\left[\frac{-i\pi}{\lambda d}\left(x^2+y^2\right)\right]\times\exp\left[\frac{i2\pi}{\lambda d}(x\xi+y\eta)\right]dxdy$$

where λ is the wavelength, d is the distance and a is the amplitude. In Digital holography, we deal with discrete representations of this transform since the hologram is discretized at the CCD into NxM samples at intervals of Δx and Δy in the x and y directions. Δx and Δy being the pixel pitches of the sensor. Direct discreteization of the Fresnel integral gives the following

$$\Gamma(m,n)=\exp\left[\frac{-i\pi}{\lambda d}\left(m^2\Delta\xi^2+n^2\Delta\eta^2\right)\right]\times\sum_{k=0}^{M-1}\sum_{l=0}^{N-1}t(k,l)\exp\left[\frac{-i\pi}{\lambda d}\left(k^2\Delta x^2+l^2\Delta y^2\right)\right]\exp\left[i2\pi\left(\frac{km}{M}+\frac{ln}{N}\right)\right]$$

Here $\Gamma(\xi,\eta)$ is the matrix of *N*x*M* points which describes the amplitude and phase distribution of the real image and $\Delta\xi$ and $\Delta\eta$ are the pixel pitches in the reconstructed images. For a thorough investigation of the resulting numerical algorithm, and the range of d over which it is useful, the reader can consult [8]. We assume we have available to us, a hologram of *N*x*M* size recorded with us of an object placed at a distance d from the camera. To calculate the real image field from this hologram, the following method is used.

i) The first complex chirp is calculated and multiplied by the original hologram. To calculate the chirp NxM computations are needed. This can be speeded up using Vector multiplications (for ex in Matlab) but the number of computations remain the same.

ii) A Discrete fourier transform of this matrix is taken. This is done using the FFT algorithm.

iii) The resultant FFT is multiplied with the second chirp factor which must be computed in the same manner as the first.

In order to speed up the Fresnel reconstruction, we note that the input chirp is independent of the input hologram field. The

second chirp and the constant factors are also independent of the input. If we precalculate a range of these matrices for different distances and load the corresponding data from memory during reconstruction, we can save $2NxM$ computations. This is advantageous for real time high resolution digital holographic systems. The time take to load a pre-calculated matrix is significantly less than the time it takes for 'on the fly' calculation. The computation reduces to 2 vector multiplications and the FFT algorithm. The algorithm now becomes

i) Load the two chirp values for the reconstruction distance d and multiply first chirp by hologram
ii) Take FFT
iii) Multiply by second chirp.

We further note that for the case of human visualization of reconstructed holograms, which is of sole importance in holographic 3D-TV[9] and in applications such as holographic endoscopes[10], the phase factors (step iii) can be neglected. This offers an additional speedup on large matrices. To test the improvement in reconstruction time, we used sections of a sample hologram of a macroscopic object of height 3cm recorded in an in-line like geometry on a 1392x1040 CCD ,pixel size 6.45µm (AVT Dolphin) using a 785nm laser. The average times taken for reconstruction and speed up achieved on a computer (Intel Pentium 4 3.0Ghz CPU 1Gb RAM), is shown in the table below.

Hologram size	No loading(time in seconds)	With loading (time in seconds)	Speed up
100x100	0.0613	0.04731	1.30x
200x200	0.1027	0.07023	1.46x
500x500	0.4390	0.26449	1.66x
1000x1000	1.7360	0.99297	1.74x
2000x2000	7.1904	4.22684	1.70x

A large number of these chirp matrices which cover a large distance can be stored permanently in memory and can be accessed by the program whenever the reconstruction is demanded for a particular distance. Recently the use of graphics cards for General purpose computing is becoming popular. Algorithms designed to exploit the parallel many-core capability of the GPU offer a significant speedup (5x-20x) over CPUs. GPGPU as it is called has already been used by a few groups to show the speed of reconstruction of holograms on the GPU architecture [11,12]. Here we show how the reconstruction and preloading works on a NVIDIA Geforce graphics card on a AMD Athlon 64 X2, 2.31Ghz, 2 Gb RAM . We use the Jacket[13] engine for Matlab to run our code on the GPU. The results are shown in Table 2

Hologram size	No loading(time in seconds)	With loading (time in seconds)	Speedup
100x100	0.0629	0.0555	1.13x
200x200	0.0646	0.0522	1.23x
500x500	0.0854	0.0672	1.27x
1000x1000	0.1819	0.0775	2.34x
2000x2000	0.5336	0.2514	2.12x

III. CONCLUSIONS

We have shown the benefits of using a table of precomputed chirp matrix and phase factors on the speed of digital hologram reconstruction on normal CPUs and GPUs. The speedup improves with larger matrices and occurs due to the fact that loading large data from memory takes very little time compared to calculation 'on the fly'. In this paper we have limited our investigation to the direct method (see Equation 2) of computing the Fresnel transforms which is made up of two chirp multiplications and a FFT algorithm [8]. Other methods of reconstruction also require calculation of chirp data which is independent of the input hologram. The convolution approach for example [8] is based on the description of the Fresnel Transform as a chirp multiplication in the Fresnel domain. This method requires calculation of a chirp and two FFTs. Thus precalculating will lead to a time saving of half as that in the direct fresnel approach. The slightly more accurate method based on the Fresnel-Kirchoff transformation requires FFT followed by multiplication by a chirp like function followed by a second FFT. Since this chirp like function (which reduces to a chirp in the paraxial Fresnel approximation) is is independent of the input hologram field, its recalculation will also result in considerable time savings.

REFERENCES

G[1] U. Schnars and W. Juptner, "Digital recording and numerical reconstruction of holograms," Meas. Sci. Technol. 13, 85–101 (2002).
[2] P. Marquet, B. Rappaz, P. J. Magistretti, E. Cuche, Y. Emery, T. Colomb, and C. Depeursinge, "Digital holographic microscopy: a noninvasive contrast imaging technique allowing quantitative visualization of living cells with subwavelength axial accuracy," Opt. Lett. 30, 468-470 (2005).
[3] C. Wagner, W. Osten, S. Seebacher, "Direct shape measurement by digital wavefront reconstruction and multiwavelength contouring," Opt. Eng. 39 79-85 (2000).
[4] B. Javidi and E. Tajahuerce, "Three-dimensional object recognition by use of digital holography," Opt. Lett. 25, 28-30 (2000)
[5] Yann Frauel, Thomas J. Naughton, Osamu Matoba, Enrique Tajahuerce, and Bahram Javidi, "Three-dimensional imaging and processing using computational holographic imaging," Proceedings of the IEEE, vol. 94, no. 3, pp. 636-653, March 2006.
[6] Digital Holography and Three-Dimensional Display Principles and Applications, Poon, Ting-Chung (Ed.) 2006, XIII, 430 p.
[7] The Fast Fourier Transform, Brigham, E.O, New York: Prentice-Hall, (2002)
[8] D. Mas, J. Garcia, C. Ferriera, L.M. Bernardo, "Fast algorithms for free space diffraction patterns calculation," Opt. Comm. 164,233245,(1999).

[9]L. Onural and H. Ozaktas, "Signal processing issues in diffraction and holographic 3DTV," in Proc. EURASIP 13th European Signal Processing Conference (2005).
[10] S. Schedin, G. Pedrini, H. J. Tiziani, and A. K. Aggarwal, "Comparative study of various endoscopes for pulsed digital holographic interferometry," Appl. Opt. 40, 2692-2697 (2001).
[11] L. Ahrenberg, P. Benzie, M. Magnor, and J. Watson, "Computer generated holography using parallel commodity graphics hardware," Opt. Express 14, 7636-7641 (2006).
[12] Tomoyoshi Shimobaba, Yoshikuni Sato, Junya Miura, Mai Takenouchi, and Tomoyoshi Ito, "Real-time digital holographic microscopy using the graphic processing unit," Opt. Express 16, 11776-11781 (2008)
[13] www. accelereyes.com

Twin removal in digital holography by means of speckle reduction. (Revised May 2009)

David S. Monaghan*[1], Damien P. Kelly [1], Nitesh Pandey [1] and Bryan M. Hennelly [a].

[1] Department of Computer Science, National University of Ireland, Maynooth, Co. Kildare, Ireland.

***Abstract* -- A method for numerically removing the twin image in on-axis digital holography, based on multiple digital holograms, is discussed. The digital holograms under examination are captured experimentally using an in-line modified Mach-Zehnder interferometric setup and subsequently reconstructed numerically. The technique is suitable for a transmission geometry. Each individual hologram is recorded with a statistically independent diffuse illumination field. This is achieved by shifting a glass diffuser in the *x-y* plane of the object path. By recording the holograms in this manner the twin image, from a numerical reconstruction, appears as speckle. By reducing this speckle pattern the twin image can be effectively removed in the reconstruction plane. A theoretical model is developed and experimental results are presented that validate this model.**

***Index Terms*—Digital Holography, On- Axis, Speckle, Twin reduction**

I. Introduction

In recent years there has been a great deal of interest in the field of Digital Holography (DH)[1-5] and 3D display[6, 7] and capture technology. This is apparent by the number of paper published in the literature. Holography[8, 9] is a method for capturing the complex field of an object and thus limited three-dimensional structures can be obtained. Recent technological improvements, such as CCD cameras, high-powered desktop computers and spatial light modulators, have made DH a viable alternative to traditional holography. DH boasts advantages such as digital storage, processing and compression of holograms, transmission over existing digital infrastructure. In this paper we will examine a method of twin removal in digital holography based on a speckle[10, 11] reduction technique.

II. Theory

In the follwoing section we present a simple theoretical model to describe the behaviour of our optical system. Our aim here is not to conduct a fully rigorous examination of the complex interaction of multiple speckle fields and various apertures in the system but rather to present a plausible description of the complex behaviour of the system. A more complete analysis would take us far beyond the scope of this manuscript. A colluminated plane wave is generated using a spatial filter and lens as depicted in Figure. 1. This colluminated plane wave is then incident on a diffuser. We assume that the diffuser is optically rough and imparts a random phase to the plane wave front that emerges from the diffuser. This random phase field now propagates to the object plane where it illuminates our transmissive target. We describe the random field that illuminates our object as

$$U_{\mathrm{R}}(X) = a_{\mathrm{R}}(X)\exp\left[j\phi_{\mathrm{R}}(X)\right], \tag{1}$$

where $a_{\mathrm{R}}(X)$ and $\phi_{\mathrm{R}}(X)$ are random amplitude and phase values respectively. We note that the random phase field at the output of the diffuser gives rise to both random amplitude and phase values (a_{R} and ϕ_{R}) at our object plane, due to diffraction introduced by the finite extent of the diffuser. For simplicity however we assume that the diffuser is sufficiently large and the distance d_1 sufficiently small (see Figure 1) such that the resulting speckle field in the object plane may be assumed to be delta correlated. We describe the effect of our transmissive object as

$$U_{\mathrm{T}}(X) = a_{\mathrm{T}}(X)\exp\left[j\phi_{\mathrm{T}}(X)\right], \tag{2}$$

and write the field immediately after our object as

$$U(X) = U_{\mathrm{T}}(X)U_{\mathrm{R}}(X). \tag{3}$$

This combined field, $U(X)$ is now allowed to propagate to the CCD plane where it interfers with an ideal unit amplitude plane wave, $R(x) = \exp[j2\pi(z\text{-}z_c)/\lambda]$ and the resulting interference pattern is recorded. We write the continious intensity distribution incident upon the camera face as

$$H(x) = \left|u_z(x) + R(x)\right|^2, \tag{4 a}$$

$$H(x) = I_z + I_{\mathrm{R}} + u_z(x)R^*(x) + u_z^*(x)R(x), \tag{4 b}$$

where I_z, and I_{R} are the DC terms corresponding to the object and reference intensities respectively and '*' denotes complex conjugate operation. The latter two terms in Eq. (4 b) correspond to the real and twin image terms respectively. The field u_z is related to our object field $U(X)$ by a Fresnel transform

$$u_z(x) = \Im_z\{U(X)\}(x),$$
$$u_z(x) = \frac{1}{\sqrt{j\lambda z}}\int U(X)\exp\left[\frac{j\pi}{\lambda z}(x-X)^2\right]dX, \tag{5}$$

where $\Im_z\{\ \}$ is the Fresnel transform operator. We now make some more simplifying approximations. In practical DH systems the continuous intensity field, Eq. (4 b) is recorded by

Manuscript submitted May 29th 2009. Corresponding author: D. S. Monaghan e-mail: davidm@cs.nuim.ie Ph +35317083849, fax +35317083848.

a camera of finite physical extent using finite size pixels located at fixed distances from each other. Each of these factors, act to significantly limit the imaging performance of DH systems and we refer the reader to [12] for more detail. However for our purposes we do not need to consider these aspects of the imaging process to get across the essence of our idea and so for simplicity we assume that the continuous field $H(x)$, Eq. (4 b) is available to us. We note that the DC terms can be removed either numerically[13] or by recording the reference and object intensities separately and subtracting them from the captured hologram. Setting $z = z_c$ in Eq. (4 b), removing the dc terms and performing an inverse Fresnel transform yields the following result

$$A(x) = U(X) + \Im_{-z}\left\{u_z^*(x)\right\}(X), \tag{6 a}$$

$$A(x) = U(X) + \tilde{U}(X) \tag{6 b}$$

where $\tilde{U}(X)$ is the twin image term.

To remove the twin image term requires that we capture multiple digital holograms using a series of statistically independent speckle fields to illuminate our object. We assume that each of these statistically independent fields has the same average intensity M. Each of the resulting digital holograms are then reconstructed and averaged on an intensity basis in the object plane. We will now examine what happens to the real and twin terms as we average them on an intensity basis in the object plane. Let us first consider the real image term. Using a random speckle field, denoted 'n', to illuminate our object the resulting reconstructed intensity pattern of the real image term is given by

$$I_n(X) = U(X)U^*(X),$$
$$I_n(X) = \left|a_T a_{Rn}\right| \exp\left[j\left(\phi_T + \phi_{Rn}\right)\right] a_T a_{Rn} \left| \exp\left[-j\left(\phi_T + \phi_{Rn}\right)\right],\right.$$
$$I_n(X) = \left(\left|a_T\right|\left|a_{Rn}\right|\right)^2. \tag{6}$$

We now average N of these intensity distributions formed by N statistically different speckle fields

$$I^{AR}(X) = \frac{I_1 + I_2 + ... + I_N}{N},$$
$$I^{AR}(X) = \left|a_T\right|^2 \left(\frac{\left|a_{R1}\right|^2 + \left|a_{R2}\right|^2 + ... + \left|a_{RN}\right|^2}{N} \right),$$
$$I^{AR}(X) = \left|a_T\right|^2 (M) \tag{7}$$

where I^{AR} represents the result of averaging together N real image intensity reconstructions. We turn our attention to the term in round brackets in Eq. (7) and note that the sum of N statistically different intensity patterns as N goes to infinity reduces to the average intensity value for an individual speckle distribution. Therefore we may replace the term in the round brackets in Eq. (7), by the average intensity value for a given speckle field, M. It is important to note that the intensity distribution for our object field, $\left|a_T\right|^2$, is contained in Eq. (7).

We now consider the twin image term. Examining the derivation of Theorem 3 in Ref. [14] we find that $u_z^*(x) = \Im_{-z}\left\{U^*(X)\right\}(x)$. Using this result we re-write the twin image term $\tilde{U}(X)$ as

$$\tilde{U}(X) = \Im_{-2z}\left\{U^*(X)\right\}(X). \tag{8}$$

The corresponding intensity is given by

$$\tilde{I}_n(X) = U_n(X)U_n^*(X)$$
$$\tilde{I}_n(X) = \left(\int a_{Rn} a_T \exp\left[j\left(\phi_T + \phi_{Rn}\right)\right] \exp\left[\frac{j\pi}{2\lambda z}\left(X - X_1\right)^2 \right] dX_1 \right)$$
$$\times \left(\int \left(a_{Rn} a_T\right)^* \exp\left[-j\left(\phi_T + \phi_{Rn}\right)\right] \exp\left[\frac{-j\pi}{2\lambda z}\left(X - X_2\right)^2 \right] dX_2 \right) \tag{9}$$

This result means that each intensity distribution due to the twin image term generates is a statistically independent speckle pattern. Like in the previous case the $a_T \exp\left(j\phi_T\right)$ term remains constant however now each component is multiplied by a random phase and then Fresnel transformed. Thus averaging over N intensity patterns gives the following result

$$\tilde{I}^{TR}(X) = \frac{\tilde{I}_1 + \tilde{I}_2 + ... + \tilde{I}_N}{N}$$
$$\tilde{I}^{TR}(X) = M. \tag{10}$$

This latter equation suggests that the twin image becomes gradually reduced as more intensity distributions are averaged together. Finally it is important to consider that cross-terms (interference between the real and the twin image) that arise when we calculate the intensity of Eq. (6 b). This interfernce term can be re-expressed as

$$CT = \left|U\right|\left|\tilde{U}\right| \cos\left(\theta_R\right) \tag{11}$$

where θ_R can be shown to be a random variable. Thus we see that the interference term described in Eq. (11) will average to zero and can be neglected. Although the analysis here is presented for transmissive objects (see Ref. [15]), it also seems to apply to reflective objects too as a new series of experimental results indicate. We would like to acknowledge that the theoretical description provided is relatively simplistic however it does capture some essence of the underlying physical behavior of the system, as we shall now demonstrate with a series of experimental results

III. RESULTS

The experimental set-up is shown in Figure 1. A 678nm meter laser is used. The wave-plate in this set-up is used in conjunction with a polarising beam splitter to allow the laser power between the two paths to be adjusted. A piezo mirror, electronically controlled, is employed to impart a phase-shift into the object path of the set-up.

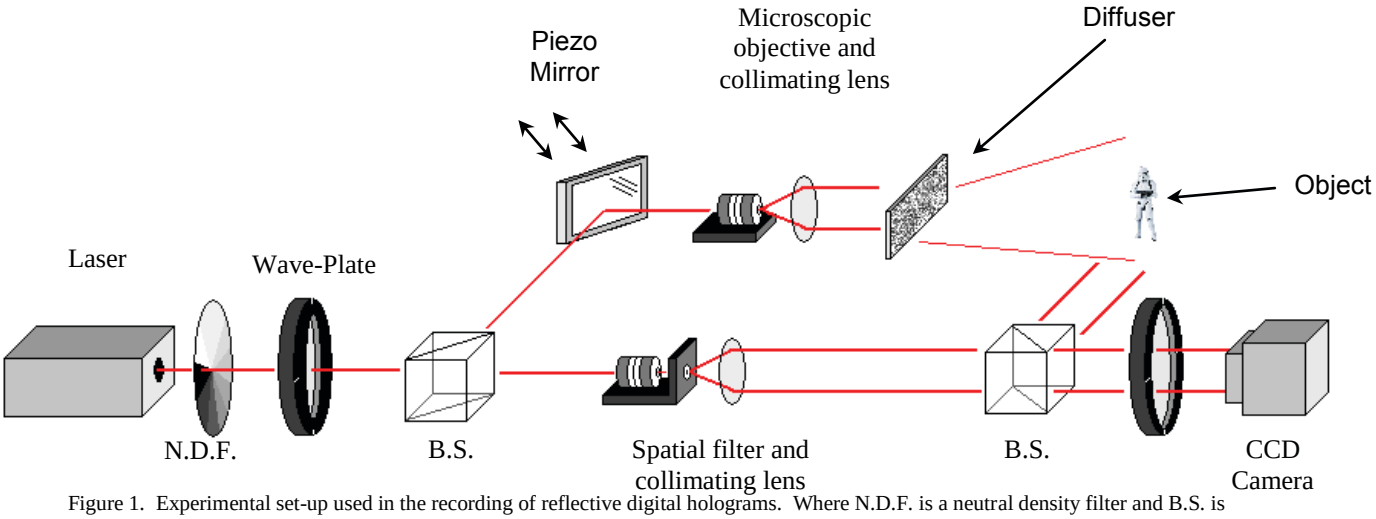

Figure 1. Experimental set-up used in the recording of reflective digital holograms. Where N.D.F. is a neutral density filter and B.S. is a polarising beam splitter.

This allows a Phase Shift Interferometry (PSI)[16, 17] digital hologram to be captured. The *x-y* position of the diffuser is moved in between each capture of a digital hologram to provide a different and statistically independent speckle pattern on each hologram.

All the holograms presented in Figure 2 are reflection holograms and were recorded using the experimental set-up shown in Figure 1. The reconstruction distance for these holograms is 285mm. They have been numerically reconstructed using the direct method (Fast Fourier transform based technique) to implement the discrete Fresnel transform[14 & 18], (also see Eq 5).

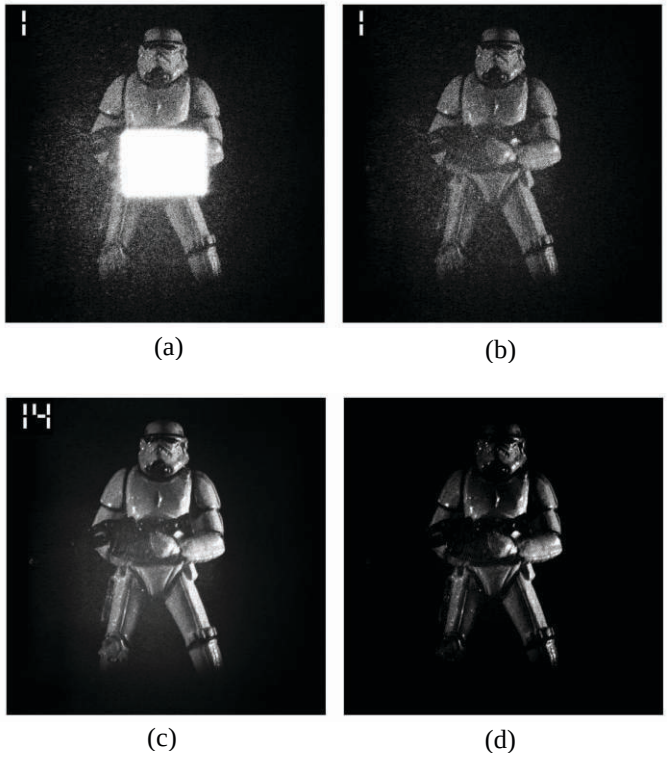

(a) (b)

(c) (d)

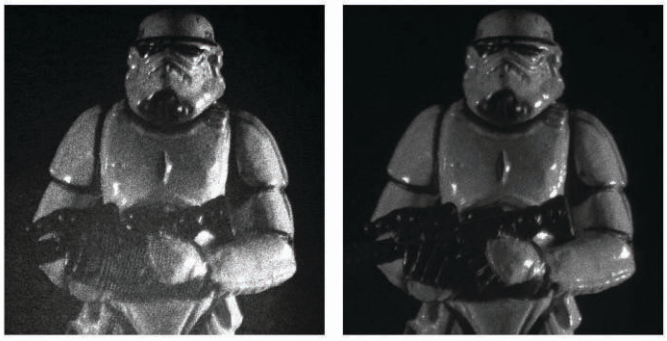

(e) (f)

Figure 2. Numerical reconstructions of a digital hologram showing (a) the DC term, twin and object, (b) single hologram and twin, (c) 14 holograms added together, (d) post-processing of (c), (e) zoomed in portion of (c) for comparison with 14 PSI holograms added together in (f).

Figure 2(a) shows a reconstruction that contains a strong DC component (or zero order term), the twin term and the original object. The DC component arises due to the intensity terms that appear as a product of the holographic process. In Figure 2(b) the DC component had been removed by a numerical high-pass filter and it can be clearly seen that the resultant reconstruction contains the original object and the twin term, which has been reconstructed as a speckle pattern due the introduction of the diffuser (see Figure 1). Figure 2(c) shows the results when 14 separate holograms how been added together on an intensity basis. It can be seen that the twin term has been significantly reduced when compared with Figure 2(b). The process of addition has produced a background DC term, which has been removed in Figure 2(d). This DC term has been removed by subtracting the mean value of the background from the entire reconstruction. Figure 2(e) and (f) show a comparison between the speckle reduction method, (e), and a PSI method, (f).

IV. CONCLUSION

The presence of a twin image in on-axis digital holography is a fundamental property of a holographic imaging system. The removal or reduction of this twin image is of principal importance in digital holography as it is present in the reconstructed image as a source of noise. In this paper we have examined a method of twin removal based on a speckle reduction technique. We have shown that this method can be applied to reflective objects in digital holography.

REFERENCES

[1] J. W. Goodman and R. W. Lawrence, "Digital image formation from electronically detected holograms," Appl. Phys. Lett. **11,** 77–79 (1967).

[2] U. Schnars and W. Juptner, "Direct recording of holograms by a CCD target and numerical reconstruction," Appl. Opt. **33,** 179–181 (1994).

[3] E. Tajahuerce and B. Javidi, "Encrypting three-dimensional information with digital holography," Appl. Opt. **39,** 6595–6601 (2000).

[4] M. Liebling, T. Blu, and M. Unser, "Complex-wave retrieval from a single off-axis hologram," J. Opt. Soc. Am. A **21,** 367–377 (2004).

[5] L. Onural and P.D. Scott, "Digital decoding of in-line holograms," Opt Eng **26**, pp. 1124–1132. (1987)

[6] U. Gopinathan, D. S. Monaghan, B. M. Hennelly, C. P. M. Elhinney, D. P. Kelly, J. McDonald, T. J. Naughton, and J. T. Sheridan, "A projection system for real world three-dimensional objects using spatial light modulators," J. Display Technol. 4(2), pp. 254–261, 2008.

[7] D. S. Monaghan, U. Gopinathan, D. P. Kelly, T. J. Naughton, and J. T. Sheridan, "Systematic errors of an optical encryption system due to the discrete values of a spatial light modulator," Opt. Eng. 48(2), p. 027001, 2009.

[8] D. Gabor, "A new microscopic principle," Nature (London) **161**, 777 (1948).

[9] D. Gabor, "Microscopy by reconstructed wavefronts," Proc. R. Soc. A **197**, 454 (1949).

[10] J. W. Goodman, *Speckle Phenomena in Optics*, Roberts Company, 2007

[11] J. W. Goodman, "Some fundamental properties of speckle," J. Opt. Soc. Am. 66(11), pp. 1145–1150, 1976.

[12] D. P. Kelly, B. M. Hennelly, N. Pandey, T. J. Naughton, W. T. Rhodes, "Resolution limits in practical digital holographic systems," (Under Review 2009).

[13] T. Kreis and W. Juptner, "Suppression of the dc term in digital holography," Opt. Eng. 36, pp. 2357–2360, 1997.

[14] F. Gori, "Fresnel transform and sampling theorem," Opt. Comm. 39, 293–297 (1981).

[15] D. S. Monaghan, D. P. Kelly, N. Pandey, B. M. Hennelly, "Twin removal in digital holography via speckle reduction," (Under Review 20009).

[16] I. Yamaguchi and T. Zhang, "Phase-shifting digital holography," Opt. Lett. 22, pp. 1268–1270, 1997.

[17] S. Lai, B. King and M. A. Neifeld**, "**Wave front reconstruction by means of phase-shifting digital in-line holography," Opt. Comm. **173**, 155-160 (2000)

[18] J. Goodman, Introduction to Fourier Optics, 2nd ed., McGraw-Hill, New York, 1966.

Review of Twin Reduction and Twin Removal Techniques in Holography

Bryan M. Hennelly, Damien P. Kelly, Nitesh Pandey, David Monaghan

***Abstract*—In this paper we review the major contributions over the past sixty years to the subject of twin reduction and twin removal in holography. We show that this collective work may be broken down into a number of categories including the well known techniques of off-axis holography and phase retrieval.**

***Index Terms*—Holography, In-Line, On- Axis, Twin Reduction**

I. Introduction

Holography was invented by Gabor in 1948[1,2]. In his initial experiments, involving electron microscopy, an object was irradiated with a radiation beam of strong coherence. The waves weakly scattered by the object interfered with the background wave on a photographic film where this interference pattern was recorded. This recorded intensity distribution contains information about the amplitude and the phase of the incident object wavefield. The limits to the Gabor experiment are the resolution of the material film and the coherence of the radiation source. Gabor also showed how it was possible to reconstruct the original object wavefield by illuminating the recorded film transparency with the original background wave. However, the image of the reconstructed object is marred by the presence of a twin image, an inherent artifact of the method. After the invention of the laser methods would later be invented to cleverly evade this twin image by using new experimental architectures, but this would impose greater restrictions on the system, in particular on the resolution of the film. However for certain radiation sources these new experimental architectures have no physical implementation or only crude and expensive equivalents. In these cases one must rely upon the initial Gabor architecture and the twin image remains a problem that must be dealt with. Such is true for many cases including x-ray holography, gamma-ray holography and electron holography. In the case of digital (optical) holography the Gabor like in-line architectures also offer advantage as discussed below.

Crystallographic structure is often determined using diffraction methods. While electron emission holography is useful for studying surface structure, it's anisotropic nature prevents the study of internal structure. The more isotropic scatter of x-rays overcomes this limitation. Improvements in x-ray detectors have enabled the application of x-ray holography for crystallography[3] which is especially useful because the recovered phase information offers an improvement over traditional diffraction techniques. As in the case of gamma-ray holography[4] and electron emission holography[5-10], the in-line architecture is used and the short distance between the source and the object implies that the twin image will be located very close to the reconstructed atom image. This creates a detrimental and unavoidable source of noise. Low voltage and high voltage electron holography are particularly useful in the imaging of weakly scattering objects such as DNA molecules[7-8]. The severe aberrations caused by lenses in electron imaging makes the in-line set-up the method of choice. Another advantage in this case is that the phase sensitivity of in-line electron holography is particularly high.

Manuscript submitted May 29th 2009. The research leading to these results has received funding from the European Community's Seventh Framework Programme FP7/2007-2013 under grant agreement no. 216105. All authors are with the Computer Science Department, National University of Ireland Maynooth, Ireland. Corresponding author: Bryan Hennelly, ph +35317083849, fax +35317083848, email: bryan.hennelly@gmail.com

II. Twin Reduction By Subtraction

In 1951, soon after Gabor's invention and many years before any off-axis architecture would be developed Bragg and Rogers developed an innovative solution to the twin image problem[11-12]. The basic idea is that the disturbance caused by the unwanted twin image on the wanted plane is, in fact, its own hologram. If a second hologram is taken from the original object, which accurately reproduces the disturbance that is due to the unwanted image at the wanted plane, the first reconstruction can be corrected by subtraction. Using a collimated light source we must take the second hologram at twice the distance of the first, since the wanted and unwanted images are formed at equal distances from the hologram on either side of it. The divergent case is somewhat more complicated. It is notable that the method works well with both phase-contrast and amplitude-contrast. This method fell into obscurity until later advances in digital technology allowed for a simplified subtraction process[12]. A similar subtraction based technique is reported in 1956[13], where two holograms must be recorded and the object must be repositioned for the second recording enabling a canceling of the twin image term. Xiao et. Al. showed[14] how the Bragg and Rogers method could be applied in x-ray holography in real time by recording two holograms while taking advantage of the penetration property of x-ray radiation.

III. Twin Elimination by Off Axis Holography

After the invention of the Laser, Leith and Upatnieks proposed[15] in 1963 a new experimental optical architecture

that enables the complete separation of the twin image term and the zero order term from the wanted image. In their method the reference beam was incident on the hologram plane at some angle relative to the normal. In this way the twin images were modulated on well-separated carrier spatial frequencies. The range of separation of the terms is dependent on the angle of the reference beam. The significantly increased bandwidth of the hologram places a much greater requirement on the resolution of the recording material. Furthermore the architecture imposes the need for numerous optical elements, in particular a beam splitter, which are not readily available in many areas of holography. The increased bandwidth of the hologram for this set-up poses a problem for digital holography. In DH, the pixilated recording cameras have resolutions an order of magnitude less than commercial photo materials. Thus the bandwidth is already severely limited and the use of an off-axis architecture will only serve to limit it further. Nevertheless Cuche et. al. proposed[16] and experimentally validated the off axis technique for real time digital holographic recording. In this case it is possible to digitally spatially filter the hologram to completely remove the DC term and the twin image. In 1966 an alternative to the off-axis method was proposed[17] for recording in the Optical Fourier Transform domain. In this case the reference beam, a point source in the object plane, can be placed adjacent to the object to effectively create an off axis hologram in the Fourier domain and to spatially separate the twin images.

IV. Twin Reduction By Fraunhofer

In 1966 another twin reduction method was proposed[18] by effectively recording in the far field of the object. When replayed in the far field the image of the object will appear but the twin image will be so spread out that it appears as a DC term and is therefore effectively removed. A year later the method was reviewed and applied to particle analysis[19] and this was followed by a further reassessment almost a decade later[20]. The method was also applied to in-line electron holography to view undecagold cluster. The method is found to work well with the phase contrast technique. In [22] Garcia et. al. extensively review lensless in-line holographic microscopy and show that the twin image is of no consequence in the reconstructions. They comment that this is because of the diverging reference beam. While the reconstruction of the object image converges upon reconstruction, the out of focus twin image continues to diverge and effectively forms the Fraunhofer case where it is a constant DC term in the 'far-field.'

V. Twin Reduction By Single Sideband Elimination

In 1968 Bryngdahl and Lohmann developed[23] a method to suppress the twin image. The method consists of filtering out half of the spatial frequency spectrum from the transmitted signal during the recording of the hologram and then filtering out half of the spatial frequency spectrum from the signal during the reconstruction process. The authors suggest that the result of this process will be that "each point scatterer in the object will cause only one half of a zone-plate pattern in the hologram plane." The reconstructed signal will have the twin images on separate sides of its Fourier spectrum and they can be easily isolated by spatial filtering.

VI. Twin Removal By Phase Retrieval

The 1970s and 1980s saw the development of a new field of research for recovering the phase of a wave field. These methods do not require interference and are collectively known under the name of "phase retrieval algorithms." We can divide these phase retrieval schemes into two subsets; (i) deterministic[24] and (ii) iterative[25-27]. Deterministic phase retrieval algorithms are based on analysing the propagation of an intensity diffraction pattern. Iterative methods on the other hand rely on recursive 'ping pong' algorithms that converge over time based on some constraints that are imposed in every iteration of the algorithm. They are often highly reliant on some initial condition set at the outset of the iteration process. These ping pong algorithms often require two recorded diffraction patterns but some have been developed that can work with only a single recorded intensity and a suitable constraint. While both deterministic and iterative phase retrieval algorithms have both been shown to work with some success, the iterative class has received by far the greatest attention in the literature. In [28] Gerchberg demonstrated how phase retrieval could be used with electron microscopy to recover the phase of the wave field. Despite the initial promise of phase retrieval algorithms, they have never managed to achieve results on a par with holographic methods. However there has been considerable interest in their usefulness in removing the twin image for in-line holography[29-41].

Twin removal has been successfully accomplished with both deterministic phase retrieval[29] and iterative phase retrieval[30-41]. In [29] deterministic phase retrieval is combined with numerical simulations of light propagation to solve the twin image problem. In [30] and [31] Liu and Scott performed the first investigation of using iterative phase retrieval for removing the twin image. The authors note that "retrieval of phase permits separation of real-object distributions from the twin-image interference that accompanies conventional optical reconstruction." However, this algorithm is limited to purely absorbing objects and cannot recover phase shifts caused by transmissive objects. Unfortunately the same can be said for many similar algorithms that followed. Liu continued to improve upon these algorithms by incorporating into them a noise constraint based on a model of additive noise[32]. Koren et. al. developed[33-34] a new constraint for these iterative twin removal algorithms. The noticed that the out of focus image was considerably larger in area than it is in focus counterpart and they unitized this fact to form their constraint. They showed their algorithm to work for complex objects as well as absorbing objects. These phase retrieval twin removal algorithms were soon successfully applied to in-line x-ray holography[35-36]. In [37] another constraint is developed for these ping-pong algorithms, this time to remove the twin image from electron holographic images. In the object plane the phase is replaced with a parabolic phase (similar to the expected shape of the object surface) and in the image plane the intensity is replaced with the measured intensity. The method only works well with pure amplitude objects.

Advances were made in understanding the sampling requirements of these phase retrieval algorithms in [38]. For real absorbing objects another iterative algorithm has been developed[39] to remove the twin image, this time utilizing both the Gerchberg-Saxton algorithm and the Fraunhofer technique. The iterative phase retrieval algorithm was extended for the case of multiple recordings of different in-line holograms in [40]. Very recently[41] improvements have been made on the iterative technique by using a better model of the object. This improved method works well for phase objects as bell as for pure absorbing objects.

VII. Twin Reduction By Linear Filtering/Digital Decoding

The first digital signal processing technique for the removal of the twin image[42] appeared in 1979 but provided poor results and received little interest. Improved DSP based algorithms were developed some years later by Onural and Scott[43-45]. They described linear filtering operations to decode the information contained in the holograms. The filter is a series expansion of the inverse of that operator that maps object opacity function to hologram intensity. However their work did not allow for phase objects. Further advances in linear filtering for twin reduction that did allow in some cases for phase objects.[46] Maleki and Devaney [47] have proposed a deconvolution algorithm to remove the twin but the method is plagued with the singularity problem, and the calculation is complex. Spence et. al. described another non iterative method[48] but this too is limited to non phase objects. Yang et. al. have developed an algorithm[49] that seems quite similar to previous work on subtraction holography discussed earlier. They devise a DSP method that relies on multiple reconstructions and subtractions. A similar method is developed in [50], seemingly unaware of work in [49], however their algorithm requires two in-line holograms to be captured.

VIII. Twin Removal By Phase Shifting Holography Or Some Form Of Phase Modulation

In 1997 Yamaguchi and Zhang developed a new method[51] for recording digital holograms free from the twin image, known as 'phase shifting digital holography. The method allowed for the use of the in-line architecture but required a number of separate interferograms to be captured in which a phase shift is introduced to one of the interfering wavefields between capture. These phase shifts are usually effected by rotation of a quarter or half wave plate or through the minute vibration of a mirror. A similar method is presented in [52]. Chen et. al. have presented a method[53] that allows for the phase-shifting technique to be applied with an arbitrary phase shift and just two captures. Kim et. al. have proposed a method[54] for removing the twin image from a white light real time holographic system by utilizing polarization optics and the addition of images. However their method is based on the triangular interferometer that has numerous disadvantages. For complex gamma ray holography a phase shifting technique[55] has also been applied based on changing the phase of the nuclear scattering amplitude by detuning from the resonance. Gabor and Goss also implemented an early technique[56] based on phase shifting in which two holograms were captured with a quarter wave phase shift was used between captures. Reconstruction was optical and required the use of a "quadrature prism" to combine the previous captures and remove the virtual image. In [57] a number of these phase modulation twin removal methods are reviewed. In the case of optical scanning holography, techniques have been proposed[58-60] to remove the twin was proposed involving simultaneous acquisition of sine and cosine Fresnel zone-lens plate coded imagesand adding the two holograms.

IX. Twin Reduction By Adding Images At Different Focus

A number of related techniques have appeared in the literature relating to twin removal in inline electron holography[9,10, 62,63]. It appears that one of the most successful methods for twin reduction in electron holography is by recording multiple holograms of the same objects with different wavelengths and then superimposing the intensities of the reconstruction. The out of focus twin image will change for each wavelength and average out. A similar technique has also been developed based on distance instead of wavelength[62,63]. By recording a series of holograms of the same objects but at different distances implies that the out of focus images will be different in each reconstruction and will integrate to approximate a constant value if a sufficient number of holograms are recorded and reconstructed.

X. Twin Removal By Spatial Filtering Of Reconstruction Planes

Pedrini et. al. propose the first instance[64] of the spatial filtering of reconstruction planes of digital holograms. This involves cutting out the wanted digitally reconstructed image from its surrounding pixels. However this area still contained considerable noise from the unwanted twin image. In [16] traditional spatial filtering in the Fourier domain was applied to an off axis digital hologram. Denis et. al. have proposed a novel method[65] of spatially filtering the reconstruction domain. It was shown that by cutting out the reconstructed focused unwanted twin and returning to the plane of the virtual wanted image by numerical propagation one could free oneself of the unwanted noise. The method was proposed only in the area particle holography and the removal of the twin images was a manual operation. In this paper we propose the use of a similar technique for macroscopic objects. We discuss for the first time the relative spreading of the unwanted twin image and the wanted image and how one might manage this spreading in the numerical reconstruction techniques.

XI. DC Removal

Throughout this discussion we have paid little attention to the zero order term – i.e. the intensity terms that appear as a by product of the holographic process. In some cases this artifact is far noisier than the unwanted twin Many of the methods discussed above will remove this term in addition to removing the unwanted twin. A number of methods have been

developed in the literature to remove this term alone to augment those metthods that do not. These methods are based on spatial filtering of the hologram[66], subtracting stochastically different holograms[67], phase-shifting[68] and by subtracting the numerical generated intensity of the object and reference waves from the digital hologram[69].

XII. Conclusion

In this paper we have categorically reviewed the subject of twin reduction and twin elimination in holography. This subject is of paramount importance in interference imaging due to the presence of the twin as a source of noise in the reconstructed image. We have reviewed over sixty years of research on this area. This paper will serve as a valuable reference to those interested in this subject.

References

[1] D. Gabor, "A new microscopic principle," Nature (London) **161**, 777 (1948).

[2] D. Gabor, "Microscopy by reconstructed wavefronts," Proc. R. Soc. A **197**, 454 (1949).

[3] M. Tegze and J. Faigel, "X-ray holography with atomic resolution," Nature (London) **380**, 49 (1996).

[4] P. Korecki and J. Korecki, "γ-Ray Holography – Three-Dimensional Imaging of a Local Atomic Structure" Hyperfine Interact. **144**, 85 (2002).

[5] J. F. Arocena, T. A. Rotwell, and M. R. A. Shegelski, "Iterative reconstruction of in-line electron holograms," Micron **36**, 23 (2005)

[6] J.C.H. Spence, "STEM and Shadow-imaging of Biomolecules at 6eVBeam Energy," Micron 28, 116, 1997

[7] H. -W. Fink, H. Schmid, E. Ermantraut, and T. Schulz, "Electron holography of individual DNA molecules," J. Opt. Soc. Am. A **14**, 2168-2172 (1997)

[8] T. Matsumoto, T. Tanji and A. Tonomura: "Visualization of DNA in Solution by Fraunhofer In-Line Electron Holography: II. Experiments." Optik 100 (No.2) (1995) 71-74

[9] S.Y. Tong, H. Hua Li, and H. Huang, "Energy extension in three-dimensional atomic imaging by electron emission holography," Phys. Rev. Lett. **67**, 3102 (1991).

[10] J. J. Barton, "Removing multiple scattering and twin images from holographic images" Phys. Rev. Lett. **67**, 3106 (1991).

[11] W. L. Bragg and G. L. Roger, Elimination of the Unwanted Image in Diffraction Microscopy Nature (London) **167**, 190 (1951).

[12] G. L. Rogers, "In-line soft-x-ray holography: the unwanted image," Opt. Lett. **19**, 67- (1994)

[13] P. Kirkpatrick and H. M. A. El-Sum, "Image formation by reconstructed wave fronts. I. Physical principles and methods of refinement," J. Opt. Soc. Am. **46**, 825- (1956)

[14] T. Xiao; H. Xu; Y. Zhang; J. Chen; Z. Xu, "Digital image decoding for in-line X-ray holography using two holograms," Journal of Modern Optics, 45:2, 343 – 353

[15] E. Leith and J. Upatnieks, J. Opt. Soc. Am. **53**, 1377 (1963).

[16] E. Cuche, P. Marquet and C. Depeursinge, "Spatial filtering for zero-order and twin-image elimination in digital off-axis holography," Appl. Opt. **39**, 4070 (2000).

[17] G. W. Stroke, D. Brumm, A. Funkhouser, A. Labeyrie and R. C. Restrick, "on the absence of phase-recording or 'twin-image' separation problems in 'Gabor' (in-line) holograms" BRIT, J. APPL. PHYS., 1966, VOL. 17, 497

[18] J. B. DeVelis, G. B. Parrent Jr., and B. J. Thompson, "Image Reconstruction with Fraunhofer Holograms," J. Opt. Soc. Am. **56**, 423-(1966)

[19] B. J. Thompson, J. H. Ward, and W. R. Zinky, "Application of hologram techniques for particle size analysis," Appl. Opt. **6**, 519- (1967)

[20] G. A. Tyler and B. T. Thompson, "Fraunhofer holography applied to particle size analysis: a reassessment," Opt. Acta 23, 685-700 (1976).

[21] T. Matsumoto, T. Tanji, A. Tonomura, "Phase-contrast visualization of an undecagold cluster by in-line electron holography" Ultramicroscopy 54 317 (1994)

[22] J. Garcia-Sucerquia, W. Xu, S. K. Jericho, P. Klages, M. H. Jericho, and H. J. Kreuzer, "Digital in-line holographic microscopy," Appl. Opt. **45**, 836-850 (2006)

[23] O. Bryngdahl and A. Lohmann, "Single-Sideband Holography," J. Opt. Soc. Am. **58**, 620- (1968)

[24] M. R. Teague, "Deterministic phase retrieval: a Green's function solution," J. Opt. Soc. Am. **73**, 1434- (1983)

[25] R. W. Gerchberg and W. O. Saxton, "A practical algorithm for the determination of phase from image anddiffraction plane pictures," Optik 35, 227–246 (1972).

[26] J. R. Fienup, "Reconstruction of an object from the modulus of its Fourier transform," Opt. Lett. **3**, 27- (1978)

[27] J. R. Fienup, "Phase retrieval algorithms: a comparison," Appl. Opt. **21**, 2758- (1982)

[28] R.W. Gerchberg. "Holography without fringes in the electron microscope" Nature **240** (1972), p. 404.

[29] J.B. Tiller, A. Barty, D. Paganin, K.A. Nugent, "The holographic twin image problem: a deterministic phase solution," Optics Communications 183 2000.7–14

[30] G. Liu and P. D. Scott, "Phase retrieval for in line holograms," in *Proceedings of the Nineteenth Annual Conference on Information Sciences and Systems* (Johns Hopkins U. Press, Baltimore, Md., 1985), pp. 237-241.

[31] G. Liu and P. D. Scott, "Phase retrieval and twin-image elimination for in-line Fresnel holograms," J. Opt. Soc. Am. A **4**, 159- (1987)

[32] G. Liu, "Object reconstruction from noisy holograms," Optical Engineering 29(01), pp.19-24 (1990)

[33] G. Koren, D. Joyeux, and F. Polack, "Twin-image elimination in in-line holography of finite-support complex objects," Opt. Lett. **16**, 1979-(1991)

[34] G. Koren, F. Polack, and D. Joyeux, "Iterative algorithms for twin-image elimination in in-line holography using finite-support constraints," J. Opt. Soc. Am. A **10**, 423- (1993)

[35] S. Lindaas, M. Howells, C. Jacobsen, and A. Kalinovsky, "X-ray holographic microscopy by means of photoresist recording and atomic-force microscope readout," J. Opt. Soc. Am. A **13**, 1788-1800 (1996)

[36] Kodama, M. Yamaguchi, N. Ohyama, T. Honda, K. Shinohara, A. Ito, T. Matsumura, K. Kinoshita, K. Yada, "Image reconstruction from an in-line X-ray hologram with intensity distribution constraint," Opt. Commun. **125**, 36-42, (1996)

[37] L. Bleloch, A. Howie, and E. M. James, "Amplitude recovery in Fresnel projection microscopy," Appl. Surf. Sci. **111**, 180 (1997).

[38] J. Miao, D. Sayre, and H. N. Chapman, "Phase retrieval from the magnitude of the Fourier transforms of nonperiodic objects," J. Opt. Soc. Am. A **15**, 1662-1669 (1998)

[39] X. M. H. Huang, J. M. Zuo, and J. C. H. Spence, "Wavefront reconstruction for in-line holograms formed by pure amplitude objects"Appl. Surf. Sci. **148**, 229 (1999).

[40] Y. Zhang, G. Pedrini, W. Osten, and H. Tiziani, "Whole optical wave field reconstruction from double or multi in-line holograms by phase retrieval algorithm," Opt. Express **11**, 3234-3241 (2003)

[41] T. Latychevskaia and H.-W. Fink, "Solution to the Twin Image Problem in Holography," Phys. Rev. Lett. **98**, 233901 (2007).

[42] Marie**,** K.H.S., Bennett, J.C., Anderson, A.P. Digital processing technique for suppressing the interfering outputs in the image from an inline hologram, *Electron Lett, 15 (1979) 241-243*

[43] L. Onural and P. D. Scott, "A digital filtering system for decoding in-line holograms," in *Proceedings of the 1985 IEEE Conference on Acoustics, Speech, and Signal Processing* (Institute of Electrical and Electronics Engineers, New York, 1985), pp. 708-711.

[44] L. Onural, "Digital decoding of in-line holograms," Ph.D. dissertation (State University of New York at Buffalo, Amherst, New York, 1985).

[45] L. Onural and P.D. Scott, Digital decoding of in-line holograms. Opt Eng **26**, pp. 1124–1132. (1987)

[46] K. A. Nugent, "Twin-image elimination in Gabor holography," Opt. Commun. **78**, 293 (1990).

[47] M. H. Maleki and A. J. Devaney, "Noniterative reconstruction of complex-valued objects from two intensity measurements," *Optical Engineering* **33**(10), pp. 3243–3253, 1994.

[48] J.C.H. Spence, X. Zhang and W. Qian, in: Electron Holography, eds. A. Tonamura, L.F. Allard, G. Pozzi, D.C. Joy and Y.A. Ono (Elsevier Science, 1995) pp. 267-276.
[49] S. Yang, X. Xie, Y. Zhao, C. Jia, "Reconstruction of near-field in-line hologram," Optics Communications **159** 1999.29–31
[50] A. Zhang and X. Zhang, "Reconstruction of a complex object from two in-line holograms," Opt. Express **11**, 572-578 (2003)
[51] Yamaguchi and T. Zhang, "Phase-shifting digital holography," Opt. Lett. **22**, 1268-1270 (1997)
[52] S. Lai, B. King and M. A. Neifeld**, "**Wave front reconstruction by means of phase-shifting digital in-line holography," Opt. Commun. **173**, 155-160 (2000)
[53] G. L. Chen, C. Y. Lin, H. F. Yau, M. K. Kuo, and C. C. Chang, "Wave-front reconstruction without twin-image blurring by two arbitrary step digital holograms," Opt. Express **15**, 11601-11607 (2007)
[54] S.-G. Kim, B. Lee, and E.-S. Kim, "Removal of bias and the conjugate image in incoherent on-axis triangular holography and real-time reconstruction of the complex hologram," Appl. Opt. **36,** 4784–4791 (1997).
[55] P. Korecki, G. Materlik, and J. Korecki, "Complex gamma-ray hologram: solution to twin images problem in atomic resolution imaging," Phys. Rev. Lett. **86,** 1534–1537 (2001).
[56] D. Gabor and W. P. Goss, "Interference Microscope with Total Wavefront Reconstruction," J. Opt. Soc. Am. **56**, 849- (1966)
[57] Y. Takaki, H. Kawai, and H. Ohzu, "Hybrid Holographic Microscopy Free of Conjugate and Zero-Order Images," Appl. Opt. **38**, 4990-4996 (1999)
[58] K. Doh, T. -C. Poon, M. H. Wu, K. Shinoda and Y. Suzuki, "Twin-image elimination in optical scanning holography," Optics & Laser Technology**, 28**, 135-141 (1996)
[59] P. Sun and J.-H. Xie, "Method for reduction of background artifacts of images in scanning holography with a Fresnelzone-plate coded aperture," Appl. Opt. **43,** 4214–4218 (2004).
[60] T. -C. Poon, T. Kim, G. Indebetouw, B. W. Schilling, M. H. Wu, K. Shinoda, and Y. Suzuki, "Twin-image elimination experiments for three-dimensional images in optical scanning holography," Opt. Lett. **25**, 215-217 (2000)
[61] K. Doh, T.-C. Poon, and G. Indebetouw, "Twin-image noise in optical scanning holography," Opt. Eng. **35,** 1550–1555 (1996).
[62] Weierstall, U., Huang, X. and Spence, J., Twin image suppression and forward focussing in low voltage in-line electron holography. *Proc. MSA,* ed. G. Bailey. Jones & Begell, New York. 1997
[63] Lin, J. A. and Cowley. J. M., Reconstruction from in-line electron holograms by digital processing. *UltramieroAcopy***.** 19, 179 189, 1986
[64] Pedrini, P. Fröning, H. Fessler, and H. J. Tiziani, "In-Line Digital Holographic Interferometry," Appl. Opt. **37**, 6262-6269 (1998).
[65] Loıc Denis, Corinne Fournier, Thierry Fournel, Christophe Ducottet, "Twin-image noise reduction by phase retrieval in in-line digital holography," Proceedings of SPIE Vol. **5914**, 59140J-1 (2005)
[66] T. Kreis and W. P. O. Juptner, "Suppression of the dc term in digital holography," Opt. Eng. 36, 2357 (1997).
[67] N. Demoli, J. Mestrovic, and I. Sovic, "Subtraction Digital Holography," Appl. Opt. **42**, 798-804 (2003)
[68] Y. Zhang, Q. Lü and B. Ge, "Elimination of zero-order diffraction in digital off-axis holography," Opt. Commun. **240**, 261-267, (2004).
[69] G. -L. Chen, C. -Y. Lin, M. -K. Kuo, and C. -C. Chang, "Numerical suppression of zero-order image in digital holography," Opt. Express **15**, 8851-8856 (2007)

Section 6B

INTELLIGENT SYSTEMS

Generating Initial Codebook of Vector Quantization Based on the Maximum Repulsion Distance

Chen Gang, Zhong Sheng
The International School of Software, Wuhan University, Wuhan, China
aeassist@yahoo.com.cn

Abstract

A definition of repulsion distance is given in this paper. After an investigation on some experiments to compare the performance of two important existing algorithms that generate initial codebook of vector quantization, a new algorithm is proposed on the concept of repulsion distance. Some further experiments with the new algorithm are performed to verify the feasibility of it and to show its performance advantages. Finally, some atypical cases when using these algorithms are discussed.

Keywords: vector quantization, initial codebook, repulsion distance

1. Introduction

Vector quantization is a widely used technique that compresses signals. In vector quantization, every *K* contiguous signal values are combined into a group, forming a *K*-dimensional signal vector. And then, all these vectors which form a training set, are employed to perform vector quantization. Given a training set of vectors in the *K*-dimensional space, the codebook generation algorithm can find out an appropriate division of all these vectors. Every area in the division is named a cell. The aim of vector quantization is to represent every vector in the training set with the codevector of its corresponding cell. During this process, the deviation between the codevector and the original vector is referred to as distortion. The codebook achieves its excellent performance when its distortion is minimal. Generally speaking, it is very difficult to generate a global optimal codebook. Thus, common algorithms usually generate a local optimal solution.

Generating codebook is the most important step in vector quantization. The LBG algorithm[1], proposed by Linde, Buzo and Gray in 1980, is the most frequently used algorithm of generating codebook. It begins from an existing initial codebook, and iterates to generate the final codebook, according to the necessary conditions of optimal vector quantizers, that is, the Nearest Neighbor Condition, the Centroid Condition, and the Zero Boundary Probability Condition. For the performance of the codebook is always getting better after any iteration, the LBG algorithm is convergent. However, a large quantity of experiment data shows that the rate of convergence and the performance of the final codebook with LBG algorithm are directly influenced by the initial codebook. So, it is a problem deserving of study in vector quantization how to generate a better initial codebook.

To select randomly an enough number of vectors from the training set as the initial codebook is one of the usual ways to generate an initial codebook. In this way, an initial codebook can be generated in a very short time, for it needs only a small amount of calculation. However, in many cases, the initial codebooks generated in this way are not satisfying enough. Besides, there are many other feasible algorithms that generate initial codebook, such as the deleting algorithm[3], the pairwise nearest neighbor algorithm, the product algorithm[1,4,5], the splitting algorithm[2], the variance classifying algorithm, and so on.

2. Common Algorithms

The deleting (DEL) algorithm is widely used to generate initial codebook in literatures on statistical clustering. This algorithm begins from the entire training set of vectors, and then selectively deletes vectors until the number of the vectors remain comes up to the requirement. Thus,

the vectors remain just form the initial codebook. Suppose $d(\boldsymbol{x}, \boldsymbol{y})$ measures the distortion between vectors $\mathbf{x}$ and $\mathbf{y}$, the DEL algorithm can be described as follows.

(1) Initial state: given a threshold ε which is a proper constant, given the training set of vectors $X = \{\boldsymbol{x}_i, i = 0,1,2,\cdots,N-1\}$ whose size is N, given the codebook $C = \{\boldsymbol{y}_i\}$ whose size is m (at the very beginning, $m = 0$), and given that the size of the final codebook should be M ($M > 1$);

(2) Set $i = 0$, $C = C \bigcup \{\boldsymbol{x}_i\}$, $m = m + 1$;

(3) Set $i = i + 1$, if $i == N$, go to (4); otherwise, go to (5);

(4) Set $\varepsilon = \varepsilon \times \theta$, $i = 1$, here θ is a positive decimal which is less than 1;

(5) If $\boldsymbol{x}_i \in C$, go to (3);

(6) Find $\boldsymbol{y}_j \in C$, so as to make sure $d = d\left(\boldsymbol{x}_i, \boldsymbol{y}_j\right) = \min\limits_{0 \le k \le M} d\left(\boldsymbol{x}_i, \boldsymbol{y}_k\right)$;

(7) If $d < \varepsilon$, go to (3);

(8) Set $C = C \bigcup \{\boldsymbol{x}_i\}$, $m = m + 1$;

(9) If $m < M$, go to (3); otherwise, stop.

In addition to the basic deleting algorithm, the pairwise nearest neighbor (PNN) algorithm proposed by Equitz, et cetera is also a kind of deleting algorithm. This algorithm firstly considers each vector in the training set as the codevector, that is to say, each vector occupies its own cell. And then, the pairwise nearest two cells are merged into a new cell continually, until the number of the cells achieves requirement. Likewise, suppose $d(\boldsymbol{x}, \boldsymbol{y})$ measures the distortion between vectors $\mathbf{x}$ and $\mathbf{y}$, the PNN algorithm can be described as follows.

(1) Set the number of codevectors $n = N$, all the cells are $R_i, i = 0,1,2,\cdots,N-1$, and the corresponding centroids are $\boldsymbol{y}_i = \boldsymbol{x}_i, i = 0,1,2,\cdots,N-1$;

(2) Calculate the distortion of each pairwise vectors $\boldsymbol{y}_l$ and $\boldsymbol{y}_m$, i.e. $d\left(\boldsymbol{y}_l, \boldsymbol{y}_m\right)$, $0 \le l < m \le n-1$;

(3) If $d\left(\boldsymbol{y}_i, \boldsymbol{y}_j\right) = \min\limits_{0 \le l < m \le n-1} d\left(\boldsymbol{y}_l, \boldsymbol{y}_m\right)$, $0 \le l < m \le n-1$, merge cells R_i and R_j, meanwhile, update codevector $\boldsymbol{y}_i$ to $\boldsymbol{y}_i = \dfrac{\left\|R_i\right\| \cdot \boldsymbol{y}_i + \left\|R_j\right\| \cdot \boldsymbol{y}_j}{\left\|R_i\right\| + \left\|R_j\right\|}$, here, $\left\|R_i\right\|$ is the number of vectors R_i contains. And then, if $j = n-1$, remove the codevector $\boldsymbol{y}_j$; otherwise, set $\boldsymbol{y}_j = \boldsymbol{y}_{n-1}$, $R_j = R_{n-1}$, and remove the codevector $\boldsymbol{y}_{n-1}$, set $n = n-1$;

(4) If $n == M$, stop; otherwise, go to (2).

To compare the performance of the final codebooks generated by the two algorithms (DEL and PNN), we carried out an experiment on the two-dimensional surface. First of all, we generated several points on the two-dimensional surface to constitute the training set of vectors. And then, we use these algorithms respectively to generate two initial codebooks, which will then be passed to the LBG iterations. At last, we can judge which algorithm generates a better initial codebook from the final distortion of them after the LBG iterations.

We did two groups of experiments. In each group, we generated randomly 100 two-dimensional vectors (points) to constitute the training set. The difference is that in the first group, all the points in the training set were distributed within a circular region with center at the point $(0, 0)$ and radius equal to 0.5. While in the second group, all the points in the training set were distributed within a rectangular region enclosed by four lines: $x = -0.5$, $x = 0.5$, $y = -0.5$, $y = 0.5$. In each group, the final codebook contained only 5 codevectors, and, the experiment was repeated 10,000 times. We recorded how many times one of the two algorithms respectively generated a better initial codebook during the process.

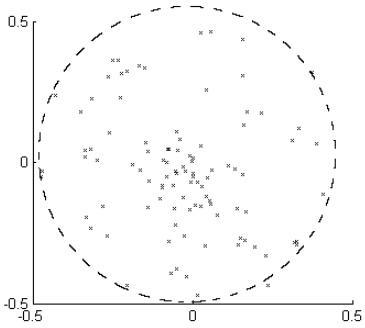

Figure 1. Training points within a circular region

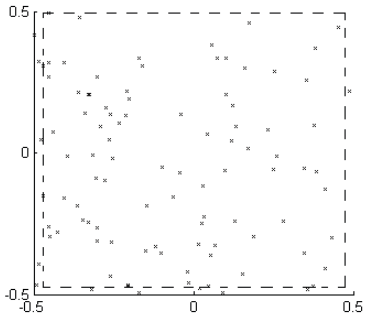

Figure 2. Training points within a rectangular region

The distribution of the training set of points in the two groups of experiments, drawn with Matlab, are shown in Figure 1 and Figure 2.

The results of the experiments are shown in Table 1 and Table 2. Note that, since sometimes codebooks generated by the two algorithms may result in the same performance, they two may be considered as "better" in one experiment. So, the sum of the number of their times better is greater than 10,000.

Table 1. Results of the 1st group

Algorithm	Times better	Conclusion
DEL	5853	DEL is better.
PNN	4994	

Table 2. Results of the 2nd group

Algorithm	Times better	Conclusion
DEL	5215	PNN is better.
PNN	6531	

We can draw a conclusion from the results above that the DEL algorithm and the PNN algorithm perform differently in different circumstances. When the training points are in a circular region, the DEL algorithm performs better; but when the training points are in a rectangular region, the PNN algorithm performs better.

3. The Algorithm Based on the Maximum Repulsion Distance

From the experiments, we know that the performance of the final codebooks developed from the initial ones which are respectively generated by the DEL algorithm and the PNN algorithm are similar to each other. To try to get an even better performance, we proposed a new algorithm of generating initial codebook, which is based on the maximum repulsion distance, the MRD algorithm. This algorithm is on the basis that the initial codevectors should be as dispersive as possible. That is to say, the initial codebook must be good enough only if all the codevectors are selected from different cells of a good division of the training set of vectors. Thus, to ensure that the codevectors are as dispersive in the training set as possible, and that they are selected from different cells, the MRD algorithm will always select the farthest vector from the selected codevectors as the next one added into the initial codebook in every iteration.

We introduced the concept of the repulsion distance to measure how far a vector is from all the vectors in a vector set. Suppose there is a vector $\boldsymbol{v}$ and a vector set $X = \{\boldsymbol{x}_i, i = 1, 2, \cdots, N\}$, the repulsion distance between $\boldsymbol{v}$ and X is defined as: $rd(\boldsymbol{v}, X) = \min_{1 \le i \le N} d(\boldsymbol{v}, \boldsymbol{x}_i)$, here, $d(\boldsymbol{x}, \boldsymbol{y})$ is the distortion of two vectors. Thus, the algorithm of generating initial codebooks based on the maximum repulsion distance can be described as follows.

(1) Initial state: given the training set of vectors $X = \{\boldsymbol{x}_i, i = 0, 1, 2, \cdots, N-1\}$ whose size is N, given the codebook $C = \{\boldsymbol{y}_i\}$ whose size is m (at the very beginning, $m = 0$), and given that the size of the final codebook should be M ($M > 1$);

(2) Calculate the centroid $\boldsymbol{c}$ of X;

(3) Find $\boldsymbol{v} \in X$, so as to make sure $d(\boldsymbol{v}, \boldsymbol{c}) = \max_{0 \le i \le N} d(\boldsymbol{x}_i, \boldsymbol{c})$. Set $C = C \cup \{\boldsymbol{v}\}$, $m = m + 1$;

(4) Find $\boldsymbol{v} \in X$, so as to make sure $rd = rd(\boldsymbol{v}, C) = \max_{0 \le i \le N} rd(\boldsymbol{x}_i, C)$. Set $C = C \cup \{\boldsymbol{v}\}$, $m = m + 1$;

(5) If $m < M$, go to (4); otherwise, stop.

As other algorithms of generating initial codebooks, the MRD algorithm can't get a global optimal solution either, but a local optimal solution. The feasibility of this algorithm can be explained as follows.

Before step (3) is executed, there is only one vector in the codebook. This vector must belong to a certain cell from a division of the training set of vectors. In each iteration, every vector that is selected as the next codevector is the farthest one from the codevectors which have already been selected. Suppose the candidate vector is $\boldsymbol{x}$, and the nearest codevector in current small-size codebook is $\boldsymbol{y}$, then the repulsion distance

$rd = d(\boldsymbol{x}, \boldsymbol{y})$. If $\boldsymbol{x}$ and $\boldsymbol{y}$ don't belong to a same cell, the algorithm gains its end. Otherwise, suppose $\boldsymbol{x}$ and $\boldsymbol{y}$ do belong to a same cell, then the diameter of the cell should be $rd = d(\boldsymbol{x}, \boldsymbol{y})$ at least. Because rd is the maximal repulsion distance, the distance from any other vectors in the training set to the existing codebook should be less than rd. Then, the "largest" cell is the one containing $\boldsymbol{x}$ and $\boldsymbol{y}$, and it should be split to create more codevectors in initial codebook. Thus, $\boldsymbol{x}$ is also a best one to be selected in this iteration.

To test the performance of the algorithm, we repeated the two groups of experiments above, with the new algorithm joined in. The initial states, conditions and requirements remained the same. The results are shown in Table 3 and Table 4.

Table 3. Results of the 1st group

Algorithm	Times best	Conclusion
MRD	4764	MRD is the best.
DEL	4116	
PNN	3430	

Table 4. Results of the 2nd group

Algorithm	Times best	Conclusion
MRD	4674	MRD is the better than DEL.
DEL	3907	
PNN	5011	

Note that, since sometimes two/three algorithms may perform just the same, they two/three can be best in one experiment.

We can see from the results above, that under different circumstances, the MRD algorithm is better than the DEL algorithm, and sometimes, better than the PNN algorithm. Even in the cases that PNN performs best, the gap between MRD and PNN is still small.

4. Discussion

The basic idea of the MRD algorithm is, when selecting initial codevectors, selecting the farthest vector from the existing codevectors so that all the initial codevectors are in different cells according to the final division. That decreases both the total iterations needed by LBG and the distortion of the final codebook. Thus a good codebook is generated.

In the experiments above, the MRD algorithm performs satisfyingly. In many cases, the performance of the codebook generated by the MRD algorithm is pretty good.

However, the MRD algorithm is not able to recognize the noise in the training set of vectors. So, in some untypical cases, when the training vectors are distributed in a special way, the MRD algorithm will tend to select the vectors which are farthest without considering any other conditions. This may lead to a bad initial codebook.

For instance, in a untypical case, the training set of vectors consists of 112 randomly generated points on a two-dimensional surface. Among them, 100 points are distributed in a circular region with center at the point $(0,0)$ and radius equal to 0.5. However, around this region, 4 groups of noise points are located in small circular regions at $(1,0)$, $(0,1)$, $(-1,0)$ and $(0,-1)$. Every group has 3 points.

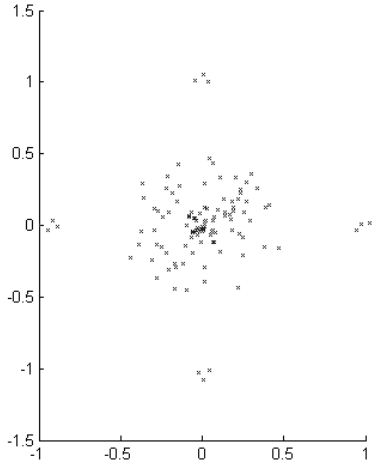

Figure 3. Training set with noise

Like the experiments above, we repeated 10,000 times.

The distribution situation of the training set of points as well as the noise points in this experiment, drawn with Matlab, is shown in Figure 3. And the result is shown in Table 5.

Table 5. Results of the special case

Algorithm	Times best	Conclusion
MRD	3231	DEL is the best.
DEL	9278	
PNN	3214	

In such a case, because of the existing of the 12 noise points, the performance of the MRD algorithm suddenly drops, worse than the DEL algorithm.

However, in the real world, the probability of

this case is quite small. So, from a statistical point of view, the MRD algorithm achieves averagely high performance. Finally, how to filter the noise and how to improve the performance of the MRD algorithm under a variety of circumstances, are problems that deserve further study.

5. References

[1] LINDE Y, BUZO A, GRAY R M. An algorithm for vector quantizer design. IEEE Transactions on communications, 1980, 28(1): 84-95.

[2] Sheng Yuanjun, Liu Kejun. An Algorithm of Setting VQ Initial Codebook Based on the Principle of Cell Distortion Balance. Journal of Harbin Engineering University, Vol. 21, No. 5, Oct. 2000.

[3] Sun Shenhe, Lu Zheming. Technique and Application of Vector Quantization. Beijing: Science Press, 2002.

[4] MAKHOUL J, ROUCOS S. Vector quantization in speech coding. Proceedings of the IEEE, 1985, 73(11): 1551-1585.

[5] GRAY R M. Vector quantization. IEEE ASSP Magazine, April 1984: 4-27.

[6] Lee K F. Automatic speech recognition - the development of the SPHINX system. Boston: Kluwer Academic Publishers, 1989.

[7] Abut H, et al. Vector Quantizer of Speech and Speech-Like Waveforms, IEEE ASSP-30, 1982: 423-435.

[8] S.P.Lloyd, Least Squares Quantization in PCM, IEEE Trans on Information Theory, Vol.28, 1982, No.2: 129-137.

Investigating the Influence of Population and Generation Size on GeneRepair Templates

Amy FitzGerald
Department of Computer Science
National University of Ireland, Maynooth
Kildare, Ireland
amy.fizgerald@nuim.ie

Diarmuid P. O'Donogue
Department of Computer Science
National University of Ireland, Maynooth
Kildare, Ireland
diarmuid.odonoghue@nuim.ie

Abstract— **In 2005 Lolle *et al* published controversial findings showing that the *Arabidopsis thaliana* plant repairs invalid genetic information using the grandparent as a kind of repair template. We have previously shown how a genetic repair operator (GeneRepair) can be used to correct invalid individuals in an evolutionary strategy. It has been shown that superior results are produced when the individual's grandparent is used as the repair template in comparison to using the individual's parent. This paper investigates whether the results produced by GeneRepair templates are affected by parameters of population size and number of generations. The results indicate that the grandparent template outperforms the parent template regardless of population or generation size. These findings further supports the controversial theory of Lolle *et al*.**

Keywords-component GeneRepair; evolutionary strategy; non-mendelian inheritance;population size, generation size, Arabidopsis thaliana

I. INTRODUCTION

Evolutionary Strategies (ES) are based on the Darwinian principle of survival of the fittest. Their expected success is based on the fact that they mirror biological evolution. ES have been shown to be successful when used on problems with large search spaces, but traditional ES are ill-suited to constraint based problems [1]. Three approaches have been adopted to enforcing constraint upon an ES: penalty points [2], modified ES operators and genetic repair. In this paper we evaluate a modified ES that incorporates a genetic repair process.

In 2005 Lolle *et al* published a controversial paper showing that the *Arabidopsis thaliana* plant used a genetic repair process to correct invalid genetic information [3]. The corrected individuals appeared to be repaired using information originating in the grandparent generation – information that *apparently* by-passed the parent generation. This radical form of non-Mendelian inheritance was treated with much skepticism by some of the scientific community.

In this paper we modify a traditional ES to mirror this genetic repair technique. We compare the effect of population and generation size on the results produced, using both the parent and grandparent template to repair invalid individuals. Invalid individuals are those that do not satisfy the constraints of a given problem – the biological equivalent of producing a viable individual/phenotype. For this paper we have used the TSPLIB eil51 51 city Travelling Salesman's Problem (TSP) to evaluate our hypothesis and compare results. The results show that as the evolutionary strategy is modified to more closely mirror biology, the grandparent repair becomes a superior candidate for use as a repair template than the parent.

II. GENEREPAIR

GeneRepair [4] is an operator which repairs invalid individuals produced by crossover or mutation in an evolutionary strategy. An example of an invalid individual for the TSP would be an individual with duplicate cities. The GeneRepair operator would ensure that this individual satisfies the problem constraints by replacing the duplicate city with any missing city.

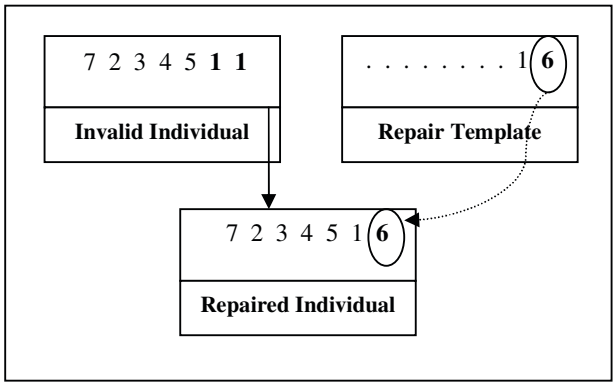

Figure 1. An Individual with an invalid duplicate gene

As we can see in Fig. 1 the individual is invalid as it has a duplicate of city 1. GeneRepair is invoked to repair this error by replacing the duplicate with a missing city. In order to decide which city to replace GeneRepair uses a template. Our research compares the use of the individual's parent and the grandparent as possible repair templates.

III. RESULTS

We ran an experiment to compare grandparent and parent GeneRepair with a population of ten for five hundred thousand generations on the eil51 TSP to investigate the consequences of change in generation and population size on

the success of the GeneRepair templates. We ran this experiment 260 times. Our results are presented in two separate subsections. In the first subsection we present the results produced by the 260 runs. We sample these results at 100,000, 250,000 and 500,000 generations and at each point we compare the use of parent and grandparent templates. In the second subsection we analyze the best result produced using the parent template and compare it to the best result produced using the grandparent template. We sample both of these files at 50, 500, 5000, 50000 and 500000 generations and compare the best parent solution and the best grandparent solution at each point.

A. Comparison of Final Results Produced by Parent and Grandparent Templates

In previous research [5] we have shown how the grandparent can be used as a template for repair in an ES to successfully find near optimal solutions to constraint based problems. In this paper we investigate whether change in population size or number of generations has an effect on those findings. We have used a population of ten for this set of experiments which is a tenth of the population used in our previous publication. The mutation rate set to two for all experiments. This mutation rate is based on the findings from the investigation carried out in mutation rates by Mitchell [6].

In this first set of results we compare the final results produced by each of the 260 experiments carried out using the parent template to repair invalid individuals to the 260 experiments carried out where the grandparent template was used. Each of the experiments was run for 500,000 generations. In Fig. 2 below you can see that each of the grandparent experiments produced a smaller tour length and so a better result that its parent counterpart.

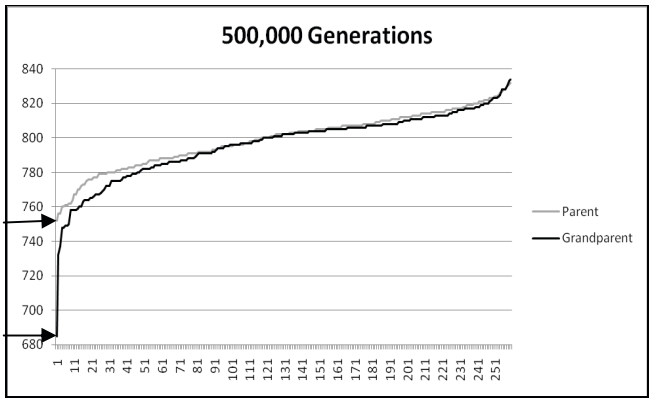

Figure 2. Results for 260 experiments after 500,000 Generations

We went on to sample each of these results at 100,000 and 250,000 generations. In Fig. 3 the result of each experiment is shown after 100,000 generations. It can be clearly seen that there is a significant gap between the tour length produced using the grandparent template and the tour length produced using the parent template for the majority of the results.

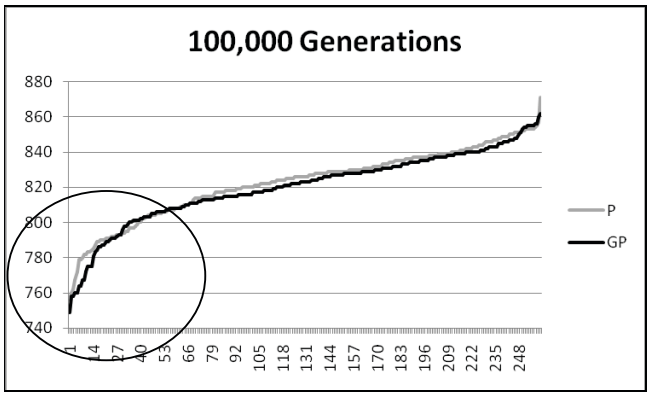

Figure 3. Results for 260 experiments after 500,000 Generations

In Fig. 4 below we can see that the gap between the results produced when using the parent and grandparent templage has grown when the results were sampled at 250,000 generations. The grandparent produces superior results to its parent template for every experiment. You can also see that the best results produced by the grandparent, as highlighted in Fig. 4 are signicantly better than those produced by the parent template.

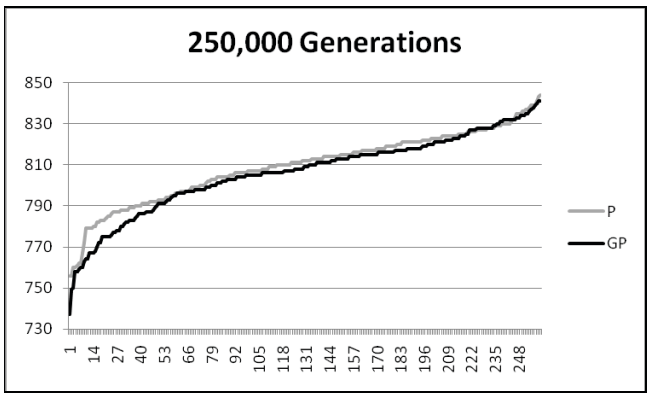

Figure 4. Results for 260 experiments after 500,000 Generations

If we analyze the results produced by the experiment as illustrated in Fig. 2, it is clear that grandparent is superior to parent as a candidate for a GeneRepair template even though the population size was one tenth of the size in previously published results. By not only looking at the final result but also sampling the experimental results at two separate points we can see that the grandparent template produces superior results to the parent template regardless of generation size. If we go on to analyze these results further we can see that while the average grandparent has a lower tour length than the average parent the standard deviation across the results produced by the grandparent template is much wider (See Table 1). Perhaps it is this diversity within the grandparent that allows us to produce better results through wider exploration of the search space.

TABLE I. EXPERIMENTAL RESULTS FOR 260 RUNS

Template	*Tour Length*	
	Average	*Standard Deviation*
Parent	799.2769	16.06984
Grandparent	796.2654	19.63673

B. Analysis of Best Parent and Best Grandparent Results

This second section of our results compares and analyzes the best result produced when using the parent template compared to the best result produced when using the grandparent template as highlighted in Fig. 2. We have sampled these results at five different points in the experiment to compare parent and grandparent GeneRepair at five different generation sizes. The results in Fig. 5 compare best results produced by both grandparent and parent GeneRepair after 50 generations. The lines in the graph below indicate the tour length (Y-axis) produced for the eil51TSP at that particular generation (X-axis). We can see that only after 50 generations a small but significant gap has formed between the use of grandparent and parent templates. We can also identify that using the parent template has caused the decrease in tour length to somewhat plateau in comparison to the steady improvement of results when using the grandparent template.

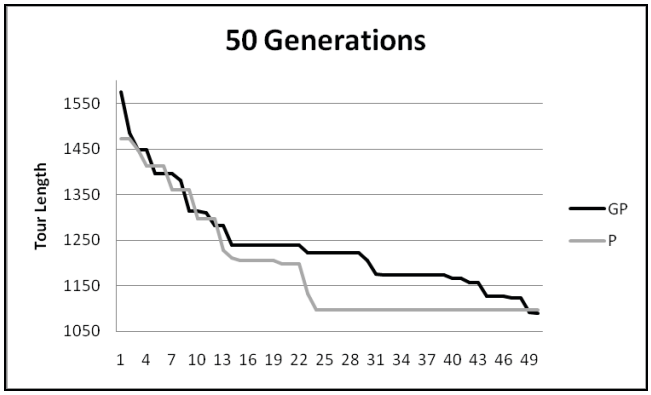

Figure 5. Results after 50 Generations

In Fig. 6 below we can see that the gap between the results produced by the grandparent and parent template has grown significantly after 500 generations. Grandparent appears to continue to evolve while once again the parent template has caused a plateau in the results.

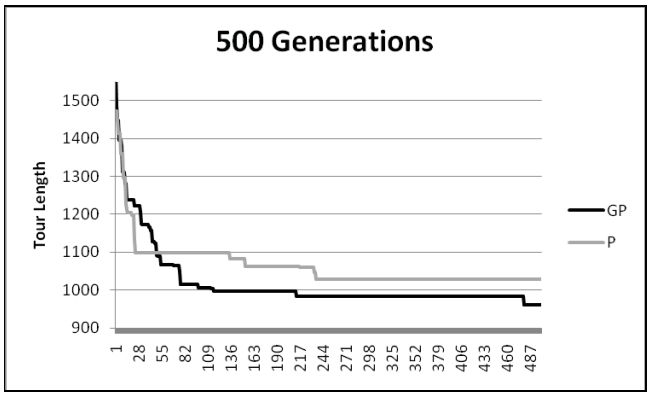

Figure 6. Results after 500 Generations

We have sampled the experiment at 5 different points; 50, 500, 5000, 50,000 and 500,000 generations. The only time that parent produces better results is at 5,000 generations but even at this point the difference between grandparent and parent is minimal in comparison to the difference between them at each of the other sampled points. (See Table 2 & Fig. 7)

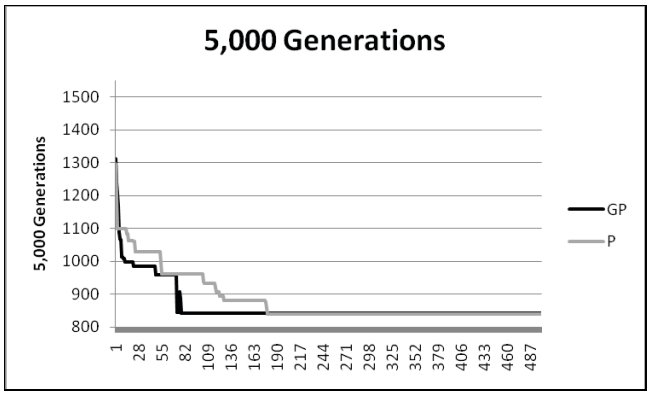

Figure 7. Results after 5,000 Generations

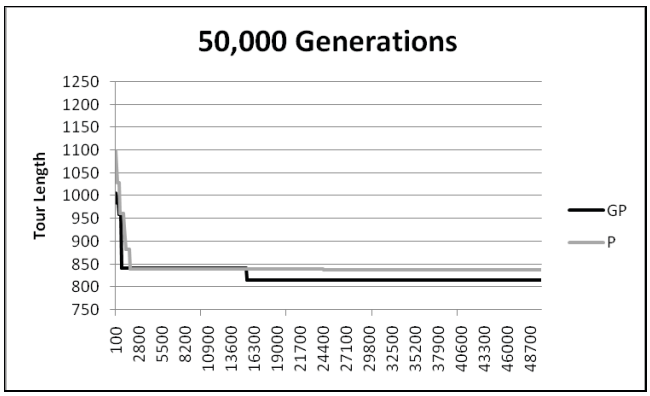

Figure 8. Results after 50,000 Generations

When the results are next sampled at 50,000 generations grandparent is significantly better than parent again which concretes the finding that the result at 5,000 generations was a definite outlier for the parent template in comparison with the constant positive results for the grandparent template (Fig. 8)

The last sample of the results was taken at 500,000 generations and the gap between the parent and grandparent template has once again grown. The final results shown in Fig. 9 illustrate that on completion of the experiment the grandparent template has produced a significantly lower tour length than the parent template.

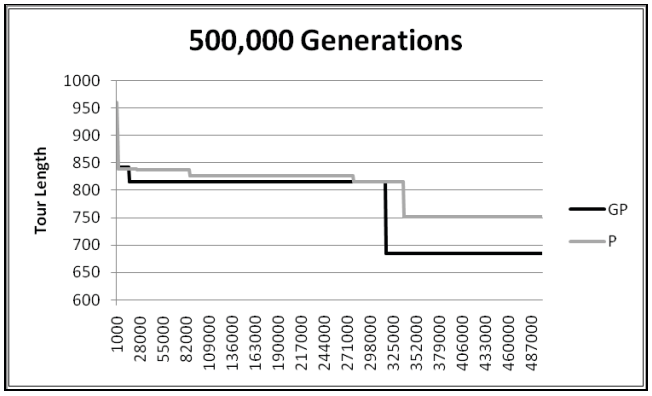

Figure 9. Results after 500,000 Generations

TABLE 2 provides a summary of the results as sampled at the five points explained above. We can see that the difference between the grandparent and parent template becomes more apparent as you increase the number of generations in the experiment. Not only is grandparent a superior repair template, it is impervious to both population size and the number of generations. We can see that it is resistant to changes in the population as this experiment gives the same conclusion as previously published results [5] even though the population used for the results shown in this paper is a tenth of what it was for previous experiments. We have also shown that it is resistant to changes in the number of generations by sampling the results at five different points and comparing the parent template to the grandparent template at each of these points (See Table 2).

TABLE II. FINAL RESULTS

Number of Generations	*Repair Template*	
	Parent	*Grandparent*
50 Generations	1098	1092
500 Generations	1028	960
5000 Generations	839	842
50000 Generations	837	816
500000 Generations	752	685

IV. CONCLUSION

Previous results [5] have illustrated that the grandparent is a superior repair template to the parent when used by GeneRepair in an ES. This paper goes on to show that the superiority of the grandparent repair template is invariant across many population and generation sizes. The population used for the experiments illustrated in this paper was set to 10 in comparison with a population of 100 in previously published results [5]. The final 260 experiments were analyzed at three different generation sizes. The results showed that at each of the sampled points the grandparent template outperformed the parent as a repair template. The results also showed that the grandparent template continuously produced superior results and so at each sampled point in the experiment it was a new best result produced by the grandparent being compared to the parent. The grandparent continually produced superior results as opposed to one superior outlier.

We then went on to examine the best result produced by the parent template in comparison to the best result produced by the grandparent template. The experiment was sampled at five different generation sizes and four out of five of these samples were positive that that the grandparent is a superior template. The one sample that was not positive was too weak to suggest that the parent template was superior. It is also to be expected with a stochastic method such as ES that a small proportion of the results will be unreliable due to the strong influence of outliers on the overall results.

The results presented in this paper strongly support the controversial findings of Lolle *et al* [3] where they show that in the biological environment of the *Arabidopsis thaliana* plant the grandparent template is successfully used as the repair template to correct invalid genetic information. This paper concludes that not only is it possible to use the grandparent as a template for repair, it is shown to be superior to using that of the parent regardless of population and generation size.

ACKNOWLEDGMENTS

The research of Amy FitzGerald carried out as part of her PhD is funded by IRCSET. The authors acknowledge the CS Dept of NUIM for access to the CREIG cluster to run the above.

REFERENCES

[1] Coello Coello, C., "Theoretcial and Numerical Constraint Handling Techniques in Evolutioanry Algorithms: A Survey", Comp. Methods in App. Mathematics and Engineering,Vol 191(11,12),pp.1245–1287 (2002)

[2] Kalyanmoy, D., "An Efficient Constraint Handling Method for Genetic Algorithms", Comp. Methods in Applied Mechanics & Engineering, Vol 186(2-4), pp. 311-338 (2000)

[3] Lolle, S.J., Victor, J.L., Young, J.M., Pruitt, R.E., "Genome-wide non-mendelian inheritance of extra-genomic information in Arabidopsis" Nature, vol.434, pp. 505–509, 2005

[4] Mitchell, G.G., O'Donoghue, D.P., Trenaman, A., "A New Operator for Efficient Evolutionary Solutions to the TSP" Applied Informatics vol. 0-88986-280-X, pp. 771-774, 2000.

[5] FitzGerald, A., O'Donoghue, D.P. *"Genetic Repair for Optimization under Constraints",* 10th Intl Conference on Parallel Problem Solving From Nature (PPSN2008),Dortmund,Germany,pp399-408, 2008.

[6] Mitchell, G.G., "Evolutionary computation applied to Combinatorial Optimization Problems", PhD Thesis, Dublin City University, Dublin Ireland, 2007

Intelligent Learning Systems Where are They Now?

George G. Mitchell, Colm P. Howlin

Research and Development Laboratory CCKF Ltd.,
Tallaght, Dublin 24, Ireland.
{george.mitchell, colm.howlin} @cckf-it.com

***Abstract*— This paper documents the work in progress in creating a new Intelligent Learning System. The paper introduces the issues of relevance when developing such systems. It examines briefly the state of the art followed by key approaches to addressing the major research questions in the field. We introduce the *Realise*^{it} *system* outlining the philosophy behind the system. and also the novel approach which we are taking to its implementation. Following this we explore the as yet unanswered research questions which must be addressed in order to develop what we believe is a truly intelligent learning system; one which can appropriately and intelligently guide learners (students) along their individual learning paths throughout their lives.**

***Keywords*— Intelligent Learning, ITS, Artificial Intelligence, Data Mining, Knowledge Management.**

I. INTRODUCTION

Over the last twenty years we have seen an explosion in the number of computer based training systems (also: VLE, LMS, LCMS, ITS and e-learning). With the internet we have a plethora of web based learning systems, all of which can utilise a variety of ways to present the material to students: text, graphics, audio and movies. The majority of educational institutions at third level have now implemented some form of managed learning environment comprising a backbone Virtual Learning Environment [1] of Moodle, Blackboard, Caroline, etc. These systems essentially provide knowledge management of the educational content, assessment and also a level of administrative assistance. To increase the attractiveness of these systems to learners, over the last few years these systems have embraced new educational technologies. The use of this technology has long been questioned, particularly around issues of relevance such as - to what extent do these new technologies assist the student in gaining the required knowledge?

A number of education technology researchers have investigated this issue, for example Clark and Mayer [2] have investigated an *interaction enhanced* e-Learning system (using natural language, first and second person pronouns for assessment and feedback). Their approach to using novel technology was benefit driven, not just because it was available but because following scientific investigation it was found to be superior to other (evaluated) approaches.

However, adding new technology to a learning system that does not contain any real intelligence raises many questions. Many of the aforementioned VLEs utilise homogeneous learning paths for all learners. These systems achieve an economical educational approach both in terms of finance and educational benefit to all students. More flexible approaches which adapt to individual learners' needs have been attempted. One of the primary research areas is Intelligent Learning Systems [3, 4] (sometimes referred to as Intelligent Tutoring Systems). This is an area of AI research which fundamentally highlights where cognitive interaction of man and machine are critical for the best performance of both systems.
Some researchers have suggested that further work is required to improve issues around homogenised e-Learning systems together with poor support and feedback for the individual learners.

II. INTELLIGENT TUTORING SYSTEM

An Intelligent Tutoring System (ITS) as defined by the AAAI [5] is "educational software containing an artificial intelligence component. The software tracks students' work, tailoring feedback and hints along the way. By collecting information on a particular student's performance, the software can make inferences about strengths and weaknesses, and can suggest additional work." The AI element is the key component to individualised learning systems. Over the last ten years a number of different systems have been developed which provide intelligent tutoring. These systems, however, have developed along very narrow lines in terms of subject area and educational objectives. An example is algebra for first year university Mathematics students. Tom Murray a significant researcher and author in the ITS and adaptive learning systems field, was critical that the ITS field lacked vision [6]. In 1999 he summarised the focus of research in ITS as applying to: particular subject domains (like algebra or calculus), learning environments which embodied either an instructional metaphor or a traditional curriculum metaphor only and those which were pedagogy or performance oriented solely. His 1999 summary of the state of the art sadly remains largely unchanged today. Murray identified a number of areas which he felt were important for future research in order to move the field forward. He noted that these were neglected in the work up to 1999, and today they remain largely uninvestigated.

One central element of research which has been identified as requiring significant exploration is the human computer interaction in learning systems. How information is presented to the learner is a complex problem, requiring the direct input from a number of interdisciplinary specialists such as: HCI, Educationalists (both pedagogical and andrologogical), Cognitive Science and Software Engineering.

III. Man & Machine

Understanding the needs of both man & machine is critical when creating an effective intelligent and adaptive learning system. It is *relatively* straightforward to assess the state of knowledge in an artificial system. However, it is somewhat more *complex* to assess the current state of knowledge in a human learner. From a human psychology perspective, through profiling and observation of the individual, an estimation of the knowledge profile of the user is possible. The degree of belief one places in this is influenced by a number of correlated factors including: the level of profiling, and the techniques used in this profiling [7]. Effective user profiling is closely associated with the development of a highly coupled human computer interaction [8]. Many studies have identified differing profiling techniques (e.g. learning style profiles [9, 10, 11]), all of which can profile particular elements of the user, using questions ranging from 10 in number to 1000 or more. New approaches that have been used to successfully assess the interaction of users and systems, include those which combine traditional profiling with theories of *Cognitive Load* [12] on a student as he/she interacts with the system. Measuring passive interactions with the systems through various techniques such as head and eye tracking, or EEG, can assist in improving our understanding of the HCI process and what most suitably works with individual learners [13].

IV. Realise[it] Intelligent Learning Systems

The Realiseit Intelligent Learning System is currently a work in progress, (see Figure 1, which depicts a typical view in the system). A number of key modules have been completed including the Artificial Intelligence Engine (AIE), see Figure 2. The AIE is tasked with providing the differing system modules with the specific intelligence to dynamically modify and develop each student's learning path.

The approach builds upon the current state of knowledge concerning expert systems. This is achieved through the use of *evidence based decision (EBD)* making. Our EBD approach utilises proactive and passive assessments coupled with profiling to create an evidence profile which can feed into an innovative blend of allied algorithms such as: Bayesian Reasoning [14], Simulated Annealing [15], Information Theory [16], Graph Theory [17], Fuzzy Logic [18], Classification Trees [19], Nonlinear and Ordinal regression techniques [20].

The Realise[it] system attempts to embrace the issues raised by Murray. The learning system is enhanced with a blend of methodological approaches including instructional metaphor, traditional curriculum metaphors, pedagogy-oriented and performance oriented metaphors, all united in a single environment. This approach facilitates the larger objective of enabling the system to be applicable across a variety of differing subject areas such as Math, Science, Languages, Business, History and Social Sciences.

Figure 1 Screenshot of Realise-it Intelligent Learning System

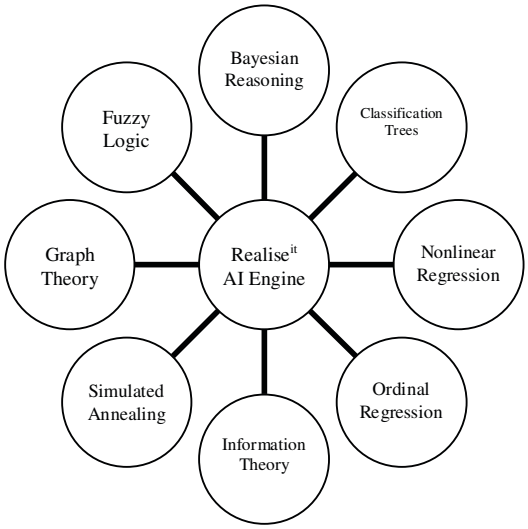

Figure 2 Artificial Intelligence Engine

The primary goals of the Realise[it] project that have been achieved so far provide the following core design features:

- Multi disciplinary learning approach. The system provides a single environment for the student to learn a broad range of subjects such as Languages, Math, Science and History. A learning objective for one individual may include learning items drawn from different subjects. This novel approach is as a result of trials which have shown that individual student learning paths typically require skills drawn from a broad range of disciplines.

- Individual dynamic learning paths. Each individual learner has a dynamic learning path for their particular learning objective. The learning path is integral to the navigation through the educational material and is consulted (and possibly modified) continuously during a learning session. This technique is one of our approaches to ensure that the user can always determine "where am I?" in relation to their progress towards intended learning objectives.

- Focus on individual learning and appropriate learning designs. The system is designed to reduce the technology noise that is often present in eLearning applications. This is particularly acute when significant amounts of valuable "learning time" are devoted to solving technology problems, instead of addressing learning problems.

- Flexible and adaptable learning environments. The system has been designed to embrace Cognitive load theory [21] and its impact upon Learning Design, creating a modern flexible learning system. Using the Learning Design approaches and standards of IMS Global (IMS-LD) [22] as a foundation, our system is self-intelligent. This provides intelligent flexibility to an individual learner's desired pedagogical (or andrologogical) approach.

Trials of the system are currently underway and it is expected that further publications will document the results of these trial when they have been completed (expected later in 2009).

V. Future Work

At present we have identified two key areas of further research which we expect will significantly enhance the understanding of intelligent learning systems. Initially we will focus on how intelligent learning systems can become even more intelligent and how they can best be utilised in an efficient *man and machine* manner. To achieve this a more full understanding of the profile of both the learner and the content is required. We will focus on:

- Behavioural assessment & modelling
- Cognitive assessment & modelling
- Learning style assessment & modelling

This will enhance our approach to developing a suite of tools to accurately instruct and assess the individual learner across a range of differing specialist fields, subject areas and multi disciplinary learning path objectives. This will ensure that the system continuously adapts (a) assessment methods, (b) content delivery vehicles and (c) the learning paths for a wider range of subjects and individual learners.

A second key area of work is *how* to fully embrace interoperability and usage of differing educational content. Content presentation and navigation is tightly coupled with the advantages of technology drive education and also cognitive loading. Improper usage of technology may purely divert attention away from the learning objective. Equally it is likely that cognitive profiling may indicate where novel usage of new technology may be more effective, for example with special case learners such as those who have an intellectual disorder or an attention deficit disorder.

It is the marrying of cognitive psychological techniques and artificial intelligence techniques that, we suggest, will bring about the next generation of intelligent learning systems.

VI. Summary

In this paper we have briefly explored the work in progress in creating the Realise[it] Intelligent Learning System. The paper introduced the issues of relevance in developing such a system. It examined briefly the state of the art followed by key approaches to addressing the major research questions in the field. We introduced the Realise[it] system outlining the philosophy behind the system and also the novel approach which we are taking to its implementation. Following this we identified the outstanding research questions which must be addressed to ensure a truly intelligent learning system which can appropriately guide learners along their individual learning paths.

REFERENCES:

[1] Anderson, T. (Ed.) (2009), Theory and Practice of Online Learning, 2nd Edition, Athabasca University Press, Edmonton, Canada.

[2] Clark, R.C., Mayer, R.E. (2003), E-Learning and the Science of Instruction: Proven Guidelines for Consumers and Designers of Multimedia Learning, Jossey-Bass/Pfeiffer, San Francisco, CA, USA.

[3] Weber, G. and Specht, M. (1997) User modeling and adaptive navigation support in WWW-based tutoring systems, Proc. 6th International Conference on User Modeling, pp.289–300.

[4] Brusilovsky, P., Karagiannidis, C., and Sampson, D. (2004), Layered Evaluation of Adaptive Learning Systems. International Journal of Continuing Engineering Education and Lifelong Learning 14 (4/5) 402 – 421.

[5] http://www.aaai.org/AITopics/pmwiki/pmwiki.php/AITopics/IntelligentTutoringSystems

[6] Murray, T., Authoring Intelligent Tutoring Systems: An Analysis of the State of the Art, International Journal of Artificial Intelligence in Education (1999), 10, 98-129.

[7] Gasparetti, F., & Micarelli, A., (2005) User Profile Generation Based on a Memory Retrieval Theory, Proceedings of the 1st International Workshop on Web Personalization, Recommender Systems and Intelligent User Interfaces (WPRSIUI 2005), pp 3-7.

[8] Gray, W. D., Sims, C. R. & Schoelles, M. (2005). Cognitive Metrics Profiling. In. 49th Annual Conference of the Human Factors and Ergonomics Society. Santa Monica, CA: Human Factors and Ergonomics Society.

[9] Zhang, L. (2003). Does the big five predict learning approaches? Personality and Individual Differences, 34, pp1431–1445.

[10] Bidjerano, T., & Yun Daia, D., (2007). The relationship between the big-five model of personality and self-regulated learning strategies. Learning and Individual Differences 17(1), pp 69-81.

[11] T. Chamorro-Premuzic, A. Furnham (2008). Personality, intelligence and approaches to learning as predictors of academic performance. Personality and Individual Differences 44, pp1596–1603.

[12] Clark, R. C., Nguyen, F., & Sweller, J. (2006). Efficiency in learning: Evidence-based guidelines to manage cognitive load. San Francisco: Pfeiffer.

[13] Salmerón, L., Baccino, T., Cañas, J.J., How Prior Knowledge and Text Coherence Affect Eye Fixations in Hypertext Overviews, The 28th Annual Conference of the Cognitive Science Society (CogSci 2006) pp715-719.

[14] Gerenzer G., Hoffrage U., (1995) How to improve Bayesian reasoning without instruction: frequency formats. Psychological Review 102, pp. 684-704.

[15] S. Kirkpatrick, S., Gelatt, C.D., Vecchi, M.P., (1983) Optimization by Simulated Annealing, Science, New Series, Vol. 220, No. 4598, pp. 671-680.

[16] MacKay,D.J.C., (2002) Information Theory, Inference & Learning Algorithms, Cambridge University Press, New York, NY.

[17] West, D.B., (2001). Introduction to Graph Theory, second ed. Prentice-Hall, Upper Saddle River, NJ.

[18] Zadeh, L.A., (1988) Fuzzy Logic, Computer, v.21 n.4, p.83-93.

[19] Rokach, L., Maimon, O., (2008) Data Mining with Decision Trees Theory and Applications, Series of Machine Perception and Artificial Intelligence Vol 69, World Scientific Publishing, Singapore.

[20] Harrell, F.E., (2001) Regression Modeling Strategies with Applications to Linear Models, Logistic Regression, and Survival Analysis, Springer Series in Statistics.

[21] Dror, I. E., Schmitz-Williams, I.C., & Smith, W. (2005). Older adults use mental representations that reduce cognitive load: Mental rotation utilises holistic representations and processing. Experimental Aging Research, 31(4) 409-420.

[22] IMS Learning Design specification, http://www.imsglobal.org/learningdesign/ (last accessed 29 May 2009).

AN IMPROVED HAPTIC ALGORITHM FOR VIRTUAL BONE SURGERY

Denis Stack, Joe Connell

Cork Institute of Technology

ABSTRACT

With the rapid development of virtual environments as part of surgical training in bone surgery, the specific challenge of feedback to the haptic device controlling the virtual drill continues to receive attention. This paper reviews the evolution of relevant haptic algorithms and measures the relative performance of those which are proxy and non-proxy based using real force data. An improved proxy-based feedback algorithm is also presented for use in a temporal bone surgery simulator. This new algorithm uses a spherical proxy which prevents the dynamic object, drill burr, from passing through gaps smaller than its own size.

1. INTRODUCTION

Traditionally, the milling procedure for temporal bone surgery has been taught to students through demonstration and practice on cadaveric specimens. Variations in the supply of these specimens coupled with technical advancements in visualisation have contributed to the development of virtual temporal bone surgery simulators. Examples include [1], [2], [3] and [4]. Simulators can also offer the facility of integrating patient-specific data. This means surgeons can perform a dry run prior to actual surgery. Central to a simulator's effectiveness is the handheld or haptic device which takes the place of the surgical drill. It is imperative that the user experiences through haptic feedback forces consistent with those experienced during a real drilling procedure. This is one of the bigger challenges in this area.

Typically, in a bone milling simulator, the underlying data derives from CT scans and is rendered on screen in 3D. Forces must be calculated based on the interaction between the virtual drilling tool and the voxels representing bone. This is in contrast to traditional haptic methods which calculated forces based on explicit surfaces.

The approach to calculating these forces can be broadly divided into two main categories: proxy-based and non proxy-based. Typically, proxy-based algorithms calculate the output based on a spring-damper force between the proxy position and the user effector position, [2], [5] and [6]. Non proxy-based algorithms calculate haptic forces based on the intersection between virtual drill burr sphere and voxels, e.g. [3] uses a system of virtual springs, while [1] and [7] use algorithms based on sample points on the drill tool.

In this paper, an improved proxy-based haptic algorithm is presented which maintains proxy-surface contact while preventing the proxy becoming immersed within the volume. It uses a new, more complex method of force calculation which achieves greater accuracy when compared with real-world force data. A second, non-proxy based algorithm similar to [1] is also presented, and the online haptic data repository discussed in [1] is used to evaluate both algorithms.

The paper is organised as follows: Section 2 discusses the evolution of haptic algorithms relevant to bone surgery, Section 3 describes the proposed proxy-based and non proxy-based algorithms in detail, Section 4 presents results and performance evaluation and Section 5 outlines future work.

2. EVOLUTION OF RELEVANT ALGORITHMS

McNeely et al [8] used a voxmap-point shell algorithm to provide haptic feedback, in which the dynamic object is represented by surface sample points. In each haptic frame all points are checked for intersection with voxels from the object being explored. If a point is found to be in contact with the object then a normal is traced towards the centre of the dynamic object. All normals are then summed and scaled to give an overall force vector.

Bryan et al [3] projected virtual springs outwards from the surface of the drill burr sphere. These form a force field which strives to maintain a minimum separation distance between burr and bone. The limitation here is that only bone surface information is used. Volumetric information is not used which rules out the possibility of varying forces according to bone density.

Petersik et al [7] developed a haptic interaction algorithm based on 26 pre-computed sample points on a spherical drill surface. A drawback with non proxy-based algorithms such as this is that a sufficiently forceful push by the user can cause the virtual burr to become completely immersed in the bone. To counteract this a basic proxy method was implemented for use only when immersion occured.

Lundin et al [5] developed a new, point-based, proxy algorithm for direct volume haptics. Material properties such

as stiffness, friction and penetrability were included. As explicit surfaces do not exist in a volumetric representation of an object, a local surface was extracted in each haptic frame.

Vidholm et al [6] presented a proxy-based algorithm based on a combination of [5] and [7]. A spherical proxy prevents the burr passing through small holes in the volume. However, when exploring complex surfaces, the spherical proxy can become completely immersed within the volume causing the algorithm to fail.

Eriksson et al [2] modified an algorithm based on that in [6] to address the immersion problem. Using an iterative approach to keep the proxy in contact with the surface of the object, and thus never completely immersed, the proxy's centre is maintained on the surface of the volume. The disadvantage is that the algorithm behaves as if the proxy were a point and therefore the haptic probe can pass through tiny gaps in a volume.

Morris et al [1] present a method similar to [7] except that the spherical drill burr is discretized using evenly-spaced volume sample points rather than surface samples only.

The algorithms discussed above can be divided into two categories: proxy-based, [2] [5], [6] , and non-proxy based, [1], [3], [7]. The three non proxy-based algorithms were developed using a Phantom Premium haptic device [9] which has improved stiffness over the lower-end Phantom Omni device [9].

Until Morris et al [1], there were no concrete standardized methods for evaluating haptic algorithms. Now, an online data repository allows haptic algorithm developers to compare output with real-world data collected from a force probe. This proves extremely useful for comparing the relative performance of algorithms and it is used here to compare the non proxy-based algorithm in [1] with the proposed improved proxy-based algorithm. The algorithm in [1] represents the most recent development in the non proxy-based class of haptic bone surgery algorithms.

3. HAPTIC ALGORITHMS

This section describes the two haptic algorithms chosen for implementation and performance evaluation using a Phantom Omni.

3.1. Non Proxy-Based Algorithm

In each haptic frame, bone voxels which are found to intersect with the drill burr sphere contribute individual unit forces which act to push the drill burr out of the volume. The unit forces are then summed to yield an overall force vector which is then scaled down to prevent instability caused by a large initial contact force. The bone voxels were used directly to compute the force, which with adequate voxel resolution is sufficient.

3.2. Improved Proxy-Based Algorithm

Similar to [2] and [6], this algorithm uses a spherical proxy which remains in contact with the bone surface as the user effector penetrates the volume. A local surface is generated in each haptic frame, to which the proxy is bound, and thus the proxy can follow complex surfaces.

In [2], [5] and [6], the force sent to the haptic device is calculated using the well-known Hooke's law $F = -kx$ for a virtual spring connecting the user position to the proxy position, where x is user penetration distance and k is a spring constant. This is in contrast with the non proxy-based algorithm discussed in Section 3.1, in which output force varies linearly with penetration *volume* into the immersed portion of the virtual burr. It was found by comparison with real-world force data that this volume approach provided more accurate results, as shown in Section 4. In this improved proxy-based algorithm, instead of using Hooke's law, force is varied as if there were a sphere penetrating the volume by a distance equal to that between the proxy and user effector thus mimicking the non proxy-based algorithm.

For a sphere intersecting a planar surface, the volume v of the intersecting sector is

$$v = \frac{\pi}{3}h^2(3r - h) \tag{1}$$

where r is the radius of the sphere and h is the penetration distance into the volume. Initially, output force was varied according to Equation 1 and scaled down by a constant, a. This constant may be varied to adjust the stiffness of a surface. The radius r of the virtual sphere should be chosen to be more than a few voxels. A larger r will simply scale up the resultant force linearly.

To remove the simplification of a local surface being planar, the output of Equation 1 must again be scaled by the ratio

$$b = \frac{intersectingvolume}{sectorvolume} \tag{2}$$

where $intersectingvolume$ is the total volume of voxels intersecting the proxy sphere, and $sectorvolume$ is the volume of the proxy sphere which would have intersected the object volume had the surface been planar. The total output force in a given haptic frame is thus

$$F = a * b * \frac{\pi}{3}h^2(3r - h) \tag{3}$$

When the user effector is in free space, proxy position and user position are identical. When contact with the bone is detected, the proxy position is then set and constrained to the surface of the bone while the user effector penetrates the volume. Local surface gradients are calculated by checking a spherical volume around the proxy centre position equal to the virtual drill burr volume. Each bone voxel found to intersect the proxy sphere contributes a unit length vector

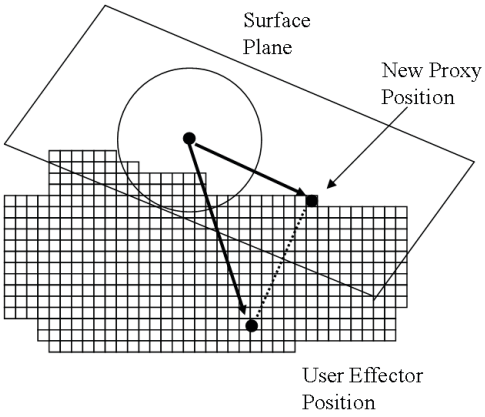

Fig. 1. Proxy Movement

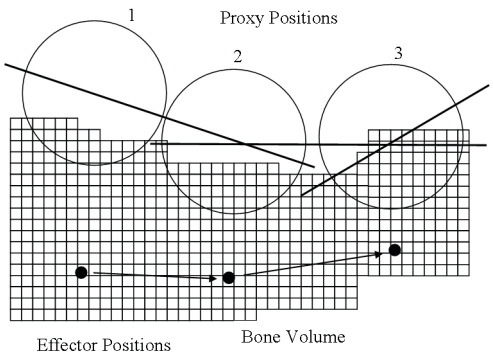

Fig. 2. Proxy Immersion

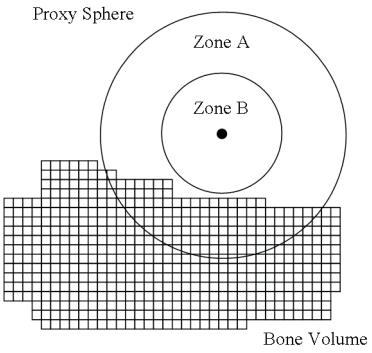

Fig. 3. Proxy Zoning

which is traced towards the centre of the proxy. These unit vectors are summed and the result normalized to give the local gradient vector.

In each haptic frame, the proxy moves along the surface plane by an amount equal to the projection of the vector between proxy and effector onto the surface plane. This is illustrated in Figure 1. Since a new proxy surface is constructed in each frame, deformation of bone does not adversely affect the algorithm.

When exploring concave surfaces using this algorithm, the proxy will inevitably become immersed within the bone volume thus causing algorithm failure. As haptic frames are executed, the increasing number of proxy contact voxels can cause the bone to eventually consume the proxy, as illustrated in Figure 2. This problem is also identified in [2]. It is also possible that the proxy may 'veer off' a convex surface thus losing contact with all voxels and resulting in failure to calculate a local surface gradient.

To prevent the proxy from becoming immersed within the volume, two zones are defined within the proxy sphere, as illustrated in Figure 3. While contact with some surface voxels is required to calculate a surface gradient, deep immersion within the bone must be avoided. Zone A in Figure 3 is the permitted zone for contact voxels; zone B is the prohibited zone. If the proxy reaches a particular position which results in bone voxels in zone B then the algorithm automatically adjusts the proxy position to empty zone B of voxels. Conversely, if exploring a convex surface, the proxy may veer off the surface thus losing contact with all bone voxels, even though the user effector is still inside the volume. To prevent this, the proxy position is adjusted in each frame to keep Zone B close to bone voxels so that there will always be bone voxels in Zone A.

Surface friction is implemented in a manner similar to [5].

4. EVALUATION AND RESULTS

Both algorithms were implemented on a temporal bone surgery simulator using SensAble's Open Haptics toolkit [10] and a Phantom Omni device. This toolkit facilitates low-level communication by directly sending forces and reading device position. Simulator visualization used a combination of VTK and OpenGL. The simulation was run in Windows XP on Intel Core Duo E8600 CPUs running at 3.33 GHz Windows XP.

The online haptic data repository in [1] was used to compare both haptic algorithms' output with real-world force data. For each haptic frame, a root-mean-squared method was used for accuracy evaluation. The overall normalized RMS error e is given as

$$e = \frac{\frac{1}{N}\sum_{i=1}^{N}|Fr_i - Fa_i|}{|Fr_i max|} \tag{4}$$

where N is the number of force trajectory samples, Fr_i is the real force at sample i, Fa_i is the algorithm's output force at sample i and $Fr_i max$ is the magnitude of the maximum real output force.

Table 1. Algorithms' Performance

Algorithm	Improved Proxy	Hooke Proxy	Non Proxy
Normalized RMS Error (%)	9.96	13.08	9.90
Frame Time (ms)	0.376	0.374	0.135

Table 1 shows the results obtained for an input trajectory of 4,000 samples. The accuracy of the improved proxy and non-proxy based algorithms is comparable. Average execution times per haptic frame are also shown.

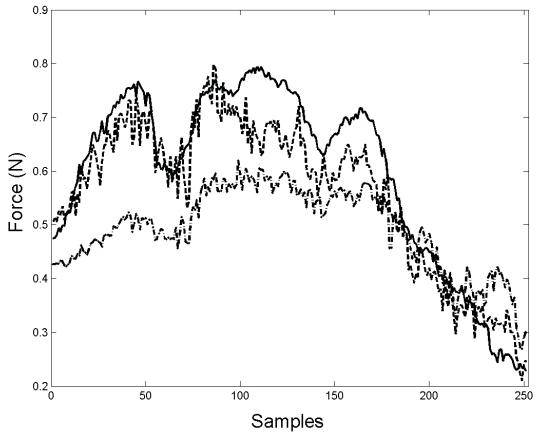

Fig. 4. Real World Forces (solid) vs. Non-Linear Force Calculation (dashed) vs. Hooke's Law Force Calculation (dash-dot)

5. CONCLUSION AND FUTURE WORK

An improved proxy-based and a non-proxy based algorithm were implemented and their performance was measured against real-world force data with both achieving comparable accuracy. The improved proxy-based haptic algorithm offers the potential advantages of controlling material parameters such as friction, stiffness, viscosity and penetrability as in [5]. These properties are difficult to implement without a proxy. When the non proxy-based algorithm was used with the Phantom Omni, the maximum bone stiffness which could be achieved without instability was poor, even when employing averaging methods such as in [7] and multi-gain methods such as in [1]. The improved proxy-based algorithm achieves greater stiffness without instability. Another advantage of using a proxy-based algorithm is that the pop-through problem of non proxy-based algorithm is eliminated. Future work will examine the effect of surface friction on the accuracy of the proposed proxy-based algorithm. Also, while the haptic evaluation method due to Morris et al is useful for evaluating haptic algorithms exploring the surface of an object, a method for comparing the haptic forces involved when drilling bone to real-world data is still needed.

6. REFERENCES

[1] Morris, D.: Haptics and Physical Simulation for Bone Surgery. PhD Thesis, Stanford University. (2006)

[2] Eriksson, M.: Haptic and Visual Simulation of a Material Cutting Process. Licentiate Thesis, TRITA-STH Report 2006:03 ISSN 1653-3836 ISRN/STH/–06:3–SE (2006)

[3] Bryan, J.: A Virtual Temporal Bone Dissection Simulator. Master's Thesis, Ohio State University (2001)

[4] Agus, M., Giachetti, A., Gobbetti, E., Zanetti, G., Zorcolo, A.: A Multiprocessor Decoupled System for the Simulation of Temporal Bone Surgery. Comput. Visual Sci. 5: 3543 (2002)

[5] Lundin, K., Ynnerman, A., Gudmundsson, B.: Proxy-based Haptic Feedback from Volumetric Density Data. Proc. Eurohaptics, pp. 104-109. (2002)

[6] Vidholm, E.: Visualization and haptics for interactive medical image analysis. Digital Comprehensive Summaries of Uppsala Dissertations from the Faculty of Science and Technology 386. 83 pp. Uppsala. ISBN 978-91-554-7067-8. (2008)

[7] Petersik, A., Pfessler, B., Tiede, U., Hoehne, K.H., Leuwer, R.: Haptic Volume Interaction with Anatomic Models at Sub-Voxel Resolution. Proc. 10th Symp. On Haptic Interfaces For Virtual Envir. and Teleoperator Systs. 0-7695-1489-8/02 (2002)

[8] McNeely, W. A., Puterbaugh, K. D., Troy, J. J.: Six Degree-of-Freedom Haptic Rendering Using Voxel Sampling. Proc. 26th Conference on Computer Graphics and Interactive Techniques pp. 401 - 408 (1999)

[9] SensAble Technologies, http://www.sensable.com/products-haptic-devices.htm

[10] OpenHaptics, http://www.sensable.com/openhaptics-academic-edition-faqs.htm

Corpus Design Techniques for Irish Speech Synthesis

Amelia C. Kelly, Harald Berthelsen, Nick Campbell, Ailbhe Ní Chasaide, Christer Gobl
Phonetics and Speech Laboratory, SLSCS, Trinity College Dublin, Ireland
kellya16@tcd.ie, berthelh@tcd.ie, nick@tcd.ie, anichsid@tcd.ie, cegobl@tcd.ie

***Abstract*—Unit selection is a data-driven approach to speech synthesis that concatenates pieces of recorded speech from a large database in order to create novel sentences. Many corpora are available in the English language, including the Arctic database [1], which allows a user to create small, reliable speech synthesisers using only a small set of recorded sentences. Such resources for minority languages are scarce however, despite their increasing importance for the survival of such languages. This paper describes the current research in creating efficient Irish language corpora for speech synthesis. Corpus design techniques are discussed, in particular, two methods of data reduction that are applied to an aligned spoken corpus of Irish in order to create smaller, more efficient speech corpora.**

Index Terms: speech synthesis, corpus design, Arctic, Irish

I. Introduction

The unit selection method of speech synthesis is a data-driven, concatenative technique that draws on a large database of recorded speech, from which it can select speech segments and join them together to create novel utterances. The content of the speech database, or corpus, is vital to the performance of the synthesiser on which it is built. Naturally it is impossible to create a corpus that contains every speech sound in the language in every context in which it can be spoken, however the use of an overly large corpus will significantly slow down the performance of the synthesiser. As a result there exists a trade off between the quality and the performance of the corpus with respect to size. The Arctic database for English is an example of a corpus has been designed to address this trade-off, and is intended to be as compact as possible, while still containing the greatest diversity of linguistic units in a variety of contexts. The benefit of such a corpus is that it is freely available for download and can be used with the open-source Festival Speech Synthesis System [2] to create a personal speech synthesiser.

Despite the advances in speech technology, resources remain scarce for endangered minority languages that have experienced a decline in the number of native speakers. Irish is an example of such a language that has fallen further behind in technology development due to the lack of resources available and to the lack of commercial incentive. Since speech technology has a crucial role to play in education and accessibility, speakers of minority languages are becoming particularly disadvantaged [3].

This study aims to address the scarcity of resources for the Irish language by creating an Irish speech database that, like the Arctic database, is recorded by a number of speakers and freely available for download. This short paper outlines the approach adopted in creating an Irish language speech database and discusses two techniques[1] for designing the corpus and determining its content. The process begins with a large amount of annotated sentences, of which a subset is selected based on criteria that would deem certain sentences more suitable than others for inclusion in the final corpus. The first technique, as used to create the Arctic database, employs a greedy algorithm [4] to select only the most phonetically diverse sentences for the corpus, so that the greatest number of contextually dependent speech units are found in the smallest set of sentences. The second is a novel technique which effectively removes over-represented and therefore redundant units from the corpus, by determining which units get selected more by the unit selection synthesiser, and removing all similar ones that tend not to be chosen. Both methods result in a smaller subset of sentences being chosen for the corpus. While the first method is anticipated to select only linguistically diverse sentences, the second method will contain the best quality examples. Since the techniques will be carried out on a recorded, annotated corpus, the better method can be determined by comparing the coverage of each database and by evaluating the synthetic speech output from synthesisers based on the corpora. The techniques can then be used to reduce large amounts of data to a smaller subset before recording. The creation of small, efficient spoken Irish corpora will contribute greatly to the growing demand for minority language speech technology, in particular to the creation of Irish synthesisers.

II. Approach

Creating a corpus involves (i) selecting source material, (ii) analysing the corpus to determine unit coverage statistics, (iii) selecting the most phonetically varied sentences from the source material, and (iv) recording a speaker, [5].

A. Gathering and analysing source material

Resesarch by the Phonetics and Speech Laboratory in Trinity College Dublin has resulted in the creation of the first Irish unit selection speech synthesiser, available to use at *http://www.abair.ie*. The corpus of roughly 9,000 sentences used to create this synthetic voice draws from internet news sites and out-of-copyright works of fiction and is also used as the source text for testing the two data reduction techniques to

[1] Currently being developed by Harald Berthelsen and Amelia Kelly

create small corpus subsets. Most of the text is specific to the Gaoth Dobhair dialect of Irish, but in order to create a more adaptable speech database, a core of dialect-neutral text should be used as the basis set, and corpora of other Irish dialects can be created by adding dialect-specific texts to the basis set. The source material can then be analysed to get statistics on the frequency of occurrence of linguistic units in order to compare the linguistic unit coverage of the selected subsets.

B. Sentence selection techniques

1) The Greedy Algorithm: The greedy algorithm is an iterative technique that allows the creation of smaller corpora by choosing a subset of sentences from the basis set so that the largest number of linguistic units in context are represented in the smallest number of sentences. This is achieved by first choosing a unit size by which to define linguistic unit coverage. In this study, the base unit originally chosen was the diphone, that is the measurement from the midpoint of one phoneme to the midpoint of the adjacent one. At this time, the criteria for whether a sentence gets included in the subset depends on how phonetically varied the sentence is, given by the distribution of phones, diphones and triphones within the sentence. For example the word "cat" contains three phones (/k/, /ae/ and /t/), four diphones (the transition from silence the beginning of the word is given by /#-k/, followed by /k-ae/, /ae-t/, and the transition back to silence /t-#/) and three triphones (/#-k-ae/, /k-ae-t/ and /ae-t-#/). The algorithm will iterate through the sentences and choose the one with the most number of unique linguistic units, removing it from the basis set to be stored as the first sentence of the corpus subset. The algorithm will repeat this until a specified number of sentences have been collected. The smallest corpus that achieves maximum occurrence of these features is said to be the one with the best linguistic unit coverage.

2) The Waste Disposal Method: The waste disposal method does not focus on the linguistic variability within a sentence, but instead removes sentences from the corpus if the units in the sentence are satisfactorily represented elsewhere in the database. A sentence can be deemed redundant, and therefore removed from the basis set, if it can be synthesised using units from the rest of the corpus and the synthesised version is shown to be acoustically similar to the original recording. This can be achieved by removing a sentence from the corpus, and then attempting to synthesise that sentence using only the sentences that remain in the database. The synthesised version can be compared with the original recording using acoustic distance measures (eg. Euclidean distance between Mel-frequency cepstral coefficients (MFCC) vectors [6]) and perceptual tests (like those conducted for the Blizzard Challenge[2]). If they are similar, it may then be concluded that the sentence can be removed from the database without degrading the quality of the synthesiser.

C. Experiment Design

The data reduction techniques outlined above are performed on the basis set of 9000 Irish sentences. The greedy algorithm technique is implemented to create corpora that vary in size by increments of one hour, resulting in the creation of 8 corpora. The linguistic coverage is then ascertained for each corpus subset in order to show how the coverage increases with increasing corpus size. The most efficient corpus will be the smallest sized one that has the maximum amount of coverage. For the waste disposal method, just one corpus needs to be created that has minimum unit redundancy. The unit coverage for this corpus can then be compared with that chosen from the greedy algorithm technique. Further comparison of the methods can be carried out by recording a speaker reading the prompt sets for each corpus and creating synthesisers out of the resulting recorded speech databases. Evaluating the synthesisers by designing perception test will provide further information as to the merit of each data reduction technique.

[2]The Blizzard Challenge, http://festvox.org/blizzard/

III. Conclusion

The main focus of this research is to provide speech technology resources for the Irish language. The creation of small freely-available corpora will allow the creation of efficient and intelligible speech synthesisers, which are indispensable for use as teaching and learning resources and accessibility tools for the visually and vocally disabled. The size of the speech database used for synthesis will determine its quality and speed. In order to determine the most suitable database in terms of size and content, two data reduction techniques are described in which sentences can be selected from a large body of data to form small corpora of maximum linguistic coverage. Further comparisons can be made between the methods by evaluating the quality of synthetic voices based on the corpora. Further challenges involved in distributing the recorded speech databases are selecting and recording a speaker for each major dialect of Irish. By gathering a core set of what can essentially be considered dialect-neutral material, supplementing it with dialect-specific material, and applying the data reduction techniques described above, we hope to create freely-available Irish corpora, in keeping with the growing need for minority language speech technology resources.

IV. Acknowledgements

The CABÓGAÍ II project is funded by Foras na Gaeilge.

References

[1] Kominek, J. and Black, A. W., "CMU ARCTIC databases for speech synthesis", Language Technologies Institute, Carnegie Mellon University, Pittsburgh, PA, 2003.

[2] Black, A. W., Taylor, P. and Caley, R., "The Festival speech synthesis system", http://festvox.org/festival, 1998.

[3] Ní Chasaide, A., Wogan, J., Ó Raghallaigh, B., Ní Bhriain, Á., Zoerner, E., Berthelsen, H. and Gobl, C., "Speech Technology for Minority Languages: the Case of Irish (Gaelic)", Interspeech, Pittsburgh, PA, 2006.

[4] van Santen, J. P. H. and Buchsbaum, A. L., "Methods for Optimal Text Selection", Eurospeech, Greece, 1997.

[5] Ni, J., Hirai, T., Kawai, H., Toda, T., Tokuda, K., Tsuzaki, M., Sakai, S., Maia, R. and Nakamura, S., "ATRECSS – ATR English Speech Corpus for Speech Synthesis", The Blizzard Challenge 2007 – Bonn, Germany, August 25, 2007.

[6] Vepa, J., King, S. and Taylor, P., "Objective Distance Measures for Spectral Discontinuities in Concatenative Speech Synthesis", Proceedings of the IEEE workshop on Speech Synthesis, 2002.

Sponsored by

NUI MAYNOOTH
Ollscoil na hÉireann Má Nuad

sfi
science foundation ireland
fondúireacht eolaíochta éireann

Microsoft

Maynooth Campus
Conference & Accommodation

Fáilte Ireland
National Tourism Development Authority

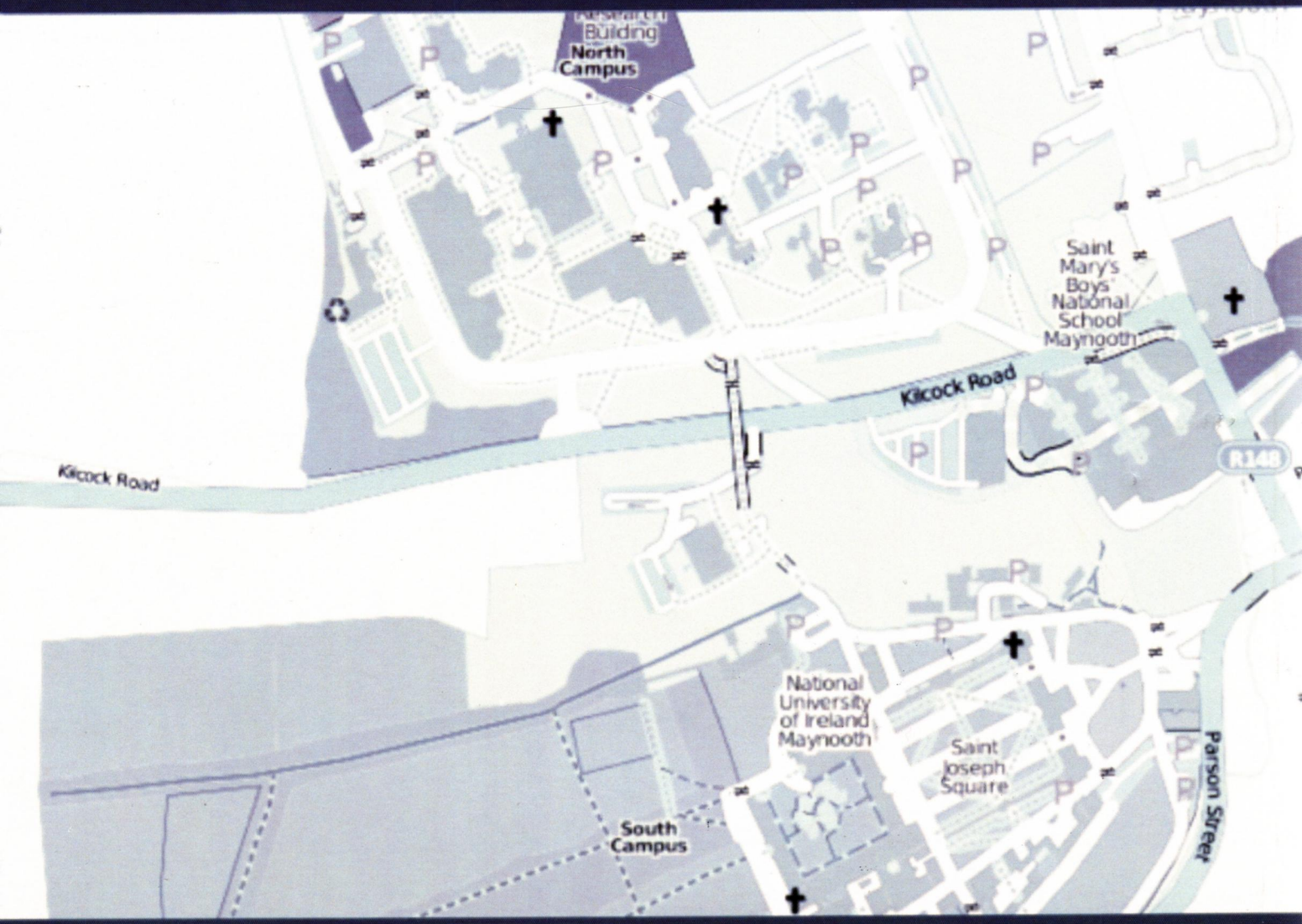

ISBN 978 0 901519 67 2